europhysics
conference
abstracts

16 th European Conference on

Controlled Fusion and Plasma Physics

Venice, March 13-17, 1989

Editors: S.Segre, H. Knoepfel, E. Sindoni

Contributed Papers
Part II

lished by: European Physical Society
s Editor: Prof. K. Bethge, Frankfurt/M.
aging Editor: G. Thomas, Geneva

VOLUME
13 B
Part II

XVI FUSION VENEZIA 1989

S. Giorgio Maggiore Island

A4
B
C1
C2

16th European Conference on

Controlled Fusion and Plasma Physics

Venice, March 13-17, 1989

Editors: S. Segre, H. Knoepfel, E. Sindoni

Contributed Papers

Part II

EUROPHYSICS CONFERENCE ABSTRACTS is published by the
European Physical Society,

PREFACE

The 16th European Conference on Controlled Fusion and Plasma Physics was held in Venice, Italy, from 13th to 17th March 1989 by the Plasma Physics Division of the European Physical Society (EPS).

The Conference has been organized under the sponsorship of the Italian National Research Council (CNR), the Italian Commission for Nuclear and Alternative Energy Sources (ENEA) and the International School of Plasma Physics "Piero Caldirola" (ISPP).

The programme, format and schedule of the Conference were determined by the International Programme Committee which was appointed by the Plasma Physics Division of the EPS.

The programme included 17 invited lectures, 23 orally presented contributed papers and more than 450 contributed papers presented in poster sessions.

This 4-volume publication contains all accepted contributed papers received in due time by the Organizers. It is published in the Europhysics Conference Abstracts Series. The 4-page extended abstracts were reproduced photographically using the camera-ready manuscripts submitted by the authors. The invited papers will be published in a special issue of the journal "Plasma Physics and Controlled Fusion" and sent free of charge to each registered participant.

The organizers would like to acknowledge the skillful and dedicated support given by Maria Polidoro of the ENEA Fusion Department at Frascati to the editing of these four volumes.

The Editors

INTERNATIONAL PROGRAMME COMMITTEE

S. Segre (Chairman), University of Rome II, Rome, Italy
K. Appert, CRPP, Lausanne, Switzerland
H.A.B. Bodin, Culham Laboratory, Abingdon, United Kingdom
F. De Marco, ENEA, Frascati, Italy
E. Fabre, Ecole Polytechnique, Palaiseau Cedex, France
M. Fontanesi, CNR, Milan, Italy
V.E. Golant, Joffe Physics Institute, Leningrad, USSR
J. Jacquinot, JET, Abingdon, United Kingdom
G.M. Mc Cracken, JET, Abingdon, United Kingdom
J. Nührenberg, MPI, Garching, F.R.G.
J. Tachon, CEN, Cadarache, France
F. Wagner, MPI, Garching, F.R.G.
R.R. Weynants, ERM, Brussels, Belgium

ORGANIZING COMMITTEE

M. Fontanesi (Chairman), CNR, Milan
H. Knoepfel, Associazione Euratom-ENEA, Frascati
M. Lontano, CNR, Milan
G. Malesani, CNR, Padua
E. Sindoni, University of Milan, Milan
M. Polidoro, ENEA, Frascati

CONTENTS

PAPER IDENTIFICATION

Each paper is identified with a 6 character code. The code u v wx yz has the following structure:

u - type of contribution; u = O, P for oral and poster contributed paper

v - the day of event; v = 1,2,3, ...9 for Monday morning, Monday afternoon, Tuesday morning, ... to Friday morning

wx - the topic and subtopic of the contribution

yz - progressive number within session and topic

Example

P4 F6 11

P	4	F6	11
Paper type	Half-day number of event	Topic and Subtopic	Progressive number
Poster	Tuesday afternoon	Plasma heating and current drive Current drive and profile control	Poster number 11

TITLE LIST OF CONTRIBUTED PAPERS

A. TOKAMAKS

A1. Experiments

A3. Theory

B. STELLARATORS

C. ALTERNATIVE MAGNETIC CONFINEMENT SCHEMES

C1. Reverse field pinch

D. INERTIAL CONFINEMENT

F2. Electron cyclotron resonance heating (ECRH)

F3. Lower hybrid heating (LHH)

F4. Alfvén and other RF-methods

G. GENERAL PLASMA THEORY

H. DIAGNOSTICS

I. BASIC COLLISIONLESS PLASMA PHYSICS

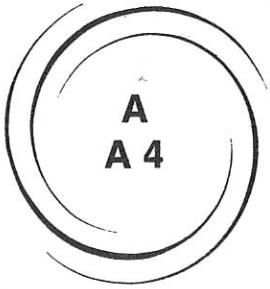

TOKAMAKS

MHD PHENOMENA (SAWTEETH, DISRUPTIONS, ETC.)

FAST CRASH AND DEPENDENCE OF SAWTEETH ON TRANSPORT COEFFICIENTS FROM REDUCED-MHD SIMULATIONS

G. Vlad

Associazione EURATOM-ENEA sulla Fusione, C. R. E. Frascati,
C.P. 65 - 00044 - Frascati, Rome, Italy

A. Bondeson

Centre de Recherches en Physique des Plasmas, Ass. Euratom-Confédération Suisse,
Ecole Polytechnique Fédérale de Lausanne, 21 Av. des Bains
CH-1007 Lausanne, Switzerland

1. INTRODUCTION

Sawtooth oscillations of the central temperature occur in practically all tokamaks under a variety of experimental conditions. A theoretical model for the sawteeth was first proposed by Kadomtsev [1]. His model is based on the resistive reconnection of an $m=1/n=1$ kink deformation which occurs when the safety factor in the centre q_0 falls below unity. Recent experimental data indicates that the Kadomtsev model is not always applicable and suggests that the central q may be significantly less than unity while the discharge is still sawtoothing [2]. Furthermore, measurements on JET indicate that the growth-time of the instability leading to the internal disruption is too short to be connected with a resistive mode [3,4].

Numerical simulations of sawteeth, generally consistent with the Kadomtsev model, have been performed by several different groups [5-7]. However, all computations carried out so far have been made with plasma parameters far from those characteristic of current experiments. In this paper, we present self-consistent simulations over a wide range of plasma parameters to obtain the dependence of characteristic features of the sawteeth on the transport coefficients. The simulations are based on the standard, straight cylinder, low-β, reduced-MHD equations with self-consistent evolution of the electron temperature, including a highly anisotropic thermal diffusivity and ohmic heating [7]. Comparison of the simulation results concerning, e.g., period, growth-time of the instability and collapse time, with experimental data shows excellent agreement for Lundquist numbers up to about 10^7 (corresponding to machines of the size of Frascati Tokamak, FT). An important effect found in these self-consistent simulations is that the current profile is significantly modified by the sawteeth, leading to a very flat distribution in a central region accompanied by a sharp drop outside the reconnection layer. This profile makes it possible to turn on the resistive kink instability with a large growth-rate by a minute change in central q. Thus, the Kadomtsev model, with some modification of the current profile, appears to describe the sawtoothing in, at least, small and medium sized tokamaks very well.

2. DEPENDENCE ON TRANSPORT COEFFICIENTS

We have chosen as a reference case a typical ohmic discharge in FT, with the toroidal field $B_T=6$ T, $a=0.20$ m, $R=0.83$ m, $q_a=2.6$, central density $n(0) \sim 1.8 \cdot 10^{20}$ m^{-3} and central temperature T(0) between 500 and 1000 eV. With these parameters, the Alfvén

time is $\tau_A \sim 0.085$ ms, the Lundquist number is $S = \tau_R/\tau_A \sim 10^7$, the normalized parallel thermal conductivity is $\chi_\parallel \sim 20$ and the normalized temperature (which equals β_{pol}/q_a^2) is $T \sim 0.02 \div 0.04$.

In general terms, the sawtoothing is a nonlinear, dissipative system, in which relaxation oscillations occur, and one must expect its behaviour to depend on the dissipation coefficients.We find that this is indeed the case. Varying $\chi_\perp(0)$ (and thus $\beta_{pol} \propto 1/\chi_\perp$) with S and ν fixed, we found distinct relaxation oscillations only for β_{pol} above some threshold value. This happens because the sawtooth period decreases as the energy confinement is reduced and below a certain value of β_{pol} the successor oscillations of one crash do not have sufficient time to decay before the next crash occurs. Regular oscillations are then lost and the mode energies never relax to a quiescent phase. When periodic sawteeth occur, their period scales as $\tau_{saw} \propto (\beta_{pol})^{0.8}$. The character of the sawteeth is also dependent on the viscosity. Changing the viscosity ν at fixed S and β_{pol}, distinct relaxations occur when $\nu \geq \chi_\perp$, whereas for low viscosity irregular behaviour arises. The sawtooth period scales approximately as $\tau_{saw} \propto \nu^{0.3}$. We note that the experimental result (found in Doublet III, TFTR and ASDEX) for the viscosity, $\nu \approx \chi_\perp$, is just inside the region where the simulations give regular-looking sawteeth.

3. SCALING WITH MACHINE SIZE

In comparing tokamaks of different sizes, the primary variations are those in the Lundquist number S, while νS and $\chi_\perp S$ ($\propto \beta_{pol}$) stay relatively constant. We therefore use the reference parameters of FT and scale these by introducing an enhancement factor E for $\chi_\perp$, ν and η, and use $\nu \approx \chi_\perp$. Figure 1a shows the sawtooth period as a function of S for our reduced-MHD simulations together with experimental data points. To account for the dependence on β_{pol}, we apply the approximate scaling of Sec. 2 for fixed S, $\tau_{saw} \propto (\beta_{pol})^{0.8}\,\nu^{0.3}$ with $\nu \propto \chi_\perp \propto (\beta_{pol})^{-1}$, and thus we have plotted $\tau_{saw}/(\beta_{pol})^{0.5}$. The agreement is

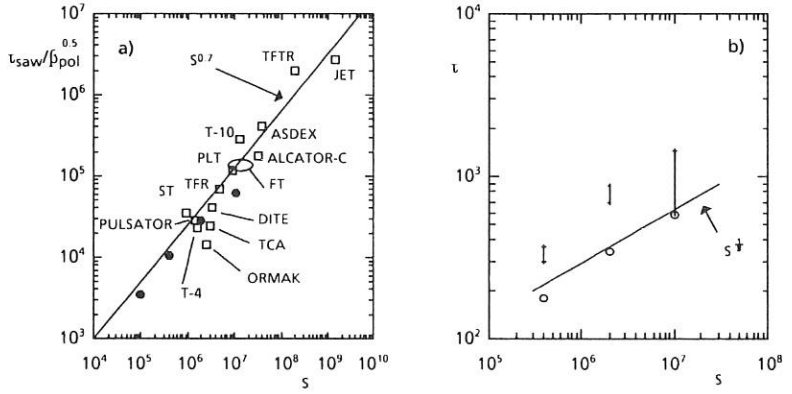

Fig. 1 - a) Normalized sawtooth period $\tau_{saw}/\tau_A\ \beta_{pol}^{0.5}$ vs Lundquist number S: black circles are the simulation results obtained for $\beta_{pol}/q_a^2 \approx 0.02$ varying S while keeping νS and $\chi_\perp S$ fixed ($\nu S \approx 24$ and $\chi_\perp S \approx 10$). b) Growth time of the linear instability (open circles) and collapse times of the central temperature (crosses; for each value of S are shown the minimum and maximum values observed among several teeth)

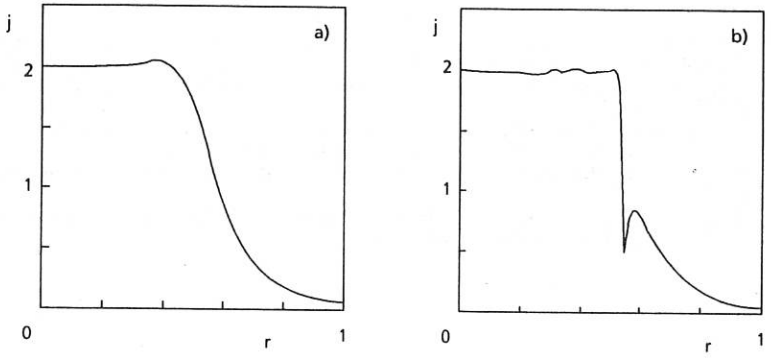

Fig. 2 - a) Current density profile j(r) (m = n = 0) for S = 2·10⁶, at the time of maximum growth rate ; b) current density profile during the nonlinear phase

striking; it is also seen from Fig. 1a that with τ_R/τ_E fixed, $\tau_{saw} \propto S^{0.7}$. Figure 1a gives a strong indication that the Kadomtsev-like sawteeth simulated here are in agreement with experimental results for S up to 10^7.

In Figure 1b we show the collapse time of the temperature and the growth time of the linear instability in the nonlinear simulations, for three values of E. Notably, both of these times scale weakly with S, and at $S = 10^7$ they are in good agreement with observation on FT. The linear growth rate scales approximately as $S^{-1/3}$. This is as expected from linear theory if the shear at the q=1 surface is independent of S. We emphasize that in the self-consistent simulations the shear at the q=1 surface is approximately independent of S. This is due to the sharp current gradient at just outside the reconnection surface, where the current drops significantly over one resistive layer width (Fig. 2a). As noted already by Kadomtsev [1], surface currents are generated by the sawteeth themselves during the reconnection phase (Fig. 2b), because the single helicity reconnection in general gives rise to profiles in which B_θ is discontinuous. During the ramp phase of the sawtooth, the surface current diffuses but at the beginning of the next crash, the current profile has a finite jump over a short distance. The shear varies considerably within one resistive layer width, between practically zero on the inside to about 0.3 on the outside, even though the resistive layer shrinks with increasing S. Thus the equilibrium profiles are dependent on the S-value, making the effective shear for the linear instability almost independent of S. The scaling of the growth-rate with S is strongly affected by this self-consistency, which has hitherto been ignored. With this type of profile for $S = 2 \cdot 10^6$, the linear growth rate of the resistive kink mode changes from 0 to $10^{-3}\ \tau_A^{-1}$ by a change of less than $2 \cdot 10^{-3}$ in central q, i.e., the threshold for instability is very steep.

In conclusion, the reduced-MHD model gives results in excellent agreement with experiments concerning sawtooth period and crash times, for low and medium-size tokamaks. An important factor allowing the fast crash time at high S is the very sharp drop in the current profile at the reconnection radius. This gives rise to an almost discontinuous dq/dr, and therefore allows the instability to be turned on at high growth rate by a minute change in central q.

REFERENCES

[1] B.B. Kadomtsev: Fiz. Plasmy 1, 710 (1975) (Sov. J. Plasma Phys. **1**, 389 (1975))
[2] H., Soltwish, W. Stodiek, J. Manickam, J. Schluter: Proc.11th Int. Conf. on Plasma Physics and Controlled Nuclear Fusion Research 1986 (Kyoto, 1986), IAEA, Vienna (1987) **1**, 263
[3] D.J. Campbell, R.D. Gill, C.W. Gowers, et al.: Nucl. Fusion **26**, 1085 (1986)
[4] J. A. Wesson: Plasma Phys. Controlled Fusion **28**, 243 (1986)
[5] B.V. Waddell, M.N. Rosenbluth, D.A. Monticello,R.B. White: Nucl. Fusion **16**, 528 (1976)
[6] R.E. Denton, J.F. Drake, R.G. Kleva, D.A. Boyd: Phys. Rev. Lett. **56**, 2477(1986)
[7] A. Bondeson: Nucl. Fusion **26**, 929 (1986)

Q-PROFILES IN JET

R D Gill, A W Edwards, B Keegan, E Lazzaro, J O'Rourke,
A Weller and D Zasche

JET Joint Undertaking, Abingdon, Oxon., OX14 3EA, UK

1. **INTRODUCTION** Tokamak q-profiles play a central role in the determination of plasma stability and q(r) towards the plasma centre is particularly important for the sawtooth instability. On JET, q(r) has been determined from magnetic measurements and Faraday rotation. Further information about the position of the q=1 surface has been found from the sawtooth inversion radius, the position of the snake and the resonance effect observed on visible light and X-ray emission during pellet injection. In addition the shear at the q=1 surface has been measured from pellet ablation [1]. This result is supported by the movement of the snake caused by a sawtooth crash. A summary of these data will be made after presenting the new results from pellet ablation.

2. **PELLET ABLATION EFFECTS** During the injection of solid D_2 pellets into JET a large drop in the soft X-ray and visible light emission has been observed as the pellet crosses the q=1 surface (fig.1). The minor radius (r_1) of the minimum of the emission has been found to be very well correlated with the sawtooth inversion radius (r_{1X}) determined from tomographically reconstructed soft X-ray camera data. The position of the q=1 surface within a sawtooth cycle has been established in a plot (fig.2)

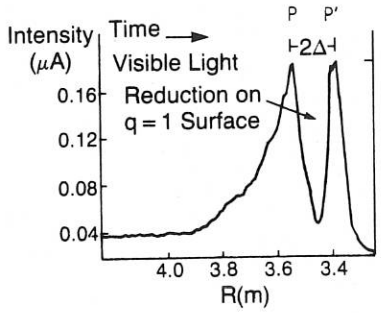

Fig.1 Visible light emission during pellet ablation.

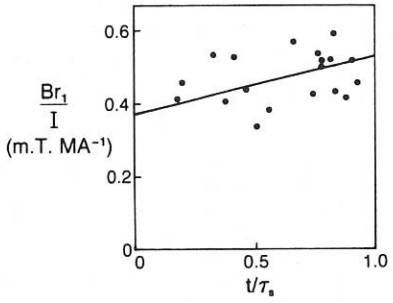

Fig.2 Correlation plot for q=1 surface.

of normalised radius (r_1 B/I) versus normalised time t/τ_s with τ_s the sawtooth period. The normalised radius is used as it has been previously observed that $r_{INV} \alpha$ I/B. Despite considerable scatter, the data is consistent with a previous observation [2] on the movement of the snake oscillation which showed that r_1 moved outwards during the sawtooth cycle by ~30%. r_{1X} corresponds to the value of r_1 at the start of the sawtooth cycle.

3. **DETERMINATION OF dq/dr** The physics of pellet ablation is well understood: the plasma electrons move along their magnetic field lines and lose energy in the ablation cloud which surrounds the pellet (of radius r_p) and protects it from direct heating (fig.3). The ablated

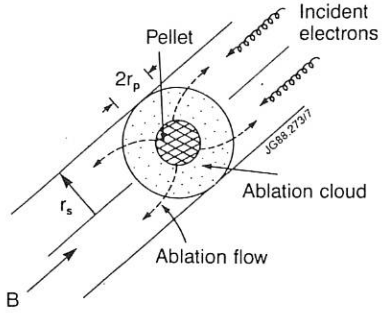

Fig.3 Pellet ablation processes.

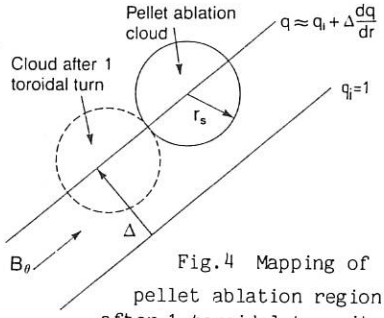

Fig.4 Mapping of pellet ablation region after 1 toroidal transit.

material expands radially up to a critical radius [3] ($r_s \approx 3.5 r_p$ for JET) and then flows along the field lines. The relative velocities are such that the plasma electrons can make many (~10) toroidal transits of the torus while the pellet ablation cloud crosses a flux surface. On a non-rational q-surface electrons from many parts of the flux surface can interact with the pellet. However, for integer q, the flux tube closes on itself thereby reducing the reservoir of available electrons. The cold ablated electrons cool the plasma slowly compared with the time for the cloud to cross the magnetic surface and q is not expected to be modified on this timescale. On integer q-surfaces the effects of shear must also be considered and it can be shown that in order to have an appreciable reduction in ablation rate $dq/dr < q/\pi r$, ie., the shear must be small. If $q=q_o(1+\alpha r^s)$ the condition becomes $(q-q_o)/q<1/\pi s$ and this condition is only likely to be satisfied on the q=1 surface. This provides an explanation for the lack of observation of a dip in ablation rate on surfaces other than q=1. It can also be shown that large effects would not be expected on rational non-integer surfaces either.

Values of dq/dr on the q=1 surface may be found by considering the degree of overlap of the pellet ablation cloud with electrons which have made one toroidal transit of the machine (fig.4). Some overlap will occur, corresponding to points P and P' of fig.1 when

$$\frac{dq}{dr} = \frac{r_{s1}}{\pi r \Delta}$$

where $2\Delta = PP'$ and r_{s1} is the radius of the pellet cloud when it reaches q=1 and is determined from pellet ablation rate calculations and a knowledge of the plasma density and temperature profiles. Putting typical values into the equation above gives $dq/dr = 5\times10^{-2}$ m^{-1} and for a parabolic profile (s=2) $(1-q_o) = 10^{-2}$ showing a q_o extremely close to one. Similar calculations for a number of different shots (fig.5) show some scatter but suggest that dq/dr does not change appreciably throughout the sawtooth cycle.

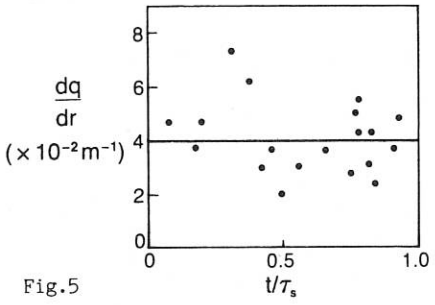

Fig.5

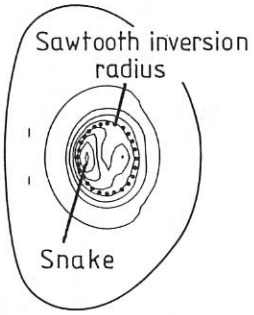

Fig.6

dq/dr deduced from pellet ablation. Tomographically reconstructed snake.

4. **THE SNAKE** The snake is also clearly associated with the q=1 surface and makes an inward step in minor radius of ≈30% coincident with a sawtooth crash. During the slow ramp phase of the sawtooth the change in central q caused by diffusion can only be about $\delta q \approx 0.02$ and therefore to provide the required shift of the snake the q-profile must be very flat. For a parabolic profile, a central q-value very close to 1 results ($q_o = 0.97$).

Detailed tomographic analysis of the snake shows that although it is clearly associated with the q=1 surface it lies to the inside of the sawtooth inversion radius determined just before pellet injection (fig.6).

5. **FARADAY ROTATION** Direct measurements of q(r) have been made on JET using a 6 channel far-infrared polarimeter [4] which determines line integrals of $(n_e B_{\|})$. Inversion of the experimental data requires knowledge of the flux surface shapes and these are calculated from an equilibrium code which uses data from magnetic measurements at the plasma periphery; this information is supplemented in the central regions by the soft X-ray tomographically determined iso-emissivity surfaces and sawtooth inversion surfaces. For ohmic discharges the q-profiles determined have central q values of $q_o \sim 0.7$-0.9 and these are significantly below 1 even when the known errors of ~15% are taken into account. The measurements also determine the position of the q=1 surface in good agreement with the sawtooth inversion radius (fig.7).

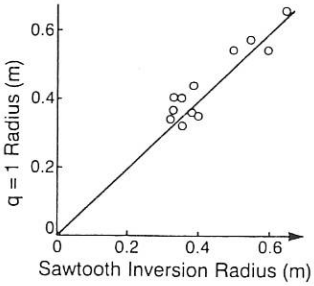

Fig.7 Position of q=1 from FR.

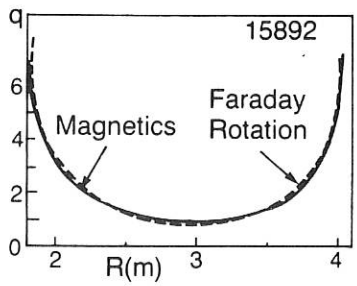

Fig.8 q(r) from magnetics and FR.

6. **MAGNETICS RECONSTRUCTIONS** Information provided by a variety of measurements can be used to define a sequence of nested reconstructions of the pressure profile and q(r) which satisfy the equilibrium equation

$$R^2\nabla\cdot(R^{-2}\nabla\psi) = -\mu R_o J(\psi,p)$$

with ψ the magnetic flux function [5]. In the simplest approach only the external magnetic fields are used and the solutions are insensitive to the central value of q. Further restriction of the problem by the imposition of integral constraints improves the determination of internal characteristics. For example, a self consistent analysis of the polarimeter measurements can be made by requiring that the solution of the GS equation also gives the best fit to the measured values of the Faraday rotation (FR) angles. The analysis gives q(r) with an accuracy varying from 3% at the edge to 20% at the centre. Generally the analysis done independently of the FR data shows q_o dropping below 1 at the onset of sawteeth and good overall agreement on the shape of q(r) (fig.8). Adding the FR data gives lower values of q_o.

7. **DISCUSSION** Overall q(r) in JET is well determined, but on the critical issue of the value of q_o the information falls into two categories: the data obtained by indirect means from the snake, pellet ablation etc., points to q_o very close to 1; whereas the more direct determinations from magnetics and FR give values significantly below 1 even if the errors (15-20%) are taken into consideration. Compatibility between these data can be obtained if it is assumed that q(r) has a rather complicated behaviour with a local flattening at q=1 and a more rapid drop towards the plasma centre. This profile shape would have many implications for theories of the sawtooth instability mechanism.

We would like to thank J Peters for his computational assistance.

REFERENCES

[1] R D Gill et al., JET P(88)59
[2] A Weller et al., Phys.Rev.Lett. 59(1987)2303
[3] P B Parks, Nucl.Fus. 20(1980)311
[4] J O'Rourke et al., Contr.Fus. & Plas.Heat. (Dubrovnik) 12B(1988)155
[5] E Lazzaro and P Mantica, Plas.Phys. & Contr.Fus. 30(1988)1735

INSTABILITIES OF BEAM-HEATED L-TYPE AND H-TYPE ASDEX PLASMAS

O. Klüber, J. Gernhardt, S. von Goeler[1]), M. Kornherr, K. Toi[2]), H.P. Zehrfeld

Max-Planck-Institut für Plasmaphysik, EURATOM Association, Garching bei München, Fed. Rep. of Germany

INTRODUCTION

This paper summarizes the investigations on MHD modes occurring in beam-heated ASDEX plasmas and supplements them by some new observations and discussions of the mode structure. Particular attention is given to the connection between oscillatory mode activity and relaxation phenomena, namely sawteeth, disruptions and ELMs, the latter occurring only in the H-regime. The relaxation processes, however, are not the main topic of this paper. For the understanding of the mode behaviour to be discussed in what follows it is important to note that in no case the onset of neutral injection leads immediately to H-type behaviour. Rather, an L-type phase extending over at least ~ 30 ms preceeds the L to H transition.

Discussion of mode structure and mode propagation.

It is generally accepted that Mirnov oscillations with the poloidal and toroidal mode numbers m and n, respectively, are created by currents flowing parallel to the field lines on rational magnetic surfaces q=m/n. In a torus, the slope of the field lines varies poloidally which leads to a variation of the poloidal wavelength: it is larger at the outside of the torus according to cos m (θ-λ sin θ) /1/. Furthermore, model calculations performed by one of the authors /2/ have shown that the mode amplitude is larger at the outside, too; typical out-in ratios range between 2 and 5. Formally, this variation can be ascribed to sidebands m = ± 1 whereas the current creating this structure is flowing on just one rational surface.

The analysis of the ASDEX data has shown that the mode structure agrees to the conception exposed above as far as the phases are concerned; the amplitudes, however, fit into this model only in rare cases. The out-in amplitude ratio varies between 20 and 0.5, apparently depending on the mode type (in addition, an up-down asymmetry exists which is nearly the same for all modes and is not discussed in this paper.) These experimental findings can be ascribed to the simultaneous occurrence of different modes i.e.currents flowing on different rational surfaces. In lowest order a mode cluster m-1,m,m+1 is sufficient to describe the observations. It has to be postulated then that the leading mode which defines the m number of the observed structure imposes its frequency onto the sideband or satellite modes.

[1]) Plasma Physics Laboratory, Princeton University, Princeton NJ, USA
[2]) Institute of Plasma Physics, Nagoya University, Nagoya, Japan

The field perturbation $\underline{\tilde{B}}$ is frozen within the plasma i.e. it moves at the velocity

$$\underline{v}^* = \underline{v} + \nabla p_i \times \underline{B} / (en_e B^2). \qquad (1)$$

Here, $\underline{v}$ denotes the macroscopic motion which in the case of ASDEX is the toroidal rotation caused by the unidirectional neutral injection. The second term is the contribution of the ion pressure gradient to the diamagnetic drift velocity /3/. This equation allows for determining the mode frequency via $v_{pol} = \omega_{pol}\, r$ and $v_{tor} = \omega_{tor}\, R$. In the case of co-injection (the only scenario treated here), both terms tend to cancel each other. From a discussion of the profiles /3/ it can be taken that modes located near the magnetic axis propagate according to the toroidal rotation while modes located near the boundary tend to move in the opposite direction. Thus, the study of mode propagation and frequency provides a very valuable tool in investigating MHD phenomena.

Sawteeth, m=1 oscillations and satellites.

The OH target plasmas of the ASDEX device are generally subject to sawteeth preceded by m=1/n=1 oscillations. The application of neutral injection leads always to an increase of the sawtooth period. In both confinement regimes, a critical power level is found above which sawtooth activity vanishes in the course of the NI pulse: After the first relaxation, the m=1/n=1 mode develops again but it attains a more or less stationary level without giving rise to sawteeth. The further temporal evolution depends on the confinement regime: If the plasma remains in the L-type state the mode may continue up to the end of the injection pulse or it may develop into fishbone-like bursts. After an L- to H-transition, however, the amplitude of the continuous m=1 mode always decreases drastically but it revives repetitiously in a fishbone-like manner indicating that the q value on axis remains close to unity.

The mode frequency of typically 10 to 30 kHz is clearly governed by the toroidal rotation of the central plasma as is shown by Doppler measurements. Regardless on the waveform - precursor of sawtooth, continuous mode of fishbone-like burst - and regardless on the confinement regime the m=1 mode is always accompanied by a satellite, i.e. an n=1 Mirnov oscillation with exactly the same frequency and similar temporal behaviour of the amplitude.

The poloidal mode number m - preferrably 4 or 5 - exceeds always the q value at the boundary (separatrix effects not included); hence an external kink is a plausible candidate. The out-in ratio of the amplitudes is extremely large and may amount up to 20 or more which indicates a cluster of modes coupled such that the maxima coincide at the outside of the torus. Presumably, such cluster comprise all mode numbers between 1 and the dominant m value which would explain the mode coupling satellite extending over the total plasma cross section.

Most puzzling, in some cases, this structure is superimposed by an m=0/n=1 component at same frequency which - due to the large amplitude ratio of the m > 0 satellite - is most prominent at the inside of the torus. Thus the signals from the Mirnov coils located in a poloidal plane at the high field side of the torus are in phase while those from the outer

coils exhibit the well-known picture of a propagating mode. On the basis of plausible assumptions it is possible to separate the m=0 component /3/. It is difficult to comment on the significance of this phenomenon since its occurrence cannot be attributed to characteristic parameters such as q, $\beta_p + l_i/2$ etc.

m=2 modes and disruptions.

L-type plasmas in ASDEX are not susceptible to disruptions below the density limit. If q approaches 2, a large m=2/n=1 mode develops which usually persists over hundreds of milliseconds without leading to disruptions. Frequently, the island size is appreciable and impairs the confinement. In H-type discharges, disruptions preceded by large m=2 oscillations occur preferrably if the β limit is approached. The way the m=2 mode is initiated is reported in ref. /4/.

The moderate amplitude ratio of the order 3 fits into the picture of just one mode. The direction of propagation is still that of the toroidal rotation while the frequency is appreciably smaller than that due to the central rotation velocity which indicates the enhanced competing effect of the diamagnetic drift.

Localized $m \geq 3$ modes and their relationship to the confinement regimes.

The m=1/n=1 and m=2/n=1 modes discussed in the preceding sections are localized in that they propagate according to eq. (1). Another localized n=1 mode was first observed in the L regime by one of the authors /5/. The m number is m* = 3 or 4, where m* is smaller than but close to the boundary q value (separatrix effects disregarded). This mode propagates in the diamagnetic drift direction at a frequency which is typically below 10 kHz, i.e. less than that of the m=1 mode. In favourable cases, the double frequency feature is clearly seen in the raw data. Using an ideal filter method /5/ the two components can be separated.

Surprisingly, in contrast to the behaviour of the satellite mode, the out-in ratio of the amplitudes is nearly unity or even less which corresponds to a cluster of modes coupled such that the maxima coincide at the inner side of the torus.

All these features indicate the occurrence of a mode originating near (but inside) the separatrix which apparently is decoupled from the central m=1 activity. Unfortunately, this statement has to be qualified according to the following experimental findings: In sawtoothing L-type discharges, there is generally an interval between sawteeth, in which the m=1 oscillation and its satellite is not detectable. This behaviour, however, holds also for the m* mode, apart from a short period after the sawtooth crash. Furthermore, there is a puzzling connection between the number m* of the mode discussed here and the mode number m_s of the satellite governed by the m=1, namely

$$m^* = m_s - 1 \qquad (2).$$

Simple relationships, however, between the frequencies of both modes or the sums or differences of them were not found.

It was already stated that the m* mode is observed in the L regime. After the L to H transition, it vanishes rapidly, i.e. within a few milliseconds. It reappears on the same time scale if, after the termination of the NI heating pulse, the plasma returns into L-type behaviour. During the H phase, the m* mode occurs only during the so-called edge-localized modes or ELMs which in general is masked by the signals due to the inward motion of the plasma column caused by the rapid decrease of β_p. Using particular evaluation techniques /6/, however, it is possible to separate both types of signals. It is seen that the m* mode and the ELM relaxation develop simultaneously. Hence, this mode is no precursor to the ELM other than the characteristic precursors of sawteeth and disruptions.

In the L phase, the m* mode develops at rather low β values. Furthermore, there is no threshold for the onset of ELMs. From this it is inferred that this mode is driven by current density rather than by pressure.

SUMMARY

The variety of MHD oscillations in beam-heated ASDEX plasmas can be systemized to some extent: rules can be established. The underlying physics, however, are not yet understood.

REFERENCES

/1/ V.G. Merezhkin, Sov.J. Plasma Phys. 4(2), 152, 1978

/2/ G. Fussmann, B.J. Green, H.P. Zehrfeld, Plasma Phys. and Contr. Nucl. Fus. Res. 1980 (Proc. 10th Int.Conf. Brussels 1980), Vol. I, IAEA, Vienna (1980) 353.

/3/ O. Klüber et al., IPP Report III/140 (1989)

/4/ O. Klüber, J. Gernhardt, K. Grassie et al., Proc. 13th Europ. Conf. on Contr. Fusion and Plasma Heating, Vol. 10c, Part I, 136 (1986)

/5/ K. Toi, J. Gernhardt, O. Klüber, M. Kornherr, to be published Phys. Rev. Letters

/6/ S. von Goeler, O. Klüber et al., submitted for publication to Nucl. Fusion.

Sawteeth in TFTR*

K. M. McGuire, R. Buchse[1], A. Cavallo, E. D. Fredrickson, A. Janos, G. Kuo Petravic, D. Mansfield, Y. Murakami[2], W. Park, and W. Stodiek.

Princeton University, Plasma Physics Laboratory
Princeton, N.J. 08543 U.S.A.

Introduction

In this paper we will look at experimental data from the soft x-ray camera and local ECE T_e measurements. An attempt will be made to understand the relationship between the temperature island and the displacement of the hot temperature core. A comparison between the temperature island size and the movement of the hot core will be made in order to identify the type of instability involved at the sawtooth crash. In addition the $\tilde{B}_\theta$ signal observed on the magnetic loops during the precursor phase will be used in an attempt to measure the motion of the magnetic axis during the sawtooth crash phase. Simulations of the of m/n = 1/1 mode during the sawtooth crash will be compared in detail with the soft x-ray and local ECE T_e measurements in order to understand the shape of the hot region as the temperature decreases at the sawtooth crash.

Experimental results

Many kinds of sawteeth are observed on TFTR[1], in ohmic and neutral beam heated plasmas. It is found that most sawteeth have little or no precursor activity before the sawtooth crash. However with closer inspection it is found that a rapidly growing mode is observed during the final collapse itself. This rapidly growing mode is easier to observe if the plasma has some toroidal rotation, which can be obtained with neutral beam injection. Reconstruction of the soft X-ray signals and the local temperature from ECE signals, have been used to obtain information about the internal phenomenology of sawteeth on a fast time scale during the final crash phase[2].

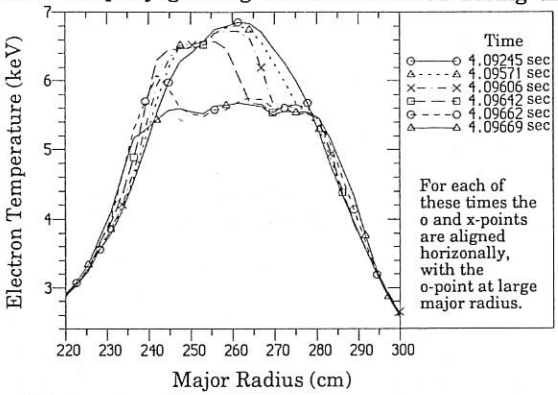

Figure 1a. Shows a sawtooth crash on TFTR with T_e profiles from the grating polychrometer during the crash phase.

The local temperature method of reconstruction is

limited to changes in the emission which are slow compared to the rotation of the plasma. However, this method of reconstruction is extremely powerful on TFTR due to the large rotation velocities obtained with neutral beam injection. The analysis of many sawtooth crashes on TFTR leads to the following overall picture: (a) the magnetic axis or hot temperature core moves away from the center as the temperature island structure grows, (b) when it moves about half the radius of the q=1 surface, it starts to deform in shape and becomes somewhat non-circular, (c) the cold island region pushes the hot core against the q=1 surface, and then the heat spreads poloidally around the q=1 surface, (d) the cold region grows to form the new plasma core. This picture of the sawtooth crash is observed on all types of sawteeth on TFTR. These features of the sawtooth crash are shown in fig. 1a - 1b, where the timing and position of the temperature island is chosen so that it is at large major radius.

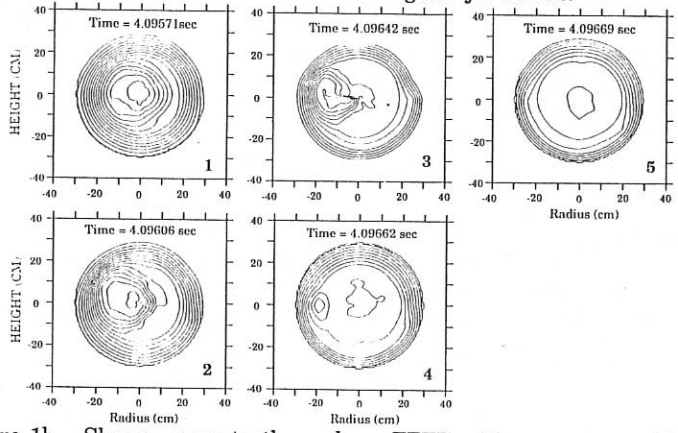

Figure 1b. Shows a sawtooth crash on TFTR with reconstructed local temperature data using the method of rotation of the plasma to obtain a poloidal distribution of the Te profile.

In a large tokamak like TFTR, the sawtooth crash time on the central T_e and line integral density can be as fast as ≈ 40 μsec. The relative change in $\Delta T_e / T_e \approx$ 40% and $\Delta T_i / T_i \approx$ 30%. However the topology of the temperature island and the motion of the hot core does appear to be consistent with reconnection type phenomena. The present sawtooth theories must explain the "Kadomtsev-like" reconnection, the fast T_e and n_e crash times, fast motion of the trapped fast ions [3], and slow neutron drops[4] at the sawtooth crash. The time scale for the complete crash, as measured by the central local temperature, is about 40μs, which is much too fast for a classical Kadomtsev-like resistive reconnection process.

Measurements of the temperature island width and the magnetic oscillations

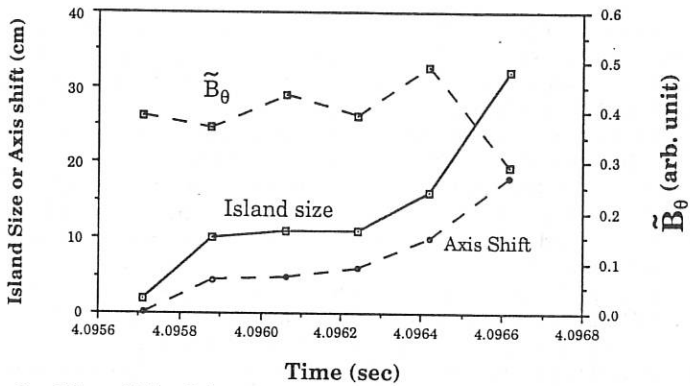

Figure 2. The width of the temperature island and the axis shift of the temperature hot spot, during the crash phase of a sawtooth, as measured by the local temperature profiles. The amplitude of the $\tilde{B}_\theta$ signal observed on the magnetic loops during the precursor phase is also shown.

during the crash phase are shown in fig.2. As the temperature island increases in width from ≈ 3cm to 30cm, the external magnetic loop signal $\tilde{B}_\theta$ does not change in amplitude. The signal detected on the loops is an m/n = 4/1 and 3/1 mode coupling out from the m/n = 1/1 in the core, therefore it seems reasonable that the larger the 1/1 mode the larger the amplitude of the $\tilde{B}_\theta$ signal at the coils. In other examples, it is found that the $\tilde{B}_\theta$ signal does increase as the temperature island grows, in near agreement with MHD code calculations.

The high frequency turbulence, measured with external magnetic loops, does not show the enhanced levels during the crash phase of the sawtooth as might be expected from a stochastic model for the sawtooth crash mechanism. However the new microwave scattering system on TFTR will address this question of turbulence during the sawtooth crash phase.

Local T_e and line integral x-ray measurements do not agree on the shape of the hot spot just before the crash of the sawtooth[5]. Simulation results are obtained by best fitting the raw experimental data, using a model of a shifted core with circular to elliptical shape. During the growth of the island shaped region, from 4.0957 to 4.0965sec (see fig. 2) the agreement between the simulations is remarkably good. The "hot spot" in the final phase of the sawtooth crash, is nearly circular on the local Te reconstruction but is somewhat island shaped on the x-ray simulation results. The difference in shape could be caused by the fact that the x-rays are sensitive to n_e and Z_{eff} and these quantities may not follow the flux surfaces, generally it is believed that T_e is constant on a flux surface.

Discussion

The flat region on the temperature profile which we interpret as a temperature

island grows to a large size before the sawtooth crash. The motion of the temperature "hot spot" is "Kadomtsev-like", that is, as expected from the Kadomstev reconnection model, except for the time scale involved. If the island detected by the $\tilde{B}_\theta$ loops was a magnetic island, then the measured $\tilde{B}_\theta$ signal should increase more than was observed. This implies that the magnetic axis may not be moving as much as required, if the temperature island is a representation of the magnetic island. Nevertheless the possibility that the magnetic island is not large at the sawtooth crash and that the large temperature island is caused by a stochastic process cannot be ruled out from the present data.

The stability of the m=1 mode at low beta and low $q_0 \approx 0.7$ has being studied in detail by Manickam and others[6]. Indications are that at high beta, $\beta_\theta > 1$[7], the m = 1 mode is unstable for $q_0 - 1 > 0.1$. For neutral beam heated discharges described in this paper, the T_e and T_i are high and $\beta_\theta \approx 1.0$. In addition a large part of the current can be carried by beam and bootstrap driven currents. For both these reasons the q_0 on axis may not reach 0.7, as was observed in OH discharges on other tokamaks[6].

Conclusions

It is found that the "hot spot" is near circular on the local T_e reconstruction but is somewhat island shaped on the x-ray tomography reconstruction during the final phase of a sawtooth crash. This leads to the conclusion that, for the x-ray diagnostic the n_e and z_{eff} may have changed and this should be taken into account. No cold bubble is observed on TFTR during a slow or fast sawtooth crash on the local temperature measurements. However it may be present on the x-ray tomography[8]. As the temperature island increases in width from ≈ 3cm to 30cm, the external magnetic loop signal $\tilde{B}_\theta$ does not change in amplitude. This problem will be resolved with a q profile measurement on TFTR. Further study is needed to address the question of mode coupling from the m/n = 1/1 to the higher mode numbers, this will lead to a better understanding of the magnetic island size during the sawtooth crash.

References

[1] McGuire, K. M., et al. (1986). IAEA (Kyoto) Vol. I 421.
[2] Kuo-Petravic, G., Princeton Plasma Physics Report PPPL 2556.
[3] Goldston, R. J., et al, Nucl. Fusion 27 (1987) 921.
[4] Lovberg, J. A., et al (1988) Princeton Plasma Physics Report PPPL 2558.
[5] Murakami, Y., (1989) to be published, (private communication).
[6] Soltwisch, H., et al (1986) IAEA (Kyoto) Vol. I 263.
[7] Bussac, M, N., et al, Phys. Rev. Lett. 35 (1975) 1638.
[8] Buchse, R, private communication

*Supported by DoE contract No. DE-AC02-76-CHO-3073

[1] Max-Planck-Institut fur Plasmaphysik, Garching, FRG
[2] University of Toyko, Toyko, Japan

Axisymetric Beam-driven Modes during High Power NBI on TFTR*

E. D. Fredrickson, K. M. McGuire, R. J. Goldston, C. Z. Cheng

Princeton University, Plasma Physics Laboratory
Princeton, NJ 08543, USA

Introduction

A new beam driven instability has been observed on TFTR during high-power neutral beam heating. It is observed during the initial beam injection phase of TFTR supershot plasmas. The mode is observed best with a very low initial density and well conditioned limiters to minimize edge recycling. The duration of the mode is short, beginning about 50 msec after beam turn-on and lasting for approximately 50 msec (Fig. 1). There is no observed degradation in fast beam ion or plasma confinement due to the mode. The instability typically has a (m,n)=(2,0) standing wave structure, although m numbers as high as 4 and (m,n)=(2,1) standing mode structures have also been observed. Typical mode frequencies lie in the range from 20 kHz up to 150 kHz. The mode amplitude is small, $\tilde{B}/B_{\phi}$ at 50 cm from the plasma edge is about 3×10^{-5}. The soft x-ray camera shows that the mode is localized near the edge of the plasma.

Experimental Results

(a) Mode Structure

The mode is observed during the initial phase of beam injection. At that time edge densities are in the range 2-4 x $10^{18}/m^3$, Z_{eff} is typically about 5, the edge electron temperature is about 100eV and the magnetic field is 4.8T on axis. The mode appears shortly (50 msec) after beam turn-on and persists for less than 50 msec. The edge density typically increases less than 20% during the first 100msec of beam injection. The (parallel) beam injection energy is approximately 105 keV with deuterium, but there is also a substantial fraction of the beam ions in the half and third energy components. For these parameters, the electron thermal velocity is about 4 x 10^6 m/sec, the beam ion velocity is about 3 x 10^6 m/sec and the Alfven velocity is 5.2 x 10^7 m/sec. Data is available for cases with q(a) approximately 4, 6 and 8.

The most striking feature of this new mode is that it is a *standing* wave. Analysis of data from the 30 channel internal Mirnov coil array [1] for a typical $q(a) \approx 8$ case shows a clear m=2, n=0 standing wave (Fig. 2). The mode structure in this example is quite complex, however. The $q(a) \approx 8$ cases have dominant (2,0) modes (possibly with multiple radial mode numbers) as well as higher m=3 and m=4 modes all present simultaneously (Fig. 3). At moderate $q(a) \approx 6$, the dominant mode structure was still (m,n)=(2,0), but

now (1,0) and (3,0) modes could also be seen. At the lowest q(a)≈4, the dominant modes became (m,n)=(2,1) standing waves with (m,n)=(3,1) traveling waves also present.

There is good evidence that the mode is localized to the edge region of the plasma. The mode is not visible on the chord averaged soft x-ray data (5 mil Be filters). However, with the filters removed and the camera sensitive to ultra-soft and VUV emission, dominantly from the edge, the mode is visible. Further, it is observed that small gas puffs preceding beam injection can stabilize the mode. As the gas puffs have their strongest effect at the plasma edge, this implies the the mode is also localized there.

(b) Frequency Spectrum

As to be expected from the complexity of the spatial structure, the frequency spectrum of the modes is also rich. As in the spatial structure, there is a qualitative difference in the spectra between the q(a)=4, 6 and 8 cases. For the q(a)≈4 case, there are two well defined peaks of nearly equal amplitude at 20 kHz and 30 kHz corresponding to the (m,n)=(3,1) traveling wave and the (2,1) standing wave respectively. The 20 kHz peak is broader (width is about 5 kHz) than the 30 kHz peak (width of about 1.0 kHz).

At q(a)≈6, where (2,0) standing waves and (3,0) and (1,0) traveling waves are present, the frequencies are no longer constant in time. The dominant (2,0) mode appears at 32kHz. Within 30ms the frequency has increased to 50kHz and the mode amplitude has become small. A very weak (1,0) mode appears and disappears at the same time with a frequency about 10 kHz below that of the (2,0). A weak (3,0) mode is also present at roughly twice the frequency of the (2,0). The richest structure occurs in the high q(a) cases (Fig. 3). The simplest description of the phenomena would assume the presence of two strong, non-linearly interacting modes (2,0) modes at 42 kHz and 50 kHz. As both positive and negative frequencies are present, all the sum and difference frequencies would be represented. The 32 kHz peak would be 2 x 42 kHz - 50 kHz, the 58 kHz peak would be 2 x 50 kHz - 42 kHz. The next grouping of peaks could be described in the same fashion. The 84 kHz and the 100 kHz peaks would be twice the 42 and 50 kHz peaks, respectively. The 92 kHz peak is 42 + 50 kHz. The interactions continue, up to the 168 kHz peak which is 4 x 42 kHz. The physical process which could give rise to such a description is unclear. It is not possible at this point to state whether there is a broad (in frequency space) driving term which excites narrow band modes (the 34, 42, 50, and 58 kHz quadruplet may be different radial eigenmodes), or whether there exists a continuum of mode freqencies excited by discrete resonances with specific beams.

(c) Scaling

The scaling with q(a) has been extensively discussed above. While the results are mostly qualitative, the changes in mode frequency and structure do roughly keep the parallel phase velocity near the injected beam velocity. Under some conditions the mode amplitude is observed to scale well with

counter power - but in contrast, ABM's are also observed with co-parallel injection only. Gas puffing, hence higher edge densities, seems to stabilize the modes (perhaps in contradiction to global Alfven wave models). However the mode amplitude does not seem to scale well with edge density. The range of toroidal field available for scaling was insufficient to draw conclusions.

Discussion

Circumstantial evidence supports the conclusion that the ABM instability is a beam driven mode. The mode is only observed during beam heating. It is present during the initial phase of neutral beam injection, before global plasma parameters (density, electron termperature or plasma current profile) have changed much from the ohmic phase. Finally, the mode frequency is close to the calculated beam poloidal transit frequency. Details of the beam ion/wave interaction are not understood, nor is the radial eigenfunction of the mode known. However, there is strong evidence that this is an edge mode. It appears sensitive to edge parameters (it disappears with heavy gas puffing) and it is observed on ultra-soft x-ray emission, but not soft x-rays. The global Alfven branch[2] would appear to be a likely candidate for the instability, but the minimum in the Alfven frequency is typically greater than 0.5MHz (Fig. 4), much higher than the range of frequencies of the dominant modes (20-60 kHz). It is of interest to note that the edge electron thermal velocity ($\approx 4 \times 10^6$m/sec) is also close to the parallel phase velocity of the mode, thus electron Landau damping may be important in calculations of the mode stability.

*Supported by US DoE contract No. DE-AC02-76-CHO-3073

[1]E. D. Fredrickson, K. M. McGuire, et al., Rev. Sci. Instrum **57** (1986) 2084.
[2]K. Appert, R. Gruber, et al.,Plasma Physics **24** (1982) 1147.

Figure Captions

Fig. 1a. Traces showing the rise in stored energy as the neutral beams are turned on and the amplitude of the $\partial B/\partial t$ signal. The initial spike is the ABM with the later rise being the turbulent fluctuations always seen with beam heating.

Fig. 1b. Raw data from the main 15 coil poloidal array of Mirnov coils. The data clearly shows the m=2 standing mode structure.

Fig. 2 Snapshots at 4 times through one period of the mode. Circles are data from the main poloidal array, triangles are data from coils at different toroidal locations.

Fig. 3 Spectrum of the fluctuations on one coil for shot 37570. The peaks are labeled as to their poloidal and toroidal mode numbers.

Fig. 4 The fundamental Alfven frequency profile for a q(a)≈6 plasma. The actual mode frequency varied from 32kHz to 50kHz. (Where $\omega_A \equiv V_A/q(r)R_0$.)

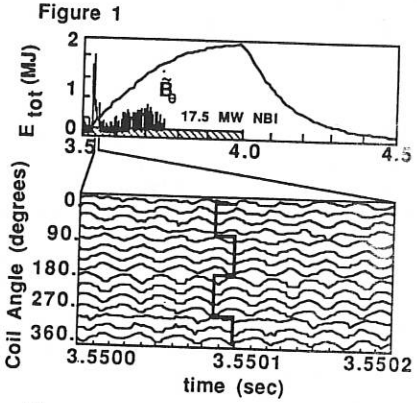

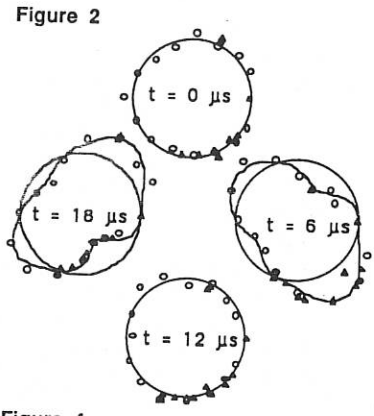

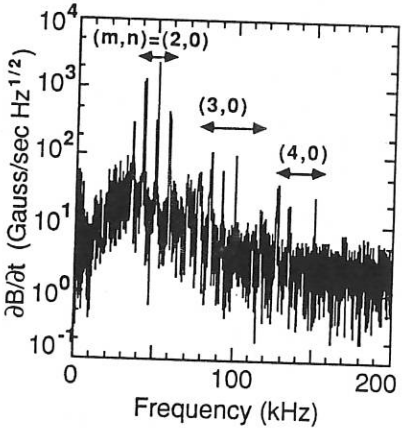

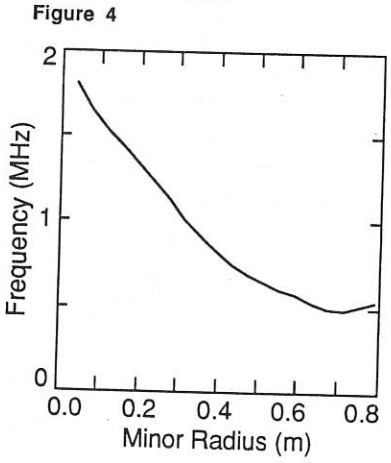

MEASUREMENTS OF THE TOKAMAK SAFETY FACTOR PROFILE BY MEANS OF DRIVEN RESONANT ALFVEN WAVES

H. Weisen, G.G. Borg, B. Joye, A.J. Knight, J.B. Lister

Centre de Recherches en Physique des Plasmas
Association Euratom – Confédération Suisse
Ecole Polytechnique Fédérale de Lausanne
21, av. des Bains, CH-1007 Lausanne/Switzerland

Alfvén waves are launched in the TCA tokamak (R, a = 0.61, 0.18 m, B_ϕ = 0.78–1.51 T, $I_p \leq 170$ kA and $n_e \leq 1.5 \times 10^{20}$ m^{-3}) by an external antenna structure [1]. An Alfvén resonance occurs wherever the local Alfvén velocity matches the externally imposed wave velocity, $\omega/k_{||}$. In the large aspect ratio approximation the resonance condition can be written as,

$$\omega^2\rho(0) = K\,[n + m/q(r)]^2 \,/\, [\rho(r)/\rho(0)]\,, \qquad (1)$$

where (n,m) are the toroidal and poloidal mode numbers respectively, $\rho(r)$ is the local mass density, and $q(r)$ is the local safety factor.

When the central line densities for which the resonance condition is satisfied at a given radius are known for two identical discharges, with, for example, (n,m) = (1,1) and (2,0) excitation, the local value of q can be obtained directly. To see this, we rewrite Eq. (1) as,

$$\omega^2\rho_0\,\rho^*(r) \propto [n + m/q(r)]^2\,, \qquad (2)$$

where ρ_0 is the central mass density and $\rho^*(r)$ is the mass density profile normalised to its value at r=0. We assume that $q(r)$ and $\rho^*(r)$ are independent of ρ_0. This allows us to write Eq. (2) with (n,m) = (1,1) and (2,0) and solve for the safety factor to obtain,

$$q(r) = \left[2(\rho_{01}/\rho_{02})^{1/2} - 1\right]^{-1}\,, \qquad (3)$$

where ρ_{01} and ρ_{02} are the values of the central density when the (1,1) and the (2,0) modes are resonant at a given radius, r. The ratio of ρ_{01} and ρ_{02} can be obtained from electron line density measurements, assuming that the (1,1) and the (2,0) discharges have the same effective ion mass, $\rho(0)/n_e(0)$. To ensure this condition the ohmic discharge was disturbed as little as possible by using a minimal RF power.

The required mode numbers, (n,m) = (1,1) and (2,0), were determined by the relative phasing of the antennae and the RF power delivered to the plasma was 40 kW, at 2.04 MHz. The resonance positions were found by observing the associated density oscillations using a phase contrast imaging interferometer [2].

Figure 1 shows the radial profile of the amplitude and phase of the line density oscillation obtained for the same line averaged electron density in both the (1,1) and (2,0) continua. Although the two continua were observed to have the same threshold density, the (1,1) resonance layer appears at a larger radius than the (2,0) layer at this density, somewhat above the threshold, as a result of its dependence upon the safety factor. Figure 2 shows how the resonances moved to the plasma edge as the density increased.

Figure 3 shows the positions of the resonance layers for the (1,1) and (2,0) modes plotted as a function of line density measured for B_ϕ = 1.51 T and I_p = 125 kA. The difference in the rate of outward movement of the (1,1) and (2,0) resonances as the density increased illustrates the q dependence of the (1,1) layer. Although this discharge showed sawtooth behaviour, the ensuing modulation was not resolved in the measurements; the frequency response of the instrumentation provided an average over the sawtooth period.

Figure 4(a) shows the q profile deduced from the measurements of Fig. 3. As the density increase at low power was often insufficient to force the (2,0) resonance layer out to $r/a > 0.7$, we have added points at larger radii by using the Abel inverted density profile obtained from an eight chord far infrared interferometer (when available), together with the (1,1) resonance layer profiles. These are the filled circles in Fig. 4.

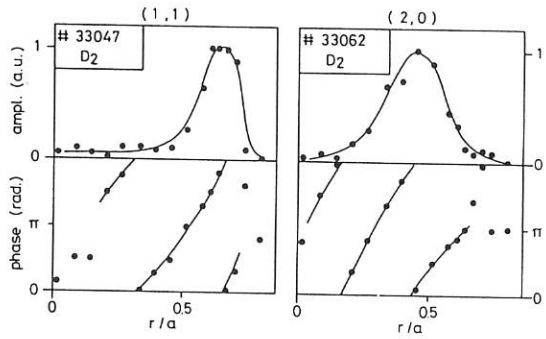

Fig. 1. Radial profiles of the synchronous line density oscillations obtained at the same values of line density and excitation frequency for (1,1) and (2,0) excitation.

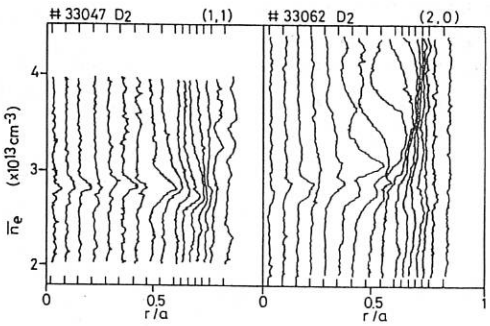

Fig 2. The density fluctuation amplitude plotted as a function of line density at 16 radial locations for the (1,1) and (2,0) discharges.

Figure 4(a) shows data taken from a sawtoothing discharge. This q profile is within a few percent of unity from $r/a = 0$ to $r/a \approx 0.4$, which corresponds, within one centimetre, to the sawtooth inversion radius obtained from soft x-ray measurements. The profile extrapolates well to the cylindrically equivalent safety factor at the edge, $q_I = 5\times10^6 a^2 B_\phi / R I_p$, in this case $q_I = 3.2$. The q_I values are indicated by the crosses in Fig.4.

Figures 4(b) and (c) show the q profiles for discharges with the same toroidal field as Fig. 4(a) but with plasma currents of 70 kA and 50 kA, respectively. Both these profiles also extrapolate well to the corresponding values of q_I, 5.7 and 7.9, respectively. These profiles do not have the flat central region shown in Fig. 4(a) and indicate a more peaked plasma current. Figure 4(b) shows q values in the central region slightly above unity, while 4(c) has central q values substantially above unity. Neither of these two discharges showed any sawtooth behaviour (the onset of sawteeth in TCA corresponds to $q_I \approx 5$).

Figure 4(d) shows the q profile for a discharge with a reduced toroidal field of $B_\phi = 1.16$ T and a larger plasma current of $I_p = 135$ kA. The reduced toroidal field, together

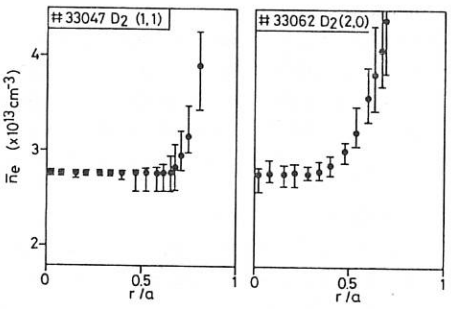

Fig. 3. Resonance layer positions for the (1,1) and (2,0) modes as a function of the central line density.

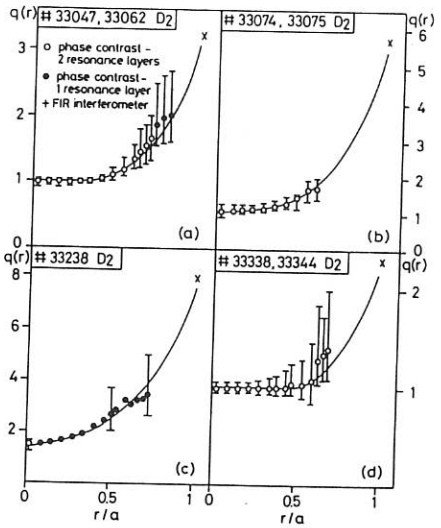

Fig. 4. Safety factor profiles for
(a) B_ϕ= 1.51 T, I_p = 125 kA,
(b) B_ϕ= 1.51 T, I_p = 70 kA,
(c) B_ϕ= 1.51 T, I_p = 50 kA,
(d) B_ϕ= 1.16 T, I_p = 135 kA.

with the higher plasma current, caused q_I to decrease to 2.3. Again, the measured q profile extrapolates well to this value. The reduced edge value of the safety factor was not associated with a reduced central value, compared to the case of Fig. 4(a). However, the central flat region has extended so that $q(r)$ stays close to unity out to $r/a \approx 0.5$. This distance corresponds to the increased sawtooth inversion radius observed on the soft x-ray signals.

Sawtooth resolved measurements show a strong modulation of the KAW phase and amplitude for $(n,m) = (2,0)$, equivalent to a 3% change in line density. The modulation by sawteeth is much weaker for $(n,m) = (1,1)$, suggesting that the change in mass density at the sawtooth collapse is compensated by the change in q. From Eq.(2) this suggests $\Delta q/q \approx -\Delta\rho/\rho \approx 3\%$, that is, the collapse expels a small amount of current together with the particles which carry the current.

Different techniques have so far yielded different measurements of $q(0)$. Our results indicate a flat q profile during sawteeth with q close to unity in the central region. This is consistent with the quasi-interchange sawtooth collapse model proposed by Wesson [3].

We are grateful for the support of the TCA team in this work, which was partly supported by the Fonds National Suisse de la Recherche Scientifique.

REFERENCES

[1] G.A. Collins et al., *Phys. Fluids*, **29**, 2260 (1986)
[2] H. Weisen, *Rev. Sci. Instrum.*, **59**, 1544 (1988)
[3] J.A. Wesson, *Plasma Phys. Contr. Fusion*, **28**, 243 (1986)

$\ell = 1$ HELICAL COIL EXPERIMENTS ON TOKOLOSHE TOKAMAK

G NOTHNAGEL, D SHERWELL, J D FLETCHER, D E ROBERTS, J A M de VILLIERS, D F B LOUW and J R O'MAHONY

ATOMIC ENERGY CO., PELINDABA, SOUTH AFRICA

Introduction A set of complete, resonant, helical windings ($\ell = 1, 2, 3$) has been installed on Tokoloshe ($R/a = .52m/.24\,m, B_T = .6\,T, I_p > 100\,kA$). The $\ell = 1$ coil has a winding law of the form $\theta = \phi + 40^{\circ} \sin\theta$ chosen to minimize the 3/1 sideband, and which gives a 2/1 satellite island of approximately one third the size of the primary 1/1 island. Other sidebands are small. In this paper the first experimental results are presented.

Experimental results Experiments to date have been limited by power supplies to $\ell = 1$ coil currents $I_1 \leq 6\,kA, I_1/I_p \leq 6\,\%$. I_1 is switched on at some chosen time during a shot, has a rise time of approximately $3\,ms$, and decays resistively over the shot duration (Fig. 1 D). The Spitzer time to the $q = 1$ surface is $15\,ms$. We have results in the case I_p is parallel or antiparallel to B_T (resonant and nonresonant helical perturbation respectively), and in the case I_1 is reversed. Observations at the $q = 1$ resonant surface are made with a single surface barrier diode at a tangent radius just outside the radius of inversion. Mirnov and hard X-ray signals are monitored.

In the resonant case with $I_1 = -6\,kA$, a maximum reduction of relative sawtooth amplitude ($\Delta A/A$) of about 50 % is achieved as shown in Fig. 1 A. Similar amplitude reduction under reversed helical current is observed (Fig. 1 B) but with considerably more complicated soft X-ray signal. Fig. 1 C shows a reference shot ($I_1 = 0$).

In the non-resonant case with $I_1 = -6\,kA$, a maximum reduction of $\Delta A/A$ of about 50 % is again observed (Fig. 2 A). With $I_1 = +6\,kA$, minor changes in $\Delta A/A$ are observed (Fig. 2 B). The dependence of observations on the sign of I_1 is surprising but may be due to an asymmetry in the outer flux surface relative to the poloidal limiter. Changes in sawtooth modulation of the $m = 2$ Mirnov signal and hard X-rays are in line with changes in $\Delta A/A$, supporting the soft X-ray results (Fig. 3). The soft X-ray signal saturates quickly in the early cooling phase as is particularly clear when comparing Fig. 2 B with Fig. 2 C. For limited helical currents $I_1 < 6\,kA$ we have not attempted to distinguish a clear trend in $\Delta A/A$ with coil current, as the observations only become significant at $I_1 \sim 6\,kA$.

Further we find that the observed time for an effect on the soft X-ray signal is 3-5 times the Spitzer value to the radius of inversion, and that major disruptions are not precipitated. The latter observation confirms the smallness of the 2/1 satellite which is not expected from experimental results with the $\ell = 2$ coil (Ref 1) to cause disruption.

In equilibria with $B_T = 0.35\,T, I_1 = 6\,kA\,(I_1/I_p = 8\,\%)$ the above results persist with $\Delta A/A$ reduced by about 50 %. Here a general decrease in 2/1 amplitude is often observed, accompanied by a lengthening of the shot (Fig. 4). These discharges have not yet been considered in depth, but pulse lengthening has been related to profile modifications

which may then occur in our experiments, and affect sawtoothing.

Discussion Partial sawtooth suppression has been achieved for limited coil currents where $I_1/I_p \leq 6\,\%$. This is to be compared with TOSCA resonant coil experiments where suppression was achieved for $I_1/I_p \sim 25\,\%$ (Ref. 2). Our power supplies are being upgraded in order to attempt full suppression and to more thoroughly characterise the above observations. The striking experimental results, however, have been first the non-resonant nature of this stabilization, which occur independently of coil helicity (Figs. 1 A, 2 A), and second that disruptions are not induced for currents as high as $6\,kA$. Numerical field line tracing on smooth peaked profiles with $q(0) = 0.7$, and with $q(a) = 3.5$ and radius of inversion $r_1 = 9\,cm$ as observed, show global stochasticity as the $1/1$ and $2/1$ islands overlap when $I_1 = 6\,kA$. We do not then believe that we have peaked q-profiles on Tokoloshe. Further, island size for peaked profiles is strongly dependent on coil resonance so that our observations do not directly implicate the $1/1$ island in sawtooth suppression as in the Kadomtsev crash theory. Field line tracing does however reveal that flux surfaces are given a $1/1$ helical shift Δ_h by the $\ell = 1$ coil. Δ_h is found to be approximately constant for given q and a wide range of flat, peaked and shifted equilibria, to scale linearly with I_1, and to undergo a resonance at $q = 1$. Fig. 5 shows Δ_h against q for flat q profiles at $6\,kA$. It is seen that the resonance width depends on helicity but that Δ_h can in either case be large for $q \to 1$. Flux surfaces can then in principle have a structure reminiscent of the $1/1$ internal kink mode in modern sawtooth crash theory (Ref. 3) if $q \sim 1$ and flat inside, but sheared outside, the radius of inversion. In terms of that theory, sawtoothing persists as observed because the stabilizing effect of line bending remains small for $I_1 \sim 6\,kA$ but the radial shift to the $q = 1$ surface of the magnetic axis in the crash is reduced by Δ_h, thus reducing $\Delta A/A$. The resonance width in q for helically non-resonant mode suppression is $\mid 1 - q \mid \sim 10^{-3}$ (Fig. 5) consistent with theory. Our single soft X-ray diode is presently being supplemented by a diode array in order to directly detect this shift.

Conclusion Preliminary observations with the $\ell = 1$ helical coil are then tentatively consistent with equilibria with low shear central q profiles, and do not seem to support the $1/1$ island growth of the Kadomtsev model. Profile modification at low B_T may occur which suggests a competing mechanism for sawtooth suppression that requires further investigation.

References

[1] Roberts, D.E. et al these proceedings

[2] McGuire, K M et al. 9th Eur. Conf. Contr. Fusion and Plasma Phys. Oxford, 93 (1979)

[3] Aydemir, A.Y. Phys. Rev. Litt. **59**, 649 (1987).

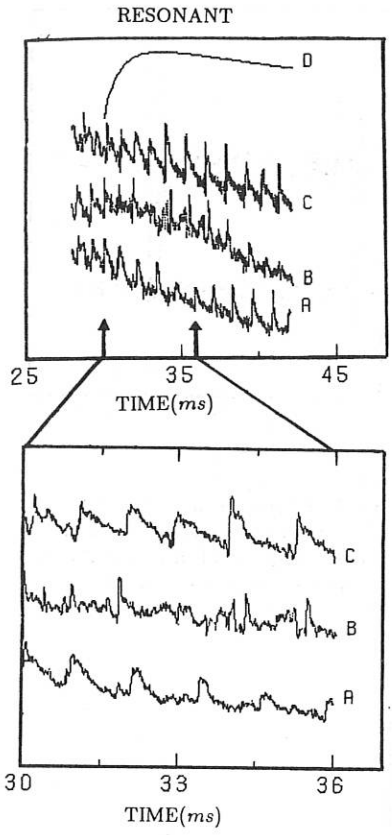

Figure 1: Effect of the $\ell = 1$ coil on $\Delta A/A$ for the case of resonant helicity:
A. $I_1 = -6\,kA$
B. $I_1 = +6\,kA$
C. A reference case with $I_1 = 0$
D. I_1 coil current ($I_{max} = 6\,kA$)

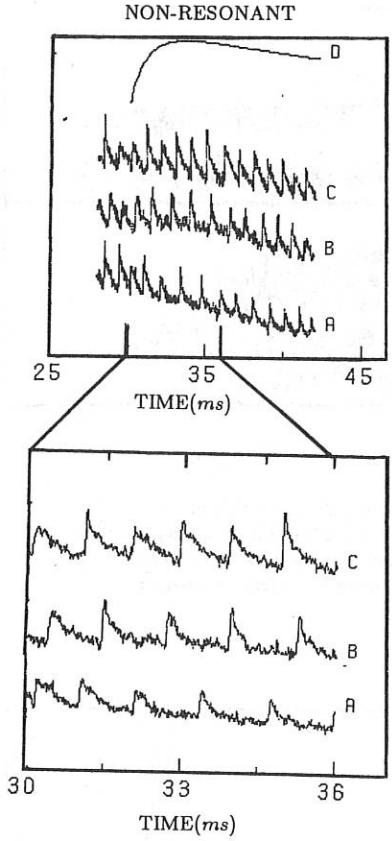

Figure 2: Effect of the $\ell = 1$ coil on $\Delta A/A$ for the case of non-resonant helicity:
A. $I_1 = -6\,kA$
B. $I_1 = +6\,kA$
C. A reference case with $I_1 = 0$
D. I_1 coil current ($I_{max} = 6\,kA$)

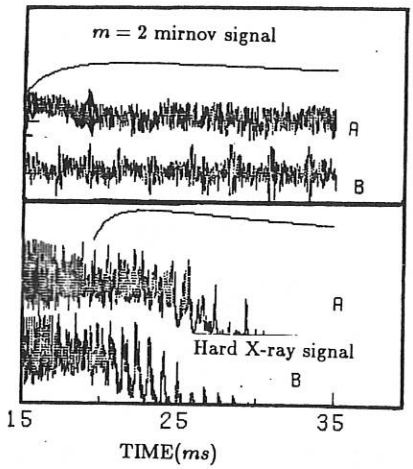

Figure 3: The effect of the $\ell = 1$ coil on the $m = 2$ Mirnov sawtooth modulation and hard X-ray sawooth modulation (cases A) compared to reference cases (B).

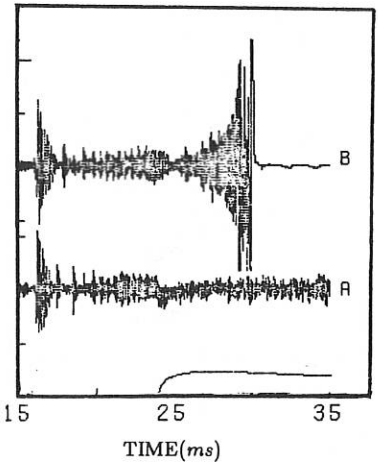

Figure 4: Change of $m = 2$ Mirnov amplitude and extension of the pulse length by application of the $\ell = 1$ helical perturbation (A) compared to a reference case (B).

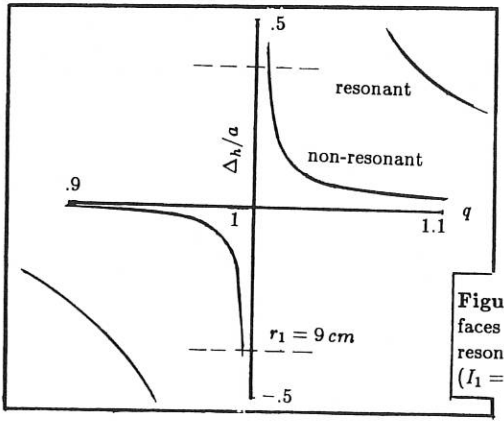

Figure 5: Helical displacement of flux surfaces for equlibria with flat q profiles for resonant and non-resonant $\ell = 1$ windings ($I_1 = 6\,kA$).

MODE LOCKING WITH A RESONANT HELICAL ℓ=2 COIL ON TOKOLOSHE TOKAMAK

D E Roberts, J D Fletcher, D Sherwell, G Nothnagel, J A M de Villiers, D F B Louw and J R O'Mahony.

Atomic Energy Corporation of South Africa

Introduction

Interest in the possibilty of control of the 2/1 tearing mode in tokamak plasmas has led to studies of the effect of external current carrying windings on ATC, Pulsator, Tosca, JIPP-TII, HT-6B and TBR1. We report here the first results obtained with a resonant ℓ=2 winding on "Tokoloshe" tokamak.

Experimental Details

The ℓ =2 winding is one of three (ℓ=1, 2 and 3) installed on Tokoloshe for instability studies [1]. A winding law $\theta=\Phi/2+48^{\circ}\sin\theta$ was chosen to minimize in particular the 3/1 sideband and measurements have been made with ℓ=2 pulses of ≤4.5kA and ≤30ms duration. The target plasmas had peak current I_p~120kA and duration ~45ms [2]. In particular two phases of the discharge were studied: (A) near peak I_p when q(a)~3, q(0)>1 and $\tilde{B}_\theta(2/1)/B_\theta$ was large (>1%) and (B) during strong gas puffing later in the discharge when q(a)~3.5, $\tilde{B}_\theta(2/1)/B_\theta$ was small (<0.1%) and $\tilde{B}_\theta$ was strongly modulated by sawtoothing. Two resonant and two non-resonant combinations of directions of B_T, I_p and I_2 have been studied so far (Fig 1).

Results and Discussions

The first effect seen with increasing I_2 is a marked distortion of the 2/1 Mirnov signal from a Fourier analysing coil (FAC). With sufficiently large I_2 mode locking occurs while further increase of I_2 leads to a major disruption.

During phase (B), measurements were made of the time to disruption, t_d, from the start of the ℓ=2 pulse, as a function of I_2. The reference plasmas (I_2=0) disrupt reproducibly with t_{do}=12.5 ± 1.5ms. For the non-resonant configuration (+-+) no effect on the plasma was seen and $t_d \sim t_{do}$. For (+++), t_d decreases when I_2 is above a certain level [Fig 2]. If we postulate that a critical island size Δ_{2c} must be exceeded for a disruption, and if the field penetration time to r_2 is t_R,

$$I_2(1-e^{-td/tI})(1-e^{-td/tR})=I_{2c}\alpha\,\Delta^2_{2c}$$

where t_I is the rise time of the ℓ =2 pulse. Fitting this relation to the measured t_d versus I_2 (Fig 2) yields estimates of t_R and I_{2c}: t_R=3.9ms, I_{2c}=800A. For (++-) we get a similar curve and t_R=3.4ms, I_{2c}=1200A. The estimated t_R

are consistent with the vacuum chamber field penetration time of ~0.7ms and a Spitzer time to r_2 of ~3ms. The different values of I_{2c} for (+++) and (++-) are believed to be due to the different orientations of the islands at the limiter in the two cases. For the lower I_{2c}, one island is on the side where the flux surface, measured with Hall probes, touches the limiter. The island sizes predicted by Poincaré plots for a given I_{2c} are consistent with disruption (large islands approaching the limiter and with extensive regions of stochasticity) within the uncertainties imposed by q'.

The behaviour of the 2/1 mode in phase (A), for a reference shot (I_2=0), is shown in Fig 3(a). $\tilde{B}_\theta$(a) reaches large values (~20G, see Fig 4) which are normally about the size observed before a major disruption on Tokoloshe. Indeed, a slight deterioration of wall conditions can lead to a minor or major disruption near peak $\tilde{B}_\theta$(a). The estimated maximum island width is W=2(a-r_2), where r_2 is the radius of the q=2 surface, and so is consistent with this, though errors due to uncertainty in q' are about a factor of two. When $\tilde{B}_\theta$ is large, poloidally asymmetric slowing down of the mode is observed and sometimes complete locking. The poloidal asymmetry is probably due to the outer flux surface leaning on the inside of the limiter.

Applications of a resonant (+++) ℓ =2 pulse with $\tilde{B}_\theta(\ell=2) \gtrsim \tilde{B}_\theta(2/1)$ leads to mode locking (Fig 3(b) and (c)). The time to lock is quite reproducible and the ℓ =2 pulse was switched off soon after the lock for these results. This normally leads to re-rotation of the mode though the lock duration is not too reproducible, at least for large $B_\theta(2/1)$. The orientation of the FAC is such that for the (+++) configuration the mode always locks following a positive half cycle of B_θ and restarts with a negative half cycle. For (++-) this is reversed (Fig 3(c)), as expected (Fig 1). Preliminary comparisons with the mode locking theories of Nave and Wesson [3] and Hender et al [4] show satisfactory quantitative agreement.

Integration of $\tilde{B}_\theta$ to give $\tilde{B}_\theta$ shows clearly that only the velocity and not the amplitude is strongly effected by the ℓ=2 coil (Fig 4). We have found an operating region where the B_θ amplitude is reduced (by $\leq$ 30%) by the ℓ=2 pulse but this is not routinely observed.

Attempts to suppress the 2/1 mode by applying reversed I_2 to a mode locked as above have not yet proved successful. The locked mode is in an unstable equilibrium with respect to the second I_2 pulse, which tends to rotate it so that the fields are no longer cancelling.

The disruptions produced by the ℓ=2 coil normally show no $\tilde{B}_\theta$ precursor signal above the noise level, or indeed any other precursor signals. The disruption is marked by a sudden loss of runaway electrons and a rapid decrease in soft X-ray intensity. Presumably, some cases of precursorless disruptions seen in other tokamaks could be due to locked modes - caused however by field inhomogeneties rather than externally applied radial fields as

here. The onset of mode locking is found to give distinctive signatures on other diagnostics than $\tilde{B}_\theta$, including a reduction in Hα intensity and Langmiur probe saturated ion current and a pronounced reduction in hard X-ray intensity.

References

[1] D.P. Coster, J.A.M. de Villiers, J.D. Fletcher, G. Nothnagel, J.R. O'Mahony, D.E. Roberts, and D. Sherwell, in Controlled Fusion and Plasma Phys. (Proc. 14th Eur. Conf. Madrid, 1987), vol 1, 240.

[2] D.E. Roberts, J.A.M. de Villiers, J.D. Fletcher, J.R. O'Mahony and A. Joel, Nucl. Fusion 26 (1986) 785.

[3] M.F.F. Nave and J.A. Wesson, in Controlled Fusion and Plasma Phys. (Proc. 14th Eur. Conf. Madrid, 1987), Vol 3, 1103.

[4] T.C. Hender, G.G. Gimblett and D.C. Robinson, in Controlled Fusion and Plasma Heating (Proc. 15th. Eur. Conf. Dubrovnik, 1988) Vol 1, 437.

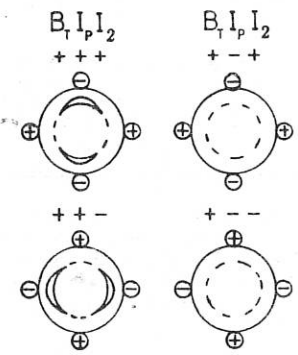

Fig. 1.
Different combinations of directions of B_T; I_p and I_z.

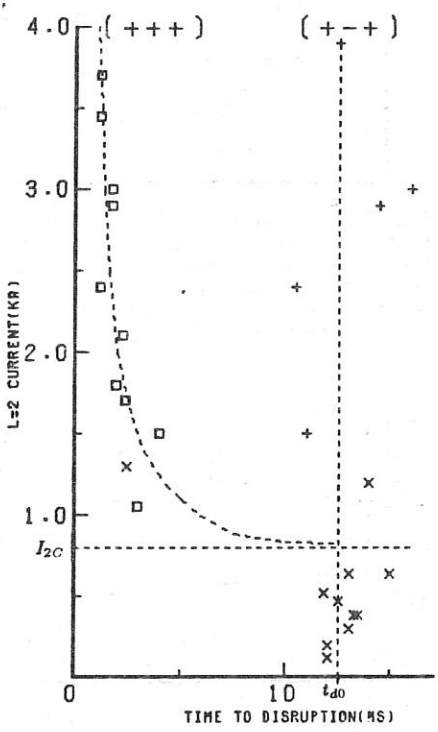

Fig. 2.
Disruption characteristics for (+++) and (++-) configurations. The disruption time t_{d0} is a Characteristic of the reference shot.

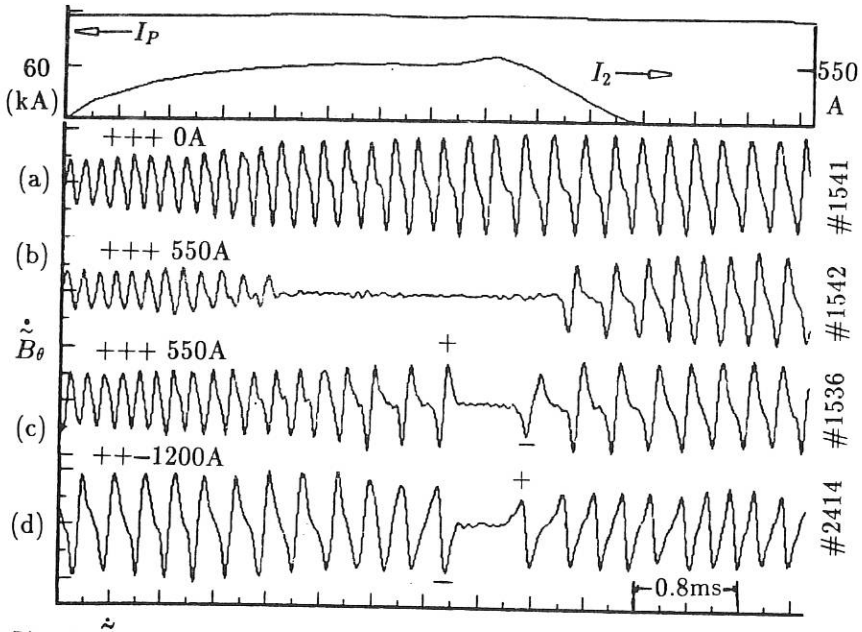

Fig. 3. $\dot{\tilde{B}}_\theta$ signals showing mode slowing down and locking. (a) Reference, (b) and (c) (+++) and (d) (++-) configurations. Note that the (+++) configuration leads to slowing down and locking in phase with the tendency to lock even with I_2=0 (a) and that the duration of the locked phase is B_θ amplitude dependant. For the (++-) configuration (c) the change in phase imposed on the natural slowing is clearly seen.

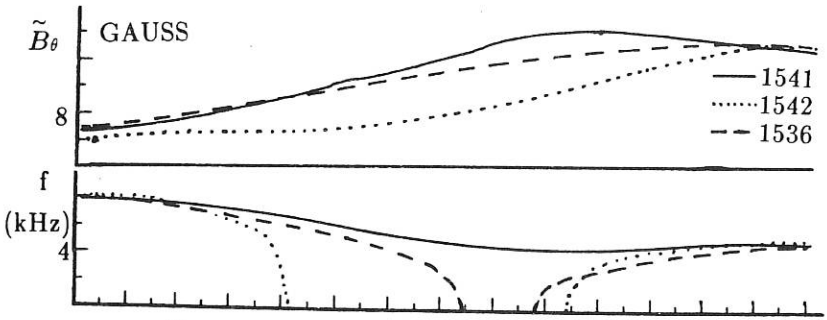

Fig. 4.(a) $\tilde{B}_\theta$, from integration of $\tilde{\dot{B}}_\theta$, showing no clear reduction in amplitude of the 2/1 mode during ℓ=2 induced locked phases of different duration. (b) The mode frequency averaged over a poloidal cycle.

SPECIFIC TURBULENCE ASSOCIATED WITH SAWTOOTH RELAXATIONS IN TFR PLASMAS.

F. GERVAIS, D. GRESILLON, P. HENNEQUIN, A. QUEMENEUR and A. TRUC

PMI - ECOLE POLYTECHNIQUE - PALAISEAU (FRANCE)

J. ANDREOLETTI, C. LAVIRON and J. OLIVAIN

DRFC/SPPF - C.E.A.-CEN CADARACHE (FRANCE)

INTRODUCTION

Recently we reported [1, 2] the existence of a specific turbulence during the sawtooth relaxation which superimposes the quasi-stationary (QS) turbulence.

Experimentally it corresponds to bursts of fluctuations observed on the high frequency side of the QS spectrum. The bursts appear synchroneously with the relaxation and globally last 60 μs. It has been shown that the specific fluctuations cover the 0.4 to 3 MHz domain depending on the wave number and, at least, the 3 to 17 cm^{-1} observed wave number range. In this range, the k spectrum follows a $k^{-5\pm1}$ rapidly decaying variation The phase velocity of this turbulence is typically 8.10^3 m/s, i.e. 4 times higher than the one of the QS turbulence.

A CO2 coherent scattering diagnostic is used to perform the experiments. The scattering volume consists on a vertical chord which is radially scanned. The presently reported experiments, performed on TFR Tokamak, concern k = 5 or 7 cm^{-1}. A careful analysis of the temporal amplitude variation lets us define three stages in the turbulent process (Fig.1), in agreement with the soft X Ray signals. Each stage typically lasts 20μs. The first stage is associated with a displacement of the hot core. The increase of fluctuations amplitude is clear but modest. The second stage coincides with the main crash of the emissivity signal. Its amplitude is large. Finally, a third stage coincides with the reorganisation process during which the central region of the plasma recovers its symmetry. During this phase, the amplitude and spectrum of the turbulence are comparable with the ones of the first phase. The following reported data is uniquely concerned with the second phase and our attention is focused on the spatial localization of the specific turbulence.

SPATIAL LOCALIZATION

The specific turbulence power $\Delta S(\omega)$ is defined as the difference between the instantaneous spectrum and the average QS spectrum. By radially scanning the scattering volume, the frequency integrated specific turbulence power $\Delta\tilde{n}^2$ is measured and gives us Fig.2. From the scattered dots a first conclusion is drawn: the specific fluctuations only exist at the interior of the q=1 surface. The large dispersion of the points lets us suspect that a hidden parameter plays an important part.

Azimutal Localization

By following the m=1 precursor mode, observed on the soft X ray signals just at the interior of the inversion radius ($r < r_1$), the azimutal position of the cold side at the beginning of the first phase (fast displacement of the hot core) is noticed as Θ. We define a radius r_0 where the turbulence is supposed to be maximum. From the raw experimental points on Fig.2 we took r_0 = 3cm. Then Θ_0 is the azimutal angle of the r_0 circle intersection with the axis of the scattering volume. The amplitude of the specific fluctuations $\Delta\tilde{n}^2$ is symmetrical in $(\Theta - \Theta_0)$ and then Fig.3 can be presented as a function of $(\Theta - \Theta_0)^2$. The amplitude drastically depends on $(\Theta - \Theta_0)^2$, following an approximately exponential law. It is maximum for $\Theta = \Theta_0$ with an experimentally observed half width of ~ 60°. We conclude that the turbulence is azimutally localized on the cold side.

Radial Localization:

If we add in Fig.2 the points obtained by extrapolating to the maximum of the fluctuations (i.e. for $\Theta = \Theta_0$), we get an envelop (the dashed line on Fig.2). From this azimutal and radial analysis we conclude that the fluctuations exist in a cell localized around a ring of radius $r_0 \sim 2.5\ \text{cm} \sim r_1/2$.

Numerical Model:

The experimentally observed signals are the result of several convolutions. To estimate with more care the spatial parameters of the turbulence cell, we try to adapt a spatial level model decaying in both the r and Θ directions with gaussian profiles. Several hypothesises concerning the k spectrum of the turbulence have been tested. These are: isotropic turbulence, radial k_r turbulence, and azimutal k_Θ turbulence. The results of the analysis are compared with the experiment and we conclude:

- The turbulence cell is located on the cold side.
- Its azimutal half width is 60 ± 8° (for k = 5 cm^{-1})
- An isotropic spectrum in an asymmetrical cell (asymmetrical gaussian function) with r_0 = 2 cm, Δr_i = 0.3cm in the interior direction and Δr_e = 2 cm in the exterior direction gives satisfactory comparison; however, whereas a pure k_r spectrum is definitively discarded, a k_Θ spectrum with r_0 = 3 cm, $\Delta r_i = \Delta r_e$ = 2 cm is also possible.

Heat Flux

The heat flux outside the q=1 surface is not azimutally symmetrical. Analysis of the soft X rays signals lets us define the azimutal direction in which the heat flux appears "sooner and faster". Assuming a constant rotation velocity of the hot core, the heat flux appears to be directed 130° away of the hot side i.e. apparently at one corner of the turbulence cell. If we share Andreoletti's model [3] ,the plasma rotation would be modified by the turbulent kink. The edge part ($r < r_1$) rotation slows down whereas the one of the most central part speeds up, producing a twisted state. Under these conditions, the direction of the "sooner and faster" heat flux agrees with the central position of the turbulence cell (Fig. 4).

With the same approach we observe a temporal and spatial localization of some turbulence in conjunction of the q=2 minor disruptions.

CONCLUSION

A cell of turbulence, localized in the interior of the q=1 surface with an azimutal full width extension of about 120° has been detected and analysed. Its life time coincides with the collapse of the sawtooth. These observations are in fair agreement with the so called "magnetodrift" turbulence in the sawtooth disruption model proposed by Andréoletti.

REFERENCES

[1] Equipe TFR , A Truc

C.R. Acad. Sc. Paris, T 304, Série II, n°7 (1987).

[2] J. Andréoletti, F. Gervais, J. Olivain, A. Quéméneur, A. Truc, D. Grésillon

EUR-CEA-FC 1336 (1988); accepted for publication in Plasma Physics and Controlled Fusion.

[3] J. Andréoletti

International Workshop on "Turbulence in MHD flows" Cargèse (France) 1988 (to be published by Elsevier) and in this conference (P2 A3 5).

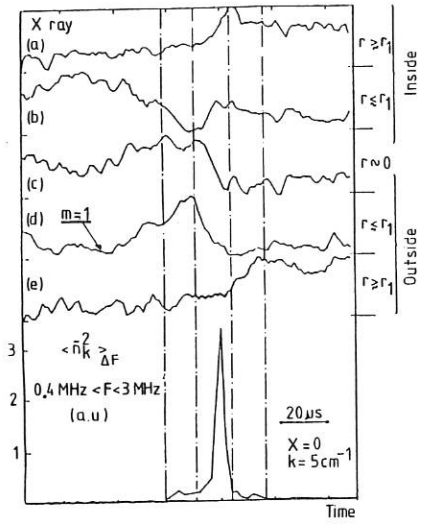

Fig.1 Temporal analysis

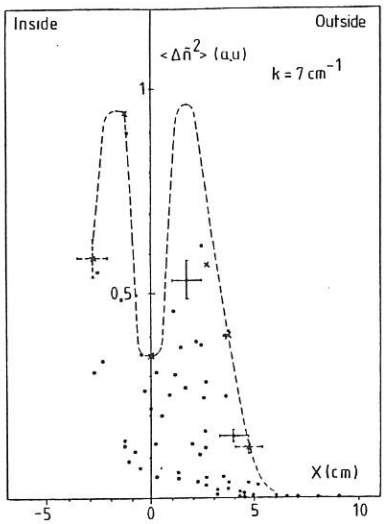

Fig2 Radial analysis

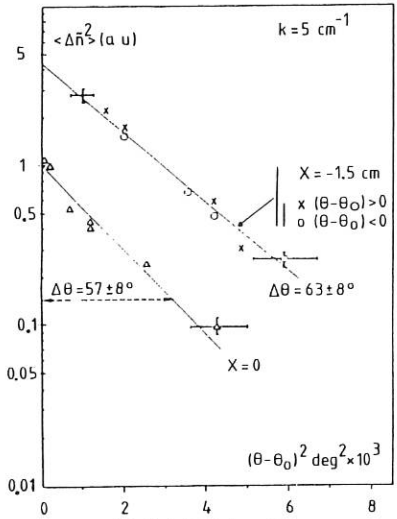

Fig.3 Azimutal analysis

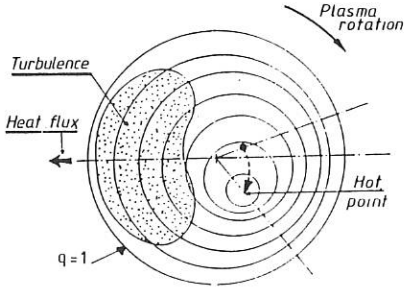

Fig. 4. Spatial localization during the collapse

(TFR plasma rotation is fast. Thus twisting is expected to be strong. ~ 50°)

IDEAL BALLOONING STABILITY OF JET DISCHARGES

R.M.O. Galvão[1], J.P. Goedbloed[2], G. Huysmans[2], E. Lazzaro,
J. O'Rourke, G. Schmidt[3], P. Smeulders.

JET Joint Undertaking, Abingdon, Oxon., OX14 3EA, UK.
[1]Instituto de Pesquisas Espaciais and Universidade de São Paulo, Brazil
[2]FOM-Instituut voor Plasmafysica, Nieuwegein, The Netherlands
[3]Princeton Plasma Physics Laboratory, Princeton, New Jersey, USA

INTRODUCTION

Conditions under which ballooning modes are expected to be excited have recently been obtained in two different types of discharges in JET. In the first type, discharges with β approaching the Troyon-Sykes-Wesson critical value β_c for optimised pressure profiles have been produced at low toroidal fields ($B_T \approx 1.5T$). In the second type, extremely high pressure gradients have been produced in the plasma core through pellet injection in the current rise phase of the discharge followed by strong additional heating [1]. The stability of these discharges has been studied with the stability code HBT [2] coupled to the equilibrium identification code IDENTC [3].

The equilibrium pressure and diamagnetic function profiles are determined in IDENTC by an optimisation procedure to fit the external magnetic measurements. The resulting pressure profile in the equatorial plane is then compared with the profile derived from 'direct' measurements, i.e., electron density and temperature profiles measured by the LIDAR diagnostic system [4], ion-temperature profile measured by the charge-exchange diagnostic system [5], and ion density profile calculated from the Z_{eff} and electron density profiles. Furthermore, the value of the safety factor q on axis is compared with that determined from polarimetry [6]. When good agreement is found, the output data from IDENTC is passed directly to HBT to carry out the stability analysis. When there is not a good agreement, as in the case of pellet discharges with highly peaked pressure profiles, the equilibrium is reevaluated using the 'experimental' profile and the data from polarimetry.

HIGH-β DISCHARGES

A series of discharges at low plasma current and low toroidal field ($I_p \approx 1.5MA$ and $B_T \approx 1.5T$) with strong ion cyclotron heating have been produced in JET to attempt reaching the critical value $\beta_c \approx 0.028\ I_p(MA)/a(m)\ B_T(T)$ of β for ideal MHD stability. In Fig.1 we show the experimental data for shot 14729 which has one of the highest values of the ratio β/β_c obtained so far, viz., $\beta/\beta_c \approx 0.6$. We note that after t = 47s the central electron temperature starts to show some spikes superimposed on the usual sawteeth. These spikes are well correlated with the MHD activity measured by external coils. Furthermore, the activity after t = 47.5s seems to increase for larger values of the toroidal mode number n. To investigate a possible role of ballooning modes, we have carried out a stability analysis at t = 48.0s, when LIDAR data are available. In Fig. 2 we show the pressure

profile determined by IDENTC normalised by the maximum electron pressure determined by LIDAR. There is no ion temperature profile available for this shot and for the stability calculations the magnitude of the total pressure is determined by the value of the poloidal beta, $\beta_I = 8\pi S\langle p\rangle/\mu_o I_p^2$, where S is the area of the cross-section of the plasma column and $\langle p\rangle$ the plasma average pressure. The plasma is found unstable in the central region indicated in the figure and becomes unstable by crossing the boundary of the first stability region. The unstable region is localised inside the q = 1 surface and thus the consequence of the instability is probably to help trigger the sawtooth crash.

DISCHARGES WITH PELLET FUELLING

Discharges with strong pressure gradients (dp/dr > 300kPa/m) have been produced in JET with pellet injection followed by strong additional heating. In Fig. 3 we show the experimental data for shot 17749. The pellet is injected at t = 42s, during current rise, followed one second later by strong heating. We notice that the value of β saturates at a constant value $\beta_I \simeq 0.4$ and that at t = 44.2s it starts to drop although the total heating power is approximately constant. This drop in the value of β_I is strongly correlated with an initial increase in the n = 4 MHD activity followed by a sharp increase in the n = 2 coupled with the n = 3 activity, whereas there is no n = 1 activity. Analysis of the fast X-ray emission indicates that the n = 2 activity is related to an odd poloidal mode number $m \geq 3$. In Fig. 3a, iv we show also the trace of β_I for shot 17747. In this shot there was no pellet injection but the level of heating power was the same as in shot 17749. The pressure profile is much broader for the no pellet shot (Fig. 4a) and there is no drop in the value of β_I at constant heating power.

The stability of these discharges has been analysed using the experimental profiles and the value of $q_o \simeq 1.2$, determined by IDENTC from polarimetry data. Shot 17749 is found unstable around the regions of maximum pressure gradient, but stable at the centre. The discharge without pellet injection 17747 is stable. The unstable region in the shear vs pressure gradient diagram has been determined by increasing β_I while keeping constant the values of q_o and q_1 ($q_o = 1.2$; $q_1 = 4.07$ for shot 17747 and $q_1 = 3.83$ for shot 17749). Again the plasma becomes unstable by crossing the boundary of the first stability region. Because the unstable magnetic surfaces are localised in the middle of the plasma, one expects that the consequence of the ballooning instability to be just an enhanced transport in this region. The rate of decay towards a stable profile, is however, constrained by transport from the centre of the plasma and to the plasma boundary. This leads to the somewhat slow relaxation of the value of β observed experimentally.

CONCLUSIONS

High-β discharges have been shown to be ballooning unstable at the centre of the discharge although β is below the critical value given by the Troyon-Sykes-Wesson limit. The pellet discharge 17749 has been found to approach the unstable region for ballooning modes from the first stable region. Access to the second stability region would require a larger

pressure gradient and current profile control to keep $q_o > 1.2$.

REFERENCES

[1] The JET Team, 12th International Conference on Plasma Physics and Controlled Nuclear Fusion Research, Nice, France, 1988. Paper IAEA-CN-50/A-IV-1.

[2] J.P. Goedbloed, G.M.D. Hogweij, R. Kleibergen, J. Rem, R.M.O. Galvão and P.H. Sakanaka, Proceedings of the 10th International Conference on Plasma Physics and Controlled Nuclear Fusion Research, London, 1986, (IAEA, Vienna, 1987), Vol. II, p. 165.

[3] E. Lazzaro and P. Mantica, Plasma Physics and Controlled Fusion 30, 1735 (1988).

[4] H. Salzmann, J. Bundgaard, A. Gadd, C. Gowers, et al., Rev. Sci. Instrum. 59, 1451 (1988).

[5] M. von Hellermann, et al., Ion Temperature Profiles in JET, this conference, paper P4 A1 12.

[6] J. O'Rourke, J. Blum, J. Cordey, A. Edwards et al., Proceedings of the 15th Conference on Controlled Fusion and Plasma Heating, Dubrovnik, 1988, Europhysics Conference Abstracts 12B, Part 1, p. 155.

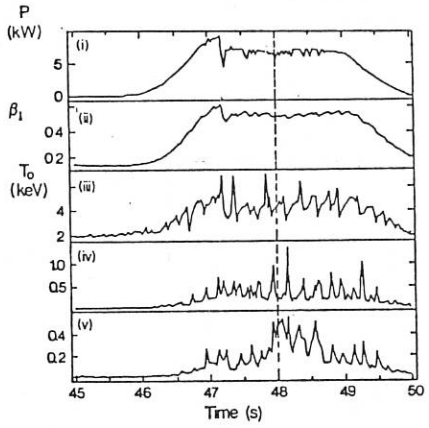

Fig. 1: Experimental data for #14729:
i) total radio-frequency power;
ii) Shafranov's poloidal beta;
iii) central electron temperature from electron cyclotron emission;
iv) n = 1 and
v) n = 3 MHD activity in arbitrary units.

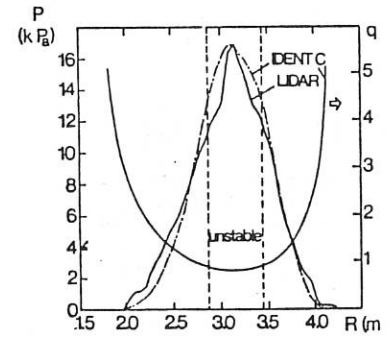

Fig. 2: Electron pressure profile measured by the LIDAR diagnostic system (full line) at t = 48s and corresponding renormalised total pressure and q profiles determined by the equilibrium code IDENTC. The indicated region is unstable to ballooning modes.

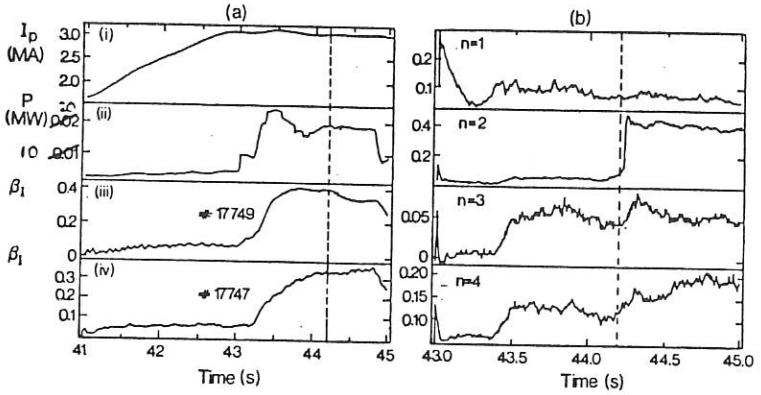

Fig.3(a): Experimental data for #17749: i) plasma current; ii) total heating power (NBI + ICRF + OHMIC); iii) & iv) Shafranov's poloidal beta (including trace for #17747). A 4mm pellet is injected at t = 42s in #17749; (b) MHD activity for #17749 (arbitrary units).

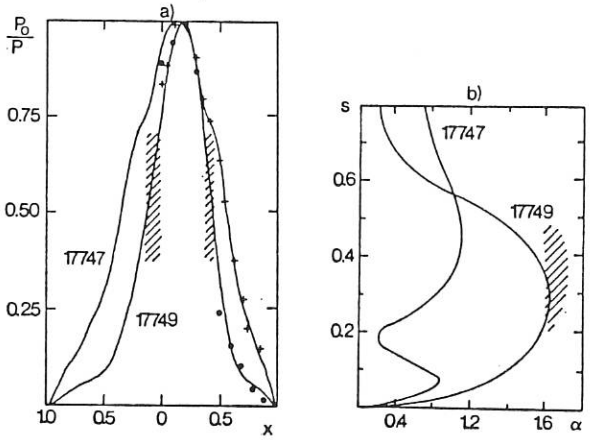

Fig.4(a): Normalised total pressure profiles for #17747 and 17749 used in the stability calculations. The horizontal axis is the radial position in the equatorial plane normalised to the half-width of the plasma cross-sections (a ≈ 1.18m). The crosses and dots represent the experimental pressure profiles for #17747 and 17749, respectively. The maximum pressures are approximately 75kPa for #17747 and 156kPa for #17749. The shaded region for shot 17749 is unstable to ballooning modes; (b) Corresponding $s = 2(\psi/q)(dq/d\psi)$ vs $\alpha = -(4q^{*2}/\epsilon B^2)\sqrt{\psi}\, dp/d\psi$ stability diagram, where $q^* = \epsilon B \int d\ell/\mu_o I_p$.

FISHBONE-LIKE EVENTS IN JET

M.F.F.Nave[1], D.Campbell,E.Joffrin,F.Pegoraro,F.Porcelli,
P.Smeulders,K.Thomsen

JET Joint Undertaking, Abingdon, Oxon, U.K.
[1] Laboratorio Nacional de Engenharia e Tecnologia Industrial, Sacavem, Portugal

Introduction

A variety of MHD activity has been observed in JET during auxiliary heating experiments. In particular, periodic bursts of oscillations detected in several diagnostics show signatures similar to that of the 'fishbone' instabilities /1/. Here we describe the characteristics of these instabilities, discuss the operating conditions under which they are observed, and compare these with the predictions of theory.

Observations

Additional heating experiments in JET have been carried out at total powers of up to 34MW. Two methods of auxiliary heating are employed: (co-directional) neutral beam injection (NBI), with up to 21MW of 80keV deuterons, and ion cyclotron resonance heating (ICRH) using (mainly) first harmonic heating of a minority species (H or ^{3}He) at powers up to 18MW. Both types of heating produce fishbone-like bursts. We believe that this is the first observation of such bursts in radio frequency heated plasmas.

'Fishbones' in JET occur as repetitive bursts lasting a few milliseconds , with a repetition time of ~ 10ms and are observed in electron cyclotron emission (ECE), soft X-rays (SXR) and magnetics diagnostics (figure 1). Sometimes continuous MHD oscillations are observed instead (figure 1). Both forms of activity are usually superimposed on sawtooth oscillations, although in a few cases bursts have been observed during the sawteeth-free periods /2/.

The frequency of the observed oscillations lies typically in the range 6-10 kHz for both ICRH and NBI discharges.(There are however exceptions of ICRH discharges with very low frequencies of ~ 1kHz and NBI discharges with frequencies as high as 20kHz). A typical burst and its frequency spectrum are shown in figure 2. For the NBI discharges, the frequency of the oscillations is of the order of the bulk rotation frequency, as determined by X-ray spectroscopy of Doppler-shifted impurity emission lines. However, such high frequency in the ICRH case is difficult to explain by the plasma rotation velocity. In these discharges it has also been observed that the frequency of the fishbone-like oscillation is ~ 3 times higher than the frequency of sawtooth precursor activity which is usually of the same order as the bulk rotation frequency /3/. Perhaps the closest similarity between our observations and those reported from PDX /1/ lies in the observed slowing down of the frequency of the MHD oscillation during a burst. It is found that the the decrease in frequency is faster when the the plasma current is higher. Magnetic mode analysis in ICRH and NBI discharges reveals an $n = 1$ toroidal component rotating in the direction of the plasma current, which is also in the direction of the ion diamagnetic drift. Magnetic poloidal structure cannot be precisely estimated, but tomographic reconstruction of soft X-rays (figure 3) and ECE signals shows an $m = 1$ kink centered on the sawtooth inversion radius. An $m = 2$, $n = 1$ component has also been observed outside the sawtooth inversion radius.

While the MHD characteristics of this activity exhibit similarities with those observed in PDX discharges, analysis of the effects of these bursts on fast particle populations in JET plasmas reveals no significant modification of the high energy plasma component which could be associated with the bursts (figure 4). The two principal diagnostics of fast particle distributions in JET are the neutral particle analyser (NPA) and the total neutron yield. Both show the influence of sawteeth and subordinate relaxations, the former by an enhanced level of charge exchange neutral losses following a sawtooth collapse, and the latter through a sawtooth modulation of the total neutron emission. However, no such effects are observed during fishbone-like bursts, at least not within the time resolution of the relevant diagnostics. It is possible that the larger size of the JET plasma leads to confinement of the fast particles which are predicted to be resonantly scattered by the instability /4,5/. An alternative explanation migth be the low amplitude of the poloidal field fluctuation associated with the bursts ($b_p / B_p \sim 10^{-4} - 3 \times 10^{-4}$). It should be noted that a fall in neutron

production is observed during continuous MHD activity. However, this can probably be explained as a result of the observed decrease in temperature associated with such activity.

Fishbone-like bursts are observed over a wide range of the JET operating space. They occur in both the L and H confinement regimes and are more common at low values of the edge safety factor q (or high values of plasma current). Since $\beta_p \alpha I_p^{-2}$, the rather unexpected result is that this activity is often observed at low rather than high values of β_p , though there appear to be a threshold value of $\beta_p \sim 0.1$ for their occurrence (figure 5). It has also been observed that the fishbone-like activity occurs at low β_p compared to that of sawtooth-free regimes. The influence of the bursts on plasma confinement is still being assessed. While, in certain regimes, high current discharges are found to have lower confinement than that predicted by the Goldston L-mode scaling, it is not clear that this should be associated with enhanced levels of MHD activity, rather than, say, heating deposition profile effects.

Theoretical considerations

Theory models /4,5/ suggest that the fishbone instability is caused by the resonance between an m = 1, n = 1 mode and trapped energetic ions inside the q = 1 surface. These trapped energetic ions can be either produced by neutral beam injection or can be accelerated by ICRH waves.

It has been recently shown /6/ that fishbones and sawtooth supression in the presence of energetic ions are intrinsically related as both phenomena can be explained in terms of a single dispersion relation encompassing the resonant and non-resonant fast ion contributions. This is illustrated by fig.6, representing the stability plane identified by the parameters

$$\beta_p^* = -8\pi/(r_0^2 B_p^2 (r_0)) \int_0^{r_n} dr\, r^2\, dp/dr \qquad , \beta_{ph}^* = -8\pi/(r_0^2 B_p^2 (r_0)) \int_0^{r_n} dr\, r^{3/2}\, d(r^{1/2} p)/dr$$

where β_p^* is the beta poloidal of the bulk plasma , and β_{ph}^* is the beta poloidal of the hot ions, both calculated at the position of the q = 1 surface, $q(r_0) = 1$. The stable regime lies below the solid line,extending to values of β_p^* as high as three times the ideal MHD m = 1 instability threshold, β_p^{mhd} /7/ (in fig.6 we have assumed $\beta_p^{mhd} = 0.2$). Fishbone oscillations are excited just outside the stable domain. The fishbone frequency in the plasma rest frame is predicted to range between the ion diamagnetic frequency, $\omega_{*_i} = (cT_i/(eBr_0 p))\, dp/dr$,for low values of β_{ph}^* /5/, and the fast trapped ion precession frequency, $\overline{\omega}_{Dh} = c E_h/(eBr_0 R_0)$ with E_h the average fast ion energy, for high values of β_{ph}^* /4/. Further away from the stable domain (i.e. outside of the dashed lines in fig.6) ideal MHD internal kink are unstable. (Values of $r_0/a = 0.4$ and of $\omega_{*_i}/\overline{\omega}_{Dh} = 0.2$ have been assumed in fig.6.) The stable domain shrinks considerably as the q = 1 radius is increased. In addition β_p^{mhd} is lower at large r_0 /7/. These considerations may account for the increasing difficulty in stabilising sawteeth and for the more likely occurrence of fishbones at high currents, as roughly $r_0 \alpha 1/q$. Also, for comparable values of β_{ph}^* , fishbones on the high frequency side of the spectrum can be expected to be more easily excited at high currents. The stable domain disappears as ω_{*_i} becomes comparable to $\overline{\omega}_{Dh}$ Then, the fishbone frequency becomes tied to ω_{*_i} (The conditions for fishbones excitation in this regime have been discussed in Ref.5.).

Comparison between the theory and the experimental results is complex because of the difficulties associated with the determination of the fast ion profiles (entering β_{ph}^* ; note that the pressure of the fast ions can be slightly hollow near the axis for the minority ions, specially during off-axis ICRH heating), and the plasma gradients at the q = 1 surface. In addition, the plasma rotation frequency ,which accounts for a Doppler shift in the predicted mode frequency, is estimated with uncertainties. Here we shall mention three examples:

(i) a slow frequency ICRH pulse (#14010, $P_{RF} \approx 7$MW, $I_p \approx 3$MA),
where $\omega_{*_i} \approx 3\times10^3\ s^{-1}$, $\overline{\omega}_{Dh} \approx 5\times10^4\ s^{-1}$ (assuming $E_h \approx 0.5$ MeV) and $\omega \approx 2.5\times10^3\ s^{-1}$;

(ii) a combined ICRH + NBI pulse (#15750, $P_{RF} \approx 8$MW, $P_{NBI} \approx 5$MW, $I_p \approx 6$MA),
where $\omega_{*_i} \approx 0.8\times10^3\ s^{-1}$, $\overline{\omega}_{Dh} \approx 7\times10^4\ s^{-1}$ (assuming $E_h \approx 0.5$ MeV) and $\omega \approx 1.6\times10^4\ s^{-1}$; and

(iii) an NBI pulse (#16883, $P_{NBI} \approx 13$MW, $I_p \approx 4$MA),
where $\omega_{*_i} \approx 7\times10^3\ s^{-1}$, $\overline{\omega}_{Dh} \approx 1\times10^4\ s^{-1}$ (assuming $E_h \approx 40$ keV) and $\omega \approx 5.6\times10^4\ s^{-1}$

In example (i) we have an ICRH discharge consistent with values of β_p^* and β_{ph}^* to the left of the stable domain, where the predicted frequency is $\omega \sim \omega_{*_i}$ .In the NBI examples (ii) and (iii), ω is of the order of the plasma rotation frequency, so the corresponding mode frequency in the plasma rest frame is difficult to determine. The second example shows an intermediate frequency,

$\omega_{*_i} < \omega < \omega_{Dh}$. In the third case, the frequency is higher than the characteristic frequencies. However since $\omega_{*_i} \sim \omega_{Dh}$, the expected rest frame frequency is also of the same order.

References

/1/ K. McGuire et al., Phys. Rev. Lett. 50,891 (1983)
/2/ D.J. Campbell et al., Phys. Rev. Lett. 60, 2148 (1988)
/3/ D. Stork et al., Procc. 14th EPS Conference vol.I, p.306 (1987)
/4/ L.Chen, L.B. White and M.N.Rosenbluth, Phys. Rev. Lett. 52, 1122 (1984)
/5/ B. Coppi and F. Porcelli, Phys. Rev. Lett. 57, 2722 (1986)
/6/ F. Pegoraro et al., IAEA-CN-50/D-4-6 (Nice, 12-19 October 1988)
/7/ M.N.Bussac et al., Phys. Rev.Lett. 35, 1638 (1975)

Figure captions

Figure 1 - Temperature and ICRH power versus time for a discharge showing both bursts and continuous oscillations. Both types of activity are out of phase on each side of the centre indicating an m = 1 mode.

Figure 2 - Magnetic signal of a fishbone-like event and its power spectrum showing a peak frequency at 9kHz.

Figure 3 - Soft X-ray emission reconstruction showing an m = 1 structure associated with a fishbone-like oscillation.

Figure 4 - Neutron flux and temperature versus time. No change in Φ_n is observed associated to the bursts seen in the T_e trace.

Figure 5 - Total diamagnetic beta poloidal versus the total input power for fishbone-like events observed during the first 6 months of 1988.

Figure 6 - Stability regimes in the β_p^* - β_{ph}^* plane (see definitions in the text). The 'stable' area corresponds to the sawtooth-free domain, outside of which the fishbone domains are indicated.

Figure 1

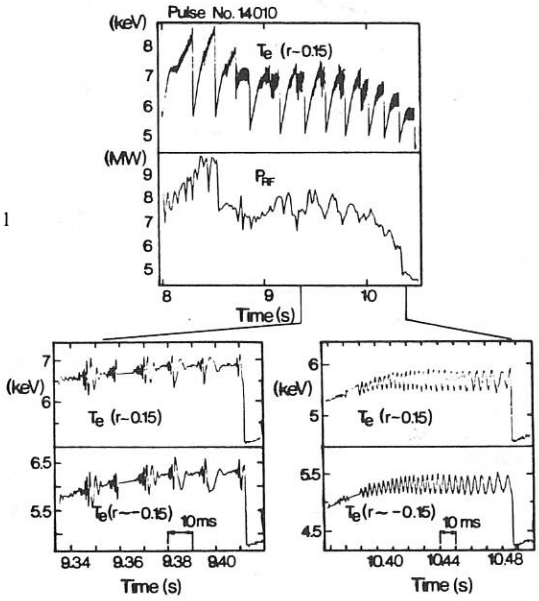

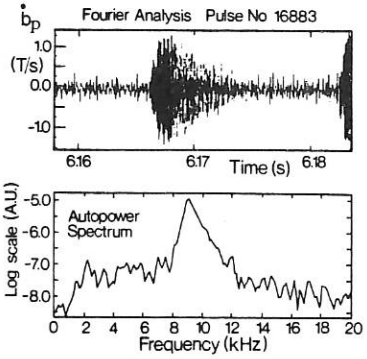

Figure 2

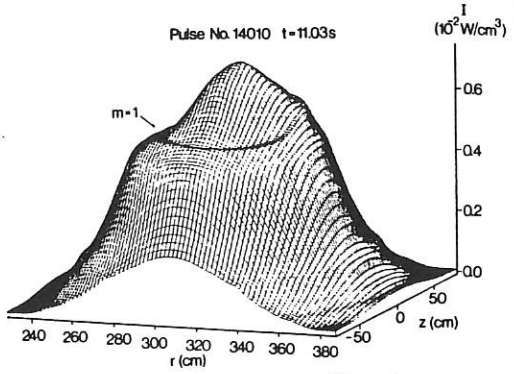

Figure 3

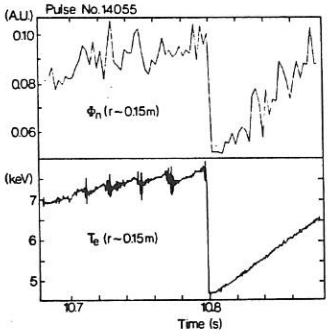

Figure 4

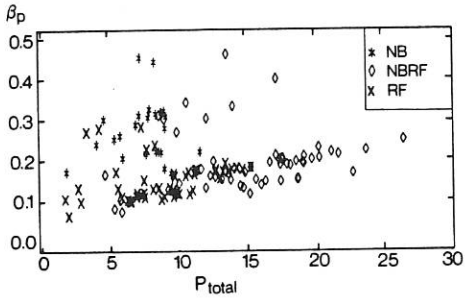

Figure 5

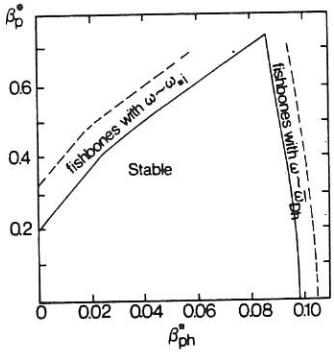

Figure 6

SAWTEETH AND THE m=1 MODE IN JET

D J Campbell, A W Edwards and D Pearson[1]

JET Joint Undertaking, Abingdon, Oxon, OX14 3EA, U K
[1] *Imperial College of Science and Technology, University of London, U K*

Introduction – Sawtooth activity in JET exhibits considerable complexity, the sawtooth cycle being interrupted by a variety of mhd phenomena: subordinate relaxations, 'fishbones' and quasi–continuous mhd oscillations. However, detailed experimental investigations of the sawtooth collapse in JET have shown that the instability is not directly related to this activity, but occurs as a rapidly growing m=1 instability which leads to a convective flow in the plasma core and a rapid loss of energy from the central region[1]. Here we consider the relationship between the m=1 activity observed during the sawtooth cycle and the sawtooth collapse and discuss the implications of this relationship for theories of the sawtooth instability.

Observations – To investigate the detailed evolution of mhd structures in JET, soft X–ray tomography and ECE reconstructions have been used to analyse the evolution of the plasma during a sawtooth cycle. Two perpendicular soft X–ray diode arrays permit the reconstruction of the contours of X–ray emission from the plasma with a time resolution of 10 μs[1]. In addition, localised ECE measurements from a calibrated 12–channel grating polychromator are used to reconstruct two–dimensional contours of electron temperature by exploiting the rotation of mhd structures in the plasma and by using assumptions about the rotational symmetry of these structures[2] (in cases considered here, it is assumed that m=n). This effectively limits the time resolution of the technique to the rotational period of the structure in question, which, in JET, is usually 100 μs – 5 ms. While this allows slowly growing and decaying mhd activity (eg successor oscillations) to be analysed, the timescale of the sawtooth collapse (~100 μs) limits the application of the ECE technique during the collapse to plasmas with very high power NBI heating, where rotational frequencies ~20 kHz can be produced.

As reported previously[3-4], sawtooth activity in JET varies greatly, depending upon such factors as plasma density, current and heating regime. Nevertheless, the sawtooth collapse mechanism is independent of this variation[4-5] and, in particular appears to be independent of the presence or absence of precursor oscillations. The collapse leads to the formation of a hot crescent, as the plasma centre is displaced by a cold 'bubble', behaviour which closely resembles the model due to Wesson[6], which postulates that $|1 - q_0| \leq 10^{-2}$. This remains true even in cases where q_0 ~ 0.7, as is observed during sawtooth stabilization in JET[7-8]. Although it is rapidly cooled, the crescent may persist for tens of milliseconds after the collapse, causing successor oscillations. This behaviour is illustrated in figure 1, where, for the first time, it has been possible to compare the details of the collapse of sawteeth by two independent diagnostics. The dynamics of the collapse reconstructed from ECE are in striking agreement with that deduced using the soft X–ray tomography, and are a confirmation of the fact that the soft X–ray emission predominantly reflects the evolution of the electron temperature and, it is reasonable to conclude, that of the magnetic surfaces (as argued in [9]).

In some cases a structure resembling a magnetic island is observed in reconstructions of

successor oscillations to sawteeth and partial sawteeth[2]. This raises the question of what role, if any, is played by magnetic islands in the sawtooth instability. Figure 2 compares ECE reconstructions of successor oscillations for two sawtooth collapses. As indicated in the figure, these reconstructions are carried out for the first successor oscillation after the collapse. In case (i), the successor has the form discussed above, ie it is a warm crescent–shaped object. However, in (ii) the crescent–shaped object is cooler than the plasma core, resembling a magnetic island, and it is surrounded by a ring of warmer plasma which is the residue of the hot crescent formed by the displacement of the core.

Further investigation of cases such as (ii) suggests that the 'island–like' object is not involved in the collapse, but is simply the residue of a pre–existing island which has survived the collapse. Evidence for this can be deduced from figure 2(ii), where large precursor oscillation to the sawtooth collapse can be observed and where, furthermore, the successor oscillation to the collapse is in–phase with the precursor oscillation. ECE reconstructions of the precursors show the island–like structures in the plasma when difference techniques are used to 'enhance' the images. Although it has not yet been possible to follow the evolution of such an island through the sawtooth collapse, the fact that many sawtooth collapses occur without such structures strongly suggests that they are not an essential component of the sawtooth instability. Further evidence for such an interpretation comes from observations of the 'snake' perturbation in JET[10]. This phenomenon, believed to be caused by a magnetic island on the q=1 surface, is observed to persist through many sawtooth collapses. As in the cases considered here, it has not yet been possible to analyse the detailed evolution of the 'snake' through the collapse, and the nature of its interaction with the sawtooth instability remains open.

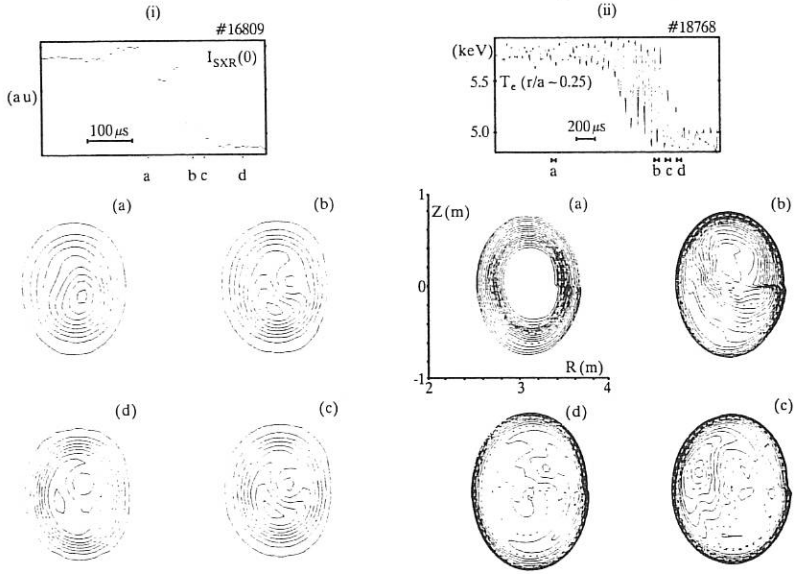

***Fig 1** : (i) Reconstruction of sawtooth collapse using soft X–ray tomography. (ii) Reconstruction of sawtooth collapse using ECE.*

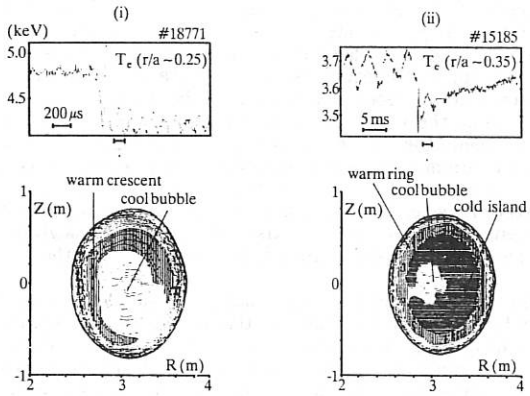

***Fig 2** : (i) ECE reconstruction of successor oscillation showing warm crescent structure. (ii) reconstruction of successor to another collapse showing cool island–like structure.*

The growth and decay of these magnetic islands during the sawtooth cycle can, however, be followed in detail, and figure 3 illustrates such a case. This shows that the island observed in the successor oscillation gradually reconnects in an annulus about the plasma centre on a timescale of ~50 ms, resulting in the formation of a flat shoulder in the electron temperature profile in the region of the sawtooth inversion radius, which presumably represents the location of the q=1 surface. Although the island does not reconnect the plasma centre, a small drop in the central temperature is often observed during this time. A remarkable aspect of the time development shown in figure 3 is that, as the annular reconnection approaches completion, a second, highly localised, island

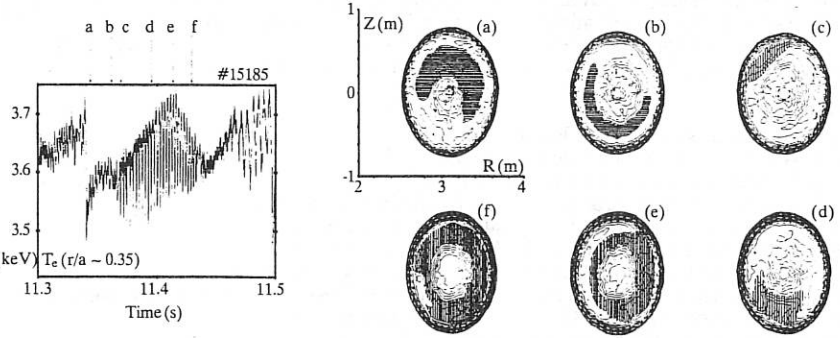

***Fig 3** : ECE reconstructions of mhd oscillations during sawtooth ramp phase showing cycles of island growth and reconnection in annulus about plasma core.*

emerges at the X–point of the old island (timeslices (c) to (f)). This new structure grows and again reconnects in a ring about the plasma centre. Once this reconnection is complete, the cycle recommences. There are several points to note here: firstly, that the cycle of island growth and reconnection is out of phase with the sawtooth cycle and, indeed, the sawtooth collapse does not appear to be related to a particular island amplitude; secondly, that the reconnection is always observed to occur in an annular region, and has never been observed to involve the plasma centre; thirdly, that although this behaviour is very common (it has previously been referred to as a 'slow' partial sawtooth[8]), it is not always present and, therefore, does not appear to be a necessary feature of the sawtooth cycle; finally, the existence of such islands throughout the sawtooth cycle suggests that a q=1 surface exists throughout the sawtooth cycle, a result which generalizes and confirms that obtained from observations of the 'snake'.

Discussion – While the results presented here clarify the phenomenology of the sawtooth cycle in JET, the fundamental problem, ie the nature of the sawtooth instability, remains unsolved. The striking agreement between soft X–ray and ECE reconstructions of the sawtooth collapse confirms the remarkable similarity reported previously between the observed behaviour and that predicted by the quasi–interchange model[6]. Nevertheless, this agreement appears paradoxical if a q=1 surface exists throughout the sawtooth cycle and if, indeed, q_0 - 0.7 in at least some cases. It is clear, however, that the experimental results are not in agreement with Kadomtsev–like models which are based on full reconnection[11]. This is also true for more recent models[12-13], although the observed growth time of the instability remains the more fundamental objection to these (and indeed all existing) theories. While it is impossible to exclude the possibility that a very small amplitude tearing mode (width ~1 cm say) is present at the start of the sawtooth collapse, it is clear from the JET results that it is the geometric rearrangement of the plasma core which is responsible for the observed collapse rather than a reconnection of the core. The cause of the subsequent loss of energy from the core also remains problematic, however.

These results may have wider implications for the evolution of the q–profile. As noted above, the observation of cycles of reconnecting islands throughout the sawtooth period generalizes the deduction from 'snake' observations that a q=1 surface exists throughout the sawtooth cycle. In addition, such cycles of islands may contribute to the maintenance of localised regions of very low shear in the q–profile[14], which may have important consequences for theories of the stability of the m=1 mode.

References

[1] A W Edwards et al, Phys Rev Lett **57** 210 (1986).
[2] E Westerhof and P Smeulders, to be published.
[3] D J Campbell et al, Nucl Fus **26** 1085 (1986).
[4] D J Campbell et al, Proc 11th IAEA Conf, Kyoto, 1986, **1** 433.
[5] R D Gill et al, Proc 15th EPS Conf, Dubrovnik, 1988, **1** 350.
[6] J A Wesson et al, Proc 11th IAEA Conf, Kyoto, 1986, **2** 3.
[7] J O'Rourke et al, Proc 15th EPS Conf, Dubrovnik, 1988, **1** 155.
[8] D J Campbell et al, Proc 12th IAEA Conf, Nice, 1988, Paper IAEA–CN–50/A–7–2.
[9] P A Duperrex et al Proc 15th EPS Conf, Dubrovnik, **1** 362.
[10] A Weller et al, Phys Rev Lett **59** 2303 (1987).
[11] B B Kadomtsev Fiz Plazmy **1** 710 (1975).
[12] T Sato et al, Proc 12th IAEA Conf, Nice, 1988, Paper IAEA–CN–50/D–3–2.
[13] A Y Aydemir et al, Proc 12th IAEA Conf, Nice, 1988, Paper IAEA–CN–50/D–3–1.
[14] R D Gill et al, JET Preprint JET–P(88)59, to be published.

AN ANALYSIS OF PLASMA ION TOROIDAL ROTATION DURING LARGE AMPLITUDE MHD ACTIVITY IN JET

J A Snipes, H Weisen[1], H P L de Esch, R Galvao[2],
T C Hender[3], E Lazzaro, D Stork,
M von Hellermann, D Zasche[4]

JET Joint Undertaking, Abingdon, Oxon, OX14 3EA, UK
[1] CRPP/EPFL, 21, Av. des Bains, CH-1007 Lausanne, Switzerland
[2] Instituto de Pesquisas Espaciais and the Universidade de Sao Paulo, Brazil
[3] UKAEA, Culham Laboratory, Abingdon, Oxon OX14 3DB, UK
[4] Max-Planck-Institut fur Plasmaphysik, D-8046 Garching, FRG

Introduction A detailed study of plasma ion toroidal rotation in JET during large amplitude MHD activity has revealed a strong viscous force that couples plasma ions to MHD modes. Depending on the MHD modes present, this force can couple across all of the plasma cross section, across only the central region, roughly within the q=1 surface, or across only the outer region outside the q=1.5 surface. The force acts to flatten the ion toroidal rotation frequency profile, measured by the JET active charge exchange spectroscopy diagnostic [1], across the coupled region of plasma. The frequency of rotation in this region agrees with the MHD oscillation frequency measured by magnetic pick-up coils at the wall. The strength of the force between the ions and modes becomes evident during high power NBI when the mode locks [2] and drags the ion toroidal rotation frequency to zero, within the errors of the measurements. The present theories of plasma rotation either ignore MHD effects entirely [3], consider only moderate n toroidal field ripple [4], or low n ripple effects [5].

Sawtooth Related MHD Modes As observed previously on JET [6] and on ISX-B [7], the measured MHD frequency of m=1, n=1 modes agrees well with the central plasma ion toroidal rotation frequency. Sawtooth precursor and postcursor oscillations driven by m=1, n=1 modes at the q=1 surface are toroidally coupled to n=1 modes near the plasma boundary with higher m numbers also with n=1. These coupled modes maintain the same oscillation frequency as the m=1, n=1 mode, but have $m/n \approx q_{\psi}(a)$. That is, modes at the plasma edge take on the rotation frequency of the driving mode from the q=1 surface. Thus, even for very peaked ion toroidal rotation profiles, the measured MHD oscillation frequency at the edge agrees with the plasma ion rotation frequency measured in the center during NBI.

Figure 1a shows an example of a reasonably peaked ion toroidal rotation frequency profile during sawtooth related MHD activity. Note that, during sawtoothing, the ion rotation profile is always flat across the central region, which is roughly the extent of the q=1 radius. In the top traces, the central ion rotation frequency closely follows the peaks of the MHD oscillation frequency. The measurement of the MHD frequency is made by a zero crossing frequency to voltage converter with an n=1 combination of poloidal field pick-up coils as input. The rapid collapses in the MHD frequency are partly real changes in the oscillation frequency (that are to rapid to be observed by the charge exchange diagnostic due to its 50 msec integration time and 50 msec dead time) and partly due to the MHD signal dropping below the threshold of the frequency to voltage converter.

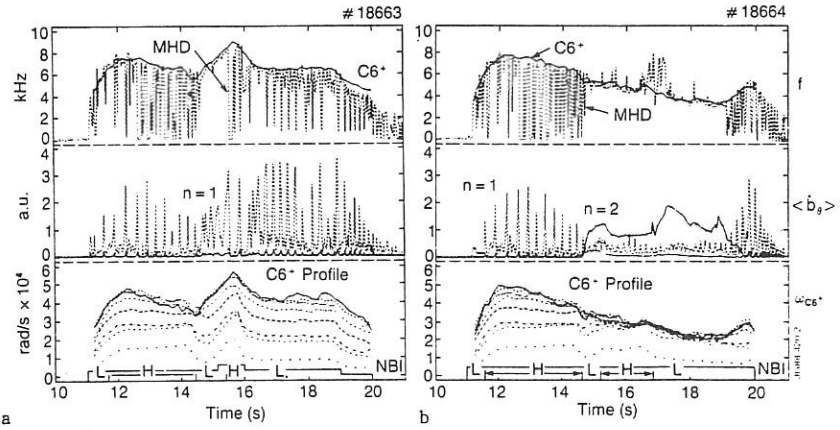

Figure 1. a) A discharge with sawtooth related MHD activity showing good agreement between the central charge exchange toroidal rotation frequency and the n=1 MHD frequency at the edge, together with the n=1, 2 and 3 rectified and smoothed MHD amplitudes and the C 6^+ rotation profile. b) A similar discharge but with a large n=2 mode that flattens most of the C 6^+ rotation profile. The times during H and L mode are indicated during the NBI. The spacing between the charge exchange channels is 10 - 15 cm.

Persistent Rotating MHD Modes When the MHD oscillations persist for more than about 300 msec, the ion toroidal rotation frequency profile flattens over an even larger region than the q=1 radius, sometimes flattening as much as 70% of the plasma cross section. Figure 1b shows an example with an oscillating predominantly n=2 mode that persists for about 5 sec. The discharge begins much like the previous one in Figure 1a with a peaked rotation profile during sawtooth related activity, then during the persistent n=2 mode, the rotation profile flattens out to roughly the q=1.5 radius. The spacing between channels of the charge exchange diagnostic is about 10 - 15 cm. The measured m number at the edge was found to be a mixture of 4 and 5, so linear toroidal coupling to the m=3, n=2 mode is expected. Note that the profile begins to peak up again as the n=2 mode decays away after about 19 sec. Similar rotation profile flattening is also observed during persistent n=1 or n=3 oscillations. Note, however, that while the MHD frequency increases proportional to n, the ion rotation frequency agrees with the n=1 oscillation frequency.

Rotation During Quasi-Stationary Modes (QSM) The agreement between the ion rotation frequency and the n=1 frequency becomes particularly apparent during high power NBI when mode locking occurs, which brings the mode to rest. Under most conditions, the ion toroidal rotation profile collapses

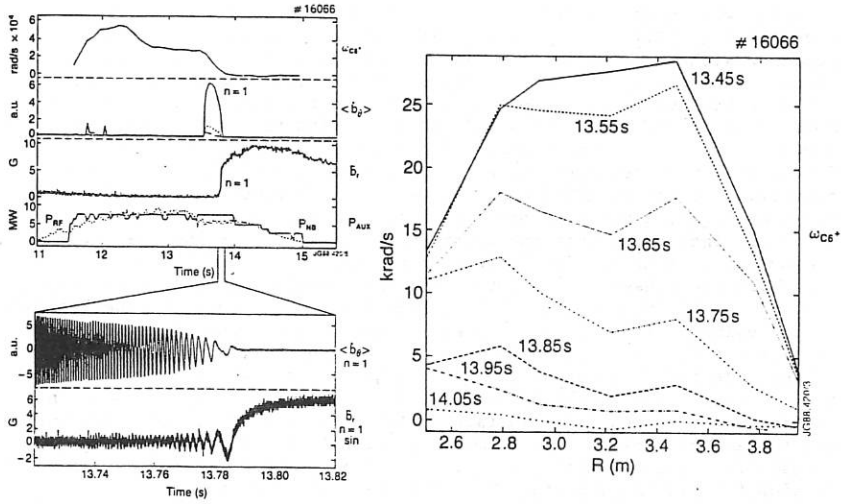

Figure 2. Mode locking during NBI + ICRH showing the subsequent collapse of the C 6^+ ion toroidal rotation profile. The time traces are the ion rotation near the center; the rectified amplitude of the n=1, 2 and 3 oscillations; followed by the locked mode radial field amplitude; and the NB and ICRH power. The expanded time traces show the n=1 oscillations slowing down and locking together with the sine component of the QSM.

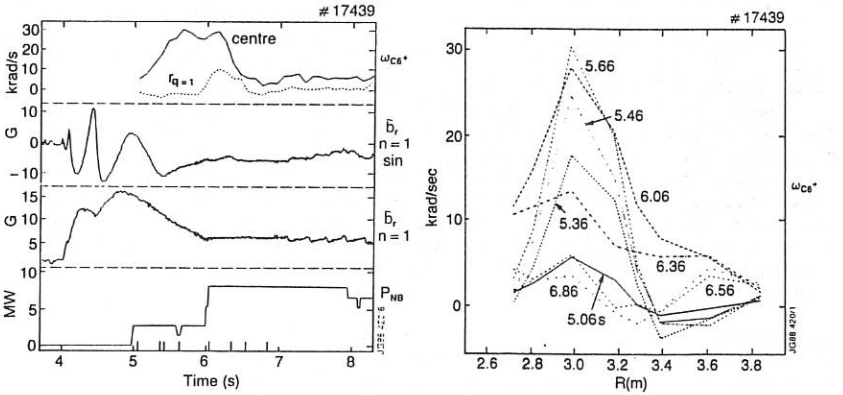

Figure 3. Pellet injection at 3 sec during the current rise drives an MHD mode that becomes a QSM at 4 sec and remains locked during NBI. Plasma ion rotation occurs within the q=1.5 surface despite the QSM at the boundary until a q=1 surface emerges in the plasma at about 6.5 sec, after which the central rotation also comes to rest, within the errors of the measurements.

to zero, within the errors of the measurements, within 100 - 300 msec of mode locking. Figure 2 shows an example of mode locking during NBI combined with ICRH. A monster sawtooth collapse at about 13.5 sec drives a large predominantly n=1 mode unstable. Almost immediately, the central rotation frequency begins to drop as the mode frequency slows down. The mode locks at about 13.79 sec and the entire ion toroidal rotation profile comes to rest, within the errors of about $\pm$ 5 krad/sec, in about 200 msec. This time lag is believed to be due to the inertia of the ions. Note, however, that the Ni XXVII ion toroidal rotation from the central region of the plasma, which has a sampling rate of 20 msec, comes to rest in about 120 msec, indicating that the 100 msec sampling rate of the charge exchange diagnostic is artificially increasing the time delay.

While the behavior in Figure 2 is what normally happens, there are special cases with NBI after pellet injection in the current rise where the outer region of the plasma is locked by the QSM, but the inner region, roughly within the q=1.5 surface, is allowed to rotate (Figure 3). A pellet injected at 3 sec drove an oscillating mode, which becomes a QSM at about 4 sec with a dominant mode number of m=2, n=1. The ion rotation continues within the q=1.5 surface despite the presence of the QSM, until a q=1 surface emerges in the plasma at about 6.5 sec, according to equilibrium code calculations, after which time the rotation profile remains flat at approximately zero despite continued NBI.

Conclusion and Comparison with Theory Plasma ion toroidal rotation is strongly coupled to MHD activity through a viscous force between the ions and the modes that equilibrates the plasma rotation and MHD oscillation frequencies. Sawtooth related modes flatten the ion rotation profile within the q=1 surface. Persistent modes lasting for more than about 300 msec can flatten the ion rotation profile across more than 70% of the plasma cross-section. Quasi-stationary modes that come to rest can also bring the plasma rotation to rest, within the errors of the measurements, in 100 - 300 msec despite NBI. Nonetheless, central plasma rotation can occur during QSM's near the plasma boundary when q(0) > 1.

These results indicate that MHD effects should be taken into account in theories of plasma rotation to obtain a more accurate description of the rotation. The observed time required for the ions to lock to the mode is 100 - 300 msec, and appears to be independent of the mode amplitude for the cases studied, suggesting that it may be fundamentally due to the plasma inertia. The extent of flattening of the ion rotation profile, however, seems to be well correlated with rational q surfaces, indicating that toroidally coupled MHD modes are indeed responsible for flattening the rotation profile.

References

[1] A Boileau, et al, to appear in Plasma Physics and Cont Fusion.
[2] Snipes, J A, et al, Nuclear Fusion, 28 (1988) 1085.
[3] Stacey, W M, et al, Nuclear Fusion, 26 (1986) 293.
[4] Boozer, A H, Physics of Fluids, 23 (1980) 2283.
[5] Mynick, H E, Nuclear Fusion, 26 (1986) 491.
[6] Stork, D, et al, 14th EPS Conf on Plasma Phys and Cont Fusion, Madrid, Vol I, (1987) 306.
[7] Isler, R C, et al, Nuclear Fusion, 26 (1986) 391.

DISRUPTION MEASUREMENT IN THE MT-1 TOKAMAK BY MICROCHANNEL PLATE DETECTOR

S. Kálvin, J.S. Bakos, G. Bürger, B. Kardon,
G. Petravich, G. Veres, S.Zoletnik

Central Research Institute for Physics
H-1525 Budapest-114 P.O.B. 49 Hungary

INTRODUCTION. VUV and soft X-ray radiation measurements have been performed on the MT-1 tokamak ($R = 40cm, a = 6.5 - 9cm, B_t = 1T, I_p \leq 30kA$) during disruptions using a MicroChannel Plate (MCP) detector. This technique enabled us to measure along several chords with one MCP detector from the UV energies up to a few keV.

MEASUREMENT METHOD. The MCP [1] can be thought of as a set of many ($\approx 10^5$) photomultipliers. These microscopic photomultipliers cover an area of a few cm^2 (in our case a circle with 27mm diameter). The electrons emitted by the MCP are collected by an anode system. A slot aperture images the plasma on the MCP.The viewing geometry of the device is determined the slot aperture and the arrengement of the anodes. Twelve poloidally arranged anodes view the central 10 cm diameter part of the plasma column.

In front of the slot aperture different foils were applied as filters. The resulting energy sensitivity of the MCP-foil system was estimated[4,5]. The approximate energy bands, where the full device is sensitive, are the following in our case: $2\mu m$ aluminium foil: $30-80eV$ and $400eV-10keV$, $0.2\mu m$ carbon foil: $80-300eV$, $10\mu m$ beryllium foil: $600eV-10keV$.

The gain of the MCP can be varied by changing the supply voltage. The output current of the MCP is limited. In our case this value is $\approx 50nA/anode$. If the output current exceeds this limit the MCP signal saturates. For a given photon flux the gain must be set to a value where the output current is maximal but does not exceed the saturation limit. The signal of the anodes was amplified with 2 μs time response. In the case of the Al and C foils this time resulution was reached, but in the case of the Be foil the statistical fluctuations due to the low photon flux were substantial. [2]

RESULTS. Measurement series were made to investigate the time evolution of the radiation profile in different energy bands during disruptions. Filter foils were changed from shot to shot during series of similar disruptive discharges. The disruptions were periodic density limit disruptions[3] with q_{lim} between 3 and 8.

The high energy band of the sensitivity with Al foil is nearly the same as the band with Be foil. The Be foil signal can be used to correct the Al foil signal for the high energy band contribution. This correction was negligible so the signal obtained with the Al foil corresponds to the radiation in the 30-80eV band. The relative photon fluxes for different foils were estimated from the foil absorbtion data[4],from the MCP energy sensitivity[5] and from the applied MCP gain. The ratios are 120 : 1 : 0.12 for Al : C : Be foils.

Fig. 1. shows examples of a series of shots. Before disruptions the central chord signals at higher energies (Be foil) increase faster than at low energies (C foil) indicating increasing electron temperature. At disruptions the low energy signals (Al foil) have high peaks *Fig. 2*), while the higher energy signals drop (*Fig. 3-4*). The drop is more pronounced for the Be foil. This may be caused by cooling of the central part of the plasma. The time scale of the drop for the Be foil is shorter ($\approx 20\mu$s) than for the C foil ($\approx 40\mu$s). The width of the peaks on the Al foil signals is approximately 100μs. The bolometer signal shows similar jumps at disruptions. From this it was concluded that the increase of the plasma electromagnetic radiation during disruptions occurs at energies below 80 eV. *Figs. 2-4.* show the line integrated radial profiles of the radiation during disruptions. The drop in the C and Be signals of the central chords are accompanied by an increase in the outer chords. The position of the inversion radius is the same for these two foils. The peak in the Al foil signal is present at every chord but it is higher for the central chords. This means that during disruptions enhanced low energy radiation is present in the whole cross section of the plasma.

References

[1] J.L. Wiza, Nucl. Instr. and Meth. **162** 587 (1979)

[2] S. Kálvin, J.S. Bakos,G. Bürger,B. Kardon,G. Petravich,S. Zoletnik, USX and SX radiation measurement of fusion plasma by MicroChannel Plate, Central Research Inst. for Phys. report KFKI (1989)

[3] S. Zoletnik,Periodic disruptions in the MT-1 tokamak Central Research Inst. for Phys. report **KFKI-1988 -64/D** (1988)

[4] B.L. Henke et. al., At. DATA, Nucl. DATA Tables **27** 1 (1982)

[5] G.W. Fraser, Nucl. Instr. and Meth. **195** 523 (1982)

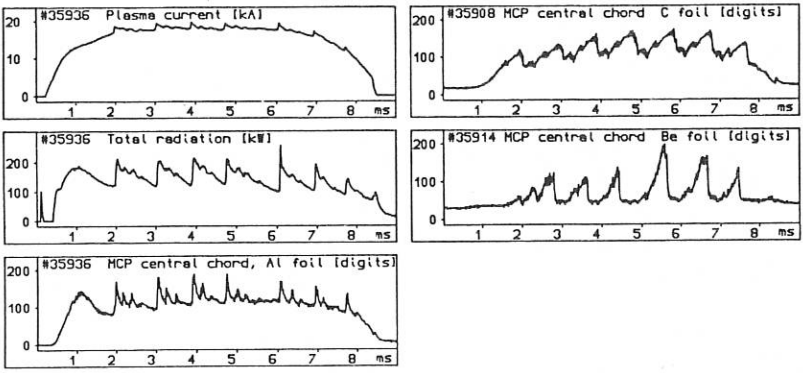

Fig. 1. Plasma current, total radiation (measured by a piroelectric crystal detector), and MCP signals of disruptive discharges. The MCP signals measured with different foils were obtained during a series of similar shots. The plasma parameters were $q_{lim} \approx 5, \bar{n}_e = 2.7 \times 10^{13} cm^{-3}$. The MCP gain was different for different foils.

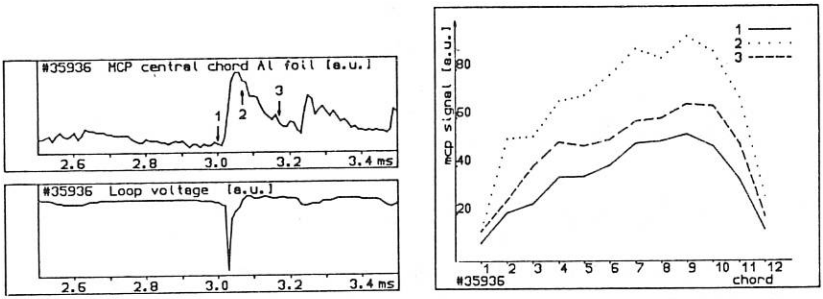

Fig. 2. Time evolution of the line integrated radiation profile in the 30-80eV energy window during a disruption. The signal of channel 6 is shown on the left side. The distributions were taken at $-30\mu s, +30\mu s$ and $+140\mu s$ relative to the loop voltage peak, which was used as a time reference. Channel 12 looks to the inner side of the torus.

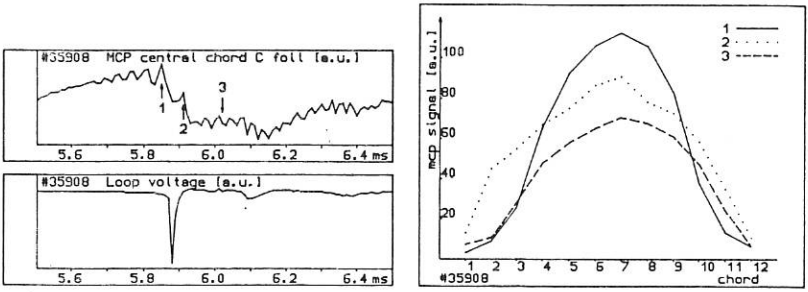

Fig. 3. Time evolution of the line integrated radiation profile in the 80–300eV energy window during a disruption. The distributions were taken at the same time instances (relative to the loop voltage peak) as in *Fig. 2.*

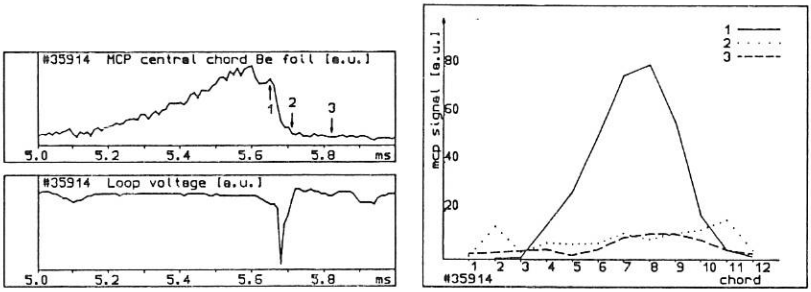

Fig. 4. Time evolution of the line integrated radiation profile in the 600eV–10keV energy window during a disruption. The distributions were taken at the same time instances (relative to the loop voltage peak) as in *Fig. 2.*

IDEAL AND RESISTIVE STABILITY NEAR THE BETA LIMIT IN DIII-D

T. Taylor, E. Strait, L. Lao, A. Turnbull, J. Lee, M. Chu, J. Ferron,
G. Jackson, A. Kellman, E. Lazarus,* T. Osborne, M. Schaffer, R. Stambaugh

General Atomics, P.O. Box 85608, San Diego, California 92138-5608 U.S.A.
*Oak Ridge National Laboratory, Oak Ridge, Tennessee U.S.A.

The maximum achievable beta in the DIII-D tokamak scales linearly with normalized current, $\beta_T(\%) \leq 3.5$ I/aB (MA/m/T).[1] This scaling has been confirmed in neutral beam heated single null divertor H-mode discharges over the range of normalized current, $I_N = I/aB$ (MA/m/T), from $0.6 < I_N < 1.8$, or equivalently $9 > q_{95} > 3$ for the discharge shape shown in Fig. 1(a). q_{95} is the inverse of the rotational transform at 95% of the enclosed poloidal flux. Although similar discharges have been obtained at low $q_{95} \approx 2$, and $I_N \approx 3.1$,[2,3] the beta limit has not been reached in these discharges owing to insufficient heating power and energy confinement time.[4]

Discharges that approach the beta limit in DIII-D exhibit one of three distinct types of behaviour: 1) quiescent operation, 2) sudden disruption, and 3) beta saturation and collapse. The behavior varies in discharges otherwise very similar as shown in Fig. 1(b). The three discharges shown were part of a series, having identical shape, plasma current, and q_{95}, and with the wall conditions as identical as possible. One discharge was stable near the beta limit with $\beta_T > 3$ I/aB for 1 sec, another ended in a sudden disruption at 3.37 sec, and a third discharge, similar to the previous two with the exception of a small increase in the electron density prior to neutral power injection, shows a decrease in beta beginning at 2.75 sec, and saturation at a lower value of beta.

Sudden disruptions caused by the $n = 1$ ideal kink instability limit beta to 3.5 I/aB in DIII-D. Disruption at high normalized beta, $\beta_N = \beta_T\ (\%)/I_N\ (MA/m/T)$ is accompanied by the rapid growth of a non rotating mode with toroidal mode number, $n = 1$. The growth time of this mode is typically 20 to 200 μsec or 10 to 100 poloidal Afvén times. This is demonstrated in Fig. 1(c), where the disrupting discharge of Fig. 1(b) is shown on an expanded time scale. At 3370.6 msec an n=1 perturbation appears, with an initial growth time of $\approx$30 μsec, as shown on the poloidal magnetic field measurement from two probes separated 170° toroidally.

Fast disruptions at high beta, $\beta_N > 3$, almost always immediately follow a sawtooth crash, suggesting that the changes in pressure and current density profiles resulting from the sawtooth crash trigger the external kink instability. The emission from a central viewing soft X-ray (SXR) chord shows a sawtooth crash just after 3370.5 msec, which can also be detected by a slight increase in the emission from a SXR chord viewing the plasma at 90% of the minor radius [Fig. 1(c)]. Approximately 50 μsec after the increase, there is an large decrease in the SXR emission from the outer viewing chord, and an increase in the D_α emission from the divertor region, indicating an edge localized mode, or ELM. Within 50 μsec of the beginning of the sawtooth crash, the $n = 1$ mode appears on the magnetic probe signals.

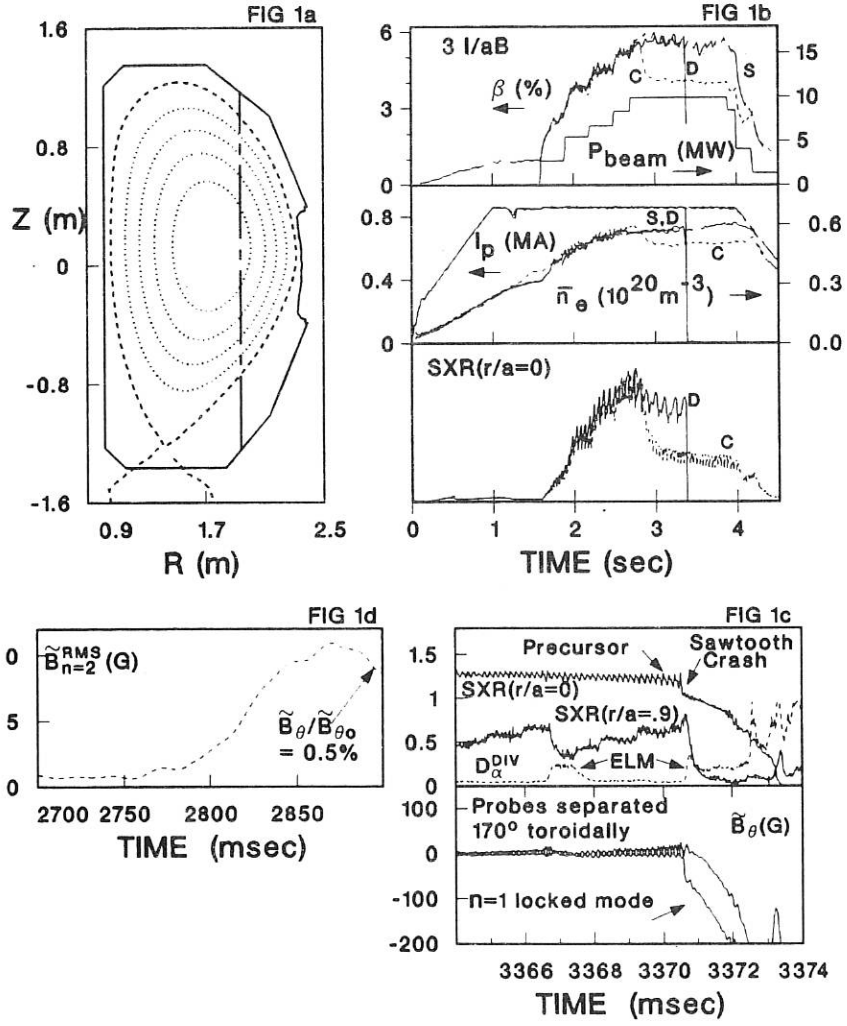

Fig. 1. (a) Equilibrium flux contours of a high beta discharge, $\beta_T = 6\%$. (b) Traces of a series of nearly identical discharges; chain-dashed traces (S), discharge runs stably at high beta; solid traces (D), discharge disrupts; dashed traces (C), discharge saturates at lower β-value. (c) Expanded traces of discharge that disrupts; and (d) expanded trace of rms level of $n = 2$ magnetic fluctuations for the discharge that exhibits saturation.

Stability against ideal modes was calculated with the code GATO[5] using equilibria reconstructed using external magnetic measurements and the measured pressure profile.[6] The total pressure is obtained from measured profiles of electron temperature, ion temperature, electron density and visible Bremsstrahlung, and the calculated fast ion contribution. The reconstructed pressure profile near the peak in a sawtooth cycle is shown as the solid curve in Fig. 2(a). For this case stability to the $n = 1$ kink is found with only weak wall stabilization, $r_{wall}/a = 2.2$. The actual location of the resistive vessel for DIII–D single null divertor plasmas is $r_{wall}/a = 1.3$–1.5. This suggests that the discharge should be stable against the $n = 1$ kink, but the DIII–D vessel has many large ports, and the "effective" wall location for stability might be somewhat larger.

The influence of the sawtooth on the kink mode stability was modeled by generating equilibria with the same discharge cross section, the same plasma current and q, and total pressure (β_T) as the measured case, but with pressure and current profiles consistent with those following a sawtooth crash and the occurrence of an ELM.[7] The pressure on axis was decreased by approximately 20% based on SXR emission data. The pressure gradient at the plasma boundary was decreased by a factor of four, consistent with the effect of an ELM. The resultant pressure profile is shown as the dashed curve in Fig. 2(a). The current profile was slightly broadened consistent with a sawtooth crash resulting in a 30% decrease in the shear near the $q = 2$ surface. This new equilibrium is more unstable to the $n = 1$ ideal kink, as is shown in Fig. 2(b). For moderate wall stabilization ($r_{wall}/a \approx 1.7$) the profile changes caused by the sawtooth plus ELM can reduce the calculated kink mode beta limit to the observed value of $\beta_N = 3.5$.

In most discharges at high normalized beta in DIII–D, beta saturation and/or collapse caused by low n resistive pressure driven modes prevents the discharge from reaching the ideal kink mode limit. Beta saturation is accompanied by the slow growth of an $n = 3$, 2, or 1 mode. The growth time of this mode is typically 10 to 100 msec, or approximately 10^4– 10^5 poloidal Alfvén times as shown in Fig. 1(d). These modes often saturate at some moderate level ($\tilde{B}_\theta/B_{\theta 0} \leq 0.5\%$) and the discharge continues with degraded energy confinement as in Fig. 1(b). At moderate q, $2.5 < q < 5$, the modes sometimes do not saturate but lead to a complete collapse, the collapse being a direct consequence of a large $n = 1$ mode ($\tilde{B}_\theta/B_{\theta 0} > 1\%$).[3,8]

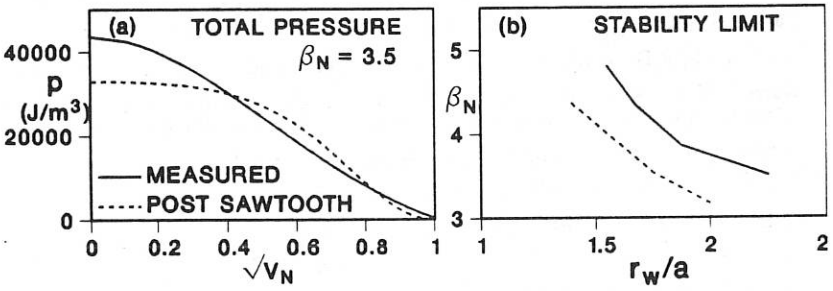

Fig. 2. (a) Pressure profiles for stability analysis, $\sqrt{V_N}$ is an equivalent radial coordinate; and (b) stability boundary for the $n = 1$ ideal kink, instability is above and to the right of the curves.

The threshold in β_N for onset of these modes varies considerably, continuous and coherent modes appearing at β_N as low as 2 in some discharges and in other discharges not appearing for β_N up to 3.5. The threshold can be increased by appropriate cleaning and conditioning of the first wall and careful attention to the details of the discharge evolution, an indication that small changes in the pressure and current density profiles can lead to the difference between stability and instability. The ability to effectively clean and condition the graphite wall in DIII–D, primarily by baking overnight and helium glow conditioning between tokamak discharges, has proved crucial in obtaining quiescent discharges near the ideal kink beta limit.

These low n continuous modes are believed to be resistive pressure driven modes. Equilibria using pressure profiles measured when these modes are present have all been calculated to be stable against ideal modes $n = 4$, 3, and 2, with no wall stabilization. Resistive stability calculations have been completed with the code CART–II.[9] As beta is increased, the modes $n = 1$, 2, 3, and 4 are calculated to be unstable, and the prevalent mode is of the resistive ballooning type with a linear growth rate dependence on resistivity and toroidal mode number of $\gamma \propto \eta^{1/3} n^{2/3}$. The shorter wavelength resistive ballooning modes are more strongly stabilized by finite Larmor radius, and the most unstable modes become the low n modes, $n = 1$, 2, 3, and 4, as observed experimentally.

These low n resistive modes are the most frequently observed MHD activity at high normalized beta in DIII–D. We have begun to evaluate what changes in the pressure and current profiles lead to stability and are optimistic that modification of these profiles by RF heating and current drive will prove effective techniques by which these modes can be avoided. However, the frequent observation of resistive modes in DIII–D and their adverse effect on confinement at beta values significantly below the limit imposed by ideal modes calls for more careful consideration of resistive pressure driven modes in future scaling studies.

This work was supported by U.S. Department of Energy under Contract No. DE-AC03-89ER51114.

REFERENCES

1. Strait, E.J., *et al.*, in Plasma Physics and Controlled Nuclear Fusion Research (Proceedings of 12th International Conference, Nice, 1988), IAEA-CN-50/A-II-1.
2. Taylor, T.S., *et al.*, GA–A19134 (1988), submitted to Physical Review Letters
3. Stambaugh, R.D., *et al.*, Plasma Physics and Controlled Fusion **30** (1988) 1585.
4. Burrell, K.H., *et al.*, Plasma Physics and Controlled Nuclear Fusion Research (Proceedings of 12th International Conference Nice, 1988), IAEA-CN-50/A-III-4.
5. Bernard, L.C., *et al.*, Comput. Phys. Comm. **24** (1981) 377.
6. Lao, L., *et al.*, GA–A19063, submitted to Nucl. Fusion.
7. Gohil, P., *et al.*, Phys. Rev. Letters 61 (1988) 1603.
8. Strait, E.J., *et al.*, GA–A19214 (1988), submitted to Physical Review Letters.
9. Lee, J.K., *et al.*, GA–A19521 (1988), submitted to Nuclear Fusion.

LOCALIZED DENSITY, SPACE POTENTIAL, AND MAGNETIC FLUCTUATION MEASUREMENTS DURING MHD OSCILLATIONS ON TEXT

P.M. Schoch, K. A. Connor, T. P. Crowley, J. W. Heard[2], R. L. Hickok, S. C. McCool[1], V. Simcic, B. A. Smith[2], A. J. Wootton[1], and X. Z. Yang[3]

Rensselaer Polytechnic Institute, Troy, NY; [1]Fusion Research Center, The University of Texas at Austin, Austin, TX; [2]Magnetic Fusion Science Fellowship Program, Oak Ridge Associated Universities; [3]Institute of Physics, Academia Sinica, Beijing, PRC

1. INTRODUCTION

A Heavy Ion Beam Probe has been used on TEXT to detect fluctuations associated with MHD activity. The results are interpreted in terms of fluctuations in potential, density and magnetic field. Two types of discharges were studied: discharges with sawteeth and discharges with high m=2 Mirnov activity. The density and magnetic fluctuations associated with the Mirnov oscillations show a strong radial dependence. For sawteething plasmas, we show for the first time that there are strong potential sawteeth with an inversion radius.

The Heavy Ion Beam Probe (HIBP) on TEXT consists of injecting a beam of Tl^+ ions into the plasma, with detection of Tl^{++} ions produced by electron impact ionization. [1] The total current, I_s, the kinetic energy E, and the toroidal displacement ϕ_{tor} of the secondary beam are measured, and, in particular, the fluctuation levels of these signals, $\tilde{I}_s/I_s$, $\tilde{E}$, and $\tilde{\phi}_{tor}$. The detected secondary current is given by:

$$I_s = I^+_0 \, (n_e\langle\sigma v\rangle^{1-2})_{sv} \exp(-\int n_e\langle\sigma v\rangle^{1-2} dl_{in}) \; \exp(-\int n_e\langle\sigma v\rangle^{2-3} dl_{out})$$

Here I^+_0 is the initial primary current, the exponentials describe the attenuation over the input beam path l_{in}, and over the output path l_{out}. The factor $(.)_{sv}$ describes the ionization in the sample volume. The ionization rates for Tl^+ to Tl^{++} and Tl^{++} to Tl^{+++} are $\langle\sigma v\rangle^{1-2}$ and $\langle\sigma v\rangle^{2-3}$ respectively. For fluctuations with small radial coherence lengths, and plasma temperatures $T_e > 100ev$ ($\langle\sigma v\rangle \sim$ constant), then $\tilde{I}_s/I_s = (\tilde{n}/n)_{sv}$. However, for the fluctuations discussed here the input and output beam attenuation cannot be ignored, and calculations are being performed to quantify this effect. $\tilde{E}$ is a true local measurement of $\tilde{\phi}$, the plasma potential fluctuation level in the sample volume. $\tilde{\phi}_{tor}$ is related to the magnetic field fluctuation level. Tonetti and Connor [3] have shown that if a tokamak is toroidally symmetric then the toroidal velocity of the secondary particles is a localized measure of the magnetic vector potential in the toroidal direction, so fluctuations in the ion's toroidal velocity are a measure of $\tilde{b}_\perp$. However in TEXT the discrete toroidal coils complicate the geometry, and the analyzer measures the toroidal displacement of the secondary beam, not the velocity. Computer simulations are under way to determine what fraction of the toroidal displacement is a local measurement, and what fraction is a line integrated effect. Presently, we cannot provide quantitative values of $\tilde{n}/n$ or $\tilde{b}$ for the cases discussed below.

2. MHD UNSTABLE DISCHARGES

Control of gas puffing and impurities allows the production of discharges with large amplitude Mirnov oscillations. The discharges produced for this study used a major radius R_p = 1m, minor radius a_p = 0.26m, toroidal field B_ϕ = 2T, plasma current I_p = 200kA ('MHD' safety factor at the edge q_a = 3.2), and line of sight average density $\bar{n_e} = 2x10^{19}m^{-3}$ in H working gas. The soft X ray arrays show no apparent sawtooth activity.

Figure 1 shows the various signals during the large Mirnov activity. Figure 1a) shows a Mirnov coil signal ($\alpha\ d\tilde{b}/dt$). The m = 2 oscillation at 4kHz exists for times > 100ms: the amplitude $\tilde{b}_{rms} \sim 2x10^{-3}T$ is >100 times larger than that of a normal MHD stable discharge. Figure 1b) shows the sum or secondary beam current I_s, figure 1c) the plasma potential ϕ and figure 1d) the secondary beam toroidal displacement ϕ_{tor}.

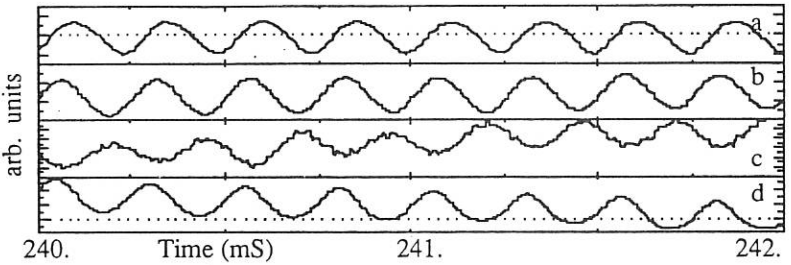

Fig. 1a) Mirnov coil signal, b) HIBP sum signal (density), p-p oscillations is ≈15% of average signal, c) space potential, ≈50vp-p, and d) toroidal motion (magnetic field)

Because the oscillation is approximately stationary the full scanning capability of the HIBP can be used. Figure 2a) shows that the amplitude of the Mirnov coil output ($\alpha\ d\tilde{b}/dt$) changes by < 30% over a 100ms time period. During this time, HIBP sample volume is slowly scanned from the machine center to the edge. The results are shown in figure 2b) for the sum signal $\tilde{I}_s$ ('density'), figure 2c) for $\tilde{\phi}$ (plasma potential), and figure 2d) for $\tilde{\phi}_{tor}$ ('magnetic'). The horizontal axis is marked, with both time and the radial location, $\rho \approx r/a_p$, which that time corresponds to. Both $\tilde{I}_s$ and $\tilde{\phi}_{tor}$ show maxima at ρ = .38 and .72 $\tilde{\phi}$ is almost constant in radius. Since the potential measurement is made relative to the vacuum vessel, the oscillation shown in figure 2c represents a radial electric field change only at the plasma edge.

Figure 3 shows relative phase measurements, made as a phase comparison for each half cycle. Figure 3a) shows the relative phase between I_s and a Mirnov coil at r = 0.295m as a function of plasma radius: the phase is nearly constant in the plasma center and in the region of the two amplitude peaks. Figure 3b) shows the relative phase between $\tilde{\phi}$ and the Mirnov coil signal: the phase shows little spatial dependence, again indicating that the entire plasma potential is fluctuating uniformly. Figure 3c) shows the relative phase between $\tilde{\phi}_{tor}$ and the Mirnov coil: the result is similar to that for the relative phase of I_s and the Mirnov coil (fig 3a). Thus when I_s and $\tilde{\phi}_{tor}$ show amplitude maxima, they are nearly in phase. In the plasma edge and near amplitude minima, the phases of I_s and $\tilde{\phi}_{tor}$ are not so close. This is clearly shown in figure 3d), where the relative phase between I_s and ϕ_{tor} is shown. The phase between $\tilde{\phi}_{tor}$

and the Mirnov coil shows an $\approx\pi$ change at ρ=.48, which is a relative minimum in amplitude. This is the same phase change as is expected for b_θ across a tearing mode rational surface.

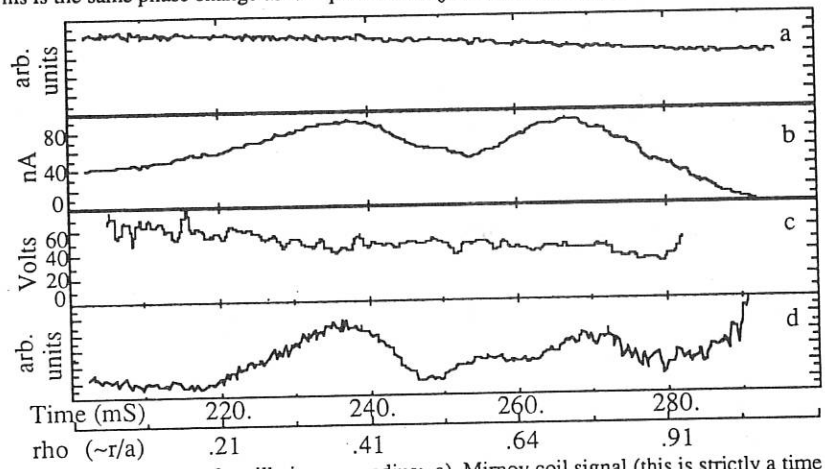

Fig. 2 Amplitudes of oscillations vs. radius: a) Mirnov coil signal (this is strictly a time history not a radial scan), b) I_s(density), c) E, and d) ϕ_{tor}(magnetic field).

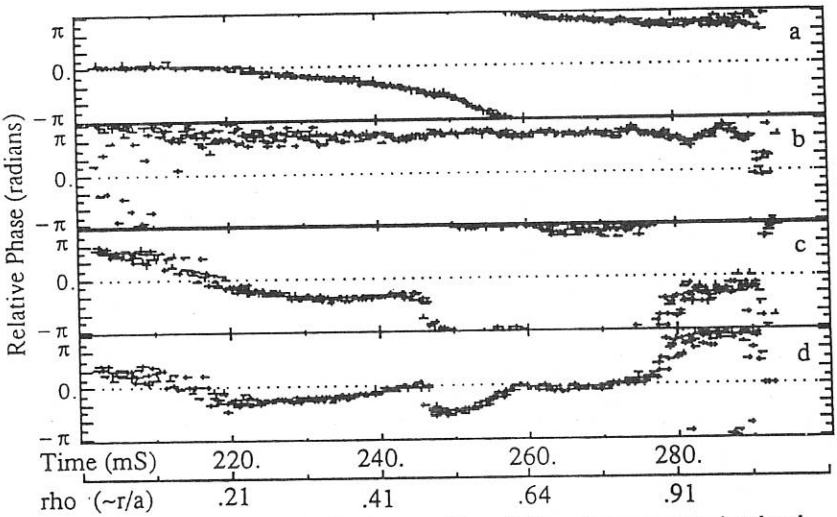

Fig. 3 Phase shift between signal pairs vs. radius: a) Phase between sum signal and Mirnov coil, b) phase between space potential and Mirnov coil, c) phase between toroidal position and Mirnov coil, and d) phase between sum signal and toroidal position.

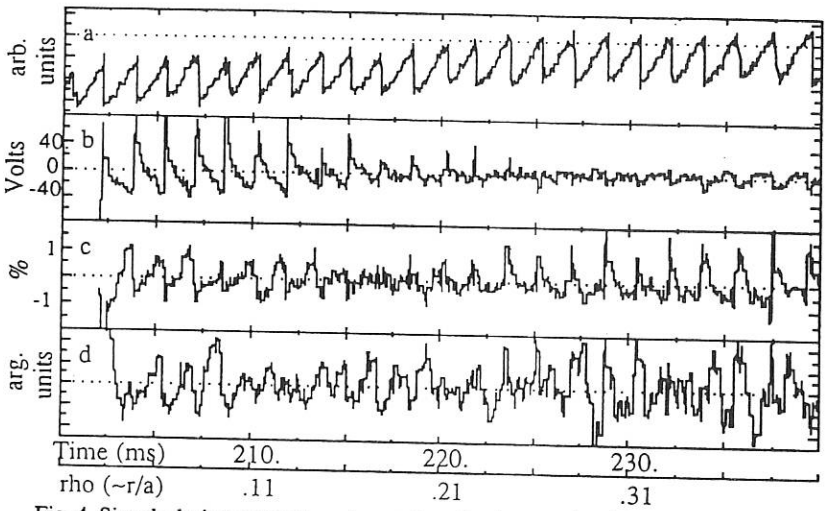

Fig. 4 Signals during sawteeth: a) central cord soft x-ray signal (not scanned), b) space potential, c) sum signal (density), and d) toroidal position (magnetic field).

3. SAWTEETH

Figure 4 shows data taken during a sawteething discharge, $B_\phi = 2T$, $I_p = 200kA$, and $n_e = 2x10^{19}m^{-3}$ in H working gas. Fig 4a) shows a central cord soft x-ray signal. The HIBP sample volume was slowly swept from the plasma interior out toward the plasma edge. Figure 4b) shows the fluctuating part of the potential, 4c) the sum signal (density), and 4d) the toroidal position (magnetic field). The space potential exhibits a sawtooth nature with the strongest variations at or near the plasma center, with inverted signals outside of $\rho=0.25$. Since TEXT has a negative potential well the potential looks like sawteeth, that is that the magnitude increases up to the time of a crash. The potential sawteeth are about 10% of the central potential.

The sum signal also shows sawteeth behavior with a smaller inversion radius. The toroidal signal is noisier than the others, but if several cycles are compared it appears that the toroidal motion also has a sawtooth characteristic with an inversion radius of $\rho=0.25$.

SUMMARY

The HIBP has made measurements of density, space potential, and magnetic oscillations on TEXT sawteeth and MHD. The measurements show interesting radial variations that are not yet explained, and the relative effect of local vs. path integration is not yet determined (except for the space potential which is a local measurement).

REFERENCES

1. P. M. Schoch, et. al., Rev. Sci., Instrum. 59 (1988).
2. G. Tonetti and K. A. Connor, Plasma Physics 22 (1980).

STUDY OF SAWTOOTH-CORRELATED DENSITY FLUCTUATIONS NEAR THE Q=1 SURFACE ON TEXTOR.

M. Jadoul , G. Waidmann

Laboratoire de Physique des Plasmas - Laboratorium voor Plasmafysica ,
Association "Euratom-Etat belge" - Associatie "Euratom-Belgische Staat" ,
Ecole Royale Militaire - Koninklijke Militaire School ,
Brussels, Belgium

Institut für Plasmaphysik, Kernforschungsanlage Jülich GmbH ,
Association EURATOM-KFA, P.O.B. 1913, D 5170 Jülich, FRG

1. Introduction

Details of the sawtooth activity in the tokamak plasma are still unresolved and under discussion since their first observation [1] more than a decade ago. A reconnection, a turbulent and a quasi-interchange model [2-4] were meanwhile proposed. Here we present experimental data obtained by ECE-radiation detection and by a 150 GHz millimeter wave scattering system, in the q=1 region. These measurements for the first time support strongly a model which predicts a rotating turbulent domain before the sawtooth crash event.

2. Experimental methods and observation of precursor oscillations

The sawtooth activity was generally observed by a 10 channel heterodyne ECE-system with a 2 cm radial resolution and a time resolution better than 100 μsec. Figure 2 shows the relative variation of the temperature profile observed during one shot. The transition from normal to inverted sawteeth is indicated by the polarity change and allows a good localisation of the inversion radius.

The inversion and mixing regions were scanned centimeter by centimeter with a 2 mm wavelength collective scattering diagnostic. The scattering volume has a 2 cm radial width and is formed by a pair of movable parabolic antennae mounted in the vacuum vessel. Fluctuations were observed in the 200 kHz to 3 MHz frequency range. The density fluctuations were found to be very enhanced at the end of the sawtooth period (fig 1). Precursors were systematically observed when the scattering volume was in a 6 cm wide region centered on the inversion radius. High and low field side precursors are shown in fig. 1 for temperature signals inside the inversion radius and for density fluctuation signals.

The phase of the ECE precursors with respect to the sawtooth crash was highly stable from sawtooth to sawtooth and from shot to shot. An m=1 mode is also recognized from these signals. The density fluctuation precursors were always clearly detected but their shape was somehow irregular. In particular a precursor peak was sometimes split into two peaks, indicating some structure of a turbulent region. For these reasons fig 1 presents averages over ~10 sawteeth. In this average, the turbulent region fills about

180° of the precursor poloidal rotation angle as can be seen on figure 1.b.

From the phase between ECE and density fluctuation precursors, one can see that the turbulent region was cooler. This becomes specially clear in fig 1.a since the scattering volume was located on an ECE measurement position (T1).

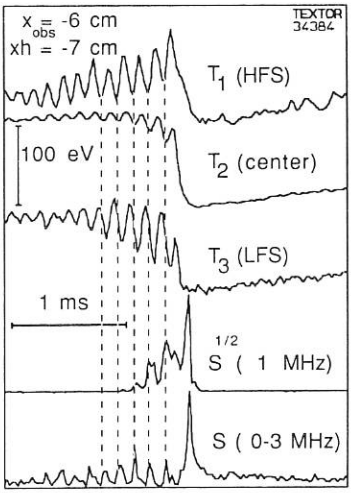

Fig. 1 a

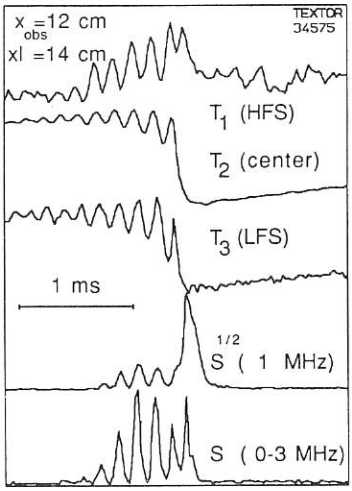

Fig. 1 b

Fig. 1 a: Precursor oscillations on ECE temperature signals (T_1,T_2,T_3) inside the inversion radius and density fluctuations (S) on the high field side a little inside the inversion radius. (x,xh,xl are defined in figure 2)

Fig. 1 b: The same with the scattering volume on low field side.

3. Spatial and frequency development of enhanced fluctuations

The spatial characteristics of the sawtooth-correlated fluctuations can be best described when relating it to the variation of the temperature profile during the crash (fig. 2.a), and when considering a broad frequency band centered around 1 MHz. An example of a spectral density evolution before and at the sawtooth crash, inside the inversion surface is shown on figure 3. It shows a dominant effect occurring around 1 MHz and a peak at a smaller frequency. At the moment of the crash the spectrum shifts to lower frequencies as is already mentioned in [5].

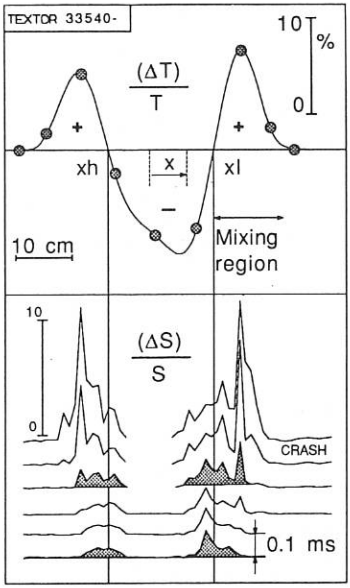

Fig. 2 a : Relative temperature variation profile due to the sawtooth crash as a function of radial distance inside the plasma.
ΔT = T(after crash) - T(before crash)

Fig. 2 b : Relative density fluctuation (S) variation profile at 1 MHz, before and at the sawtooth crash. (Precursors are smoothed out).

The precursor oscillations develop before the sawtooth crash. From figure 2.b, a multipeak structure can be seen in this precursor region with an approximate symmetry between high and low field side.

Shortly before and during the crash a sharp peak of turbulence grows just outside the precursor region (hatched on figure 2.b). At the same time the central temperature falls and a heat pulse will appear outside the inversion radius in the mixing region. The turbulence maximum is remarkably close to the maximum of this heat pulse and has a width of about 2 cm (which is our spatial resolution !). It is this latter sudden increase of turbulence which appears to correspond to earlier observations on TEXT and TFR ([5],[6]).

After this event lasting less than 1 ms, the turbulence relaxes.The heat pulse then propagates to the plasma edge. A small but detectable turbulence pulse was observed over a 15 cm radial distance, propagating almost at the same speed. A few times we have also observed irregular successor oscillations.

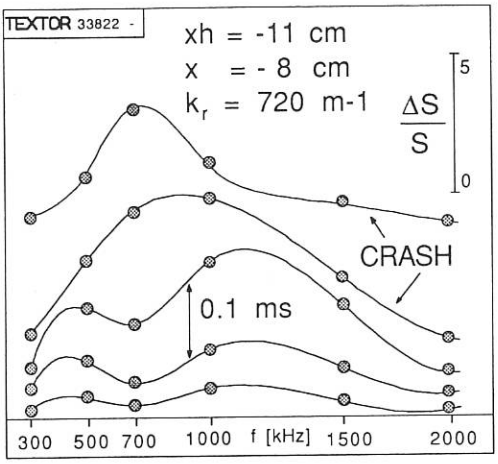

Fig. 3 : Relative variation of the density fluctuation spectrum (S) a little before and at the sawtooth crash.

4. Discussion of the results

The theory of Dubois and Samain [3] explains the sawtooth disruption as a consequence of an increased transport caused by magnetic modes growing on the separatrix of an m=1 island. We have measured density fluctuations that may clearly be associated with these modes. They show up in the form of precursor bursts which are correlated in time and space with the m=1 island detected from ECE signals. Moreover this region is located on the ECE inversion points and some spatial structure is indicated (fig. 2). The frequency spectra also support this view (fig. 3). Indeed one should expect it to be determined by the kinetic Alfvén wave dispersion relation [7]:

$$\frac{\omega^2}{k_{||}^2 v_A^2} = \frac{\lambda_i}{1 - I_0(\lambda_i)\, \exp(-\lambda_i)} + \frac{Te}{Ti}\lambda_i \quad , \quad \lambda_i = k_r^2 \rho_i^2 \quad , \quad \rho_i : \text{Larmor radius}$$

The width of the spectrum is then the consequence of our wavevector resolution (Δk_r = 320 m^{-1}) and the k_r dependence of this relation. The experimental central frequency and width of the dominant peak agree within 20% with this dispersion relation.

5. References

[1] v. GOELER,S. et al. Phys. Rev. Lett. 33,1201 (1974) .
[2] KADOMTSEV B.B. Fizika Plasmy 1,710 (1975) .
[3] DUBOIS,M., SAMAIN,A., in Plasma Physics and Controlled Nuclear Fusion Research (Proc. 7th Int. Conf. Innsbruck, 1978) Vol. 1, IAEA, Vienna (1979) 615.
[4] WESSON J. EPS-Conf. Budapest (1985) Post deadline paper.
[5] BROWER D.L. et al. EPS-Conf. Madrid (1987) 1314 .
[6] J. ANDREOLETTI et al. (1988) Submitted to Plasma Physics .
[7] A. HASEGAWA and C. UBEROI , The Alfvén Wave (1982) .

DETAILED STRUCTURE OF THE q PROFILE AROUND q=1 IN JET

B. Pégourié, M.A. Dubois

Association EURATOM-CEA sur la Fusion Contrôlée
CEN Cadarache B.P. n°1, 13108 Saint-Paul-lez-Durance, France

and R.D. Gill

JET Joint Undertaking, Abingdon, Oxon, OX143EA, UK

1- INTRODUCTION

The limitation of ablation on rational surfaces has been shown to be an efficient mechanism of striation formation during pellet ablation [1]. In JET, a very large striation is observed when the pellet crosses the q=1 surface [2]. This paper presents a thorough analysis of the pellet ablation in this region and shows that an extended shearless zone around q=1 is necessary to reproduce the experimental signal. Such a feature is likely to be an essential ingredient in the understanding of internal disruptions.

2 - DESCRIPTION OF THE MODEL:

The basic idea is that dark striations correspond to locations where ablation is lower than average, i.e. that the available electron energy is lower there than at other radii. This can be understood as follows for electrons of parallel velocity $v_{//}$: the pellet, surrounded by its neutral cloud (of effective diameter Φ_p), moves across the discharge with a velocity v_p. It interacts during $\delta t=\Phi_p/v_p$ with every toroidal shell of infinitesimal thickness. Therefore, all the electrons located at a distance smaller than $\delta t\, v_{//}$ from the pellet (following the field line) are intercepted by the neutral cloud.If the pellet is on a resonant magnetic surface, (corresponding to a rational q value $q_R=m/n$), the field line has a finite length $L(q_R)$. If $L(q_R) < \delta t\, v_{//}$, the energy flux on the neutral cloud vanishes after $\delta t' = L(q_R) / v_{//}$, leading to the following reduction of the local ablation rate:

$$\alpha_R = \frac{L(q_R)\, v_p}{v_{//} \Phi_p} \qquad (1)$$

The influence of a rational surface extends until the difference of poloidal rotation (after m toroidal turns) reaches the angular sector sustained by the neutral cloud. Inside this region, the shape of the striation is linked to the q profile by the relation:

$$\alpha = \alpha_R \left(1 + (\alpha_R^{-1} - 1) \left(\frac{2\pi m r}{\Phi_p} (q_R^{-1} - q^{-1}) \right)^{1/3} \right) \qquad (2)$$

provided the width of the striation is larger than Φ_p.

Inside Δr ,the observed H_α signal is assumed to be proportional to the matter deposition profile:

$$\Delta M = 4\pi r_p^2 \dot{r}_p \eta \Delta r / v_p \qquad (3)$$

where r_p is the pellet radius and η the ice density. The expression of $\dot{r}_p$ given in [3] can be revised to take into account the shape of the striation α and the maxwellian distribution of the electrons f(E); leading to:

$$\dot{r}_p = 5.14\ 10^{-9} r_p^{-2/3} n_e^{1/3} \left(\int_0^\infty E^{4.92} f(E)\, \alpha^3\, dE \right)^{1/3} \qquad (4)$$

where n_e is the local electron density.

This model can be used to determine the details of the q profile around a resonant surface displaying a striation at this location, provided q_R is known. Indeed, Φ_p (the only free parameter of the model) can be determined from the experimental value of α_R by equations (1), (3) and (4); and then the q profile computed from the experimental shape factor α by equations (2), (3) and (4).

3- THE q PROFILE AROUND q=1 IN JET:

An exemple is given for JET shot 9228 the main parameters of which are: $n_e(0) = 3.7\ 10^{19}\ m^{-3}$, $T_e(0) = 3.6$ keV, $q_\psi(a) = 4.8$, and q=1 at $r \approx 51$ cm in the equatorial plane. The pellet has an initial radius $r_{p0} \approx 2.2$ mm and is injected with a velocity $v_p \approx 10^3\ ms^{-1}$.

On figures 1a to d, comparisons between model and experiment are shown for different q profiles around q=1: for a smooth q profile ($\nabla q \approx 0.25\ m^{-1}$, fig.1a), the computed striation is too shallow and considerably narrower than the observed one. The large dip of about 14 cm wide exhibited by the experimental signal implies the presence of a flattening of roughly the same extent on the q profile [4]. This flattening is modelled with a constant q gradient: $\nabla q \approx 0.03\ m^{-1}$ (fig.1b, and curve labelled b on fig.2) and a zero q gradient (fig.1c and 2, curve c). These two cases emphasize the extreme sensitivity of α to the details of the q profile. Finally, the best fit of the experimental data is displayed on figure 1d and the corresponding q profile on

figure 2, curve d.The diameter of the neutral cloud deduced from the maximum depth of the striation α_R is Φ_p = 0.7 cm. Outside the striation, the residual discrepancy between the computation and the experimental signal is ≤20% and local variations of the latter do not exceed this value. Expecting a similar accuracy inside the striation leads to $\delta q/q \leq 2.5\ 10^{-4}$. Therefore, the extremely flat region ($\nabla q \approx 0.003\ m^{-1}$) of about 8 cm wide around q=1 is not an artifact of the computation.

4- DISCUSSION:

Two effects are neglected in this model: the radial heat and matter transport and the density structure of the neutral cloud which is not - stricto sensu - a perfectly absorbing sphere. However, for a given q profile, they both tend to smooth the resultant striation. Therefore, to take them into account will strengthen further the strong q flattening at the center of the striation, which gives yet more confidence in the reality of this feature.

The existence and persistence of an extended shearless annular region in the vicinity of the q=1 surface should be taken into account in any theory of the internal disruption. It is likely that this zone acts as a control to release the energy accumulated at the center of the discharge. The precise mechanism can be studied using pellet ablation as a shear diagnostic since an hypothetical q=1 island would be distinguishable by this method, even if local temperature gradients are very low. A first step is to study this shoulder on the q profile at several times in the sawtooth period, to check if its evolution is consistent with normal resistive diffusion.

REFERENCES:

[1] M.A. Dubois, B.Pégourié, Cargèse workshop Nonlinear processes in Vlasov plasmas (1988), Editions de Physique (Orsay); and B.Pégourié, M.A.Dubois, submitted to Nuclear Fusion (1989).

[2] R.D. Gill et al., submitted to Nuclear Fusion (1989).

[3] P.B. Parks, R.J. Turnbull, Phys. Fluids **21** (1978) 1735.

[4] R.D. Gill et al., this conference.

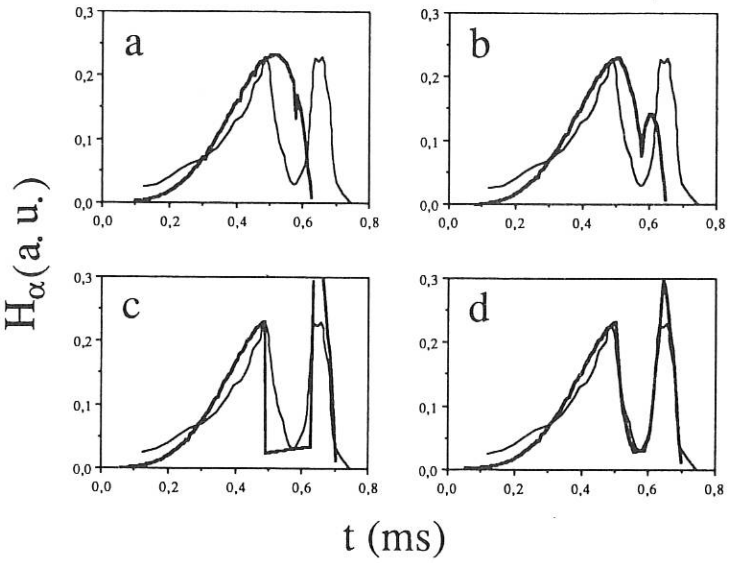

Figure 1: Comparison between experimental (thin line) and computed (thick line) signals for different q profiles around q=1:
a. Smooth q profile (without flattening), b. Constant q gradient,
c. Zero q gradient, d. Optimized q profile to best fit data.

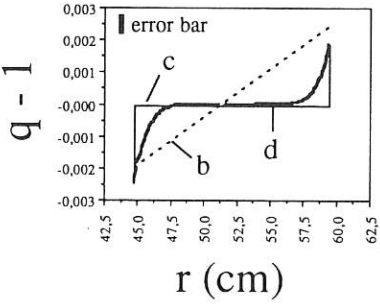

Figure 2 : (q -1) profile around q=1 in the three cases b,c and d. For case d the error bar is indicated in the upper left corner of the figure.

ALPHA PARTICLE LOSSES DURING SAWTOOTH ACTIVITY IN TOKAMAS

D. Anderson and M. Lisak

Institute for Electromagnetic Field Theory
Chalmers University of Technology
S-412 96 GÖTEBORG, Sweden

The time evolution of the prompt losses of fusion produced alpha particles in Tokamak plasmas characterized by sawtooth activity is investigated. The variation of the alpha particle loss rate during a sawtooth period is shown to contain a characteristic high intensity burst during the magnetic reconnection stage following the sawtooth crash. The spectrum of the lost alpha particles is composed of two parts: (i) directly lost particles giving rise to a peak at the particle birth energy and (ii) accumulated particles, which have suffered significant slowing down and are lost during the reconnection stage. These latter particles give rise to a broad spectrum slightly down-shifted due to additional slowing down during the reconnection stage.

Significant sawtooth activity seems to be an inherent part of present day Tokamak plasma behaviour. Although a strong effort is being made to conceive methods for sawtooth suppression, it seems likely that sawtooth oscillations will be present also in Tokamak operation near ignition conditions.

The emission and loss rate of high energy fusion products are strongly affected by sawtooth oscillations. The sawtooth induced variation of fusion neutron emission has recently attracted considerable attention and it has been shown that profile effects play an important role for the prediction and interpretation of neutron emission measurements.

The purpose of the present work is to investigate the effect of sawtooth activity on the loss rate of fusion produced alpha particles. In particular it is shown that, in addition to a slowly varying background loss, bursts of unconfined alpha particles should appear at the sawtooth crash. The bursts are caused by particles which have been accumulating during the sawtooth rise, but which are lost due to increased velocity space loss regions and/or redistributed density profiles during the magnetic reconnection stage of the sawtooth crash.

The emission rate, $\dot{N}$, of fusion products can be written

$$\dot{N} = \int_V n_A n_B \, \overline{\sigma v} \, \ell \, dv \qquad (1)$$

where n_A and n_B denote the densities of the reacting species, $\overline{\sigma v}$ the reaction rate, ℓ the local loss fraction and V the plasma volume. Assuming $\overline{\sigma v} \sim T^\gamma$ where T is the plasma temperature and radial profiles according to $(1-r^2/a^2)^m$, eq. (1) can be rewritten in terms of on axis values

$$\dot{N} \sim n_A(0)\ n_B(0)\ T^{\gamma}(0) \int_0^1 (1-x^2)^q \ell(x)\ x\ dx \qquad (2)$$

where $q = m_A + m_B + \gamma m_T$.

Consider the case of neutron emission from thermal D-D reactions. In this case $\gamma \simeq 2$, $\ell(x) = 1$ and eq. (2) implies the following result for the change in the neutron emission as caused by sawtooth induced changes in plasma parameters:

$$\frac{\Delta \dot{N}}{\dot{N}} \simeq \frac{2\Delta n_D(0)}{n_D(0)} + \gamma\ \frac{\Delta T(0)}{T(0)} + \frac{2\Delta m_D + \gamma \Delta m_T}{2m_D + \gamma m_T} \qquad (3)$$

The last part involving profile changes plays an important role for the interpretation of neutron yield variation during sawtooth oscillations.

In the case of charged fusion products, $\ell(x) < 1$, which gives rise to a new effect, a loss burst during the reconnection stage of the sawtooth crash, when the plasma profiles adjust to the new conditions. The physical explanation of the burst is that confined particles accumulated during the sawtooth build up phase have a radial profile which broadens and/or have a loss factor, $\ell(x)$, which increases. Present day experimental evidence suggest that both mechanisms are operative. However, in both cases particles generated during a sawtooth period, t_s, are lost during a reconnection time, t_r, cf. [2]. This implies an amplification factor $t_s/t_r >> 1$ for the loss intensity, thus generating a burst.

This scenario can be made more quantitative as follows:
For moderate direct particle losses, the local loss fraction $\ell(x)$ can be approximated as, [1]

$$\ell(x) \simeq \begin{cases} \frac{1}{\sqrt{8A}}\ (1 - K_S + x + K_S x^2) & x_S < x < 1 \\ 0 & 0 < x < x_S \end{cases} \qquad (4)$$

where A is the aspect ratio and $x_S = 1 - 1/K_S$ with

$$K_S \equiv \left(\frac{A}{ME_b(\mathrm{MeV})} \right)^{1/2} \frac{2ZI(MA)F(1)}{1+[3(1+1/A)]^{1/2}} \qquad (5)$$

In eq. (5), M and Z denote the mass and charge numbers of the particle, E_b its birth energy and F(x) the normalized flux function which is determined by the current profile (total current I).

As an illustration, the present analysis is applied to the INTOR Benchmark experiment, cf. [2]. For the loss rates before (0) and after (1) the sawtooth crash we obtain

$$\frac{\dot{N}_1}{\dot{N}_o} \simeq 5 \tag{6}$$

The burst intensity, N_{burst}, can be estimated for the two cases:
(i) no spatial or velocity space redistribution occurs during reconnection but the current profile changes from parabolic to flat. This implies

$$\frac{\dot{N}_{burst}}{\dot{N}_o} \simeq 20 \tag{7}$$

(ii) full spatial and velocity space redistribution during reconnection plus a flattening of the current profile. This increases the burst intensity to

$$\frac{\dot{N}_{burst}}{\dot{N}_o} \simeq 35 \tag{8}$$

Collisional slowing down effects can be discussed as follows: The time evolution of the alpha particle distribution function, f_α, is (neglecting energy diffusion)

$$f_\alpha(v) \sim \frac{1}{v^3}\left[H(v-v_\alpha e^{-t/\tau_s}) - H(v-v_\alpha)\right] \tag{9}$$

where τ_s is the collision time and H(v) denotes the Heaviside step function. Eq. (9) pictures a slowing down front at $v=v_\alpha \exp(-t/\tau_s)$ sliding along the steady state distribution $f_\alpha(v) \sim 1/v^3$ towards thermal energies. The confinement properties of an alpha particle depends on its energy, E, through $K_s \sim 1/E^{1/2}$, which determines the radius of confinement, x_s, cf. eqs. (4) and (5). Thus, as E decreases the loss rate is reduced. A rough estimate of the effect of slowing down on the loss rate of the burst is obtained by evaluating the losses for the average energy of the time dependent distribution over a sawtooth period. The average energy, $\bar{E}$, is

$$\bar{E} = E_\alpha \frac{\tau_s}{2t_s}\left[1-\exp(-2t_s/\tau_s)\right] \tag{10}$$

This reduces the losses as obtained in eqs. (7) and (8), e.g. in case (i) we now obtain $\dot{N}_b/\dot{N}_o \simeq 7$. Significant slowing down during the sawtooth build up phase implies that the spectrum should be very broad. Furthermore, the spectrum of the accumulated particles can be expected to be slightly down-shifted due to additional slowing down during the reconnection time, t_r. This energy shift, ΔE, is determined by

$$\Delta E = E_\alpha \frac{\tau_s}{2t_r}\left[1-\exp(-2t_r/\tau_s)\right] \tag{11}$$

The present theory is qualitative on several points. Nevertheless, several features of the recently observed losses of 15 MeV protons in JET, [2], seem to be consistent with the present model, in particular the characteristic burst feature as well as the broad and downshifted spectrum of the burst.

References

[1] D. Anderson and P. Batistoni, Nucl. Fus. (to appear).

[2] G. Martin, O.N. Jarvis, J. Källne, V. Merlo, G. Sadler, and P. Van Belle, Physica Scripta, T16, 1987, 171.

[3] E. Bittoni and M. Hąegi, Proc. 15TH European Conf. on Contr. Fus. and Plasma Phys., Dubrovnik, 1988, part I, 298.

FEEDBACK STABILISATION OF DISRUPTION PRECURSOR OSCILLATIONS

A W Morris, S Arshad [1], C Balkwill, G Fishpool[2], P S Haynes, T C Hender, J Hugill, P C Johnson, J B B Percival, D C Robinson, D L Trotman, A J Vickers

UKAEA Culham Laboratory/Euratom Fusion Association, Abingdon, Oxon, U.K.

Introduction

The major disruption has been one of the failings of the tokamak since its inception, and despite the improvements in the operating systems of modern large tokamaks, it is still not possible to run a tokamak with no disruptions in a regime that is reactor-relevant. This is reflected in the designs of "next step" devices such as ITER [1] where the design has to withstand the large electromechanical and thermal stresses of disruptions. A new experiment has been started on the DITE tokamak to study further the problem of using magnetic feedback to stabilise the MHD instabilities seen as precursors to major disruptions – similar experiments have been performed in the past [2,3] demonstrating some instability control, but without successful prevention of the disruption itself. This report describes preliminary measurements of the plasma response to applied helical fields as a function of plasma parameters, which reveal properties of the equilibrium and dictate the transfer function of the remainder of the feedback loop.

Experimental Configuration

As in earlier experiments the mode is detected by Mirnov coils and the feedback applied by a helical magnetic field. The DITE system is designed to minimise phase lags in the system, so both detectors and driving coils are placed inside the vacuum vessel, which consists of 12–25mm thick stainless steel sectors separated by 0.5mm thick bellows. Figure 1 shows the layout of the detector and saddle coils. The detectors consist of 4 arrays of 8 large B_r and B_θ coils ($nA = 0.49, 0.091\text{m}^2$, respectively). The detector arrays are positioned in the bellows sectors on $R = 1.17$m, $a = 0.28$m at $\phi = 22.5°, 90°, 202.5°, 270°$ and are spaced with $\Delta\theta = 45°$, except at the outboard midplane where there are B_θ coils at $\pm 6.5°$ to simulate the proposed JET arrangement.

The feedback magnetic field is provided by 8 saddle coils on $R = 1.19$m, $a = 0.26$m centred in the thick sectors at $\phi = 0°, 112.5°, 180°, 292.5°$, with toroidal extent 20° and at $\theta = \pm 45°, \pm 135°$. The coils are formed from bare stainless steel plate. They are connected to form quadrupole fields at each toroidal location, and opposite saddles are connected to form two independent $m = \pm 2, n = 1$ windings. These are powered by two 5kA, 60V transistor amplifiers, which can drive 500A in each coil at 10kHz or 1kA at 5kHz, corresponding to $B_r(m = 2, n = 1) \sim 1$G at $r = 20$cm. The amplifiers will be converted to current mode when the feedback loop is closed.

[1]University College, University of Oxford, U.K.
[2]Imperial College of Science & Technology, University of London, U.K.

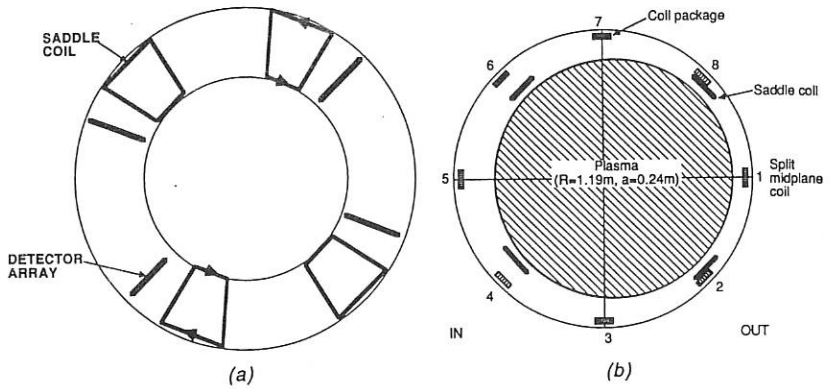

Figure 1: *Schematic layout of DITE feedback windings and detectors (a) plan, (b) poloidal section*

To create the input signal for feedback, opposite pairs of detector arrays are combined to form two $m,n = 2,1$ sensors: $V_1 = \sum_i A_i[\dot{B}_\theta(\theta_i, \phi = 22.5°) - \dot{B}_\theta(\theta_i, \phi = 202.5°)]$ and a similar expression for the other pair of detector arrays, where the weights A_i are set by multiplying DACs. This allows any combination of the signals to be formed, thus enabling the mutual inductance,including the plasma-induced coupling, of the detectors and the driving saddles to be nulled. The phase of the feedback loop is adjusted by mixing the two signals with different amplitudes: this adjusts the phase in the *spatial* domain, not the temporal domain, and allows optimum frequency response. The phase and gain of the feedback loop can be functions of 3 parameters: time, mode frequency and mode amplitude – these parameters are to be used as real-time addresses of a 3-dimensional pre-programmed look-up table. This approach should allow for compensation of any phase errors in the electronics and for effects of the resistive liner.

Initial results – measurements of the plasma response

Previous experiments [2,3] and theory [4,5] show that an applied helical field is modified by the plasma. The response is different for resonant and non-resonant helicities of the applied field. The saddle coils on DITE are configured to produce no net helicity (i.e. $B_{m=2,n=1} = B_{m=-2,n=1}$) and so, in the absence of plasma, there should be no signal on coils displaced toroidally by 90° from the saddle loops. This is observed when one $m = 2, n = 1$ winding is driven at fixed frequency. In the presence of plasma, however, a signal is expected since the two opposite helicities no longer cancel. A substantial signal is indeed observed on these detectors, providing clear evidence of plasma response.

Figure 2 shows how the spatial structure of this signal varies with $q(a)$ for sawtoothing discharges with $I_p = 100$kA, $R = 1.19$m, $a = 0.23$m and $\bar{n}_e \sim 3 \times 10^{19}$m^{-3} when

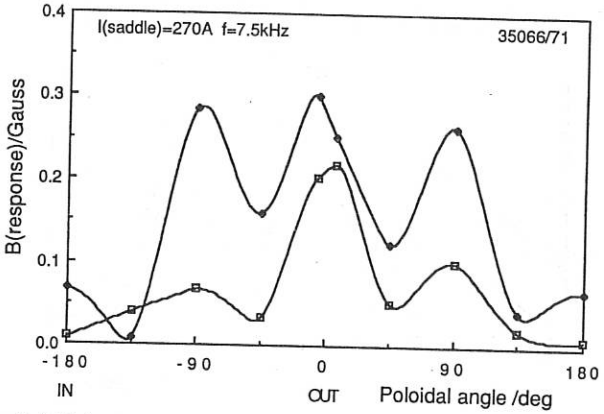

Figure 2: *Poloidal structure of plasma response* ($B_\theta(n = \text{odd}, \phi = 90°)$) *at different* $q(a)$: • : $q_{cyl}(a) = 3.3$; □ : $q_{cyl}(a) = 5.6$

the driving frequency is 7.5kHz. The response is deduced from the cross-spectrum of $B_\theta(n = \text{odd}, \phi = 90°)$ and I_{saddle} at the drive frequency. It is seen that the basic structure is an $m = 2$ standing mode as expected (there is a π phase change at each minimum), but there are substantial $m = 1, 3$ toroidal sidebands. A comparison with theory is given in ref [5]. The majority ($\gtrsim 75\%$) of the response varies as $\sin(m\theta + \phi)$ as expected, but a small $\cos(m\theta + \phi)$ or $\sin(m\theta + 3\phi)$ component may also be present. The rapid appearance of the standing wave ($\lesssim 100\mu s$)suggests that it is indeed due to an ideal-MHD effect rather than resistive penetration, at least initially. Further the response is only a weak function of frequency (3.5–17.5kHz). The amplitude of the response is typically $\sim 0.2 - 0.6$G for 300-500A in the saddle coils, and is approximately in agreement with theoretical predictions [5]. There is a small background MHD mode at $\sim$ 10kHz in these discharges at a level of $\sim 0.1 - 0.3$G, with $m = 2$ and toroidal sidebands. It is notable that this mode apparently does not lock to the applied perturbation at the current levels used, but co-exists at a different frequency, even when the driving frequency is within the $\sim$ 1kHz linewidth of the background mode. The phase relative to the driving field is the same for all shots examined, indicating that the $\Delta' = 0$ boundary is not crossed [4], as expected given the background MHD activity.

The plasma response is calculated to be a function of Δ' and so the response is expected to change as the plasma becomes more unstable. This is indicated in Figure 2, as the background MHD activity increases by a factor of ~ 5 as $q(a)$ falls over this range. Figure 3 shows the change in the response amplitude as the density is increased at constant $q(a)$, when again the natural mode amplitude increases. Some asymmetry is apparent in the spatial structure of the response close to the disruption boundaries.

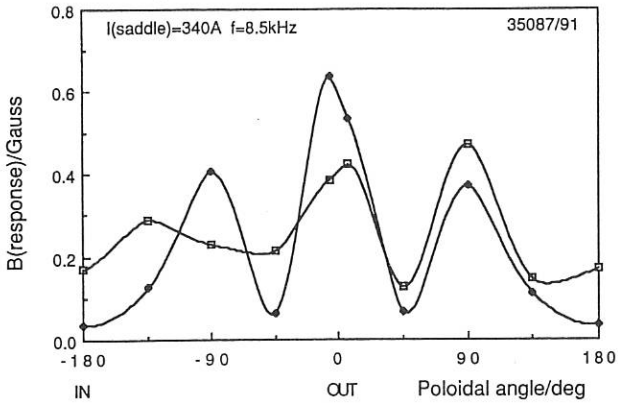

Figure 3: *Plasma response at different* $\bar{n}_e$ *with* $q_{cyl}(a) = 3.3$. $\bullet$: $\bar{n}_e = 1.2 \times 10^{19} m^{-3}$; $\square$: $\bar{n}_e = 4.7 \times 10^{19} m^{-3}$. $\bar{n}_e$(disruption) $= 5.0 \times 10^{19} m^{-3}$.

Conclusions

A flexible configuration of detectors and saddle coils has been installed in DITE for experiments on magnetic feedback control of disruption precursors. Initial open loop experiments demonstrate the existence of a standing wave driven by the applied helical field, approximately consistent in many cases with theoretical predictions. The magnitude and spatial structure of this plasma response are relatively weak functions of plasma parameters except close to the disruption limit, and it is likely that the standing wave can be adequately eliminated from the $m = 2, n = 1$ feedback signal.

Acknowledgements

The authors are very grateful to M Hugon, G F Neill, J Snipes , P E Stott and N V Ivanov for advice, to the DITE technical staff under R W Storey for operation of DITE, to the COMPASS group for the loan of the power amplifiers, and to A Simonetto for analysis software. This work is being performed under an Article 14 contract for JET.

References

[1] Post, D "ITER: Physics Basis" 12th IAEA Conf, Nice, Paper F-II-1 (1988)

[2] Bol, K *et al* Proc 5th IAEA Conf, Tokyo, **1**, 83 (1974)

[3] Gvozdkov, Yu V; Ivanov, NV; Kakurin, AM, Sov J Plasma Phys **6**, 130 (1980)

[4] Ellis, JJ *et al* Proc 10th IAEA Conf, London **1**, 163 (1984), Lee, JK *et al* Nucl Fusion **23**, 63 (1983)

[5] C Balkwill *et al*, this conference

PLASMA RESPONSE TO MAGNETIC FEEDBACK ON DITE

C Balkwill, S Arshad[1], S C Cowley[2], P S Haynes,
T C Hender, J Hugill, P C Johnson, A W Morris,
J B B Percival, D C Robinson, D L Trotman and A J Vickers

UKAEA/Euratom Fusion Association, Culham Laboratory, Abingdon, Oxon, UK.

Introduction

A set of saddle coils and mode detector coils have been installed within the vacuum vessel on DITE, to allow active magnetic feedback of the (2,1) mode; a fuller description of this system is given in Ref [1]. In this paper we describe the theoretically predicted response of the plasma to the applied fields and compare the results with experimental observations.

Plasma Response Theory

For resonant harmonics the requirement that the applied magnetic fields satisfy perturbed force balance ($\nabla \tilde{P} = \tilde{J} \times B$), will give rise to strong deviations from the vacuum field structure. To study this problem in toroidal geometry we consider the case $q > 1$, so that we need only retain the resonant surfaces of the $m = 2$, $n = 1$ mode and its side-band $m = 3$, $n = 1$ in an inverse aspect ratio (ϵ) expansion (although the modes $m = 1$ to 3, $n = 1$ are retained in the expansion). In an analogous fashion to Ref [2], we find the relation between B_i^r, the radial field at $q = i$, $\Delta_i' = \lim_{\delta \to 0}[B_i^{r\prime}/B_i^r]_{r_s-\delta}^{r_s+\delta}$ at r_s where $q = i$ ($i = 2, 3$), and the $n = 1$ poloidal Fourier components of the applied feedback currents I_i (i=1,2,3):-

$$\left[\begin{pmatrix} \Delta_2' & 0 \\ 0 & \Delta_3' \end{pmatrix} + \begin{pmatrix} F_{11} & F_{12} \\ F_{21} & F_{22} \end{pmatrix}\right] \begin{pmatrix} B_2^r \\ B_3^r \end{pmatrix} = \begin{pmatrix} C_{11} & \cdots & C_{13} \\ \vdots & & \vdots \\ C_{31} & \cdots & C_{33} \end{pmatrix} \begin{pmatrix} I_1 \\ I_2 \\ I_3 \end{pmatrix} \qquad (1)$$

where the F_{ij} and C_{ij} are equilibrium dependent constants which may be calculated using a version of the code described in Ref [3], modified to incorporate the feedback current terms. In the limit of infinite aspect ratio Eq(1) reduces to

$$(\Delta_2' + F_{11}) B_2^r = C_{22} I_2 \qquad (2)$$

[1]University of Oxford.
[2]Princeton Plasma Physics Laboratory, Princeton, USA.

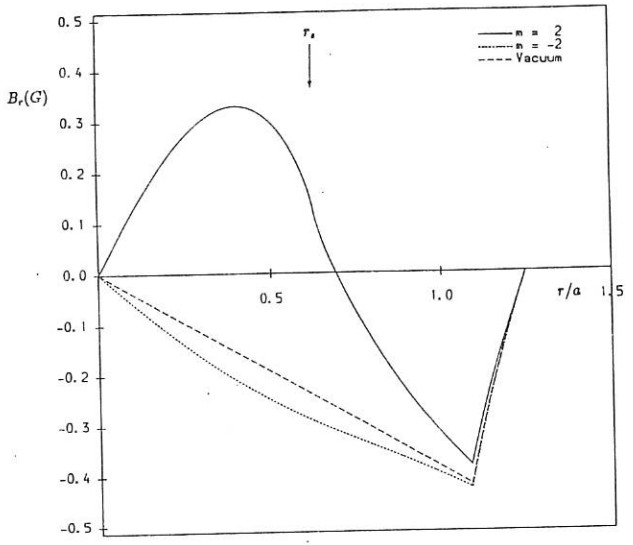

Figure 1: *Predicted radial variation of B_r for $m = \pm 2$, $n = 1$. Lengths are normalised to the plasma limiter radius, (a), with the saddle coils at $r/a = 1.08$, the detector coils at $r/a = 1.17$, and the wall at $r/a = 1.25$.*

with $F_{11} \equiv -\Delta'_0$, the value of Δ' in the absence of the feedback current. By solving equation (1) numerically or by directly integrating the force balance relation in cylindrical geometry we can predict the expected response of the plasma to the feedback fields; these results are described in the next section.

Comparison with Experiment

The saddle coils on DITE have no net twist and thus generate equal and opposite amounts of $(\pm m, n)$ components. However only one of these components $(+m$ or $-m)$ is resonant and subject to significant changes due to the plasma response. Figure 1 shows the theoretically predicted radial variation of B_r in steady state $(\Delta'_2 = 0)$, for the components $m = \pm 2$, $n = 1$ with $q_a = 4.4$, $\beta = 0\%$ and an applied saddle coil current of 280 A. It can be seen that the resonant mode $(m = +2)$ is significantly modified from the vacuum field. The deviation between the $m = \pm 2$ components should give

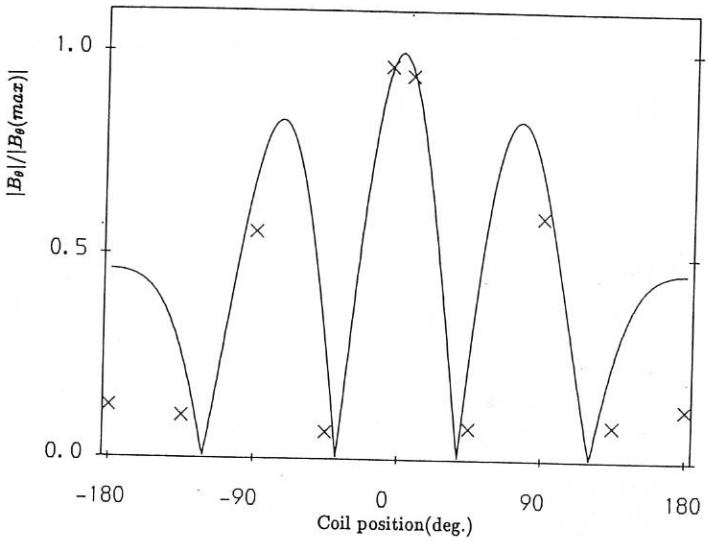

Figure 2: *Comparison of measured (×) and theoretically predicted B_θ (solid line).*

rise to an effect most easily detected in the experiment by measuring the magnetic oscillations at 90° toroidally from a driven set of saddle coils; in vacuum the saddle coils produce $\vec{B}(\phi = 90°) \equiv 0$ and thus any measured oscillations are due to the plasma response (or a natural mode). Figure 2 shows the poloidal variation of the measured B_θ amplitude at $\phi = 90°$ and $f = 7.5$ kHz for an applied saddle coil current of 280 A at 7.5 kHz. It should be noted that the natural mode frequency in this case ~ 10.5 kHz and thus the response measured at 7.5 kHz (in Fig 2) is driven directly by the saddle coils. Examination of the phase of the fluctuations described in Fig 2 indicates that they are probably due to a standing wave [1]; which is as expected, since oscillating a single $n = 1$ set of saddle coils drives a standing wave directly.

From Fig 1 we see that there is $\sim 10\%$ reduction of the $m = +2$ component relative to the $m = -2$ component. This plasma response corresponds to a $B_\theta(\phi = 90°) \sim 0.15$ G (for a saddle coil current of 280 A); this is in reasonable agreement with the experimentally measured B_θ value (~ 0.2 G of $m = 2$, $n = 1$).

For Figure 1 we have assumed that the steady state has been achieved and that there has been sufficient time for tearing to occur at $q = 2$. In the opposite limit, $B_r(q = 2) = 0$, we find very similar results for the response amplitude.

The peak B_θ values in Fig 2 show a strong ballooning characteristic with the B_θ peaks being far larger on the outboard ($\theta = 0°$) than on the inboard side ($\theta = \pm 180°$).

This is partly due to a geometric effect, since the plasma is centred 2 cm farther out than the detector coils. The ballooning effect is however, mainly due to constructive at ($\theta = 0°$) and destructive (at $\theta = \pm 180°$) interference between the $m = +2$ mode and its side-bands $m = 1$ and 3. A toroidal calculation solving Eq(1) for the DITE coil current distribution ($I_1 : I_2 : I_3 = -0.13 : 1.0 : 0.048$) assuming $q = 1.1(1 + 3.0r^2)$ gives the magnitude of these side-bands and gives reasonable agreement with the experimentally measured B_θ (see solid line in Fig 2).

Conclusions and Discussion

It has been shown that the plasma response causes resonant harmonics (in particular $m = 2$, $n = 1$) to deviate significantly from their vacuum values. The theoretically calculated response, including toroidal effects, appears to be in reasonable agreement with the DITE experimental results. It should be noted however that the poloidal variation and magnitude of the plasma response are strong functions of the current profile for fixed q_a (and may also be functions of β particularly near the β limit). Thus care must be exercised in drawing conclusions from comparisons with the experiment.

Since the plasma response is a function of the stability parameter Δ'_0 (cf Eq(2)), its measurement should allow the onset of instability to be detected and may provide information about the current profile. Understanding of the plasma response is also an important prerequisite to the active feedback experiments.

Acknowledgements

This work was performed under an Article 14 contract with the JET Joint Undertaking. We are grateful to our JET colleagues, in particular P Stott, J Snipes and G Neill, for useful conversations and comments. The authors are also very grateful for the assistance of the DITE technical staff under R W Storey, to the COMPASS group for the loan of the power amplifiers and to A Simonetto for analysis software.

References

[1] A W Morris et al, 'Feedback Stabilisation of Disruption Precursor Oscillations', This conference.

[2] J W Connor et al, Phys. Fluids **31** (1988) 76.

[3] J W Connor et al, 'Tearing and Micro Tearing Instabilities in the Tokamak', Proc 12th IAEA Conf, Nice, 1988

Sawtooth Activity during Impurity Accumulation in ASDEX

R. Nolte, G. Fussmann, O. Gruber

Max-Planck-Institut für Plasmaphysik
D-8046 Garching, Fed. Rep. of Germany

Introduction

Previous investigations in ASDEX have revealed that sawteeth instabilities not only result in a flattening of density and temperature in the plasma center but lead also to a reduction of impurity concentration in this region /1/. This counteracting mechanism is most important in regimes with peaked density profiles (e.g. pellet injection, IOC, Counter-NBI), because here the dominating neoclasssical effects induce a strong inward drift of impurities. In ASDEX-discharges with peaked density profiles we generally observe an increase of the sawtooth repetition time ending with complete suppression of sawteeth. The subsequent accumulation of impurities then leads to a central radiation collapse.

Invoking the Kadomtsev model of the sawtooth relaxation /2/ this behaviour may be explained by the influence of impurities on the evolution of the conductivity profile during the sawtooth rise. If a rapid influx of impurities keeps the conductivity profile flat after the sawtooth crash, the current profile will not be able to peak again to bring q below the critical threshold $q_{crit} < 1$ for sawtooth initiation. In this picture the sawtooth repetition time should be related to the resistive time scale $\tau_j = \mu_0 r_1^2 \sigma / 15$, where σ and $r_1 \simeq a/3$ denote the conductivity and radius of the sawtoothing region respectively.

In a similar way, it has recently been demonstrated that peaking of the Z_{eff}-profile can explain the suppression of sawteeth during pellet refuelled discharges in ALCATOR C /3/.

In this paper we present a detailed study on the behaviour of sawteeth during Counter-NBI discharges with additional ICRH, which showed density peaking and a remarkable content of light impurities after the onset of ICRH. By investigating the temporal change of $Z_{eff,0}$ and $T_{e,0}$ it is possible to get information about the influence of the central concentration of impurities on the quenching of sawteeth activity.

1. Sawteeth activity in discharges with Counter-NBI and ICRH

In ASDEX density peaking was observed for Counter-NBI discharges ($P_{NBI} = 1.05$MW) with additional ICRH at plasma currents of 380kA /4/ ($q_a = 3.0$, no peaking found for slightly higher currents). Although the discharges were different in ICRH-power ($P_{ICRH} = 0.65 - 1.95$MW), peaking factor, impuritiy concentration ($Z_{eff} = 3.5 - 4.0$), total radiated power P_{rad} and SX-radiation, they all showed great temporal coherence in the evolution of the sawtooth oscillations. This is depicted in Fig. 1, where SX-traces of discharges with different ICRH-powers are reproduced. Before $t = 1.25$s there is only very little phase difference between the sawteeth of different discharges. After this time the discharges evolve differently, ultimately showing sawtooth quenching succeded by a disruption within less than 0.2s.

The discharges with $P_{ICRH} \leq 1.0$MW behave almost like discharges without ICRH. The sawtooth repetition time τ_R increases from about 8ms to roughly 15ms before the sawteeth are suppressed completely. At higher ICRH-powers strong modification of the sawtooth are to be seen. Actually a rapid rise phase at the beginning can be distinguished from a slow slope phase extending until sawtooth crash.

2. The influence of impurities on sawteeth suppression

The following discussion is based on the assumption that after the sawtooth crash flat q- and T_e-profiles are established within a core region $r < r_1 \simeq a/3$. The related profiles of current density j and conductivity σ are also essentially flat at this time, but central heating tends to restore a peaked T_e-profile on a short time scale $\tau_{T_e} \sim r_1^2/5\chi$ with a thermal conductivity of orders of $1\text{m}^2/\text{s}$. The j-profile develops towards the peaked conductivity profile $\sigma \sim T_e^{1.5}/Z_{eff}$ but is largely delayed because of the very long diffusive time scale $\tau_j \sim r_1^2\mu_0\sigma/15$ $((\mu_0\sigma)^{-1} \simeq 0.015\text{m}^2/\text{s})$. After the repetition time τ_R a sufficient large increase of Δj_0 on axis (i.e. a decrease of Δq_0) is reached by which the next sawtooth is triggered. Impurities can change the outlined procedure by changing the conductivity via radiation losses ($\dot{T}_e < 0$) as well as by central accumulation ($\dot{Z}_{eff} > 0$). The total change of the conductivity on axis,

$$\langle \frac{\dot{\sigma}_0}{\sigma_0} \rangle = \frac{3}{2} \langle \frac{\dot{T}_{e,0}}{T_{e,0}} \rangle - \langle \frac{\dot{Z}_{eff,0}}{Z_{eff,0}} \rangle$$

averaged over a sawtooth period is therefore an important quantity. As soon as $\langle \dot{\sigma}_0/\sigma_0 \rangle$ is approaching negative values sawtooth quenching is expected because no peaked j-profile will be restored under this conditions.

In fig. 2 the central values of the two contributions $3/2\langle \dot{T}_e/T_e \rangle$ and $\langle \dot{Z}_{eff}/Z_{eff} \rangle$ are compared for the discharge with $P_{ICRH} = 0.65$MW and the upper of the two discharges in fig. 1 with 1.70MW. The temperature change was taken from the ECE-diagnostic. Z_{eff} was derived from data of the visible Bremsstrahlung diagnostic /5/. To provide sufficient time resolution the density from the HCN interferometer was taken to correct $Z_{eff} \sim P_{Brems}\sqrt{T_e}/n_e^2$ which normally is evaluated with Thomson scattering data (sampled every 15ms).

We notice that in both cases a crossing occurs at times $t^* = 1.2$s and $t^* = 1.4$s after which $\langle \dot{\sigma}_0/\sigma_0 \rangle < 0$. This behaviour reflects qualitatively the observation presented in fig. 1. In reality, however, the true quenching time is delayed about 60ms and 200ms respectively. As to be seen in fig. 2 the transition to $\langle \dot{\sigma}_0/\sigma_0 \rangle < 0$ is caused by both, a decrease of the central T_e-variation and an increase of the Z_{eff}-variation. In contrast to the large decrease of the central T_e-variation the corresponding variation at larger radii stays about constant. This observation may be explained by assuming a non-central triggering event during the late sawtooth phase $t > t^*$.

3. The dependence of the repetition time τ_R on σ

From our picture a scaling of the sawtooth repetition time τ_R with τ_j is to be expected. To check such a dependence we plot in fig. 4 τ_R as a function of the conductivity σ_0 on axis for the lower of the two discharges in fig. 1 $P_{ICRH} = 1.7$MW. 1. The approximate scaling of τ_R with σ for most of the sawteeth is obvious. Deviating points are those of the last two sawteeth before suppression. This finding is contrary to the results

reported in /6/ where a scaling of τ_R with the timescale of heat transport $\tau_{T_e} = r_1^2/5\chi$ is predicted.

4. Analysis of the current profile during sawteeth

To get more insight into the sawtooth mechanism we have started to analyze the sawtooth behaviour using measured n_e-, T_e-, P_{rad}-profiles, the sawtooth event times and a current profile mixing as in the Kadomtsev model using the TRANSP-code. Fig. 4 shows the resulting time behaviour of $q(0)$ with and without full current mixing for a Counter-NBI discharge with $q(a) = 2.5$. The measured sawtooth inversion radius can only be recovered with a weaker current mixing than predicted by the Kadomtsev model. This is in line with the results of section 2 suggesting a non-central mechanism for the sawtooth trigger. During the last large sawteeth in the beam-heated phase the influence of the j-mixing model on $r_{q=1}$ is reduced. T_e- and n_e-data show in all cases a much broader region of inverted sawteeth than can be generated by the Kadomtsev formulation. After the last sawtooth the decreasing T_e and increasing Z_{eff} (due to impurity accumulation) result in an increasing $q(0)$ i.e. decreasing $j(0)$ and the critical q-profile for the triggering of a sawtooth may not be reached again.

Summary

We find strong indications that quenching of sawteeth, which is preferentially observed in discharges showing peaked density profiles, can be explained by impurity accumulation. The reason is due to enhanced central radiation on account of metallic impurities (Fe, Cu) that lower $\dot{T}_e$ and in addition to the influence of low-Z impurities (C, O) increasing $\dot{Z}_{eff}$ after each sawtooth crash. Both effects finally prevent a peaking of the conductivity profile. A further support for this interpretation and the underlying physical picture is obtained from the sawtooth repetition time which scales approximately proportional to the central conductivity.

References

/1/ G. Fussmann et al., Proceedings of th 14th European Conference on Contolled Fusion and Plasma Physics, Madrid 1987

/2/ B. B. Kadomtsev, Sov. J. Plasma Physics **1** (1975) 389

/3/ M. Greenwald et al., paper presented at the Workshop on Pellet Injection, Gut Ising 1987

/4/ F. Ryter et al., this conference

/5/ H. Röhr, K.H. Steuer, ASDEX-Team, Rev. Sci. Instruments **59** (1988) 1875

/6/ F. Alladio, M. Ottaviani, G. Vlad, Plasma Physics and Controlled Fusion **30** (1988) 597

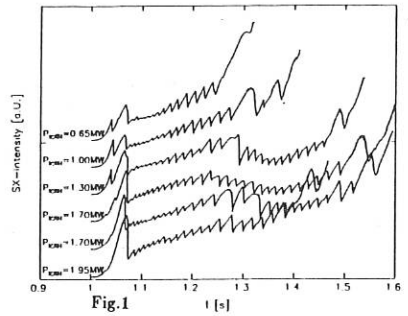

Fig.1

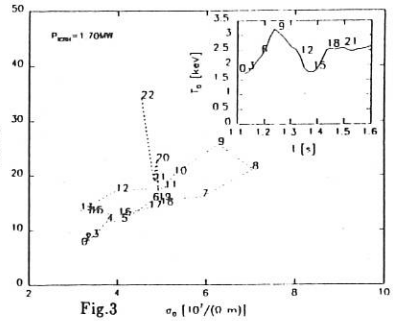

Fig.3

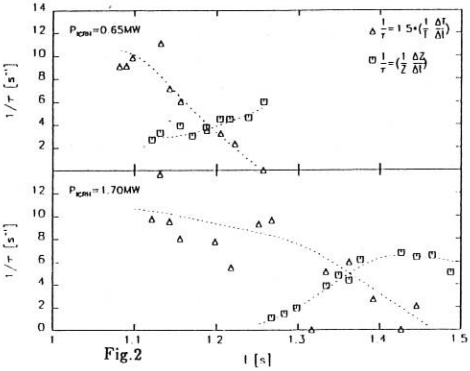

Fig.2

Fig.1: SX-Intensity showing the coherent sawtooth behaviour for discharges with CTR-NBI (1.05MW) and ICRH. NBI from 1.05s, ICRH from 1.10s until disruption. The traces are shifted equally against each other.

Fig.2: Contribution of the variation of $T_{e,0}$ (triangles) and $Z_{eff,0}$ (squares) to the variation of conductivity σ_0 on axis during sawtooth rise (see text).

Fig.3: Scaling of the sawtooth repetition time τ_R with conductivity σ_0. The numbers on the $T_{e,0}$-trace indicate the position of the sawtooth events (see text).

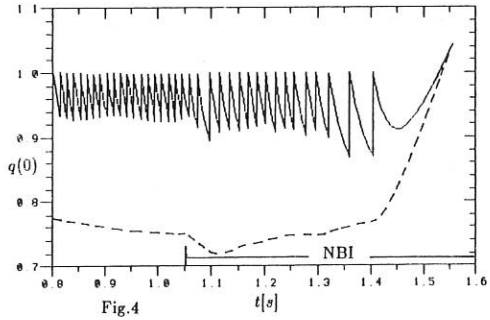

Fig.4

Fig.4: Time evolution of $q(0)$ with (solid line) and without (dashed line) full current mixing for a Counter-NBI discharge calculated using the TRANSP-code.

INVESTIGATION OF AXISYMMETRIC SPLITTING INSTABILITIES OF A TOKAMAK PLASMA

R.Weiner, S.C.Jardin*, N.Pomphrey*
MPI für Plasmaphysik, Boltzmannstr. 2, D-8046 Garching
*) Princeton University, PPPL, P.O.Box 451, Princeton, NJ 08543

Abstract

A recently published study, [1], suggests that elongated tokamak plasmas with sufficiently large pressure are susceptible to an ideal axisymmetric splitting instability (n=0, m=2). We find, using the Princeton Tokamak Simulation Code (TSC) [2], that these configurations are stable to all even poloidal mode number deformations. We extended our investigation of splitting modes by considering the deformation of an elliptic plasma to a doublet. Here we determined the critical coil currents in a set of pinching coils needed to split the plasma apart.

Introduction

Advanced tokamaks such as CIT or ITER will operate with highly shaped plasma cross sections, with elongations of $\kappa = 2$ or more. It is well known that these configurations are susceptible to an ideal MHD antisymmetric vertical displacement instability (n=0, m=1) which has to be stabilized by passive wall structures and active feedback systems. Here we consider the stability of these configurations to an even mode number symmetric splitting instability (n=0, m=2). Previous analytic calculations, [3], have shown these modes to be stable. However, in a recent numerical study, [1], the authors conclude that elongated cross section tokamak plasmas are unstable with respect to an ideal MHD splitting instability (n=0, m=2) if the plasma beta exceeds a critical value, depending on the elongation. They maintain that elliptical cross section tokamaks with R/a = 3.2 and with $\kappa = 2.6$ are unstable to splitting for $\beta_t > 5\%$, and that $\kappa = 4.0$ plasmas are unstable to splitting for $\beta_t \geq 1.0\%$. We have investigated the splitting behaviour of highly shaped TCV [4] tokamak plasmas by performing simulations using TSC [2] and found no indication of these symmetric splitting instabilities even for high elongations of $\kappa = 3.7$ and high toroidal beta of $\beta_t = 25\%$. To force splitting and to produce indented plasma shapes, we introduced additional coils ("pinching coils")

on both sides of the plasma midplane waist. By ramping the currents in these coils we found stable doublets with bifurcated magnetic axes even at high pressure (e.g. $\beta_t \approx$ 26%). If the current in the pinching coils exceeded a critical value, we were able to split the plasma apart. The critical current is a decreasing function of the plasma β.

Numerical Simulation

We have carried out a series of TSC simulations to investigate splitting modes in the absence of the vertical instability by considering a TCV plasma with a plasma current of $I_p = 1.2\ MA$ and enforcing up/down symmetry. An input dataset for the TCV tokamak was provided by F.B.Marcus [4]. Here the vacuum vessel and the external coils of the TCV tokamak are modelled by single grid conductors as illustrated in the figures. Additional divertor coils and pinching coils on both sides of the plasma have been introduced to allow the investigation of divertor plasmas and to squeeze the plasma in order to produce doublets. We studied limiter and divertor plasmas with elongations between $\kappa = 3$ and $\kappa =$ 3.7 and a toroidal beta lying between $\beta_t = 6\%$ and $\beta_t = 32\%$. The current in each pinching coil ranged from 0 kA to 200 kA. Starting the simulation with a divertor plasma ($\kappa = 3$, $\beta_t = 11\%$) as illustrated in Fig.2, the current in the pinching coil was ramped to a certain value and then kept constant. For pinching coil currents of $|I_{pinch}| \geq 175kA$ per coil, the plasma always split into droplet pairs. Snapshots of equilibria during the splitting phase are shown in Fig.4a, b, and c. Pinching coil currents of $|I_{pinch}| \leq 175kA$, however, allow stable single magnetic axis or doublet equilibria. The flux and current density contours of a stable equilibrium with $\beta_t \approx 26\%$ and $|I_{pinch}| = 100kA$ is shown in Fig.3, with a bifurcated magnetic axis at $R = 0.92m$ and $z = \pm 0.18m$. Having found a stable solution, the pressure was increased in time until the plasma split. In this manner we determined the critical pinching coil currents as a function of the toroidal beta. The results of the simulations are summarized in Fig.1, where the critical pinching coil current $|I_{pinch}|$ is plotted versus the toroidal beta. If the pinching coil currents are below the critical value the plasma is stable to the splitting instability. In particular, for all cases studied, the plasma was found to be stable to splitting for $|I_{pinch}| = 0$, which corresponds to an elliptical shape.

Conclusion

The splitting of tokamak plasmas has been studied in case of the TCV tokamak. For highly elongated equilibria with elliptical cross sections we found no indication for the symmetric splitting instability (n=0, m=2). To split the plasma apart additional pinching coils were necessary. Here we determined the corresponding critical pinching coil currents as a function of the critical toroidal beta. Below the critical values we found a broad range of stable single magnetic axis configurations and doublets with a bifurcated magnetic axis, even at high pressure. We conclude that the splitting instabilities are of no concern for present envisaged advanced tokamaks.

Acknowledgements

We would like to thank F.B. Marcus for providing us with a TCV input dataset for the TSC code and for stimulating discussions

References

[1] Y. Nakayama, T.Sato, K.Matsuoka; Phys. Fluids **31** (3), March 1988, 630

[2] S.C.Jardin, N.Pomphrey, J.DeLucia; JCP **66** (1986) 481

[3] G. Laval, R. Pellat, J.S. Soule; Phys. Fluids **17** (1974) 835, R. Dewar, et al; Phys. Fluids **17** (1974) 930, P.H. Rutherford; PPPL 976 (1973)

[4] F.B. Marcus, private communication, CRPP, Lausanne

Fig.1

Stability diagram:

Current in pinching coils versus toroidal beta

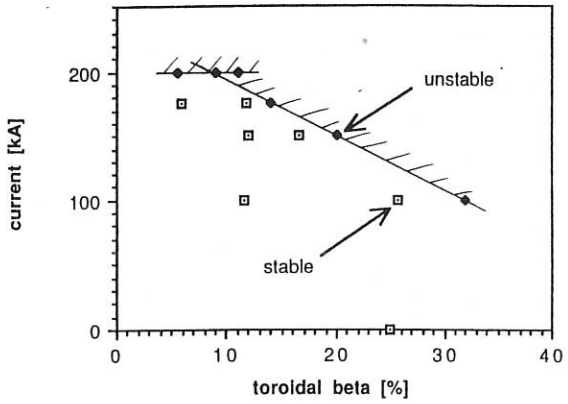

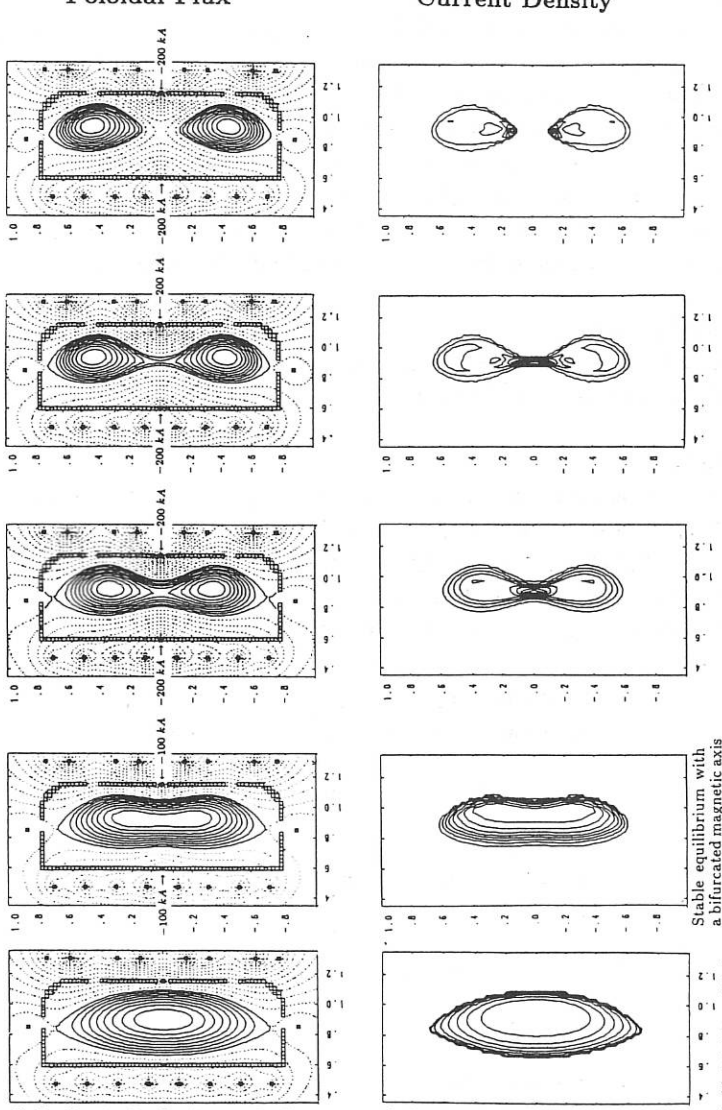
Poloidal Flux
Current Density
Fig.2
Fig.3
Fig.4a
Fig.4b
Fig.4c
Stable initial equilibrium
$I_p \approx 1.2\ MA$, $\beta_t \approx 11\%$
Stable equilibrium with
a bifurcated magnetic axis
$I_p \approx 1.2\ MA$, $\beta_t \approx 26\%$
$|I_{pinch}| = 100\ kA$
Fig.4a,b,c: Snapshot sequence of equilibria during the splitting phase
$I_p \approx 1.2\ MA$, $\beta_t \approx 11\%$, $|I_{pinch}| = 200\ kA$

SIMULATION OF ASDEX UPGRADE SHOT SCENARIOS WITH POWER SUPPLY CONSTRAINTS

R.Weiner, H.Bruhns, S.Cha, O.Gruber, K.Lackner, U.Seidel
MPI für Plasmaphysik, Boltzmannstr.2, D-8046 Garching

1. Introduction

ASDEX Upgrade, presently under construction at IPP Garching, is a divertor tokamak allowing experiments with elongated plasmas of Single and Double Null shapes. For this tokamak, we have performed a series of dynamical simulations during the start up, the flat top and the shut down phase, using the Princeton Tokamak Simulation Code (TSC) [1]. In the simulations, we have included all coil groups, i.e. the ohmic heating system, the poloidal field coils external to the TF magnets, the inner control coils as well as passive structures such as passive conductors and the vacuum vessel. The feedback control of the plasma position by the inner control coils and the external poloidal field coils, both during regular shot scenerios and for disruption simulations under realistic power supply constraints, is studied. In the following we describe in somewhat more detail two applications, the simulation of a complete discharge including the start up phase and a plasma disruption. Although in both cases of the simulation, model assumption are required for the thermal energy transport, the emphasis is here on the aspects of plasma position and shape control and the electrodynamics of the poloidal field circuits.

2. Complete Discharge Simulations

Numerical simulations of complete Single Null discharges including start up, flat top and shut down phase during 10 sec have been performed. The interaction of the plasma with the poloidal field coil system and passive wall structures have been taken into account by modelling the vacuum vessel, the top - bottom unsymmetric passive conductors and the poloidal field coils as illustrated in Fig.1. In the simulations plasma current and poloidal field coil currents as determined from the Garching equilibrium code, have been preprogrammed and correction currents have been determined by position and plasma current feedback systems. The desired currents consist of pre-

programmed and feedback currents. By comparing desired and actual currents the feedback voltages have been determined. For energy transport, a model by Coppi and Tang [2] was taken which describes the L-mode scaling and consequently underestimates the expected β and τ values during additional heating by a factor of order 2.

In an example, the simulation of a Single null shot is started with a plasma current of 100 kA. Due to power supply limitations, the current ramp rates in the poloidal field coils are not sufficient during the initial plasma current rise for obtaining divertor configurations. Therefore the discharge is started as a limiter plasma at the torus inner wall needing less PF currents compared to those of divertor plasmas. Additional precharging of PF coils is necessary and the resulting stray field is compensated by the inner control coils. After break down a divertor equilibrium is provided as soon as possible, in our example at time $t \approx 80\ msec$. During the expansion phase the major radius increases to about 1.65 m and the plasma is displaced vertically by $\approx$ 15 cm. The evolution of the 99% surfaces of equilibria from the inboard limiter to a divertor plasma during 80 msec is shown in Fig.1. The final cross sectional shape is obtained after $\approx$ 200 msec. During the pure ohmic heating phase up to 1.5 sec, the plasma current is raised to 1.2 MA as shown in Fig.2a and the poloidal beta evolves to about $\beta_p \approx 0.2$ (Fig.2b). The auxiliary heating of $\approx$ 10 MW is started during the plasma current ramp up phase as the necessary changes in the PF currents going from low to high β_p help to save Vsec. The flat top is reached after 2.5 sec with a plasma current of 1.6 MA, a poloidal beta of ≈ 0.7 and a density of $\approx 1.5 \cdot 10^{20}\ m^{-3}$. At the end of the flat top and auxiliary heating phase (t = 7 sec) the plasma current is ramped to the initial value within 3 sec and the plasma is moved to the inside limiter again.

Presently we are optimizing the Single Null shot scenarios by readjusting the preprogrammed quantities especially the plasma position, the currents of the external shaping coils and of the OH coils, where we take into account also the actual voltage supply restrictions. We are trying to optimize also the feedback coefficients for the plasma current control and the control of the radial plasma position in order to avoid radial overshoots which would cause the plasma to touch the outboard limiter (the ICRH antenna) during the start up phase.

3. Simulation of Single Null Plasma Disruptions

Several scenarios for plasma disuptions in ASDEX Upgrade have been simulated to assess the limits up to which - with the foreseen power supplies - discharges can be sufficiently controlled to avoid strong wall contact and terminal current quench after a partial disruption. As one result of such simulations we show the time trajectory of the magnetic axis position in the R - z plane for the case of a high - β_p Single Null disruption in ASDEX Upgrade (Fig.3). For such a simulation we distinguished three phases:

- A short stable discharge phase which serves to produce reasonable initial conditions for the plasma configuration. During this period (which corresponds to the first 4 msec in Fig.3) the plasma position is controlled by the feedback system acting on the interior control coils. With proper choice of initial parameters, heating power and energy transport model, the radial and vertical plasma excursion during this phase are kept to less than 3 mm.
- Plasma disruption phase (from 4 msec to 5 msec). We simulate the consequences of the thermal quench phase of a minor disruption by transiently increasing the factor in front of our heat conductivity expression from 1 to 500. The plasma loses its equilibrium position, the plasma current decreases from 1.6 MA to 1.58 MA and the β_p value reduces from 1.6 to 0.7.
- Recovery phase (from 5 msec to 30 msec). After the thermal quench phase the heat conductivity enhancement factor is reset to the original value. Due to the action of the feedback systems, the plasma position and the current converge back to their original values.

Acknowledgements

We would like to thank S.C. Jardin and N. Pomphrey for helpful discussions.

References

[1] S.C.Jardin, N.Pomphrey, J.DeLucia; JCP **66** (1986) 481

[2] S.C.Jardin et al.; Nuclear Fusion Vol.27, No.4 (1987)

Fig.1: Evolution of the 99% flux surfaces during the start up phase of a Single Null discharge. Also shown the modelling of passive structures and the poloidal field coils.

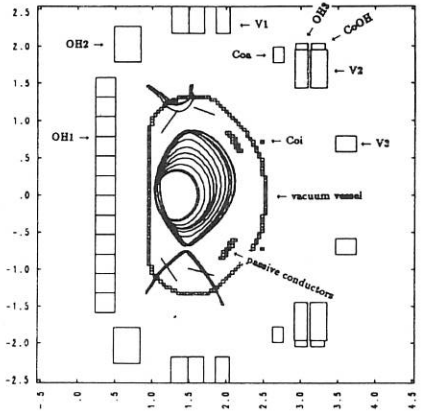

Fig.2a: Plasma current in kA of a Single Null discharge: 2.5 sec current ramp up, 4.5 sec flat top, 3 sec shut down.

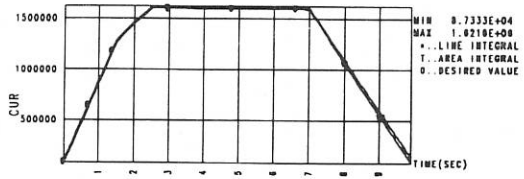

Fig.2b: Poloidal beta and internal inductance during a complete discharge. Auxiliary heating is applied at time T = 1.5 sec.

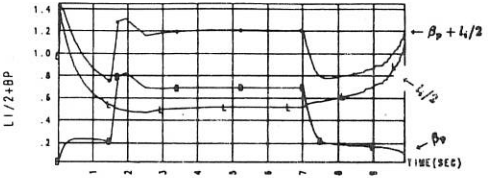

Fig.3: Trajectory of the mag. axis position during a minor disruption (Time: 0 sec → 0.03sec)

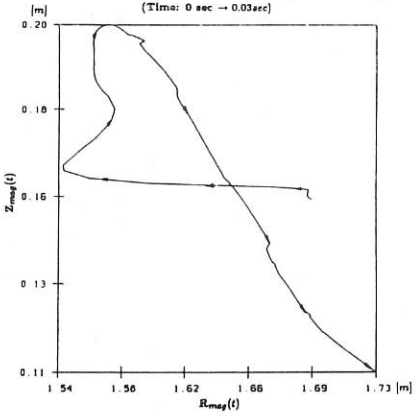

MHD Activity in PBX-M

S.M. Kaye, S. Preische, N. Asakura, R. Bell, R. Fonck, A. Holland, H. Kugel, B. LeBlanc, M. Okabayashi, S. Paul, M. Reusch, N. Sauthoff, S.Sesnic, H. Takahashi

Princeton Plasma Physics Laboratory, Princeton University, Princeton, N.J. 08543, U.S.A

Introduction

Magnetic activity leading to disruptions was found to be the ß-limiting mechanism in low-q ($2 \le q \le 4.5$) discharges in the PBX tokamak [1]. This activity was characterized by low frequency (few to 25 kHz) m=3/n=1 oscillations growing over the course of tens of μsec to two msec, and culminating in a plasma disruption or a large sawtooth-like event followed several msec later by a disruption. Both theoretical analyses and experimental data indicated that the observed growing mode could be explained to zeroth order by destabilization of the ideal n=1 external kink mode [2,3]. Theory further showed that a conducting wall in close proximity (a few cm) to the plasma could effectively stabilize these external kinks for higher-$<ß_t>$ operation.

In recognition of these results, the PBX tokamak was modified by installing close fitting conducting plates to stabilize the ideal surface kinks, and by allowing plasma operation at larger major radius for increased indentation (to date, indentations of up to 24% have been achieved, in comparison to the PBX maximum of 20%). A cross-section of the PBX-M device is shown in Fig. 1. Also shown in the figure are the equilibrium flux surfaces for an I_p=590 kA, B_t=1.2 T, indentation=24%, and q_{edge}=3.5 plasma. The inboard and upper passive plates are for stabilizing the n=0 vertical instability, while the outer sets of plates are meant to stabilize the n=1 ideal surface kink. The passive plates are 1.25" thick aluminum plates bonded to a thin stainless steel sheet, with an L/R time of 20 msec. The plates are electrically connected toroidally and vertically, except for one toroidal gap, and Rogowski coils are situated at various toroidal locations on legs connecting the top and bottom outermost plates in order to monitor the induced currents in these plates. Once the problem of external kinks is eliminated by the plates, PBX-M will pursue its primary goal of probing the second stability regime to ballooning modes utilizing indentation and current and pressure profile control.

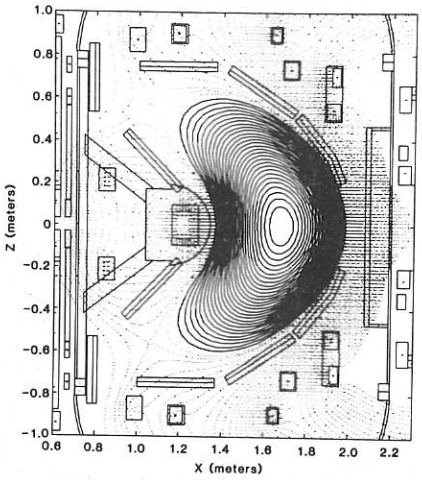

Fig. 1 Equilibrium flux plot of a 24% indented PBX-M plasma

This paper will focus on preliminary observations of magnetic activity associated with disruptions and the change in broadband magnetic activity across H-mode transitions. The magnetic activity in PBX-M is measured by a toroidal array of six Mirnov coils situated on the outer midplane approximately 20 cm from the plasma edge, and a poloidal array of 20 coils with plasma/coil separations varying from several to ≥30 cm, depending on the locations of the coils. All coils are calibrated up to approximately 250 kHz.

Low-q Operation

One of the distinct differences between PBX and PBX-M to date has been the facility with which PBX-M is able to operate at $q \le 3$. Here, q is taken to be the MHD q at the 95% flux surface. As was seen in PBX,

the ability to operate at q≤3.5 was limited by poor discharge survivability [1]. All plasmas with q≤3.5 would disrupt, and it was difficult to achieve q≤3.5 under any circumstances, with the occurrence frequency of the low-q discharges being only about 1/5 of that for q>4. Additionally, discharges with q≤3.5 could be achieved only with large current ramps (>1.5 MA/sec).

In contrast, PBX-M plasmas have routinely operated at q<3, and down to approximately 2 with no perceptible decrease of discharge survivability in the q=2 to 3 range. This is shown in Fig. 2, where the number of shots in each q-bin is plotted in histogram form. The data contained in the figure are approximately evenly divided between OH and NBI (P_{inj}≤2.5 MW) discharges. The data shown are taken from discharges with indentations >5%, and those discharges with q≤3 are limited to indentations ≤17%. The low-q discharges in PBX-M could be achieved with little or no current ramping (≤0.5 MA/sec). Although the data in Fig. 2 are only a preliminary statistical evaluation of discharge survivability, the ability to operate at q<3 in PBX-M utilizing little current ramping may indicate the beneficial effects of both increased indentation and the stabilizing effects of the passive plates.

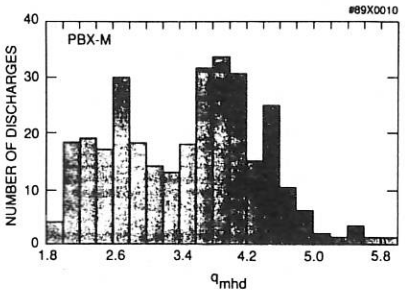

Fig. 2 Distribution of accessible q in PBX-M for indentations >5%. Both OH and NBI were used.

Disruption Scenarios

Approximately 80% of the discharges used for constructing Fig. 2 disrupted. The reasons for this are twofold, but both are related to the, as yet, non-optimal plasma control system because of the limited operational lifetime of PBX-M. The first reason for disruption is due to the loss of vertical control of the plasma, and the second is due to the loose coupling between the plates and the plasma edge. Typical plasmas have an edge-to-plate separation of ≥10 cm near the outer midplane, and, therefore, the full stabilizing effect of these plates may not yet be realized. This is especially true if either the plates are not perfectly conducting and the mode is not purely ideal. Nevertheless, studies of the disruption characteristics of PBX-M plasmas have hinted at the beneficial effect that the plates have on the MHD modes leading up to the disruption.

Unlike the PBX plasmas, however, the disruptions in PBX-M have no typical single type of precursor activity. The disruption precursors are seen to be either at high (50 to 70 kHz with short toroidal coherence lengths) or low (few kHz) frequency. The low frequency activity is sometimes seen to grow as the mode locks, and the high frequency activity appears to be localized on the inboard side of the plasma. In some cases, only a growing, locked, n=1 mode is seen prior to the disruption.

One interesting sequence of events leading to a disruption is seen in Fig. 3. The figure is a composite of (from the top) edge and central chord integrated soft X-ray emissivity, outer midplane Mirnov coil, plasma current, currents measured on two hockey stick passive stabilizer plates approximately 180° apart toroidally, midplane H_α, and a flux difference measurement indicating n=0 vertical motion. In this example, a low frequency (2 to 3 kHz) n=1 oscillation was seen to grow at 525 msec. The oscillation was seen on the soft X-rays, Mirnov, and passive plates. The H_α trace shows an increase, indicating enhanced interaction with the wall during the time of the n=1 mode. The mode appeared to begin to lock near 530 msec, and then grew, resulting in another n=1 helical perturbation, as seen on the plate currents, and a rapid decrease in soft X-ray emissivity and further increase in the plasma/wall interaction. Some fluctuations were seen on the plasma current trace, although the current did not start to decrease until about one to two msec later, when the plasma exhibited n=0 vertical motion. The vertical motion was most probably due to rapid inward motion of the plasma caused by the loss of energy at 531 msec, and it sometimes occurred simultaneously with the n=1 helical perturbation.

While the discharge in Fig. 3 is meant to display some of the qualitative features of the PBX-M disruptions, there are certain reproducible features that indicate the stabilizing effect of the plates for a range of

discharge characteristics and heating powers.These include 1)the observation that n=1 plate currents are induced in response to the n=1 fluctuations in the plasma, 2) the fact that the growth time of the mode can be longer than those in PBX discharges with similar discharge conditions, and 3) mode amplitudes at the coil which are comparable for similar discharge conditions in PBX and PBX-M even though the observation point in PBX is at a 50% greater distance than that in PBX-M, perhaps indicating a smaller amplitude at the source. It is unlikely that the source region for these fluctuations is drastically different in PBX and PBX-M for similar discharges.

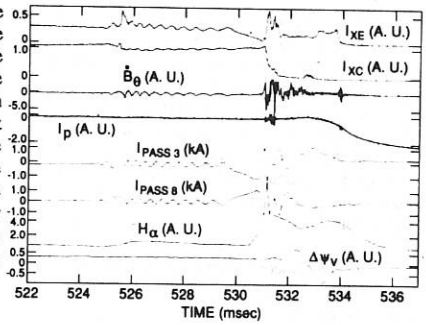

Fig. 3 Sequence of events leading up to one type of disruption on PBX-M.

H-Mode Plasmas

H-mode transitions, with concommitant drops in the H_α emission and rises in plasma density, have been routinely observed in separatrix-limited PBX-M plasmas. The transitions were observed with only ~1MW of neutral beam heating power, less than the ~2.5 MW power threshold required for PBX H-modes. It has been reported elsewhere that the H-mode transition is accompanied by a drop in broadband magnetic activity near the x-point [4], indicative of stabilization of microtearing modes [5]. The 20 coil poloidal Mirnov array in PBX-M enables us to study the full poloidal dependence of the change in magnetic activity across the transition.

Fig. 4a shows the time traces of the raw Mirnov signal measured at a coil situated near the top of the plasma and one at the midplane on the inboard side. The H-mode transition in this shot occurs at 554 msec. At this time, the broadband activity near the top of the plasma decreases, in accord with the previously reported observations. However, the new feature reported here is the observed increase of the signal level on the midplane. The full poloidal dependence of the change in MHD signal level is shown in Fig. 4b. Plotted in this figure is the activity enhancement across the transition at each coil for two frequency ranges, 30 to 50 kHz, and 70 to 100 kHz. The activity enhancement is defined to be the ratio of signal level after to that before the transition, and was calculated from the Fourier transforms of the signals of length 5 msec both before and after the transition. The activity enhancement peaks and is ≥ 1 (increase of signal level) at the midplane, especially in the higher frequency range. Off the midplane, the activity enhancement is ≤ 1 (decrease in signal across the transition), with the largest decrease in signal near the top and bottom of the plasma (near the x-point). Little correlation between signals at different poloidal locations was observed.

An examination of the signals from flux loops and Mirnov coils was made to see if the MHD behavior noted in Fig. 4 could be ascribed to sudden changes in the plasma boundary position or shape at the time of the transition. No such sudden change was apparent. We, therefore, conclude that the observed behavior is due to changes in the amplitude and/or configuration of the source of these fluctuations.

Conclusions

The primary aim of this report is to present preliminary magnetic fluctuation data from the PBX-M tokamak in an attempt to find some indication of the beneficial effects of the close fitting conducting plates for plasma edge stability. While PBX-M plasmas are observed to disrupt, it is believed that the underlying cause of the disruptions is the non-optimal use of the plasma control system leading, in part, to a loose coupling between the plasma edge and the conducting plates. If both the plates and the plasma were ideally conducting, a separation of ~10 cm would be sufficient for stabilization. Any resistivity of the plates or plasma leads to less plate stabilization, and the plate-to-plasma separation would have to be further reduced to enhance the stabilizing effect. The plasmas reported here had a maximum power injected of 2.5 MW; it is

consequently believed that the electron temperature was not very high. A study to detail the stabilizing effects of a resistive plate is presently underway.

Despite the non-ideal characteristics of the plasma and plate, there are indications of a beneficial effect due to the presence of the plates. These are 1) the ability to operate routinely at q<3 with no perceptible decrease in discharge survivability down to q=2, 2) the sometimes slower growth rate and 3) the smaller amplitudes of the low frequency disruption precursor activity, and 4) the fact that n=1 plate currents are induced in response to n=1 fluctuations in the plasma. We, additionally, report on the observations of the change in broadband activity across the H-mode transition, showing that while the signal level is seen to decrease across the transition off the midplane, a dramatic increase in signal level is seen at coils situated on the midplane.

The PBX-M project is supported by U.S. Dept. of Energy Contract #DE-AC02-76-CHO-3073

References

1) S.M. Kaye et al., accepted for publication in Nucl. Fusion (1989)
2) K. Bol et al., Phys. Rev. Lett., 57 (1986) 1891
3) G.L. Jahns et al., Nucl. Fus., 28 (1988) 881
4) M. Malacarne et al., Plasma Phys. and Controlled Fusion, 29 (1987) 1675
5) N. Ohyabu et al., in Proc. of Fifteenth European Conf. on Controlled Fusion and Plasma Heating (Dubrovnik, Yugoslavia, May 1988) Vol. 12B, Part 1 (1988) 227

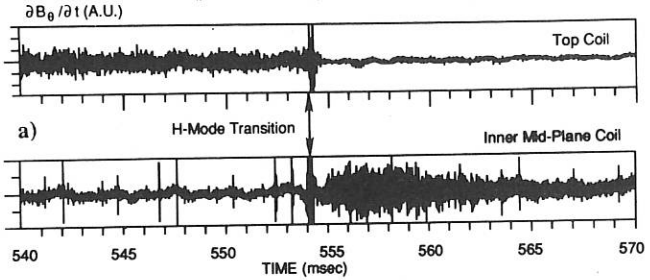

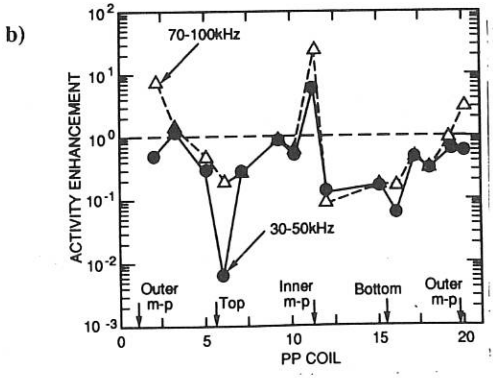

Fig. 4a) Raw signals from two Mirnov coils (top and inner mid-plane) showing the change in broadband activity across the H-mode transition.

4b) Poloidal distribution of the activity enhancement across the H-transition for two frequency ranges. The activity enhancement is defined as the ratio of the signal level after the transition to that before the transition.

EXPERIMENTAL INVESTIGATIONS OF THE INTRINSIC PROFILE FORMATION NEAR RATIONAL SURFACES IN TOKAMAKS

J. Schlüter, H. Soltwisch

Institut für Plasmaphysik, Kernforschungsanlage Jülich GmbH, Association EURATOM/KFA, P.O. Box 1913, D-5170 Jülich, FRG

During regular sawtooth activity in Ohmically heated Tokamaks the amplitude of the precursor oscillations caused by an $m = 1$, $n = 1$ tearing mode passes the detection limit only a short time before the sawtooth crash. The mode is expected to be stable or stay at an undetectable, nonlinearly saturated level only if the slopes of the current density and pressure profiles are reduced near the $q = 1$ magnetic surface. With the TEXTOR tokamak operating at $q = 2.1$ at the limiter, such a plateau in the current density distribution could be resolved recently /1/. Up to now, however, corresponding deformations of n_e and T_e profiles have not been observed, presumably because of the limited resolving power of the diagnostics.

This paper presents high resolution measurements of n_e and T_e profiles during the quasi-stationary phase of Ohmically heated sawtoothing TEXTOR discharges obtained by a nine-channel HCN laser interferometer and a 40 channel mode analyzer (Fig. 1). T_e is derived from the soft x-ray (SXR) continuum by the application of a modified absorber foil method. Signals from highly reproducible plasmas positioned at slightly different major radii are combined to increase the virtual number of diagnostic chords (and thus the spatial resolution) by a factor of five. In addition, a relative calibration of the SXR detector channels is enabled by the horizontal displacement of the plasma column. Signal components that are not correlated with the sawtooth phase are eliminated by forming a coherent average of a large number (~100) of sawteeth measured in 3-4 consecutive discharges /2/. The high shot-to-shot reproducibility needed has been achieved by conditioning and carbonizing the walls very carefully /3/ and by controlling many parameters during a discharge. The soft x-ray spectrum is found to be free of metal lines (which is important for the application of the absorber foil method), and from the enhancement of the continuum by a factor of 3 over pure deuterium bremsstrahlung a Z_{eff}-value of about 1.3 is deduced. In order to account for residual shot-to-shot variations, the signals are normalized to the total number of electrons and the total radiation, respectively, obtained by integrating the output of all chords. The corrections are less than 1% for the line densities and smaller than 10% for the continuum intensities.

As a result of this signal generation and processing, the sawteeth in TEXTOR are represented by two sets of almost noise-free profiles for the interferometric phase shifts $\Delta\varphi(R)$ and the emitted soft x-ray intensities $I_{SXR}(R)$ which are equidistantly separated in time by intervals of $\tau/100$ (with R being the major radius and $\tau \simeq 20$ msec the mean sawtooth period). From these profiles local values of the electron density n_e and the

emissivity ε as well as their variation during a sawtooth cycle can be deduced under the assumptions of eccentric flux surfaces and constant n_e and ε on a given surface. The inversion procedure performed on $\Delta\varphi(R)$ and, for more detailed information, also on $\Delta\varphi - \overline{\Delta\varphi}$ results in $n_e(\rho,t)$ and $\Delta n_e(\rho,t) = n_e(\rho,t) - \bar{n}_e(\rho)$ (see Figs. 5b and 4b; the bar indicates the average over a sawtooth period and ρ denotes the surface radius). The eccentricity $\delta(\rho)$ of the flux surfaces required to match the asymmetry of the phase shift profile follows fairly exactly a smooth parabolic dependence $\delta(\rho) = \delta_0(1 - (\rho/a)^2)$ with an axis shift δ_0 of about 4 cm.

For the inversion of $I_{SXR}(R)$ a method proposed by Gottardi /4/ is applied which yields also the shift δ of the flux surfaces. Figure 2 shows that $\delta(\rho)$ has the same parabolic dependence except for the region 5 cm $< \rho <$ 10 cm inside the $q = 1$ radius ρ_1, where the surfaces appear to be shifted much stronger. To resolve this discrepancy, both sides of the $I_{SXR}(R)$- distribution are inverted independently for $R < R_0$ and $R > R_0$ under the assumption of an undisturbed parabolic shift (Fig. 3). The condition of constant emission on a given surface is surprisingly well satisfied for $\rho > \rho_1$, but again strong deviations from symmetry are observed for $\rho < \rho_1$. However, if we invert $I_{SXR} - \bar{I}_{SXR}$ to obtain the differential emissivity $\varepsilon - \bar{\varepsilon}$, this loss of symmetry disappears (see Fig. 4a), indicating that the sawtooth process takes place on the unperturbed surface structure.

These observations may readily be explained by postulating a small run-away current of less than 1 kA flowing solely inside the $q = 1$ surface with the drift surfaces of the energetic particles displaced outward with respect to the flux surface pattern. If these run-away electrons touch the $q = 1$ surface at $R = R_0 + \rho_1$, they will be lost from the plasma since this point acts as a virtual scrape-off limiter. Thus the bremsstrahlung of the run-away electrons adds to the thermal continuum radiation inside the $q = 1$ surface preferentially towards the outboard side and with the exception of a small region $R_0 - \rho_1 < R < R_0 - \rho_1 + \Delta\rho$ with $\Delta\rho \simeq 2$ - 4 cm. Therefore the branch of $\varepsilon(\rho)$ obtained by inverting $I_{SXR}(R < R_0)$ may be used to study the flattening of the profile also somewhat inside of ρ_1.

Dividing $\varepsilon(\rho)$ by $n_e^2(\rho)$, we obtain a profile which is merely a monotonic function of T_e. By calibration at two radial positions with T_e-values measured by standard techniques, we finally get T_e-profiles of very high spatial resolution without destroying localized structures in the corresponding ε/n_e^2-distribution. Figure 5a clearly shows stationary indentations in the wings of the T_e-profiles which are most likely related to the vicinity of a rational q surface.

At the inversion radius ρ_i, where both n_e and T_e stay constant throughout a sawtooth period and which is located somewhat inside the $q = 1$ surface ($\rho_i = 12.5$ cm $< \rho_1 \simeq 15$ cm as determined from Faraday rotation measurements), the density gradient varies during the sawtooth rise from 5×10^{11} cm^{-4} to -2×10^{11} cm^{-4}. Immediately before the sawtooth crash this value is still a factor of 4 smaller than the corresponding value provided by a parabolic profile $n_0(1 - (\rho/a)^2)$. A shoulder in the density distribution is present for all times. For the T_e-profile the gradient at ρ_i varies from -10 eV/cm to -30 eV/cm, but shoulder formation is observed only towards the end of the sawtooth rise (note that the strong structurization on $\varepsilon - \bar{\varepsilon}$ for $\rho < \rho_i$, which is similar to the one on $n_e - \bar{n}_e$, is strongly diminished by the division by n_e^2). After the sawtooth crash the positive density gradient balances the negative temperature gradient to result approximately in a zero pressure gradient.

References

/1/ Soltwisch, H., Stodiek, W., Manickam, J., Schlüter, J., *Proc. 11th Int. Conf. Plasma Phys. Contr. Nucl. Fusion Research, Kyoto 1986*, Vol. 1, p. 263, IAEA, Vienna, 1987.

/2/ Soltwisch, H., Rev. Sci. Instrum. **59**, 1599 (1988).

/3/ Winter, J., Waelbroeck, F. et al., J. Nucl. Mat. **128-129**, 841 (1984).

/4/ Gottardi, N., J. Appl. Phys. **50**, 2647 (1979).

Figure Captions

FIG. 1: Plasma cross-section shifted to 3 of 5 different positions together with the chord systems for interferometry/polarimetry and SXR mode analysis ($R_0 \simeq 1.75$ m, $a = 0.42$ m, $B_t = 2.26$ T, $I_p = 380$ kA).

FIG. 2: Surface shift δ versus surface radius ρ as derived by Gottardi's inversion method /4/; dotted line: δ [cm] $= 4.4 \times (1 - (\rho/a)^2)$.

FIG. 3: Time-averaged local emissivity $\bar{\varepsilon}$ by independent inversion of $\bar{I}_{SXR}(R)$ for $R < R_0$ and $R > R_0$ under the assumption of a parabolic surface shift (dotted line in Fig. 2).

FIG. 4: Modulations of (a) the local continuum emissivity $\varepsilon(\rho, t) - \bar{\varepsilon}(\rho)$ and (b) the electron density $n_e(\rho, t) - \bar{n}_e(\rho)$ at 10 equidistant times during a sawtooth period.

FIG. 5: (a) electron temperature $T_e(\rho, t)$ and (b) electron density $n_e(\rho, t)$ at 10 equidistant times during a sawtooth period.

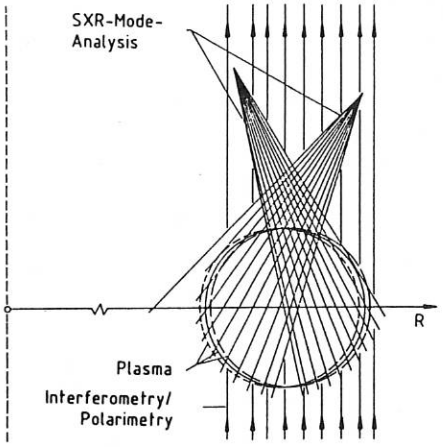

Fig. 1

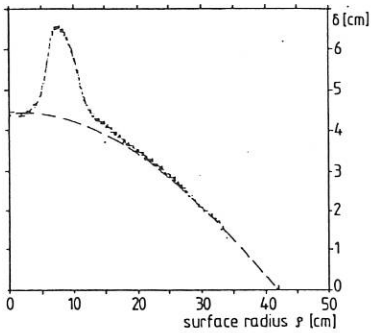

Fig. 2

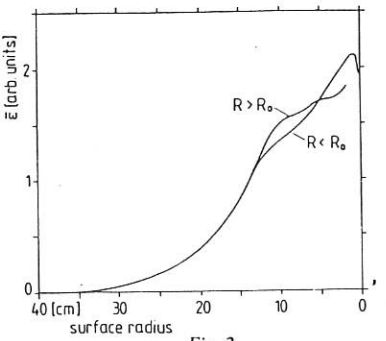

Fig. 3

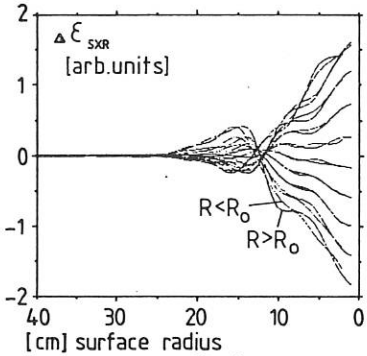

Fig. 4a

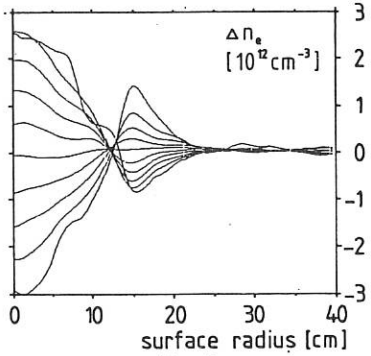

Fig. 4b

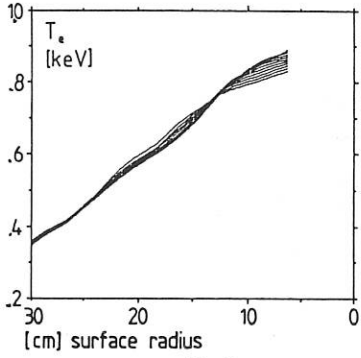

Fig. 5a

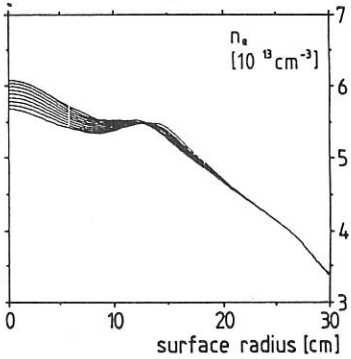

Fig. 5b

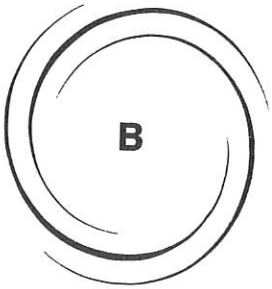

STELLARATORS

ECRH AND ICRF HEATING EXPERIMENTS IN CHS

S.Okamura, M.Fujiwara, M.Hosokawa, K.Ida, H.Idei, H.Iguchi, S.Kubo, K.Masai, K.Matsuoka, S.Morita, K.Nishimura, N.Noda, H.Sanuki, T.Shoji, C.Takahashi, Y.Takita, H.Yamada, Y.Abe, A.Ando, T.Aoki, D.-G.Bi*), J.Fujita, S.Hidekuma, O.Kaneko, T.Kawamoto, A.Mohri, A.Nishizawa, S.Sobhanian†), S.Tanahashi, K.Tsuzuki, K.Yamazaki

Institute of Plasma Physics, Nagoya University, Japan
*) Southwestern Institute of Physics, Leshan, China
†) Department of Physics, University of Tabriz, Iran

1. Introduction

CHS (Compact Helical System) is a torsatron-type device which has an l=2/m=8 helical structure. Its major radius is 1 m and minor radius is 0.2 m with helical pitch modulation $\alpha^* = 0.3$. Maximum toroidal magnetic field at the helical winding center (B_0) is 1.5 T. The main purpose of this experiment is to investigate the plasma confinement and MHD characteristics in low aspect ratio ($A_p = 5$) helical systems. Three heating systems (ECH, NBI and ICRH) have been developed for the plasma production and heating. In this paper we report the initial experimental results on the confinement of ECH plasma and ICRF plasma production.

2. Magnetic Field Configuration

Although the magnetic field configuration is primarily determined by the design of helical coils, there is still possibilities of varying the configuration with different settings of axisymmetric poloidal coils. CHS has four pairs of poloidal coils, three of which (TVF, SF, IVF) are independently excited while OVF coils are excited by the same power supply as the helical coils. Therefore we can select three free parameters to characterize the poloidal field. Decomposing the poloidal field structure into multipole components, we selected the dipole (vertical) and quadrupole components as two free parameters and set the condition of the minimum stray field around the machine as the third free parameter.

Variation of vertical field determines the horizontal position of the magnetic surface. Figure 1 shows important parameters characterizing the magnetic field configuration as a

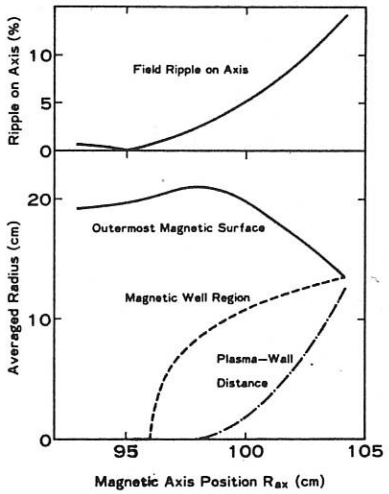

Fig. 1 Dependence of magnetic field configuration on magnetic axis position

function of the magnetic axis position, when the vertical field is varied under the condition of minimum stray field. The quadrupole component is fixed so that the toroidally averaged quadrupole component generated by the helical coils should be reduced by 50 % with the additional quadrupole field generated by the poloidal coils.

The plasma size is largest when the magnetic axis position is shifted inward by about 2 cm from the center of the helical coils. At the same position, the outermost magnetic surface determined by the magnetic field ergodicity touches the inner wall of the vacuum chamber. When the magnetic axis is shifted outward, the ergodic region exists between the outermost magnetic surface and the chamber wall. The magnetic well region is defined as the region where the specific volume of the magnetic surface is radially decreasing ($d^2V/d\psi^2 < 0$). When the magnetic axis is shifted inward, the magnetic field ripple along the axis is reduced.

3. ECH Experiments

The main purpose of ECH experiments in 1988 was to study the basic confinement characteristics of CHS plasma. A 28 GHz gyrotron was used for the plasma production and heating. The magnetic field is set around 1 T in order to locate the fundamental resonance layer near the magnetic axis. The microwave is launched through the port located at the inside of the torus. With this setting, it is possible to have the microwave reach the

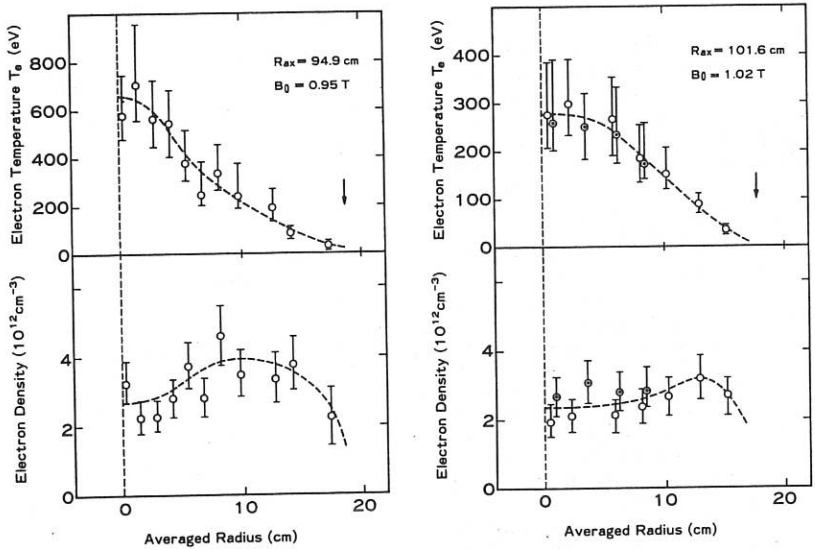

Fig. 2 Electron temperature and density profiles for two different magnetic field configurations. Different temperature scales are used for the convenience of profile comparison.

fundamental resonance layer from the high field side, which should give a higher heating efficiency for a high density plasma. However we have not observed such effects mainly because the heating power (typically 100 kW) is not enough to heat the high density plasma. The electron temperature measured by the Thomson scattering system was 200 - 900 eV at the plasma center which depends on the density (2 - 6 $\times 10^{12}$ cm^{-3}). The electron energy decay time was in the range of 1 - 6 msec.[1)]

In order to study the difference of plasma transport in various magnetic field configurations, we measured the electron temperature and density profiles with the Thomson scattering system for several different cases. We selected following positions of magnetic axis for three typical configurations in Fig. 1.

Case 1 : R_{ax} = 94.9 cm, no field ripple on the magnetic axis.
Case 2 : R_{ax} = 97.4 cm, largest plasma size.
Case 3 : R_{ax} =101.6 cm, sufficient spacing between the outermost magnetic surface and the vacuum chamber wall.

Figure 2 shows the electron temperature and density profiles of hydrogen discharges for two of these cases. Gas fueling rate is controlled to keep the line averaged density roughly constant for these discharges. The magnetic field strength was adjusted to place the ECH fundamental resonance layer at the magnetic axis position. The profiles are plotted as a function of the averaged minor radius. The position of the calculated outermost magnetic surface for each configuration is indicated by an arrow. For the Case 3, the measurements were made for both sides of the profile and double circles are for the measurements on a different side from others. The fitting curves are drawn by hand.

The biggest difference between these profiles is the central temperature (the scales for temperature are two times different for two figures). The launched microwave power is about the same ($P_{MW} \simeq$ 100 kW) for these cases. The radiation power monitor (pyroelectric detector) showed a much smaller signal for the Case 3 which is the indication of reduced plasma interaction with the wall. The shapes of the profiles are also different for these two cases. The Case 1 gives more peaked temperature profile which corresponds to the narrower central hollow in the density profile.

The profiles for the Case 2 is intermediate for the shape and the peak value between the Case 1 and 3. Figure 3 shows the dependence of plasma energy on the magnetic axis position. The total electron energy is calculated by integrating over the temperature and density profiles. The diamagnetic signal gives the total

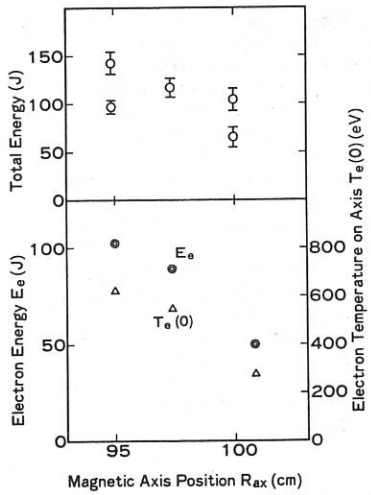

Fig. 3 Dependence of energy on magnetic axis position

energy including the ion contribution. The dependence of total energy on the magnetic axis position was obtained in the different series of the experiments. All these measurements show the better plasma parameters for the inwardly shifted magnetic configuration.

The possible mechanisms for such dependences are the difference of heat deposition profiles and the confinement of high energy electrons. The low ripple magnetic field enhances the power deposition of cyclotron damping at the center of the plasma which raises the central temperature. Inwardly shifted configuration is also better from the aspect of high energy electron's orbit loss. Because the density was low for these experiments, the drift frequency for the high energy electrons ($\gtrsim$ 1 keV) becomes comparable to the collision frequency. In such situation, the confinement of high energy electrons affects the bulk confinement.

4. ICRF Plasma Production Experiments

The ICRF plasma production experiments in CHS have an objective of supplying the currentless plasma for the continuous setting of magnetic field strength. Two types of antennas are installed. The Nagoya Type-III antenna has a carefully designed conductor (10 cm wide and 50 cm long) which fits the magnetic field lines in parallel. This antenna is designed to excite the ion Bernstein wave or Alfven wave depending on the magnetic field setting. The poloidal antenna consists of a pair of quarter-turn conductors located at the outer side of the torus. It is designed to excite the whistler wave. Each antenna has a Faraday shield.

Figure 4 shows the line averaged densities of the hydrogen plasma produced by ICRF heating only for the magnetic axis position R_{ax} = 97.4 cm. The plasma is produced over the all range of magnetic field setting of CHS device (from 0.15 T to 1.5 T) with either antenna system. In the experiments with the Type-III antenna, ion heating was also observed. The ion temperature measured by the time-of-flight type neutral particle energy analyzer was 130 eV. The electron temperature measured by the Thomson scattering was 120 eV for the discharges at B_0 = 1.1 T.

The possible mechanisms of electron heating are, for the Type-III antenna, the Alfven resonance of the shear Alfven wave, and for the poloidal antenna, the electron Landau damping of the whistler wave.

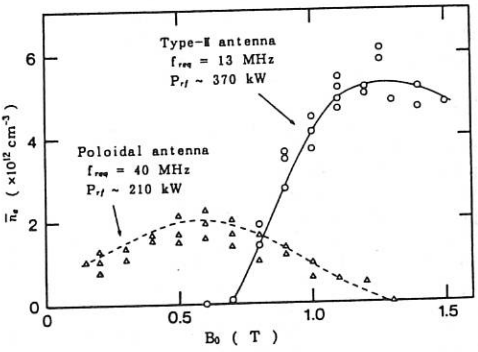

Fig. 4 Line averaged density of ICRF plasma vs. magnetic field

REFERENCE

[1] K. Matsuoka et al. : IAEA-CN-50/I-I-3 in Plasma Physics and Controlled Nuclear Fusion Research (Proc. 12th IAEA Conf., Nice, 1988).

SECOND STABILITY STUDIES IN THE ATF TORSATRON

M. Murakami, B. A. Carreras, J. H. Harris, F. S. B. Anderson[1], G. L. Bell[2], J. D. Bell[3], T. S. Bigelow, R. J. Colchin, E. C. Crume, N. Dominguez, J. L. Dunlap, A. C. England, J. C. Glowienka, L. D. Horton, H. C. Howe, R. C. Isler, H. Kaneko[4], R. R. Kindsfather, J. N. Leboeuf, V. E. Lynch[3], M.M. Menon, R. N. Morris[3], G. H. Neilson, V. K. Paré, D. A. Rasmussen, J. B. Wilgen, and W. R. Wing

Oak Ridge National Laboratory, Oak Ridge, Tennessee 37831-8072, U.S.A.

INTRODUCTION

The Advanced Toroidal Facility (ATF) is a stellarator designed to have direct access to the second stability (β self-stabilization) regime [1]. This regime should be reached when deepening of the magnetic well, caused by increased Shafranov shift with increasing beta, stabilizes pressure-driven (interchange) instabilities. In the initial operating phase, ATF was operated with magnetic islands due to field errors [2,3] (now being corrected). The resulting reduction in effective plasma radius and edge transform caused larger Shafranov shift and improved stability properties for a given value of β. Thus, field errors may actually have facilitated access to the second stability regime. We discuss (1) experimental conditions for these studies, (2) the theoretical threshold for the second stability regime, (3) magnetic fluctuation measurements and predicted β self-stabilization, and (4) confinement behavior.

EXPERIMENTAL CONDITIONS

ATF is a continuous-coil, ℓ=2, 12-field-period torsatron with major radius R_0 = 2.10 m, average minor radius $\bar{a}$ = 0.27 m, magnetic field on axis $B_0 \leq 2$ T, and rotational transform $0.3 < \iota(r) < 1.0$. It

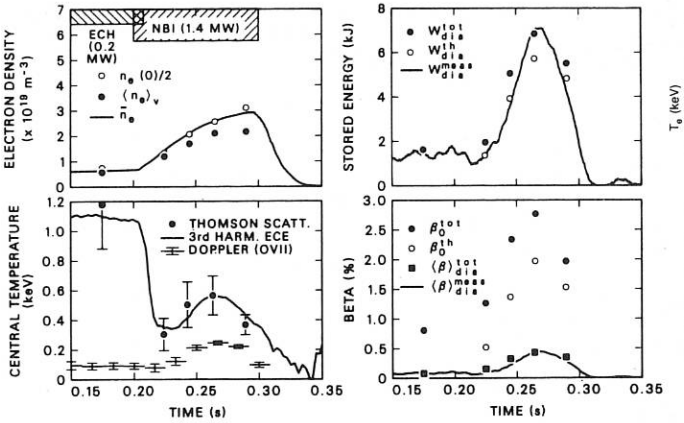

Fig. 1. Characteristics of a typical discharge.

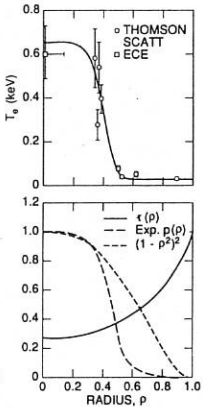

Fig. 2. Radial profiles of electron temperature, rotational transform, and total pressure.

---

[1]University of Wisconsin, Madison, WI, U.S.A.

[2]Auburn University, Auburn, AL, U.S.A.

[3]Computing and Telecommunications Division, Martin marietta Energy Systems, Inc.

[4]Kyoto University, Uji, Kyoto, Japan

has a 0.2 MW, 53 GHz ECH system for currentless target plasma production and a 2 MW, 40 keV, 0.3 s co-plus-counter tangential neutral beam injection system for high-power bulk heating. Experiments began in January 1988. Field mapping [3] in May 1988 with an electron-beam/fluorescent screen technique revealed 6-cm-wide magnetic islands at the $\iota = 1/2$ surface and smaller ones at other rational surfaces. These islands were later found to result from the design of the current feeds to the helical and outer vertical field coils. Corrective measures were taken, and e-beam experiments to confirm the correction are now in progress.

Wall conditioning [4] (with electron cyclotron resonance and glow discharge cleaning combined with baking the vessel up to 150°C) was effective in producing ECH plasmas lasting for up to 1 s with no radiative collapse. However, neutral beam heated discharges were more sensitive to low-Z impurity radiation (particularly oxygen and carbon) [5] and thermally collapsed before the beam pulse ended[6]. Partial coverage (<30%) chromium gettering proved beneficial in extending the duration of the neutral beam pulse and substantially increased the achievable plasma density and stored energy.

Figure 1 shows the time evolution of several parameters for a typical H^+ discharge with balanced beam injection of 1.4 MW total H^0 power into the gettered torus. The stored energy, measured with a diamagnetic loop, reached $W_{dia} = 7$ kJ with $\bar{n}_e = 2.5 \times 10^{19}$ m^{-3}, $n_{e0} \equiv 5 \times 10^{19}$ m^{-3}, $T_{e0} \equiv 0.6$ keV, $T_{i0} \equiv 0.26$ keV at t = 0.265 s. This value of W_{dia} at $B_0 = 0.95$ T corresponds to volume-average β $\langle\beta\rangle = 0.5\%$. For this case, the central β is $\beta_0 = 2.8$—3.2%, depending on diamagnetic or equilibrium weighting of small anisotropic beam contributions. Figure 2(a) shows the electron temperature profile measured with Thomson scattering at $R_0 = 2.10$ m and then mapped into the radial flux coordinate ρ in the finite-β equilibrium geometry. The equilibrium was calculated by the VMEC code with the self-consistent pressure profile shown in Fig. 2(b). Such narrow T_e profiles were observed in both ECH and NBI phases and are probably due to the islands at the $\iota = 1/2$ surface, which effectively reduce the plasma radius to $r_p \equiv 0.6\ \bar{a}$. The narrow pressure profile resulted in a large outward Shafranov shift ($\delta = 0.11$ m $\equiv 0.4\ \bar{a}$).

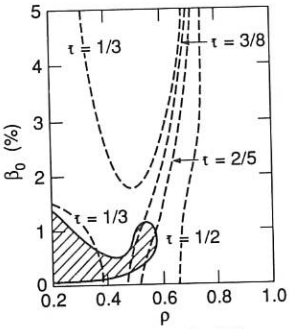

Fig. 3. Calculated ideal stability boundaries and rotational transform contour. The shaded area is the unstable region.

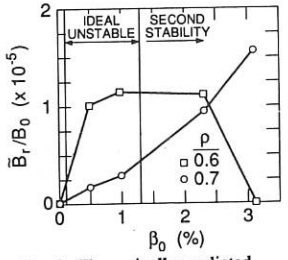

Fig. 4. Theoretically predicted levels of magnetic fluctuations versus central beta.

The field errors may also affect the sensitivity of global confinement parameters (W_{dia} and $\bar{n}_e$) to the vacuum axis shift [2]. The optimal position (at least at low β) was found to be with the vacuum magnetic axis shifted in ~5 cm from the standard configuration, and all of the experiments discussed here were conducted with this inward shift, so that $R_0 = 2.05$ m. The inward shift minimized the $\iota = 1/2$ island width in the vacuum field; significantly larger inward shifts spoiled vacuum stability properties by increasing the destabilizing magnetic hill. As discussed below, the vacuum configuration with a slight magnetic hill at $R_0 = 2.05$ m, combined with large Shafranov shift, made it possible to pass through a narrow, weakly unstable regime as β increased.

MHD STABILITY ANALYSIS

Ideal MHD stability was examined [7] using the Mercier stability criterion ($D_m > 0$) for the equilibrium sequence with the "experimental" pressure profiles. Although the criterion is an asymptotic limit for high-n modes, the stability boundaries for low-n modes generally agree well with those for the Mercier modes. At a given radius (e.g., $\rho = 0.52$, where a large ∇p exists), D_m shows weak instability in the unstable regime. The transition to second stability occurs at relatively low β_0 (= 1.3%) above which D_m increases sharply, reflecting a strong β self-stabilization effect. Complete

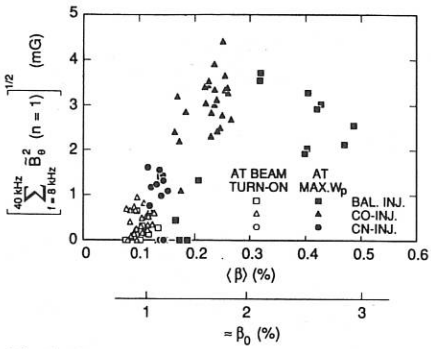

Fig. 5. Observed n=1 magnetic fluctuation amplitudes versus volume-average beta.

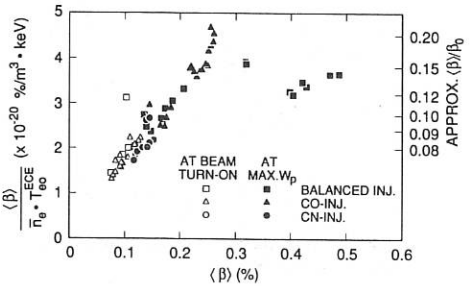

Fig. 6. Pressure "broadness" parameter ($\propto \langle\beta\rangle/\beta_0$) versus volume-average beta.

stability at all radii is attained at $\beta_0 > 1.3\%$ for zero-current equilibria (as shown in Fig. 3) and at $\beta_0 > 1.6\%$ for flux-conserving equilibria. The values achieved in the experiment (β_0 up to 3%) are well above these theoretically predicted thresholds.

Finite-resistivity plasmas exhibit fluctuations even in the second stability regime, which is an ideal MHD concept. The relevant instabilities are resistive interchange (∇p-driven) modes. Theoretically, β self-stabilization, which stabilizes the ideal modes, also reduces the saturation amplitude of the resistive modes as β increases [8]. In this sense, the resistive modes serve a probe to detect access to the second stability regime. These modes are primarily electrostatic ($\tilde{n}$ and $\tilde{\phi}$), and thus magnetic components ($\tilde{B}$) are expected to be small. The dependence of magnetic fluctuation on β_0, calculated from the saturation level of $\tilde{\phi}$, is shown in Fig. 4. Fluctuations caused by resistive interchange modes do not disappear in the second stability regime (particularly near the plasma edge), but show the effect of β self-stabilization in the region where ∇p is large (ρ=0.6) as shown in Fig. 4.

FLUCTUATION MEASUREMENTS

Initial fluctuation measurements [9] on ATF were made with a soft X-ray diode array (on loan from the Heliotron-E group) viewing the central portion of the plasma ($\rho \leq 0.5$) and Mirnov coils ($\tilde{B}_\theta$) located ~30 cm outside the plasma. The soft X-ray signals show no evidence of gross instabilities such as sawteeth or disruptions.

Spectral analysis of $\tilde{B}_\theta$ data from Mirnov coils separated in toroidal angle by $\Delta\phi = 30°$, 150°, and 180° reveals coherent fluctuations (frequency-resolved coherence function $\gamma > 0.7$) in the frequency range 8–40 kHz with amplitudes ~ 10^{-3} G. The relative phase shifts of the signals are predominantly consistent with n=1 toroidal mode symmetry, but some evidence of n=3 components is seen for $\Delta\phi = 30°$. No corresponding coherent activity is seen on the soft X-ray signals. It is difficult to determine the poloidal mode (m) number spectrum at present, because only two poloidally spaced Mirnov coils ($\Delta\theta = 150°$) were available for these experiments; the non-circular flux surface geometry of ATF further complicates the determination of mode numbers. The available spectral data indicate that the fluctuations contain at least two poloidal harmonics, one of which can most simply be interpreted as m=2.

The dependence of the $\tilde{B}_\theta$ amplitudes of the n=1 mode (integrated over 8–40 kHz) on plasma pressure, shown in Fig. 5, suggests (1) a pressure threshold for the fluctuations at $\beta_0 < 1\%$ and (2) saturation and possible reduction of $\tilde{B}_\theta$(n=1) as β_0 exceeds 1.5%. Additional trend analysis shows no obvious correlation with beam configuration or plasma current. The amplitude and overall behavior of the fluctuations are strongly reminiscent of the theoretical predictions for pressure-driven instabilities in ATF.

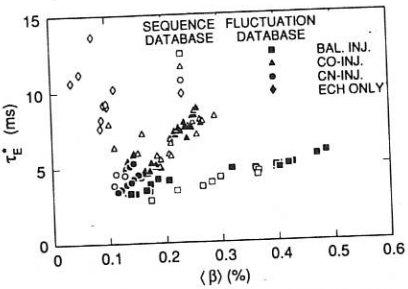

Fig. 7. Global energy confinement time versus volume-average beta.

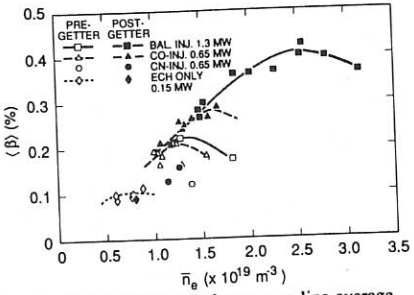

Fig. 8. Volume-average beta versus line-average electron density.

EFFECTS ON CONFINEMENT

Figure 6 shows a profile "broadness" parameter (and corresponding approximate $\langle\beta\rangle/\beta_0$ based on a few profile-analyzed cases) as a function of $\langle\beta\rangle$ for the fluctuation shot database. The pressure profiles broaden rapidly as β increases; this effect saturates for $\beta_0 \geq 1.5$ %. Although many mechanisms could be responsible for such broadening (e.g., change of heating deposition profile), this behavior is *consistent* with growth of the plasma volume and reduced fluctuations (or anomalous transport losses) as the region of magnetic well expands with increasing β. Figure 7 shows global energy confinement time (τ_E^*) versus $\langle\beta\rangle$ for data taken at maximum W_{dia} (i.e., not including data at beam turn-on) in the fluctuation database, overlaid with data from a wider "sequence"(averaged over a large number of shots) database. The improvement at high β is due to increasing $\bar{n}_e$. Figure 8 shows the dependence of $\langle\beta\rangle$ on density for the sequence database. For a given injection power and state of cleanliness, $\langle\beta\rangle$ increases roughly linearly with $\bar{n}_e$, then saturates and decreases. The saturation threshold increases with increasing heating power and improving cleanliness. This translates into an empirical scaling law, $\tau_E^* \propto P_{abs}^{-0.65} \bar{n}_e^{+0.57}$, implying that confinement deterioration is offset by the favorable $\bar{n}_e$ (or β) dependence.

More comprehensive studies in the future will be aimed at correlations of transport, β, and fluctuations. These studies will use configuration control (with vertical fields), profile variations (with limiter, *intentional* field errors, and pellet injection), and internal fluctuation diagnostics (reciprocating Langmuir probe, microwave reflectometer, and heavy ion beam probe).

ACKNOWLEDGMENTS

We acknowledge with appreciation the contributions of our many colleagues in the ATF Group. The research was sponsored by the Office of Fusion Energy, U.S. Department of Energy, under contract DE-AC05-84OR21400 with Martin Marietta Energy Systems, Inc.

REFERENCES

[1] J. F. Lyon et al., Fusion Technol. **10**, 179 (1986).
[2] M. J. Saltmarsh et al., in Plasma Physics and Controlled Nuclear Fusion Research (Proc. 12th Int. Conf. Nice, 1988) IAEA, Vienna (1989), IAEA-CN-50/C-1-2.
[3] R. J. Colchin et al., this Conference (paper P2B10).
[4] P. K. Mioduszewski et al., this Conference (paper P8B2).
[5] R. C. Isler et al., this Conference (paper P8B1).
[6] H. C. Howe et al., this Conference (paper P9B4).
[7] B. A. Carreras et al.,"A First Glance at the Initial ATF Experimental Results" (to be published).
[8] B. A. Carreras, Comments Plasma Physics and Controlled Fusion **12**, 35 (1988).
[9] J. H. Harris et al., Bull. Am. Phys. Soc. **33**, 2070 (1988).

ANALYTICAL FIELD RESULTS FOR LOW ASPECT RATIO STELLARATOR CONFIGURATIONS

F. Alladio, F. Crisanti, F. De Marco, S. Mancuso

Associazione EURATOM-ENEA sulla Fusione, C. R. E. Frascati,
C.P. 65 - 00044 - Frascati, Rome, Italy

One of the ways of exploring the existence of nonergodic vacuum magnetic configurations in nonaxisymmetric toroidal confinement systems has been through the use of the magnetic scalar potential ϕ_M [1,2]. In the absence of a macroscopic current density in a region of space, the magnetic field can be described as $\mathbf{H}=-\nabla\phi_M$, $\mathbf{B}=\mu_0(\mathbf{H}+\mathbf{M})$ where $\mathbf{M}$ is the magnetization density.

Considering the case of the volume enclosed in a torus with surface current densities flowing on its boundary, we can reproduce the magnetic field inside the domain in the following way: i) given the current j flowing on the surface we can replace it by an equivalent magnetization density $\mathbf{M}$ outside the torus so that $\nabla_A\mathbf{M}=\mathbf{j}$; ii) we then evaluate $\nabla\cdot\mathbf{M}$ outside the torus; iii) we finally solve the Laplace-Poisson scalar problem $\nabla^2\phi_M=\nabla\cdot\mathbf{M}$.

The Laplace equation, in the toroidal coordinates $(\theta,\tilde{\omega},\phi)$ with the concentration locus at $R=R_0$ [3], admits the well-known quasi-separable solution [4]:

$$\Phi_M=\sum_{q=0}^{\infty}\sum_{p=0}^{\infty}\left(L^{e,qc}_{pc}\,\phi^{e,qc}_{pc}+L^{e,qs}_{pc}\,\phi^{e,qs}_{pc}+L^{e,qc}_{ps}\,\phi^{e,qc}_{ps}+L^{e,qs}_{ps}\,\phi^{e,qs}_{ps}\right) \tag{1}$$

where $L^{e,q\binom{c}{s}}_{p\binom{c}{s}}$ are the scalar external multipolar moments and

$$\phi^{e,q\binom{c}{s}}_{p\binom{c}{s}}=\sqrt{\mathrm{ch}\theta-\cos\tilde{\omega}}\;Q^{q}_{p-1/2}(\mathrm{ch}\theta)\begin{Bmatrix}\cos\\ \sin\end{Bmatrix}(p\tilde{\omega})\begin{Bmatrix}\cos\\ \sin\end{Bmatrix}(q\phi) \tag{2}$$

are the toroidal multipolar harmonics and $Q^{q}_{p-1/2}(\mathrm{ch}\theta)$ is the second-kind Legendre function [4].

Among the various winding laws that we can try for a helicoidal surface current flowing on a circular cross section torus $\theta=\theta_*$, a simple choice is the one of constant pitch in the toroidal coordinates, i.e.,

$$\begin{cases} j_\phi=\dfrac{mI}{2R_0^2}\,(\mathrm{ch}\theta_0-\cos\tilde{\omega}_0)^2\,\delta(\theta_0-\theta_*)\cos(m\tilde{\omega}_0+n\phi_0) \\ j_{\tilde{\omega}}=\dfrac{nI}{2R_0^2\,\mathrm{sh}\theta_0}\,(\mathrm{ch}\theta_0-\cos\tilde{\omega}_0)^2\,\delta(\theta_0-\theta_*)\cos(m\tilde{\omega}_0+n\phi_0) \end{cases} \tag{3}$$

where I is the modulus of the total current flowing between two lines of null current ($m\tilde{\omega}_0 + n\phi_0 = \pi/2, 3\pi/2, \ldots$) m is the poloidal winding number and n the toroidal one. This surface current allows a fully analytical treatment when steps (i) to (iii) are followed and produces scalar external multipolar moments with only a q=n toroidal number, but with all the p poloidal numbers. In particular, we find

$$\left\{\begin{array}{l} L_{pc}^{e,ns} = \dfrac{I}{2\sqrt{2}\,\pi}(2-\delta_{po})(-i)^n \dfrac{\Gamma(p-n+1/2)}{\Gamma(p+n+1/2)} \left\{ -P^n_{p-1/2}(ch\theta_*)\left[g_{|m+p|}(ch\theta_*)+g_{|m-p|}(ch\theta_*)\right] \right. \\ \left. + \left[(p+n-1/2)\,P^n_{|p-1|-1/2}(ch\theta_*) - ch\theta_*(p-1/2)\,P^n_{p-1/2}(ch\theta_*)\right]\left[Q^0_{|m+p|-1/2}(ch\theta_*)+Q^0_{|m-p|-1/2}(ch\theta_*)\right]\right\} \\ \\ L_{ps}^{e,nc} = \dfrac{I}{2\sqrt{2}\,\pi}(2-\delta_{po})(-i)^n \dfrac{\Gamma(p-n+1/2)}{\Gamma(p+n+1/2)} \left\{ P^n_{p-1/2}(ch\theta_*)\left[g_{|m+p|}(ch\theta_*)-g_{|m-p|}(ch\theta_*)\right] \right. \\ \left. - \left[(p+n-1/2)\,P^n_{|p-1|-1/2}(ch\theta_*) - ch\theta_*(p-1/2)\,P^n_{p-1/2}(ch\theta_*)\right]\left[Q^0_{|m+p|-1/2}(ch\theta_*)-Q^0_{|m-p|-1/2}(ch\theta_*)\right]\right\} \end{array}\right. \tag{4}$$

where $P^q_{p-1/2}(ch\theta)$ is the first-kind Legendre function and $f_m(ch\theta)$, $g_m(ch\theta)$ are the first and second-kind Fock functions [3]. However, when m=1,2 or 3 configurations are considered (i.e., the ones of practical interest for stellarator designs), a truncation of the expansion to p=12 is beyond any useful numerical accuracy. From the scalar potential derived from (2) and (4), the total field can be estimated $\mathbf{B} = -\mu_0 \nabla \phi_M + B_T^0 [(ch\theta - \cos\tilde{\omega})/sh\theta]\,\hat{e}_\phi$ (5) where the second term represents a superposed toroidal field with value B_T^0 at the concentration locus of the toroidal coordinates. An additional vertical field can be added that is derived as the null toroidal winding number limit of the same winding law (3) and would thus be produced by an axisymmetric surface current flowing on the same torus $\theta = \theta_*$ with distribution

$$j_\phi = f_v \frac{B_0^T}{R_0\mu_0} \frac{m}{n\,sh^2\theta_* \sqrt{m^2 sh^2\theta_* + n^2}} (ch\theta_0 - \cos\tilde{\omega}_0)^2\,\delta(\theta_0 - \theta_*) \tag{5}$$

where f_v is a constant of order unity that has to be chosen by an optimization criterion (e.g., by maximization of the rotational transform at the edge of the configuration t_{edge}).

The scalar multipolar moments generated by (5) are

$$L_{ps}^{e,o} = -\frac{2\sqrt{2}}{\pi}(2-\delta_{po}) f_v \frac{R_0 B_0^T}{\mu_0} \frac{m}{n\,sh^2\theta_* \sqrt{m^2 sh^2\theta_* + n^2}} p\left(\int_0^{\theta_*} sh\theta_0\, Q^0_{p-1/2}(ch\theta_0) P^0_{p-1/2}(ch\theta_0) d\theta_0 \right) \tag{6}$$

A field line tracing is simple to calculate on the field expression (5) with the moments (4) describing the helicoidal field and (6) the vertical field and reduces simply to the system $d\theta/d\phi = sh\theta\, B_\theta/B_\phi$; $d\tilde{\omega}/d\phi = sh\theta\, B_{\tilde{\omega}}/B_\phi$.

The main interesting characteristic of the vacuum configurations produced is that they are able to provide extremely low aspect ratios A=<R>/<a> with a value of rotational

transform that exceeds unity when the aspect ratio is greater than 3.5. Even at A=2.7 like the case shown in Fig. 1, we can achieve $t_{edge}=2/3$ (see Fig. 4) and separatrix-like features at the edge of the configuration. The main parameters of the configuration of Fig. 1 are as follows: the surface current is distributed on a torus with R=2.26 m, a=1.05 m (so that $\theta_*=1.4$) with m=2, n=6 winding numbers, I=4.17 MA for the helicoidal field, $B_T^0=5$T at $R_0=2$ m for the toroidal field and $f_v=1.5$ which means a total net current of 0.97 MA for the vertical field. A more machine oriented configuration is the torsatron shown in Fig. 2 that is produced by 2 helical coils discretized by three filaments each and four axisymmetric return coils (see Fig. 3). This configuration has been designed to be as similar as possible as the ideal configuration of Fig. 1. Its main features are I=8.33 MA for each of the two helical coils and return currents, $I_{v1}=-2.37$ MA for the inner vertical coils and $I_{v2}=-4.49$ MA for the outer coils. The main difference is that the volume of the configuration becomes even larger (A=2.3) keeping the same value of rotational transform at the edge (see Fig. 4), but the sharp separatrix-like features of the more idealized configuration are lost. The obvious advantages of a compact torsatron configuration, which are examined in detail in [5], are briefly the lower cost of small aspect ratio machines and the high equilibrium and stability β limit, whereas

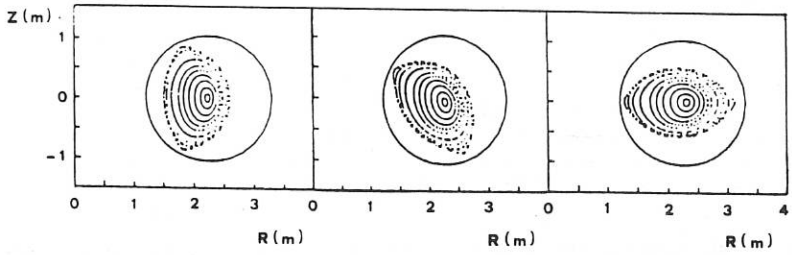

Fig. 1 - Idealized surface current stellarator configuration with m=2 poloidal and n=6 toroidal winding number with aspect ratio A=2.7 at $\phi=0, -2\pi/4n$ and $-2\pi/2n$

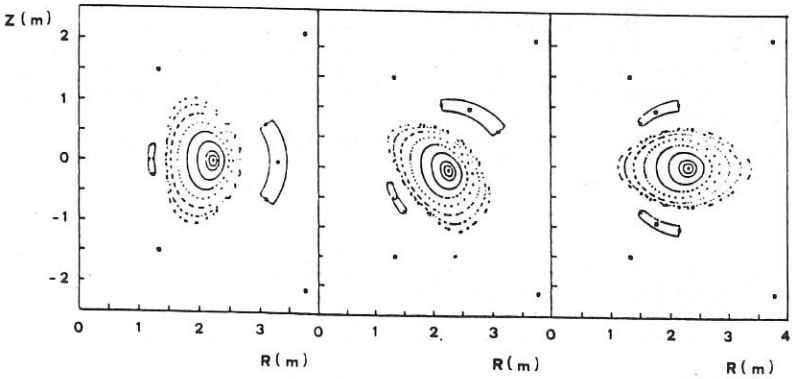

Fig. 2 - Torsatron configuration with same winding numbers and aspect ratio A=2.3 at $\phi=0, -2\pi/4n$ and $-2\pi/2n$

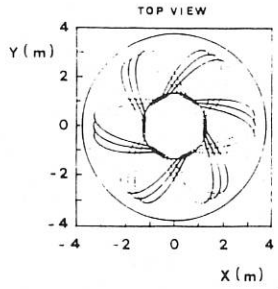

Fig. 3 - Top view of helical and vertical field coils filaments for the torsatron configuration

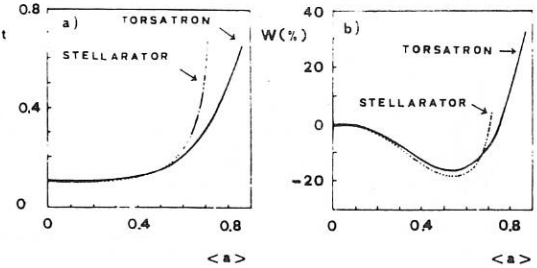

Fig. 4 - Comparison between the idealized stellarator and the torsatron configurations. a) Rotational transform t vs average minor radius <a>; b) Magnetic well depth vs <a>

the two main troublesome points, i.e., the α-particle containment capabilities of such configurations and their resilience to flux surface breaking due to field errors and beta effect are presently under investigation. Two degrees of freedom seem, moreover, to be available to deal with these two difficulties, i.e., the vertical field strength and its multipolar expansion and the unbalancing of the two helical coil currents which can change the nonplanarity of the magnetic axis.

The authors of this paper would like to express their gratitude to the ORNL Group (in particular B. Carreras, S. Hirshman, N. Dominguez and V. Lynch) for helpful suggestions and discussions and for allowing an extensive comparison with their computational codes.

REFERENCES

[1] L.M. Kovrizhnykh: Sov. Phys. Techn. Phys. 8, 281 (1963)
[2] J.R. Cary: Phys. Rev. Lett. 49, 276 (1982)
[3] F. Alladio and F. Crisanti: Nucl. Fusion 26, 1143 (1986)
[4] Morse & Feshbach: Methods of Theoretical Physics,Mac Graw-Hill, New York (1953)
[5] B.A. Carreras et al.: ORNL/TM-10030 (1988)

APPROXIMATE CONSTRUCTION OF RATIONAL MAGNETIC SURFACES IN ANALYTIC VACUUM STELLARATOR FIELDS

W. DOMMASCHK, F. HERRNEGGER, A. SCHLÜTER
Max-Planck-Institut für Plasmaphysik
IPP-EURATOM Association
D-8046 Garching bei München

1.Introduction. A systematic method is applied to reduce the size of magnetic islands in analytic vacuum field configurations where, because of technical reasons, the magnetic fields should be described by a set of Dommaschk potentials[1] of low order. In typical cases, fields with 5 or 6 toroidal periods of length L_P and poloidal mode numbers up to 4 (including axisymmetric fields) define a last closed magnetic surface with aspect ratio $A \approx 11$ to 13 and a value of the twist ι (i.e. angle of rotational transform divided by 2π) of $\iota_b = 5/7$ near the boundary.

The method of measure-preserving tangential mapping [2,3] is used to analyse the vicinity of the fixed points of the mapping. In case of 5 field periods and $\iota = 5/7$, the field line is closed while making 7 toroidal and 5 poloidal revolutions. The mapping of the plane $\phi = 0$ onto itself takes seven field periods (R, ϕ, Z are ordinary polar coordinates). Because of the stellarator symmetry, the matrix of the mapping can be obtained by integrating the field lines over just the half of that number, namely 7/2 periods. The residue R^* of the fixed points of the mapping[2] and its internal twist ι_{is} are computed from the trace of that matrix: the fixed point is of the O-type if $R^* > 0$, and is of the X-type if $R^* < 0$. Because of the stellarator symmetry, one fixed point (to be determined) of the mapping of the plane $\phi = 0$ lies inboard at $Z = 0$, and another distinct fixed point at $Z = 0$ inboard at $\phi = L_P/2R_T$ (the torus radius R_T is the reference length). The residues of these two fixed points are intended to get at small values by varying some values of the field potentials. In addition, the normalized magnetic flux $F = \oint \mathbf{A} \cdot d\mathbf{x}$ between these two closed field lines is computed and, in some cases, iterated to zero by varying another partial field ($\mathbf{A}$ is the vector potential of the magnetic field, $\mathbf{x}$ the radius vector, the line integral is performed over both closed field lines).

2.Results. For demonstration, essentially one nonresonant axisymmetric field[5] is varied to make the absolute values of the two residues sufficiently small for both closed field lines of the connectivity fitting $\iota = 5/7$. The aspect ratio is nearly kept fixed. Fig. 1 shows an example of a configuration with 7 intersections of one closed field line of the O-point type (left column: aspect ratio $A \approx 13$, $\iota_{ax} = 0.73$) and a configuration where these islands have been removed as observed from the figure (right column: $\iota_{ax} = 0.77$). Figure 2 shows a configuration with 6 field periods, small Pfirsch-Schlüter currents (measured by $\langle j_\parallel / j_\perp \rangle = 0.91$), $\iota_{ax} = 0.65$, $\iota_b = 0.96$, and without visible islands.

In a case where the islands are close to the boundary, the island structure was investigated in some detail as shown in the Figs. 3 to 6; Figure 3 shows the island structure

of three different field configurations with decreasing size of the islands. The islands of the configuration WAD321 ($R^* = 0.37 \cdot 10^{-5}$) are surrounded by an ergodic region whereas the islands of the configuration WAD042 ($R^* = 33.95 \cdot 10^{-5}$) are very thin and are surrounded by smooth magnetic surfaces; the configuration WAD847 shows two systems of islands not conneted to each other ($R^* = -1.44 \cdot 10^{-5}$). Fig. 4 shows the internal twist ϵ_{is} (over seven field periods) of the configuration WAD321 as function of the major half-axis of the magnetic surfaces within the island. The internal twist number is almost zero at the fixed point corresponding to the fact that the residue R^* is very small. Nevertheless the islands are still of finite size (left graph of Fig. 3).

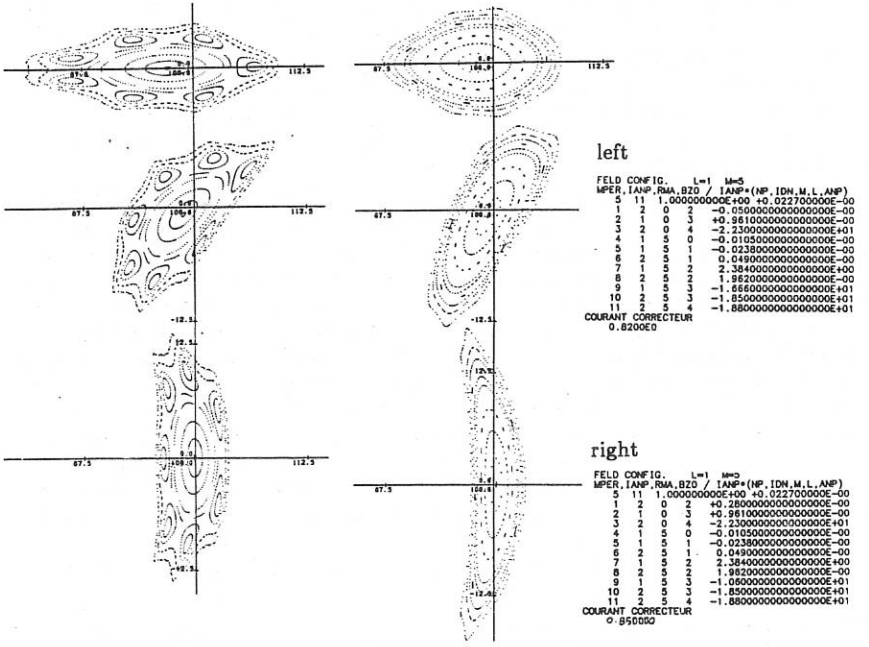

Fig.1. Reduction of island size by additional axisymmetric field components.

If, in addition, the constraint of vanishing flux between the two closed field lines is used to determine a further field and keeping both residues sufficiently small, the resulting field configuration WAD042 (right graph of Fig. 3) shows the desired property that the island size is negligibly small. One observes that the flux F decreases by three orders of magnitude simultaneously as the island size decreases.

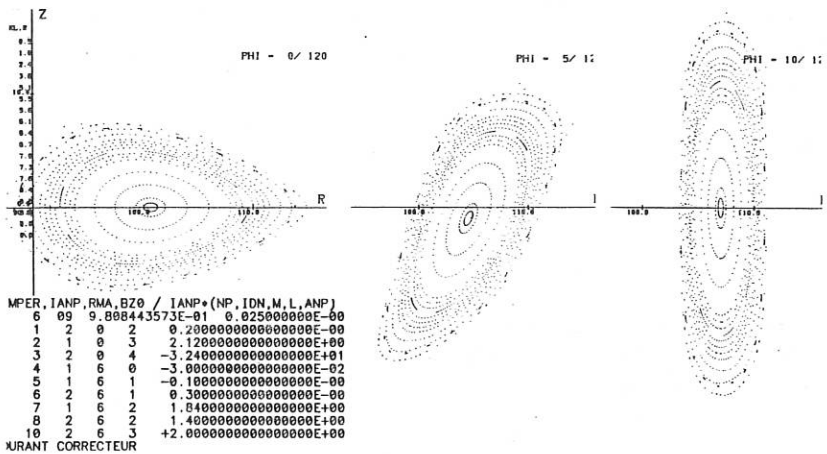

Fig.2. Field configuration with 6 field periods. The Dommaschk potentials are given in the Table where the notation of Ref.5 is used.

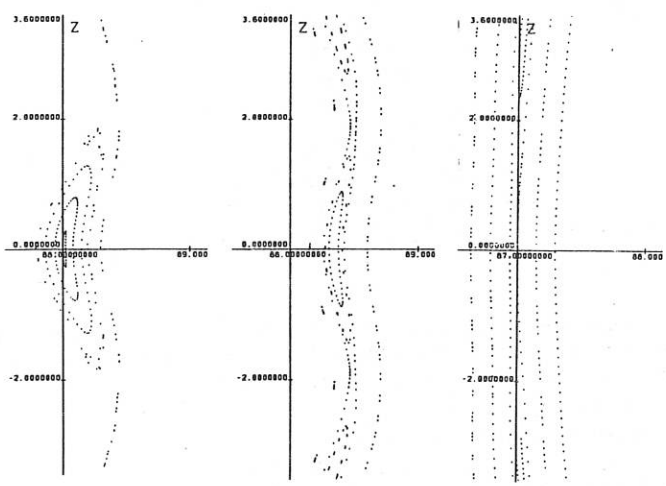

WAD321: $F = 7.4 \cdot 10^{-6}$ WAD847: $F = 6.3 \cdot 10^{-8}$ WAD042: $F = 1.0 \cdot 10^{-9}$

Fig.3. Island structure in the boundary region and residual flux in various configurations with 5 field periods.The boundary region of Helias configurations is discussed in Ref.6.

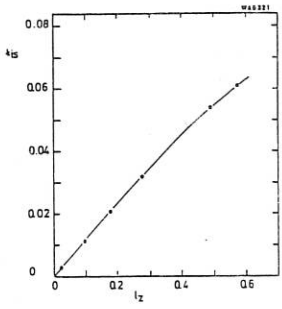

Fig.4. Internal twist ϵ_{is} of the island as function of half-axis l_y (configuration WAD321).

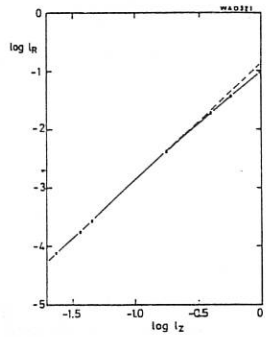

Fig.5. Dependence of the half-axis l_R of the island surfaces on l_z giving the asymptotic relation $l_R \sim l_Z^2$ as l_Z goes to zero.

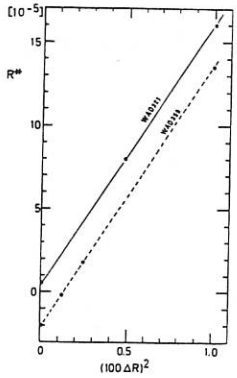

Fig.6. Residue R^* as funtion of the grid size ΔR used to compute the matrix of the mapping; left graph for islands located at inboard side and right graph for islands located at outboard side. A typical grid size used here is $\Delta R = \Delta Z = 10^{-4}$ for $R_T = 100$.

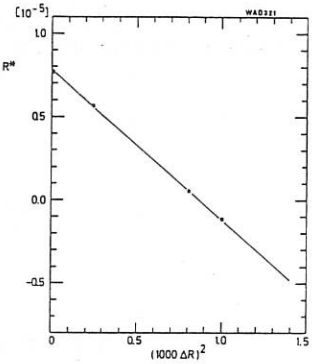

This algorithm is being used in an optimization procedure to approach analytically vacuum magnetic fields with the desired field qualities of, e.g., magnetic well, small secondary currents at ϵ_b around 0.8, and reduced particle drift.

1) W. Dommaschk, Z. Naturforsch. **36a**, 251 (1981).
2) J.M. Greene, J. Math. Physics **9**, 760 (1968).
3) J.D. Hanson and J.R. Cary, Phys. Fluids **27**, 767 (1984).
4) F. Herrnegger, Proc. 2nd Workshop on Wendelstein VII-X, SchloßRingberg 13 - 16 June 1988, F.Rau and G.G. Leotta, Eds., CEC Brussels and Luxembourg 1988, EUR 11705 EN, p. 59 - 67.
5) F. Herrnegger, Z. Naturforsch. **42a**, 1085 (1987).
6) F. Rau et al., Paper P9B8 of this Conference.

STUDIES OF ISLANDS IN STELLARATOR VACUUM FIELDS BY SOLVING A NEUMANN PROBLEM

P. MERKEL

Max-Planck-Institut für Plasmaphysik
IPP-EURATOM Association
D-8046 Garching bei München
Federal Republic of Germany

1. Introduction

Stellarator vacuum fields can be obtained by solving the Neumann problem for Laplace's equation inside the boundary of a toroidal domain. By this method a vacuum field with vanishing normal component at the boundary is computed, so that the prescribed boundary of the domain becomes a magnetic surface. For appropriately chosen parameters one finds solutions where also the magnetic field in the interior consists of a set of "good" nested surfaces [1], as shown in Fig. 1. Of course, a finer resolution of the solutions shows that islands are still present and that the field structure is in general complicated. However, one can conclude from these studies that in general the analyticity of the boundary benignly influences the regularity of the surfaces; for example, finding low aspect ratio solutions with good surfaces is easy. In the present paper the question of the regularising effect of the solution method on the structure of islands is considered. A numerical study of a class of toroidal Heliac vacuum fields was performed. A configuration with $n_p = 4$ periods, small shear and a rotational transform per period of $\iota \approx 1/3$ has been chosen, so that sizeable islands are found, although a boundary value problem is solved for a smooth boundary.

The Heliac fields are computed with the NESCOIL code. In [1], [2] one finds a detailed description: on a closed surface surrounding the Heliac boundary a surface current distribution is determined in such a way that the field $\vec{B}$ approximates the true solution of the Neumann problem. This is achieved by requiring that the normal component of $\vec{B}$ be minimized on the Heliac surface

$$F = \int_{\partial R} (\vec{B} \cdot \vec{n})^2 \mathrm{d}f = \min!$$

This method solves the boundary value problem approximately, but with arbitrarily high accuracy. One period of the outer current carrying surface and the Heliac surface are given by a parameter representation $r(u,v)$, $z(u,v)$, $v = \frac{n_p}{2\pi}\varphi$, where v is proportional to the toroidal angle, u is a poloidal angle-like variable, (r, φ, z) are cylindrical coordinates, and n_p is the number of periods.

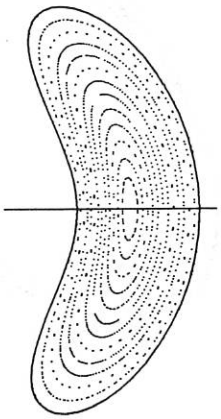

Fig.1 Poincaré plot of a Helias [3] vacuum field with "good" magnetic surfaces

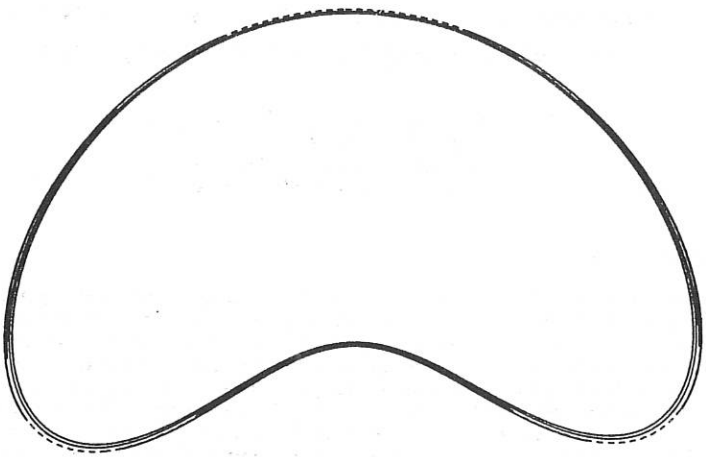

Fig.2a

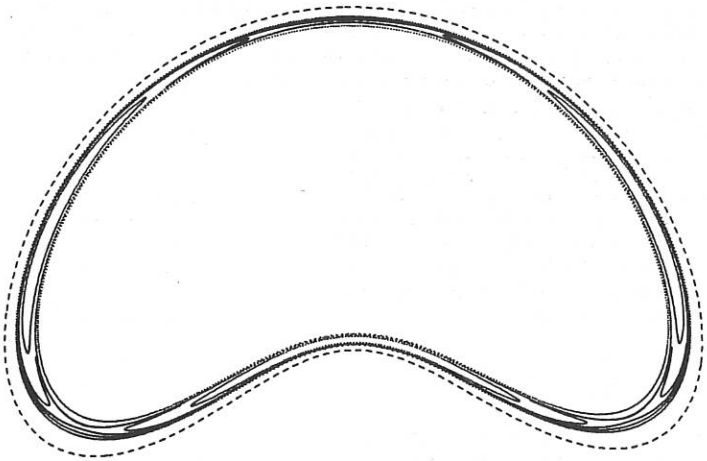

Fig.2b

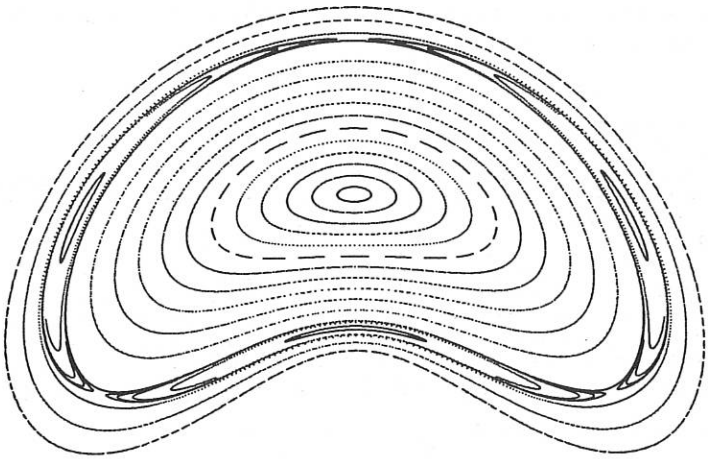

Fig.2c

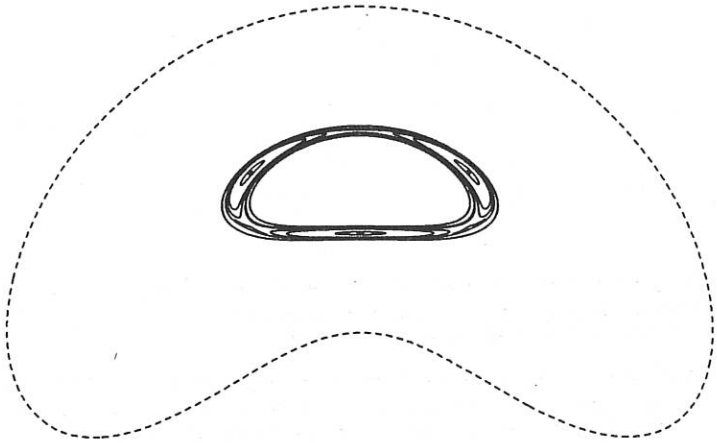

Fig.2d

Fig.2a-2d Poincaré plots of the islands at $\iota = 1/3$ are shown for different radial positions. Values of the parameter p are $p = 0.3113$, 0.313, 0.32 and 0.33. The dashed line is the Heliac boundary.

The surface current density with the same periodicity is expressed by a potential $\Psi(u,v)$ defined on the surface: $\vec{j} = \vec{n} \times \text{Grad } \Psi(u,v)$.

2. Results

The Heliac boundary is defined by the Fourier harmonics of $r(u,v)$ and $z(u,v)$ in (u,v)-space: $r_{0,0} = 10.$, $r_{01} = z_{01} = 0.96$, $r_{11} = z_{11} = 1.$, $r_{21} = z_{21} = 0.38$, $r_{2-1} = -z_{2-1} = 0.11$ and $-r_{1-1} = z_{1-1} = p$ (for notation see [2]). The class of Heliac configurations presented in Fig. 2 is obtained by varying the value of p between $0.3113 < p < 0.334$. In this way the position of the $\iota = 1/3$ resonance is shifted from the boundary to the magnetic axis.

Figures 2a-2d show Poincaré plots of the $\iota = 1/3$ islands for different positions. The Poincaré plot in Fig. 2c shows that apart from the $\iota = 1/3$ islands solutions with "good" nested surfaces are found. The boundary value problem is solved with high accuracy: For a number $N_u = 128$ and $N_v = 256$ mesh points in real space and a number of $m = 32$ poloidal and $|n| \leq 6$ toroidal Fourier modes for the potential $\Psi(u,v)$ the maximal local error on the boundary $\epsilon = (\vec{B} \cdot \vec{n})/|\vec{B}|$ is 10^{-6} ($\vec{n}$ = normal unit vector on the boundary).

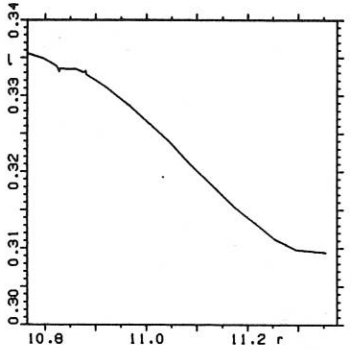

Fig. 3

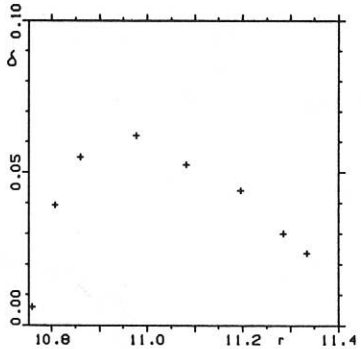

Fig. 4

Fig.3 Profile of the rotational transform for the case shown in Fig.2c.

Fig.4 The relative island thickness δ versus its radial position with the Heliac boundary at $r = 10.76$ and the magnetic axis at $r = 11.4$.

The island thickness δ versus its radial position is plotted in Fig. 4. At the Heliac boundary the condition $\vec{B} \cdot \vec{n} = 0$ forces the island thickness to $\delta = 0$. Close to the magnetic axis and close to the boundary the island thickness is in accordance with analytical arguments.

References

[1] P. Merkel, In: Theory of Fusion Plasmas, Eds. A. Bondeson E. Sindoni, and F. Troyon, Varenna, Italy, EUR 11336 EN, 25-46.

[2] P. Merkel, Nucl. Fusion **27** (1987) 867.

[3] J. Nührenberg, R. Zille, Phys. Lett. A **114** (1986) 129.

RESISTIVE BALLOONING STABILITY OF ADVANCED STELLARATORS

H.P. Zehrfeld, J. Kisslinger, H. Wobig

Max-Planck-Institut für Plasmaphysik
EURATOM Association, D-8046 Garching, Federal Republic of Germany

Abstract

Recently it has been shown that the problem of resistive ballooning stability of plasmas in axisymmetric toroidal magnetic field configurations can be treated and solved applying a variational approach [1]. The method was suggested by the observation that resistive ballooning modes, in the framework of single-fluid MHD theory, can be conceived as Euler-Lagrange equations of an appropriately constructed Lagrangian. In the present paper we extend this method to three-dimensional configurations. A unique treatment for both stellarators and tokamaks becomes possible by specifying the MHD equilibria assigned for ballooning stability analysis in terms of suitable flux coordinates.

This approach and a stability investigation for the advanced stellarator Helias will be presented.

Using particular field line coordinates in the covering space the equations describing resistive ballooning modes [2] in a three-dimensional equilibrium configuration can be written in the form

$$\frac{1}{\mu_0}\mathbf{B}\cdot\nabla\Big\{\frac{k^2}{B^2}\mathbf{B}\cdot\nabla u\Big\}+\Big\{K\frac{dp}{dV}-\frac{\rho\gamma^2k^2}{B^2}\Big\}u+K\frac{dp}{dV}v=0 \tag{1}$$

$$\mathbf{B}\cdot\nabla\Big\{\frac{\mathbf{B}\cdot\nabla v}{B^2}\Big\}-K\frac{dp}{dV}\Big\{\frac{\eta}{\gamma}+\frac{\rho\gamma^2}{\mu_0((\nabla p\cdot(k\times\nabla\sigma))^2}\Big\}u$$
$$-\Big\{\frac{\eta}{\gamma}\Big(K\frac{dp}{dV}+\frac{\rho\gamma^2k^2}{B^2}\Big)+\frac{\mu_0\rho\gamma^2}{B^2}\frac{1+\beta}{\beta}\Big\}v=0 \tag{2}$$

Here

$$K\equiv 2\boldsymbol{\kappa}\cdot(k\times\nabla\sigma)(k\times\nabla\sigma)\cdot\nabla V \qquad D\equiv 1+\frac{\eta k^2}{\mu_0\gamma} \tag{3}$$

$$k\equiv-\frac{2\pi n}{\Psi'(V)}\nabla r \tag{4}$$

with $\mathbf{k}$ being the wave vector, $\boldsymbol{\kappa}$ the curvature vector, V the volume enclosed by a magnetic surface and Ψ being the poloidal magnetic flux; all other quantities have their usual meaning. (V, τ, σ) are right-handed flux coordinates in the covering space [3] of a magnetic surfaces resulting from the Clebsch representation $\mathbf{B} = \nabla V \times \nabla \tau$. σ is related to the arc length s along a field line by $d\sigma = ds/B$.

After an appropriate transformation of the equations (1) and (2) the problem to be solved can be seen to be equivalent to the stationarity conditions with respect to u of the quadratic functional

$$L(\gamma, V, \sigma_0) = \int_{-\infty}^{+\infty} \mathcal{L}(\gamma, V, \sigma, \sigma_0, u(\sigma), \dot{u}(\sigma)) d\sigma \tag{5}$$

with the Lagrange density

$$\mathcal{L} = \frac{1}{2}(\dot{u}^T \cdot P \cdot \dot{u} - u^T \cdot Q \cdot u) \tag{6}$$

$u = (u^1, u^2, u^3, u^4)$ comprises real and imaginary parts of u and v in equations (1) and (2) and $\dot{u} = du/d\sigma$ the components $du^k/d\sigma$, $k = 1, .., 4$. Q and P are equilibrium determined symmetric matrices with nonlinear dependence on the the complex growth rate γ. Thus unstable resistive ballooning modes u are those stationary points of L with $\mathrm{Real}\{\gamma\} > 0$. P and Q are equilibrium determined real symmetric matrices with nonlinear dependence on the the complex growth rate γ. They have the structure

$$P = \begin{pmatrix} P_{11} & P_{12} & 0 & 0 \\ P_{12} & -P_{11} & 0 & 0 \\ 0 & 0 & P_{33} & P_{34} \\ 0 & 0 & P_{34} & -P_{33} \end{pmatrix}, \qquad Q = \begin{pmatrix} Q_{11} & Q_{12} & Q_{13} & 0 \\ Q_{12} & -Q_{11} & 0 & -Q_{13} \\ Q_{13} & 0 & Q_{33} & Q_{34} \\ 0 & -Q_{13} & Q_{34} & -Q_{33} \end{pmatrix} \tag{7}$$

where the matrix elements are determined by equilibrium quantities.

The field line coordinates (V, τ, σ) can be easily related to Boozer's coordinates [4] which were used to investigate ideal ballooning modes for stellarator configurations [5].

In the present paper, for the case of resistive ballooning modes, we apply a variational approach which already turned out to be successful in the case of axially symmetric equilibrium configurations [1].

The computational procedure will be applied to a Helias configuration which originally is described in Boozer's coordinates (V, u, v). Fig. 1. shows a poloidal cut of magnetic surfaces reconstructed from data in the straight-field line flux coordinates (V, u, v).

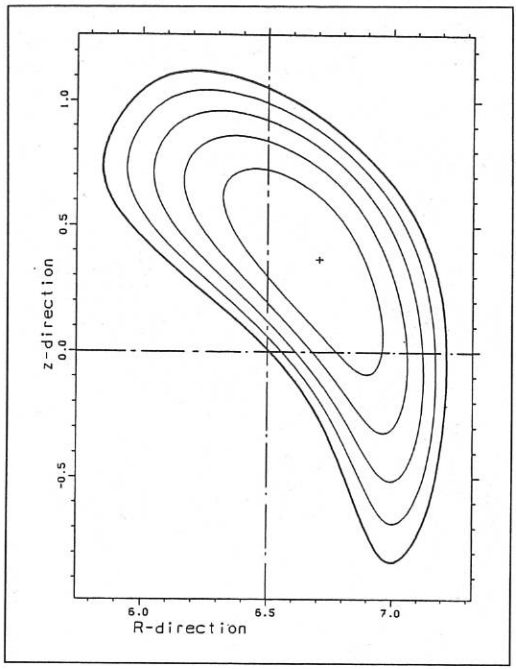

Fig. 1: Poloidal cut of magnetic surfaces of the Helias configuration reconstructed from data in straight-field line flux coordinates.

REFERENCES

[1] H.P. Zehrfeld, K. Grassie, "Resistive Ballooning Stability of ASDEX Equilibria", Nucl. Fusion **5** (1988), 891.

[2] D. Correa-Restrepo, "Resistive Ballooning modes in Three-Dimensional Configurations", IAEA-CN-41/V-3

[3] R.L.Dewar, A.H.Glasser, "Ballooning mode spectrum in general toroidal systems", Phys.Fluids **26** (1983), 3038.

[4] Boozer, A., Phys.Fluids **23** (1980) 904.

[5] J.Nührenberg, R.Zille, Proc. 12th Eur. Conf.on Contr. Fusion and Plasma Physics (Budapest, 1985), EPS, Budapest 1985, Vol.**9F**, I, 445.


PAX
TIBI
MAR
CE
EVAN
GELIS
TA-
MEVS

VACUUM FIELDS AND PARAMETER RANGE OF A MODULAR HELIAS CONFIGURATION

C. Beidler, E. Harmeyer, F. Herrnegger, J. Kißlinger , P. Merkel, A. Montvai*, F. Rau, R. Scardovelli, and H. Wobig
Max-Planck Institut für Plasmaphysik, D-8046 Garching, FRG,
EURATOM-Association.
* Guest from: Central Res. Inst. for Physics, H-1525 Budapest, Hungary.

INTRODUCTION . At IPP Garching, the stellarator experiment WENDELSTEIN VII-X is being developed. Among stellarators Helias configurations (Helical Advanced Stellarator) offer the prospects of stable plasma operation at $\langle\beta\rangle \approx 5\%$ because of the optimization of confinement, MHD-equilibrium and stability [1]. Considering ballooning modes and resistive interchange instability, Helias configurations with five field periods are preferred [2]. In the present paper the development of a modular coil system for W VII-X is described briefly, and details of the magnetic vacuum fields and the accessible parameter range are given. We concentrate on a data set named HS 5-8 with a major radius of 6.5 m and a coil aspect ratio of 5.4. Each of the 60 coils, considered to be superconducting, carries 1.75 MA at a current density of about 50 MA/m^2. The magnetic field on axis is 3 T and the maximum induction at the coil is 5.8 T . The coil set and an outer flux surface are shown in Fig. 1 .

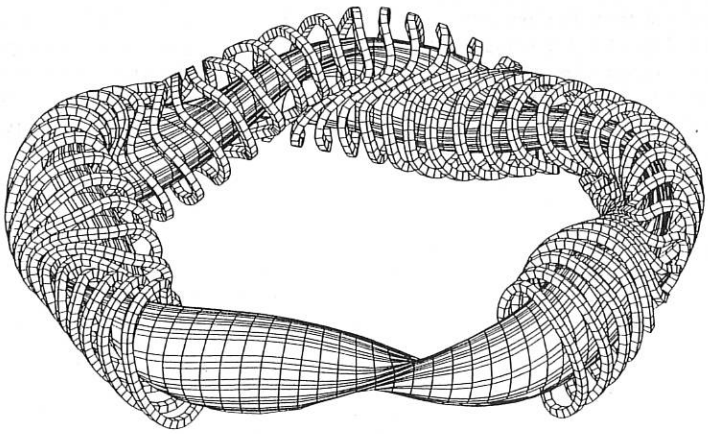

Fig. 1 : Coil set for HS 5-8 (4 of the 5 field periods), and an outer flux surface. The coils have dimensions of lateral 0.18 m and radial 0.20 m.

COIL SYSTEM . Using the NESCOIL code, [3], a system of current filaments is computed on a toroidal surface S_2, which encloses an outer magnetic surface S_1 of a given Helias configuration. Both surfaces are described in Fourier series of two angular co-ordinates. These current filaments are taken as the center lines of finite size coils which are optimized with respect to curvature, maximum distance between coils and between plasma and coils. The number of coils per field period is 12, which minimizes the modular field ripple to about 0.7% at the edge and leaves sufficient space between the coils for access to the plasma. To achieve optimum conditions the Fourier coefficients of S_2 and S_1 are modified, those of S_1 only slightly. At critical positions the coils are smoothed afterwards. This leads to a small deviation from the original Helias configuration which, after comparing it with the vacuum field of the finite coils, is acceptable in the present case. In HS 5–8 three important quantities could be made as large as possible: minimum coil curvature radius 30 cm, minimum lateral distance between coil centers 22 cm, and minimum radial distance of 36 cm between the current surface (coil center) and a flux surface with an aspect ratio of 9 .

VACUUM FIELD PROPERTIES . Up to 5 filaments per coil are used for calculating the vacuum magnetic fields; in most of the cases one or two filaments per coil have be found as sufficient. Fig. 2 shows the Poincaré plots of the vacuum magnetic field for three toroidal positions. The rotational transform is $\iota_0 = 1.02$ along the helical magnetic axis, it increases monotonically to a value of 1.2 at the edge, see Fig. 3 . This figure also shows the value of $V' = \int dl/B$ as function of the averaged radius $\bar{r}$, from which a magnetic well $(V_0' - V')/V_0' =$ -1.5% is calculated. A low neoclassical transport in the plateau regime, small Shafranov-shift and small change of ι and shear with β are expected from the low value of $\langle |j_{||}/j_{\perp}| \rangle = 0.63$. A proper combination and low number of the Fourier components , determining the magnetic field in magnetic co-ordinates, guarantees a small value for the equivalent ripple, which characterizes the neoclassical transport in the $1/\nu$-regime. The equivalent ripple amounts to less than 1% for a similar configuration, HS 5–7, which has a 20% lower value of the rotational

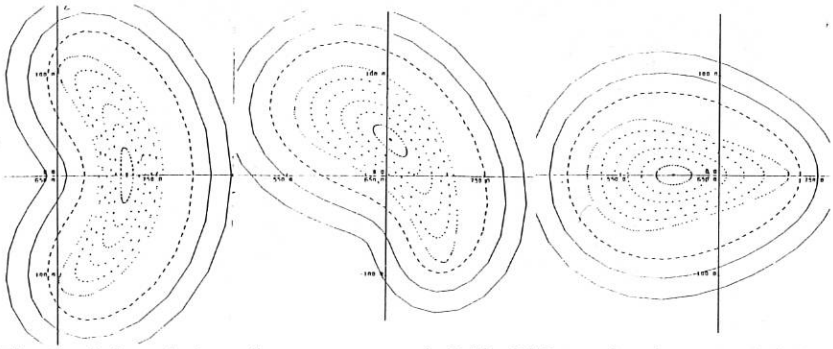

Fig. 2 : Poincaré plots of vacuum magnetic field of HS 5–8 for three toroidal plane with contours of the inner and outer boundaries of the modular coils (solid lines). The dashed line indicates the position of a tentative first wall.

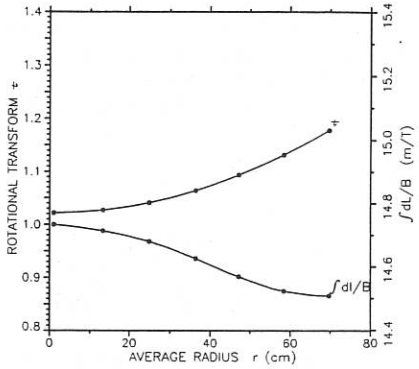

Fig. 3 : Rotational transform ι and the value of $V' = \int dl/B$ as function of the averaged radius $\bar{r}$.

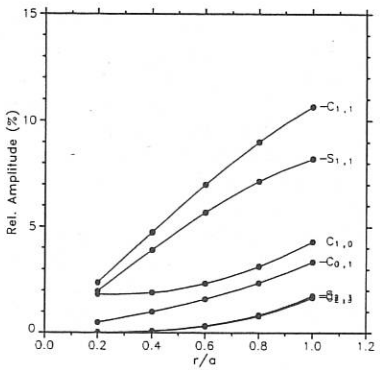

Fig. 4 : Normalized Fourier components of the field strength $|B|$. Coefficients with an edge-value below 1.5% and $C_{0,0} \sim 1$ are omitted.

transform. Fig. 4 shows the normalized Fourier components of the field strength

$$|B| = |B_0|\Big(\sum C_{n,m} cos(n\phi)cos(m\theta) + S_{n,m} sin(n\phi)sin(m\theta)\Big) \quad ,$$

where ϕ and θ are toroidal (index n) and poloidal (index m) magnetic variables [4], respectively, $B_0 = 3$ T is the average field, and $C_{0,0} \sim 1$. Adjusting in HS 5–8 the helical field components $C_{1,1}$ and $S_{1,1}$ with respect to the coefficients $C_{0,1}$ and $C_{1,0}$ yields a geometrical factor for the bootstrap current, as discussed in [5], of less then 10% of the equivalent tokamak value in the lmfp regime.

At low order rational values of the rotational transform, e. g. $\iota = 5/5$, 'natural' magnetic islands usually exist in the system of magnetic surfaces. The position and size of these islands is influenced by the choice of the initial flux surface and of the outer surface used for the NESCOIL input, and by the admitted number of Fourier harmonics determining the current lines. It is also sensitively affected by the smoothing procedure. In HS 5–8 the lowest order rational values of $\iota = 5/5$ and $5/4$ are avoided. A method to obtain a small island size, described in [6], is not yet applied. The neighbouring rational values of higher order $\iota = 10/9$ and $\iota = 15/13$ produce small islands with averaged radial dimensions of 1.5 ... 2 cm. Their average radial positions are 51 and 62 cm, respectively, inside an effective minor radius of about 70 cm.

PARAMETER VARIATION . A necessary prerequisite for an experimental device is a sufficiently broad range of variable magnetic field parameters like rotational transform and axis position. This can be achieved by a set of 4 planar external coils per field period in a helical arrangement as shown in Fig. 5 . Considering individually adjustable currents in the coils A and B allows to introduce toroidal and vertical fields as well. In Fig. 6 the dependences of ι_0 on axis, ι_a at the edge, and of the magnetic

well V'' are plotted as a function of the current in the planar coils. A current of ± 0.5 MA per planar coil and of 1.75 MA in each modular coil changes the rotational transform by about 20%. In this way configurations with rational values of $\iota = 5/5$ or $\iota = 5/4$ at the boundary are obtained. One can anticipate to use the corresponding island chain for plasma edge control.

Vertical field components, generated by opposite currents of 0.5 MA in the planar coils A and B of Fig. 5 shift the magnetic axis by about 1% of the major radius. The toroidal modulation of the field strength, introduced in this case, can be reduced considerably by using different currents in the modular coils.

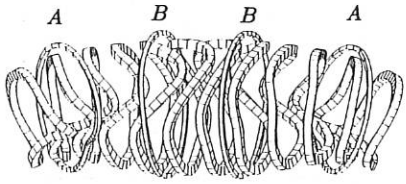

Fig. 5 : One period of HS 5–8 showing the modular coils and the external planar coils A and B for varying the rotational transform and axis position.

SUMMARY AND CONCLUSION

The configuration HS 5–8 with 5 field periods, a major radius of 6.5 m, an averaged field of 3 T, an iota-value between 1.02 and 1.2, is generated by 60 modular coils. The coils are optimized according to technical constraints and appear to be feasible; they leave sufficient access to the plasma and offer space between plasma and wall. The vacuum field properties e. g. low Pfirsch-Schlüter currents, magnetic well, low equivalent ripple, high quality of flux surfaces, are the basis for good plasma confinement and sufficient high stability-β. The adjusted combination of the field components reduces the bootstrap current to a tolerable value. A set of external planar coils allows both, a variation of the rotational transform of 10%, and also a shift of the magnetic axis of 1% of the major radius.

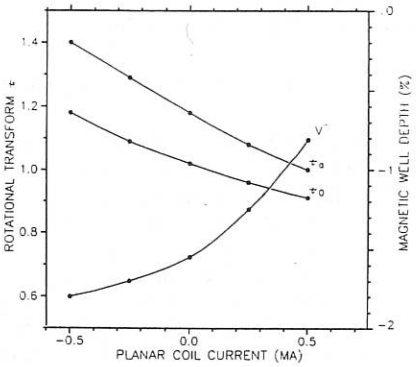

Fig. 6 : Dependences of ι_0 on axis, ι_a at the edge, and of the magnetic well V'' as a function of the current in the planar coils.

REFERENCES

[1] NÜHRENBERG, J. and ZILLE, R., Phys. Letters **114A** (1986) 129.
[2] GRIEGER, G. et. al., paper IAEA-CN-50/C-I-4, 12^{th} Conf. on Plasma Physics and Nuclear Fusion Research, Nice 1988.
[3] MERKEL, P. Nuclear Fusion 27, 867 (1987)
[4] BOOZER, A., Phys. Fluids 25 (1982) 520
[5] WOBIG, H., IPP Garching Rep. 2/297 (1988) and paper P9B3, this conference.
[6] HERRNEGGER, F., paper P2B2 ,this conference.

INVESTIGATION OF PLASMA EQUILIBRIUM CURRENTS IN A DRAKON-TYPE TRAP

V.V.Nemov

Institute of Physics and Technology, the Ukrainian SSR Academy of Sciences, 310108 Kharkov, USSR

Pfirsch-Schlüter currents are investigated in a closed magnetic trap DRAKON described in detail elsewhere /1-3/. The magnetic system in the trap contains long rectilinear sections with a longitudinal magnetic field. The sections are connected with curvilinear equilibrium elements (known as CREL) whose parameters are chosen such as to keep the Pfirsch-Schlüter currents within the CREL and prevent them from penetrating into the rectilinear sections. In this paper the plasma equilibrium currents are calculated involving numerical methods for the magnetic system formed by a solenoid with a finite number of current-carrying rings. The CREL consisting of three semitori whose planes make angles of 120° with one another /1,2/ is considered.

The principal parameters of the system under study are:

$$R=100 \text{ cm}, \ a=20 \text{ cm}, \ W = 100, \ d = \pi R/10, \ l = 2\pi R, \quad l_1 = 0.7\, l, \ R_M = 3 \tag{1}$$

where R is the semitorus radius, a is the radius of the current-carrying ring, W is the total number of these rings in both the rectilinear sections and CREL, d is the distance between the ring centers along the solenoid axis, l is the rectilinear section length, l_1 is the length of the part of the rectilinear section where the magnetic field is reduced, $R_M = I/I_1$ is the mirror ratio, I_1 is the current in the rings in the section of length l_1, and I is the current in the other rings. Fig. 1a shows a schematic diagram of the system in question and Fig. 1b some relative dimensions.

To calculate the equilibrium currents, we used the following set of differential equations derived from the ones of Ref. /4/ in the Cartesian coordinates x, y, z (see Fig.1a):

$$\frac{dx}{ds} = \frac{B_x}{B}, \quad \frac{dy}{ds} = \frac{B_y}{B}, \quad \frac{dz}{ds} = \frac{B_z}{B} \tag{2}$$

$$\frac{dP}{ds} = -\frac{1}{B}\left(\frac{\partial B_x}{\partial x}P + \frac{\partial B_y}{\partial x}Q + \frac{\partial B_z}{\partial x}G\right), \tag{3}$$

$$\left.\begin{aligned} \frac{dQ}{ds} &= -\frac{1}{B}\left(\frac{\partial B_x}{\partial y}P + \frac{\partial B_y}{\partial y}Q + \frac{\partial B_z}{\partial y}G\right), \\ \frac{dG}{ds} &= -\frac{1}{B}\left(\frac{\partial B_x}{\partial z}P + \frac{\partial B_y}{\partial z}Q + \frac{\partial B_z}{\partial z}G\right), \end{aligned}\right\} \qquad (3)$$

$$\frac{dh}{ds} = -\frac{2[\vec{B}\nabla B]\nabla\psi}{B^4} \qquad (4)$$

Here B_x, B_y, B_z are the magnetic field $\vec{B}$ components; P, Q and G are the derivatives of the magnetic surface function ψ ($\partial\psi/\partial x$, $\partial\psi/\partial y$, $\partial\psi/\partial z$, respectively), and s is the arc length of the magnetic field line. The quantity h is related to the longitudinal equilibrium current density $j_\parallel$ by

$$\vec{j}_\parallel = c\frac{dp}{d\psi}h\vec{B}, \qquad (5)$$

where $p = p(\psi)$ is the plasma pressure.

The above set of equations describes the $\nabla\psi$ and $\vec{j}_\parallel$ distributions along the magnetic field line, and hence, on the magnetic surface formed by this line. We solved this set of equations on a computer for the case of small β ($\beta = 8\pi p/B^2$) where one can make use of the vacuum magnetic field. The magnetic field and its space derivatives were calculated on the basis of well-known formulas for the magnetic field of a circular current-carrying conductor. The initial integration points were chosen on the x-axis in the z=0 plane through the centers of the rectilinear sections. At these points we assumed that $|\nabla\psi| = 1$ and the $\nabla\psi$ direction was the direction of the normal to the magnetic surface, $\vec{N} = [\vec{L}\vec{B}]$, where $\vec{L}$ is the vector tangential to the magnetic surface cross section at the initial point. With such a choice of the initial points it is easier to set initial P, Q and G values as the $\vec{L}$ vector is parallel to the y-axis due to the symmetry of the magnetic surface cross section in the z=0 plane with respect to the x-axis.

Figure 2 shows the cross sections of the magnetic surface with the initial integration point $x_0 = x_{0c} + 10$ cm (y=z=0, x_{0c} is the coordinate of the solenoid axis in the initial plane) in the z=0 plane and in the plane of joint of the rectilinear section with the CREL. The $\nabla\psi$ projections onto these planes are shown by arrows. Fig. 3a,b shows the distribution of g versus $\omega = \theta/(2\pi)$ over the magnetic surface cross section; g is related to $j_\parallel$ and h by

$$j_\parallel = \frac{2c}{\iota B_0}\frac{dp}{d\psi}g, \quad g = 0.5\,\iota B_0 B h \qquad (\text{for } \alpha = 120^\circ \quad \iota = 0.88) \qquad (6)$$

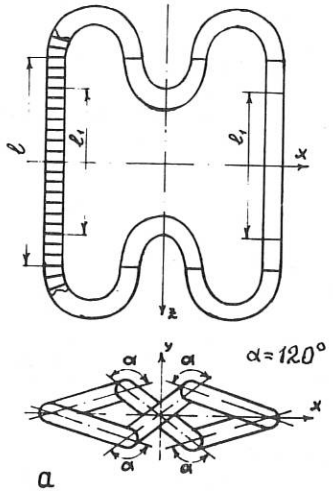

Fig. 1

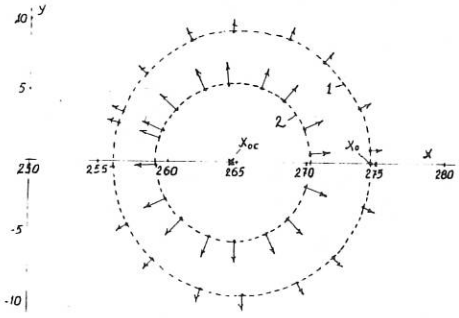

Fig. 2. 1: z=0, 2: z=0.5ℓ.

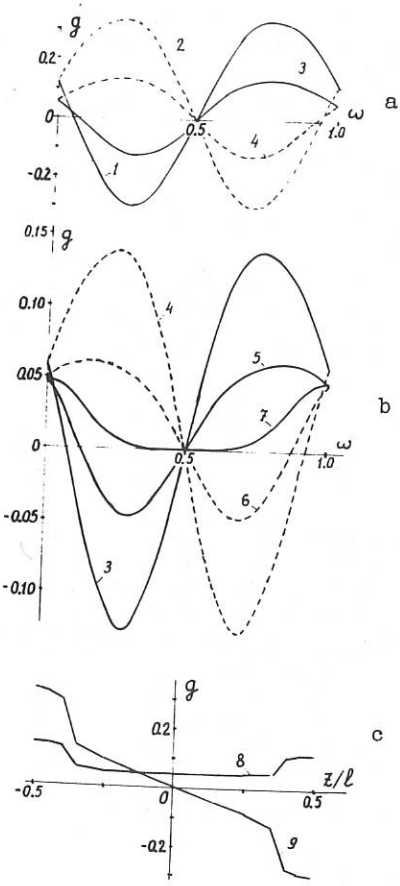

Fig. 3. 1: z=0.5ℓ, 2: z=-0.5ℓ, 3: z=0.5ℓ,, 4: z=-0.5ℓ, 5: z=0.15ℓ, 6: z=-0.15ℓ, 7: z=0, 8: ω=0, 9: ω=0.27.

where ι is the rotational transform over the solenoid length (in units of 2π), $B_0=4\pi I_1/(cd)$, $dp/d\psi$ coincides with $|\nabla p|$ at the initial point, θ is the angle round the spatial solenoid axis measured from the normal to this axis (in the rectilinear sections this normal is in the y=0 plane). We assumed the initial h to be $h_0 = 0$. The plots presented correspond to different cross sections of the rectilinear section. It can be seen that in the middle of the rectilinear section (z=0) the g distribution includes a variable in θ component of type $\cos\theta$ with the amplitude $g_m \approx 0.025$. It is about a factor of 40 smaller than for the typical Pfirsch-Schlüter current in toroidal traps ($g_m \approx 1$). The g distribution varies along the length l_1 so that along the field line g varies almost linearly (see Fig. 3c). The amplitude g_m increases at the periphery of these sections ($z = \pm l_1/2$) and the g distribution becomes roughly sinusoidal (with opposite phases on the opposite sides of the l_1 section). The g distribution also includes the component constant in θ, which is due to the choice of $h_0 = 0$. In the center of the CREL the θ dependence of g approaches a cosinusoid with $g_m \approx 1.75$ (the corresponding curve is not given).

From further calculations (the corresponding graphs are not shown here) it follows that the constant component of g can be reduced to zero by a proper choice of $h_0 \neq 0$. As the length of the rectilinear sections l is increased by a factor of 2 or 3 (provided d and difference $l-l_1$ are preserved and $W > 100$), the g_m amplitudes in the l_1 section also increase by about a factor of 2 or 3. For $R_M = 1$ the θ dependence of g does not actually change over almost the entire length l. With the magnetic surface radius increase, as the magnetic field rippling along the magnetic line of force becomes greater, the dependence of g is more complicated due to appearance of the $\cos 3\theta$ harmonic.

The increase in the $j_\parallel$ amplitude in the rectilinear sections as their length is increased is a disadvantage to this type of trap. For more complex CRELs /3/ this disadvantage might be less pronounced.

References

1. Glagolev V.M., Kadomtsev B.B., Shafranov V.D., Trubnikov B.A., in Controlled Fusion and Plasma Physics (Proc. 10th Eur. Conf. Moscow, 1981), Vol. 1, European Physical Soc. (1981) paper E-8.
2. Shafranov V.D. Phys. Fluids 26 (1983) 357.
3. Glagolev V.M., Trubnikov B.A., Churin Yu.N. Nucl. Fusion 25 (1985) 881.
4. Nemov V.V. Nucl. Fusion 28 (1988) 1727.

STABILITY OF SMALL-SCALE MHD MODES OF THE FINITE-PRESSURE PLASMA IN STELLARATOR-TYPE TRAPS

Yu.A.Zhdanov, A.Ya.Omel'chenko

Institute of Physics and Technology, the Ukrainian SSR Academy of Sciences, 310108 Kharkov, USSR

P.V.Demchenko

Kharkov State University, Kharkov, USSR

Abstract. Stability of ideal and resistive ballooning modes of the finite pressure plasma is investigated. Stability criteria of the modes mentioned are established accounting for fourth power effects in the plasma pressure.

Consider magnetic systems of the stellarator type with a spatial magnetic axis the curvature $\varkappa$ and the torsion $\varkappa$ of which are constant. The vacuum helical magnetic field potential of such systems is determined by the relation $\varphi_H = B_0 \varepsilon_\ell (R\ell/m) I_\ell(m a/R) \sin(\ell\theta - n\zeta)$ where ε_ℓ is the relative amplitude of the helical magnetic field. As is known [1], in magnetic traps mentioned the value of the shear S may be considerably reduced with the plasma pressure increasing or even it may change the sign what will lead to the additional destabilization of local modes. Therefore it seams reasonable to investigate the plasma stability in stellarator-type traps accounting not only for the second but for the fourth order terms in plasma pressure.

Stability of ideal ballooning modes. In the frame of ideal magnetic hydrodynamics the ballooning mode stability may be described in CHT representation [2] with the second order differential equation relative to the amplitude of radial plasma displacement. Using the technique of averaging over fast oscillations of metrics [3] the small oscillation equation given may be cast in the form:

$$S^2 \frac{d}{dt}\left[(1+t^2)\frac{d\bar{f}}{dt}\right] - \left[U_0 + \frac{U_1}{1+t^2}\right]\bar{f} = 0, \qquad (1)$$

where

$$U_0 = 4\frac{a^2}{R^2}\beta_\theta\left[R^2K^2\frac{\mu+2\varkappa_0 R\mu_4}{\mu} - (\mu+\varkappa_0 R)^2 - R^2K\frac{3\mu_4'+a\mu_4''}{2\mu}\cdot\frac{\xi}{a} - \frac{RB_0^2}{2}V_{vac.}''\right] + 6(ka)^4\beta_\theta^4,$$

$$U_1 = -16(ka)^2\beta_\theta^2 S + 24(ka)^4\beta_\theta^4, \quad \bar{f} = \langle f\rangle_{\theta,\zeta}.$$

μ_H and V''_{vac} are the vacuum rotational transform and the magnetic "hill" respectively.

To the small oscillation equation (1) there corresponds the potential energy functional of the form

$$W \sim \int dt \left[S^2 (1+t^2) \left(\frac{d\bar{f}}{dt} \right)^2 + \left(\mu_0 + \frac{\mu_1}{1+t^2} \right) \bar{f}^2 \right]$$

Substituting the test function $\bar{f} = (1+t^2)^{-1/2}$ into the said functional we find the stability criterium for the ideal ballooning modes in the finite pressure plasma,

$$\frac{1}{2} S^2 + 4 \frac{a^2}{R^2} \beta_\theta \left[R^2 k^2 \frac{\mu + 2\varkappa_0 R - \mu_H}{\mu} - (\mu + \varkappa_0 R)^2 - R^2 k \frac{3\mu_H + a\mu''_H}{2\mu} \cdot \frac{\xi}{a} - \frac{R B_0^2}{2} V''_{vac} \right] \quad (2)$$

$$- 8 (ka)^2 \beta_\theta^2 S + 18 (ka)^4 \beta_\theta^4 > 0 .$$

The validity domain of the stability criterium obtained (2) with respect to the parameter β_θ values is determined by the requirement that oscillating parts of the amplitude f be small as compared with the averaged $\bar{f}$ $(\beta_\theta \leq \beta_\theta^* \sim R/4a)$ and by the assumption about the linear character of the displacement ξ of the magnetic surface centre versus plasma pressure behaviour. The latter condition is valid if $\beta_\theta < \beta_\theta^* < \beta_\theta^{crit.}$ For $\beta_\theta \to \beta_\theta^{crit.}$ the sharp increase of the displacement ξ values occurs what corresponds to the loss of equilibrium in the system. In particular in the $\ell = 2$ torsatron in a currentless regime the magnitude $\beta_\theta^{crit.} \simeq \varepsilon_2^2/2$. As the parameters of the "U-2M" torsatron under design [4] are: $A = 170/30$ and $\varepsilon_2 = 0.37$ the relations for β_θ mentioned above are valid up to $\beta_\theta \lesssim 1.4$, we use the criterium (2) to analyze the stability of ideal ballooning modes in this device. In Figs. 1-2 there are shown $S - \beta_\theta$ diagrams of plasma stability with respect to the excitation of ideal ballooning modes and Mercier modes at the plasma periphery accounting for β_θ^4 - terms (Fig.1) and for β_θ^2 -terms (Fig.2).

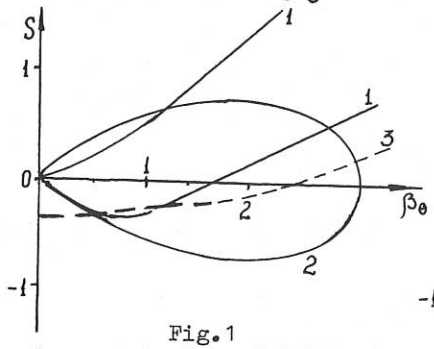

Fig.1

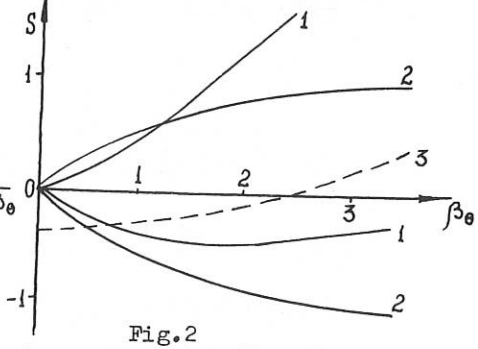

Fig.2

Curve 1 is the stability boundary of ideal ballooning modes, 2 is the stability boundary of Mercier modes, 3 is shear S .

From the diagrams presented it follows that the influence of finite pressure effects leads to noticeable narrowing of the ideal ballooning mode stability region limited by $\langle\beta_\theta\rangle<1.1$ and it points to the possibility of stabilization of Mercier modes on increasing the plasma pressure.

Stability of resistive ballooning modes. Three-dimensional problem about the resistive ballooning mode stability, as shown in [5], may be reduced to a two-dimensional one with respect to angular variables and in a CHT-representation it is described by a system of second order differential equations for the amplitude of the radial displacement of plasma ξ and the plasma pressure perturbation P.

$$\hat{L}_{\parallel}\left(\hat{L}^{*}_{\perp M}\hat{L}_{\parallel}\xi\right)+\frac{p}{p_0'}\left[W_0+\hat{L}_{\parallel}A_M\right]-\frac{4\pi^2 g\,\rho_0\gamma^2}{\varphi_{12}}\hat{L}_{\perp M}\xi=0. \qquad (3)$$

$$\left[q^2\hat{L}_{\parallel}^2-\gamma^2\tau_t^2\right]\frac{\delta P}{p_0'}=q^2\left[\hat{L}_{\parallel}^2-\hat{L}_{\parallel}\hat{\mathcal{D}}^{-1}\hat{L}_{\parallel}\right]\xi+\frac{\varphi_{12}\rho_0\gamma^2}{4\pi^2 p_0'^2}\frac{q^2 g_{33}}{\sqrt{g}}\hat{L}_{\parallel}A_M\cdot\xi \qquad (4)$$

Here $P=\delta P-\xi p'$, $\hat{L}^{*}_{\perp M}=\hat{L}_{\perp M}\hat{\mathcal{D}}^{-1}$, $\hat{\mathcal{D}}=1+\frac{n^2q^2\rho}{\sigma\gamma}\hat{L}_{\perp M}\cdot\frac{g_{33}}{\sqrt{g}}$, $\tau_t=\frac{R^2q^2}{\gamma_0 p_0}$,

γ_0 is the adiabatic power, σ, ρ_0 and p_0 are the conductivity, the density and the equilibrium pressure of the plasma, γ is the growth rate of unstable perturbations.

By averaging over fast oscillations of the metrics the system of equations (3)-(4) is reduced to a one-dimensional equation with respect to the variable $t=S\gamma(\theta\to\gamma)$ which in the threshold vicinity ($\gamma\to 0$) in the resistive limit ($|\Delta'|\gg 1$) assumes the form

$$\Gamma S^2\frac{d^2\bar{\xi}}{dt^2}-\left[V+U_0+\frac{U_1}{1+t^2}\right]\bar{\xi}=0, \qquad (5)$$

where

$$V=\frac{\Gamma^2}{N_S^2}(1+t^2)(1+2R^2K^2q^2)$$

$$U_0=4\frac{a^2}{R^2}\beta_\theta\left[R^2K^2\frac{\mu_\gamma+\varkappa_0 R}{\mu_\gamma+\mu_H-\varkappa_0 R}-R^2K\frac{\mu_\gamma'+\mu_H'}{\mu_\gamma+\mu_H-\varkappa_0 R}\xi'-(\mu_\gamma+\mu_H)^2-\right.$$

$$\left.-R^2K\frac{3\mu_H'+a\mu_H''}{2(\mu_\gamma+\mu_H-\varkappa_0 R)}\cdot\frac{\xi}{a}-\frac{RB_\theta^2}{2}V_{vac}''\right]-6(ka)^4\beta_\theta^4,$$

$$U_1=-16(ka)^2\beta_\theta^2 S+40(ka)^4\beta_\theta^4,$$

$$\Gamma=\frac{\gamma\tau_S}{n^2q^2},\quad \tau_S=a^2\sigma,\quad N_S=\frac{\tau_S}{\tau_\theta}\frac{1}{n^2q^2},\quad \tau_\theta=\frac{Ra}{C_A},$$

C_A is the Alfven velocity.

The analysis of the eq.(5) for the slow resistive mode ($t \ll 1$) shows that the mode mentioned will be unstable if two unequalities $U_1 < 0$ and $U_0 + U_1 < 0$ are fulfilled simultaneously. Using of the unequalities obtained for the stability calculations of slow modes in "U-2M" torsatron shows that in the region $\beta_\theta \lesssim 1.4$ the excitation of the mode noted does not occur. The excitation of the slow mode is possible with plasma pressure increasing when the shear S and, respectively, the magnitude U_1 change their signs.

The excitation of the less localized ($t \gg 1$) fast resistive mode (g -mode), as the analysis of eq.(5) shows, occur if

$$-(\mu_J+\mu_H)^2+R^2K^2\frac{\mu_J+\varkappa_0 R}{\mu_J+\mu_H-\varkappa_0 R}-R^2K\frac{\mu_J'+\mu_H'}{\mu_J+\mu_H-\varkappa_0 R}\xi'-$$
$$-R^2K\frac{3\mu_H'+a\mu_H''}{2(\mu_J+\mu_H-\varkappa_0 R)}\cdot\frac{\xi'}{a}-\frac{1}{2}RB_0^2V_{vac}''-\frac{3}{2}(ka)^2\beta_\theta^2<0. \qquad (6)$$

In the region where the unequality (6) holds the growth rate of unstable perturbations of a g -mode is determined by a relation

$$\gamma=\frac{|U_0|^{2/3}(nq)^{2/3}}{(\tau_\theta^2\tau_S)^{1/3}(1+2R^2K^2q^2)|S|^{2/3}} \qquad (7)$$

The numerical analysis of finite pressure plasma stability in "U-2M" device shows that for arbitrary values of the parameter β_θ the fast resistive mode on the plasma column periphery is unstable.

References

1. V.D.Pustovitov, V.D.Shafranov. In "Voprosy teorii plazmy", Coll.ed.by B.B.Kadomtsev, Energoatomizdat, 1987, p.146-291 (In Russian).
2. J.W.Connor, R.J.Hastie, J.B.Taylor. Proc.Roy.Soc., 1979, v.A365, p.1-17.
3. A.B.Mikhailovsky, E.I.Yurchenko. Plasma Phys., 1982, v.24, N8, p.977-985.
4. V.E.Bykov, A.V.Georgievsky et al. "Voprosy atomnoi nauki i tekhniki, ser. "Termoyaderni sintez", 1983, N1,p.46-50.
5. V.V.Demchenko, A.B.Mikhailovsky, A.Ya.Omel'chenko. Preprint KhFTI-84-3, Moscow, 1984, 12p. (In Russian).

IDEAL MERCIER STABILITY FOR THE TJ-II*

A. Varias, A.L. Fraguas and L. García
CIEMAT-EURATOM Association
E-28040 Madrid, Spain

B.A. Carreras, N. Domínguez and V.E. Lynch
Oak Ridge National Laboratory
Oak Ridge, Tennessee 37831, U.S.A.

Introduction

The hardcore winding of the four period heliac TJ-II is composed of a circular coil and a helical winding with separately controllable currents. This makes the TJ-II a very atractive flexible heliac with a broad range of controllable rotational transform and magnetic well [1]. The configurations obtained by varying the rotational transform ι and the magnetic well have different MHD properties. The standard configuration (Configuration A), with $\iota = 1.44$, has an average stability beta limit of $\langle\beta\rangle \approx 2$ %, as shown in Ref. 2. Howewer, by varying the magnetic well at constant transform, a more stable configuration (Configuration B) can be found with higher beta limits.

Vacuum Configurations

Vacuum field configurations are determined with fixed TF coil line currents, fixed VF coil line currents, and various circular coil (I_{cc}) and helical coil (I_{hc}) line currents. The parameters that characterize the two considered configurations are:

	ι_0/N	I_{cc}	I_{hc}	Well
Config. A	0.36	219	95	3%
Config. B	0.36	105	82.5	4%

The boundary of the confinement region is Fourier analyzed in a form suitable as input for the VMEC equilibrium code [3]. The selected modes are distributed in a rectangle in an (m,n) mesh. The analysis [4] of a sequence of fittings using

different numbers of modes shows that more than 100 Fourier amplitudes are needed to reproduce with VMEC the vacuum results (rotational transform profile and magnetic well). In the two configurations considered in this work, the poloidal number m takes values from 0 to 7 and the toroidal number n ranges from -12 to 12.

Equilibrium Calculations

The fixed boundary equilibria for the two configurations under study were obtained from VMEC using a mesh of 31 points in the radial coordinate. The number of modes for the calculation of the finite beta equilibria was equal to that needed to specify the boundary; that is, 138 for both configurations. The total average force for the equilibrium configurations was less than 10^{-9}.

We considered a sequence of zero current equilibria with the pressure prof $p \alpha (1- \phi)^2$ where ϕ is the normalized toroidal flux. Figure 1 shows the flux surfaces at $\beta = 0$ for the two configurations.

Mercier Stability

The stability analysis shows that a beta stability limit exists for the standard configuration (Configuration A) around $< \beta > \approx$ 2.5%. Howewer, the configuration with a deeper magnetic well (Configuration B) is stable for this value of beta. In fact, this configuration is stable up to $< \beta > \approx$ 3%. These results show that the stability limit of the TJ-II heliac device is higher than the threshold of the average beta (2%) calculated for the standard configuration. They also suggest the possibility of finding configurations stable to average beta values higher than 3%. Figure 2 shows the results of the Mercier criterion for these critical beta values. Work is under way to study the stability of other accesible configurations with deeper magnetic wells.

References

* Research sponsored in part by the Office of Fusion Energy, U.S. Department of Energy, under contract DE-AC05-84OR21400 with Martin Marietta Energy Systems, Inc.

[1] T.C. Hender et al., *Fusion Technology* **13** (1988) 521.

[2] Nührenberg J., R. Zille and S.P. Hirshman, *14th Eur. Conf. on Conr. Fusion and Plasma Phys., Madrid 1987,* ECA Vol. 11d, Part I, 415.

[3] S.P. Hirshman, W.I. van Rij and P. Merkel, *Comput. Phys. Commun.* **43** (1986) 143

[4] A. Varias et al., Bull. Am. Phys. Soc. **33**, (1988).

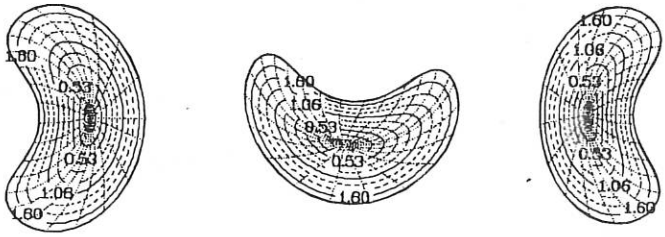

Configuration A

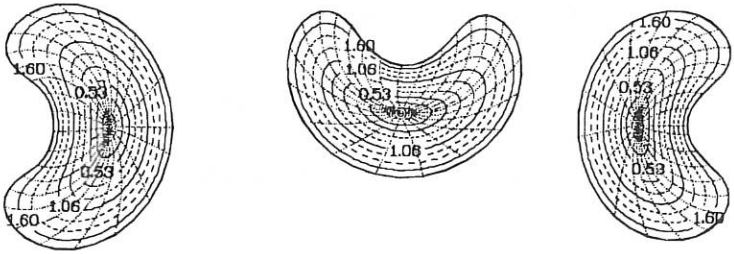

Configuration B

Fig. 1 Flux surfaces of the two considered configurations at different toroidal angles with $< \beta > = 0$.

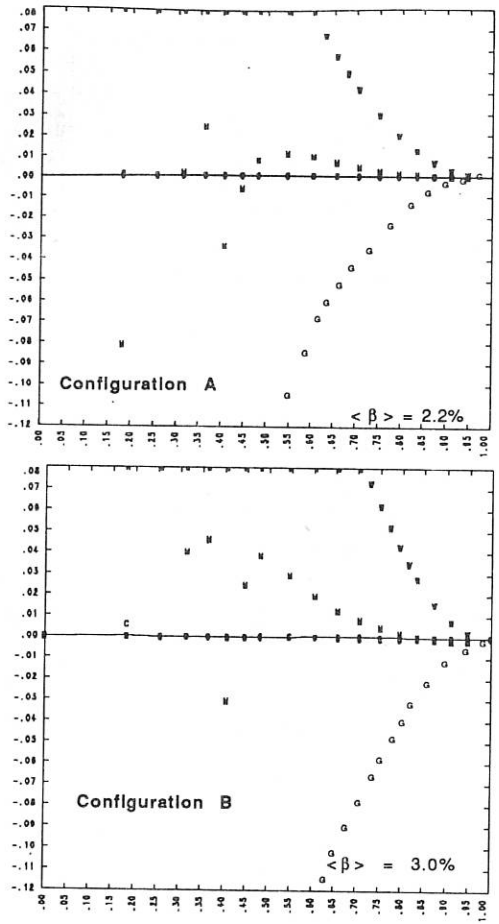

Fig. 2. The Mercier criterion (M) and the contributions from the shear (S), the magnetic well (W), the net currents (C) and the geodesic curvature (G) for Configuration A (top) for $< \beta > = 2.2\%$ and for Configuration B (bottom) for $< \beta > = 3.0\%$.

STABILITY OF LOCAL MODES IN LOW-ASPECT-RATIO STELLARATORS

L. Garcia
Universidad Complutense and Association CIEMAT-EURATOM. 28040 Madrid, SPAIN

B.A. Carreras, N. Dominguez
Oak Ridge National Laboratory. Oak Ridge, Tennessee 37831, USA.*

The studies of MHD stability properties of stellarator-type configurations are complicated by the three-dimensional (3-D) nature of the equilibrium of these configurations. Usually, the unstable modes are pressure-driven and very localized around the rational surface. The 3-D Mercier stability criterion for local instabilities [1] is therefore adequate for most of the stability studies. The method has been implemented in different 3-D equilibrium codes and is widely employed in stability calculations for stellarators.

We use an average method based on vacuum flux coordinates [2] to study the equilibrium of low-aspect-ratio configurations. The specific vacuum flux coordinates (ρ, θ, φ) are those described by Boozer [3]. The radial variable is ρ, while θ and φ are, respectively, poloidal and toroidal-like angles. The Jacobian is $D = B_v^2/\rho B_0 g_B$. The only vacuum magnetic field covariant component different from zero is $B_\varphi = g_B$, while $B_0 \pi \rho^2$ is the toroidal flux.

At finite beta, to leading order, $B_\varphi = F$ and the averaged pressure p are functions of the averaged poloidal flux ψ only [2]. We have developed a computer code to invert the Grad-Shafranov-type equation for ψ, that results at lowest order [4]. The equilibria obtained are used to evaluate the 3-D Mercier criterion for local instabilities:

$$D_M = D_S + D_W + D_I + D_G \geq 0$$

This form of the Mercier criterion utilizes the same conventions as that given in Reference [5]. D_S gives the stabilizing contribution of the shear, D_W is the contribution of the magnetic well, D_I is the contribution of net currents, and D_G gives the contribution due to the geodesic curvature. To calculate the integrals involved, we expand all the quantities in averaged and varying components up to a given order. At lowest order, the different terms can be written as follows:

---

* Operated by Martin Marietta Energy Systems, Inc., under contract DE-AC05-84OR21400 with the U.S. Department of Energy.

$$D_S = \frac{s}{64\pi^2 \iota^2}\left(\frac{d\iota}{ds}\right)^2,$$

$$D_W = \frac{\mu_0 B_0 g_B}{2\pi \iota^2 \Phi_e^4} s \frac{dp}{ds}\frac{d}{ds}\iint\left\langle\frac{B^2}{B_v^2}\right\rangle \frac{\rho\, d\rho\, d\theta}{|\nabla s|^2}\left[\frac{d^2V}{ds^2} - 2\pi\mu_0 B_0 g_B \frac{dp}{ds}\frac{d}{ds}\iint\left\langle\frac{1}{B^2 B_v^2}\right\rangle \rho\, d\rho\, d\theta\right],$$

$$D_I = \frac{\mu_0 B_0 g_B}{8\pi \iota^2 \Phi_e^2} s \frac{d\iota}{ds}\left[\frac{1}{\Phi_e}\frac{dI}{ds}\frac{d}{ds}\iint\left\langle\frac{B^2}{B_v^2}\right\rangle \frac{\rho\, d\rho\, d\theta}{|\nabla s|^2} - \frac{d}{ds}\iint\left\langle\frac{\bar{J}\cdot\bar{B}}{B_v^2}\right\rangle \frac{\rho\, d\rho\, d\theta}{|\nabla s|^2}\right],$$

$$D_G = \left(\frac{\mu_0 B_0 g_B}{2\iota \Phi_e^2}\right)^2 s\left\{\left[\frac{d}{ds}\iint\left\langle\frac{\bar{J}\cdot\bar{B}}{B_v^2}\right\rangle \frac{\rho\, d\rho\, d\theta}{|\nabla s|^2}\right]^2 - \frac{d}{ds}\iint\left\langle\frac{(\bar{J}\cdot\bar{B})^2}{B_v^2 B^2}\right\rangle \frac{\rho\, d\rho\, d\theta}{|\nabla s|^2}\cdot\frac{d}{ds}\iint\left\langle\frac{B^2}{B_v^2}\right\rangle \frac{\rho\, d\rho\, d\theta}{|\nabla s|^2}\right\},$$

where the integrals are calculated over contours of constant ψ, $s = \Phi/\Phi_e$, being Φ the toroidal flux, and Φ_e its value at the edge. V is the volume enclosed by each flux surface, ι is the rotational transform, J is the current density, I is the toroidal current on each flux surface, B and B_v are, respectively, the finite beta and vacuum magnetic fields, and the angle brackets $\langle\ \rangle$ denote average over the toroidal angle φ.

At lowest order, B^2 / B_v^2 and $\bar{J}\cdot\bar{B} / B_v^2$ are independent of the toroidal angle φ, so we can write:

$$\left\langle\frac{1}{B^2 B_v^2}\right\rangle = \left\langle\frac{1}{B_v^4}\right\rangle\left\langle\frac{B^2}{B_v^2}\right\rangle^{-1}, \qquad \left\langle\frac{(\bar{J}\cdot\bar{B})^2}{B_v^2 B^2}\right\rangle = \left\langle\frac{\bar{J}\cdot\bar{B}}{B_v^2}\right\rangle^2\left\langle\frac{B^2}{B_v^2}\right\rangle^{-1}$$

All the terms involved in the two-dimensional (2-D) integrals can be calculated from the averaged equilibrium quantities ψ, F and p, the vacuum magnetic field and the averaged metric elements.

We compare the results obtained using this 2-D method with 3-D calculations made with the VMEC code [6]. First, we present results for the CT6 configuration [5], a 6-field-period l=2 torsatron with a plasma aspect ratio of 3.8, and ι ranging from 0.32 at the magnetic axis to 0.95 at the edge. The pressure is proportional to ψ^2 in these calculations, and they assume zero net current within each flux surface. The 3-D Mercier criterion for this profile gives stability for

the full beta range; this is also the case for the 2-D Mercier criterion using CHAV, and the values for D_M given by both codes are very close. The main difference comes from the term due to the geodesic curvature, which is more destabilizing in the full 3-D calculations. For this sequence, the equilibrium shift and well depth results of both codes are almost the same. Figure 1 shows the results for an equilibrium with $\beta_0 = 11.7\%$. The values for the different components using both codes are very close.

Second, we present results for the 4-field-period flexible heliac TJ-II [7]. The particular case considered has an ι profile ranging from 1.46 at the magnetic axis to 1.48 at the edge, and the well depth is 2.3%. As in the previous case, the pressure is proportional to ψ^2, and we impose zero net current within each flux surface. The equilibrium shift and well depth results are very similar. The calculations of the Mercier criterion using VMEC show that the configuration is unstable for this pressure profile. However, with CHAV, it appears to be stable. As in the case of CT6, the difference comes from the geodesic curvature term, but now is much marked. The helical terms are more important in this case, and higher order terms must be introduced in the expansion to obtain a more realistic result for the local stability calculations.

In conclusion, the 2-D Mercier criterion calculated using this average method gives slightly more optimistic results than the 3-D calculations, due to the geodesic curvature term. These differences are stronger for helical axis configurations, probably because of the helical shift.

REFERENCES

[1] MERCIER, C., LUC, H., Lectures in Plasma Physics, Commission of the European Communities, Luxemburg (1974).

[2] HENDER, T.C., CARRERAS, B.A., *Phys. Fluids* **27** (1984) 2101.

[8] BOOZER, A.H., *Phys. Fluids* **25** (1982) 520.

[4] GARCIA, L., et al., 12th IAEA Conf. on Plasma Phys. and Contr. Nucl. Fusion, Nice, 1988. Paper C-I-5-1.

[5] CARRERAS, B.A., et al., *Nucl. Fusion* **28** (1988) 1195.

[6] HIRSHMAN, S.P., VAN RIJ, W., MERKEL, P., *Comput. Phys. Commun.* **43** (1986) 143.

[7] HENDER, T.C., et al., *Fusion Technol.* **13** (1988) 521.

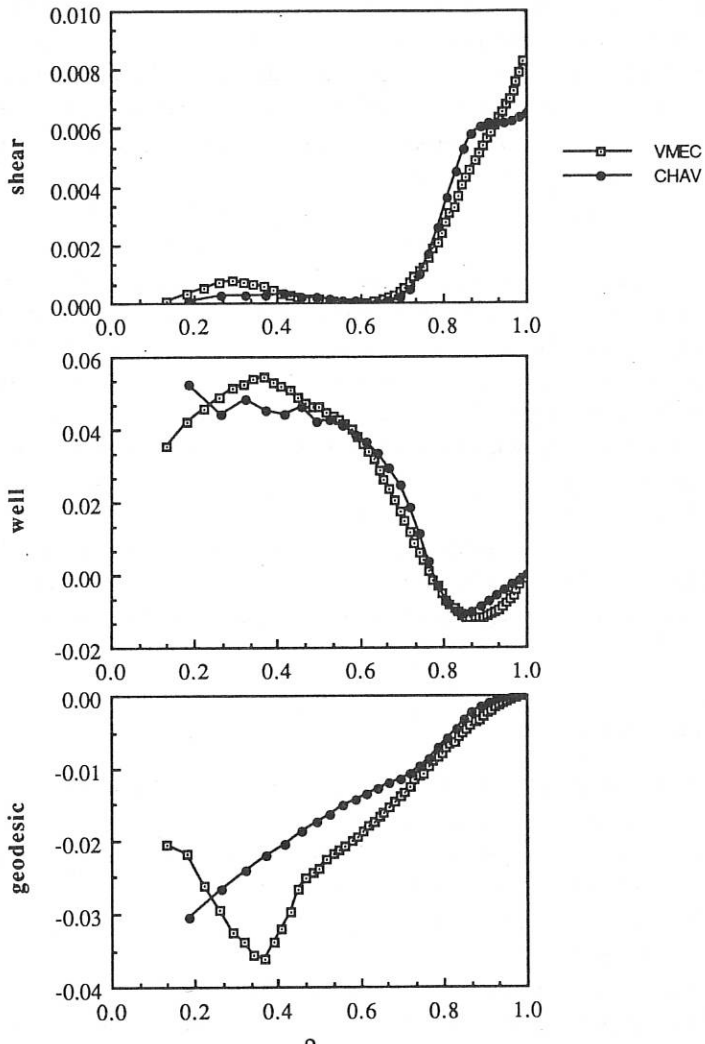

FIG. 1. Radial dependence of the contributions to the Mercier criterion using VMEC and CHAV. The plotted values are for a $\beta_0 = 11.7\%$. The radial coordinate is $\rho = \sqrt{s}$.

CORRECTION OF FIELD ERRORS IN THE ATF TORSATRON*

R. J. Colchin, J. H. Harris, F. S. B. Anderson[a], A. C. England, R. F. Gandy[b], J. D. Hanson, M. A. Henderson[b], D. L. Hillis, T. C. Jernigan, D. K. Lee[c], V. E. Lynch[c], M. Murakami, G. H. Neilson, J. A. Rome, M. J. Saltmarsh, C. M. Simpson[d]

Fusion Energy Division, Oak Ridge National Laboratory, Oak Ridge, Tennessee, U.S.A.

ABSTRACT An electron beam has been used to trace the flux surfaces in the ATF torsatron. The flux surfaces were found to have islands at the location of low-order resonances, signifying the existence of field errors. Careful measurement of the magnetic fields from individual coil sets ruled out misalignments as the cause of the errors. Subsequently, the field errors were identified as magnetic dipoles arising from uncompensated current feeds to both the helical and vertical field coils. Extensive modeling calculations were carried out to find ways to minimize the errors, and the bus work was modified. Preliminary flux surface scans indicate a large reduction in the size of previously existing islands.

FLUX SURFACE MAPPING A beam of electrons was used to map out flux surfaces in the ATF[1] torsatron. The beam was detected when electrons impinged on a phosphor-coated screen located $\sim 180°$ toroidally away from the gun. The electron gun was mounted on a probe drive that could scan the entire cross section within the last closed flux surface in ATF. Light from the phosphor-coated screen[2] was detected by an image-intensified CCD television camera that viewed the screen at an angle through a nearby port. All experiments were conducted with a steady-state magnetic field of ≤ 0.1 T. First the magnetic axis was located by moving the electron gun in increments until a single spot was obtained. The gun was then translated at the rate of 1 mm/s along a vertical or horizontal chord, allowing for a complete scan of the flux surfaces within a few minutes. Data were viewed directly on a TV monitor and stored on video tape. Data were analysed by transferring frames from video tape to a computer, where the image was enhanced and transformed to remove spatial distortions due to the viewing angle of the camera.

Flux surface scans revealed the existence of a number of low-order rational surfaces. With the position of the gun known from the scan rate, it was possible to determine the rotational transform ι as a function of distance from the magnetic axis. Figure 1

*Research sponsored by the Office of Fusion Energy, U.S. Department of Energy, under contract DE-AC05-84OR21400 with Martin Marietta Energy Systems, Inc.

[a]Torsatron/Stellarator Laboratory, University of Wisconsin, Madison, Wisconsin.

[b]Auburn University, Auburn, Alabama.

[c]Computing and Telecommunications Division, Martin Marietta Energy Systems, Inc.

[d]University of Maryland, College Park, Maryland.

shows ι versus distance for the "standard" field configuration in ATF. The experimentally determined values of ι compare well with calculated values, except where islands were observed at low-order resonant surfaces. The largest islands were detected at the $\iota = 1/2$, $2/3$, and 1 resonant surfaces, as can be seen in Fig. 1. The extent of the $\iota = 1$ island could not be determined since it intercepted the screen holder at the edge of the viewing surfaces. The islands observed at the $\iota = 1/3$, $1/2$, and $2/3$ resonant surfaces are shown in Figs. 2(b)–2(d). The largest island, at $\iota = 1/2$, has a maximum width of 6 cm.

An island ~2–3 cm wide at $\iota = 1/2$ had been expected owing to the perturbing influence of the earth's field. The fact that the island was twice that size signaled the presence of field errors. When the magnetic field was scanned between 0.1 T and 0.02 T, the island size did not change appreciably, indicating that the field errors were either intrinsic to the coils and feeds or due to linearly induced fields. Configurations other than the "standard" magnetic field configuration were also run. These measurements made it possible to eliminate the inner vertical field coils as the field error source. The possible sources of error fields were coil misalignments, perturbations from ferromagnetic materials, or fields from uncompensated currents in coil leads.

MAGNETIC FIELD COIL ALIGNMENT MEASUREMENTS A slight (~1 cm) tilt or shift of one coil was regarded as a likely source for the field error. A search for such errors was made by measuring the radial field B_r of individual coil pairs and using this information to determine their axes.[3] These measurements were made using a precision positioning apparatus located near the centerline of ATF to locate a Hall-effect probe. From these measurements the two helical field coils were found to be aligned to within $\leq$3 mm. The inner and mid-vertical fields were also found to be well aligned. Data for the trim vertical field coils (which are in the same coil bundle as the outer vertical field coils) were somewhat confused by ferromagnetic objects located just outside these coils. However, the perturbations were too small to have caused the observed islands.

MODELING TO DETERMINE THE FIELD ERROR SOURCE AND CORRECTION A careful review of the coil feeds and bus work revealed four locations where ~600 cm^2 dipole loops were created. These occurred at the four helical coil current feeds, where it was not possible to have closely spaced parallel leads. Smaller uncompensated current dipoles were also found in the current leads feeding the outer vertical field coils. Model computations were performed to determine the effect of these perturbations, and the result is shown in Fig. 2(a); the errors in the current feeds give a good match in both island size and phase to those measured using the electron beam [Figs. 2(b)–2(d)].

The four helical coil current feed errors could not be eliminated without modifications to the structural support of ATF. Modeling calculations showed that symmetrization of these errors by the addition of eight more dipole error fields, equally spaced around ATF, would eliminate the islands. This solution was adopted, and the vertical field bus work was redesigned to decrease the area of uncompensated current feeds near the coils.

FLUX SURFACE MAPPING RESULTS AFTER ERROR FIELD CORRECTIONS Preliminary results of the flux surface structure have been obtained after modifications to the bus work. The same electron beam technique was used as has been previously described. A plot of ι versus vertical distance is shown in Fig. 3. The islands which previously existed in the outer half of the ι profile (i.e., $\iota = 1/2$, $2/3$) were greatly reduced in size. In particular, the $\iota = 1/2$ island width was reduced to ~2.5 cm. However,

islands in the inner half of the ι profile now exist which had previously been either small or nonexistent. The largest of these islands occurs at $\iota = 1/3$. Efforts are presently under way to understand the remaining perturbations causing these inner islands and to minimize them.

SUMMARY Data obtained from flux surface mapping showed the existence of intrinsic islands, indicating the presence of field errors. The use of a fluorescent screen as a detector for an electron beam proved to be a very efficient and graphically descriptive method of mapping torsatron flux surfaces. Data from the magnetic field alignment probe ruled out coil misalignments as the principal cause of the islands. Modeling studies showed that the likely source of the field errors was uncompensated currents in coil feeds. These coil feeds were modified, and scans of the flux surfaces show that the size of the $\iota = 1/2$ and $2/3$ islands has been greatly reduced.

ACKNOWLEDGEMENT This research was sponsored by the Office of Fusion Energy, U.S. Department of Energy, under contract DE-AC04-84OR21400 with Martin Marietta Energy Systems, Inc.

REFERENCES

[1] J. F. Lyon, B. A. Carreras, K. K. Chipley, M. J. Cole, J. H. Harris, T. C. Jernigan, R. L. Johnson, V. E. Lynch, B. E. Nelson, J. A. Rome, J. Sheffield, and P. B. Thompson, Fusion Technol. **10** (1986) 179.

[2] G. L. Hartwell, R. F. Gandy, M. A. Henderson, J. D. Hanson, D. G. Swanson, C. E. Bush, R. J. Colchin, A. C. England, and D. K. Lee, Rev. Sci. Instrum. **59** (1988) 460.

[3] R. J. Colchin, J. H. Harris, D. K. Lee, J. A. Rome, A. I. Fedotov, F. I. Ozherel'ev, O. S. Pavlichenko, D. P. Pogozhev, V. M. Zalkind, and J. D. Treffert, Rev. Sci. Instrum. **57** (1986) 1233.

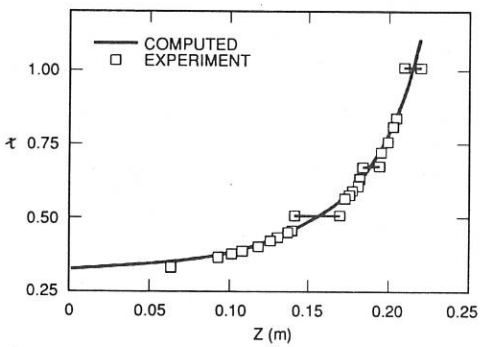

FIG. 1. Plot of the rotational transform parameter ι versus the radius (along the Z axis) Islands at $\iota = 1/2$, $2/3$, and 1 are shown by straight lines.

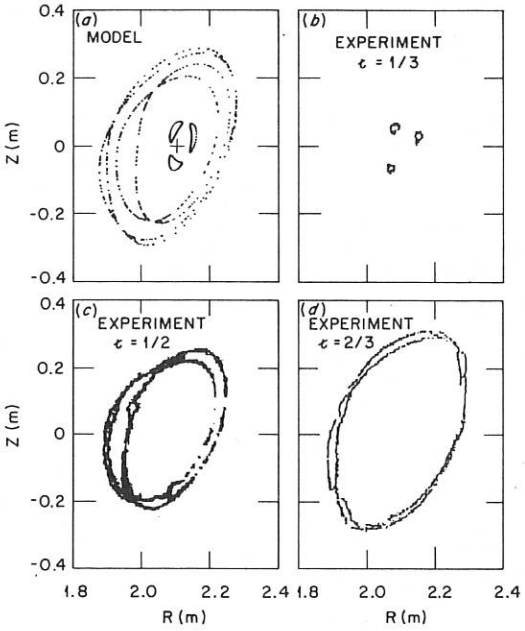

FIG. 2. (a) Computed islands at $\iota = 1/3$, $1/2$, and $2/3$ assuming field errors due to uncompensated currents in coil feeds. (b)-(d) Corresponding measured flux surfaces.

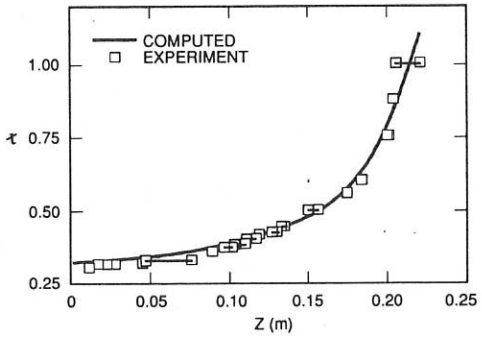

FIG. 3. Plot of the rotational transform parameter ι versus radius (along the Z axis) after error field correction. Islands are noted by straight lines.

IMPURITY STUDIES IN THE ADVANCED TOROIDAL FACILITY

R. C. Isler, L. D. Horton, E. C. Crume, H. C. Howe, and G. S. Voronov†

Fusion Energy Division, Oak Ridge National Laboratory
Oak Ridge, TN 37831
U.S.A.

Abstract

Impurities have played an important role in the initial stages of operation of the Advanced Toroidal Facility (ATF).[1] Cleanup practices have been adequate enough that plasmas heated by ECH only can be operated in a quasi-steady state; however, neutral-beam injected plasmas always collapse to a low temperature. It is not clear whether impurity radiation is actually responsible for initiating the collapse, but at the time the stored energy reaches a maximum, there are indications of poloidal asymmetries in radiation from low ionization stages, such as observed in marfes, which could play a dominant role in the plasma evolution.

ECH plasmas and cleanup

The earliest ATF plasmas were heated with only 200 kW of 53 GHz, second harmonic gyrotron power. Discharge cleaning in this period was accomplished using a 2.45 GHz, 4 kW, ECR source. The discharges exhibited uncontrollable rises in electron density and spectral line radiation because of impurity influxes, and they always collapsed to low temperature plasmas before the end of the ECH pulse. This behavior is illustrated by the O V emission from shot 679 (100 ms ECH pulse) shown in Fig. 1 where arrows indicate the time of collapse. Following a rapid increase in radiation from intermediate stages of ionization, such as O V and O VI, a precipitous temperature drop occurs at 50 ms leaving O II and O III as the dominant oxygen ions. The electron density falls along with the temperature because of recombination. The addition of glow discharge cleaning together with baking the vacuum vessel reduced the impurity content significantly. Within 10 days of this type of cleaning, discharges could be operated up to 280 ms (shot 1080), and within two weeks, collapses could be avoided completely as illustrated by the O V signal from shot 1156 which decays only when the ECH is turned off at 450 ms. Discharges up to 1s long have been operated with no observable buildup of contaminants.

NBI plasmas

Quasisteady operation has not been achieved with neutral beam injection. Following the onset of injection, the electron density and stored energy both rise briefly, but in typical non-gettered operation they start to decrease at 50-70 ms after injection starts. Figure 2 shows the behavior of the central electron and ion temperatures during 100 ms of 750 kW NBI. The 200 kW ECH heating is operated from 0-400 ms. The electron temperatures are measured continuously from electron cyclotron emission and the ion

---

†Institute of General Physics, Moscow.

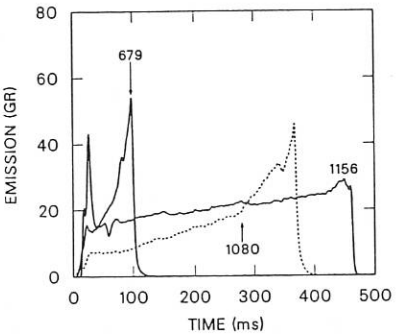

Fig. 1. O V emission for specified shot numbers

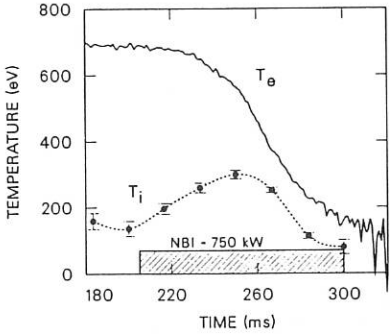

Fig. 2. Time history of $T_e(0)$ and $T_i(0)$ during 750 kW NBI injection.

temperatures are obtained from the Doppler widths of the O VII line at 1623 Å averaged over 16 ms intervals. The neutral beam pulse clearly heats the ions initially, but similar heating is not observed in the electrons. Both temperatures fall after 260 ms. It is still an open question whether impurity radiation alone is responsible for the inability to maintain the electron temperature at a high level during NBI.

Detailed interpretation of impurity behavior is complicated by the rapidly changing temperature and density, but certain general aspects are readily deduced. Characteristic carbon signals are shown in Figs 3 and 4 for a discharge in which injection lasts from 100-200 ms. It is noteworthy that the C III radiation, one of the most intense transitions, is relatively weak in the target plasma, 7 GR, and that after injection it increases by a factor of 10 up to the peak of the stored energy at 150 ms. Even so, it radiates only 13 kW out of 400 kW of absorbed power. Typically, the radiated power at the time of the peak in the stored energy is only 30-40% of the absorbed power. The intense peak in the C III emission that develops after 170 ms is the result, not the cause, of the severe drop in T_e; it appears only when the temperature is low enough for C III to be a dominant ion.

Radiation from C V and C VI are used to determine the carbon density during injection. The C VI signal comes overwhelmingly from charge-exchange excitation $(CXE)^2$, and is proportional to the C^{6+} density in the interior of the plasmas. Emission from the 2271Å line of C V (Fig. 4) indicates a substantial fraction of C^{5+} is also present in the center. This conclusion is drawn from the difference between the radiation when injection from the two beams is alternated from shot to shot. The grazing incidence spectrometer on ATF has a field of view that encompasses only beam #1. The trace in Fig. 4a is taken with beam #1 operating and is the sum of electron excited and charge-exchange excited emission, whereas Fig. 4b is recorded with only beam #2 operating and, hence represents only electron excitation, i.e., the signal is related only to the density of C^{4+} and not to C^{5+}. The difference of the two signals, which depends only on the C^{5+} density, is shown in Fig. 4c. The fact that the carbon is not burned out in the center implies that the diffusion coefficients are rather high, 1-2 X 10^4 cm^2/s. The rapid rise of the CXE signals when the beam is turned on provides a measure of the carbon content before its concentration changes substantially from that of the ECH target plasma. Subsequent evolution is representative of the change in the impurity

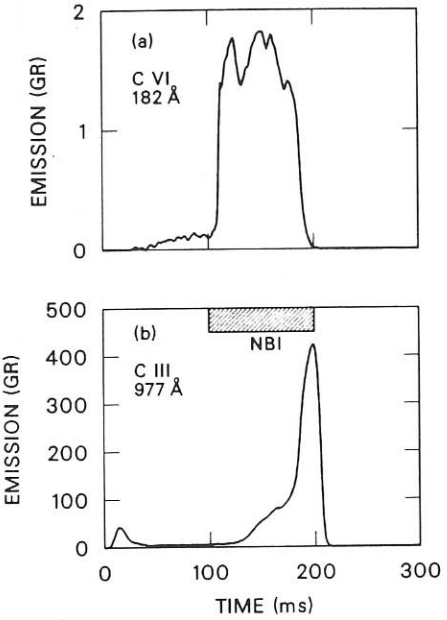

Fig. 3. Emission from a CXE line and a strong $\Delta n=0$ line in NBI discharges.

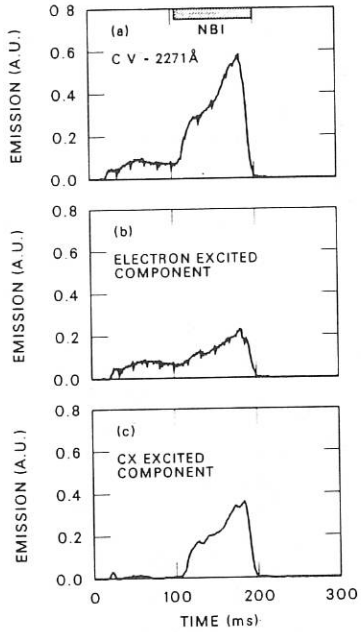

Fig. 4. C V emission (2271 Å), (a) CXE and electron excited, (b) electron excited only, and (c) CXE only.

level as the discharge progresses. For a wide variety of conditions, analysis shows that the central densities of oxygen, carbon, and nitrogen all increase by factors of 1.5-3. The increase appears to result from a greater influx during injection; there is no strong evidence that injection engenders accumulation.[3] Because the electron density also rises, Z_{eff} does not increase very much; it remains in the range 1.5-2.0. Gettering approximately 30% of the vacuum vessel with chromium reduces the edge radiation by factors of 3-4 in ECH plasmas, although the central densities change by only about 30%. Higher electron densities can be achieved by gettering, but the discharges still terminate similarly to ones where gettering is not employed.

The relatively low impurity content and low fraction of radiated power at the time of the peak in the stored energy would make it seem unlikely that impurities alone are responsible for the collapse, but modelling studies using the PROCTR code indicate that this may indeed be the case for the plasmas described here which have substantially reduced volumes because of the presence of large magnetic islands. Also, there are some indications that marfe-like structures, which could drive the collapse, may develop just prior to the time the stored energy peaks. Fig. 5 shows the chordal signals from C IV and their Abel inversions as a function of vertical position for several times. Up to

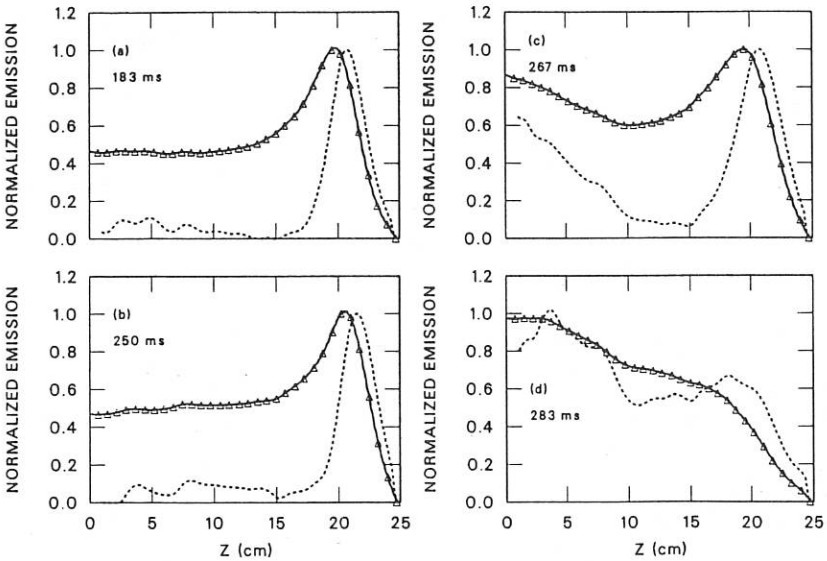

Fig. 5. Chordal signals (solid lines) and Abel inversions (dashed lines) for the 1548 Å line of C IV. Neutral beam injection lasts from 200-300 ms.

50 ms after injection the signal is peaked in the periphery as expected. At 267 ms, 17 ms after the start of the collapse, a second peak ostensibly appears in the center of the plasma. No tenable physical explanation for such a central peak has been found, however. It is believed that a strongly radiating, poloidally localized source located in the midplane may be giving a false impression of the radial distribution.

Summary

Vessel cleaning techniques have reduced the low-Z content to about $0.02n_e$ and allowed quasi-steady operation of ECH plasmas. Impurities still present a problem in NBI plasmas which eventually collapse to a low temperature where 100% of the input power is radiated. It is still uncertain whether the impurity radiation can initiate the collapse. Reduction of island widths by correcting field errors should provide more insight into this problem.

Acknowledgement

Work sponsored by the Office of Fusion Energy, U. S. Department of Energy, under contract No. DE-AC05-84OR21400 with Martin Marietta Energy Systems Inc.

References

1. J. F. Lyon et al., Fusion Technol. **10**, (1986) 179.
2. R. C. Isler, Physica Scripta **35**, (1987) 650.
3. W VIII-A TEAM, NI GROUP, Nucl. Fusion **25** (1985) 1593.

EDGE PLASMA AND DIVERTOR STUDIES IN THE ATF TORSATRON*

P. K. Mioduszewski, T. Uckan, D. L. Hillis, J. A. Rome, R. H. Fowler,
J. C. Glowienka, M. Murakami, and G. H. Neilson

Oak Ridge National Laboratory
Oak Ridge, Tennessee 37831, U.S.A.

1. Introduction

During the first operating period of the Advanced Toroidal Facility (ATF), currentless plasmas have been generated and heated with up to 0.2 MW of electron-cyclotron power (ECH) and up to 1.5 MW of neutral beam injection (NBI) [1]. ATF is an l= 2, 12-field-period torsatron with a major radius R_0 = 2.1 m, an average plasma radius a = 0.27 m, and a mean field of $B_0 \leq 2$ T. The ECH system consists of one 53.2 GHz, 200 kW, CW gyrotron which provides fundamental heating at B_0 = 1.9 T and second harmonic heating at B_0 = 0.95 T. Two neutral injectors are installed, aligned for tangential injection in opposing directions (co- and counter-injection). Each beam can inject up to 1 MW into the torus at energies up to 40 keV, with pulse lengths up to 0.3 s. For future long pulse or steady state operation, we are investigating options for continuous particle control and edge modifications with a divertor.

2. Experimental Arrangement

The poloidal cross-section of the plasma is a function of the toroidal angle. At $\phi = 0^0$ and 30^0 the plasma is vertically elongated, while halfway in between, at $\phi = 15^0$, it is horizontally elongated.Toroidal cuts through the vacuum vessel at $\phi = 0^0$ and 15^0 and the corresponding poloidal cross-sections are shown in Fig. 1. The figure shows the main plasma, limited by the last closed flux surface (LCFS), and the plasma edge. It has been observed in Heliotron-E that

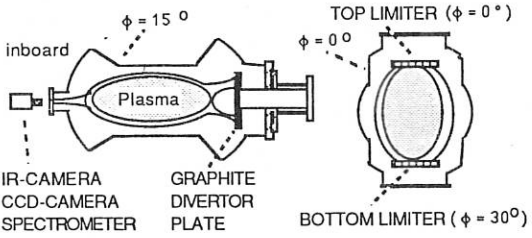

FIG.1 Poloidal cross-section of the plasma at toroidal angles of $\phi = 0^\circ$ and 15°, showing the plasma edge and the arrangement of limiters and the graphite plate.

*Research sponsored by the Office of Fusion Energy, U.S. Department of Energy, under contract DE-AC84OR21400 with Martin Marietta Energy Systems, Inc.

the plasma leaves the confinement zone in distinct flux bundles intercepting the wall as "divertor stripes" [2]. As indicated schematically in Fig. 1, two stripes leave the confinement zone towards the outboard wall and one towards the inboard wall. Because of the complicated structure of the plasma edge, the diagnostics system was designed to determine a) the global configuration, i.e. the location and extent of the stripes, and b) the local plasma parameters within the stripes. The main edge diagnostics that have been used so far are the instrumented limiters, the instrumented divertor plate, and an array of H_α-monitors.

The instrumented limiter system is comprised of one moveable top and bottom module, each with a vertical stroke of 25 cm and a toroidal separation between the two units of one field period. Each module consists of 11 individual graphite tiles, mounted on a water-cooled stainless steel base plate. The tiles form calorimeter arrays for measurements of the energy deposition profile and the total deposited energy. The central tile incorporates Langmuir probes and a gas puff nozzle. The drawing in Fig. 2 shows the schematic arrangement of the top limiter and the central tile.

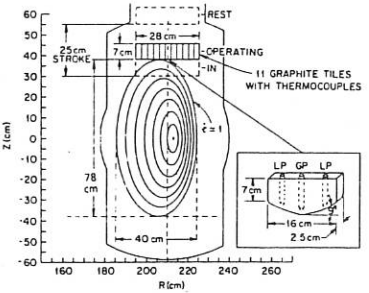

FIG. 2 Location of the top rail limiter in the ATF vessel.The inset shows the central tile.

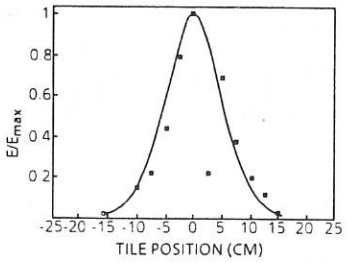

FIG. 3 Energy deposition profile on the top limiter located at z = 39 cm

A system consisting of a graphite divertor plate and an infra-red (IR) or charge-coupled device (CCD) camera is used to study the divertor configuration. Figure 1 indicates the location of the divertor plate; it has a diameter of 50 cm and can be positioned between the wall and the LCFS. The pattern of particle and heat fluxes on the divertor plate can be observed with CCD- or IR-camera repectively. A multi-purpose image processing system has been developed for fast aquisition, display and analysis of these 2-dimensional patterns. For measurements of local plasma parameters, Langmuir probes are imbedded in the graphite plate at three locations. Observing particle fluxes to the divertor plate while scraping off the edge plasma with top and bottom limiters, will allow us to determine the connection lengths in the plasma edge as a function of radial position.

The H_α-monitors view the wall, the gas puff location, the location of neutral beam injection, and the limiter. The observed signals serve as a relative measure of particle fluxes. Because of the complicated structure of the plasma edge, the determination of the integrated global particle flux requires detailed transport modeling of the neutral hydrogen and is in progress.

3. Modeling of the Plasma Edge

Particle flow from the confined plasma to the vacuum vessel wall has been studied by following field lines and single particle orbits. A realistic multifilament model for the vacuum magnetic field was combined with a detailed computer model of the ATF vacuum vessel to determine the interception of the field lines with the vacuum vessel. Magnetic field lines as well as 1-keV particles were launched randomly from locations 1 to 3 cm outside the LCFS. The result showed both field lines and particles being funneled to form narrow stripes at the wall. The stripes were similar for the field lines and the 1-keV particles. Modeling the interception of the field lines with the outboard divertor plate showed two distinct stripes with the location depending on the radial position.

4. Results

A typical limiter energy profile of a 0.25 s discharge is shown in Fig. 3. The plasma was sustained by 170 kW of ECH with an additional 600 kW of NBI from 0.15 s to 0.25 s; the maximum line-averaged density was 1.5×10^{19} m^{-3}. The vertical position of the limiter was at 39 cm which corresponds approximately to the LCFS. The central tile received an energy of 860 J, the total energy deposited on one limiter was 4 kJ. From the width of the energy deposition profile, the scrape-off length of the heat flux was determined to be $\lambda_q = 2.3$ cm, similar to values obtained in tokamaks. To determine the average power flux as well as the contributions from ECH and NBI, limiter position scans were performed for ECH-only as well as for (ECH+NBI) discharges. The total deposited energy at the top limiter as a function of position is shown in Fig. 4.

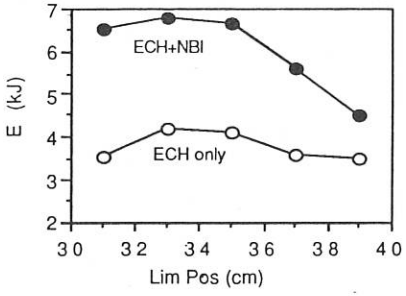

FIG. 4 Total energy deposited on top limiter during 0.25 s discharge as a function of limiter position

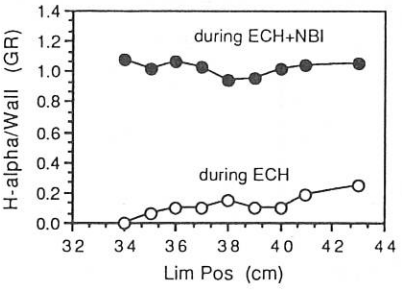

FIG. 5 H_α-radiation from the wall at 70 ms (ECH) and 150 ms (ECH+NBI) into the discharge

The ECH-only discharges are suitable for estimating the power flux. The average ECH input was 170 kW for a duration of 0.25 s. The energy deposition at the LCFS (39 cm) was 3.5 kJ, corresponding to an average limiter power flux of 14 kW. Hence, the total power flux to both limiters was 16.5 % of the input power. Knowing the power to the central tile as well as the e-folding length of the power flux, the power flux density at the LCFS could be calculated and was approximately 270 W/cm^2. This is consistent with Langmuir probe measurements which indicate temperatures and densities at the LCFS of 12 eV and 3×10^{18} m^{-3} respectively.

The (ECH+NBI) discharges were sustained for 0.25 s by 170 kW of ECH, with an additional 740 kW of NBI for 0.1 s. The total input energy increased by a factor of 2.75. As Fig. 4 shows, the energy on the limiter increased only by a factor of 1.3 at the LCFS and by 1.6 at 33 cm. At the LCFS, an incremental energy of 1 kJ was deposited by NBI, corresponding to a power flux of 10 kW. Accounting for both limiters, the fraction of NBI power that is transported to the limiters, is only about 3 %. Since, on the other hand, the stored energy in the bulk plasma increased typically by a factor of 2.5 with NBI, we conclude that energy transport from the center does not occur by conduction and convection to the plasma edge, but by mechanisms that transport energy directly to the wall such as radiation and charge-exchange processes. This is consistent with measurements of the H_α radiation at the vessel wall. When the limiters were inserted well into the confined plasma, most of the plasma should have been scraped off, causing the particle flux to the wall to vanish. As Fig. 5 shows, this is actually the case for the ECH phase of the discharge while during the NBI phase the particle flux to the wall is hardly influenced by the limiter position. Whether or not these observations can be explained e.g. by charge-exchange processes or by other mechanisms such as orbit losses, will be studied further.

Some initial experiments with the divertor plate have confirmed modeling results on the "divertor stripes". A position scan of the divertor plate has provided first information on the stripes. The Langmuir probes on the plate were used to measure the ion saturation current as a function of plate position. As a result, three curves were obtained which represent the particle flux in the stripe, each at a different position. Figure 6 shows one example (the zero position corresponds to the plate located at the wall). The figure shows that the stripes were very narrow with only 2 cm half-width and particle fluxes of several times 10^{17} cm^{-2} s^{-1}. Stripe position and half-width did not change with NBI. The particle flux was three times higher during NBI than during ECH-only which is consistent with the change in line-average density.

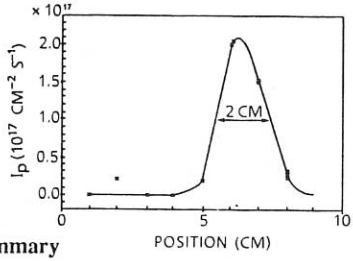

FIG. 6 Particle flux in the "divertor stripe" as a function of the divertor plate position

5. Summary

First plasma edge data have been obtained during the initial operating period of ATF. For discharges with 170 kW of ECH power, 600 kW of NBI power, and line-average densities of 1.5 x 10^{19} m^{-3}, the plasma parameters at the LCFS were: $n_e = 3 \times 10^{18}$ m^{-3}; $T_e = 12$ eV; heat flux 150 - 300 W/cm^{-2}, decay length $\lambda_q = 2$ cm. The fraction of the input power that was deposited on the limiters was 16 % in ECH discharges and 3 % in NBI discharges. The particle flux in the divertor stripes was several 10^{17} cm^{-2} s^{-1} with a half-width of 2 cm. Location and width of the stripes did not change when the neutral beam was injected into the ECH plasma.

6. References

[1] M.J. Saltmarsh et al., IAEA-CN-50/C-1-2, IAEA Conference Nice, France, Oct. 1988
[2] O. Motojima et al., J. Nucl. Mater. 128 & 129 (1984) 524

EXPERIMENTAL RESULTS OF MAGNETIC SURFACE MAPPING IN THE STELLARATOR W VII-AS

R. Jaenicke, K. Schwörer*, E. Ascasibar**, P. Grigull, H. Hailer*, I. Lakicevic, M. Zippe

Max-Planck-Institut für Plasmaphysik, IPP-EURATOM Association, D-8046 Garching b. München, Federal Republic of Germany
*Institut für Plasmaforschung der Universität Stuttgart, D-7000 Stuttgart 80, Federal Republic of Germany
**Guest from: C.I.E.M.A.T., E-28040 Madrid, Spain

Before starting plasma experiments in the new modular stellarator W VII-AS the magnetic surfaces have been studied in detail. W VII-AS has small shear, and by means of a superimposed toroidal field the rotational transform ι can be varied between about 0.25 and 0.70. Further details of the different coil systems, the expected shape of the vacuum magnetic surfaces etc. can be found in Ref. [1]. Two different methods have been applied to map the vacuum magnetic surfaces. Both methods use a directed electron beam source that can be positioned on an arbitrary magnetic surface in the poloidal cross section. At magnetic fields $B_o > 0.2$ T and electron energies < 150 eV used in the experiments single electrons emitted parallel to the magnetic field follow almost exactly the magnetic field lines.

The first or standard technique uses a capacitive point probe which is scanned across the poloidal cross section to detect the positions of the electron beam transits [2]. The electron gun is pulsed in this case so that the number of toroidal revolutions can be derived from a time-of-flight measurement. In this way the rotational transform can be calculated from the definition $\iota = (n + \Delta n)/m$ where n and m are the numbers of the poloidal and toroidal transits, respectively. The deviation Δn from a rational value $\iota = n/m$ can be determined rather accurately for $\Delta n << 1$ by comparing the measured transit positions with the prediction from a field line tracing code.

Fig. 6 shows an example of a measured $\iota(\bar{r})$ profile. The average radius $\bar{r}$ of the cross section of the magnetic surface is used as a radial magnetic field coordinate. The measured ι-values are compared with values calculated from two versions of the W VII-AS field line tracing code. The first one (Code, old) is the original version of this code used to design the W VII-AS modular field (MF) coils [1]. It predicts ι-values which are typically only 1.5 % smaller than the actual values. By decreasing the MF-coil radius by about 1 mm (compared to an average coil radius of about 50 cm) the agreement can still be improved (Code, new).

A much faster detection of the electron beam is achieved with the second method. It uses a fluorescent rod to record the positions of the electron beam transits and has been applied for the first time at the Stellarator WEGA at IPF, University of Stuttgart [3]. The rod coated with a fluorescent powder (ZnO_2 : Zn) emits light usually at both intersection points with the magnetic surface under consideration when it is struck by a

continuous electron beam. To gain a complete surface picture the rod has to be swept over a poloidal cross section. Recording was done with a CCD TV-camera together with an image processing system which adds together at first the individual light points to a complete surface picture and then also several surfaces with different radii $\bar{r}$ of a given magnetic field configuration. With this technique up to a few hundred toroidal transits can be detected with a spatial resolution of a few mm. Therefore, it is suited to investigate magnetic surface structures up to rather tiny details.

Sometimes also toroidal transit numbers can be deduced from the fluorescent rod pictures, especially in cases with small shear and when at least one surface with a rational ι-value happened to be found resulting in a discrete number of light points. Such an example is shown in Fig. 5, and the ι-values calculated from these surface pictures have also been included in Fig. 6.

In addition, the fluorescent rod pictures can be used to compare the measured shape and spatial position of magnetic surfaces to numerical predictions. Examples for a magnetic surface with an extreme triangular and an extreme elliptical shape [1] are given in Figs. 1 to 4. Again, very good agreement is found. Only in the case of Figs. 3 and 4 a systematic radial shift of < 1 cm can be seen which seems to be larger than the experimental error.

Summarizing the results of all the surface mapping experiments we can state that it has been demonstrated in the Stellarator W VII-AS that it is possible to produce excellent magnetic surfaces in good agreement with the numerical predictions by means of modular field coils [1]. Fig. 5 shows an example typical for the situation at low ι-values where closed magnetic surfaces extend even beyond the limiter ($\bar{r} \lesssim 18.5$ cm). At high ι-values the last closed magnetic surface is given by a magnetic separatrix (Fig. 8). This separatrix is usually determined by one of the 5/m resonances which are a consequence of the five toroidal field periods and the pentagonal shape of the magnetic axis [1]. An example of a higher order 5/m resonance with m = 11 is presented in Fig. 7. Imperfections e.g. in the coil shapes and/or alignment which are not included in the code lead to additional perturbation fields. They produce large magnetic islands especially at major resonances like ι = 1/2 and 1/3, but smaller islands have also been found at higher order resonances. An example is shown in Figs. 1 and 3 where close to the boundary the resonance ι = 2/5 results in islands which are not predicted by the field line tracing code (Figs. 2 and 4).

REFERENCES

[1] Kisslinger, J., Rau, F., Wobig, H., in Fusion Technology (Proc. 12th Symp. Jülich, 1982), Pergamon, Oxford (1983) 1051

[2] Sinclair, R.M., Hosea, J.C., Sheffield, G.V., Rev. Sci. Instrum. 41 (1970) 1552

[3] Hailer, H., Massig, J., et al., in Controlled Fusion and Plasma Physics (Proc. 14th Eur. Conf. Madrid, 1987), Vol. 1, European Physical Society (1987), 423

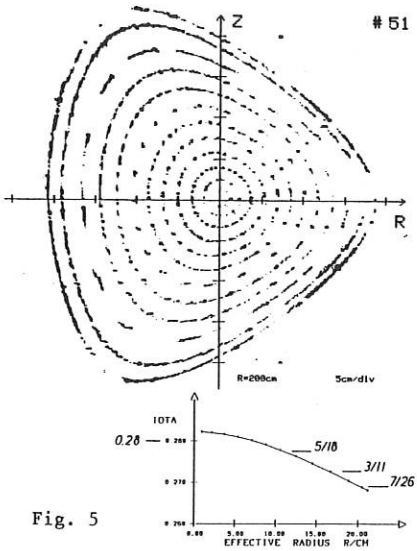

Fig. 5

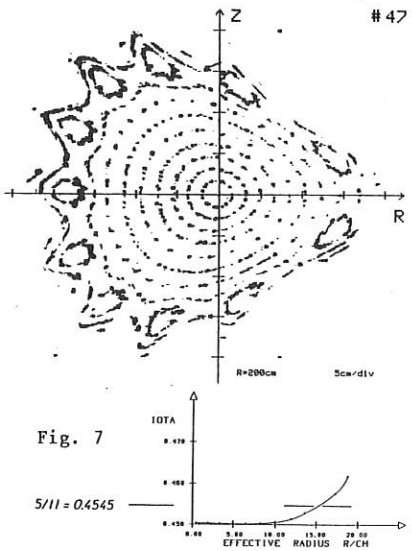

Fig. 7

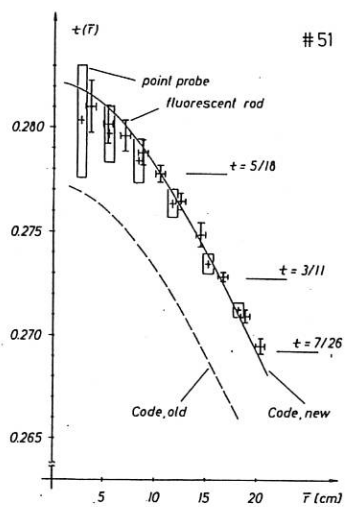

Fig. 6

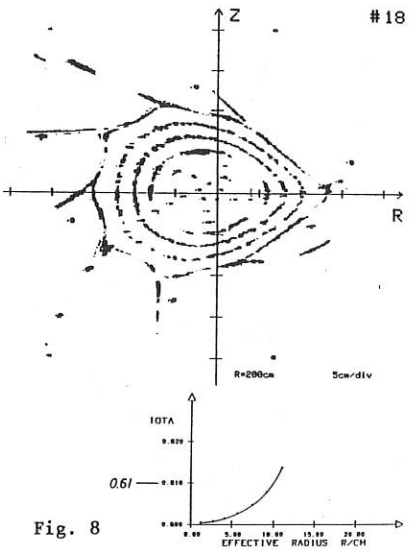

Fig. 8

SOURCES OF TOROIDAL CURRENT IN THE WENDELSTEIN VII-AS STELLARATOR

U. Gasparino, H. Maaßberg, W VII-AS Team*, NI Team**
Max-Planck Institut für Plasmaphysik
Association EURATOM-IPP, D-8046 Garching, FRG

ECRH Group†
Institut für Plasmaforschung der Universität Stuttgart
D-7000 Stuttgart, FRG

INTRODUCTION - The nearly shearless modular stellarator Wendelstein VII-AS (major radius $R = 2\ m$, averaged minor radius $< a > = 0.2\ m$) started plasma operation in October '88. As in W VII-A, also in W VII-AS a strong correlation between the global confinement properties and the value of the rotational transform ι has been observed in "net-current-free" plasmas. Apart from the confinement degradation at values of ι corresponding to low order rational values, already observed in W VII-A, broader intervals of degraded confinement are also found at values of $\iota = \frac{5}{m}$ (m integer) where, due to the five field period structure of the machine, the vacuum field configuration presents natural magnetic islands /1/. In the first months of operation particular attention has been paid to the investigation of 2^{nd} harmonic Electron Cyclotron Resonance Heating (ECRH) in the ι-region $\frac{1}{2} \leq \iota \leq \frac{5}{9}$. The vacuum ι-profile can be affected by toroidal currents. At $B_0 \simeq 1.25\ T$ (2^{nd} harmonic heating) a current I_P causes a change $\Delta\iota_a \simeq 0.014 \cdot I_P(kA)$ at the boundary value ι_a or the rotational transform ($\Delta\iota_a \propto \frac{I_P}{B_0}$). For the ranges of B_0 and ι currently under examination, the maximum tolerable I_P for operation in the good confinement ι-interval is about $1\ kA$. Within neoclassical theory radial diffusion drives a net current ("bootstrap-current") peaked in the pressure gradient region. The existence of this current component is experimentally supported. Since the magnitude of this current is related to plasma energy, the existence of a critical current I_P can influence the maximum achievable energy. Operation at values of ι corresponding to good confinement properties during the whole duration of the discharge could require an external ι-profile control acting on the current profile itself and not merely obtained by having two channels of current of different sign at different radii. Due to the possibility of controlling the profiles of the absorbed power and of the driven current, electron cyclotron waves are a natural candidate for current profile control. The strong dependence of global confinement properties on the ι-profile puts a particular interest in the investigation of the toroidal current sources. Furthermore, the "net-current-free" regime of operation of most Stellarator-devices gives the opportunity of observing and studying non inductive currents without the presence of an "obscuring" Ohmic current. The results of the analysis of the toroidal current in W VII-A /2/ are reconfirmed.

AUXILIARY HEATING SOURCES - Three different auxiliary heating systems will be used in W VII-AS: Neutral Beams Injection ($H^0, 1.5\ MW$, tangential injection) Electron Cyclotron Resonance Heating ($70\ GHz, 1.0\ MW$), and Ion Cyclotron Resonance Heating

* E. Anabitarte, S. Besshou, R. Brakel, R. Burhenn, G. Cattanei, A. Dodhy, D. Dorst, A. Elsner, K. Engelhardt, V. Erckmann, D. Evans, U. Gasparino, G. Grieger, P. Grigull, H. Hacker, H.J. Hartfuß, H. Jäckel, R. Jaenicke, S. Jiang, J. Junker, M. Kick, H. Kroiss, G. Kühner, I. Lakicevic, H. Maaßberg, C. Mahn, W. Ohlendorf, F. Rau, H. Renner, H. Ringler, J. Saffert, J. Sanchez, J. Sapper, F. Sardei, M. Tutter, A. Weller, H. Wobig, E. Würsching, M. Zippe

** K. Freudenberger, F.P. Penningsfeld, W. Ott, E. Speth

† W. Kasparek, G.A. Müller, P.G. Schüller, M. Thumm, R. Wienecke

1.0 MW). So far, the neutral beam lines have only been tested, while ECRH has routinely been used (up to three gyrotrons). During the neutral beam lines testing discharges (unbalanced injection) some beam induced current has been observed. The W VII-AS ECRH system consists of four 200 kW , 70 GHz , 3 s pulse-length gyrotrons, highly oversized circular waveguide transmission lines and quasi-optical wave launch antenna. Before reaching the plasma the Gaussian beam is reflected by focusing movable mirrors. After reflection a microwave beam of parallel plane phase-fronts (bringing to a lower beam divergence in a refractive plasma) with an half width radius $\simeq$ 1.5 cm is obtained. The plasma column is not axisymmetric with respect to the injection plane also for exactly perpendicular injection the toroidal angle of the ray will be affected, in a finite density plasma, by refractive effects. The mirrors can be tilted in both toroidal and poloidal direction, so that the sign and the magnitude of the toroidal angle of injection, as well as the vertical position at which the beam reaches the resonant layer, can be choosen. After a description of the theoretical model, results obtained in a single shot analysis and by scanning the toroidal ECRH injection angle will be presented.

THEORETICAL MODEL - Within neoclassical theory, electron transport is related to the deviation of the electron distribution function from the Maxwellian, a theoretically consistent description of transport (including the influence of auxiliary heating) would require the solution of the related Fokker-Planck equation in full phase space. This is not possible at present time. With respect to the toroidal current the problem can be simplified if the bootstrap current and the auxiliary heating driven current are described as independent processes. Through the comparison of a set of discharges it will be also experimentally possible to distinguish between the two sources (while on a single shot data analysis only the total contribution can be measured).
Neoclassical transport in the non-axisymmetrical geometry of W VII-AS has been investigated by means of the DKES-code /3/. The induced bootstrap current as well as the radial transport has been obtained as a function of the local plasma parameters for several magnetic surfaces.
The Electron Cyclotron Current Drive efficiency is estimated by means of a Hamiltonian 3-D ray tracing code based on the cold plasma dispersion relation and an absorption coefficient for general angle of propagation (relativistic Doppler shifted resonance relation) based on a Maxwellian distribution function. The self-adjoint approach is used. It is to be noticed that the angle of injection experimentally determined by the orientation of the reflecting mirror, is usually slightly different from the angle formed by the rays and the magnetic field at the resonant layer. This last angle is the physically important one and can only be theoretically evaluated by determining the ray trajectories under the hypothesis of geometrical optics of the ray tracing. This causes an uncertainty in the evaluation of the current drive efficiency for small angles of injection, where the dependence of the efficiency on the angle is very strong. With the increase of the injection angle this uncertainty becomes negligible. Quasi-linear and trapped particle effects are outside the present description. Heating of electrons trapped in the field ripple of the 3-D magnetic field topology of W VII-AS /3/ and quasi-linear effects can contribute to a degradation of the current drive efficiency. The linear model used in the ray-tracing is expected to give an upper limit for current drive efficiency.

FREE CURRENT, SINGLE SHOT ANALYSIS - In some set of discharges the current was left free to evolve, no loop voltage being externally applied. Under stationary condition the loop voltage (V_{loop}) would be zero and the total driven current value can be directly measured removing the uncertainty coming from the evaluation of the plasma conductivity (strongly dependent on temperature profile and Z_{eff}) generally required to determine the current I_P from the measured V_{loop}. In the series #906 $\div$ 923 two gyrotrons were applied (X-mode 2^{nd} harmonic, total injected power $P_{inj} \simeq 350$ kW). The microwave radiation was

launched nearly perpendicularly to the magnetic field, this should minimize its contribution to the total current (see next paragraph). During the second gyrotron pulse (200 ms) the toroidal current saturated at a value $I_P = +1.5\ kA$ in the resistive time scale $\frac{L}{R} \simeq 100 \div 150\ ms$. This value is of the order of the electron bootstrap current $I_B = +1.4 \div 0.95\ kA$ (for $Z_{eff} = 2 \div 4$, respectively) theoretically calculated using the measured Thomson profiles (central density $n_{e,0} = 1.9 \cdot 10^{19}\ m^{-3}$, central temperature $T_{e,0} = 0.8\ keV$). The ion bootstrap current (ion temperature $T_{i,0} \simeq 0.2\ keV$) and ECRH driven current (ray-tracing calculation evaluates total absorption with an efficiency of $\eta = +1\ A/kW$, see next paragraph) are also expected to give a smaller positive contribution to the measured current.

SCAN IN THE ECRH ANGLE OF INJECTION - Two gyrotrons (X-mode 2^{nd}-harmonic, $P_{inj} = 180\ kW$ each) were used in a set of discharges dedicated to the investigation of electron cyclotron current drive. The first gyrotron (with an angle of injection nearly perpendicular, with respect to the external magnetic field) produced and mantained a target plasma over a pulse length of 500 ms. The second gyrotron with a pulse length of 150 ms, long enough to reach a second stationary state, was switched on $\simeq$ 190 ms later. The toroidal angle of injection of this second gyrotron was then scanned from a value corresponding to nearly perpendicular propagation to an angle nearly 40° from the perpendicular. To have similar plasma conditions during the angle scan the boundary value ι_a was fixed by a feed-back current control (during the scan the net current is kept under 50 A). Line density ($\simeq 4 \cdot 10^{18}\ m^{-2}$) is nearly stationary during the whole plasma discharge and highly reproducible from shot to shot. The diamagnetic energy W_P increases during the second pulse from $1.1 \pm 0.1\ kJ$ to $1.3 \pm 0.1\ kJ$ no correlation with $k_{\|}$ being noticeable. The measured loop voltage is clearly correlated with the angle of injection (see Fig. 1). This correlation is pointed out in Fig 2 where the loop voltage at the time $t = 300\ ms$ is reported as a function of the angle of injection (at the reflecting mirror) after having redefined as zero the V_{loop} observed during the shot with minimal $k_{\|}$. The behaviour of the observed loop voltage with the change of the injection angle is in very good agreement with the behaviour of the current drive efficiency evaluated theoretically by means of the ray tracing code (Fig. 3). The fact that the loop voltage remains clearly negative, also when the injection angle of the second gyrotron corresponds to optimal current drive efficiency, is an indirect proof of the existence of a further predominant positive current source. This component is theoretically identified with bootstrap current. Due to the observed very small dependence of plasma energy and density on the injection angle of the second gyrotron, the loop voltage relative to the boostrap current (and to the current driven by the first gyrotron, whose injection angle remain fixed) will be nearly independent on the $k_{\|}$ of the second gyrotron and would be responsible of a ΔV_{loop} contribution nearly constant for all the shots of the $k_{\|}$-scan. The different behaviour of V_{loop} at the change of the injection angle can be in this way brought back to a direct current drive of the second gyrotron. For a quantitative comparison with theoretical predictions the equivalent current must be determined from the observed ΔV_{loop}. Thomson profiles are missing for this series. A temperature profile with a central temperature $T_{e,0} \simeq 1.2\ keV$, supported by ECE and X-ray signals and in agreement with the observed diamagnetic energy is assumed. The density dependence of the result is much weaker than the temperature dependence and a density profile with central density of $n_{e,0} \simeq 1.4 \cdot 10^{19} m^{-3}$ reproducing the observed line density, is assumed. With these profiles the ray tracing evaluates strong absorption for injected X-mode polarized waves, but passing from perpendicular to oblique injection the absorbtion coefficient as well as the percentage of the injected X-mode polarized wave slightly decreases (10% effect). The maximal current drive efficiency is $\eta_{max} = -23\ A/kW$ (corresponding to an injection angle $\simeq 15°$), as reported in the ordinate of Fig. 3. A quantitative agreement with the observed loop voltage would require, for the second gyrotron, an absorbed power $P_{abs} = 150 \div 180\ kW$ assuming $Z_{eff} = 3 \div 4$, respectively.

CONCLUSIONS - In the advanced stellarator Wendelstein VII-AS net toroidal currents (of the order of few kA) are experimentally observed even in absence of externally driven ohmic currents. These currents must be the sum of (at least) two components of different physical origins. A theoretical description based on neoclassical bootstrap current and electron cyclotron driven current explains the observed behaviour. In particular, the theoretically predicted dependence of the ECRH driven current on the angle of injection has been experimentally observed. Due to the experimental uncertainties (especially for the strong dependence on Z_{eff} of the quantitative results) the substantial quantitative agreement found between theory and experiment should be judged with some care. More definite results are expected to be achievable for the next future.

REFERENCES

/1/ H. Renner et. al., invited paper, this conference
/2/ U. Gasparino et. al., Plasma Phys. and Contr. Fusion, 30 (1988), 283
/3/ H. Maaßberg et. al., this conference

Fig. 1 V_{loop} *dependence on the angle of injection of the second gyrotron:*
a) $\rightarrow 2°$
b) $\rightarrow 4.9°$
c) $\rightarrow 9.7°$
d) $\rightarrow 13.9°$
e) $\rightarrow 18.2°$
f) $\rightarrow 22.5°$
g) $\rightarrow 26.8°$
h) $\rightarrow 31.2°$
i) $\rightarrow 36.2°$
j) $\rightarrow 40.1°$

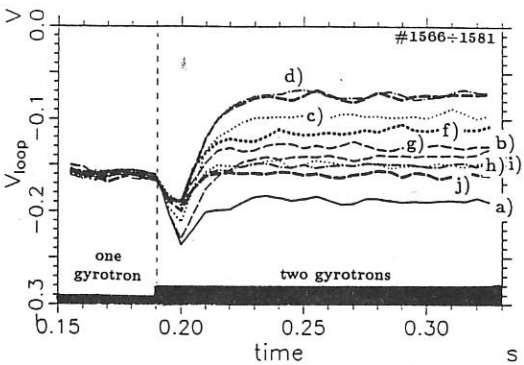

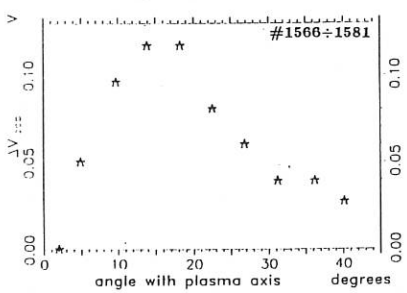

Fig. 2 Same as Fig. 1, defining as $V_{loop} = 0$ *the loop voltage relative to the smaller angle of injection.*

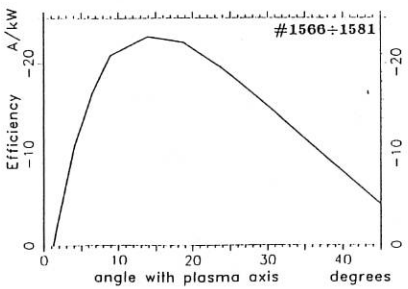

Fig. 3 ECRH current drive efficiency evaluated from the ray tracing code. To be compared with Fig. 2.

NEOCLASSICAL TRANSPORT IN THE W VII-AS STELLARATOR

H.Maassberg, U. Gasparino, G. Kühner, H. Ringler
W VII-AS Team* and NI Team**
Max-Planck Institut für Plasmaphysik
Association EURATOM-IPP, D-8046 Garching, FRG
ECRH Group†
Institut für Plasmaforschung der Universität Stuttgart
D-7000 Stuttgart, FRG

Abstract

For the rather complex magnetic field topology of W VII-AS stellarator, the full neoclassical transport matrix with radial electric field included in both the plateau and long mean free path regime is calculated using the DKES code. The toroidal resonance for larger radial electric fields is found to be important for the ion transport coefficients with up to seven roots of the ambipolarity condition in the LMFP regime. Temperature and density profiles measured by Thomson scattering for the first ECF heated discharges (at 2^{nd} harmonic) are analysed, the electron heat conduction coefficient is estimated and compared with the neoclassical prediction.

Introduction

The new W VII-AS stellarator is characterized by a rather complex magnetic field topology /1/. The representation of magnetic field strength on flux surfaces, which determines the neoclassical transport properties, leads to a very large number of Fourier coefficients in magnetic flux coordinates. In Figure 1 the $|\mathbf{B}|$-contours for approximately half minor radius are plotted. The particles trapped in the absolute minimum, B_{min}, contribute significantly to the neoclassical transport in long mean free path (LMFP) regime, more than 20 Fourier coefficients in the $|\mathbf{B}|$-representation are necessary (e.g., with only 7 Fourier coefficients, the particle transport coefficient is decreased by a factor of about 2). Consequently, simple analytic estimates of the neoclassical transport coefficients are unqualified and a full numerical solution of the drift kinetic equation is used (DKES code /2/) to compute the full transport matrix.

After 2 months of plasma operation in the W VII-AS stellarator, the experimental database for analyzing the energy transport is only small. Up to now, electron density and temperature profiles from the Thomson scattering diagnostic are available for 2^{nd} harmonic ECF maintained discharges ($B_0 \approx 1.26$ T) with heating power up to 500 kW (3 gyrotrons) mainly at rotational transforms $\iota > 0.5$. For these conditions with moderate T_e, the electron collisionality is typically close to the plateau regime. In the LMFP-regime ($1/\nu$-regime), the neoclassical transport is expected to determine the experimental energy balance analogous as in HELIOTRON-E (/3/). Modeling the energy source and loss terms with regard to the experimental conditions, the energy balance equation is used to fit the electron temperature profile yielding the experimental electron heat conduction coefficient.

Neoclassical Transport Code

The DKES code (Drift Kinetic Equation Solver /2/) is based on the linearized monoenergetic drift kinetic equation in magnetic flux coordinates for each particle species with radial electric field included. As the poloidal component of the ∇B-drift is neglected, the solution depends only on the $|\mathbf{B}|$-Fourier spectrum independently for each magnetic surface. Typically, about 200 Fourier harmonics for both poloidal and toroidal angle and up to 150 Legendere polynomials in pitch angle are used to represent the neoclassical deviation of the distribution function from the Maxwellian. Especially in the LMFP with moderate radial electric fields, this large number of basis functions is necessary for the estimation of the non-diagonal term of the monoenergetic Onsager transport matrix. For each magnetic surface, the 3 monoenergetic transport coefficients are computed for varying collisionality and radial electric field (more than 200 values with up to 10 min. CPU on the CRAY 1 for each run). On this grid of storaged monoenergetic transport coefficients, the energy convolution is performed based on bi-cubic interpolation resulting in

* ** † see paper of Gasparino, U. et al., this conference

the full transport matrix D_{ij} which is slightly different defined with respect to the Onsager form (but more practical for an experimental environment):

$$\Gamma = -n \cdot \{D_{11}(\frac{n'}{n} + \frac{q\Phi'}{T}) + D_{12}\frac{T'}{T} + D_{13}E_{\|}\}$$

$$Q = -nT \cdot \{D_{21}(\frac{n'}{n} + \frac{q\Phi'}{T}) + D_{22}\frac{T'}{T} + D_{23}E_{\|}\}$$

$$j_{\|} = -\{D_{31}(\frac{n'}{n} + \frac{q\Phi'}{T}) + D_{32}\frac{T'}{T} + D_{33}E_{\|}\}$$

where Γ is the particle flux, Q the heat conduction, $j_{\|}$ the toroidal net current density, $\Phi' = -E_r$ the radial electric field and $'$ denotes the radial derivative (flux coordinate). For a fixed magnetic configuration (defined by rotational transform, ι, vertical field, B_z, and pressure profile, $\beta(r)$) the monoenergetic transport coefficients are computed for different minor radii, cubic interpolation in r is applied in connection with the energy convolution algorithm. For larger values of radial electric field, high resolution is necessary close to the toroidal resonance, $E_r = \iota v r B_0/R$, strongly affecting the ion transport coefficients in both the plateau and the LMFP regime. Due to this toroidal resonance, several roots of the ambipolarity condition (up to 7 values for radial electric field) can exist in the LMFP regime. In Figure 2, the electron and ion transport coefficients versus E_r are shown with a 2nd maximum in the ion transport coefficients at the toroidal resonance. This result is contrary to the simple picture of radial electric field based on the Shaing-Houlberg transport model /4/ (only 2 stable and 1 instable root possible). In general, however, with the condition of ambipolarity, the radial electric field, particle and energy flux and the bootstrap current can be calculated for a given density and temperature profile. First calculations indicate, that the neoclassical radial electric field is negative in the plateau regime (typical for NBI heated discharges) and can become positive in the LMFP regime (ECF heated discharges). For an axisymmetric field, DKES computations were compared with Monte Carlo simulations /5/, nearly identical particle and energy transport coefficients were found. Furthermore, the bootstrap coefficient, D_{31}, was tested using the relation to particle transport /6/, reliable agreement was found.

The particle and energy transport coefficients in the plateau regime are comparable to those of an equivalent axisymmetric case showing some improvement due to the advanced stellarator concept. In the W VII-AS configuration, however, the strong localized minimum in $|\mathbf{B}|$ (see Fig. 1) leads to a rather large fraction of trapped particles contributing significantly to the transport. An additional B_z-field affects this fraction of trapped particles and their radial drift. Calculations show, that an additional B_z-field of $\pm$ 300 G changes the neoclassical particle and energy transport coefficients by a factor of 2; the bootstrap current coefficients, however, are found to be nearly unaffected by the B_z-field. The electron energy transport coefficient, D_{22} (called heat conduction coefficient χ in the next section), is typically by a factor of 3 larger than the coefficient D_{21}. Furthermore, the density profiles are broader than the electron temperature profile justifying the diffusive ansatz for the heat conduction coefficient fit.

1st Estimates of Electron Heat Conduction

Electron density and temperature profiles are measured by the Thomson scattering diagnostic in a series of discharges similar as in the old W VII-A stellarator (a new single shot system is under construction). The quality and reliability of these profiles depends mainly on accurate control of all machine parameters (e.g. gas feed), but also on the stability of the discharges, in some cases, current control by a small loop voltage increases the reproducebility. Within a series, only discharges with nearly indentical values of line density and energy content are used. In future, also the ECE temperature measurements which are absolutely calibrated should be used to confirm the Thomson profile data. For estimating the electron heat conduction on the basis of the energy balance equation, the local power source and loss terms must be known. For the low density ($n_e < 3 \cdot 10^{13}\ cm^{-3}$) discharges with 2^{nd} harmonic ECF heating at $B_0 \approx 1.26$ T in the first 2 months of operation, the radiation losses and the collisional power transfer to the ions are rather small: each of the order of less than 35 kW. The experimental estimation of absorbed ECF power is deduced from ECE data after a gyrotron is switched off: the local power absorption is given by the transient decay of electron temperature. However, at 2^{nd} harmonic heating, only 7 radial ECE channels are available and the separation between ECF power deposition and the range with heat transport is not very reliable. Simulations of the switch off phase indicate, that the power deposition

range is limited to the inner ECE channels. However, the estimation of the total absorbed power (and ECF heating efficiency) is rather inaccurate. Consequently, we assume about 75% of gyrotron power being absorbed, this is consistent with single pass ray tracing calculations (nearly full absorption) and the ECE data. The deposition profile is mainly determined by the broadness (half witdh diameter about 3 cm), the distance of the ECF beam from the magnetic axis and the resonant magnetic field value: the power deposition profile is modeled by a shifted Gaussian (standard deviation $\sigma = 1.5$ cm) centered at at r_{abs} depending on the value of magnetic field on axis. The fit of the heat conduction coefficient based on energy balance depends only linear on the value of total absorbed power leading to an uncertainty of less than a factor of 2 for $r > r_{abs}$. The power loss terms are estimated by an average oxygen radiation model renormalized to the bolometry data and by the usual collisional power transfer to the plasma ions. Doing this, the power source model depends only slightly on the value of Z_{eff} which is rather unknown for this type of discharges. With this source model, the electron energy balance equation is integrated with the ansatz of a power series in normalized minor radius for the logarithm of the heat conduction coefficient, the coefficients of the power series are calculated by weighted least square fit to the electron temperature profile. For the electron density representation, a standard least square best fit is used.

The profiles (shots 185-206) in Figure 3 are the 1st Thomson series of W VII-AS stellarator measured at the 1st day of operation! The H_2 discharge heated with $P_{abs} \simeq 130$ kW with 1 gyrotron was not stable: the central density increases up to the cut-off limit. The time of the Thomson profile, however, was close to the maximum of the energy content. In this series, the ECF power was deposited in the center, at $\iota \simeq 0.53$ the outer part of the plasma radius was destroyed by natural islands related to $\iota = 5/9$. The profiles (He discarges in shots 906-923) shown in Figure 4 are more typical for the first two months: much broader temperature and density profiles, the ECF power was absorbed ($P_{abs} \approx 300$ kW with 2 gyrotrons) more outside. For both cases, the least square best fit of χ has an accuracy of about 50% within the gradient region of electron temperature mainly determined by the scattering of the Thomson data and the uncertainty of absorbed power. In the central part as well as at outer radii, the error is expected to be much larger. However, the best fit suppresses strong local changes in electron heat conduction and in the central part, due to the relative large experimental error bars of Fig. 4 which are used as weighting functions, χ^{ex} is mainly influenced by larger radii. For comparison, the neoclassical coefficients χ^{DKES} and χ^{H-H} based on the Hinton-Hazeltine model /7/ and the old W VII-A anomalous coefficient χ^{an} /8/ are also shown. In all analyzed profiles, χ^{ex} increases strongly at outer radii, but for some profiles also in the central part for very flat T_e profiles (tendency for even hollow $T_e(r)$). For most of the analyzed profiles, the agreement of χ^{ex} and χ^{an} is much better at outer radii than in the example of Fig. 4, but the ratio of χ^{ex} to χ^{DKES} is much larger than in the central part of Fig. 3. Furthermore, for the series in Fig. 4 a neoclassical bootstrap current of about 1 kA is expected from DKES code (for $Z_{eff} \simeq 3$), I_b is in reasonable agreement /9/ with the measured toroidal current.

Conclusions

The neoclassical transport in W VII-AS with the complex field structure is described using the DKES code, the full transport matrix is computed with radial electric fields included. For the discharges of the 1st two months of plasma operation with 2^{nd} harmonic ECF heating, the experimental values of the electron heat conduction coefficient are governed by anomalous transport. In this regime of plasma parameters, the heat conduction is larger than the neoclassical prediction.

References

/1/ J. Kisslinger, F. Rau and H. Wobig, Fusion Tech. (Proc. 12th Symp. 1982), Pergamon (1983), 1051
/2/ S.P. Hirshman et al., Phys. Fluids **29** (1986), 2951
/3/ T. Obiki et al., 12th Int. Conf. on Plasma Phys. and Contr. Nucl. Fus. (1988), IAEA-CN-50/C-1-1
/4/ K.C. Shaing et al., Plasma Phys. and Contr. Nucl. Fusion Res., **2**, IAEA Vienna (1984), 189
/5/ W. Lotz and J. Nührenberg, Phys. Fluids, **31** (1988), 2984
/6/ H. Wobig, Report **IPP 2/297** (1988)
/7/ F.L. Hinton and W.N.G. Hazeltine, Rev. Mod. Phys., **48** (1976), 239
/8/ G. Grieger et al., Plasma Phys. and Contr. Fusion, **28** No. 1A (1986), 43
/9/ U. Gasparino et al., this conference

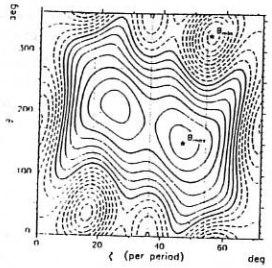

Fig. 1: $|\mathbf{B}|$ contours on magnetic flux surface: $r \simeq 10$ cm, $\iota \simeq 0.51$ (for vacuum field).

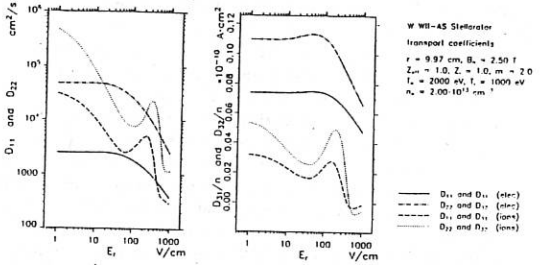

Fig. 2: Neoclassical Transport coefficients (DKES code) D_{11} and D_{22} (on the left) and D_{31} and D_{32} (on the right) versus radial electric field, E_r.

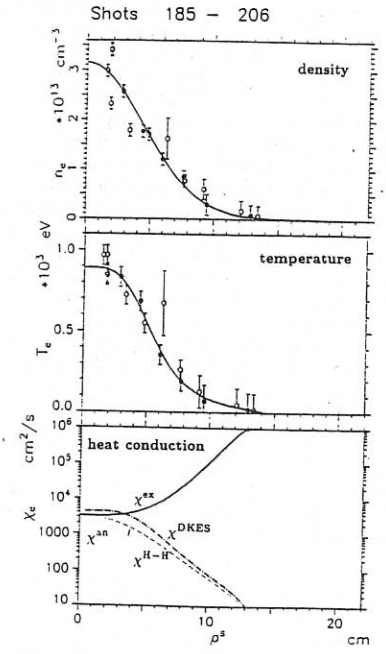

Fig. 3: $n_e(r)$ and $T_e(r)$ by Thomson scattering diagnostic and fit of electron heat conduction, $\chi(r)$, for H_2 discharge with $P_{abs} \simeq 130$ kW (1 gyrotron) at $r_{abs} \simeq 3$ cm ($B_0 \simeq 1.274$ T with resonance on axis).

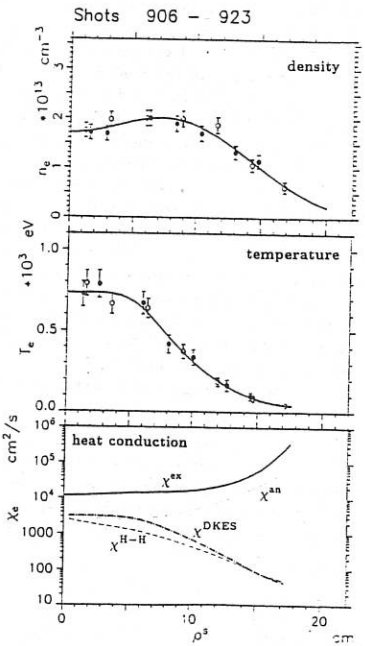

Fig. 4: $n_e(r)$ and $T_e(r)$ by Thomson scattering diagnostic and fit of electron heat conduction, $\chi(r)$, for He discharge with $P_{abs} \simeq 300$ kW (2 gyrotron) at $r_{abs} \simeq 5.5$ cm ($B_0 \simeq 1.256$ T with resonance shifted inside).

NEUTRAL GAS TRANSPORT AND PARTICLE RECYCLING IN THE W VII-AS STELLARATOR

F. Sardei, H. Ringler, A. Dodhy, G. Kühner,
W VII-AS Team*
Max-Planck-Institut für Plasmaphysik
Association EURATOM-IPP, D-8046 Garching, FRG
ECRH Group**
Institut für Plasmaforschung der Universität Stuttgart
D-7000 Stuttgart, FRG

Introduction

In the W VII-AS stellarator plasma particle and power balance will be strongly affected by the distribution of the ion sources and charge exchange losses (similar as in W VII-A [1]), which are poorly known from experimental data. Furthermore, the control of the plasma density critically depends on the recycling processes in the plasma boundary region and at the limiters and walls.

Results for a model plasma

Before the W VII-AS operation was started, model plasmas were used to study the neutral gas transport behaviour with the 3D DEGAS code [2]. For a neutral source due to limiter recycling a simulation was performed to investigate to what extent the neutral density distribution is affected by the asymmetries of the flux surfaces and wall structures. The T_e, T_i and n_e profiles were taken from model calculations with the TEMPL plasma transport code ($T_e(0)$ = 1.9 keV, $T_i(0)$ = 500 eV, $n_e(0) = 2 \times 10^{13}$ cm^{-3} for an ECF input power of 720 kW) [3].

The typical cross section of the W VII-AS toroidal sector modelled for the neutral transport calculations is shown in Fig. 1. The limiter, the bulge for the NBI ports and the geometry of the magnetic surfaces (see Fig. 1) introduce asymmetries in the torus, which directly affect the neutral density distribution. Figure 2 shows the radial profiles of the neutral density at the poloidal angles $\theta = 0^o$, 90^o, 180^o, 270^o. As shown by the $\theta = 90^o$ profile, the neutral density has a maximum at the limiter face and drops by 2 orders of magnitude to the plasma centre. In the opposite direction with respect to the limiter, $\theta = 270^o$, the density is significantly lower, reaching a maximum of 1/3 of the limiter value. Along the horizontal chord, $\theta = 0^o$ and $\theta = 180^o$, the neutral density profiles are fairly symmetric up to a distance of ≈12 cm from the magnetic axis. The relatively high gradients of these profiles reflect the smaller plasma radius along this chord, associated with the asymmetry of the magnetic surfaces (see Fig. 1). Due to this asymmetry, the central neutral density is mainly determined by the neutrals penetrating the plasma in the horizontal direction. At $r > 15$ cm, well inside the scrape-off region, the profiles diverge from each other, reflecting the asymmetry introduced by the bulge. Within the bulge, the neutral density is fairly constant and amounts to roughly 1/4 of the limiter value.

In the following, results from neutral transport simulations are discussed for a typical deuterium discharge from the first months of W VII-AS operation.

Discharge parameters and Hα-monitoring system

The analysis is based on a ECF (70 GHz) heated deuterium discharge at the 2nd harmonic, with 1.25 T at the plasma centre and the external rotational transform ι being ≈ 0.53 at the plasma edge. Electron density and temperature profiles, measured by Thomson scattering, were available at 200 ms (Fig. 3). Stationary plasma conditions were maintained by one gyrotron heating with 150 kW input power and by external gas input linked to a feedback control of the plasma density. A plasma current induced either by ECF and/or by plasma pressure [4] was controlled and kept below ≈ 500 A by the OH-transformer. The measured T_e, n_e profiles covered a plasma radius extending up to the separatrix, which was located at r_{eff} = 17.5 cm, about 2.5 cm outside the last flux surface not intersected by the limiter. A clear-cut separation of the plasma from the scrape-off region is not possible for this particular discharge type with edge ι values close to the 5/9 resonance, because of the strong poloidal deformation of the flux surfaces crossing the limiter. A more effective limiting of the plasma is provided in this case by the separatrix, outside of which the open field lines lead to a flattening of the temperature and density profiles.

An absolutely calibrated Hα monitoring system [5] installed at W VII-AS yields information about particle recycling at both limiters (two toroidal positions for the bottom and one for the top limiter) and at two "triangular" magnetic surface cross sections close to and far from a gas feed inlet, respectively.

Results for first W VII-AS discharges

The DEGAS code simulation at the "triangular" cross section near the gas inlet was used to find estimates for T_e, n_e between separatrix and wall, which were consistent with both the measured gas input rate and Hα signal close to the gas inlet. These estimates were then used in the limiter and wall recycling simulations. The time histories of the measured Hα-signals from the limiters and the "triangular" cross sections are shown in Fig. 4a,b. The neutral fluxes and densities were estimated by scaling the calculated Hα emission rates to agree with the measured ones.

The calculated total refuelling rate of the plasma inside the separatrix due to limiter and wall recycling and to external gas feed amounts to 2.5 x 10^{20} ions/s. 83 % of this ionization source are provided by the limiter, 13 % by the wall and 4 % by the gas puffing. This corresponds to a global recycling coefficient of 0.96. From the calculated refuelling rates and a plasma ion content of 8.9 x 10^{18} particles inside the separatrix, as resulting from the measured electron densities (Fig. 3) and an assumed z_{eff} of 3, a global particle confinement time of 36 ms is estimated for this time of the discharge. The plasma refuelling efficiencies as fractions of the neutrals ionizing inside the separatrix are 0.65 for the limiter, 0.44 for the wall and 0.29 for the external gas source. The small values for the wall and gas puff sources are directly

related to the large volume of the boundary region between separatrix and wall (more than twice the volume of the confined plasma). On the other hand, this has the advantage of improving the decoupling between the plasma and the wall, thus reducing the wall loading by high energetic charge exchange neutrals.

The given refuelling rates and efficiencies from wall recycling and gas puffing may have a considerable error margin due to their sensitivity to the unknown plasma density and temperature in the boundary region. Furthermore, the flux of ions incident to the wall at the position of the Hα viewing line may not represent a good average of the ion fluxes over the entire torus wall. However, these uncertainties do not strongly affect the global recycling coefficient and τ_p, since recycling from the limiter is the main refuelling mechanism to the bulk plasma.

Experimental indication of a recycling coefficient close to one for the discharge type discussed here is given after a second gyrotron is switched on for about 100 ms (see Fig. 4b). During that time a constant plasma density is maintained without any external gas feed and the Hα signals at the triangular cross sections close to and far from the gas inlet coincide (see Fig. 4b). The amplitude of all signals (Figs. 4a,b) is considerably higher than before the 2nd gyrotron was added. Considering that at stationary conditions the externally supplied neutral flux equals the fluxes absorbed by wall and limiters and that the absorbed fluxes linearly scale with the recycling fluxes, gas puffing proves to be a very efficient density control mechanism for high recycling ECF discharges.

For the same discharge, the calculated average neutral densities at the limiters and wall due to the recycling sources are 2.9×10^9 cm^{-3} and 3.9×10^8 cm^{-3}, respectively. The total ion power loss due to charge exchange with all neutrals is 3.1 kW. The total electron power loss due to ionization, excitation and dissociation is 2.0 kW.

REFERENCES

[1] H. Ringler et al., Plasma Phys. and Contr. Nucl. Fusion, IAEA-CN-47/D-V-1 (1987), Vol. 2, 603
[2] D.B. Heifetz et al., J. Comput. Phys. 46 (1982), 309
[3] H. Wobig, Notes on the W VII-A and W VII-AS Stellarators, Ringberg (1986), Internal Report
[4] U. Gasparino et al., this conference
[5] T. Uckan, ORNL/TM-10698.

*,**: see U. Gasparino et al., this conference

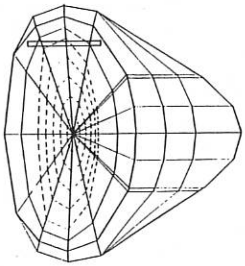

Fig. 1: Vertical cross-section of the modelled W VII-AS torus at the position of the module connecting flanges, including the wall, the bulge for the NBI ports, the flux surfaces and one of the limiters.

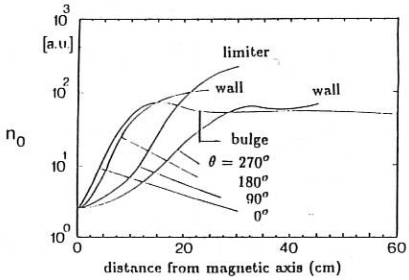

Fig. 2: Radial distributions of the neutral density at the poloidal angles $\theta = 0^o$, 90^o, 180^o, 270^o in the vertical cross-section shown in Fig. 1.

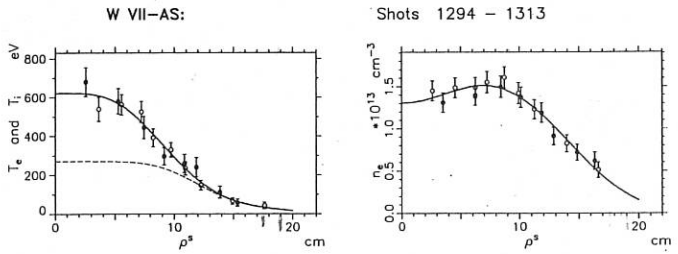

Fig. 3: Radial Te and n_e profiles vs. effective radius at $\Delta t = 0.2$ s from Thomson scattering. Full circles represent measurements on lh side of the profile.

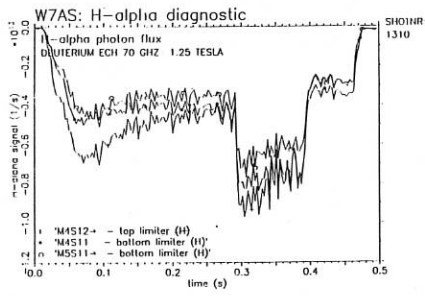

Fig. 4a: Hα-photon fluxes vs. time from ECE discharge looking at top and bottom limiter, plasma cross-section elliptical (a second gyrotron was switched on between 0.3 and 0.4 s).

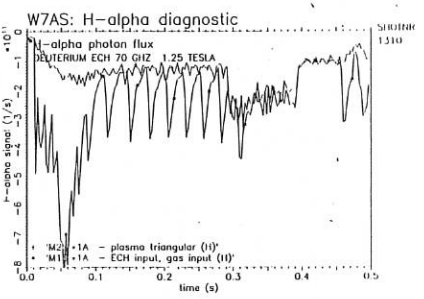

Fig. 4b: Hα-photon fluxes vs time at two triangular plasma cross-sections, with and without gas inlet. The large spikes reflect the pulse sequence from the gas inlet.

INNER SIDE ELECTRON CYCLOTRON EMISSION(ECE)MEASUREMENTS DURING ELECTRON CYCLOTRON RESONANCE HEATING (ECRH) IN L-2 STELLARATOR

D.K.Akulina, A.N.Nakladov, O.I.Fedyanin, V.I.Chepizhko*
General Physical Institute, Moscow, USSR
* Gosstandart USSR, Khar'kov, USSR

INTRODUCTION

High-power electromagnetic waves radiated by gyrotron on the electron cyclotron(EC) frequency - f_{He} are successfuly used for electron heating up to thermonuclear temperature both in current and currentless plasma /1-5 /. In addition to electron heating some phenomena like a deformation of electron distribution function , an enhancement of trapped particles population, a variation of MHD activity were observed. These phenomena prevail in the low density plasma . When plasma density is higher then $\bar{n}_e > 10^{13}$ cm^{-3} a distribution function approachs to the Maxwellian one and the diagnostics which are responsible for electron temperature measurements are in good agreement. As for low-density experiments some unpleasant phenomenon, like decreasing of bulk heating efficiency, is observed / 3,5 /.

EXPERIMENTS ON L-2 STELLARATOR

The experiments at H= 1,35 tesla main toroidal field on axis with 37,5 GHz /200 kW / 10 ms gyrotron were carried out.For L-2 stellarator (R=100 cm, a=11,5 cm) after neutral gas breakdown the plasma density equal to $\bar{n}_e \leq 10^{13}$ cm^{-3} was produced and heated with ordinary wave polarization launch in equatorial plane from low-field side of magnetic field on the fundamental (n =1) harmonic frequency ($E \| H \perp k$). In the experiments up to 50 % of the power was absorbed and plasma was heated to 0,6-1 keV.The electron temperature was measured by several methods: laser Tomson scattering, visible spectroscopy,x-ray radiation and second cyclotron harmonic radiation (ECE) technique. Diamagnetic signals and their derivatives are simultaneously carried out.The ECE measurements were performed by superheterodyne receiver in 80-71 GHz band in the equatorial plane from the high - field magnetic side (see Fig.1). The diagnostic window was placed at the distance ~30 cm from the gyrotron one and it inner side location permits to observe ECE spectra without their deformation by bulk plasma absorption of relativistically shifted nonthermal radiation / 7,8,9 /.Because of strong stray signals from gyrotron in the vicinity of second harmonic the data in f=74-76 GHz were omitted.When ECE are

used to determine $T_e(r)$ one usually suppose that the plasma optical thickness is $\tau > 1$, electron distribution function is Maxwellian one and antenna pattern divergency is small ($\alpha < 5°$). The calculations earlier performed/6/ have shown that single path optical depth is equal to $\tau > 1$ in the L-2 stellarator within $\Delta r = \pm$ 6 cm at $T_e > 0,5$keV and $\bar{n}_e \sim 1.10^{13}$cm^{-3}. In the "black" body conditions ($\tau > 1$) there is the simple relation between ECE intensity - $I(\omega, r)$ and T_e:

$$I(\omega, r) = kT_e(r)\omega^2 / 1 - e^{-\tau(r)} / 8\pi^3 c^2$$

where k- is Bolzmann constant , c-is light velosity.
If the optical depth is $\tau < 1$ or an electron distribution function is not Maxwellian, then one uses T_r - radiation temperature as the measure of energy radiation. Fig.2 shows the oscillograms $I(\omega)$ made at different frequencies, the diamagnetic signal- W_e and plasma density - $\bar{n}_e$ vs time. The main feature of $I(\omega)$ curves is the similar behaviour vs time, but the absolute value of $I(\omega)$ is quite different. For example, the higher $T_r \sim$ 4-2keV for f=73and72GHz as compared with f=77-80 GHz ($T_r \sim$ 0,8-0,9 keV) was observed. The higher ECE is probably connected with presence superthermal electrons generated during ECRH at rather low $\bar{n}_e$ /7,11/. It is possible to estimate the energy of suprathermal electrons taking into consideration the relativistic shift of energy /8/. If one suppose that electrons were born at the resonance interaction at frequency f=37,5 GHz(the gyrotron frequency), then the enhanced radiation at f=73 GHz is formed by electrons with energy up to 7 keV. It is possible to do very rough estimation of the number of electrons /8/, which is about 1% of bulk plasma density, but in spite of small number they can play a role in HF power balance. The T_r dependence vs n_e is shown in Fig.3. Let us note that $I(\omega)^r$ vs $\bar{n}_e$ curve is a strongly dependent function of breakdown discharge conditions and therefore the data spread is large. Fig.4 shows time $T_{e,r}$ decay after the gyrotron switch off. One can see that the decay constant (τ_r) is equal to τ_r=1,1-1,5 ms for f=77-80 GHz (bulk plasma) and ~ 2 times less for f=73 GHz (nonthermal). Let us note that diamagnetic decay constant is equal to 2,5-3 ms and this discrepancy is now under consideration. The $I(\omega)$ evolution vs fed power is shown in Fig.5. It is seen that there is the time saturation of T_e and the shape of curves for f=77GHz and f=73 GHz is quite different. One can see rather sharp (like threshold) increasing of f=73 GHz signals.

The performed experiments results in the following remarks: 1. The asymetry of the spectrum can be related to a nonthermal electron component which is either partialy trapped or has shifted radiation frequency 2. All frequency sharp amplitude decays after the gyrotron switgh off enable us to conclude that HF energy deposition take place along the whole small plasma radius. 3. $I(\omega)$ vs HF power curves have time saturation and for f=73 GHz looks like threshold dependance.

Fig1
L-2 chamber cross - section and /H/=const lines view.

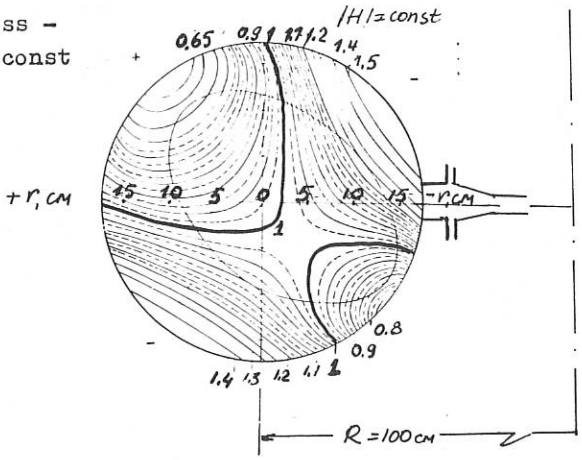

Fig.2
a) Intensities of ECE radiation on different frequencies vs time
Δ - laser data

b) Diamagnetic and plasma density signals vs time

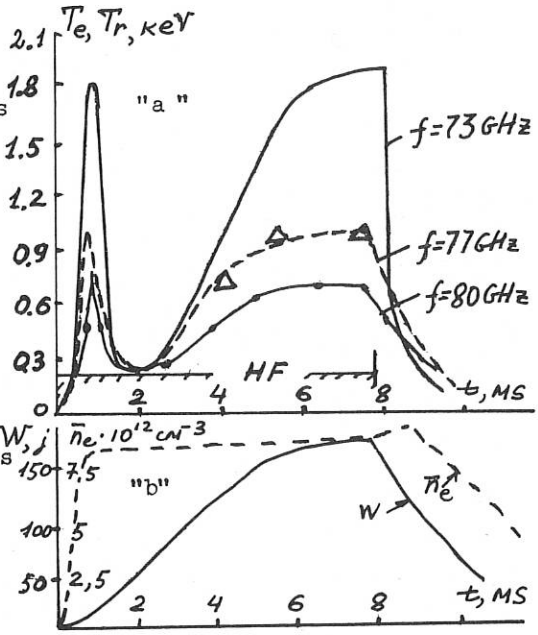

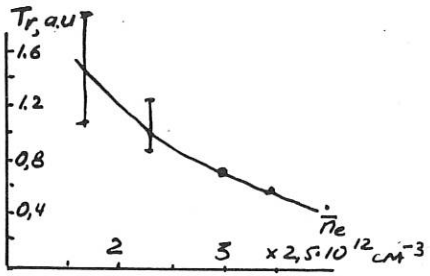

Fig 3 Temperature dependance vs plasma density.

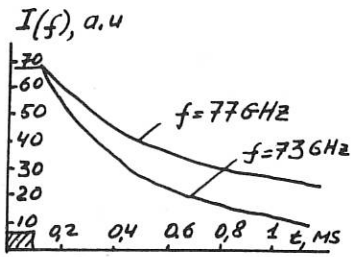

Fig 4 Decay curves for different frequencies

Fig 5
ECE intensity evolution vs fed power at
Δt= 4ms
Δ t= 6ms

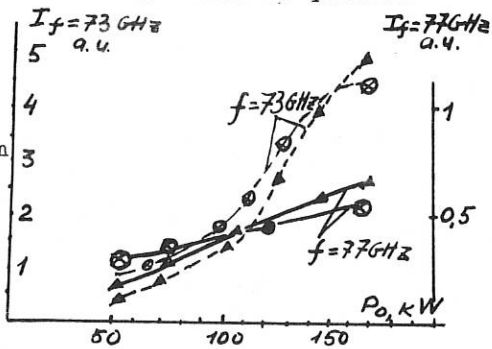

1. Alikaev V. et al. Proc.10th conf. on Plasma Physics and CTR,v.1,p.419,London,1984
2. Akulina D. et al.,Proc.15th European Conf. on CTR and Plasma Heating,v.1,p.447-451,Dubrovnik,1988
3. Erckmann H. and W-7A team Journ.of Plasma Physics and CTR v.28,n.9A,p.1277-1290,1986
4. Zushi H. et al., Preprint PPLK-R-15,Plasma Physics Lab. Kyoto Univ.,1985
5. Airoldi A. et al.,Report FP 86/13 Instituto di Fisica del Plasma,Milano,dec.1986
6. Akulina D.,Suvorov E. Proc. of Course and Workshop "Basic and advanced diagnostic techniques for Fusion Plasma" Varrena,V.1p.139-168,1986
7. O'Brien M.R.,Cox M. Start D.F.,Nuclear Fusion v.26,p.1625-1640,1986
8. C.Celata,D.Boyd, Nuclear Fusion 17(1977),735
9. A.Costley et al., J.Phys.Rev.Lett. 33,758,(1974) TFR Groupe, Report EUR-CEA FC 1091, March,1981
10. Lontano M.,et al., Nuovo Cimento v.6313,n.2,(1981).529
11. Hartfuss H. et al., Preprint IPP 2/292 Max-Planch Inst. fur Plasma Physik November,1987

POWER BALANCE STUDIES FOR RF HEATED PLASMA IN THE URAGAN-3 TORSATRON

V.L. Berezhnyi, M.P. Vasil'ev, V.S. Voitsenya,
E.D. Volkov, Ju.V. Gutarev, A.G. Dikij, G.V.Zelenin,
B.V. Kravchin, S.V. Kovalev, V.G. Konovalov,
V.I. Kononenko, V.D. Kotsubanov, G.G. Lesnyakov,
A.P. Litvinov, Ju.K. Mironov, N.I. Nazarov,
I.K. Nikol'sky, O.S. Pavlichenko, I.I. Patlay,
V .K. Pashnev, V.V. Pljusnin, N.F. Perepelkin,
A.I. Skibenko, A.S. Slavnyi, V.S. Taran, T.O.Thoryak,
S.I. Fedotov, I.P. Fomin, A.N. Shapoval, O.M. Shvets

Institute of Physics and Technology, Ukrainian
Academy of Sciences, Kharkov, USSR

Abstract

Power balance of RF heated currentless plasma in the Uragan-3 torsatron has been studied for low density quasistationary discharges (Q-discharges [1]). It was shown that the most part of RF power is absorbed and dissipated by a cold plasma mantle surrounding a hot plasma core. In the hot core energy losses are determined by electron heat conductivity and radiation.

1. Introduction

Studies of currentless plasma production and heating by RF waves in the $\omega \lesssim \omega_{ci}$ frequency range in the Uragan-3 torsatron resulted in a revelation of regime of quasistationary discharges with ion temperature up to 1,1 KeV and average beta up to 0,6% [1]. Highest ion temperature and plasma energy content realised at low electron density ($\bar{n}_e = (2\text{-}3)\cdot 10^{12}\,cm^{-3}$). The electron density increase resulted in the decrease of the ion temperature and energy content of plasma as well.

To understand the reason of this degradation of plasma energy it is necessary to analyse the power balance of RF plasma.

This report presents the results of the power balance studies in low density Q-discharges performed for the Uragan-3 torsatron before device shutdown in March 1988.

2. The experiment

The Uragan-3 torsatron has been operated with a confining field 4,4 KG. Hydrogen RF discharges were produced by one antenna which radiated the power of 0,2-0,3 MW at $\omega \simeq 0{,}8\cdot\omega_{ci}$.

Principal diagnostics were described in a paper [1]. In

this experiment electron density profiles were reconstructed from multichord interferometer data (λ = 8;2;1; 0,337 mm). The NPA with a horizontal line-of-sight scanning was used for the ion temperature profile studies. Electron temperature profiles were reconstructed from a singe-point Thomson scattering data (at the plasma axis), spectroscopic data ("carbon thermometer" at $r \approx 0.5 \cdot a$) and electric probe data (at the plasma edge). Hydrogen atom density profiles were determined from the H_β -line profiles. Radiation and charge exchange loss power P_{rad} was measured by a collimated pyroelectric detector. Total plasma energy content W_T was measured by a saddle - type magnetic coil.

3. The results and discussion

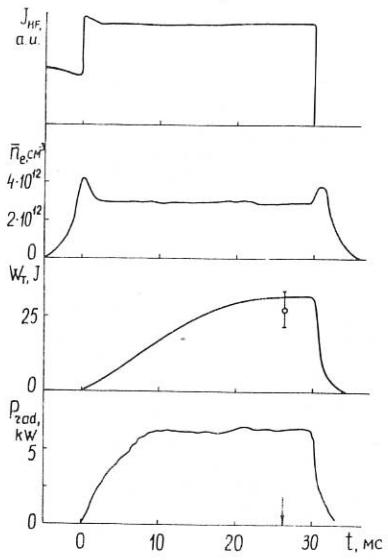

Fig.1. The time behavior of parameters (J_{HF} -antenna current, $\bar{n}_e$ -average electron density, W_T -total plasma energy, P_{rad} -pyroelectric detector power).

Figure 1 shows the time behaviour of the plasma parameters in the studied Q-discharges. Figure 2 shows T_e, T_i, n_e profiles measured at the time moment shown by an arrow at Fig.1. Electron temperature and density profiles were narrower than ion temperature one. Hydrogen atom density profile was rather flat inside of $r \leq 0,8 \cdot a$ ($n_{H0} = 1,7 \cdot 10^9$ cm^{-3}). Volume averaged loss power measured by the pyroelectric detector is equal 5 KW. Saddle coil plasma energy content evaluation agrees (within an error of 30%) with data obtained from T, n profile measurements.

The RF power deposition profiles for electrons and ions are necessary for power balance calculations. Until now we don't have a reliable data on power deposition profiles. Therefore we have limited the power balance calculations for the decaying plasma ($\Delta t \leq 0,5$ ms after RF power switch-off).

Figure 3 shows the time behavior of total plasma energy W_T, W_{e+i} and ion W_i and electron W_e energy after RF switch-off ($W_{e,i} = W_e + W_i$).

One can see that the total plasma energy decay rate is governed by a rapid electron cooling inspite of their minor role ($\simeq 20\%$) in the total energy content. The electron cooling is determined by the heatconductivity ($P_{hc} = 6$ KW) and radiation ($P_{rad} \simeq 5$ KW) and slow ion cooling is determined by a charge-exchange losses ($P_{cx} = 1$ KW). Ion-electron collisional heating is negligible ($P_{ei} \simeq 0{,}2$ KW).

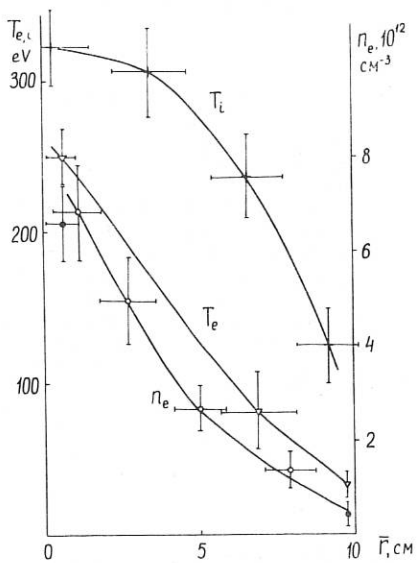

Fig.2. n_e , T_e , T_i profiles. Black points on the n_e -profile-data obtained by Thomson scattering and by electric probes.

In this regime the global energy confinement time τ_E^* equals 5 ms, the electron heatconductivity time τ_{hc}^e eqauls 1,5 ms, As the ion cooling time is goverend by charge exchange mostly, one can have only minor estimate for the ion heatconductivity time $\tau_{hc}^i \geq 30$ ms.

This power balance analysis showed that in this Q-discharges a small part of antenna radiated power ($\simeq 10\%$) is absorbed by a plasma core and ions and electrons are heated independently. High ion temperature is the result of a small power losses by ions.

It's worthwile to compare estimates of ion and electron energy confinement times with the theory predicted ones [2] .

In the studied regime the ions are in a banana regime ($\nu_i^* \lesssim 0{,}5$; $\varepsilon_h \ll \varepsilon_t$), the electrons are in a plateau regime ($\nu_e^* \gtrsim 1$). The ion energy confinement time estimate taking into account the profile data gives a value of $\tau_{hc}^i \simeq 20 \div 65$ ms which doesn't contradict to experimental data. Electron heat losses are of the order of neoclassical value in the near-axis region, but two orders of value higher at the plasma edge ($r \gtrsim 0{,}7\,a$).

Strong hydrogen atoms "burning-out" in the plasma created in the large vacuum chamber ($V = 70$ м^3) filled by the hydrogen with a molecule density of $2 \cdot 10^{14}$ cm^{-3} needs an explanation. This "burning-out" may be the result of the plasma core screening by a plasma in an ergodic layer.

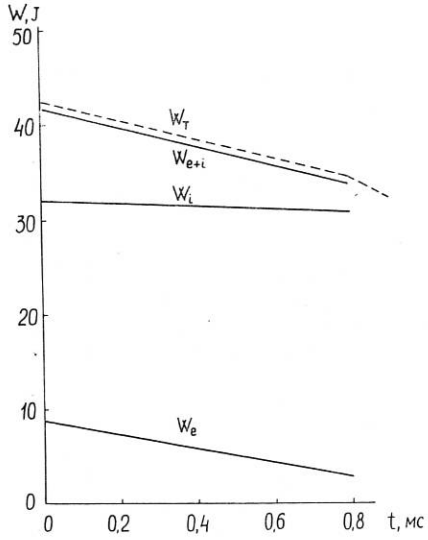

Fig.3.

(target density $\int n d\ell$ = $= 1.10^{13}$ cm^{-2}, T_e =15eV) and a plasma mantle ($n_e \simeq 1.10^{10}$ cm^{-3}, $T_e \simeq 5 \div 10$ eV) existing in the whole vacuum chamber (r =2,5 m). Nearly 90% of RF power is absorbed and lost by this cold plasma mantle.

4. Conclusion

The power balance studies for RF produced Q-discharges in the Uragan-3 torsatron showed that the main part of RF power (90%) is absorbed by a non-confined plasma which is screeing a hot plasma core hydrogen atoms coming from a vacuum chamber. The rest of power ($\simeq$ 10%) is lost from a hot plasma core mostly by electrons.

References

1. V.L. Berezhnyi, N.T. Besedin, M.P. Vasil'ev, et al., Plasma Physics and Controlled Nuclear Fusion Research 1986, v. 2. 497 (1987).
2. K.C. Djabilin, L.M. Kovrizhnykh, Fizika Plasmy (Sov.) 13, 515 (1987).

ELECTROSTATIC CONTROL OF PARTICLE FLOWS IN A STELLARATOR

R.P. Doerner, D.T. Anderson, W.N.G. Hitchon, P.G. Matthews and J.L. Shohet

Torsatron/Stellarator Laboratory
University of Wisconsin-Madison
Madison, Wisconsin 53706 (USA)

Abstract - An electrostatic method for controlling diverted particle fluxes in a stellarator has been demonstrated. Potentials applied to a defined set of divertor targets (shields) in contact with diverted flux bundles results in redistribution of plasma flow to any given divertor. Examination of the edge magnetic topology shows that **ExB** drifts just outside the last-closed magnetic surface account for the alteration of the diverted particle flows.

Experimental evidence of divertor structure has been observed in many stellarators[1,2]. These divertors usually spread the plasma flux over large regions.[3] An externally applied vertical magnetic field has been used to alter the divertor pattern in a stellarator globally.[4] We present here a method using electrostatic fields which provides local control of diverted particle fluxes in the Interchangeable Module Stellarator (IMS).

IMS is an $l = 3$, seven field-period modular stellarator with a 40 cm major radius and a 4.5 cm average plasma radius.[5] Outside the last closed magnetic surface (LCMS), is a region of ergodic field lines which extends radially for about 5 mm. Beyond this, field-line trajectories quickly coalesce to form 63 diverted-flux bundles. This divertor structure has been observed computationally[6] and experimentally.[7] Electrically-isolated stainless-steel shields placed at the locations of each of the 63 emergent bundles are used to monitor the diverted plasma flow as well as to apply an electrostatic bias to specific divertor bundles. The location of each shield is identified by both the coil support ring on which it is mounted and the poloidal angle at which it is positioned on the coil support ring as shown in Figure 1, (e.g., S8-340°).

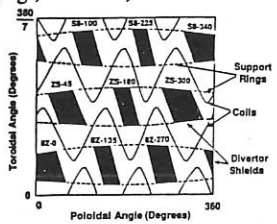

Tracing the magnetic-field lines from a given divertor shield back to a reference surface 5 mm beyond the LCMS gives an origin "map" of the field lines comprising that divertor bundle. An origin mapping of all 9 divertors in one field period is presented in Fig. 2dAny point on the reference surface is connected by field lines to at most two divertors. By following field lines parallel to the direction of the magnetic field a diagram is generated which indicates the areas of the launch surface that are connected to the various divertors (Figure 2a).

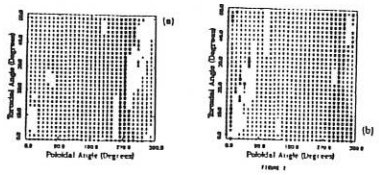

Figure 2b shows a similar map generated by following field lines in the opposite direction. Superimposing Figures 2a and 2b reveals that the field lines connecting to a given divertor originate mainly from a continuous toroidal strip on the reference surface.

It has been experimentally confirmed by launching ion-acoustic waves beyond the LCMS and monitoring the divertor shields to detect the wave,[8] that the plasma flows closely follow this mapping in IMS. The ion-acoustic wave propagation measurements[9] were also used to obtain a value for the diverted plasma flow velocity.

Measurements of the floating potential just outside the LCMS were taken during shield-biasing experiments. The regions outside the LCMS which connect to the biased divertor shield exhibited changes in the floating potential as the voltage on the divertor shield was varied. Changes in the floating potential of up to T_e, the electron temperature, were observed. A probe inserted in other origin regions, not connected to the biased shield, showed no appreciable change in floating potential when the same shield's bias was varied. Central plasma parameters also exhibit no changes during divertor-shield biasing. Measurements of the space potential show similar changes to those in the floating potential.

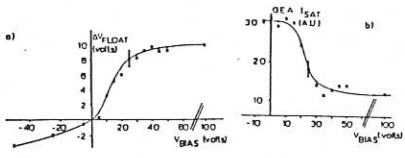

Figure 3b shows the change in the diverted ion current to a gridded-energy analyzer within a divertor when an adjacent divertor shield's bias voltage was varied. The change in current is strongly correlated with the floating potential change near the separatrix (Figure 3a). As the change in floating potential grows, with increased d.c. bias, an electric field develops between the biased and unbiased regions of the launch surface (outside the separatrix) and the diverted particle current changes. When the change in the floating potential saturates (at T_e volts) in the biased-origin region, no further changes are observed in the diverted particle currents.

A positive 50-volt potential was applied to the divertor shield in each field period which is located at a poloidal angle of 340 degrees (i.e., the S8-340° shield, see Figure 1). The ion-saturation current to each divertor within one field period was measured. The ion-saturation current to the shield located at a poloidal angle of 300 degrees (the ZS-300° shield) and the shield located at a poloidal angle of zero degrees (the 8Z-0° shield) exhibited changes. The ion-saturation current to the other shields showed no appreciable changes during biasing of the S8-340° shields. Referring again to Figure 2, the ZS-300° and the 8Z-0° origins are seen to flank the biased S8-340° origin. The diverted ion current to the ZS-300° divertor rises abruptly from 10.5 mA to 15.7 mA when the bias is applied to the S8-340° divertor shields. At the same time, the diverted ion current to the 8Z-0° divertor abruptly decreases from 8.0 mA to 2.0 mA when the bias voltage is applied.

Figure 4 shows the data obtained with this shield biasing configuration. The two traces labelled ZS-300° and 8Z-0° monitor the ion-saturation current collected by each of these divertor shields. The bias is switched on half-way through the discharge. The current to each divertor clearly exhibits an abrupt change when the bias is applied to the S8-340° shields. The total current collected by the biased shield is the trace labelled I_{bias}. The line-averaged density does not change appreciably over the course of the plasma discharge. Particularly, it does not change when the bias is applied. It is thus seen that the diverted-ion current decreases to the divertor whose origin strip is located on the positive poloidal angle

side of the biased origin. The current increases to the divertor whose origin is located on the negative poloidal angle side of the biased origin. This trend persists, even when other sets of divertor shields are biased.

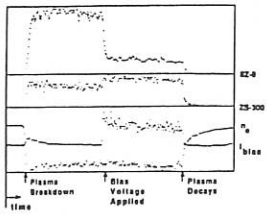

Since the decrease in current to one monitored divertor approximately equals the increase in current to the other monitored divertor, and since the currents to remote divertors exhibit only minimal changes, we conclude that the redistribution of flux is predominantly localized to those origin regions bordering the biased origin region.

The perpendicular conductivity of the IMS edge plasma is several orders of magnitude too small to account for the observed changes. Reversing the direction of the coil currents leaves the structure of the magnetic field unchanged, and should not directly change the electric field structure along a magnetic field line. Thus, one would expect to measure identical alterations to the diverted particle flows (at least to lowest order), if parallel conduction is the dominant mechanism responsible. On the other hand, reversing the direction of the magnetic field reverses the direction of any **E** x **B** drifts. If an **E** x **B** drift is responsible for the observed alterations, one would expect to see a reversal of the trend.

The measured potential changes (just outside the LCMS) due to shield biasing indicate the formation of an electric field having both radial and poloidal components. The radial component of the electric field acts to produce a poloidal drift (which pushes plasma poloidally around from one origin to a neighboring origin). The poloidal electric field component results in a radial **E** x **B** drift. The radial **E** x **B** drift resulting from shield biasing is the same order of magnitude as the measured plasma flow velocity through the divertors.[8] This radial drift acts to pull plasma out from near the LCMS on one side of the biased origin (i.e., the drift is outward) and to retard the flow of plasma out of the region near the LCMS on the other side (the drift is inward). The poloidal and radial electric fields thus act in concert.

Repeating the measurement with the S8-340 divertor shield biased to + 50 volts, but with the oppositely-directed (i.e. "negative") magnetic field does show a reversal of the change in the diverted ion current to both of the divertors described previously (the ZS-300°and the 8Z-0° divertors). This is consistent with an **E** x **B** drift acting on the diverted plasma. The diverted ion current to the ZS-300° divertor decreases by 5.2 mA, whereas with a "positively" directed magnetic field, the current increased by 5.2 mA. The change in the diverted ion current to the 8Z-0° divertor also reversed, increasing by 6.4 mA whereas it had decreased (with a "positively "directed magnetic field) by 6.0 mA. The fields and drift directions are pictorially represented in Figure 5.

Further confirmation of the **E** x **B** drift hypothesis has been obtained by operating IMS with a central magnetic field strength of 5.8 kG instead of the normal 2.6 kG. Measurements of the alterations in the diverted ion currents were made at the higher-field setting. The higher power available from the 17-GHz source (20 kW) and operation at 5.8 kG allowed the creation of plasma with ~ 2.5 times the density and electron temperature of the lower-field plasmas. The differences between the plasma parameters in the two cases provides an excellent means of verifying the **E** x **B** drift hypothesis. Table I summarizes the parameters of the two different regimes of operation and indicates the percent change in the diverted ion current to the same divertor during shield biasing for each configuration.

The higher electron temperature during 5.8 kG operation is seen to affect the shield-biasing measurements in two ways. First, the increased temperature permits a higher potential to be maintained in the origin strip. Second, the larger electron energy increases the

ion-sound speed and therefore also increases the measured diverted-plasma flow velocity. The imposed **E** x **B** drift velocity is quite similar for the two cases (due to increases in both E and B for the 5.8 kG case). However, the ratio of the **E** x **B** drift velocity to the diverted plasma flow velocity is observed to be less in the 5.8 kG case. The percent change in the diverted ion current during shield biasing is seen to scale closely with the ratio of the **E** x **B** drift velocity to the diverted plasma flow velocity.

These scaling results indicate that the dominant mechanism responsible for the redistribution of particle flux through the IMS divertors appears to be the **E** x **B** drift of the diverted plasma. This scaling indicates that this technique can be applicable to other larger stellarator devices. The plasma which is inhibited from flowing through the divertor (by the minor radially inward **E** x **B** drift) is directed to a location where the outward **E** x **B** drift enhances plasma flow through that divertor. This shows that it is possible to alter the diverted plasma flow patterns in a stellarator, using potentials applied to remote material surfaces in the edge region, without affecting the central plasma confinement properties.

This work was supported by the U.S. Department of Energy Grant No. DE-FG02-86-ER53216.A004 and Oak Ridge National Laboratory Contract No. 19X-3591-C.

References

1. Voitsenya, V.S., Voloshko, A.Y., Lats'ko, E.M., Solodovchenko, S.I., and Shtan', A.F., Nucl. Fusion 19, 1241 (1979).
2. Motojima, O., Iiyoshi, A., Uo, K., Nucl. Fusion 15, 985 (1975).
3. Gourdon, C., Marty, D., Maschke, E.K., and Touche, J., Nucl. Fusion 11, 161 (1971).
4. Doerner, R.P., Anderson, D.T., Anderson, F.S.B., Matthews, P.G., and Shohet, J.L., Nucl. Fusion, 28, 1901 (1988).
5. Anderson, D.T., Derr, J.A., and Shohet, J.L., IEEE Trans. Plasma Sci. PS-9, 212 (1981).
6. Derr, J.A., and Shohet, J.L., IEEE Trans. Plasma Sci. PS-9, 234 (1981).
7. Doerner, R.P., Anderson, D.T., Anderson, F.S.B., Shohet, J.L., and Talmadge, J.N., Phys. Fluids 29, 3807 (1986).
8. Doerner, R.P., Ph.D. Thesis, University of Wisconsin-Madison, (1988).
9. Ando, K., Ejima, S., Davis, S., Hawryluk, R.J., Hsuan, H., et al., in Plasma Physics and Controlled Nuclear Fusion Research (Proc. 5th Intl. Conf. Tokyo, 1974), Vol. 1, IAEA, Vienna (1975) 103.

FIGURE CAPTIONS

Figure 1) Schematic diagram of one field period indicating divertor shield nomenclature.
Figure 2) Each of the nine divertor-origin locations in one field period on the launch surface (a) field lines followed in the direction of B and (b) followed opposite to the direction of B)
Figure 3) The change in the potential near the last-closed magnetic surface (a) and the ion-saturation current to a divertor (b) as functions of the bias potential.
Figure 4) Experimental data showing changes in ion-saturation current to two divertors during +50-volt biasing of the S8-340° divertor shield.

B	2.6 kG	5.8 kG
n_e	2×10^{11} cm^{-3}	4.6×10^{11} cm^{-3}
T_e	8-12 eV	20-25 eV
E	8 V/cm	21 V/cm
E/B	3.1×10^5 cm/s	3.6×10^5 cm/s
V_{flow}	1.2×10^6 cm/s	2.0×10^6 cm/s
change of diverted ion current	- 62%	- 40%

TABLE I: Shield biasing results during plasma operation for two values of B.

CONVECTION, ELECTRIC FIELDS AND ECRH HEATING RATES IN THE INTERCHANGEABLE MODULE STELLARATOR

J.N. Talmadge, D.T. Anderson, F.S.B. Anderson and J.L. Shohet

Torsatron/Stellarator Laboratory
University of Wisconsin-Madison
Madison, Wisconsin 53706 (USA)

Steady-state hollow density profiles in the Interchangeable Module Stellarator (IMS) are consistent with a transport model that includes convection in the particle balance equation. Measurements of the space potential over the plasma cross-section show that the poloidal electric fields increase as the profiles become more hollow. The plasma was produced by a 7.28 GHz microwave source with a power output of 2 kW and a pulse length of 10 msec. Plasma densities are in the range of 0.5 - 3.0 x 10^{11} cm^{-3}, bulk electron temperatures are 10 eV and ion temperatures are 2-4 eV.

Density profiles vary from almost flat to very hollow with the ratio of the edge peak density to the central density in the range of 1.2 to 10.0. The hollowness increases as the electron cyclotron resonant layer is moved from the inboard side of the torus to the outboard side by increasing the magnetic field strength. In Figure 1a, the solid circles show the experimental density profile, normalized to the peak density when the central magnetic field, B_o, is 2.52 kG, which places the resonant layer close to the magnetic axis. Figure 1b shows the normalized density profile when B_o = 2.35 kG which places the cyclotron layer on the plasma edge at the inboard side of the device.

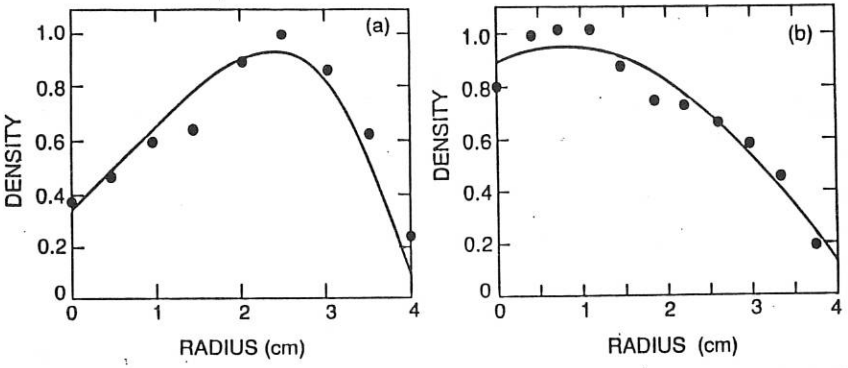

Figure 1 Normalized electron density profiles when the central magnetic field is (a) 2.52 kG and (b) 2.35 kG.

Because transport governed solely by diffusion would fill in the profiles on a time scale on the order of the confinement time, it is necessary to include convection in the particle

balance equation to explain steady-state hollow profiles. Assuming the diffusion coefficient D, ionization rate γ and convection velocity V are independent of radius (in effect considering these parameters to be global averages) this equation is,

$$r\frac{\partial^2 n}{\partial r^2} + (1 - \frac{V}{D}r)\frac{\partial n}{\partial r} + (\frac{\gamma r}{D} - \frac{V}{D})n = 0 \qquad (1)$$

In Figures 1a and 1b the solid lines show the best fit of Equation (1) to the experimental profiles. For the hollow profile V/D = 0.87 and γ/D = 0.86, while for the flatter profile V/D = 0.14 and γ/D = 0.37. If the diffusion coefficients were the same for both profiles, then for the flatter profile the convective velocity would be a factor of 6 less and the confinement time a factor of 2 greater than for the hollow profile.

The confinement time during the ECRH is determined by measuring the particle flux into the divertor regions and is given by $\tau = qnV_{pl}/I$ where n is the plasma density, V_{pl} is the plasma volume and I is the current to the shields that are mounted on the modular coil support rings.[1] The confinement time for the flatter profile was 770 ± 170 μsec and for the hollow profile was 360 ± 110 μsec, in good agreement with the factor of two determined from the steady-state profiles.

The space potential was measured for both profiles at 1 cm intervals over the plasma cross-section. In Figure 2a it can be seen that for the hollow profile, the equipotential contours do not correspond very well to the magnetic surfaces. The crescent-shaped contour on the outboard side of IMS can give rise to an E x B drift in the radial direction. Figure 2b shows that for the flatter profile, the equipotential contours correspond better to the magnetic surfaces.

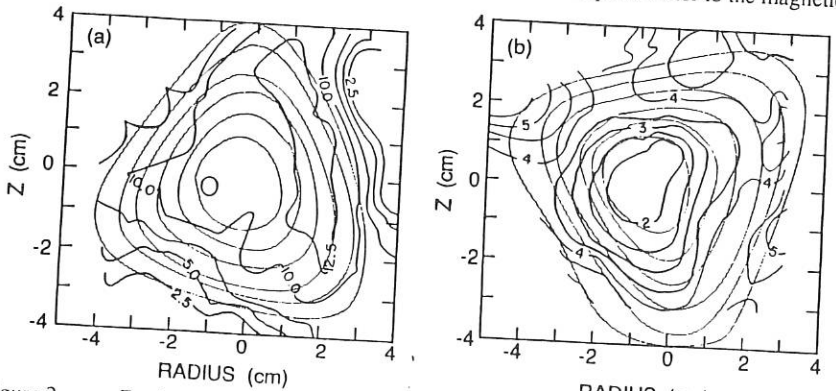

Figure 2 Equipotential contours (bold lines) and magnetic surfaces (light lines) for (a) hollow profile (contour interval is 2.5 V) and (b) flatter profile (contour interval is 0.5 V).

A numerical code was used to interpolate the potential on a flux surface and calculate the net E x B drift as a function of radius. For the hollow profile the peak convective velocity was 500 cm/sec and the radially averaged velocity was 170 cm/sec, while for the flatter

profile the values are 80 cm/sec and 30 cm/sec respectively. The local E x B drift velocities are roughly 2 orders of magnitude greater. The ratio of the convective velocities is in good agreement with the estimates made from the equilibrium profiles.

Experimental evidence suggests that non-thermal electrons may be responsible for the poloidal electric fields and the hollow profiles. The optically thin second harmonic electron cyclotron emission in the 12-18 GHz band was observed to increase with the magnetic field and peaked when the cyclotron layer coincided with a saddlepoint in the magnetic topology on the outside of the torus. Figure 3 shows the intensity at 13.0 GHz as a function of the central magnetic field. The peak in the emission corresponded to the most hollow density profile.

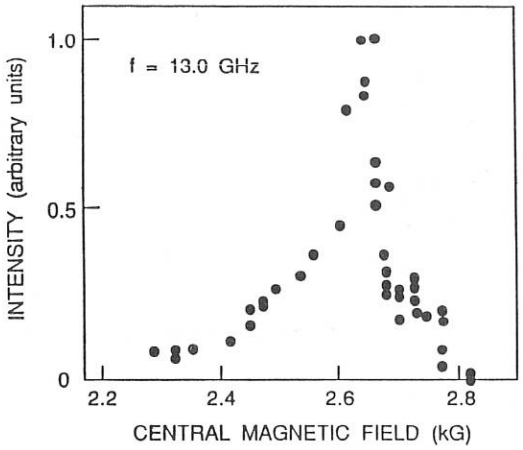

Figure 3 Intensity of the second harmonic ECE at 13.0 GHz versus central magnetic field strength.

A simple model of stochastic heating predicts increased heating as the cyclotron resonance layer is moved towards the outboard side of the torus, and peaks when the resonance layer coincides with a saddlepoint in the magnetic field. The heating rate is calculated numerically by computing the trajectory of a magnetic field line and summing the contributions of each resonance crossing. It is assumed that successive crossings of the resonance by a particle are uncorrelated. The heating rate on a flux surface ψ is given by

$$\frac{dW(\psi)}{dt} = \pi e E_{\perp}^2 \frac{1}{L} \Sigma \frac{1}{(\partial B/\partial s)_{res}} \qquad (2)$$

where $E_{\perp}$ is the perpendicular component of the electric field, L is the distance over which the trajectory of the magnetic field line is computed and $(\partial B/\partial s)_{res}$ is the gradient of the field line along its path length at the location of the resonance crossing. The volume averaged heating rate is calculated by integrating the surface averaged heating rate over the flux volume. This quantity is shown in Figure 4 as a function of the central magnetic field. The relation of the heating rate to the resonance location was demonstrated during the breakdown

phase of the discharge by monitoring the dependence of the delay time between the beginning of the ECH pulse and the production of a measureable density as a function of puff pressure, RF power and magnetic field strength.[2]

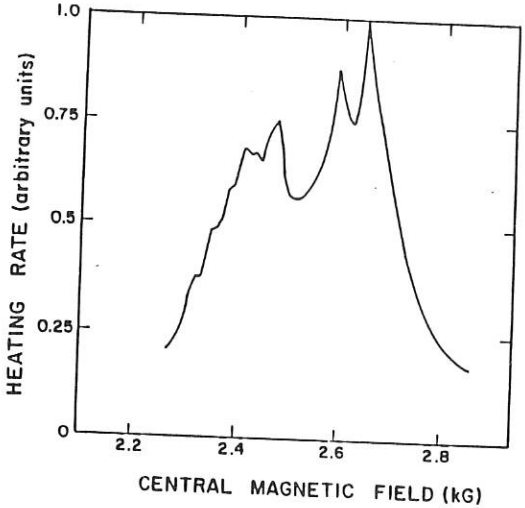

Figure 4 Volume averaged heating rate as a function of the magnetic field at the geometric center.

It appears that the increased heating rate as the resonance is moved to the outboard side may be responsible for the increase in the non-thermal electrons that show up as an increase in the electron cyclotron emission. It is this population that is thought to be responsible for the poloidal electric fields that give rise to the convection and the hollow profiles. Similar effects have been observed in the Elmo Bumpy Torus.[3]

References

1. Doerner, R.P., Anderson, D.T., Anderson, F.S.B., Shohet, J.L., Talmadge, J.N., Phys. Fluids, 29 (1986) 3807.

2. Talmadge, J.N., Anderson, D.T., Nucl. Fusion, 28, (1988) 1879.

3. Tolliver, J.S., Hedrick, C.L., Phys. Fluids, 30, (1987) 870.

INFLUENCE OF DENSITY FLUCTUATIONS ON ENERGY DEPOSITION PROFILE DURING ECRH IN L-2 STELLARATOR

Likin K.M., Ochirov B.D.*

Institute of General Physics, Academy of Sciences of USSR, Vavilov street 38, Moscow 117924, USSR
*Institute of Automation and Electrometry, Academy of Sciences of the USSR, Siberian Branch, Novosibirsk 630090, USSR

Microwave scattering measurements /1/ showed the presence of low-frequency density fluctuations in L-2 stellarator. It is thought that low-frequency oscillations are connected with transport phenomena in plasma. As it was shown in papers /2,3/ the density fluctuations also affect rays' trajectories and, therefore, they can influence upon absorption efficiency and energy deposition profile. In this report the influence of density fluctuations on absorption efficiency and energy deposition profile by ECRH simulation in L-2 stellarator is studied.

The propagation of electromagnetic waves in plasma is simulated in geometrical optics approximation /3/. 3-D code includes ray tracing and cyclotron absorption along rays' trajectories. Monte-Carlo method was employed in ray tracing code /2/. Scattering of ordinary wave to like type wave was taken into account and scattering of ordinary wave to extraordinary mode (i.e. change of wave polarization) was ignored in modelling. Scattering of incident wave occurs in poloidal plane because perpendicular component of wavenumber of drift waves is much higher than parallel one ($\bar{z}_\perp \gg \bar{z}_\parallel$). The time interval Δt was chosen to obtain total probability of scattering P equal or less than 0.1. The real wavenumber spectrum of fluctuations measured during ECRH in L-2 stellarator plasma /1/ was used in simulations. This spectrum has form close to Gaussian:

$$S(\bar{z}) = \frac{1}{(\pi \bar{z}_0^2)} \langle (\delta n/N)^2 \rangle \exp\left(-\bar{z}^2/\bar{z}_0^2\right)$$

Modelling of scattering on density fluctuations during ECRH in L-2 stellarator was carried out. The main parameters of this device are: R_0=100 cm - major radius, a_0=17.5 cm - minor radius, a_p=11.5 cm - average radius of plasma, $B_0(0)$ = 13.4 kG - magnetic field in the plasma centre. Ordinary wave (λ_0=8 mm - vacuum wavelength) was launched from low magnetic field side as Gaussian beam with width (at e^{-2} level) 57 mm and with plane phase front. Radial distributions of electron density and electron temperature used in simulations were close to experimental profiles /5/.

During debugging of the code it was found that in calculations without scattering on density fluctuations number of rays should be taken more than 13 and in modelling with scattering number of rays must be more than 65.

Figure 1 demonstrates the rays' trajectories on poloidal plane in the following regime: $n_e(r)=1.125\cdot 10^{13}\cdot [1-(r/a_p)^2]$

cm^{-3} - electron density; $T_e(r)=0.4\cdot[1-(r/a_p)^2]$, KeV - electron temperature; $B_o(0)=13.4$ kG - magnetic field; $(\delta n/n)(r)=0.1$ - relative level of density fluctuations; $\xi_c=12$ cm^{-1} - characteristic wavenumber of Gaussian spectrum of fluctuations. In the next figure (Fig.2) the absorption power profiles for the same regimes are shown. One can see that energy deposition in plasma centre is reduced when relative level of fluctuations is equal to 0.1. Also the absorption efficiency is decreased from 43% to 39%. As rays' trajectories show the diminution of absorption in regime with scattering on density fluctuations is connected with decreasing of power flux density in the plasma centre regions in comparison with calculations without scattering. The density fluctuations substantially affect absorption efficiency and energy deposition profile when the relative level of fluctuations is more than 0.1 (Fig.3). In these simulations it was supposed that profile of relative level of fluctuations was flat. Calculations for various profiles of relative level of fluctuations were carried out. These results are presented in Fig.4. As follows from this modelling the absorption efficiency and energy deposition profiles weakly depend on radial profiles of relative level of fluctuations. The small part of incident wave is scattered in plasma peripherer because of small absolute level of density fluctuations on in this region (in spite of great value of $\delta n/n$).

Summarizing we note that substantial variations in energy deposition profile and absorption efficiency were obtained for relative level of fluctuations more than 0.1. Density fluctuations in the central region of L-2 stellarator plasma ($r/a_p \leq 0.5$) essentially can determine absorption efficiency and energy deposition profile.

References

1. Batanov G.M. et al. Microwave Scattering on Plasma Density Fluctuations in L-2 stellarator. 15-th Europ.Conf.on Cont. Fusion and Pl.Heating. Dubrovnik, 1988, p.455.
2. B.Hui et al. Scattering of electron cyclotron resonance heating waves by density fluctuations in tokamak plasmas. Nucl. Fusion, v.21, N°3, 1981, p.339.
3. F.R.Hansen et al. Ordinary wave propagation in a tokamak with random density fluctuations. Nucl. Fusion, v.28, N°5, 1988, p.769.
4. Likin K.M. et al. Energy Deposition Profiles of Simulations of the ECRH in the L-2 Stellarator. 15-th Europ. Conf. on Contr. Fusion and Pl. Heating. Dubrovnik, 1988, p.451.
5. Andryukhina et al. Electron Cyclotron Heating (ECH) of Currentless and "Target" Current Plasmas by an Ordinary Wave in L-2 Stellarator. 15-th Europ. Conf. on Cont. Fusion and Pl. Heating. Dubrovnik, 1988, p.447.

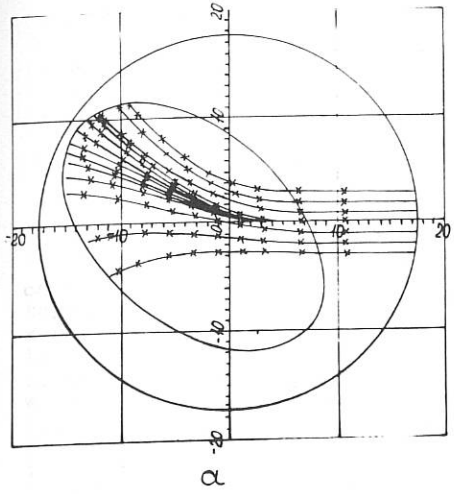

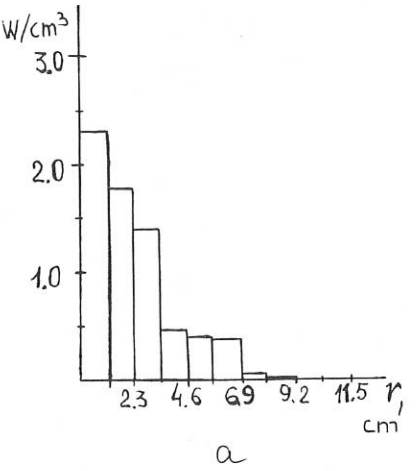

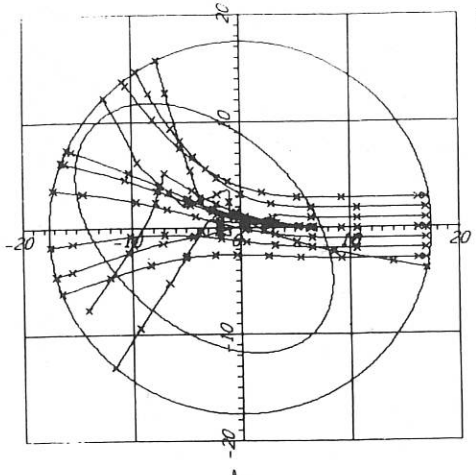

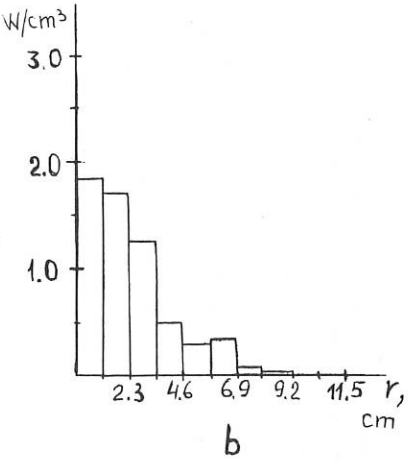

Fig.1 Rays' trajectories:
a-without scattering;
b-with scattering.

Fig.2 Absorption power profiles.

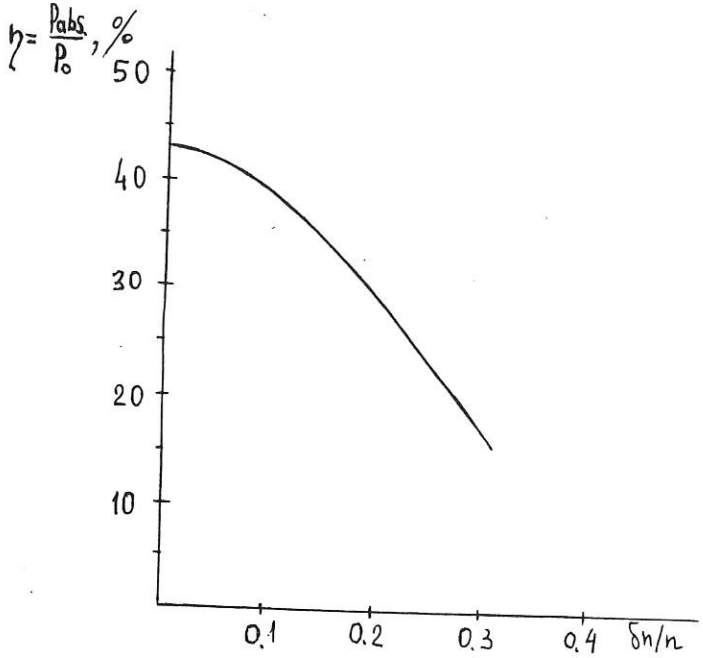

Fig.3 Absorption efficiency ($\delta n/n(r) = const.$).

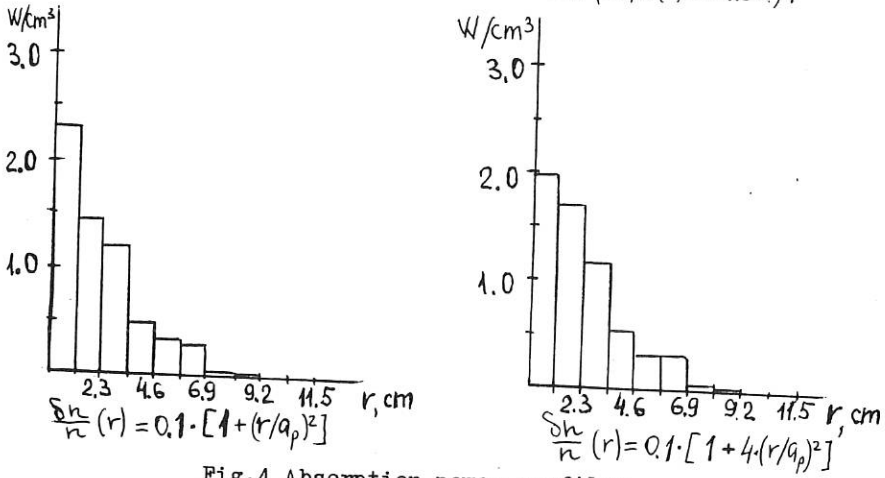

Fig.4 Absorption power profiles.

SMALL-SCALE DENSITY FLUCTUATIONS IN OHMIC AND ECR HEATED PLASMA IN L-2 STELLARATOR

Batanov G.M., Saposzhnikov A.V., Sarksyan K.A., Shats M.G.

Institute of General Physics, Academy of Sciences of the USSR, Vavilov street 38, Moscow, 117942, USSR

Density fluctuations measurements in L-2 stellarator were carried out using 2.5mm collective scattering system. Scattered waves were received at the angles θ_s =15°,30°,45° corresponding to $k_\perp$=6, 13 and 20 cm^{-1} (where $k_\perp$-is the wavenumber in poloidal plane). Homodyne detection system was used. Samples of digitized signals (sample time T=n×1μsec, where n=200-1000) were recorded and autocorrelation functions and Fourier coefficients of autocorrelation functions were calculated using FFT algorithm. Experimental set-up allows registration of frequency spectra for three angle channels simultaneously few times per each stellarator discharge.

Frequency and wavenumber spectra and intensity of the fluctuations were measured in regimes of ohmic and ECR heating of plasma [1]. Frequency spectra shown in Fig.1 were obtained in regimes of ohmic heating (Fig.1a) and ECRH ofcurrentless plasma (Fig.1b). Spectra in Fig.1 refer to the case when a helium was used as working gas. Frequency spectra for the case of ohmic heating (Fig.2a) and ECRH of currentless plasma (Fig.2b) in hydrogen are shown in Fig.2. Presented in Figs.1, 2 frequency spectra are the result of averaging over five realizations. Necessity of spectra averaging is connected with nonstationarity of spectra on time intervals greater or equal to intervals at which plasma parameters (T_e,W etc.) change. Nonaveraged frequency spectra (T=200μsec) during ECRH pulse ars shown in Fig.3. Noted in [2] burstlike temporal structure of the oscillations at fixed frequencies was observed in our experiments too. The likely explanation of spectra nonstationarity on time scales longer than autocorrelation time is connected with existence of time and spatial internal structure of the turbulence, as it have been shown in [3].

As can be seen in Figs.1,2 characteristic frequencies of fluctuations in helium plasma are higher than in hydrogen one. In hydrogen discharges (during both ECR and ohmic heating) about 50% of fluctuations' power is contained in the frequency range f=2—30kHz, whereas in helium plasma the contribution of these low-frequency fluctuations in the integral intensity is about 10% in currentless plasma and about 20%in ohmic heating regime.

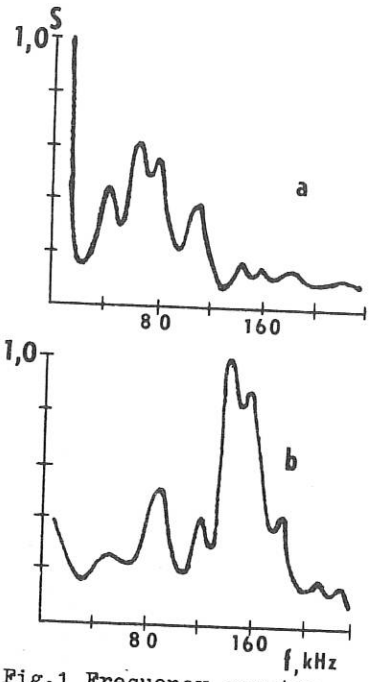

Fig.1 Frequency spectra during discharges in helium
a-ohmic heating
I_p=15 kA
b-ECH, P_{ECH}=100 kW

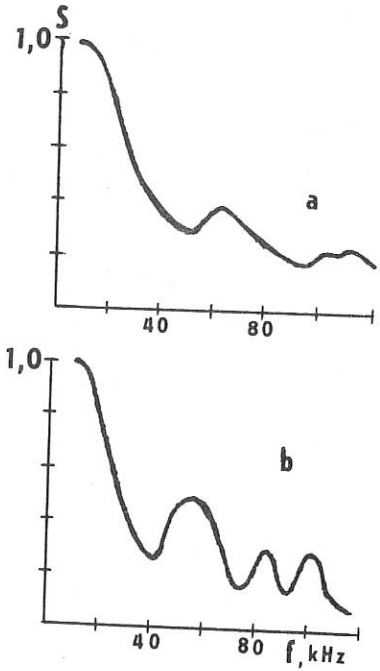

Fig.2 Frequency spectra during discharges in hydrogen
a-ohmic heating
I_p=15 kA
b-ECH, P_{ECH}=170 kW

Difference of frequency spectra in helium and hydrogen discharges may be connected with distinction in density profiles. After switching off the gyrotron power during ECH of currentless plasma low-frequency contribution in integral intensity increases with flattening of density profile. So, frequency spectra are sensitive to the density scale length and/or to kind of working gas.

Behaviour of density fluctuations intensity was studied in the regime of ECH of currentless plasma by an ordinary wave at first electron cyclotron harmonic. Microwave power launched into the stellarator chamber was equal to P_{ECH}=170 kW and absorbed power varied in a wide range (30-90 kW). In Fig.4 the correlation of central electron temperature with relative level of density fluctuations is shown. One can suppose that effect of density fluctuations on heating efficiency is connected both with the influence of fluctuations on energy

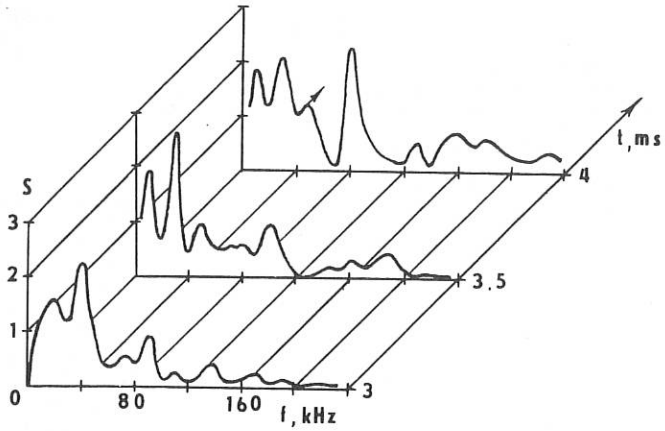

Fig.3 Evolution of density fluctuations spectra during ECRH of currentless plasma (sample time T=200μsec, P_{ECH}=170 kW, hydrogen)

transport and with scattering of the incident microwave ("heating") beam on density fluctuations. The latter is verified by calculations of energy absorption along ray tracing trajectories accounting scattering on density fluctuations[4]. Another reason for the observed strong correlation of T_e and $\delta n/n$ is the possible shift of the maximum of $k_\perp$-spectra due to the changing of T_e (the effect of integration over limited range in $k_\perp$[5]).

Effect of density fluctuations on energy transport is illustrated by correlation of nT_e/P_{abs} (proportional to energy confinement time τ_E) with $\delta n/n$ presented in Fig.5. Comparison of anomalous heat conductivity due to the electrostatic drift turbulence [6] $\varkappa_e \approx \frac{5}{3}\gamma L_n^2 (\delta n/n)^2$ with coefficient of anomalous diffusion, calculated from electron energy balance in L-2 stellarator [7] gives the same order of magnitude of $\varkappa_e \approx 10^4 cm^2/s$. This fact indicates a great role of intense ($\delta n/n \sim 0.1$) density fluctuations in transport processes.

REFERENCE

1. Batanov G.M. et al.15 Europ. Conf. on Contr. Fus. and Plasma Heating,1988,Dubrovnik,v.12B, pt.2,p.455
2. Barkley H. et al. Int. Conf. on Plasma Physics,1987, Kiev,v.3, p.24
3. Horton W. Phys. Fluids,1986,v.29, p.1491
4. Likin K.M., Ochirov B.D. - This conference
5. Van Andel H.W.H. et al.Plasma Phys. Contr.Fus.,1987,v.29,74
6. Liewer P.C. Nucl. Fus.,1985,v.25,p.543
7. Andryukhina E.D. et al.Lebedev Phys.Inst.Report,n.245,1983

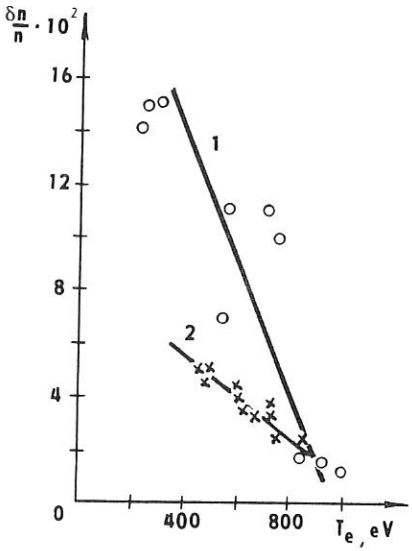

Fig.4 Correlation of central electron temperature T_e with fluctuations' level
1-P_{ECH} =170 kW, hydrogen
2-P_{ECH} =100 kW, helium

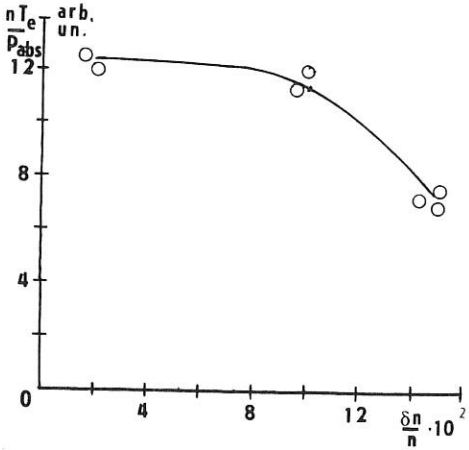

Fig.5 Correlation of nT_e/P_{abs} with density fluctuations' level $\delta n/n$ during ECH of currentless plasma (P_{ECH}=170 kW, hydrogen)

OPTICAL MEASUREMENTS OF ECRH HELIUM PLASMA IN THE L-2 STELLARATOR.

Donskaya N.P., Larionova N.F., Roshchin V.I.,
Smirnova A.D.,Voronov G.S.

General Physics Institute, Vavilova 38,Moscow, USSR.

Experiments on ECR-heating of helium plasma in the L-2 stellarator were fulfilled with the ordinary wave fundamental harmonic in 1988 [1]. This report describes in more detail optical measurements of the plasma parameters.

Microwave beam (f=37.5GHz) was launched into the chamber through the external horizontal window from the low-fild side. The lens beam-guide was used to transfer the beam to the machine. Microwave beam power at the window was about 100 Kw, beam diameter as measured at the level of .1 of central power was about 6sm, beam divergency was .02.

Helium was chosen as working gas in order to decrease radiation losses and to prevent the effect of wall conditions on the discharge parameters. In fact, the radiation losses dropped to .7 of those in hydrogen, less than 20% of plasma absorbed power was lost with radiation. The increase of plasma density during the heating puise was also smaller than in hydrogen.

Optical diagnostics used were: 1) Thomson scattering at the second harmonic of neodim-glass laser (wavelength 5300 A), 2) multichannel submillimeter interferometer at the wavelength .337mm for measurements of plasma density radial distributions, 3) spectral measurements in both quartz and vacuum-ultraviolet wavelength regions.

Gas breakdoun and plasma formation was due to microwave field, considerable role in this phenomenon could be played by X-polarised wave obtaned in the course of multiple beam reflections from metal walls of the chamber.The breakdown power F was noticeably smaller than heating power W (Fig.1). Rather small time of .5-1ms was needed for gas breakdown and plasma formation, the slow density increase due to impurities followed (Fig.2).As could be concluded from absolute spectral-line intensity measurements, density increase was due to increase in concentration of oxygen and carbon which were 4% and 1.5% correspondingly, at the end of the heating pulse.

Radiation loss power Prad=12-15Kw was considerably less then absorbed power Pabs and was aproximatelly equal to power emitted by oxigen and carbon ions.

Electron temperature evolution measured with Thomson scattering and spectral-line localisation evolution studies [3] had shown that the ECR plasma heating in the L-2 sttellarator could

develop in two different ways. Fast increase and subsequent stabilization at the level of 600 Ev of the central electron temperature was characteristic of one of these "A" regimes (Fig.3). In "B" regime central electron temperature was growing during the whole heating pulse to get .9-1.Kev at the end of it (Fig.4). Sometimes, a transition could be observed from "A" to "B" regime during the heating process (Fig.5).

"B" regime could be obtained in very narrow region of the magnetic field values : B/B<.5%. B value corresponded approximanely to central location of the ECR resonance but was also affected by some other parameteres difficult to be controlled such as profile and plasma density magnitude, microwave beam direction at the chamber entrance, ets. This B uncertainty could be due to beam refraction in plasma and, therefore, power absorbtion region changing its localization.

Shown in Fig.6 and Fig.7 is Te profile evolution in "A" and "B" regimes. In "A" regime Te(r) widened to the end of the heating pulse while Te(0) remained the same. In "B" regime Te(r) profile had been keeping its picked form during all the heating time.Difference in these Te profiles can be easily seen in Fig.8 where a transition is shown from "A" to "B" regime.

Density profile measured with HCN-laser interferometer is parabolic for the most part. Sometimes more picked profiles were observed during the heating, any correlation to heating regime, however, had not been observed.

Energy containement of the plasma electron component obtained with integration over the profiles Te(r) and Ne(r) was (140-150)J in "A" regime and (180-190)J in "B" regime in good agreement with diamagnetic measurements results. Absorbed power was 60Kw and (60-70)Kw in "A" and "B" regimes correspondingly as measured with diamagnetic signal derivative at the time when heating power had been switched off. Energy confinement time was calculated to be 2.4ms ("A" regime) and 2.8ms ("B"regime) with radiation losses having been neglected.

At present, there is no any possibility to measure space distribution of the absorbed power Q(r). An attempt was made to culculate it with help of plasma energy derivative at the time moment when heating power had been switched off.

Spectral line localization followed the electron temperature evolution with some delay .5ms due to finite velocities of impurity ionization and diffusion processes. Te(r) profile, meantime, changed because of heat conduction. Nevertheless, qualitative difference in Te(r) profiles for the abovesaid regimes are quite obvious (Fig.9). As it can be seen, narrow profile Te(r) with high central temperature Te(0) 1Kev ("B" regime) was obtained when power absorbtion maximum was located at the centre while more flat profile with central temperature Te(0) 600ev ("A" regime) corresponded to peripheral heating.

Magnetic surface structure is complex in L-2 stellarator. Slight change in the magnetic field amplitude and beam refraction on plasma inhomogenuities can make absorbtion region to

move to the saddle point of the magnetic field structure. Ray-tracing culculation results [2] are in agreement with this supposition.

REFERENCES

[1] Andryukhina E. D. et al. in Europhysics Conf. Abs. 12B (Proc. 15th Eur. Conf. Contr. Fusion and Plasma Phys., Dubrovnic, 1988) Part 2, p.447.
[2] Likin K. M. et al. ibid, Part 2, p.451.
[3] Voronov G.S., Donskaya N. P., Roshchin V. I. Preprint GFI, 265, 1987 (in Russian).

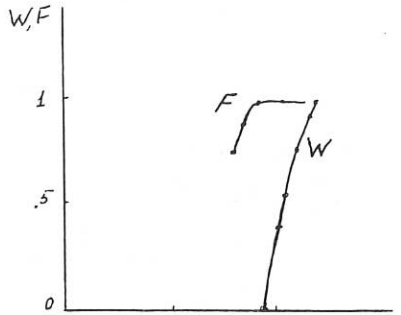

Fig. 1

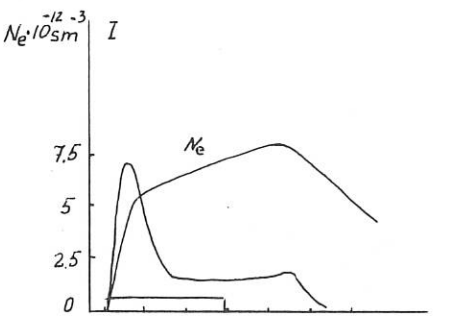

Fig. 2

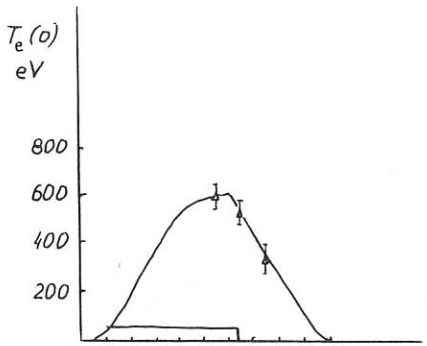

Fig. 3

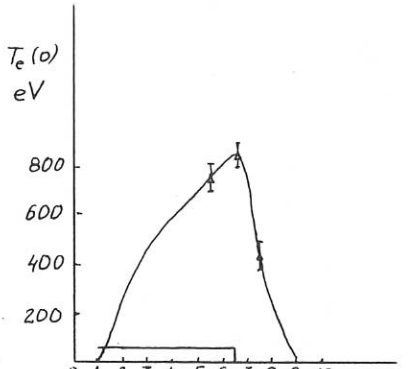

Fig. 4

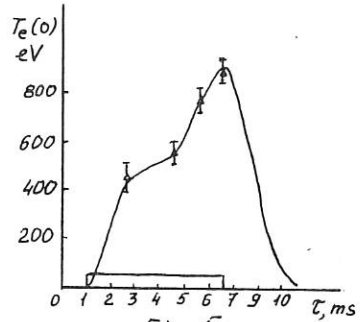

Fig. 5

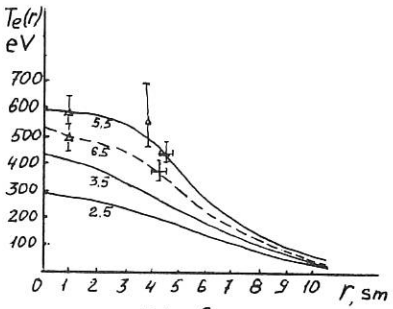

Fig. 6

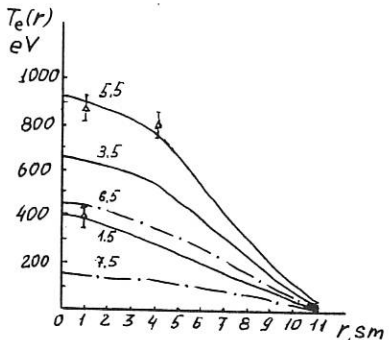

Fig. 7

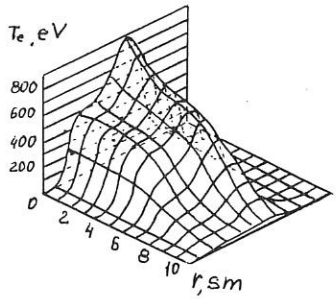

Fig. 8

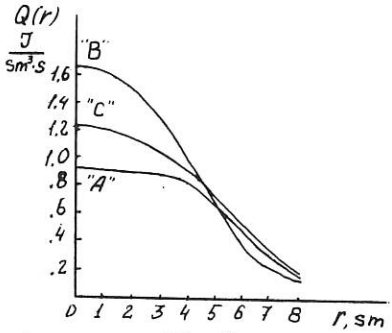

Fig. 9

OPTIMIZATION OF TRANSPORT AND DIRECT HIGH-ENERGY LOSSES IN STELLARATORS AND TORSATRONS

C. O. Beasley, Jr.*

International Atomic Energy Agency
P. O. Box 100
Wagramerstrasse 5
Vienna 1400, Austria

C. L. Hedrick and W. I. van Rij

Fusion Energy Division
Oak Ridge National Laboratory
P. O. Box Y
Oak Ridge, TN 37830, USA

In most existing stellarators and torsatrons, bulk neoclassical losses and high energy direct losses stem from departure of helically-trapped particle drift surfaces from flux surfaces, as is shown in Fig. 1. Here, ψ labels the radial coordinate of the Boozer coordinates (ψ, θ, φ). Except for "straight stellarators," in which ε_t vanishes, the displacement of the average drift surfaces from the flux surfaces greatly exceed the oscillatory displacement; hence we can neglect the oscillatory displacement.

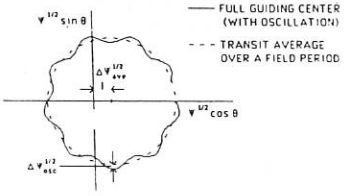

Fig. 1

The averaged motion can be described by the adiabatic invariant, J*, defined as

$$\int m v_{\parallel} \, d\ell - e\sigma \frac{2\pi}{M} \int_0^{\psi} d\psi' \iota(\psi')$$

$\sigma = \mathrm{sign}(v_{\parallel})$ (passing particles), 0 (trapped particles); $\quad d\ell = \frac{B_0 \hat{B}_0}{B} d\varphi$

and which is most pronounced for the trapped particles, as shown (for ions) in Fig. 2. (In fact, for electrons, the difference between trapped and passing particles is even more dramatic). Because the analysis becomes much simpler, most work has been done on deeply-trapped particle transport.

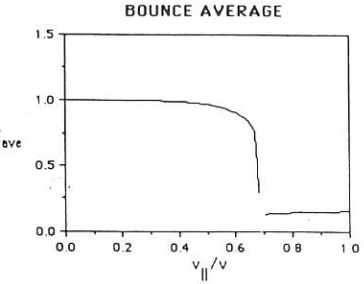

Fig. 2

Now J* = constant implies that

$$e\Phi_E + \mu B_{min} = const.$$

If Bmin and Φ_E are independent of θ, then the bounce-averaged orbits lie on a flux surface, Ψ = constant. Let us assume our magnetic field is of the form

$$B = B_0 \{ 1 - \varepsilon_t \cos\theta - [\varepsilon_h - \lambda \varepsilon_t \cos\theta] \cos(M\varphi - \ell\theta) \}$$

then

$$B_{min} = B_0 \{ 1 - \varepsilon_h - \varepsilon_t (1-\lambda) \cos\theta \}$$

The two ways of making Bmin independent of θ are ε_t optimization, as per Nuhrenberg, where $\varepsilon_t = 0$, or λ optimization, as per Mynick, where $\lambda = 1$. Of the two, ε_t optimization works to prevent displacement of both trapped and passing particles from a flux surface, while for λ optimization, only deeply-trapped particles will display this characteristic.

We may use

$$J^* = const = J_0^* + \Delta\Psi \frac{\partial J^*}{\partial \Psi} + \cos\theta \frac{\partial J^*}{\partial \cos\theta}$$

to obtain the maximum displacement of deeply-trapped particles from flux surfaces. In the $1/\nu$ regime, only $\partial J^* / \partial \cos\theta$ enters, so we find the normalized displacement shown in Fig. 3 here for three different values of λ.

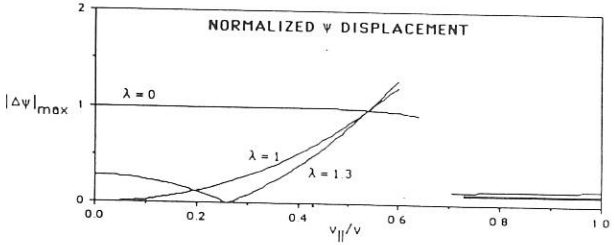

In an earlier work, we calculated transport coefficients in the $1/\nu$ regime and checked these results numerically. We found that the transport coefficients have a common geometric factor

$$G = \varepsilon_h^{3/2} \varepsilon_t^{\,2} \int d\theta \sin^2\theta \, [g_1 - g_2 \lambda + g_3 \lambda^2]$$

where g1, g2, and g3 are functions of

$$\eta = 2(\varepsilon_h - \lambda \varepsilon_t \cos\theta) / [1 - \varepsilon_h - \varepsilon_t (1-\lambda) \cos\theta] \leq 2\varepsilon_h / (1 - \varepsilon_h)$$

If we define a reduction factor

$$F = G(\lambda) / G(\lambda = 0)$$

we find that for a given ε_h, here taken to be 0.3, F has a minimum, as shown by the solid line in Fig. 4.

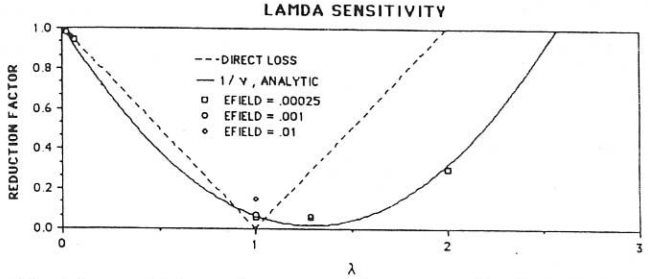

Fig. 4

To verify these $1/\nu$-regime results, we calculated F for several different λ using the DKES code; these are plotted in Fig. 4 for various electric fields. (In the $1/\nu$ regime, transport is independent of the electric field).

The dependence of the position of λ_{min} on ε_h, and its value Fmin, are shown in Fig. 5. This curve points out that λ_{min} is insensitive to ε_h. Interpretation also suggests that the most deeply-trapped particles carry more weight at larger ε_h.

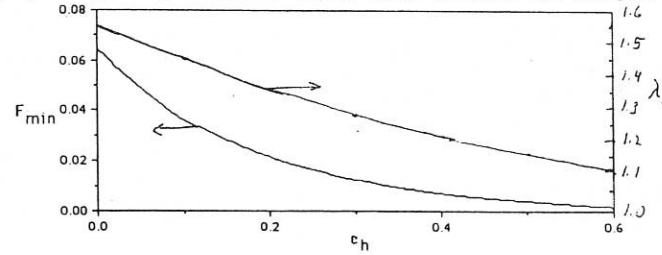

Fig. 5

Using DKES, one may calculate the value of λ_{min} at various collisionalities. Over five orders of magnitude, the optimum value remains between 1.3 and 2, as is shown in Fig. 6.

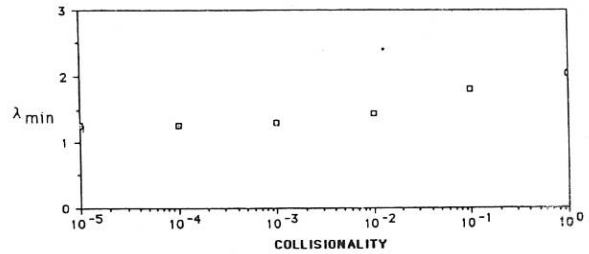

Fig. 6

In "simple" stellarator transport, characterized by $\lambda = 0$, there is a peak in the transport curve (Mt. Ripple) between the ν and $1/\nu$ regimes, as is shown in the "unoptimized" curve in Fig. 7. With λ set to 1.3, transport at the corresponding peak

is reduced by more than an order of magnitude (see "λ-optimized" curve in Fig. 7). These results were obtained using DKES. For comparison, we have also plotted the ε_t-optimized straight stellarator transport.

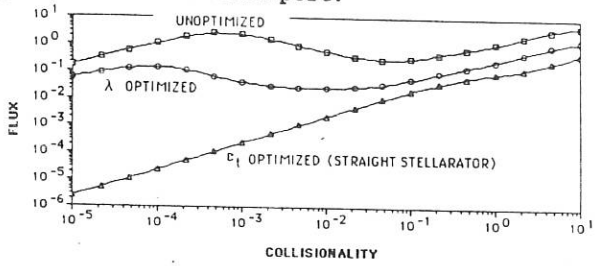

Fig. 7

While not shown here, the $1/\nu$ analysis has also been carried out for more general magnetic fields, such as the Shaing-Hokin model. The results from those calculations show that the DKES results are more general than for the model field, and apply to more realistic stellarator devices.

With regards to high-energy direct losses, Painter and Lyon have conjectured that Bmin is a good measure of direct losses of high-energy particles due to unconfined drift orbits. These losses are proportional to

$$\varepsilon_t \, |\lambda - 1|$$

This λ behavior is also shown in Fig. 4. This analysis suggests that both bulk transport losses and direct losses of high-energy particles are dependent on Bmin, and provides a simple set of guidelines for optimizing stellarator/torsatron magnetic configurations.

In summary, we find that optimization of $1/\nu$ transport also optimizes the peak transport of Mt. Ripple. That high-energy losses as well as bulk losses can be reduced by aligning Bmin = constant surfaces with flux surfaces is encouraging for future stellarator devices.

MODULAR-RIPPLE TRANSPORT IN STELLARATORS

C.D. Beidler

Max-Planck-Institut für Plasmaphysik, EURATOM-IPP Association
D-8046 Garching bei München, Federal Republic of Germany

The future stellarator experiment, Wendelstein VII-X, will be the first to employ the Helical-Axis Advanced Stellarator (Helias) concept. A distinct advantage of Helias configurations over classical stellarator/torsatron devices is their significantly reduced neoclassical transport rates, both in collisional regimes and in the long-mean-free-path regime where particles trapped in the local *helical* ripple wells of the stellarator's magnetic field make the dominant contribution to transport. Unlike the classical, continuously wound stellarator/torsatron, however, the magnetic field of Wendelstein VII-X will be produced by a large number of *discrete* non-planar coils. These *modular* coils give rise to a further ripple in the magnetic field strength and introduce a neoclassical loss mechanism not otherwise present. The magnitude of this modular ripple may be made small by using a large number of coils — added expense and restricted plasma access are the principal drawbacks to this approach.

In the present work, the additional transport introduced by the modular ripple is calculated by analytically solving the bounce-averaged kinetic equation. The solution assumes a general magnetic field model so that complicated helical ripple profiles composed of several harmonics may be treated. The deformation of modular ripple wells due to the presence of the other magnetic field harmonics is fully accounted for. This solution is used to determine the level of modular ripple transport to be expected in Wendelstein VII-X candidates for configurations with both 10 and 12 coils per field period.

The set of magnetic coordinates (r, θ_0, ϕ) will be chosen to represent physical space [1]; r is the minor radial variable defining a toroidal flux surface, θ_0 labels a field line and ϕ is the usual toroidal angle. The poloidal angle, θ, is related to the angular variables through the rotational transform, ι, by the expression $\theta = \theta_0 + \iota\phi$. In this system, the guiding-center drift-kinetic equation may be expressed as

$$\frac{v_\parallel}{R}\frac{\partial F}{\partial \phi} + \dot{\theta}_0 \frac{\partial F}{\partial \theta_0} + \dot{r}\frac{\partial F}{\partial r} = \nu B^{-1} v_\parallel \frac{\partial}{\partial \mu}\left(m v_\parallel \mu \frac{\partial F}{\partial \mu}\right) , \tag{1}$$

where $v_\parallel$ is the particle velocity along a field line, $dl = Rd\phi$ is the differential distance along a field line, ν is the 90 degree deflection frequency and $\mu = mv_\perp^2/2B$ is the magnetic moment. The magnitude of the magnetic field, B, is given by

$$\frac{B}{B_0} = -\delta(r)\cos Np\phi + \sum_{m,\ell} C_{m,\ell}(r)\cos \ell\theta \cos mp\phi + \sum_{m,\ell} S_{m,\ell}(r)\sin \ell\theta \sin mp\phi \ , \tag{2}$$

with p the number of field periods of the stellarator and N the number of discrete modular coils which make up each field period. The first term in this expression represents the modular ripple with magnitude δ, while the Fourier harmonic expansions describe the toroidal and helical nature of the stellarator field. The only restriction on such harmonics is that they be of rather low order, i.e. $m, \ell \ll N$.

Given the density and temperature ranges at which Wendelstein VII-X is expected to operate, the bulk plasma ions will find themselves in the long-mean-free-path or *collisionless* regime. In other words, the bounce frequency of ions trapped in modular ripple wells, $\omega_\delta \approx \sqrt{\delta} v_{th} N p/(2\pi R)$, is much greater than the frequency with which particles are collisionally removed from such wells, $\nu_{eff} = \nu/\delta$. As this is the case, the longitudinal adiabatic invariant, $J = \oint m v_\parallel \, dl$, is a constant of a trapped particle's motion and equation (1) may be simplified by application of the bounce-averaging operator, $\oint dl/v_\parallel$.

The resulting bounce-averaged kinetic equation is then solved in lowest non-trivial order by expanding the distribution function in terms of a local Maxwellian, F_M, and a perturbation term, f. Finally, the ratio of $\dot{\theta}_0/\nu_{eff}$ is assumed to be small, an assumption valid for all but the most energetic ions given the expected plasma parameters of Wendelstein VII-X. With the above assumptions, the kinetic equation to be solved is

$$\frac{1}{qB_0 r}\frac{\partial B}{\partial \theta_0}\frac{\partial F_M}{\partial r}\frac{\partial}{\partial \mu}(\mu J) = \nu \frac{\partial}{\partial \mu}\left(\mu J \frac{\partial f}{\partial \mu}\right) . \tag{3}$$

The form of equation (3) is made possible since particles trapped in modular ripple wells have very low parallel velocity and hence $\dot{r} \approx -(\mu/qB_0 r)(\partial B/\partial \theta_0)$ and $(\partial/\partial \mu)(\mu J) \approx -\oint (\mu B/v_\parallel) dl$. One may then solve equation (3) in the regions of phase space where local modular ripple wells exist (i.e. the range of μ values which satisfy $\kappa/B_{max} < \mu < \kappa/B_{min}$, with $\kappa = mv^2/2$ and B_{min}, B_{max} the local minimum and maximum values of B which define the ripple well) with the boundary conditions that $\partial f/\partial \mu$ be finite in the region of solution and that $f = 0$ for non-ripple-trapped particles. The solution for f is

$$f = \frac{1}{qB_0 r}\frac{\partial B}{\partial \theta_0}\frac{\partial F_M}{\partial r}\frac{(\mu - \kappa/B_{max})}{\nu} , \tag{4}$$

and the associated particle flux is given by

$$\Gamma_\delta = \frac{1}{\pi (2m^3)^{1/2}} \int d\theta_0 \int d\phi \int d\kappa \int d\mu \, \frac{B}{\sqrt{\kappa - \mu B}} \dot{r} f . \tag{5}$$

Carrying out the μ integration, the particle flux may be written in the form $\Gamma_\delta = A_\delta(\theta_0, \phi) W(\kappa)$, where

$$A_\delta(\theta_0, \phi) = \frac{2\sqrt{2}}{15\pi} \int_0^{2\pi} d\theta_0 \int_0^{2\pi} d\phi \left(\frac{1}{B\epsilon_t}\frac{\partial B}{\partial \theta_0}\right)^2 (1 - B/B_{max})^{3/2}(4 + B/B_{max}) , \tag{6}$$

where $\epsilon_t = r/R_0$ is the inverse aspect ratio of the given flux surface. The quantity

$A_\delta(\theta_0, \phi)$ contains all information relating to the magnetic field structure and is thus a convenient quantity to use in describing the neoclassical transport characteristics of a given device.

A general analytic solution of equation (6) is impossible given the very complicated magnetic field geometry introduced by equation (2). Difficulties appear not only in the expression for B itself, but also in the accompanying deformation of individual modular ripples, greatly complicating any analytic expression for B_{max}. An expression very similar to equation (6) has been analytically evaluated by several authors for rippled tokamaks in limiting cases for simple magnetic field profiles [2-4]; in the general case, these authors resorted to numerical integration. The latter approach will also be adopted here, except that no analytic form for B_{max} will be derived or assumed. Instead, for each point on a flux surface, the condition $\partial B/\partial \phi = 0$ along a field line is *numerically* solved to determine whether a local modular ripple well exists at that point, and if so, what the local value of B_{max} is.

The approach described above is used to compare the level of neoclassical transport due to particles trapped in the modular ripple with that due to particles trapped in the stellarator's *helical* ripple. The comparison will be made for the Wendelstein VII-X candidate designated HS5-7, a five field period Helias with rotational transform varying from $\iota = .76$ on axis to $\iota = .96$ at the plasma edge. The principal Fourier harmonics of the HS5-7 magnetic field, shown in Figure 1, place this configuration in the class of *transport-optimized* stellarators [5]. As such, the geometrical factor A_h which characterizes *helical* ripple transport is greatly reduced

$$A_h \approx \frac{64}{9}\epsilon_h^{3/2}\left(\frac{C_{0,1}}{\epsilon_t}\right)^2\left\{1 - \frac{6}{5}\frac{\sigma\epsilon_h}{C_{0,1}} + 0.385\left(\frac{\sigma\epsilon_h}{C_{0,1}}\right)^2\right\}, \tag{7}$$

where ϵ_h and σ are averages over the magnitudes of the various magnetic-field harmonics. (For the simplest model stellarator field, ϵ_h is identified with the magnitude of the helical ripple, $\sigma = 0$, $C_{0,1} = \epsilon_t$ and thus $A_h = 64\epsilon_h^{3/2}/9$.)

It is possible to realize the magnetic field of HS5-7 (or any other Helias) through a number of different modular coil configurations, differing in the number of discrete coils per field period, N. The principal magnetic-field harmonics are essentially identical in these various cases, only the magnitude of the modular ripple, δ, and its periodicity are effected. Large values of N reduce δ significantly but also greatly limit experimental access to the plasma. Ideally, the value of N should be as small as possible to maximize access, but also large enough to insure that modular-ripple transport does not spoil the optimization represented by equation (7).

The HS5-7 configuration is currently being considered in $N = 10$ and $N = 12$ versions. The relative magnitude of the modular ripple in each case is indicated by the dashed lines in Figure 1. The ratio of A_δ/A_h is also calculated in the two cases as a function of plasma radius and presented in Figure 2. The $N = 10$ version shows values of this ratio considerably in excess of one near the plasma edge. On the other hand, the ratio of $A_\delta/A_h < 1$ at all radii for the $N = 12$ version of HS5-7. As this latter version also allows sufficient plasma access, 12 coils per field period is deemed to be the optimum value for HS5-7.

REFERENCES

[1] A.H. Boozer and G. Kuo-Petravic, **Phys. Fluids, 24**, (1981) 851.
[2] T.E. Stringer, **Nuclear Fusion, 12**, (1972) 689.
[3] J.W. Connor and R.J. Hastie, **Nuclear Fusion, 13**, (1973) 221.
[4] R.J. Goldston and H.H. Towner, **Nuclear Fusion, 20**, (1980) 781.
[5] H.E. Mynick, T.K. Chu and A.H. Boozer, **Phys. Rev. Lett., 48**, (1982) 322.

FIGURE CAPTIONS

FIGURE 1. Fourier components of the HS5-7 magnetic field are plotted vs. normalized radius. The magnitude of the *modular* ripple appears as the dashed line for configurations with both 10 and 12 modular coils per field period.

FIGURE 2. Ratio of A_δ/A_h vs. normalized radius for the Wendelstein VII-X candidate HS5-7. Results are presented for configurations with both 10 and 12 modular coils per field period.

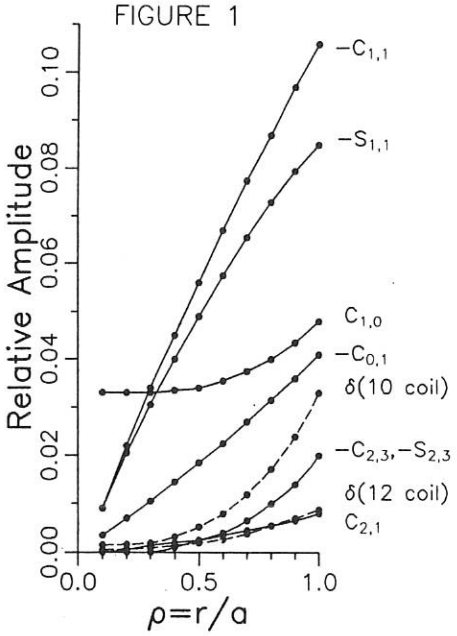

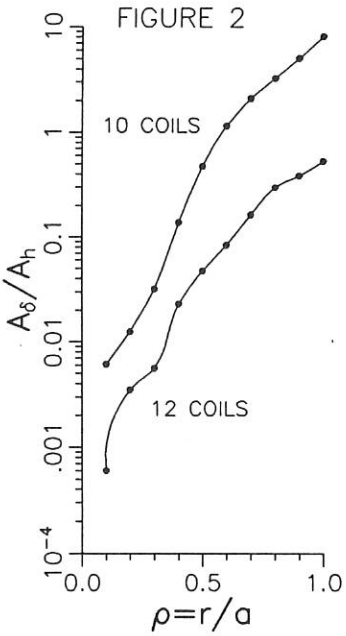

ON BOOTSTRAP CURRENTS IN HELIAS CONFIGURATIONS

C. Beidler, E. Harmeyer, F. Herrnegger, J. Kißlinger, H. Maaßberg, A. Montvai*,
F. Rau , R. Scardovelli and H. Wobig ,
Max–Planck Institut für Plasmaphysik, D–8046 Garching, FRG,
EURATOM–Association.
* Guest from: Central Res. Inst. for Physics, H–1525 Budapest, Hungary.

A Introduction. Neoclassical bootstrap currents cause severe problems in stellarators since the profile of the rotational transform is modified with increasing plasma pressure. This effect has been observed in the experiments, particularly in *Wendelstein VII-A* and *Wendelstein VII-AS*, where shear is low and with small changes of the rotational transform low order rational magnetic surfaces arise and confinement tends to deteriorate. Therefore, in future stellarators neoclassical bootstrap currents should be avoided by proper shaping of the magnetic surfaces. As has been shown by Shaing and Callen [1] bootstrap currents in stellarators can be made small by the counteracting effect of toroidal curvature and helical stellarator fields. In quasi-helically symmetric stellarators [2] bootstrap currents flow opposite to those in axisymmetric configurations, however, they are smaller than these. A certain deviation from symmetry seems to be necessary for achieving small bootstrap currents. The present paper discusses analytic theory relating bootstrap currents to neoclassical radial losses and presents some results of numerical calculations based on the DKES-code [3] .

B Analytic theory . Bootstrap currents are the result of parallel momentum balance on every magnetic surface. Particle drifts in the magnetic field lead to a distortion of the distribution function $f(v_{\|})$ and a deviation from the Maxwellian which is balanced by collisions. In the macroscopic picture this leads to tangential forces in the magnetic surface described by the anisotropic part of the pressure tensor. The momentum balance and the resulting flux-friction relations [4] have been widely used in literature to express the bootstrap current in terms of these tangential forces or so-called parallel viscosity. The flux-friction relations also contain radial plasma losses consisting of Pfirsch-Schlüter fluxes and neoclassical fluxes and therefore these equations provide a correlation between bootstrap currents and neoclassical radial losses. Such a relation has already been found by Bickerton et al. [5] for tokamaks. In [6] this proportionality between currents and fluxes has been extended to helically symmetric and quasi-helically symmetric stellarator configurations and yields

$$\eta < B^2 > I'(\psi) = C(\psi)\,(\iota - \gamma_\omega)\{\frac{\Gamma_{neo}}{N} + 0.32\,\frac{q_{e,neo}}{NT_e}\}. \qquad (1)$$

$I'(\psi)\,d\psi$ is the differential toroidal current on a magnetic surface ψ= const, η = Spitzer resistivity, ι = rotatitional transform, γ_ω = slope of the invariant direction. $\Gamma_{neo}, q_{e,neo}$

= neoclassical particle flux and electron thermal flux. $C(\psi)$ is a positive constant on the magnetic surface. Tokamak results are obtained by setting $\gamma_\omega = 0$. Equation (1) can be generalized to an arbitrary non-symmetric stellarator, in that case the coefficient $C(\psi)$ can be of either sign and the exact value has to be found from kinetic theory. Details are given in [6] .

C Quasi-helically invariant configurations . These are characterized by the magnetic field being a function of one variable $\theta - \gamma_\omega \phi$ alone (θ, ϕ = poloidal and toroidal magnetic coordinates). Since particle orbits in magnetic coordinates and consequently neoclassical effects are only determined by $B(\theta, \phi)$ and not by the shape of the magnetic surfaces, this implies, that neoclassical tokamak theory can easily be transferred to helically symmetric or quasi-helically symmetric configurations. This isomorphism has been pointed out in [7]. Based on this similarity and Eq.(1) the bootstrap current and the resulting shift of ι are evaluated for helically invariant configurations. The neoclassical fluxes are taken from ref. [8]. In the long-mean-free-path regime, where bootstrap current is largest, this leads to a total current

$$I \approx I_o \beta(0) (R/a)^2 \sqrt{\epsilon} \frac{0.3}{\iota - \gamma_\omega}. \qquad (2)$$

$I_o = 2\pi a^2 B/\mu_o R$ is a reference current with $\iota = 1$, a = av. plasma radius, $\sqrt{\epsilon}$ = number of trapped particles. In extrapolating this to a quasi-helically invariant Helias configuration with R = 6.5 m, a = 0.6 m, B = 2.5 T, $\iota = 0.85$, $\gamma_\omega = 5$ and n(0) = $10^{20}\mathrm{m}^{-3}$ the bootstrap current is 300 kA at $T_e(0) = 8$ keV. The corresponding shift of the rotational transform is $\delta\iota$ = -(0.25 -0.3) depending on the plasma profiles. Eq. (2) says that the bootstrap current in helically invariant stellarators is negative and smaller than the current in a tokamak with the same aspect ratio, the factor is $\iota/(\iota - \gamma_\omega)$.

D Non-symmetric stellarators . The shift of ι in helically invariant stellarators is still too large to be tolerable and therefore a superposition of several helical harmonics, leading to a small deviation from helical symmetry, may be necessary to reduce the bootstrap current further. In realistic Helias configurations (see [9]) the magnetic field

$$B = B_o \{ \sum_{m,n=0} C_{n,m} \cos(n\phi) \cos(m\theta) + S_{n,m} \sin(n\phi) \sin(m\theta) \} \qquad (3)$$

not only contains the dominating helical harmonic $C_{1,1}$ and $S_{1,1}$, but also the toroidal term $C_{0,1}$ and higher harmonics. In [9] an example of a five-period Helias configuration and the spectrum of B is given. The geometrical bootstrap factor $G_b f_f/f_c$ [10] , which determines the bootstrap factor in the $lmfp$-regime has been computed for various Helias configurations. For comparison, this factor is normalized to an axisymmetric configuration with the same rotational transform and the same aspect ratio. Fig. 1 shows the bootstrap factor for various Helias configurations with the magnetic field generated by coils. The case HS-5-8A is described in [9] . As can be seen, the bootstrap factor ranges between -0.1 and +0.1, which means that the bootstrap current is smaller

than 1/10 of the current in an equivalent tokamak. The dominant terms in $B(\theta,\phi)$ responsible for the bootstrap current are $C_{1,1}, S_{1,1}$ and $C_{0,1}$. The value of $C_{0,1}$ needed to compensate for the current of the helical harmonics $C_{1,1}$ and $S_{1,1}$ is roughly $|C_{0,1}| \approx 0.3 \cdot |S_{1,1}| or |C_{1,1}|$. The case HS-5081 is nearly quasi-helically invariant, symmetry-breaking terms are $C_{0,1}$ and $C_{2,2}$. Here, a toroidal term $|C_{0,1}| \approx 0.18 \cdot |C_{1,1}|$ is sufficient to reduce $G_b\, f_t/f_c$ to -0.1, without these term we find $C_b\, f_t/f_c = -(0.24 - 0.3)$.

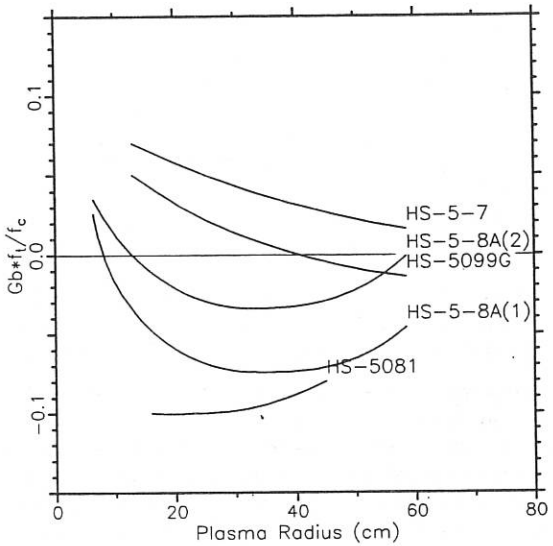

Fig. 1 *Normalized bootstrap factor $G_b\, f_t/f_c$ vs plasma radius for several 5-period Helias configurations. The configuration HS-5-8 is described in ref. [9]*

E Results of numerical calculations. Using the DKES-code [3] the coefficient of the bootstrap current can be calculated for all regimes of collisionality. This code solves the drift-kinetic equation and yields the whole transport matrix D_{ik} with the non-diagonal term D_{31} being the relevant coefficient. Numerical results of Helias configurations show negative bootstrap currents in nearly quasi-helically invariant cases (HS-5081). Fig. 2 shows the result in comparison with the coefficient of the equivalent axisymmetric case. The factor D_{31} is smaller than in the axisymmetric case, however it exhibits a strong dependence on the collisionality ν^* and the radial electric field. In the *lmfp*-regime the coefficient D_{31} changes from negative to positive, this cross-over point, however, depends on the particular magnetic surface and on the radial electric field. This feature complicates the comparison with the *lmfp*-limit G_b. A similar behaviour was also found in the other configurations listed in Fig. 1.

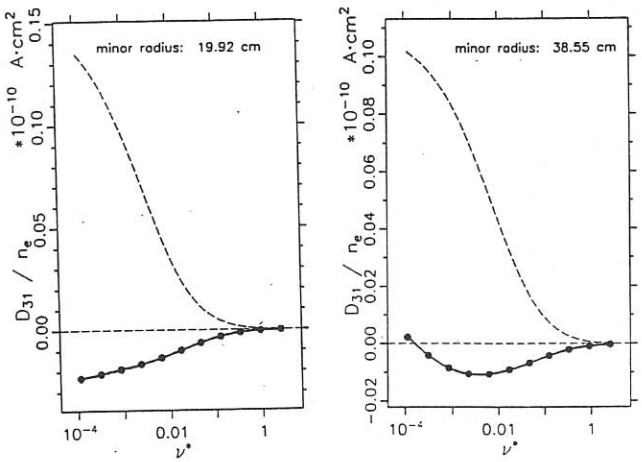

Fig. 2 *Bootstrap coefficient D_{31}/n of the Helias configuration HS-5081 vs collisionality (solid line). Broken line: equivalent axisymmetric configuration. Electric field E=0. Plasma parameter: B=3 T, T_e=2 keV, ι=0.89.*

F Summary and conclusions. Bootstrap currents in optimized Helias configurations have been computed by various methods. In 5-period configurations the current is about a factor 10 smaller than in the equivalent axisymmetric case. This low value may be acceptable in stellarator experiments, however, it is found that bootstrap currents depend sensitively on the Fourier spectrum of the magnetic field and therefore accurate calculations are required. Evaluation of the G_b-factor shows that a toroidal $C_{0,1}$-term of the order $0.3 \cdot |C_{1,1}|$ is needed for sufficiently small bootstrap currents, however, results from the DKES-code show that the size of the current also depends critically on the radial electric field and the collisionality.

REFERENCES

[1] K.C. Shaing, J.D. Callen *Phys. Fluids* **26** (1983) 3315
[2] J. Nührenberg, R. Zille, *Phys. Letters* A **129**(1988)113
[3] S.P. Hirshman et al. *Report ORNL/TM-9925*, April 1986
[4] S.P. Hirshman, D.J. Sigmar *Nucl. Fusion* **21** (1981) 1079
[5] R.J. Bickerton, J.W. Connor and J.B. Taylor *Nat. Phys. Sci.* **225** 110 (1971)
[6] H. Wobig, *Report IPP 2/297*, October 1988
[7] A.H. Boozer, *Phys. Fluids* **26**(1983) 496
[8] M.N. Rosenbluth, R.D. Hazeltine and F.L. Hinton, *Phys. Fluids* **15** (1972), 116
[9] C. Beidler et al. *paper P2B5 of this conference*
[10]T.S. Ohkawa, M.S. Shu, *Report GA-A18688* Nov. 1986

TRANSPORT MODELING OF ECH AND NEUTRAL-BEAM-HEATED PLASMAS IN THE ADVANCED TOROIDAL FACILITY

H. C. Howe, L. D. Horton, E. C. Crume, J. H. Harris, R. C. Isler,
J. B. Wilgen, and W. R. Wing

Fusion Energy Division, Oak Ridge National Laboratory
Oak Ridge, TN 37831
U.S.A.

INTRODUCTION

Results of time-dependent transport modeling of the ATF plasmas are compared with a typical ungettered, neutral-beam-heated discharge. A summary of ATF machine parameters is given by Murakami et al. [1]. The model is adjusted to give agreement between measured diagnostics signals and the corresponding values inferred from the model plasma. With this agreement, the model reproduces the main features of the discharge, including the radiation-induced temperature collapse.

MODEL

The discharges are modeled with the predictive transport code PROCTR [2], which evolves radial plasma profiles in time in the full 3D ATF geometry. Models are included for the plasma temperatures T_e and T_i, the plasma hydrogenic-ion density, and the toroidal current. In addition, a multi-charge-state impurity transport model [3], which includes radial transport and ionization and recombination between the various charge states, is used for carbon and oxygen. Neoclassical heat transport including transport due to the helical ripple [4] is assumed for both electrons (χ_e) and ions (χ_i) with a large anomalous enhancement in the outer half of the plasma (in the region $+ > 1/2$) to reproduce the narrow observed T_e profile shape [1]. This enhancement is attributed to magnetic islands due to field errors, the cause of which has been identified and is being corrected. Hydrogenic-ion and impurity diffusion are treated with a radially constant diffusion coefficient of 0.2-0.5 m^2/s with a large enhancement for $+ > 1/2$. An inward pinch is included in the impurity transport. Electron cyclotron heating (ECH) is treated using a linear-absorption, multi-pass model [5] including cutoff (for $n_e > 1.8 \times 10^{13}$ cm^{-3} in ATF). Neutral-injection heating is given by an axisymmetric neutral deposition model plus thermalization governed by a moments solution of the fast-ion Fokker-Planck equation including fast-ion loss due to charge-exchange during slowing down. Thermal neutral transport uses a cylindrical model [6] where the neutral level is determined by recycling and external fueling.

ECH PLASMA

Approximately steady-state plasmas are obtained with 200 kW of second harmonic ECH in ATF. Measured Thomson scattering T_e profiles, spectroscopic T_i values, stored energy, and spectroscopic emission levels may be reproduced using the model described

above when the impurity source rates are adjusted to give impurity levels corresponding to $Z_{eff} \approx 2$-2.5. The power balance for the ECH plasmas indicates that electron (35%) and neoclassical ion (20%) heat conduction are the largest energy losses from the plasma core with neoclassical electron heat conduction accounting for more than 50% of the total electron conduction loss. The total radiated power in the model is approximately 40% to 50% of the heating power, in agreement with spectroscopic estimates, and originates primarily from the outer regions of the plasma.

NEUTRAL-BEAM-HEATED PLASMA

Neutral-beam-injection (NBI) heated discharges exhibit dynamic behavior and do not reach a steady state in ATF experiments. During NBI heating with 650 kW of co-injection, the density ramps up nearly linearly from the value obtained in the ECH phase of the discharge (see Fig. 1). This ramp is obtained in the model by a combination of beam fueling and an external gas source, which is similar in magnitude to the gas puff introduced in the experiment. At the same time, the stored energy (Fig. 2) and plasma ion temperature rise to a peak and then fall to a low value while the electron temperature decreases monotonically from the ECH-phase value (after a small initial rise in some discharges). See Isler et al. [7] for a summary of these data. These features of the data are all reproduced by the model. Near the end of the stored-energy decrease, the spectroscopic line emission from intermediate charge states of light impurities (C, O, N) disappears due to collapse of the plasma electron temperature. This sudden collapse is reproduced in the model (see Figs. 3 and 4) when the impurity source rates are adjusted so that the predicted spectral line-integrated intensities agree with the measured intensities for spectral lines emitted from the plasma interior. This agreement occurs for $Z_{eff} \approx 2$, indicating a rise in impurity content that is approximately proportional to the rise in electron density. The unstable nature of the collapse is due in the model to the strong increase in impurity line radiation at low plasma electron temperatures ($T_e < 100$ eV). The T_e profile collapses inward from the edge as large radiation from the outer region of the plasma progressively cools adjacent interior plasma until all the stored energy has been radiated in a brief (5 - 10 ms) burst of radiation. The collapse has been simulated successfully only with the observed narrow T_e profiles, which allow the lower impurity ionization states to penetrate the outer half of the plasma, resulting in a large radiating volume. The collapse may be initiated in the model either when the plasma density reaches ECH cutoff (in ECH-only discharges) or when the total radiation exceeds the full heating power.

At the time of collapse, the model electron density shows a change in slope from an upward ramp to a slow decrease (Fig. 1). The decrease is due, in the model, to a large reduction in the ionization rate of neutrals by plasma electrons, which results from the low plasma electron temperature. Without an ionization source, the plasma density decays by cross-field diffusion. The saturation of the experimental plasma density just before the collapse is most likely due to a decrease in plasma recycling as the plasma temperature profile contracts and detaches from the wall. A similar reduction in impurity influx just before collapse would also be inferred from the detachment. This effect has not yet been

included in the model.

The model time-dependent global power balance (Fig. 5) illustrates the transient nature of neutral-injection-heated discharges. The density of the ECH discharge is adjusted in the experiment so that the central electron density is just below the wave cutoff density; thus, the ECH is cut off almost immediately by the density rise induced by NBI. The neutral-beam electron heating increases continuously during the heating pulse as the shine-through and fast-ion charge-exchange losses decrease due to the rising plasma density. The radiation also rises during injection (as a result of increased impurity influx in the model) and eventually surpasses the heating power, resulting in the temperature collapse. At the peak of the stored energy, the simulation indicates that approximately 50% of the heating power is being radiated (from the outer regions of the plasma) but this ratio is a strongly increasing function of time. The primary energy loss from the plasma core at the time of the stored-energy peak is electron (25%) and neoclassical ion (40%) heat conduction with neoclassical electron heat conduction accounting for less than 50% of the total electron conduction loss.

The plasma current also rises to a peak and then decreases to a small value at the time of collapse (see Fig. 6). The small current present during the ECH phase of the discharge may be a bootstrap current, which is not included in the model. The current during the neutral-beam phase is approximately reproduced in the model by the beam-driven current plus the induced plasma current. The current decreases after reaching a peak because of the decreasing plasma electron temperature and resulting decreasing fast-ion slowing-down time.

ACKNOWLEDGEMENT

Work sponsored by the Office of Fusion Energy, U. S. Department of Energy, under contract DE-AC05-84OR21400 with Martin Marietta Energy Systems Inc.

REFERENCES

[1] M. Murakami et al., this Conference (paper O7B1).

[2] H. C. Howe, Technical Report ORNL/TM-9537, Martin Marietta Energy Systems, Oak Ridge Natl. Lab., 1985.

[3] K. Behringer, Report JET-R(87)08, JET Joint Undertaking, Abingdon, Oxon, UK, 1987.

[4] D. E. Hastings, W. A. Houlberg and K. C. Shaing, Nucl. Fusion, **25**, 445, 1985.

[5] R. C. Goldfinger and D. B. Batchelor, in *Applications of radio-frequency power to plasmas*, pages 65-68, American Institute of Physics, 1987.

[6] K. Burrell, Journal of Comp. Physics, **27**, 88, 1978.

[7] R. C. Isler et al., this Conference (paper P8B1).

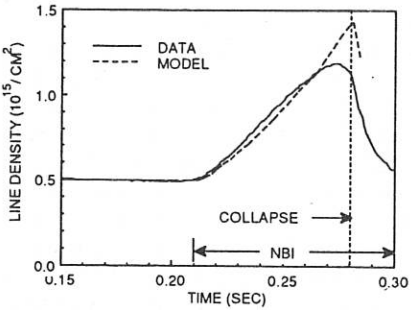

FIGURE 1 LINE-INTEGRATED DENSITY

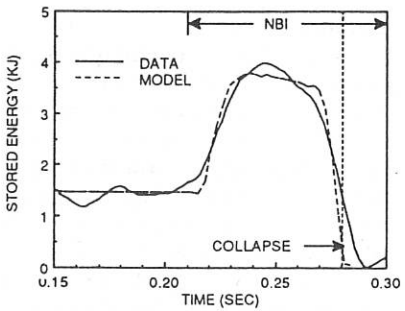

FIGURE 2 DIAMAGNETIC STORED ENERGY

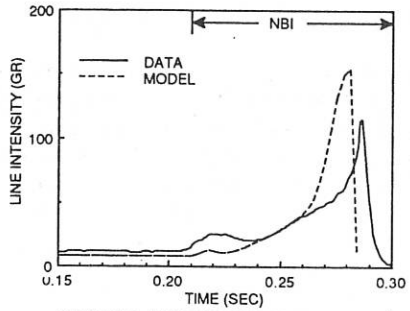

FIGURE 3 LINE INTENSITY FOR OV 760Å

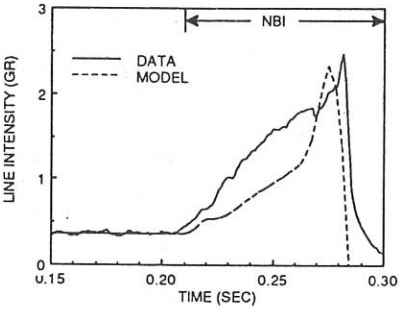

FIGURE 4 LINE INTENSITY FOR CIV 312Å

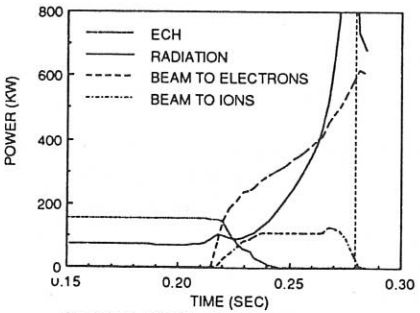

FIGURE 5 SIMULATED POWER BALANCE

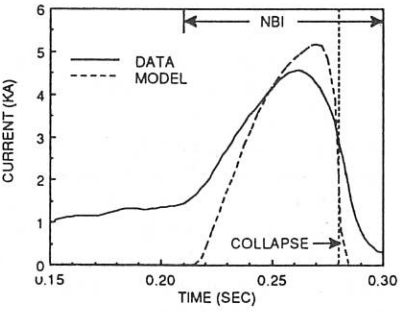

FIGURE 6 TOROIDAL PLASMA CURRENT

EQUILIBRIUM BASED ITERATIVE TOMOGRAPHY TECHNIQUE FOR SOFT-X-RAY IN W7A STELLARATOR.

A.P. Navarro, M.A. Ochando
Asociacion EURATOM / CIEMAT, 28040 Madrid, ESPAÑA
A. Weller
Max Planck Institut für Plasmaphysik, EURATOM Association, Garching, RFG

INTRODUCTION

Several algorithms have been developed for X-Ray tomography in plasmas and applied to the determination of local emissivity distribution at times of particular interest in the discharge, (sawteeth, MHD perturbations, disruptions, etc.) [1, and references there in]. Some of these techniques are based on numerical iterative techniques in order to avoid assumptions on emissivity spatial modal structure . They are able to determine any type of structures even those with very localized perturbations, that would required a great number of harmonics, and subsequently a larger amount of detector arrays, in any modal analysis [2]. Iterative numerical techniques have two main drawbacks: high computer time consumption and possibility of non-real solutions.Trying to avoid them, an iterative method, that uses as initial weights magnetic flux values derived from equilibrium calculations, has been developed. This technique can be applied to any plasma shape and even be used as a "modified Abel Inversion" when analyzing single array signals. Application using signals from a 30 detector array, have been made for NBI discharges in W7A stellarator, and the obtained reconstructions of local Soft-X-Ray emissivity are compared with theoretical estimations.

FUNDAMENTALS

Signal at one detector, (impact parameter ρ_i), in a particular array, (poloidal position δ_n) can be expressed as:

$$S(\delta_n, \rho_i) = \sum_{j=1}^{NX} \sum_{k=1}^{NY} E_0(x_j, y_k) \cdot M(n, i, j, k) \qquad (1)$$

where $E_0(x_j, y_k)$ is the local emissivity value of cell (j, k) and M(n, i, j, k) gives the contribution from that cell to that detector signal. NX, NY are the grid dimensions . Local emissivity values could be deduced from (1) by inverting M matrix but, due to its dimensions, an approximate procedure must be used.

The approach taken in this technique (EBITA : Equilibrium Based Iterative Tomography Algorithm) is to divide each detector signal between the different cells along the line of sight, weighting the process with the values of the magnetic flux, deduced from equilibrium calculation for the configuration, at each cell. Local emissivity is deduced as:

$$E(x_j, y_k) = \frac{W(j,k)}{NC(j,k)} \sum_{n=1}^{NA} \sum_{i=1}^{ND} S(\delta_n, \rho_i) \cdot \frac{M(n,i,j,k)}{WN(n,i)} \qquad (2)$$

where W is the weight matrix, WN is the weight normalization factor for each line of sight and NC the number of contributions of each cell to different detector signals. NA is the number of arrays, each one with ND detectors.

Using at expression (1) the emissivity values deduced with (2) it is possible to reconstruct the detectors signals: $SR(\delta_n,\rho_i)$. Comparison between these signals and the real values provides an estimation of the error of the inversion:

$$Er(it) = \frac{1}{ST}\left[\sum_{n=1}^{NA} \sum_{i=1}^{ND} (S(\delta_n, \rho_i) - SR(\delta_n, \rho_i))^2\right]^{\frac{1}{2}} \qquad (3)$$

where ST is the total detected signals:

$$ST = \left[\sum_{n=1}^{NA} \sum_{i=1}^{ND} (S(\delta_n, \rho_i)\right] \qquad (4)$$

Following iterations can be made by substituting the weight at each cell by the local emissivity deduced in the previous iterations. Evolution of Er(it) will measure the procedure convergence. This method has been checked for different plasma shapes. Fig. 1 shows results when applied to a triangular one, as expected at some toroidal locations in W7AS

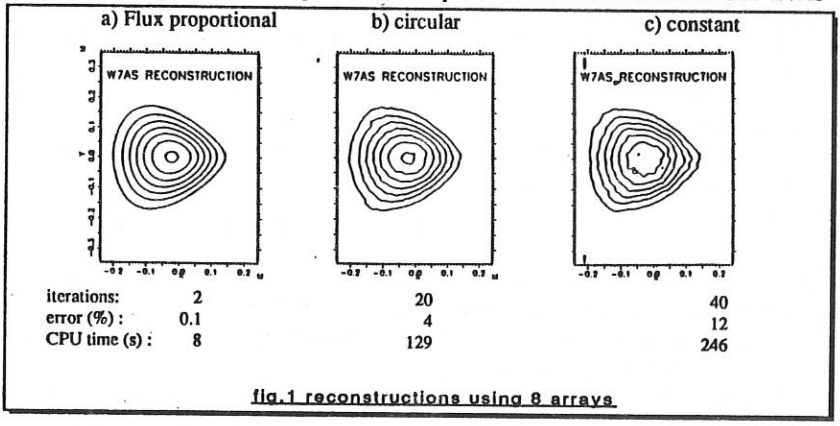

fig.1 reconstructions using 8 arrays

stellarator. Eight arrays have been used in these tests.

In cases like this with enough views it is possible to deduce the real distribution even with a wrong choice of initial weights. The only difference is the number of iterations and CPU time required. With adequate choice of initial weights even local perturbations and hollow profiles can be detected using as few as two arrays. (Fig.2).

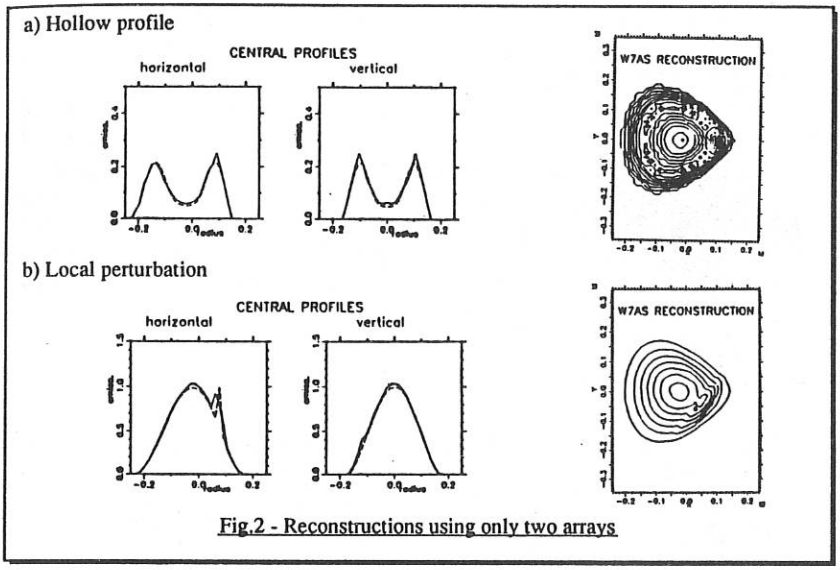

Fig.2 - Reconstructions using only two arrays

SINGLE ARRAY DATA INVERSION USING EBITA

Signals from single arrays can be inverted using EBITA by imposing an additional constraint in the iterative process: weight must be constant on the assumed equal emissivity contour shapes. This is done by averaging the emissivity obtained for those cells in the contour and using this averaged value as weight for the next iteration. The separation on each contour of this condition of equal emissivity can be defined as:

$$Ec(it) = \frac{1}{NC}\left[\sum_{j=1}^{NX}\sum_{k=1}^{NY}\frac{1}{NP(l)}\left(\frac{E(x_j, y_k) - \overline{E(l)}}{\overline{E(l)}}\right)^2\right]^{\frac{1}{2}} \qquad (5)$$

where NC is the total number of contours considered and NP(l) the number at contour l. The evolution of Ec(it) provides information about the goodness of the shape assumption to justify the obtained data.

APPLICATION TO W7A STELLARATOR

Fig. 3 shows the signal evolution in a 30 detector Soft-X-ray array located at a bottom port in the W7A stellarator, for a discharge with neutral beam injection during the interval 140 to 170 ms.

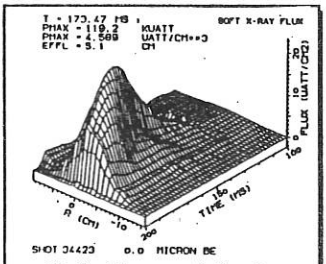

Fig.3 - X-ray evolution for W7A discharge

Assuming elliptical shape with 45° inclination for the equal emissivity contours, EBITA has been applied to the array signal profile at different times during the discharge. Fig.4 shows the evolution deduced with this technique for local emissivity during the whole shot. For each reconstruction there is indication of both errors, matching of the signals and contour shape validity defined by expressions (3) and (4).

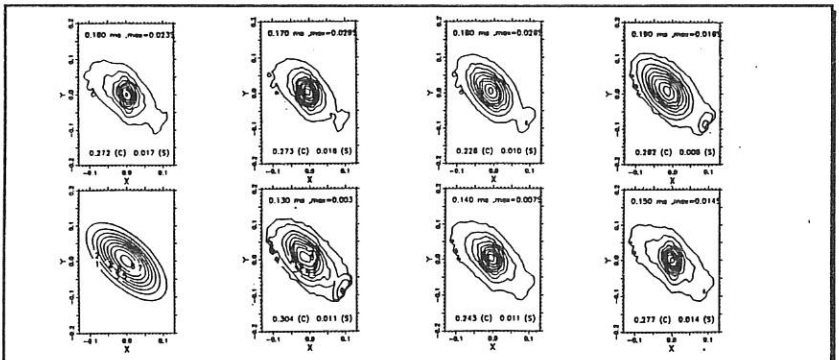
Fig. 4 - Local emissivity reconstruction for W7A discharge

REFERENCES

[1] R.S. Granetz and P. Smeulders, "X-Ray Tomography on JET", Report JET-P(87) 49.
[2] A. P. Navarro et al, Rev. Sci. Instr. 52 , 11, 1981.

BOLOMETRIC STUDIES OF PLASMA EDGE TURBULENCE. SIMULATION FOR THE TJ-II FLEXIBLE HELIAC

M.A.Ochando and A.P.Navarro
Asociacion EURATOM/CIEMAT
28040 Madrid, ESPAÑA

INTRODUCTION

Edge plasma turbulence seems to play an important role in energy and particle confinement in plasma devices [1, and references there in], and many experimental and theoretical studies are devoted to clarify and understand this role in tokamaks and stellarators. In the case of the TJ-II flexible heliac, a device aimed to the study of helical magnetic axis plasmas in a wide range of configurations [2], the turbulence level, and its influence on the confinement properties, for such wide operational space is an important part of the experimental programme. Fluctuations in basic plasma parameters, such as: electron density and temperature , floating potential and magnetic field, can be measured using standard diagnostic techniques. From these measurements particle and energy fluxes due to electrostatic and electromagnetic turbulence are deduced. Nevertheless, a direct measurement of the fluctuation effect on radiation losses would be very appreciated for the estimation of this effect on plasma energy confinement. To check the possibility of such direct measurements in TJ-II, simulations of radiation losses and the correspondent bolometer signals have been made when turbulence, modeled as a random superposition of high poloidal number, is present at the plasma edge.

TURBULENCE SIMULATION

Plasma edge turbulence is simulated by a superposition , with random phases, of magnetic islands with high poloidal number, (m in the range 10 to 40). Additional assumption is to consider a flattening, to the value corresponding to the resonance surface radius, of electron density inside the island:

$$n_e(r, \theta, t) = n_e(r_{sm}, \theta, t) \qquad \text{if } |r - r_{sm}| \le \Delta_m \qquad (1)$$

$$\Delta_m = a_m \cos(\omega_m t + m\theta + \varphi_m(t)) \qquad (2)$$

where a_m, ω_m and φ_m are the island width, rotation frequency and phase, respectively. Non-rigid rotation has been assumed with the same observed frequency for all the modes. No effect on electron temperature is either considered in order to impose the most strict scenario for the detector requirements.

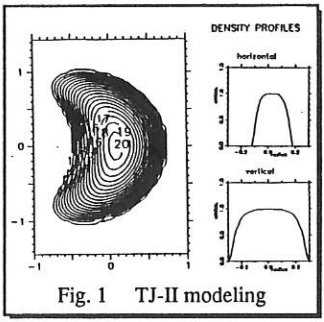

Fig. 1 TJ-II modeling

TJ-II is simulated by using the cylindrical model described in [3]. Electron density and temperature are deduced by assuming them constant on flux surfaces:

$$n_e = n_{eo}[(1 - \psi(\rho)/\psi(\rho_0)^{\alpha_1}]^{\alpha_2} \quad (3)$$

Fig.1 shows the TJ-II magnetic structure deduced with this model and the horizontal and vertical profiles obtained for $\alpha_1=\alpha_2=2$.

A turbulent layer at the TJ-II plasma edge, covering about 30% of the average plasma radius, has been simulated. Fig.2 presents the evolution of n_e contours

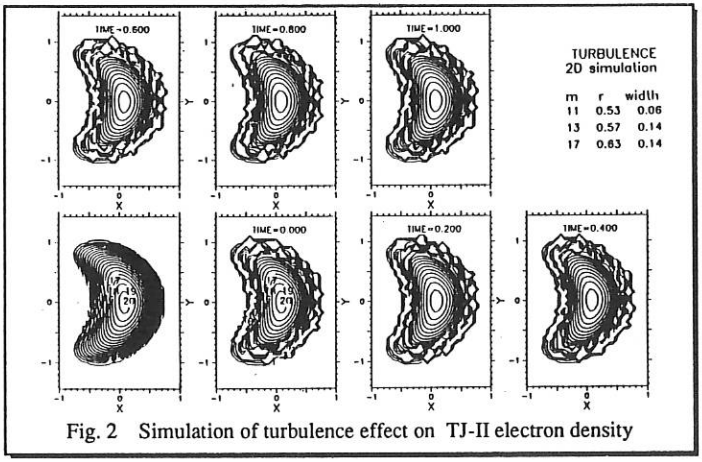

Fig. 2 Simulation of turbulence effect on TJ-II electron density

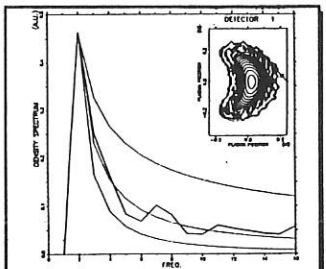

Fig. 3 $\tilde{n}_e$ spectrum

for the island structure indicated in the table inset at the figure. Fig.3 presents the frequency spectra for density fluctuations simulated with this model. They have a decay given by $A(\omega) = K\,\omega^{-1}$.

SIGNAL SIMULATION

Plasma losses are assumed due to the basic radiation processes: bremsstrahlung, recombination, synchrotron, H_α and charge exchange. Simulation of the signals produced by these losses in a 31 detector fan-like array, viewing a complete TJ-II poloidal cross section, has been made using the scheme developed at

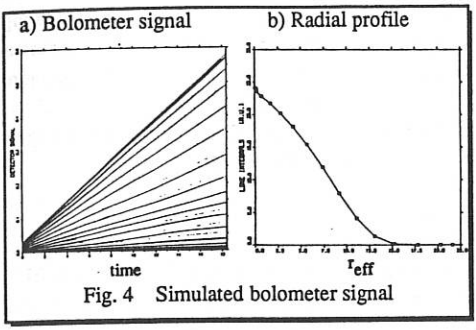

Fig. 4 Simulated bolometer signal

[4]. Detector response is assumed similar to that one from Ge bolometers used at W7A and W7AS stellarators [5], which have a very high sensitivity to temperature changes.

Typical simulated signals from these integral detectors are presented at fig. 4a. Dotted lines correspond to constant energy flux on the detector and solid ones to the case with turbulence present at the plasma edge. Fig. 4b shows the line integral radial profile, deduced from these signals for a particular time in the discharge. Effective radius, r_{eff}, defined as the radius of the equivalent circle to the contour surface tangential to the line of sight, is used in these plots in order to make possible any comparison between radial profiles obtained with detector arrays at different poloidal positions. Relationship between impact parameter and r_{eff} has been calculated numerically by following the line of sight of each detector and determining the innermost surface intersected. Fig. 5 presents the results for one array located at the equatorial midplane (▲-▲) and another at the bottom (□).

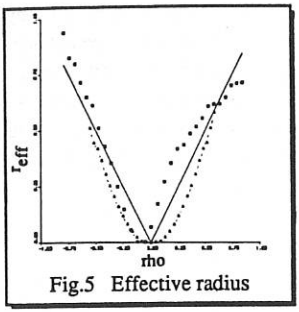

Fig.5 Effective radius

SIMULATION RESULTS

Time evolution of the array signal radial profile can be seen at fig. 6b. Superimposed it also appears the radial dependence of the amplitude, at the dominant frequency, in the frequency spectrum of each detector signal. (Lines of sight of each detector in the array are plotted at fig. 6a.)

As can be deduced from these results, radial profiles of spectrum amplitude are much more adequate to char-

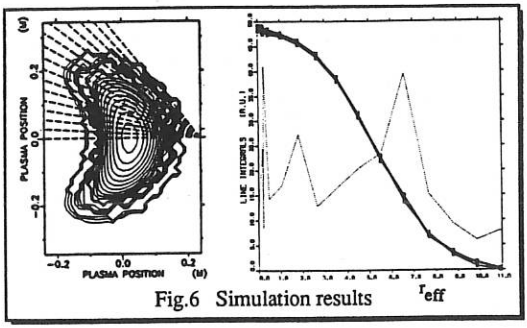

Fig.6 Simulation results

acterize edge turbulence than signal radial profiles, in which fluctuations are lower than 4%. The pronounced maximum at the outermost regions indicates the presence of a strong perturbation. The maxima at inner positions are explained by the effect of this perturbations in the signal of the detectors looking through the plasma center. This effect is more pronounced for D shaped plasmas than in circular ones and can facilitate the use of bolometers to characterize the edge turbulence because these central chords must have a higher signal level, relaxing so the requirements in signal to noise ratio value.

CONCLUSIONS

The input power in TJ-II at first operation stages will be about 200 kw so that the energy reaching detectors like above mentioned could be lower than 0.2 mw x ms. This means that only low frequency fluctuations in power losses (< 1 kHz) could be detected when high spatial resolution is wanted. Nevertheless, turbulence can be seen in a global way and only emission asymmetries from big plasma volumes could be determined by using wide angle detectors in the array. In a later operation stage, with the proyected neutral beam inyectors, heating powers of the order of Mw will be reached and therefore much higher electron density and temperature are expected, increasing noticeably the bolometer signals. Under these conditions, stronger fluctuations in the plasma energy losses would take place and edge turbulence with radial resolution should be detected with Ge bolometers.

REFERENCES

[1] P. Liewer, Nucl. Fusion **25**, 543, (1985)

[2] A.P. Navarro et al., Proc. IAEA Meeting on Plasma Confinement and Heating in Stellarators, EUR 9618 EN, Vol **II**, 563, (1984).

[3] J.H. Harris et al., Nucl. Fusion **25**, 623, (1985).

[4] M.A. Ochando, A.P. Navarro and J. Vega, IEEE Trans. on Plasma Science, in press.

[5] H.J. Jäckel et al., IPP Report 2 / 291, (1988).

PARTICLE ORBIT STUDIES AND THE STRUCTURE OF MAGNETIC FIELDS IN THE STOCHASTIC REGION OF HELICAL SYSTEMS

H. Akao, T. Watanabe† and Kyoji Nishikawa

Faculty of Science, Institute for Fusion Theory†
Hiroshima University, Japan

ABSTRACT

A new helical coil winding law is proposed which constructs preferable magnetic fields for plasma confinement, such as the deep well(12%), the large outermost magnetic surface, and the clean divertor configuration with long connection length. High accuracy codes are developed and the structure of the magnetic fields as well as particle orbits are investigated. It is found that the drift surface of the trapped particle becomes stochastic only in the outerside stochastic field region of the torus, while in the innerside, the trapped particle can form a drift surface even in the stochastic field region, which can improve the particle confinement. Particle orbits under strong rf fields are also investigated and good confinement performance for highly accelerated particles is shown.

1 New coil winding law

Although extensive studies have been carried out on the heliotron/torsatron type magnetic fields, no magnetic configuration with low aspect ratio has so far been reported that has the following characteristics simultaneously: deep well, large outermost magnetic surface, and good particle confinement. One of the reasons for this is that the outermost magnetic surface can hardly shift but diminishes its size by the control of the vertical field. It seems necessary for the current density in the outer part of the helical coil to be reduced so that the outermost magnetic surface may shift outward. Coil width modulation has been proposed as one method for this purpose. (ref. 1)

We propose a new simple winding law to realize the above situation for the $\ell=2$ heliotron/torsatron devices. In the winding law, the helical coil has a meridian cross section of rectangular shape which covers an area of constant size. The coil position and current density are simply given by

$$\begin{cases} x=(R-X\sin\theta+Y\cos\theta)\sin\phi \\ y=(R-X\sin\theta+Y\cos\theta)\cos\phi \\ z=\quad X\cos\theta+Y\sin\theta \end{cases}, \qquad J=\frac{I}{4ab}\left[1+\frac{X^2+Y^2}{(R-X\sin\theta+Y\cos\theta)^2}\cdot\left(\frac{d\theta}{d\phi}\right)^2\right]^{1/2}$$

where $I, R, \phi, \theta=\theta(\phi), a, b$ are the total current, the major radius, toroidal angle, poloidal angle, width of rectangular sides, respectively, and (X, Y) is the rotating Cartesian

coordinates on the meridian plane. For the function $\theta(\phi)$, we adopt either $\theta=m/\ell\cdot\phi$ (referred to as 'normal type' in this paper) or $\theta=m/\ell\cdot\phi+\alpha\cdot\sin(m/\ell\cdot\phi)$ ('pitch modulation type'). Moreover, we propose a 'split type' coil as another candidate which reduces the current density in the outer part of the coil more effectively. In this system, each helical coil is split into 2 coils on the meridian plane, where $\theta(\phi)$ for the split coil is given by

$$\theta_1=(m/\ell\cdot\phi+\Delta\theta)+\alpha\cdot\sin(m/\ell\cdot\phi+\Delta\theta),\ \theta_2=(m/\ell\cdot\phi-\Delta\theta)+\alpha\cdot\sin(m/\ell\cdot\phi-\Delta\theta)$$

We performed field-line tracing and particle orbit analysis, using Biot and Savart's formula and the 3D spline's interpolation code developed, which is particularly effective in the stochastic region, where high accuracy is required.

2 Magnetic Surfaces

We first show the characteristics of the magnetic surfaces. We utilized the values of the basic machine parameters for the LHS, and chose the toroidal pitch number m=10, the amplitude of pitch modulation α=0.2, and the clearance angle of split coils $\Delta\theta=\pi/6$.

In the normal type, the well depth ΔU=2.3% and the average minor radius of the outermost surface a_p=40cm when the magnetic axis is located at the center of the torus tube. In the pitch modulation type, ΔU=1.1% and a_p=44cm. As the magnetic axis shifts from the center, a_p decreases drastically in both the above types. While in the split type, outward shift of the magnetic axis can bring about the deep well (12%) as well as the large average minor radius a_p=54cm.

3 Stochastic field region

The so-called 'stochastic region' of the helical system consists of two regions. One is the quasi-stochastic layer caused by island overlapping near the outermost surface, and the other is the region of 'localized linear pattern' forming a divertor configuration near the wall, which can hardly be stochastic. In our analysis, the number of the linear patterns n depends on the rotational transform of the outermost surface ι_a, by the next relation

$$n=2\left[\frac{m}{\ell}\iota_a^{-1}-1\right]$$

As n increases, each linear pattern becomes thinner, so that low ι_a is preferable in

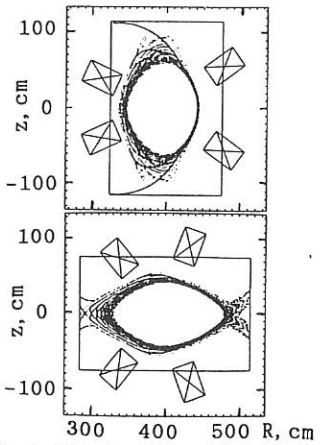

Fig. 1 Stochastic field of the split type.

terms of the buffle plate setup.

In the normal type (ϵ_A=10/12), some linear patterns cross the inner wall of the vacuum vessel. As is widely known, the pitch modulation type (ϵ_A=10/10) reduces the overall width of the linear pattern region; it increases, however, the width of the individual pattern. The split type (ϵ_A=10/20) has the most preferable divertor configuration made up of the thin linear patterns, and with small overall width. The connection length is about 100 toroidal turns for the quasi-stochastic region, and a few toroidal turns for the region of the localized linear patterns, regardless of the coil type.

4 Particle orbits

The existence has been noted of the loss region by the helical mirror trapped particles starting in the outer part of the torus. (ref. 2) It is shown that the split type coil does not cause confinement deterioration even by the positive pitch modulation, and has confinement performance almost comparable to the normal type.

In what follows, we present the results for the normal type which has the best particle confinement of the 3 types. We set the loss boundary on the vacuum vessel wall, and traced the drift orbits in the stochastic region. Figure 2(a) shows the typical velocity space loss region, where the initial location of particles is at 5cm inside of the outermost magnetic surface in the outer part of the torus. It is noted that the drift surface of a particle near this loss region is not stochastic (Fig. 3), even though it drifts in the stochastic region in the inner part of the torus. Particle loss occurs when the drift surface intersects the inner wall, as also seen from the loss position chart (Fig. 2(b)). Hence, the loss region can be reduced by

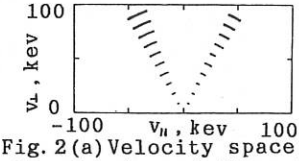

Fig. 2(a) Velocity space loss region of the outer part of the torus.

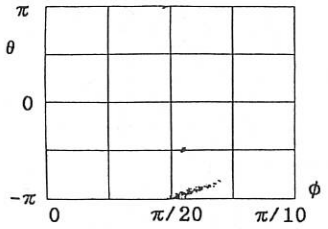

Fig. 2(b) Loss positions of the particles from the above loss region.

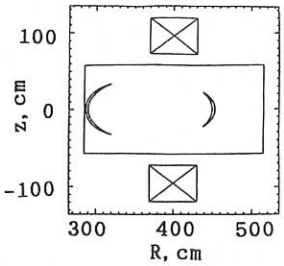

Fig. 3 Drift surface of a helical mirror trapped particle near the above loss region.

adjusting the inner wall position, provided the charge-exchange with neutral particles in that region hardly occurs. Actually, in the above example, the loss region in Figure 1 disappears by setting the inner wall position 15cm away from the present position.

Trapped particles starting in the stochastic region in the outer part of the torus is sensitive to the stochastic field structure (Fig. 4). These particles go out along the divertor field lines (Fig. 5).

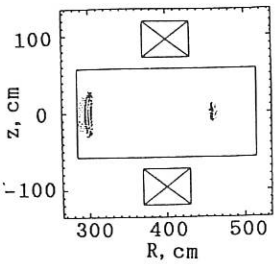

Fig. 4 Drift surface of a helical mirror trapped particle from the outerside stochastic region.

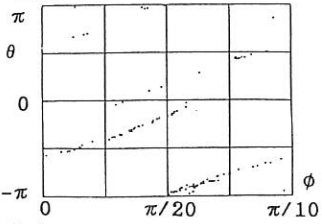

Fig. 5 Loss positions of the particles from the outerside stochastic region.

5 Rf acceleration

Figure 6 shows the particle acceleration process under a strong rf field along the z direction, where the rf frequency is chosen to be the ion cyclotron frequency for 4 tesla field; the amplitude is uniform and is 20kv/cm. The transit particle with 1kev initial energy is accelerated and converted into a 100kev trapped-detrapped particle. Some particles near the magnetic axis can be accelerated to 2 Mev. As for plasma heating, the above rf field is not realistic, for the plasma shields the electric field. It should be noted that under this rf field, the ponderomotive force plays no role in improving the particle confinement; high energy particles are confined by the magnetic field alone.

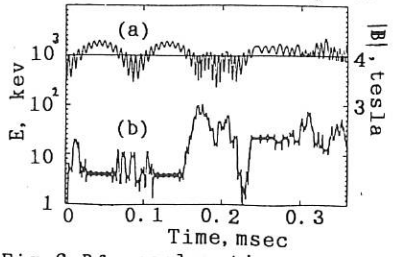

Fig. 6 Rf acceleration process of a 1kev particle
(a): |B| along the drift orbit
(b): energy of the particle

References

[1] M. Fujiwara and K. Nishimura: private communication.
[2] H. Sanuki, K. Hanatani and T. Kamimura: Proc. of US-Japan Workshop on New Generation Experiments and Reactors, Kyoto(1988), p55.

ON THE EDGE STRUCTURE OF A HELIAS CONFIGURATION

C. Beidler, E. Harmeyer, F. Herrnegger, J. Kißlinger, A. Montvai*, F. Rau ,
R. Scardovelli, and H. Wobig

Max–Planck Institut für Plasmaphysik, D–8046 Garching, FRG,
EURATOM–Association.

* Guest from: Central Res. Inst. for Physics, H–1525 Budapest, Hungary.

INTRODUCTION . The next step in the Garching stellarator programme, the experiment WENDELSTEIN VII-X, will use a Helias configuration (Helical Advanced Stellarator) with 5 field periods, aspect ratio about 10, major radius of 6.5 m, and magnetic fields up to 3 T. One of the aims of this optimized stellarator experiment is the operation at elevated average beta values of $\approx 5\%$. To reach this goal, a heating power of the order of 20 MW is necessary. This poses challenging tasks in application and removal, especially to attain a low level of impurities. The complex physics of the edge plasma, depending on internal transport processes and on effects at the plasma boundary, and the necessity of sufficient impurity control for long-pulse experiments call for knowledge of the edge structure of the magnetic topology. The edge structure is influenced by the value of the rotational transform, and by the shape of the first wall and/or the position of limiter(s). In the present investigation vacuum magnetic fields are used. This approach is justified since Helias systems have small changes of their magnetic surfaces and rotational transform profiles with beta.

VACUUM FIELD AND LIMITERS . For the present investigation the Helias system HS 5–7 is used. This configuration is similar to that described in [1], with the major difference that the edge value of the rotational transform is $\iota_a = 1$ with five associated magnetic islands, see Fig. 1 . One can anticipate to use such islands for plasma edge control. The separatrix region is 'ergodic' with some radial extension. Two tentative limiters, options A and B, are indicated in the left part of the figure: a bulged system on

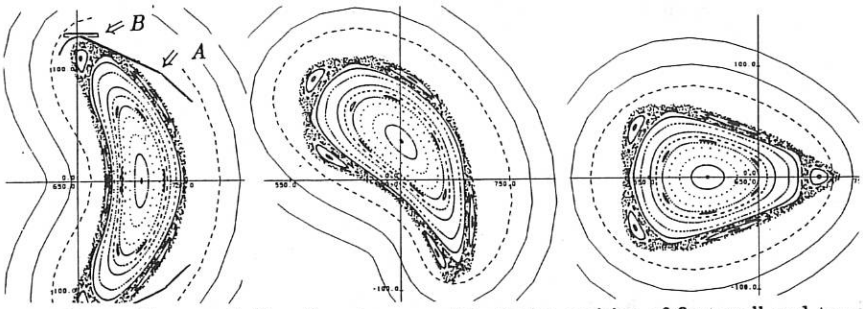

Fig. 1 : Vacuum field, coil contours, and tentative position of first wall and two limiters A and B ; toroidal planes $\varphi = 0$, $1/4$, and $1/2$ field periods.

[1] C. Beidler et al., paper P 2 B 5 , this conference.

top and bottom near the X-point, shaped smoothly towards the first wall at $\varphi \approx \pm 10^o$, and a plate at $Z = 1.3$ m with radial width $\delta R = 0.3$ m, extended between $\varphi = -3^o$ and 12^o. The magnetic topology and the limiter systems are toroidally fivefold periodic.

Fig. 2 is a close-up of the magnetic topology. Three irrational flux surfaces, with one rational surface $\iota = 15/16$ in between are shown, and the $\iota = 1$-island . It has an internal transform of $\iota_i \approx 1/7$, and a cluster of 8 sub-islands near its edge. The island and the ergodic region partially intersect the first wall between $\varphi \approx 20$ and 52^o , which is neglected in the calculation. The position of the separatrix, especially of its X-points, depends weakly on the step length of field line integration, $\delta s = 2$ to 5 cm. The radial extension of the ergodic region is uncertain, it may be enlarged by effects of the finite grid size of stored field values used for fast integration. Up to 1500 transits are calculated in this region; it may be 'open'.

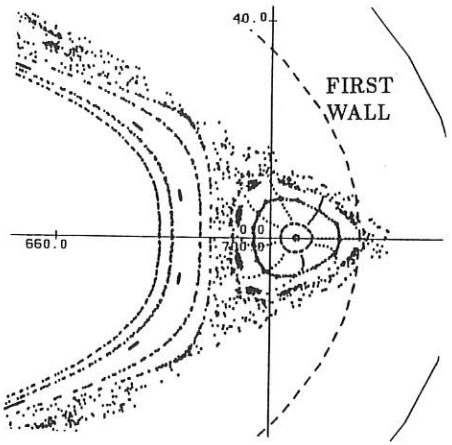

Fig. 2 : Detail of Fig. 1 at $\varphi = 36^o$.

Other magnetic topologies with irrational or rational values of the rotational transform at the edge can be produced by superposed toroidal and/or vertical fields. Limiter or separatrix dominated configurations are to be distinguished. At rational ι-values at the edge, perturbation fields may play an essential role. In cases with an irrational ι-value at the edge, the transition from closed to open topology is comparatively sharp; a substantial radial extension of an ergodic layer can be questioned.

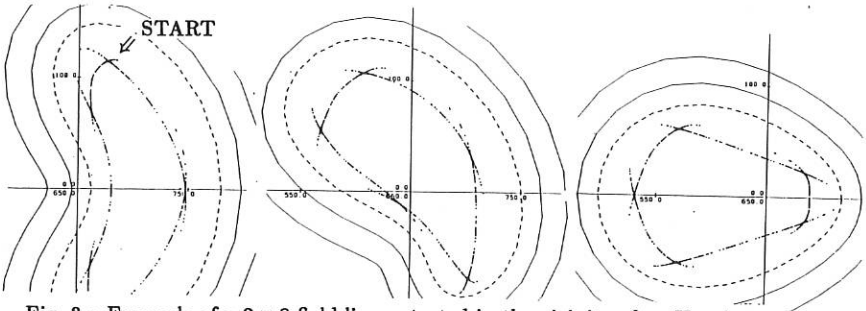

Fig. 3 : Example of a 2×8 field lines, started in the vicinity of an X-point, intersecting with first wall or limiter A after 3 to 66 transits.

EDGE STRUCTURE . The edge structure of the vacuum fields in HS 5–7 and the intersection with first wall and/or limiter is studied by following magnetic field lines started near the separatrix, in many cases near one of its X-points, at chosen toroidal and poloidal angles. The integration is done in both directions, parallel and opposite to $\vec{B}$. An example is given in Fig. 3 , where 2×8 field lines, started in the vicinity of an X-point within $\delta R = 2.5$ and $\delta Z = 1$ cm perform 3 to 66 transits around the torus. Nearly all of these field lines hit the limiter type A ; the first wall is reached after one additional transit by all 16 field lines. Four other neighbouring field lines remain after 120 transits at distances of 7 to 8 cm from the wall, and 2 cm from limiter A, respectively. Low transit numbers, typically 2 to 10 until intersection, are seen for starting points within the ergodic layer. Large transit numbers, up to more than 400 , are seen at starting points close to the X-point; these field lines leave the separatrix region always near an X-point and intersect, within one or two additional transits, with the first wall or with limiter A . In these integrations a comparatively short step length, $\delta s = 2$ cm, is required. In summary: comparatively well defined 'fans' of escaping field lines exist in HS 5–7 , and the ergodicity of the separatrix region is not effective.

HOT SPOT PATTERNS . The intersection points with the wall or with limiter A are shown in Figures 4 and 5. The pattern of the intersection points differs markedly. In Fig. 4, two 'hot spots' are seen near $\varphi = 3/8$ and $5/8$ field periods. For the whole torus a total hot spot area of about 1 m^2 is estimated. In Fig. 5, about half of the field lines end at the limiter bulges in narrow stripes. Most of them are started near one of the X-points at various toroidal and poloidal positions. In other tests 10 starting points are used at equal poloidal angles for 13 toroidal positions; the radial coordinate is extrapolated from inner magnetic surfaces. These starting points are mainly in the ergodic region.

Fig. 6 shows the connection of the wall to the limiter type B , and to points started 5 cm below it. Since this limiter is positioned outside of the separatrix, there is no direct connection, and only some part of the field lines started 5 cm below this limiter reaches the vicinity of the separatrix.

LENGTH OF FIELD LINES . A large span of the lengths of field lines is seen in the above investigations. For starting points outside the ergodic region small values of the length of a field line from wall to wall, L_{ww}, are observed, ranging between less than the length of a field period, $L_p = 8.6$ m, up to a few times this value. Towards the separatrix and close to it, up to several hundreds of transits around the machine, corresponding to values of L_{ww} up to 29 km have been seen; most of the data range between 100 and 500 m. Slightly shorter values are obtained for the limiter A as for the first wall. Field lines started inside the separatrix (and therefore not touching the wall) can be followed numerically up to ± 1500 transits around the machine, corresponding to a total length up to about ± 65 km; they attain a minimum distance of about 10 cm to the wall, and about 4 cm to the limiter A . Elements of limiter B are connected to the wall by field lines ranging between about 1 and 27 m in length. If this limiter is shifted by 5 cm downwards, local maximum values up to 350 m are seen.

SUMMARY AND CONCLUSIONS . The conditions at the edge of HS 5–7 are dominated by the proximity of the first wall in the range between $\varphi = 3/8$ and $5/8$ field periods. Some ergodicity is seen at the separatrix for $\iota_a = 1$. At this rational ι-value 5 magnetic islands are present. They are partially intersected by the first wall. There, an inhomogeneous pattern of the intersection points of field lines started close to the separatrix is seen, from which a total 'hot spot' area of the order of 1 m^2 is estimated. Due to the comparatively low transit numbers of most field lines the finite radial extension of the ergodic region cannot be utilized to increase this area. – Two tentative limiter shapes are studied which collect some part of the field lines emerging outside of the separatrix. Further refinements in geometry of first wall and limiter are in progress.

Fig. 4 : Angular plot of intersection points with first wall. Abscissa = 1 field period.

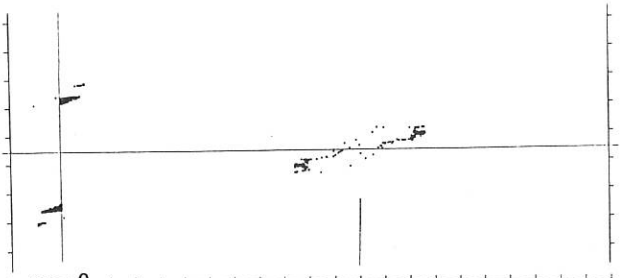

Fig. 5 : As above, limiter type A .

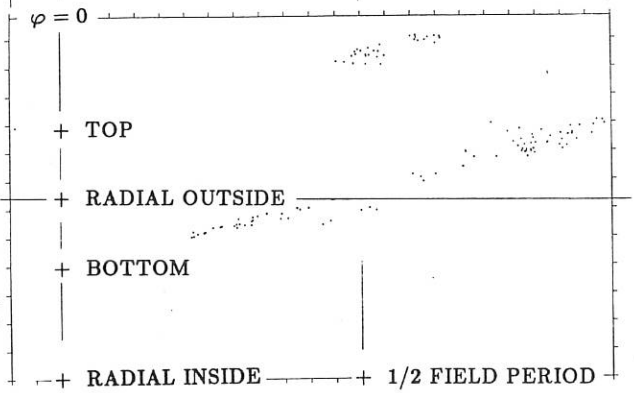

Fig. 6 : Intersection points at first wall; field lines started from limiter type B and 5 cm downwards.

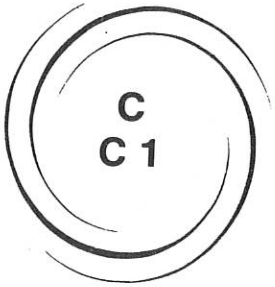

ALTERNATIVE MAGNETIC CONFINEMENT SCHEMES

REVERSE FIELD PINCH

RESULTS FROM HBTX1C WITH CLOSE AND DISTANT RESISTIVE SHELLS

B Alper, M K Bevir, H A B Bodin, C A Bunting, P G Carolan, J A Cunnane+, D E Evans, C G Gimblett, R J La Haye*, P Martin≠, A A Newton, P G Noonan, A Patel, S Robertson‡, H Y W Tsui & P D Wilcock

Culham Laboratory, Abingdon, Oxon, OX14 3DB, UK
(UKAEA/Euratom Fusion Association)

* General Atomics, San Diego, CA, USA
‡ University of Colorado, USA
≠ Istituto Gas Ionizzati, del CNR, Padua
+ University College, Cork, Ireland

Introduction

HBTX1C has operated with resistive shells to study, in particular, reversed field pinch (RFP) confinement where pulse lengths (τ_p) exceed the time constant for vertical field penetration of the wall (τ_w). Initial operation with τ_w = 0.5ms for a shell located at 1.15 times the minor radius, (see Figure 1), led to the growth of low frequency (thin shell) modes [1] which grew to termination in less than 5ms. Mode numbers and growth rates were in agreement with linear MHD theory. The installation of a secondary shell distant from the plasma at 1.6 times the minor radius has significantly altered plasma properties and improved confinement [2,3].

Thin shell operation permits dynamic control of plasma equilibrium. Using high current switching circuitry, feedback control of the horizontal position of the plasma has been successfully implemented. This has been followed by control of one phase of the external kink mode, (m,n)=(1,2), as a first step towards suppression of the growth of thin shell modes.

Operation in the ultra-low-q (ULQ) regime of unreversed discharges with $0 < q \leq 1$ has been studied for currents ranging from 80 to 260kA [4].

Plasma Stability with Resistive Shells

RFP operation with a thin shell (τ_w = 0.5ms) leads to the growth, after a brief quiescent period, of low frequency magnetic modes [1,2] which grow on timescales similar to, but slower than, the wall time for all dominant modes ($\gamma\tau_w = 0.3 \pm 0.1$ where γ is the growth rate). Large radial fields at the boundary (10-20% of the local field) lead to termination in 3-5ms. A structure is observed in the soft X-ray emission profile [5] centred at 0.6a, where a is the minor radius, which has a similar growth rate. An example of this is shown in Figure 2. Its origin is as yet unexplained. Thin shell operation is also accompanied by a factor of $\sim$3 increase in loop voltage and a corresponding decrease in energy and particle confinement compared to thick shell operation.

The inclusion of a secondary shell with τ_w = 5.5ms, positioned

outside the windings at 1.6a, Figure 1, has led to significant changes in plasma properties. In particular, the pulse duration has doubled to 6-10ms, density is typically lower with higher electron temperatures and lower loop voltages [3]. The fall in loop voltage is in line with helicity loss model for the lower measured radial fields with the secondary shell [2]. As expected from a simple ion power balance model the ratio of ion to electron temperature has fallen from ∿1.6 with the thin shell to ∿1 with the secondary shell in line with the drop in loop voltage [6]. The growth of the soft X-ray structure has been suppressed [5] and the growth of all magnetic modes has been slowed indicating non-linear effects [2]. However, the growth rate of the external kink mode, (m,n)=(1,2) increases as the current profile narrows with increasing θ [3] in accordance with linear theory [1]. As found with thin shell operation the modes rotate only very slowly or not at all.

Feedback Control Studies

The horizontal position of the plasma with the secondary shell has been controlled to ±1mm by a feedback control circuit. The plasma is moved by closing either one of two semiconductor switches (gate turn-off thyristors, GTOs) which alters the way current is shared by the parallel-connected field windings. Figure 3 illustrates the variation in Δ, the shift of the outermost flux surface, in three conditions. With the current trace shown in Figure 3a for a discharge without feedback, the variation in Δ is shown in Figure 3b, Figure 3c shows a discharge set to Δ = -4mm with the bars on the figure illustrating when the control circuit was on and Figure 3d shows three consecutive discharges with the preset offset adjusted to -1, -4 and -7mm. At -1 and -7mm, initially the outer or inner GTO turns on for ∿2ms in order to move the plasma to within the desired range. The growth of thin shell modes is believed to be the dominant cause of termination, so the observation that equilibrium control does not measureably affect plasma duration is not surprising.

As a first step towards dynamic control (or suppression) of the growth of thin shell modes, two helical windings, 90° out of phase were installed on the secondary shell to generate a helical field with (m,n) = (1,2). There was no linkage to the transformer nor toroidal field. The semiconductor switching circuitry (GTOs) used for equilibrium control has been connected to one of the two phases only, at present, and can drive a 10 Gauss helical field on-axis of either polarity. (Control of both phases is planned for the near future). The amplitude of the mode is monitored by an array of B_θ pick-up coils immediately outside the vacuum vessel and the appropriate switch is activated when this signal exceeds a preset threshold. In an analysis of discharges with and without feedback, the maximum amplitude of this phase with feedback was maintained below 50 ± 20% of its amplitude without feedback. On present evidence, the growth of the other phase appears to be unaffected. On some discharges, particularly at low θ, the (m,n)=(1,2) mode amplitude never reaches

threshold and the circuit is not activated, yet in all cases pulse duration is limited to less than 10ms.

Ultra-low-q (ULQ) Discharges

Magnetic perturbations similar to the thin shell modes in RFP discharges have been observed in ULQ discharges of up to 260kA plasma current [4]. In q=⅓ discharges, the (m,n) = (1,1) perturbation has a growth time of 1ms in thin shell operation with a rotational frequency ∿300Hz. The ULQ pulse duration can be extended by supressing the growth of this mode when the edge q is maintained within 10% of its limiting value. For example a q=⅓ pulse is extended from 5 to 10ms by increasing the loop voltage from 70 to 130V. ULQ discharges are characterised by low density ($<1.10^{19}m^{-3}$), high ion and electron temperatures (1-1.5keV and 0.6-0.8keV respectively) [6] and large resistance anomaly factors [4] (>100 for flat profiles). Particle confinement is short, estimated to be $\lesssim$50μs from soft X-ray and visible line intensities and plasma resistance is higher than RFP discharges at the same current.

Conclusions

Reversed field pinch studies with a thin shell have been extended to include operation with a secondary shell positioned outside the windings. Although far from the plasma surface, it has had a significant effect in stabilising the plasma. This is seen in a doubling of pulse duration to a maximum of 10ms, a slowing of the growth of all thin shells modes, the suppression of a structure in the soft X-ray profile and a lowering of the plasma resistance.

Feedback stabilisation of plasma horizontal position to ±1mm has been demonstrated using relatively simple circuitry. The suppression of the growth of one phase of the (m,n)=(1,2) external kink mode has been successfully implemented. Circuitry to control both phases is in hand.

Thin shell modes observed in ULQ discharge can be suppressed whilst the edge q is maintained within 10% of its limiting value.

References

[1] B Alper et al, Plasma Physics and Controlled Fusion 31 (1989) Vol.2, to be published.

[2] J A Cunnane et al, "Magnetic Fluctuation Studies in RFPs with Various Shell Times", this conference.

[3] B Alper and R J La Haye, "Plasma Confinement in HBTX with a Distant Resistive Shell", this conference.

[4] H Y W Tsui et al, "A Comparison of Magnetic Behaviour in Ultra-low-q and RFP Discharges in HBTX1C", this conference.

[5] B Alper and P Martin, "Soft X-ray Activity in RFP Plasmas with Various Shell Times", this conference.

[6] C A Bunting and P G Carolan, "Ion Temperature Measurements in HBTX1C with a Thin Shell", this conference.

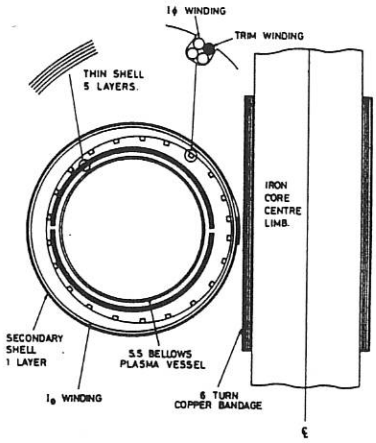

Figure 1
HBTX1C cross-section showing the shell system: thin shell, core bandage and secondary shell.

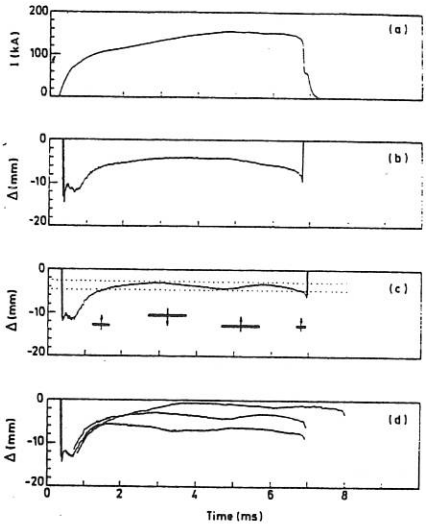

Figure 3
(a) Current trace with (b) showing displacement Δ without control, (c) with feedback control and (d) with control and Δ set to -1, -4 and -7mm on 3 consecutive discharges.

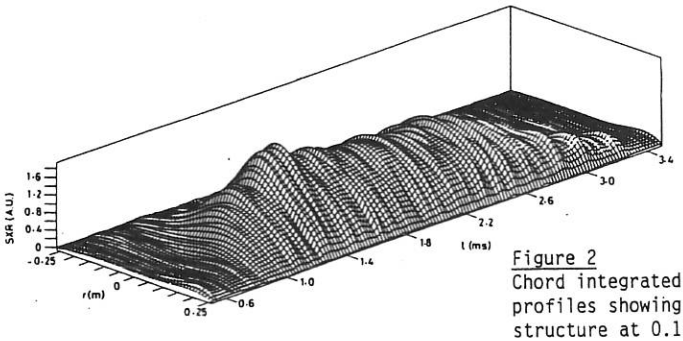

Figure 2
Chord integrated soft X-ray profiles showing growth of structure at 0.16m with time.

PLASMA PERFORMANCE IN THE RFX REVERSED FIELD PINCH

Giubbilei M., Martin P., Ortolani S., Puiatti M.E., Valisa M.

Istituto Gas Ionizzati del C.N.R., Associazione EURATOM-ENEA-CNR
Corso Stati Uniti 4, Padova, Italy

RFX is the large European RFP experiment under construction in Padova. The main parameters are listed in table I. The interest in using the Reversed Field Pinch (RFP) magnetic configuration for plasma confinement is due to its relaxation and self-organization properties, to the relatively low magnetic field and to the possibility of achieving thermonuclear fusion conditions, with significant β values, by ohmic heating only.

RFX will allow to study relaxation phenomena, the underlying MHD instabilities and the corresponding transport processes at keV temperatures in a high plasma current RFP.

In this paper the expected plasma parameters in RFX are discussed in terms of global steady-state and time dependent power balance models. Both size and current scaling from present experiments are discussed, and a steady-state transport analysis of the RFX plasma is presented.

The expected plasma performance is difficult to predict since RFX represents a significant step in parameters from existing RFP experiments. In particular the plasma current will be substantially increased and correspondingly the temperature and energy confinement could increase significantly.

For an ohmically heated system operating near the high density (radiation dominated) limit the scaling with current is determined by the scaling of beta. Assuming the three β vs I dependences: β=const, $\beta \propto I^{-1/4}$ and $\beta \propto I^{-1/3}$, reported in fig. 1 together with some experimental points, the average electron temperature and global energy confinement time scale as shown in fig. 2. As long as β is only a function of current the scaling of τ_E, $n\tau_E$ and $n\tau_E T$ is only a function of temperature and therefore the range of parameters expected for RFX can be represented on a three dimensional plot β, $n\tau_E$, T as shown in fig. 3.

These predictions appear reasonable also in the light of the initial operation of the Madison MST experiment [1], a device of comparable size to RFX with a = .52 m, where $\beta_\theta \gtrsim 0.1$, $I/N \approx 2.5\ 10^{-14}$ A·m and $Z^*_{eff} \equiv 7$ have been achieved

at 400 KA. In fact, assuming for RFX the same I/N, Z^*_{eff} and β_θ yields, at 2 MA, peak temperatures of $\approx$ 1.5 keV, densities of 10^{20} m^{-3} and energy confinement times of $\approx$ 10 ms. Therefore MST in its early operation phase has already achieved results which, allowing for inprovements and optimizations, lead to some optimism for the RFX performance.

The problem of the minimum initial voltage and of the available flux swing has been studied with a O-D time dependent model including impurity radiation losses (C and O) and a transport term modelled by specifying the β limit at which the plasma settles and writing the energy confinement time as $\tau_E = \frac{3}{16}\mu_o \frac{\beta_{\theta e} a^2}{\eta}$. The results are summarized in fig. 4 where the minimum initial voltage necessary to achieve 1 MA (with 7.5 V·s flux swing) or 2 MA (with 15 V·s flux swing) are shown as a function of the electron poloidal beta, $\beta_{\theta e}$.

The magnitude of the heat transport in Reversed Field Pinches can be discussed with reference to the classical ion perpendicular transport. In general for an ohmically heated system the global energy confinement time scales as the ratio of plasma beta to the electrical resistivity $\tau_E \propto \beta/\eta$. The classical ion transport would give a scaling as $\tau_E^{cl,i} \propto \frac{1}{\eta\beta} \cdot Z^2$ for ions of charge Z. Comparing with the classical transport of Z=1 ions we find that the ratio $\tau_E / \tau_E^{cl,i}$ only depends on β^2 and is independent on η and on any effect due to anomalies, dynamo actions and impurities incorporated in η.

With realistic values of β ($\lesssim 0.1$) it is easily found that τ_E is smaller than $\tau_E^{cl,i}$ by typically one or two orders of magnitude [2,3]. An example of a calculation done with typical profiles [2,3] and on axis beta, β_o=0.1, is given in fig. 5 and 6. In fig. 5 are shown the parallel current density profile and the corresponding dynamo electric field necessary to maintain the profile in steady-state. The corresponding electron and ion heat conduction coefficients obtained by assuming that the ohmic power goes into the electrons and the dynamo power into ion heating are drawn in fig. 6 where the values are normalized to the on axis classical ion value.

Therefore the RFP operates far from the classical ion transport limit; however if β will remain comparable to the values achieved in present experiments the ratio between the observed transport and the classical value will also remain constant but the scaling will be favourable so that thermonuclear conditions would be achieved with plasma currents $\lesssim$ 20 MA.

REFERENCES

[1] Almagri A.F. et al., "Initial Operation of the MST Reversed Field Pinch", post deadline paper, 12th IAEA Conference on Plasma Physics and Controlled Nuclear Fusion, Nice, France, 12-19 October 1988.

[2] Ortolani S., "Twenty Years in Plasma Physics", International Centre for Theoretical Physics, World Scient.Publ., Philadelphia (1984), 75.

[3] Ortolani S., 1987 International Conference on Plasma Physics, Kiev, USSR, April 6-12, 1987, Vol. 2, 802.

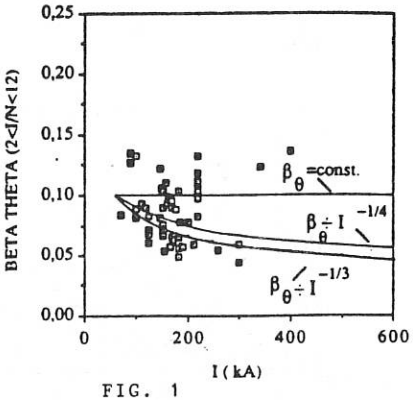

FIG. 1

TABLE I

RFX PARAMETERS

• major radius	2m
• graphite armour inner radius	0.457m
• vacuum vessel inner radius	0.475m
• vacuum vessel outer radius	0.505m
• shell inner radius	0.535m
• shell outer radius	0.600m
• shell time constant	400 ms
• flux swing	15 vs
• maximum design current	2 MA
• maximum applied toroidal field	0.7 T
• inductive stored energy	72 Mj
• capacitive stored energy	5 Mj

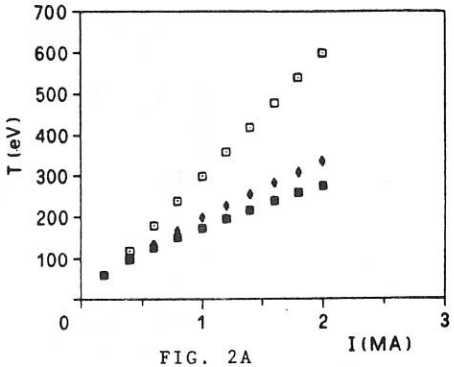

FIG. 2A

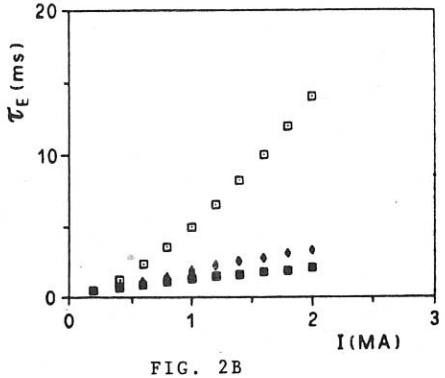

FIG. 2B

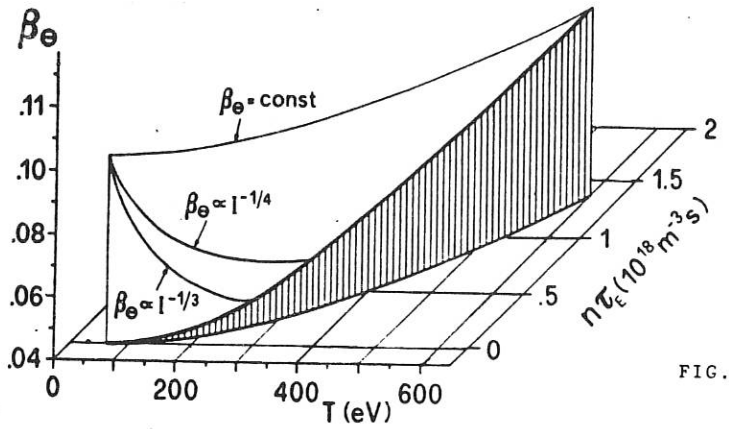

FIG. 3

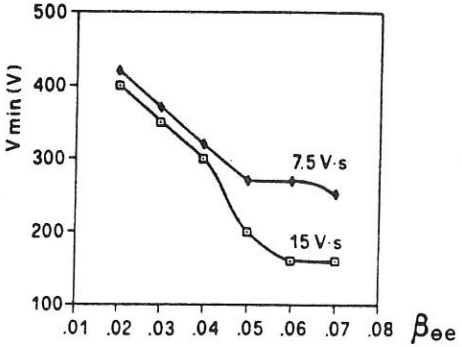

FIG. 4

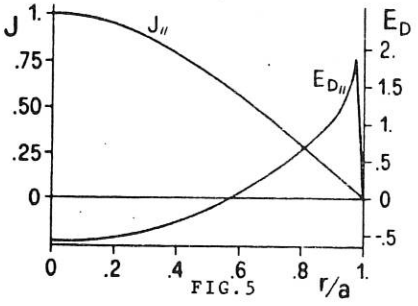

FIG. 5

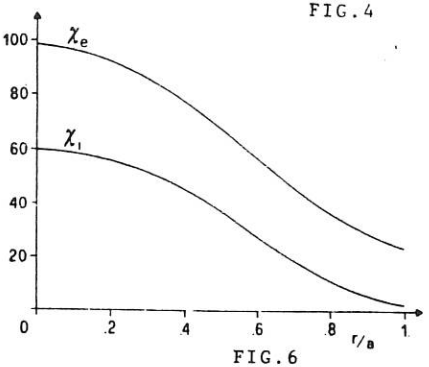

FIG. 6

PLASMA CONFINEMENT IN HBTX WITH A DISTANT RESISTIVE SHELL

B Alper & R J La Haye*

Culham Laboratory, Abingdon, Oxon, OX14 3DB, UK
(UKAEA/Euratom Fusion Association)

* General Atomics, San Diego, CA, USA

Introduction

When HBTX was operated with a resistive shell (τ_w = 0.5ms) located at 1.15 times the minor radius, pulse lengths were limited to 3-5ms [1]. This limit was not imposed by the available voltseconds but was associated with the growth of thin shell modes. Using arrays of saddle coils placed far from the plasma outside the windings system (at 1.6 times the minor radius), radial magnetic fields up to 50 Gauss were detected from these modes. Analysis of these modes showed a strong correlation between the growth of the (m,n)=(1,2) external kink mode and the plasma duration [2].

These studies prompted the idea that a secondary shell placed at the position of these coils might have a beneficial effect of suppressing the radial field and the growth of the (m,n)=(1,2) mode in particular.

Secondary Shell - Properties

A thin (0.5mm) copper shell was installed outside the windings system at 1.6 times the plasma minor radius [3]. The vertical field penetration time τ_w was 5.5ms. Linear MHD calculations show that this shell should be more effective at suppressing the growth of the low n-modes rather than the high n-modes. For example the theoretical relative increase in growth time for the n=5 mode is less than half the increase in the n=2 growth time when changing from thin to secondary shell configurations. The factor is even smaller when comparing the higher n-modes to the n=2. Thus any significant effect on plasma parameters due to the presence of the secondary shell would be indicative of the importance of the role of the external kink or of possible non-linear coupling between the modes.

Change in Plasma Confinement

The first clear observations of the benefit of the secondary shell were an increase of ~100% in the pulse length to 6-10ms and a reduction in the loop voltage, V_ϕ, see Figure 1. Another significant change was a fall in electron density n_e. With only the thin shell, attempts to reduce n_e to values below $2.10^{19}m^{-3}$ (using helium glow cleaning and low filling pressures) failed, whereas densities below $1.10^{19}m^{-3}$ could be routinely obtained with the secondary shell and electron temperatures rose from ~210eV to over 450eV. In order to compare plasma properties under similar operating conditions a series of measurements were carried out at the same density (raised by gas puffing and higher filling pressures for the

secondary shell) and are displayed in Table 1. The electron temperature with the secondary shell (270eV) is now closer to that with the thin shell (210eV). Of particular note is the loop voltage (V_ϕ) which has fallen from 67 Volts to 51 Volts. This fall cannot be explained simply in terms of the small change in electron temperature. Taking a value of Z_{eff} of 3 in both cases (as indicated by radiation measurements) and current profiles deduced from the measured values of F and θ, the Spitzer value of V_ϕ is estimated to have reduced from 17 to 11 Volts. The anomalous contribution to the loop voltage we attribute to magnetic helicity dissipation from flux intercepting the first wall [4]. Using values determined from discrete coil measurements the change in the non-Spitzer loop voltage can be accounted for by the measured fall in the flux penetrating the liner, [2].

Models of ion heating based on power balance relate the ratio of ion to electron temperature to the magnitude of the loop voltage [5]. The observations of a reduction in this ratio from $\sim$1.6 to $\sim$1 supports this trend. Energy confinement times have risen from 0.15ms to over 0.2ms with the secondary shell but (as found in changing from thick to thin shells) the poloidal beta (β_θ) has changed little.

Table 1

Parameter	Thin Shell only	with Secondary Shell
I_ϕ (kA)	170	-
n_e ($\times 10^{19} m^{-3}$)	2.1	-
τ_{pulse} (ms)	$\sim$3	$\sim$6
V_ϕ (Volts)	67	51
T_e (eV)	210	270
T_i/T_e	$\sim$1.6	$\sim$ 1.0
F	-0.26	-0.24
θ	1.65	1.60
β_θ (%)	16	16
τ_E (ms)	0.15	0.21

Unlike operation with a thick shell, it was found that plasmas with shallow reversal (F>-0.2) could not be sustained with a thin shell [1]. This still holds with the secondary shell and optimum values of F and θ have changed little. In fact the longest discharges are obtained at $F \lesssim -0.3$. Operating at deeper reversal compared to thick shell plasmas (where F was $\sim$-0.08) is estimated to contribute 15-30% of the observed increase in plasma resistance.

Multichord studies of soft-X-ray emissions from the thin shell RFP [6] showed that a secondary peak in the outer region of the plasma grew on

the thin shell timescale. The growth of this structure has not been observed after the addition of the secondary shell.

Analysis of the growth of the magnetic modes [2] indicate that the growth of all m=1 modes (ie. at both low and high n values) have been suppressed by the secondary shell indicating the presence of non-linear coupling between the modes.

Dependence on θ

Linear ideal MHD theory predicts that the external modes should grow more rapidly as the plasma current profile becomes more peaked at higher θ [1]. To test this, signals from helical windings, placed outside the secondary shell to measure the amplitude and phase of the (m,n)=(1,2) external kink were analysed as θ and F were varied. As can be seen in Figure 2 which shows the growth in amplitude of this mode with time for sample discharges at low (1.6) medium (1.9) and high (2.2) θ, the growth rate does indeed increase with θ. In these data the cut-off radius in the current profile, determined using the Modified Bessel Function Model fell from 0.75a at low θ to 0.4a at high θ. The discharge duration shortens as the mode grows faster, and termination occurs when the amplitude is ∿10 Gauss at the helical winding (or ∿50 Gauss at the plasma surface as measured by an array of discrete coils). As with thin shell operation, the mode does not rotate. Shown in Figures 3a and 3b is the dependence of growth rate of this mode for a number of discharges on θ and F respectively. The trend for the growth rate γ to rise with θ or fall with F is clearly seen. At low values of θ (1.5-1.65) occasionally no clear growth in the external kink is measured but pulses are still limited to less than 10ms.

Conclusions

A thin (0.5mm) secondary copper shell (τ_w=5.5ms) placed outside the windings system at 1.6 times the minor radius of the plasma has had the beneficial effect of doubling the pulse length in RFP discharges on HBTX1C. It has led to lower densities, higher electron temperatures and lower loop voltages. As this shell was expected to suppress the growth of only the longer wavelength modes (n∿2) and all MHD activity has been suppressed, non-linear coupling between the modes is indicated. However, the observed change in the growth rate of the external kink mode (m,n)=(1,2) which increases with increasing θ, is a prediction from linear theory.

References

[1] Alper B, et al Plas. Phys. & Contr. Fus. 31 (1989) 2, to be publ.

[2] Cunnane J A, Tsui H Y W & La Haye R J, 'Magnetic Fluctuation Studies in RFPs with Various Shell Times', this conference.

[3] Alper B, et al, 'Results from HBTX1C with Close and Distant Resistive Shells', this conference.

[4] Tsui H Y W, Nucl. Fus. 28 (1988) 1543
[5] Bunting £ A & Carolan P G "Ion Temperature Measurements in HBTX1C with a Thin Shell' this conference.
[6] Alper B & Martin P, 'Soft X-ray Activity in RFP Plasmas with Various Shell Times', this conference.

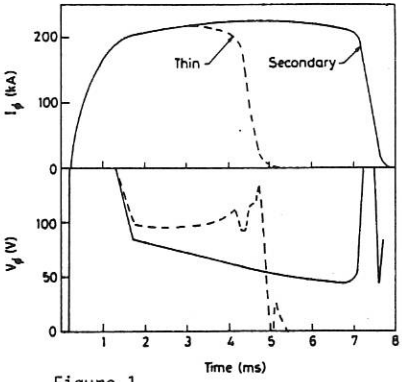

Figure 1
Comparison of current and voltage traces for thin and secondary shell operation.

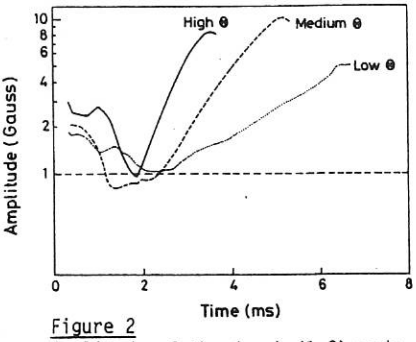

Figure 2
Amplitude of the (m,n)=(1,2) mode at the secondary shell for 3 values of θ.

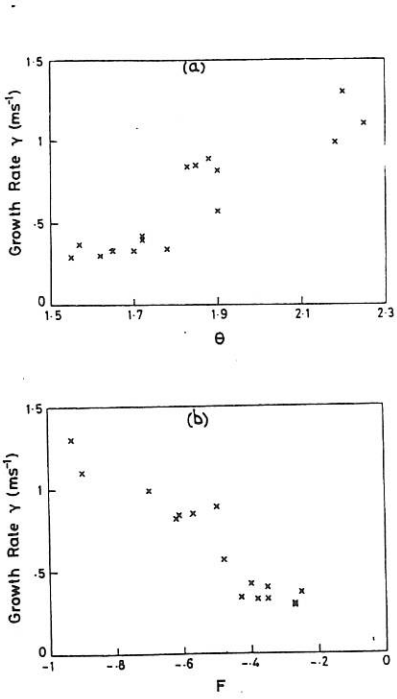

Figure 3
Dependence of growth rate of the (m,n)=(1,2) mode on (a) θ and (b) F.

THE EFFECT OF THE VELOCITY FLUCTUATIONS ON THE ION AND ELECTRON TEMPERATURE AND THE ENERGY CONFINEMENT IN THE REVERSED FIELD PINCH

A Lazaros*

Culham Laboratory, Abingdon, Oxon, OX14 3DB, UK
(UKAEA/Euratom Fusion Association)

* Euratom Fellowship, Fusion Programme

Abstract

It is suggested that velocity fluctuations (which in the dynamo hypothesis provide the anomalous voltage), also provide the power loss from the ions and the electrons (via turbulent convection) but heat the ions (via ion viscosity) faster than they cool them.

The opposite variation of the ion and the electron temperature (by limiter insertion and tile removal in the HBTX1B) is therefore attributed to the variation of the strength of the velocity fluctuations which may be affected by the wall.

Introduction

Plasma relaxation in the Reversed Field Pinch is a continuous process which sustains the configuration against magnetic resistive decay. This is done at the expense of an anomalous voltage ΔV_ϕ which in the dynamo hypothesis [1] has the form:

$$\Delta V_\phi = -\frac{1}{I_\phi} \int < \underline{\tilde{v}} \times \underline{B} \cdot \underline{j} > d^3x \qquad (1)$$

Anomalous diffusion in the RFP is believed to arise from turbulent convection in which heat transfer due to turbulent mass transfer is much faster than that due to collisions. The diffusion coefficient appropriate for turbulent convection [2] is given by $D \sim \tilde{v}_r \Lambda_\perp$ (2) where $\Lambda_\perp$ is the perpendicular correlation length.

Velocity fluctuations are also associated with the anomalous ion heating. In many RFPs it has been observed that the ion temperature is of the same order as the electron temperature ($T_i \sim T_e$). The energy confinement time τ_E in these experiments is much smaller than the classical equipartition time, τ_{ei}, therefore the ions cannot be heated up to the observed temperatures by collisions with electrons. It has been shown [3] that ion heating due to parallel viscosity given by:

$$W_i = Q_{vis} = \left(\frac{2\pi R}{\lambda_{MFP}}\right)^2 n\, T_i\, \tau_{ii} \left(\frac{du_r}{dr}\right)^2 \qquad (3)$$

can provide the required ion heating.

Experimental Results

In several cases it was observed at the HBTX1B under constant density and current that the ion and the electron temperatures (although uncoupled) change in the opposite way with the plasma resistance behaving like the ion temperature; (when T_e increases T_i decreases and visa versa). This was observed for a first time during the mobile limiter experiment [4]. When a mobile limiter was inserted into the plasma the loop volts increased with the insertion distance of the limiter, the ion temperature increased too [5] but the electron temperature had decreased. Ion and electron temperatures vs the insertion distance given in [5] are shown in Figure 1.

The same effect was observed at HBTX1B by limiter removal. At the constant current of 220 kA and the typical density of 2×10^{19} m^{-3}, the loop volts decreased from $\sim$ 33 volts to $\sim$ 22 volts, the typical ion temperature also decreased from $\sim$ 360 eV to $\sim$ 230 ev, but the electron temperature had increased from $\sim$ 350 eV to $\sim$ 460 eV [4].

The most remarkable case however was observed in the out-of-phase sawtooth oscillations [6] of the ion temperature and the Soft x-ray (SXR) time traces (associated with the electron temperature oscillation), shown in Figure 2.

Data Interpretation

When diffusion is assumed to dominate the power loss, [7] the energy density apparently is: $nT \propto WD^{-1}$ (4) where W is the power input.

Power input to the electrons is assumed to be the Ohmic heating: $W_e = nj^2$, where η ($\propto T_e^{-3/2}$) is the Spitzer resistivity and j ($\propto I_\phi$) is the current density; therefore: $W_e \propto T_e^{-3/2} I_\phi^2$ (5). Substituting equations (5) and (2) into (4) we obtain:

$$T_e^{5/2} \propto n^{-1} I_\phi^2 \Lambda_\perp^{-1} \tilde{u}_r^{-1} \qquad (6)$$

Power input to the ions is assumed to be the viscous heating rate given by equation (3). The ion mean free path is determined from the thermal velocity: $\lambda_{MPF} = v_{th} \tau_{ii} \propto T_i^{1/2} \tau_{ii}$ and the ion-ion collision time [8] is: $\tau_{ii} \propto n^{-1} T_i^{3/2}$. Substituting equations (3) and (2) into (4) we obtain:

$$T_i^{5/2} \propto n \left(\frac{d\tilde{u}_r}{dr}\right)^2 \Lambda_\perp^{-1} \tilde{u}_r^{-1} \propto n \Lambda_\perp^{-3} \tilde{u}_r \qquad (7)$$

The perpendicular correlation length $\Lambda_\perp$ was found [9] to be constant under most conditions where $\Lambda_\perp/a \sim 0.1$. In this case it follows from equations (6) and (7) that T_i and T_e (under constant density and current) depend on the single parameter $\tilde{u}_r$, i.e: $T_e \propto \tilde{u}_r^{-2/5}$ (8a) and $T_i \propto \tilde{u}_r^{2/5}$ (8b). If the strength of the velocity fluctuations increases, (due to

limiter insertion, for example), T_e will be reduced (according to equation 8a), T_i will increase (according to equation 8b) as will also ΔV_ϕ (according to equation 1). This apparently happened by limiter insertion. The variation of the main plasma parameters after tile removal can be explained if we assume that $\tilde{u}_r$ is reduced. For the coherent oscillations of T_i and T_e we suggest that an unstable mode affects $\tilde{u}_r$. As a result of this, T_i will oscillate in phase with $\tilde{u}_r$ and in anti-phase with T_e.

Conclusions

An explanation to our data can be offered if we assume that the wall determines the strength of the velocity fluctuations. Any alteration of the wall condition (which we imposed at HBTX1B by inserting a limiter and removing the tiles) may affect $\tilde{u}_r$. This is yet to be confirmed experimentally.

On the crucial question, how the velocity fluctuations affect the energy confinement, it follows that due to the opposite effect which they have on the ion and the electron temperature, they have only a minor effect on β_θ. It is however their contribution to the plasma resistance which highlights the damaging effect of the velocity fluctuations on the energy confinement in the RFP.

Acknowlegements

All of the data presented in this paper are taken and published by the HBTX experimental group. Here the data are shwon again for the convenience of the reader and I am grateful to my colleagues for their permission to present the data.

References

[1] Gimblett C G and Watkins M L, (1975); Proc. 7th EPS Conf. on Contr. Fus. and Plasma Phys. (Lausanne) Vol I, 103
[2] Rusbridge M G, (1969); Plasma Physics & Contr. Fus., Vol II, 35
[3] Gimblett C G, (1988); Private communication, also paper submitted to Europhysics Letters (unpublished)
[4] Alper B et al, (1988); Plasma Physics & Contr. Fus. Vol 30, 843
[5] Carolan P G, Bunting C A & Field A R, (1988); submitted to Plasma Physics and Contr. Fus.
[6] Hayden R J & Alper B, (1988); Proc. 15th EPS Conf. on Contr. Fus. and Plasma Physics (Dubrovnik) Vol II, 581
[7] Carolan P G, et al, (1987); Proc. 14th EPS Conf on Contr. Fus. and Plasma Physics (Madrid) Vol II, 469
[8] Braginskii S I, (1965); Reviews of Plasma Physics Vol I, 215
[9] Gee S J, (1988); PhD thesis, University of Manchester

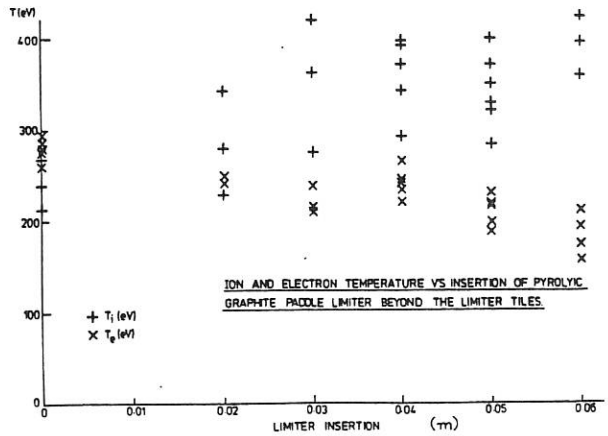

Figure 1. Ion and electron temperatures (obtained by Carolan et al, 1988) vs limiter insertion beyond the tiles.

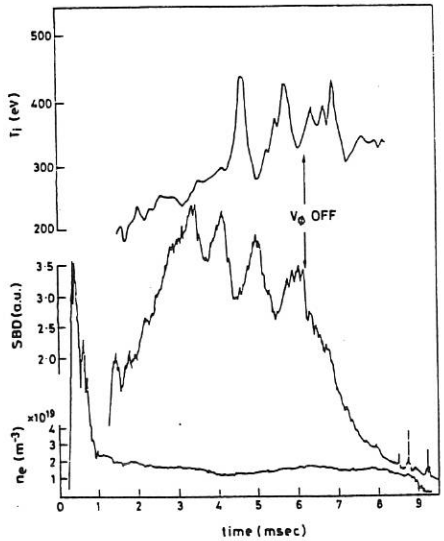

Figure 2. Ion temperature (NPA) and SXR (SBD) coherent oscillations (observed by Hayden and Alper, 1988) at constant density.

ELECTRON RUNAWAY AND HEAT LOSS IN THE RFP

A A Newton, D E Evans & H Y W Tsui

Culham Laboratory, Abingdon, Oxon, OX14 3DB, UK
(UKAEA/Euratom Fusion Association)

Introduction

Understanding transport is an important task in Reversed Field Pinch (RFP) research. In the RFP much higher values of $E/E_c \sim 0.1$ to 1 are seen than in Tokamak, here $E = V_{LOOP}/2\pi R$, $E_c = 2KT_e/e\,\lambda_o$, and λ_o is the mean free path of thermal electrons. Runaway electrons at MeV energy and their effects, viz, X-rays, wall damage, reduction in V_{LOOP} below the Spitzer value are not seen. Nevertheless, experimental observations show an excess population of electrons at energies above thermal at $W_e = 3$ to $10kT_e$ in some cases [1] with flow in the direction to carry most of the current [2,3]. In this paper we use these results to discuss the electron power balance including the application of the kinetic dynamo theory and the role of electron neutral collisions. Data used are from HBTX1B (R/a = 0.8/0.26m) with a thick shell.

Experimental Basis

In RFP the field lines "cut and rejoin", this being the intrinsic dynamo process which maintains the reversed toroidal field. Thus magnetic lines depart slightly from average magnetic flux surfaces and since $K_{||}/K_{\perp} \sim (\omega\tau)^2$ a small inclination is sufficient for parallel electron heat flow to exceed perpendicular ion conduction e.g. on ZETA (ULQ) $K_{\perp} = 10^{-2}K_{ell}$ accounted for the results with collisional parallel conductivity [4].

In modern RFP temperatures are one to two orders of magnitude higher, densities lower and mean free paths $\sim 10^3$m permitting collisionless flow. Measurements on HBTX1B at 200kA off-axis at r/a $\sim$ 0.65 by Thomson Scattering of electron velocity distributions which are interpreted as temperature and poloidal current, T_e = 250 to 450eV and $j_{\theta o} \sim 1.5$ to 3MA/m². The current density is as expected with an MBFM having on axis $j_{\phi e}$ = 4MA/m² [2]. Calorimetry at the plasma edge [3] shows heat flow in the direction of the electron current at a factor of 40 higher than the average power arriving on the walls. An electron energy analyser at 2cm insertion from the wall detects electron up to 1keV with a flow energy of 200-300eV typical of the central region and a density $\sim$1-2% [3].

Losses with Parallel Flow

Since in RFP $\tau_E << \tau_{ei}$ the electrons and ions are uncoupled we can consider the power balance of each species separately. (The ion heating by fluctuations is discussed elsewhere [5]). To further develop the parallel flow model we assume that fluctuations promote electron power loss of the form $P_L \propto n_e T_e D$ where D is an equivalent diffusion

coefficient (volume/loss time) proportional to $P_D = IV_D$. Here V_D is the dynamo contribution to $V_{LOOP} = V_S + V_D$ and V_S is the loop voltage due to Spitzer resistivity, η_S. To complete the balance we assume that electrons are heated by IV_S only and other losses such as radiation can be neglected. This formulation is justified by observations that when V_D is reduced by control of equilibrium, reduction of field errors, etc, the observed T_e and $\beta_{\theta e}$ are higher but the power input is less. The resulting scaling laws (see Table 1) give T_e and $(\beta_{\theta e})^{-1}$ increasing nearly linearly with current are closely similar to those observed with limiter tiles (see Table 2) as shown in Fig. 1. Data without tiles are a less good fit (see Fig. 1).

Table 1 - Dynamo Electron Heat Loss Scaling Laws for Electron Temperature and Beta

$$T_e \propto I^{4/5} N^{-2/5} Z^{2/5} P_D^{-2/5}$$

$$\beta_{\theta e} \quad I^{-6/5} N^{3/5} Z^{2/5} P_D^{-2/5}$$

Table 2 - Observed Scaling Laws for $T_e = A\, I^a/\bar{n}_e^{\,b}$, (eV, kA, $10^{19}m^{-3}$)

	A	a	b
With tiles	6.2	0.78	0.55
Without tiles	26.4	0.57	0.63

The above model leads to estimates for τ_{Ee} in the range up to 5ms without tiles where T_e values up to 800eV are measured (see Fig. 2).

Collisional losses based on classical parallel conduction as postulated on ZETA are independent of density (and direction of current flow) resulting in a weaker variation $T_e \propto I^{2/5}$ different to HBTX1B results.

Application of Kinetic Dynamo Theory

The KDT model [6] may be more relevant because λ_o is large and then resistivity is described by a nonlocal Ohm's law. Electron momentum diffuses outwards and is absorbed by collisions with the wall giving an effective helicity resistivity (Eqn. 6 of Ref. 6) which can be expressed as:

$$\eta_k/\eta_S = m\,(E/E_C) + c \qquad (1)$$

where c=1 and m contains the field line diffusivity D_F, magnetic configuration factor $f(\theta)$ and a correction for the average ion charge (E_C is conventionally defined for hydrogenic plasmas). We find that data from HBTX1B agrees well with the form of Eqn.(1) having well defined intercepts and slopes (see Fig. 3 and Table 3). The D_F is a factor 1.5 higher with tiles than without consistent with other observations [6].

Table 3 - Summary of Coefficients to fit HBTX1B Data to the KDT Model

	m	c	R	Z+
With Tiles	4.0	1.3	0.92	2
Without Tiles	3.8	0.6	0.95	3

+ average measured value used in η_S

Effects of Particle Recycling

The critical field E_c is proportional to the product of resistivity and density: $E_c \propto \eta_s n_e$. As classical resistivity is almost independent of density, its reduction increases the likelihood of runaway.

A steady RFP plasma, in which a radially outward particle flux is balanced by a source of new plasma internal to the discharge, is expected to exhibit a new contribution to resistivity, $\eta_t = m_e S/e^2 n_e^2$, which will add a few percent only to the ordinary Spitzer quantity under normal conditions. If the resistivity determining the critical field is now identified as the sum of classical Spitzer resistivity η_s and the new resistivity η_t, then $E_c' \propto (\eta_s+\eta_t)n_e = \eta_s n_e + m_e S/e^2 n_e$ and the existence of the particle source acts to inhibit runaway. Indeed, there now exists a lowest E_c occurring when $\eta_t = \eta_s$, ie. when $n_e = \sqrt{(m_e S/e^2 \eta_s)}$. For densities below this value, E_c increases once more.

The size of the expected effect is illustrated first by reference to normal 200kA discharges in HBTX having axial density and temperature $n_e = 1\times10^{19}m^{-3}$, $T_e = 300eV$, and the conventionally calculated $E/E_c = 0.7$. We deduce a recycling source strength $S=1.9\times10^{22}m^{-3}s^{-1}$ which marginally modifies the resistivity ($\eta_t/\eta_s = 0.08$) and the runaway parameter $E/E_c' = 0.65$. A more marked effect occurs in a high temperature (800eV) low current (80kA) and low density discharge ($3\times10^{18}m^{-3}$) for which conventionally $E/E_c = 0.83$. In this case we find $S = 1.25\times10^{21}m^{-3}s^{-1}$ produces $\eta_t/\eta_s = 0.24$ and $E/E_c' = 0.67$.

Conclusion

Although high values of E/E_c prevail in RFP no measurements show significant fast electrons above $W_e \sim 10kT_e$ suggesting that runaways are rapidly lost before reaching higher energies. Of the scalings the most consistent is the variation of measured resistivity (η_k) with E/E_c which follows the form predicted in the KDT model. Thus the electron loss processes are driven by the toroidal electric field rather than radial gradients of temperature and pressure as in classical transport. Particle recycling makes a small contribution to resistivity but fails to account for the high values of E/E_c.

Acknowledgements

The authors are grateful to many colleagues for discussions and C G Gimblett and J Sandemann for manipulation of the data.

References

[1] R J Hayden & B Alper, Plasma Phys. & Contr. Fusion 31 (1989) 2
[2] D E Evans & P D Wilcock, Rev. Sci. Instrum. 59 II (1988) 1645
[3] R F Ellis, J C Ingraham, P Noonan & H Y W Tsui, Bull. Am. Phys. Soc. 33 (1988) 1999
[4] M G Rusbridge, Plasma Physics 11 (1969) 1291
[5] B Alper et al, Proc. IAEA Conf Nice 1988, ppr CN50/C-2-2
[6] R W Moses, K F Schoenberg & D A Baker, Phys. Fluids 31 (1988) 3152

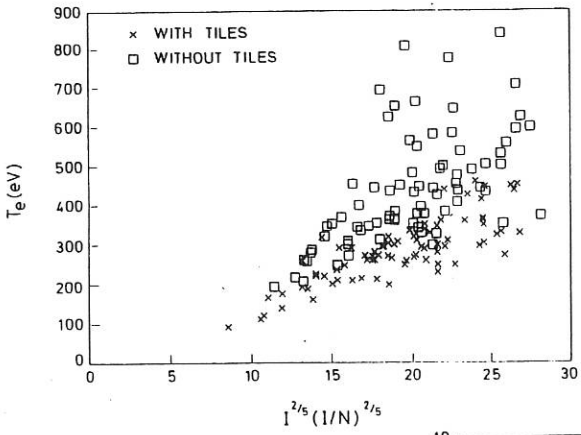

Fig 1 Plot of measured T_e vs heat loss scaling parameter for HBTX1B data with and without limiter tiles.

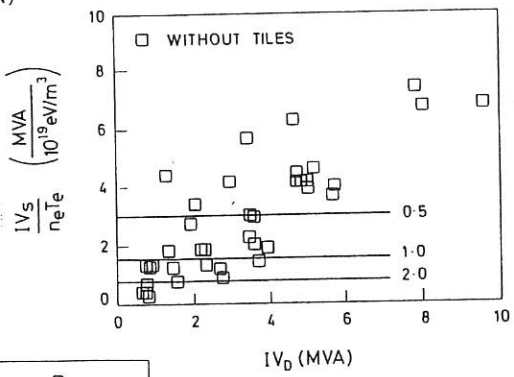

Fig 2 Plot of electron energy loss rate vs dynamo power for HBTX1B without tiles. Horizontal lines show τ_{Ee} in ms.

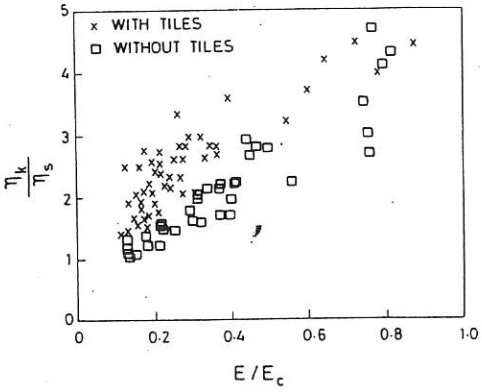

Fig 3 Plot of measured resistivity vs electric field (both normalised) to test KDT model.

SOFT X-RAY ACTIVITY IN RFP PLASMAS WITH VARIOUS SHELL TIMES

B Alper and P Martin*

Culham Laboratory, Abingdon, Oxon, OX14 3DB, UK
(UKAEA/Euratom Fusion Association)

*Istituto Gas Ionizzati del C.N.R. , Padova, Italy
(Euratom-Enea-Cnr Association)

1. INTRODUCTION

Soft X-ray (SXR) emission studies have been carried out in three version of the HBTX Reversed Field Pinch experiment, namely HBTX1B fitted with a thick shell (wall time τ_w=75 ms) [1], HBTX1C with a thin shell (τ_w=0.5 ms) and later with secondary shell [2]. The secondary shell installed on the thin shell version is a copper conductor placed outside the windings (at b=1.6a) with wall time τ_w=5.5 ms.

The experimental set-up consists of twenty surface barrier diodes arranged in a set of three fan arrays viewing the plasma through three vertical ports at one toroidal location. The diodes are fitted with 5000Å copper foils which absorb radiation below approximately 400 eV in energy.

In HBTX1B with a thick shell the SXR emission is due to Oxygen VII [3]; with the thin shell the intensity from the central chord falls by about a factor of 30, but is still above the level expected from continuum radiation. Line contribution to the emission is then dominant and a few percent concentration of Oxygen can account for the observed SXR emission intensity.

Using the Time Dependent Coronal Model [4] to predict the power radiated by Oxygen VII as a function of T_e and $n_e\tau_p$, where τ_p is the particle confinement time, and considering the measured electron temperature (~400 eV for the thick shell and ~200 eV in the lower intensity thin shell discharges) it can be seen that the factor of 30 can be justified only if, with the thin shell, $n_e\tau_p$ falls to about 1/3 of its thick shell value. This evidence of poorer particle confinement is consistent with a measured fall in the energy confinement time [2]. The chord integrated emissivity profiles are usually narrower during the operation with thick and secondary shell than with the thin shell, the Full Width Half Maximum (FWHM) of the profile being usually ≤0.5a in the former case and ≥0.6a in the latter.

2. FLUCTUATIONS IN SXR EMISSIVITY

The normalized RMS fluctuation level in SXR intensity measured along the central chord has been computed in the frequency range 0.5-35 kHz. The lower frequency limit has been chosen to exclude the slow evolution of the signal; the upper limit is such that very little power is stored in signal components with frequencies >35 kHZ. In fig.1 the RMS fluctuation level is shown as a function of the plasma resistance, R_p, computed through Ohm's law for the thick, thin and secondary shell operation. Each point corresponds to a discharge and the discharges have plasma current in the range 170-220 kA. The RMS fluctuation level shows a linear correlation with R_p, varying from ~3% at R_p~0.1 mΩ for thick shell operation at low pinch parameter (Θ~1.4) to ~18% at R_p~1 mΩ for thin shell operation at various Θ values.

The increased level of fluctuations in the higher resistance and lower energy confinement time regime is believed to be related to enhanced MHD activity needed to sustain the configuration against diffusion. Moreover in thin shell operation a background due to "thin shell" instabilities is likely to be present. In the thick and secondary shell regimes the fluctuation level increases with Θ, a trend found also in other RFPs [5,6] and correlated to an increase in MHD activity present when the configuration is further away from the relaxed state; with the thin shell the fluctuation level does not depend on Θ, indicating that "thin shell" modes play an important role independently on the value of Θ.

3. COHERENT OSCILLATIONS

In both thin and secondary shell operation large and correlated oscillations are observed in the SXR signals throughout the plasma. With standard plasma conditions the relative amplitude of the oscillations is larger with the thin shell, ranging up to 50% peak to peak; with the secondary shell they usually increase as the reversal deepens.

These coherent oscillations correspond to macroscopic changes in the chord integrated emissivity profiles, which periodically peak and flatten during the discharge as shown in fig.2 for a time interval during the current flat-top. The oscillations are correlated with analogous oscillations in global magnetic quantities, like the reversal parameter F, the average toroidal field $\langle B_\phi \rangle$, the toroidal field at the wall $B_\phi(a)$ and the Modified Bessel Function (MBF) radius. In fig.3 the SXR intensity measured along the central chord, the FWHM of the SXR profile, F, Θ, $\langle B_\phi \rangle$, $B_\phi(a)$ and the MBF radius are displayed for the same discharge as fig.2. In particular this figure shows that when the SXR intensity increases in the core of the plasma and the profiles become narrower, the current density distribution shrinks and the magnetic flux decreases. When the SXR intensity falls in the core the profiles flatten and magnetic flux is regenerated. These correlations suggest that the oscillations observed in HBTX1C are the kinetic counterpart of the current density redistributions observed in many other RFPs [3,5,6,7,8,9,10]. These have been explained as the outcome of the counteracting actions of resistive diffusion and relaxation processes [6,11] responsible for the sustainment of the RFP configuration. As can be deduced from fig.1 their amplitude grows with the plasma resistance. Nonetheless we should remark that in different plasma conditions, i.e. at low current ($I_\phi \sim 80$ kA) and shallow reversal, large coherent oscillations have been observed at very low plasma resistance [3].

As a test of the role that resistive diffusion plays in the processes underlying the coherent oscillations, fig.4 shows their period as a function of the resistive diffusion time $\tau_R \propto 2R/R_P$, where R is the major radius, for HBTX1C and other RFPs [6,7,8,9,10,11].

As expected a trend for the period to increase with τ_R can be inferred, even if a very low resistance HBTX1B-(no tiles) point [3], not shown in the figure, with period ~1.25 ms and $\tau_R \sim 27$ms, suggests a saturation could be present when the resistive diffusion time increases.

4. A NEW THIN SHELL PHENOMENON

In several thin shell discharges a secondary maximum is present in the outer part of the chord integrated emissivity profile. The amplitude of this maximum grows during the discharge, becoming sometimes larger than that of the central maximum close to the termination. An example of this is shown in fig.5, where profiles at subsequent times are displayed, the last being very close to termination.

The ratio between the secondary and the central maxima grows exponentially in time , with growth rates of the order 0.3-1 $x(1/\tau_w)$. Such values are close to those measured with magnetic coils for the growth rate of magnetic "thin shell" modes [2]: this suggests that the

growth of the structure could be related to the growth of instabilities connected with the presence of a thin shell. A preliminary tomographic reconstruction performed using codes written by P.Smeulders [12] shows that this phenomenolgy corresponds to the growth of an m=1 structure centred at +16 cm, whose width increases with time.
After installation of the secondary shell, there is much less evidence for this phenomenon.

5. CONCLUSIONS

SXR emission has been measured in three versions of the HBTX RFP experiment with the same geometry but different shell times. From these measurements a degradation of particle confinement during the operation with the thin shell is found.
Coherent oscillations in both SXR emissivity and global magnetic quantities have been observed and are consistent with the outcome of counteracting actions of resistive diffusion and relaxation processes.
A trend for the coherent oscillation period to increase with the resistive diffusion time can be inferred from experimental data from HBTX and is supported by data from other RFPs.
The RMS normalized fluctuation level in SXR intensity grows with plasma resistance, indicating enhanced MHD activity is needed to sustain the configuration against diffusion.
The growth of a structure in the SXR emissivity profile probably related to "thin shell" modes has also been clearly observed in thin shell operation .
SXR studies have thus provided a further insight into the dynamics of the RFP and have demonstrated features in thin shell operation which confirm a globally poorer confinement in this kind of operation.

ACKNOWLEDGMENTS

The authors wish to acknowledge Dr. P Smeulders for having made available his code for tomographic reconstructions. One of the authors (P.M.) would also like to acknowledge all the members of HBTX team for the support and the kind hospitality accorded during his visit at Culham.

REFERENCES

[1] Alper B et al., Plasma Physics Contr. Fusion **30** (1988) 843.
[2] Alper B, Bevir M K et al., "Results from HBTX1C with Close and Distant Resistive Shells", this conference.
[3] Hayden R J and Alper B , 'Coherent oscillations in HBTX1B RFP plasmas', Plasma Physics Contr. Fusion **31** (1989) vol.2, to be published.
[4] Carolan P G and Piotrowicz V A, Plasma Physics **25** (1983) 1065.
[5] Watt R G and Nebel R A, Phys. Fluids **26** (1983) 1166.
[6] Antoni V and Ortolani S, Phys. Fluids **30** (1987) 1489.
[7] Hirano Y et al., Proc. 10th International Conference on Plasma Physics and Controlled Nuclear Fusion Research, London, UK, 1984; vol.2 (1985) 475.
[8] Antoni V, Martin P and Ortolani S, Plasma Physics Contr. Fusion **29** (1987) 279
[9] Tsui H Y W and Cunnane J A, Plasma Physics Contr. Fusion **30** (1988) 865.
[10] Ueda Y et al., Nuclear Fusion **27** (1987) 1453.
[11] Wereley K A, Nebel R A and Wurden G A, Phys. Fluids **28** (1985) 1450.
[12] Smeulders P, Nuclear Fusion **26** (1986) 267.

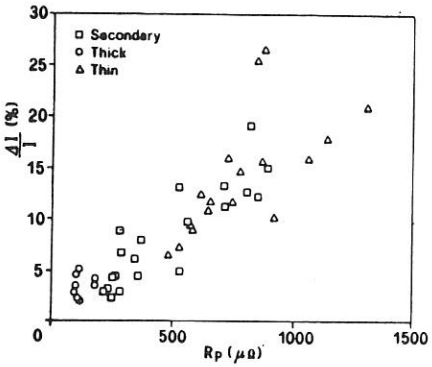

Fig.1: SXR RMS fluctuations vs plasma resistance

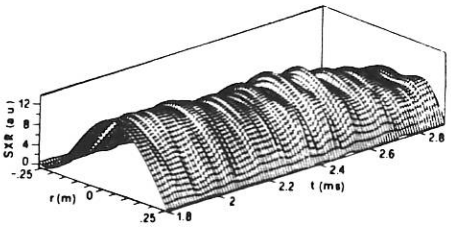

Fig.2: Coherent oscillations in the chord integrated SXR profile

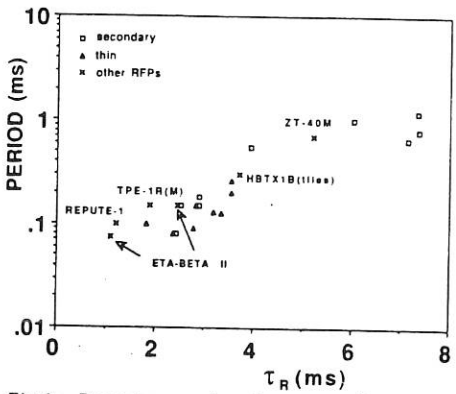

Fig.4: Dependence of coherent oscillations period on the resistive diffusion time

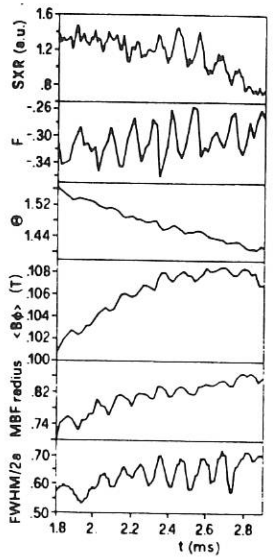

Fig.3: Oscillations in various plasma parametrs for the same discharge as fig.2

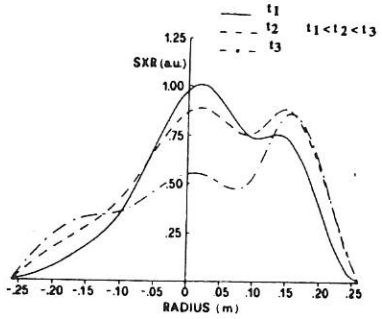

Fig.5: SXR profiles at 3 times during a thin shell discharge

MAGNETIC FLUCTUATION STUDIES IN RFPs WITH VARIOUS SHELL TIMES

J A Cunnane*, R J La Haye+ and H Y W Tsui

Culham Laboratory, Abingdon, Oxon, OX14 3DB, UK
(UKAEA/Euratom Fusion Association

* University College, Cork, Ireland
+ General Atomics, San Diego, CA, USA

Abstract RFP experiments with various shell times have been carried out in the HBTX assembly. Measurements of the edge magnetic fields reveals fluctuations thought to be related to the dynamo process and also magnetic perturbation identified as resistive shell modes. In resistive shell operation, the larger loop voltage and current termination can be associated with the growing resistive shell modes.

Introduction A conducting shell becomes a resistive shell when the pulse duration is comparable or longer than the time constant for vertical field penetration (τ_w). The properties of magnetic fluctuations and equilibrium in Reversed Field Pinches (RFP) depend on the wall penetration time for magnetic fields. These have been investigated using arrays of magnetic pick-up coils in experiments on the HBTX device fitted with shells having τ_w of 80 ms, 0.5 ms and 0.5 ms plus a 5.5ms secondary distant shell. Numerical analysis on these measurements yields information on poloidal and toroidal wavenumber (m,n) as well as frequency (f).

Equilibrium and Stability With a perfectly conducting shell, RFP operation stable to current driven modes is possible. When the profile of $\mu = \underline{j}.\underline{B}/B^2$ is expressed as $\mu(r) = \mu(0)\ (1-(r/a)^{\alpha})$ and $\mu(0) = 2\theta_0/a$, the ideal shell stable region in the $\alpha - \theta_0$ parameter space [1] is shown in Fig 1. Also plotted are the internal resistive shell modes [2] stable region and the operating values of α and θ_0 in experiments. (External resistive shell modes are always unstable). It can be seen that the RFP plasma in HBTX1B with a conducting shell of τ_w = 80 ms is stable or at least marginally stable to the ideal shell modes. In HBTX1C with resistive shell of τ_w = 0.5 ms, the time evolution of the F and θ values indicates a configuration initially unstable to both the ideal and resistive shell modes changing to ideal shell stable. However, the configuration remains unstable to the internal resistive shell modes. With the secondary shell of τ_w = 5.5 ms, the F and θ values are changed but the configuration is still unstable.

It has been suggested [3] that the dynamo arises indirectly from the

interaction of internally resonant modes. In experiments, field reversal is maintained robustly for all values of τ_w, and reversal strength seems to depend only weakly on mode amplitudes (see later).

Conducting-shell studies For conducting-shell (τ_w = 80 ms) RFPs, magnetic fluctuation activity is concentrated between 5 kHz and 80 kHz, with m = 0 and m = 1, and a broad band of toroidal wavenumbers $|n| \sim 5$-18. Fig 2 shows the n-spectrum for B_ϕ fluctuations. This broad band activity is tentatively identified as the 'dynamo' activity needed to generate toroidal field reversal. No single dominant n-mode was seen; we conjecture that the modes interact strongly to broaden the n-spectrum. By correlation of mode signals measured at different locations, mode rotations are estimated to be of the order of 10^4 ms^{-1}. No distinct precursor to discharge termination is evident in the magnetic data. With deeper field reversal, an m = 1, $|n| \sim 4$-6 helical perturbation resembling Taylor's second minimum-energy state was found. Theory predicts that this second state should exist only at deep reversal and with n = 4 for HBTX. There is very little low frequency ($f \leq 5$ kHz) activity and no discernible steady mode growth.

Resistive-shell Experiments With a resistive shell (τ_w = 0.5 ms) positioned at 1.15 times the plasma minor radius [4], fluctuations are dominantly m = 0 and 1. Low-frequency ($f << 5$ kHz) magnetic perturbations were observed to contain (m,n) = (1, -5 to -7) on-axis or internal resonant modes, with some (1, 2 to 3) externally nonresonant kinks, both growing on timescales similar to the wall time, and rotating very slowly or not at all ($\omega\tau_w < 0.1$); these growth rates correspond to those predicted by the linear theory of resistive-shell modes [2]. Non-linear theory [5] predicts mode-locking to the resistive wall. An (m, n) = (1, 9 to 11) external mode was also observed experimentally, with some (m, n) = (1, $\sim$ -13). High-frequency modes exist at much lower amplitudes (typically below 1% of mean field) and have a broad band of n-numbers each having similar magnitude remaining roughly constant throughout the discharge. The growth of the dominant modes is illustrated in Fig 3. After the electrically noisy setting-up phase, there is evidence of a brief quiescent period of about 0.5 ms before an initial prompt mode growth occurs, followed by a steady growth to large amplitude. Typical growth rates γ during this steady increase are $\gamma\tau_w = 0.3 \pm 0.1$ for all dominant modes. Large radial fields at the plasma boundary (Fig 4) up to a magnitude of the order of 10-20% of the local field) and mode growth rate acceleration were seen to precede abrupt discharge termination at less than 10 wall times. The magnetic activity at higher frequencies is stronger than that seen during conducting-shell discharges.

Experiments with Secondary Shell A secondary shell with τ_w = 5.5 ms, distant from the plasma (at 1.6 times the minor radius), has been

installed recently [6]. Growth times for the resistive-shell modes are about twice as long as those seen with the 0.5 ms shell, and typical discharge duration is correspondingly longer (up to 10 ms). Despite this, the normalised growth rate $\gamma\tau_w$ is larger with the secondary shell ($\gamma\tau_w \sim$ 2-3); linear calculations predict this for a shell distant from the plasma. The same four groups of low-frequency modes are present here as in the discharges with τ_w = 0.5 ms. Fig 3 also shows dominant mode development for this value of τ_w. The field reversal ratio at the same θ remains unchanged from the resistive-shell case despite the large change in mode amplitudes (including the internal resonant modes) at different τ_w. Theory predicts that the secondary shell should slow the growth of the low-n modes most; the slowing depends on the relative sizes of the mode wavelength and the vacuum region between the secondary shell and the plasma. The experimental observation of similar slower growth rates for all dominant modes indicates that some non-linear coupling between the modes is present. Large radial fields are still present, but at lower levels (Fig 4). The radial magnetic flux linking the wall had decreased from 51 to 32 mWb at the current flat-top and is consistent with the non-Spitzer contributions of 49 and 32 volts, according to helicity balance calculations [7], to the loop voltages of 67 and 51 volts where the estimated values for Spitzer resistivity contribution is 17 and 11 volts. The slower growth rate allows the discharge to last longer until the field perturbation is too large to sustain.

Conclusion The resistive shell stability of Reversed Field Pinch plasma has been demonstrated in a series of experiments on HBTX assembly with various shell times. Unstable modes growing on the shell timescale and having properties consistent with the predictions of thin shell theory have been identified. All dominant modes have similar growth rates and the growth of modes with higher wavenumbers is slowed more effectively by the presence of a secondary distant shell than the linear calculation predicts, both indicating non-linear effects. The higher loop voltage in thin shell operation is consistent with the larger radial field leading to extra helicity loss. The growth of these thin shell modes to large amplitude limits pulse length but does not significantly affect the higher frequency activity thought to furnish the dynamo action.

References

[1] V Antoni et al, Nucl. Fus., 26 (1986) 1711
[2] C G Gimblett, Nucl. Fus., 26 (1986) 617
[3] E J Caramana, R A Nebel, and D D Schnack, Nonlinear, Phys. Fluids, 26 (1983) 1305
[4] B Alper et al, 'RFP stability with a resistive shell in HBTX1C', Plasma Phys Contr. Fus, 31(2), Feb 1989, to be published
[5] Y L Ho and S C Prager, Phys. Fluids, 31 (1988) 1673
[6] B Alper et al, 'Plasma confinement in HBTX with a distant resistive shell', this conference
[7] H Y W Tsui, Nucl. Fus., 28 (1988) 1543

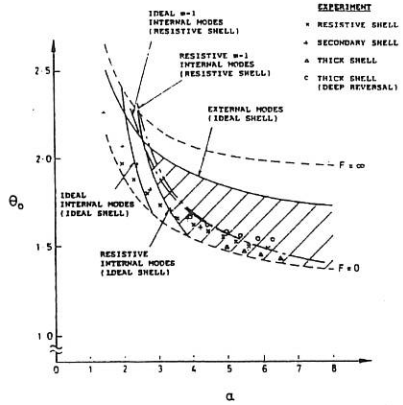

Fig 1 Stability diagram and HBTX operating parameters.

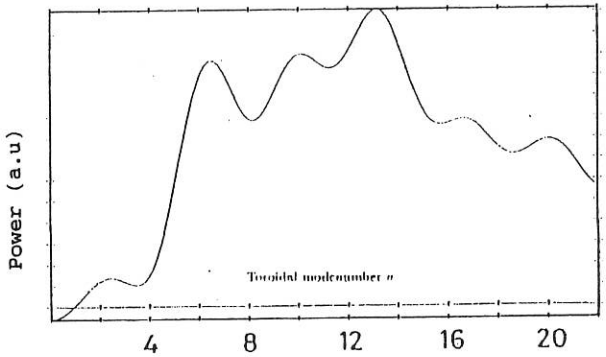

Fig 2 Toroidal modenumber spectrum of B_ϕ with τ_w = 80 ms.

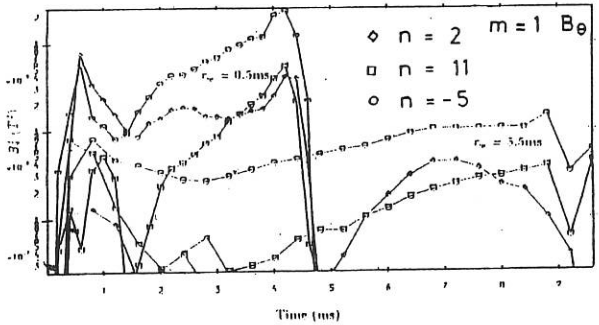

Fig 3 History of dominant B_θ m=1 modes with τ_w = 0.5 ms and with τ_w = 5.5 ms secondary shell.

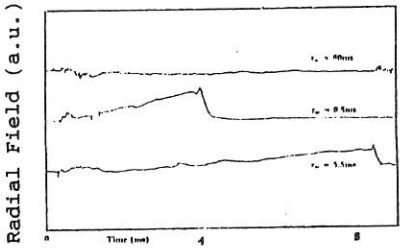

Fig 4 Local radial field at the plasma surface for various τ_w. Note the early termination of τ_w = 0.5 ms discharges due to the resistive instability growth.

Equilibrium Measurements on the REPUTE-1 RFP Plasma

H. Ji, H.Toyama, S.Shinohara, A.Fujisawa, K.Yamagishi,
Y.Shimazu, A.Ejiri, K.Shimoji and K.Miyamoto

Department of Physics, Faculty of Science, University of Tokyo,
7-3-1 Hongo, Bunkyo-ku, Tokyo 113, Japan

Introduction

Global plasma equilibrium measurements by external magnetic probes are widely introduced on the toroidal plasmas, i.e. tokamaks or RFPs, because of their simplicity and convenience. The measurement principle is based on Shafranov's toroidal equilibrium theory[1], which gives simple relations between the global equilibrium quantity and the external fields. These relations are valid in the either case of existence or absence of ideal shell just out the plasma column, however, not valid in the case of the thin (or resistive) shell, whose skin time τ_s has the same order of the current rise time τ_r. A method introduced by Swain et al.[2] is effective in this case, in which the plasma current I_p is replaced by 6 filament currents. However, by this method it is difficult to include the effect of iron core and computation requires a lot (beyond 14) of the measurement of the fields or flux loop. In this paper we introduce a simple method which is based on fitting measured fields to the vacuum approximate solution of Grad-Shafranov equation. The computation require only a few measurements (≥ 6) of the fields.

REPUTE-1 device[3] is characterized by a thin shell of $5mm$ thickness whose skin time τ_s for the penetration of the vertical field is $1ms$ compared with τ_r of $0.5ms$. The optimum discharges whose duration τ_d are about 3 times of τ_s have been obtained. In spite of various efforts including vertical-ohmic coils series connection experiments[4], toroidal ripple reduction experiments[5] and port bypass plate installation experiments[6], until now τ_d is still limited by $3.2ms$. We should think that the equilibrium of plasma is lost due to an unfavorable vertical field. In this paper we present the measurements of the time evolution of the plasma position from the flat-top phase to the termination phase, at that time the plasma begins to lose its equilibrium. The liner has a major radius R_L of 82 cm and a minor radius a_L of 22 cm.

Poloidal Array of Magnetic Probes

A poloidal array of magnetic field pick-up coils with protective covers of 0.7 mm thick stainless steel, is installed inside the vacuum vessel of 2.4 mm thick Inconel-625 at a port segment. A square cross section pipe runs poloidally between the probes which leads the coil signal wires to the feedthrough and protects them from damages by the plasma. The magnetic fields can be measured with good frequency response up to 40 kHz. The array covers all poloidal angle equally at 8 poloidal positions with a 45° separation. At each position the toroidal, poloidal and radial components of field B_ϕ,B_θ and B_r can be measured on or just out the plasma surface simultaneously.

Plasma Equilibrium Model

For the equilibrium model we assume that the plasma has a circular outermost magnetic surface which has a radius of a, as shown in Fig.1. Outside the plasma $r>a$ we use the vacuum solution of Grad-Shafranov equation

in the first approximation of the expansion in r/R[1]:

$$B_\theta(r,\theta)=\frac{a}{r}B_a+\frac{a}{2R}B_a[(1+\frac{a^2}{r^2})(\Lambda+\frac{1}{2})+\ln\frac{r}{a}-1]\cos\theta; \quad (1)$$

$$B_r(r,\theta)=\frac{a}{2R}B_a[\ln\frac{r}{a}+(\Lambda+\frac{1}{2})(1-\frac{a^2}{r^2})]\sin\theta.$$

which satisfied the boundary condition $B_\theta(a,\theta)=B_a(1+a/R\Lambda\cos\theta)$; $B_r(a,\theta)=0$ at $r=a$. Here $B_a=-\mu_0 I_p/2\pi a$, $\Lambda=\beta_p+l_i/2-1$, where β_p is the poloidal beta and l_i is the internal inductance of the unit length of the plasma column.

Determination of Plasma Position

Now we define Δ_x, Δ_y as the horizontal and vertical displacement of the outermost magnetic surface from the liner center, so the plasma major and minor radius R and a are reduced to $R=R_L+\Delta_x$; $a=r_L-(\Delta_x^2+\Delta_y^2)^{1/2}$, respectively, as shown in Fig.1. Figure 2 shows the definitions of r_i, θ_i^0 and θ_i with respect to the i-th probes. θ_i^0 is a constant and r_i and θ_i are determined from Δ_x and Δ_y. From (1) we have the fields at the i-th probe position:

$$B'_{\theta i}=\frac{a}{2R}B_a[C_0\cos\theta_i^0+C_1\cos(\theta_i^0-\theta_i)+C_2\cos(\theta_i^0-2\theta_i)];$$

$$B'_{ri}=-\frac{a}{2R}B_a[C_0\sin\theta_i^0+C_1\sin(\theta_i^0-\theta_i)+C_2\sin(\theta_i^0-2\theta_i)]; \quad (2)$$

$$C_0=\ln\frac{r_i}{a}+\Lambda;\quad C_1=\frac{2R}{r_i};\quad C_2=\frac{a^2}{r_i^2}(\Lambda+\frac{1}{2})-\frac{1}{2}.$$

There is three free parameters to determine $B'_{\theta i}$ and B'_{ri}: Δ_x, Δ_y and Λ. We use the least squares method to determine these free parameters, i.e. to fine a set of Δ_x, Δ_y, Λ which minimize

$$S=\sum_i[(\frac{B_{\theta i}-B'_{\theta i}}{\sigma_{\theta i}})^2+(\frac{B_{ri}-B'_{ri}}{\sigma_{ri}})^2] \quad (3)$$

where $B_{\theta i}$ and B_{ri} are the poloidal and radial fields measured by the i-th probe, $\sigma_{\theta i}$ and σ_{ri} are standard deviation of errors in $B_{\theta i}$ and B_{ri} measurements. Because this fitting is a nonlinear problem, Δ_x, Δ_y and Λ are calculated using Gauss-Newton Method based on linear approximation, through an iteration process. Test fitting are performed by ideal data with random error. To enable the determination, it is required that B_θ and B_r are measured at least at proper 3 poloidal positions. In fact, the calculation is usually carried out within iterations of ten times, so it is enough quick to perform it between shots as a real time routine. Note that one can not determine Δ_x and Λ separately only by B_θ measurements, because of their negative correlation.

Results of Position Measurements

Parameters of a typical discharge in REPUTE-1 RFP are shown in Fig.3(a). At $t\sim1.4ms$, I_p has the maximum value of $\sim280kA$, the loop voltage $V_l\sim150V$ and the chord-averaged electron density $\bar{n}_e\sim5\times10^{19}m^{-3}$. The discharge is not maintained to a quasi-steady state, i.e. I_p begins to fall down and V_l begins to rise up, after I_p reaches its maximum value. Figure 3(b)

shows the time evolution of Λ, Δ_x, Δ_y and Δ_t, where toroidal shift Δ_t presents distance between the magnetic axis and the center of outermost magnetic surface due to the toroidal effect: $\Delta_t = a^2/2R(\Lambda + 1/2)$ and typically $\Delta_t \sim 1cm$. Fitting errors estimated from measurement errors are enough small so can be neglected usually. The reversal ratio F and the pinch parameter Θ are also shown in Fig.3(a), where solid lines and dash lines indicate the values with and without correction according to change in the plasma position, respectively. It is shown that observed values of $F \sim -0.35$ and $\Theta \sim 2.25$ are reduced to reasonable ones of $F \sim -0.25$ and $\Theta \sim 1.90$ through the correction due to the plasma position at the current flat-top ($t \sim 1.4ms$). During the flat-top phase $\Lambda \sim -0.20$, this is consistent with the results of $\beta_p \sim 0.1$ and $l_i \sim 1.2-1.4$ [3]. $\Lambda - \Theta$ diagram is shown in Fig.4, where parameter α is defined by $\mu = \mu_0 \mathbf{j} \cdot \mathbf{B}/B^2 \propto 1-(r/a)^\alpha$.

Before I_p begins to fall down at $t \sim 1.4ms$, the plasma column starts to move outward and downward from the liner center at $t \sim 1.1ms$. This plasma column displacement, in other words plasma position instability, can be considered as an origin of the discharge termination, although its toroidal dependence is unkown. It is not clear whether the outward movement is due to either weak vertical fields or short skin time of the shell. According to measurements using an internal probe array, the penetration of the vertical fields into the shell is dependent on its distance from the torus center, i.e. the penetration at the outside of torus is faster than that at the inside of torus. It can be explained by the situation that eddy currents flowing in shell, which refuse the penetration of external fields, are disturbed by a lot of big holes existing at the outside of torus. As a result, the decay index $N = -RdB_v/B_v dR$ in the shell has a negative sign during the penetration, in spite of a positive sign after penetration. It can be considered that this negative N induce an up-down instability of the plasma column and perhaps cause the discharge to terminate.

Conclusion

A simple method is introduced to measure the plasma position, in the case of existence of a thin shell and externally applied vertical fields. The model bases on fitting measured external fields to the vacuum approximate solution of Grad-Shafranov equation, and the position determination require only a few measurements (≥ 6) of the fields. An application on REPUTE-1 RFP plasma equilibrium measurement shows that the plasma starts to move outward and downward before I_p begins to fall down. Downward movement can be explained as a result of negative N during the penetration of the vertical fields into the shell. It suggests that a faster and more precise feedback control in the vertical field coils system is necessary.

Reference

[1] V.S. Mukhovatov, V.D. Shafranov: Nucl. Fusion **11** (1971) 605.

[2] D.W. Swain, G.H. Neilson: Nucl. Fusion **22** (1982) 1015.

[3] Y. Ueda et al.: Nucl. Fusion **27** (1987) 1453.

[4] H. Toyama et al.: in Controlled Fusion and Plasma Physics (Proc. 14th Europ. Conf. Madrid, 1987), **PART 2** (1987) 544.

[5] K. Hattori, et al.: Nucl. Fusion **28** (1988) 311.

[6] H. Toyama et al.: this conference; S. Shinohara et al.: this conference.

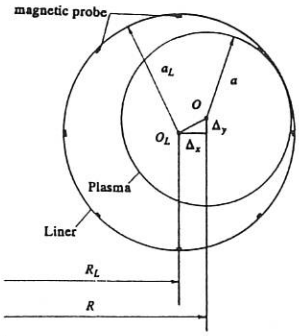

Fig. 1 Displacement of plasma from liner center and poloidal magnetic probe array.

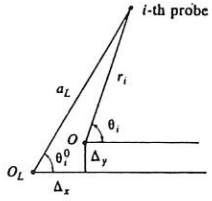

Fig. 2 Definitions of r_i, θ_i and θ_i^0 with respect to the i-th probes.

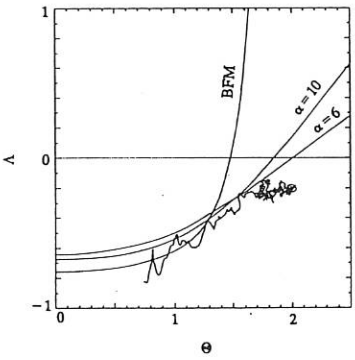

Fig. 4 $\Lambda-\Theta$ diagram. Here α is defined by $\mu=\mu_0 j\cdot B/B^2 \propto 1-(r/a)^\alpha$.

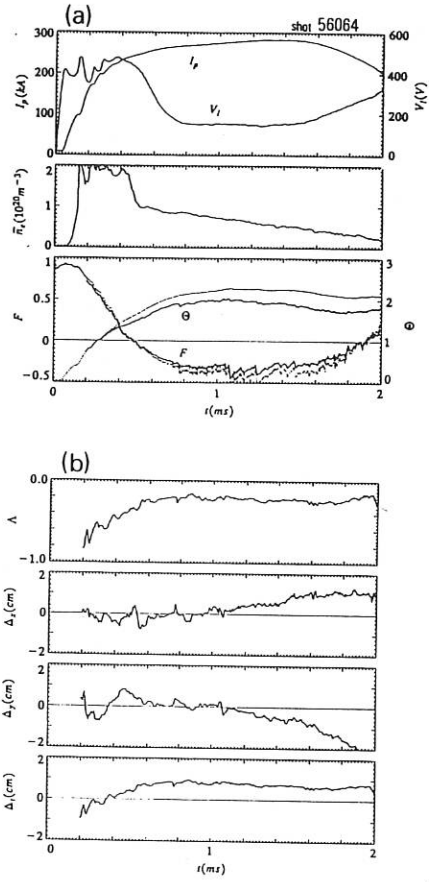

Fig. 3 Waveforms of I_p, V_l, $\bar{n}_e$, F and Θ (a); Λ, Δ_x, Δ_y and Δ_t (b) in a typical discharge.

FIELD ERROR REDUCTION EXPERIMENT ON THE REPUTE-1 RFP DEVICE

H.Toyama, S.Shinohara, K.Yamagishi, A.Fujisawa,
H.Ji, Y.Shimazu, A.Ejiri, K.Shimoji, K.Miyamoto
K.Saito*, N.Inoue*, Z.Yoshida*, J.Morikawa*

Department of Physics, Faculty of Science
Department of Engineering, Faculty of Engineering*
University of Tokyo
Bunkyo-ku,Tokyo 113, Japan

INTRODUCTION

The vacuum chamber of the RFP device REPUTE-1 [1,2] is a welded structure using 18 sets of 1 mm thick Inconel bellows(inner minor radius 22 cm) and 2.4 mm thick port segments arranged in toroidal geometry as shown in Fig.1. The vacuum chamber is surrounded by 5 mm thick stainless steel shells. The time constant of the shell is 1 ms for vertical field penetration. The pulse length in REPUTE-1 is so far 3.2 ms (about 3 times longer than shell skin time). The port bypass plates have been attached as shown in Fig.2 to reduce field errors so that the pulse length becomes longer and the loop voltage becomes lower.

MACHINE STATUS

Operations of the plasma current I_p up to 476 kA were achieved, changing the limit of charging voltage of OH power crowbar capacitor banks from 10 kV to 15 kV, but usually operated below 350 kA avoiding the wall damage. The lowest loop voltage V_l at the current flat top is 115 V (230 kA). The longest pulse length is 3.2 ms. The ion temperature measured by the Doppler broadening of CV line(2271 A) is 700 eV with the line averaged density n_e of 5 X $10^{19} m^{-3}$[3].

NUMERICAL ANALYSIS OF FIELD ERRORS

The distribution of the liner current of REPUTE-1 with and without port bypass plates is calculated using INCANET code(IHI Induced Current Analysis Code by the Network Mesh Method)[4]. The magnetic field generated by the liner current is calculated by Biot-Savart's law. The computational results show that field errors are reduced by a factor of 5, on average, by attaching port bypass plates.

EXPERIMENTAL RESULTS

PHASE 1 At first, 17 side ports were attached by the port bypass plates shown in Fig.2(a) and only one port was attached by the plate with a hole of 15 mm diameter as shown in Fig.2(b). The discharge optimization has been carried out as shown in Fig.3. The best shot of plasma current of 230 kA has shown that the plasma resistance R_p at the current flat top is 0.5 mohm; R_p is reduced 50 % compared with the discharges without port bypass plates.

PHASE 2 The bypass plates of five side ports were replaced by the plates with holes whose diameters are 30 mm (maximum) due to diagnostic requirements. An extensive series of I_p scan has been run at currents from 150 kA to 380 kA after the treatment of the carbonization, changing gas feed and the deepness of the reversal. Typically, conditions for getting good discharges are as follows; F value is -0.4 and the toroidal bias field is high; aided mode. The vertical field control is OH series mode. The ratio of the step-down transformer for OH power crowbar is 4:1. The plasma resistance R_p at the current flat top is shown in Fig.4 with and without port bypass plates as a function of the plasma current I_p. The R_p scales as $I_p^{-3/2}$ and the proportional constant(with plates) is reduced 25 % compared with no bypass plates.

PHASE 3 The port bypass plates of one side port were fully removed to install magnetic probes for equilibrium and fluctuation measurements[5]. In this case, R_p has increased 14 % compared with phase 2. In any phases, the pulse length has not been prolonged than 3.2 ms which was attained without bypass plates. The wall conditioning with the carbonization has the effect of not only eliminating pumpout phenomena but also getting higher ion temperature, typically 700 eV[3]. In these experiments, however, the carbonization has no effect on the plasma resistance.

CONCLUSION

The plasma resistance R_p at the current flat top of the best shot is reduced 50 % by attaching port bypass plates. In phase 2, the value of R_p scales as $I_p^{-3/2}$ and the value of R_p(with plates) is reduced 25 %. But the pulse length is not prolonged by this modification. The carbonization has no effect on the plasma resistance.

REFERENCES

[1] Y. Ueda et al: Nucl. Fusion **27**,1453(1987).

[2] K. Hattori et al: Nucl. Fusion **28**,311(1988).

[3] A. Fujisawa et al: Proc. 15th EPS Conf(Dubrovnik) p.549.
[4] K. Saito et al: Japanese J. Appl. Phys. **27**,1743(1988).
[5] H. Ji et al: this conference.

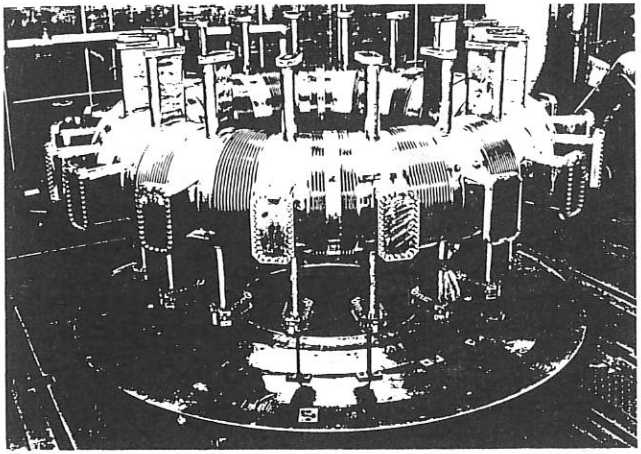

Fig. 1.

Vacuum chamber of REPUTE-1

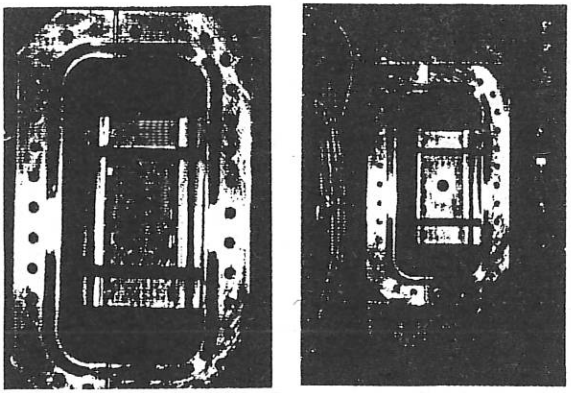

(a) (b)

Fig. 2.

(a) Bypass plates of side port
(b) Bypass plates with a hole of 15 mm diameter for phase 1 experiments

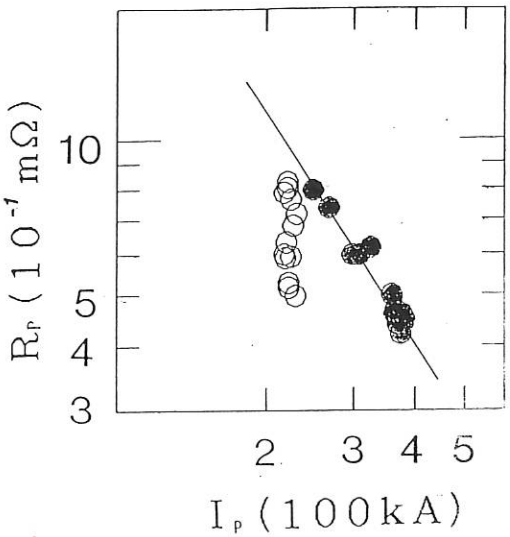

Fig. 3.

Change of plasma resistance R_p during procedure of optimization
●: closed circles; without port bypass plates as reference

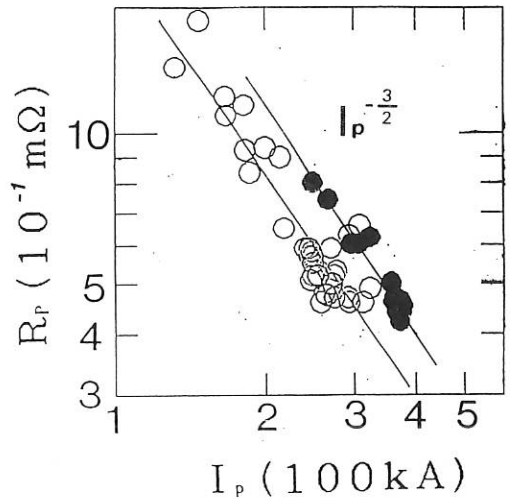

Fig. 4.

Plasma resistance R_p
vs.
plasma current I_p

o: open circles; with port bypass plates
● : closed circles; without port bypass plates

RFP Discharges with Port Bypass Plate and Trim Coil in the REPUTE-1

S. Shinohara, H. Toyama, A. Fujisawa, H. Ji, Y. Shimazu
A. Ejiri, K. Yamagishi, K. Miyamoto, Z. Yoshida,† N. Inoue†

Department of Physics, Faculty of Science,
†Department of Nuclear Engineering, Faculty of Engineering,
University of Tokyo, Bunkyo-ku, Tokyo 113, Japan

INTRODUCTION

The RFP discharges are sensitive to the error field. Near the port hole, this field generated by the liner current is large and must be minimized. In addition, plasma position control is very important to have good plasma parameters. In the REPUTE-1 RFP device (major radius R = 82 cm and minor radius a = 22 cm) [1-3], the port bypass plates and new trim coils are installed to reduce the error field and to control the external magnetic field in order to examine the effects on the plasma performance.

BYPASS PLATE

The bypass plates, located in the 54 port sections, can be expected to reduce the error magnetic field generated by a winding liner (made of Inconel 625) current [4-6]. Plates (3 mm thick SUS 304) consist of a 58 mm wide and 80 mm high plate, and two plates, 58 mm wide and 22 mm high, at the side port. At the top and bottom ports, one plate, 45 mm wide and 95 mm long in the major radius direction, is installed. Each plate has a hole of 20 - 30 mm in diameter, at the every top and bottom ports and at a half number of the side ports.

Before the installation of bypass plates, a radial profile of the vertical magnetic field B_z was measured in order to check the error field in the presence of the toroidal liner current. The probe measurements show that this error field is consistent with the results of the calculations, *i. e.*, an analytical method with a plane geometry [4,5] and a three dimensional network mesh method [6], as shown in Fig.1. Here, the effects of the iron core [7] and the up-to-down asymmetry of iron core gaps [8] are included to derive the measured field value from the liner current component. Note that the B_z value is finite in the vacuum chamber due to the toroidal effect.

In comparison to the case without bypass plates, the plasma resistance R_p, defined as the ratio of the toroidal loop voltage V_l to the plasma current I_p at the current maximum, decreased by about 25 % (Fig.2) and 40 % (Fig.3), for the cases of R = 4 and 2, respectively. Here, R is a winding ratio of the step-down transformer of the ohmic PFN power supply, and the extended empirical scalings are also shown in the figures for comparison;

broken and solid lines mean the previous results of no bypass plate with R = 4 (I_p = 240 - 360 kA) and 2 (I_p = 230 - 270 kA), respectively. This R_p scaled as -(3/2) power law of I_p, which has the same tendency with the previous results. With an increase in I_p, a reproducibility of the discharge became better. For the case of R = 4, there was no difference between the matched and high bias modes (and between with and without the carbonization) as for the R_p value, and this value was typically 0.45 mΩ at I_p = 300 kA. However, the plasma discharge duration was unchanged using the plates ($\leq$ 3.2 ms).

When the bypass plates at one side port was extracted with an insertion of poloidal magnetic probe array inside the liner (7 mm beyond the liner surface), the plasma resistance R_p decreased with I_p, but did not show a decrease (nearly constant) above I_p = 250 kA for both cases of R = 4 (Fig.5) and 2. Here, the probe jacket, made of SUS304, occupies 8 cm (in total) and 1.4 cm in the poloidal and toroidal directions, respectively. There is a possibility that this independency of I_p comes from the change of the wall condition (including the probe array) and/or from the increased error field at the one side port. Generally, the CrI intensity (4275 A) increases drastically at the end of the discharge, but, at least, a remarkable increase in this emission with increasing I_p at the flat top phase was not found.

TRIM COIL

The trim coils consist of the additional vertical (V_{ad}) and toroidal (T_{ad}) field coils wound around the torus. The V_{ad} coils are expected to act as a trimming of the equilibrium vertical field, control of the coupling between the vertical and ohmic coil systems, an active stabilization of the plasma column (decay index control) and a passive one. The V_{ad} coils are located on the eight poloidal positions around the torus.

The preliminary experiments as control of the coupling shows a wider range of the operational regime; ramp up of the plasma current from 230 kA to 285 kA by increasing the power supply voltages (from 4.7 to 6.0 kV and from 0.8 to 1.1 kV for vertical start and PFN voltages, respectively) of the vertical field coils for the fixed ones ($\sim$ 10 kV) of the ohmic coil, as shown in Fig.5. The vertical field coils were connected in series with the V_{ad} coils, and the total net turns of coils were four, which was a direction of the plasma current. During the ramp up, the ratio I_v/I_p (I_v: current of vertical field coil) was nearly constant of $\sim$ 0.017. The efficiency to ramp the plasma current by the increase in the vertical field power supply was nearly the same with the ohmic one from a view point of the necessary stored energy of the condenser bank. With an increase in the ramped plasma current, a decrease in the plasma resistance was also found (see Fig.3). By the careful trimming of the vertical field, R_p could be decreased by $\sim$ 20 % compared with the results in Fig.3 (closed triangles). These results show

that the positioning of the plasma column is very important to have the better plasma discharges.

The T_{ad} coils are expected to reduce the toroidal field ripple between the ports, although the ripple at the port section increases. The mean ripple at the minor radius r of 22 cm at the outer side of the torus decreases from 5.5 % to 3.0 % from the calculation. However, up to now, the better plasma discharge compared with the previous experiments [9] has not been found in spite of the finer positioning of the T_{ad} coils.

CONCLUSIONS

In order to get the better plasma discharges, the experiments using the port bypass plates and trim coils have been executed in the REPUTE-1 RFP device. The plasma resistance decreased in the presence of plates, and the new operational regime of ramping the plasma current with vertical trim coils was found.

REFERENCES

[1] N. Asakura *et al.*, Plasma Phys. and Contr. Fusion **28** (1986) 805.

[2] N. Asakura *et al.*, in *Proc. 11th Conf. on Plasma Phys. and Contr. Nucl. Fus. Res.* (Kyoto, 1986) **2** (1987) 433.

[3] N. Inoue *et al.*, in *Proc. 12th Conf. on Plasma Phys. and Contr. Nucl. Fus. Res.* (Nice, 1988) IAEA-CN-50/C-5-8.

[4] S. Shinohara, in *Proc. 15th Conf. on Contr. Fusion and Plasma Heating* **12B PART II** (1988) 541.

[5] S. Shinohara, Jpn. J. Appl. Phys. **27** (1988) 1299.

[6] K. Saito *et al.*, Jpn. J. Appl. Phys. **27** (1988) 1743.

[7] S. Shinohara *et al.*, J. Phys. Soc. Jpn. **52** (1983) 94.

[8] T. Fujita *et al.*, J. Appl. Phys. **59** (1986) 2277.

[9] K. Hattori *et al.*, Nucl. Fusion **28** (1988) 311.

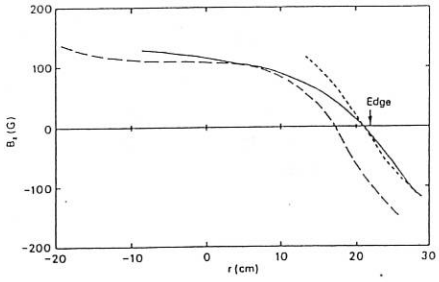

Fig.1 Radial profiles of the vertical field for the case of measurement (solid line) and calculations (dotted line [4,5] and broken line [6]) without bypass plates.

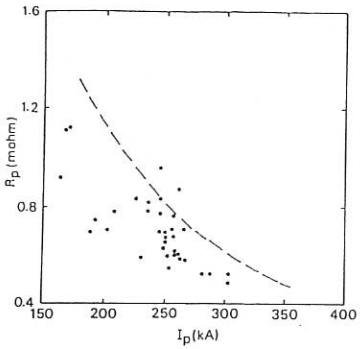

Fig.2 R_p vs. I_p with high bias mode and $R = 4$.

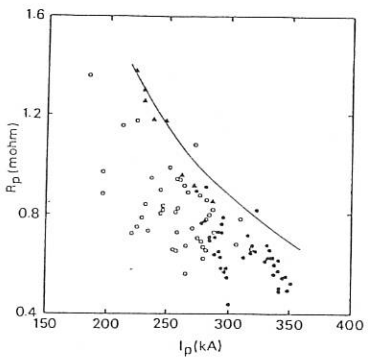

Fig.3 R_p vs. I_p with matched (open circles), high bias (closed circles) and high bias ramp up (closed triangles) modes for the case of $R = 2$.

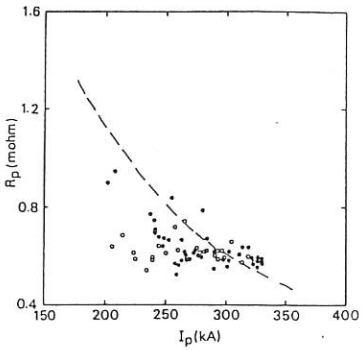

Fig.4 R_p vs. I_p with matched (open circles) and high bias (closed circles) modes with $R = 4$. Previous scaling curve is also shown.

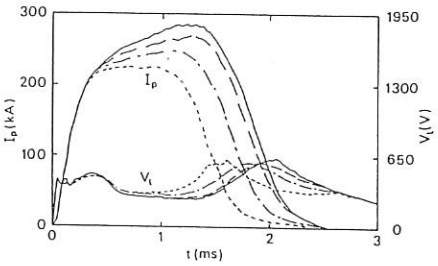

Fig.5 Time evolution of I_p and V_l with ramp up mode and $R = 2$.

EQUILIBRIUM AND STABILITY OF THE STE RFP

Sadao Masamune, Hiroshi Oshiyama

Department of Electronics and Information Science
Kyoto Institute of Technology, Sakyo-ku, Kyoto 606, Japan

ABSTRACT

A reversed-field pinch (RFP) plasma which has characteristics typical of that produced in a conventional thin metal liner has been obtained in the STE-1(M) RFP experiment. It uses a 3.4 mm thick metal chamber with four insulators for application of the toroidal voltage, along with the aided self-reversal mode for setting up the RFP configuration. Displacement of the center-of-current channel at the gap was twice as large as that far from the gap. This local displacement could be controlled with a vertical field. Initial results from the STE-2 RFP experiment will also be described.

INTRODUCTION

At first, as an introduction, we will give a brief histrical review of the study of magnetic separatrix in the STE RFP experiments. Here, STE is the acronym for separatrix test experiment.

Oshiyama proposed a method for setting up the RFP configuration with the use of the poloidal heliotron (PH) magnetic field as an initial bias, and experimental demonstration of this method was performed in a linear device[1]. This concept was applied to a toroidal device, STE-RFP, which used a glass discharge chamber. It was demonstrated that stable toroidal asymmetric RFP configuration was easily attained with the self-reversal mode using the PH bias field, when compared with the axisymmetric bias field[2,3].

In studying the magnetic separatrix in a RFP, the use of a thick metal liner appears to be required because heat flux to the wall will be highly localized under such circumstances. The STE-RFP was then modified to the axisymmetric STE-1(M)[4], whose objectives included setting up the RFP and sustaining its equilibrium in a thick metal chamber having insulator gaps. More recently, the STE-2 RFP has been constructed, in which device it is expected to establish a scenario for sustaining stable RFP with a duration much longer than the time constant of the thick metal chamber. This paper primarily includes the results from the STE-1(M) RFP experiment. Initial results from the STE-2 RFP experiment are also included.

STE-1(M) RFP EXPERIMENT

The STE-1(M) uses a 3.4 mm thick stainless steel toroidal chamber with a 24 cm major radius and an 8 cm minor radius. The chamber is insulated toroidally at four locations separated by 90° in the toroidal direction by a 5 mm thick insulator. The penetration time of the chamber for the toroidal field is 0.2 ms.

Figure 1 shows the time behavior of the loop voltage V_1, plasma current I_p, toroidal field at the plasma center $B_z(0)$, toroidal field at

the inner wall $B_z(a)$, and intensities of the H_α line and oxygen impurity lines. One-turn loop voltage higher than 400 V was applied at the initiation of the breakdown, however, we have observed no damage to the insulators. The setting-up time of RFP configuration is shorter than the penetration time of the chamber, which means that we have used the aided self reversal mode. The loop voltage for sustaining the discharge is about 150 V without a vertical field. This sustaining voltage does not strongly depend upon the plasma current, and thus, the global resistance of the plasma, $R_p = V_l/I_p$, is inversely proportional to the plasma current. It should be mentioned that net toroidal current flowing in the chamber and through the plasma at the gap is observed in the present experiment. Although this current decreases with increasing the plasma current, it still remains in the range of 10% of the plasma current for I_p of 20 kA. The toroidal field at the plasma center increases with a current up to 3-4 times the initial value, indicating that the plasma dynamo works in the STE-1(M). The RFP configuration is set up in 50-70 μs into the discharge, and is maintained for 0.2 ms.

A distinctive pressure window for stable RFP has been observed in the STE-1(M). For the filling pressure of hydrogen lower than 1 mTorr, the plasma current tends to disrupt before attaining the RFP. For the optimum filling pressure of 2 mTorr, the observed magnetic field profiles are well approximated by the Bessel functions (BF), indicating that the plasma is in a well-relaxed state. The value of F $(=B_z(a)/\langle B_z\rangle)$ and θ $(=B_\theta(a)/\langle B_z\rangle)$ are in the range from -0.2 to -0.3 and from 1.6 to 1.7, respectively, where $B_\theta(a)$ is the poloidal field at the wall and $\langle B_z\rangle$ is the average toroidal field. For a higher filling pressure, the field profiles deviate from BF and the field reversal becomes shallow.

Figure 1(e) clearly shows that the oxygen lines appear from the low ionization stage to the higher one, which is typical of a temperature increase phase. It is thus indicated that the electron temperature increases near to or slightly higher than the value restricted by the radiation barrier due to oxygen, about 20 eV. It appears that it requires more Joule input energy to show the evidence of burnthrough of the radiation barrier. It should also be noted that the time behavior of ion saturation current of an electrostatic probe showed that after its maximum at 0.7 ms, a rapid fall followed. It seems that pumpout of the density occurred in the STE-1(M).

Figure 2 shows the dependence on the vertical field B_v, (a) of the displacement of the center-of-current channel far from the gap, Δ_{av}, and of that at the gap, Δ_{gap}, (b) of the average radial field at the gap, B_r^{gap}, and (c) of the global resistance R_p at the maximum plasma current. Here Δ_{av} is the radial location of the magnetic axis determined from the poloidal magnetic field profiles, and Δ_{gap} is the displacement of the plasma column measured with a cosine coil at the gap. Time behavior of the vertical field at the gap was similar to that of the plasma current, and the value of B_v at the gap was plotted in the abscissa in Fig.2. Since skin time of the chamber for vertical field is almost the same as the current duration, Δ_{av} shows a weak dependence on B_v, while Δ_{gap} decreases almost linearly with increasing B_v. Optimization of B_v has resulted in a reduction of the resistance by 20%. Thus, in the present experiment, global equilibrium of the plasma was maintained by the thick metal

chamber, while local equilibrium at the insulator gap was improved with the external vertical field. We may therefore conclude that the global equilibrium and local one can be controlled separately for a RFP produced in a thick metal chamber.

Influence on the plasma performance of the toroidal asymmetry of time constant of the chamber brought about by vacuum flanges at the gaps should be studied carefully. Moreover, the net toroidal current might be a residual problem for the control of equilibrium.

STE-2 RFP EXPERIMENT

The STE-2 RFP uses a 2 mm thick stainless steel chamber with a 40 cm major radius and a 10 cm minor radius. No thick conducting shell has been mounted. It uses an iron core transformer with 0.3 V·s, which is five times as large as that of the STE-1(M). This machine is constructed for the purpose of establishing a scenario for sustaining a stable RFP with a duration much longer than the time constant of the metal chamber. In addition to local compensation of field errors at the gaps of the chamber, therefore, application of multipole fields are considered.

In the second phase of experiments, divertor configurations will be studied in this machine. In the design study of configurations, it has been shown that, in the axisymmetric poloidal divertor, a coaxial structure of the divertor hoop is effective in reducing derofmation of the magnetic surfaces near the outer edge[5].

To date, the STE-2 has operated as a RFP with currents up to $\gtrsim$30 kA. The RFP configuration is maintained for $\gtrsim$0.3 ms without the power crowbar being applied. Discharge optimization is in progress.

REFERENCES

[1] H.Oshiyama: J. Phys. Soc. Jpn. 49 (1980) 1199.
[2] H.Oshiyama and S.Masamune: Mem. Fac. Eng. & Design, Kyoto Inst. Tech. 33 (1984) 19.
[3] S.Masamune, S.I.Koh, and H.Oshiyama: J. Phys. Soc. Jpn. 57 (1988) 2229.
[4] S.Masamune and H.Oshiyama: Jpn. J. Appl. Phys. 27 (1988) L710.
[5] S.K.Koh and H.Oshiyama: J. Phys. Soc. Jpn. 55 (1986) 2901.

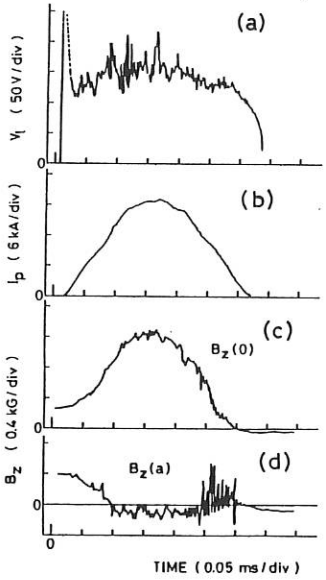

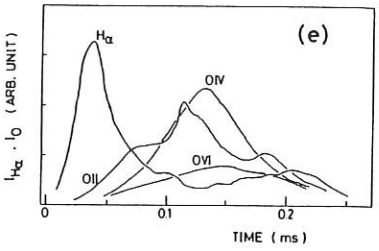

Fig.1. Discharge Characteristics of the STE-1(M) RFP.

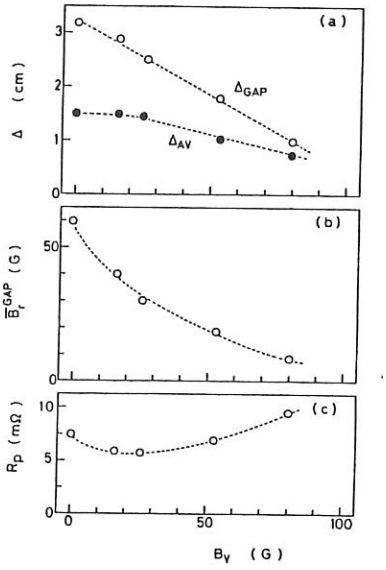

Fig.2. Dependence on the vertical field of the average and local displacements of the plasma column, radial field at the gap, and global resistance of the plasma.

EVIDENCE FOR POLOIDAL BETA LIMITED CONFINEMENT ON THE ZT-40M REVERSED FIELD PINCH

M. M. Pickrell, J. A. Phillips, C. P. Munson, P. G. Weber, G. Miller, K. F. Schoenberg, and J. C. Ingraham

Los Alamos National Laboratory, Los Alamos, NM 87545, USA

Motivation:

Confinement experiments on ZT-40M exhibit an approximate scaling of the plasma electron temperature-density product with the square of the plasma current: $n_{ave}kT_o \propto I_\phi^2$. These results are confirmed by similar performance of other RFP's.[1–4] Although the data fluctuate, and represent only well optimized discharges, the correlation suggests that the optimized poloidal beta is approximately constant: $\beta_\theta \sim$ constant. A comparison of the confinement scaling predicted by a constant beta, to the results of several RFP experiments also shows close agreement.[5]

These results suggest that the total energy transport process in the RFP adjusts to maintain an approximately constant plasma beta. Although total transport may be comprised of several competing processes, the dominant loss mechanism appears to be beta dependent. The dynamics can be modeled by a non- radiative thermal conductivity of the form: $\chi_{\text{dominant}} \propto f\,(\beta_\theta - \beta_{\text{crit}}(\vartheta_i))$ where f is some very strong function, and $\beta_{\text{crit}}(\vartheta_i)$ is either constant, or a weak function of some macroscopic plasma parameters ϑ_i. In this model, energy transport decreases to compensate for an increase of radiation, and $\beta_\theta \simeq \beta_{\text{crit}}$ is maintained.

Krypton Injection Experiment:

We tested this hypothesis on ZT-40M by mixing Krypton gas (about 3%) with the Deuterium fill, and measuring the effect of the enhanced impurity radiation on the plasma contained energy. The fraction of ohmic power radiated, ($\zeta \equiv \frac{P_{\text{radiated}}}{P_{\text{ohmic}}}$) was increased from approximately 15% to over 95%. The remaining energy loss by all other transport processes was reduced by an order of magnitude. This experiment tested whether the non radiative confinement properties of the plasma improved to compensate for the enhanced radiation loss, and consequently maintained a constant plasma beta.

In a zero dimensional model, the total confinement time and the non radiative confinement are related by: $\frac{1}{\tau_E} = \frac{1}{\tau_{E_{NR}}} + \frac{1}{\tau_{\text{radiation}}}$, where τ_E is the total energy containment time, $\tau_{E_{NR}}$ is the non radiative containment time associated with cross mean field transport, and $\tau_{\text{radiation}}$ is the confinement associated with radiation. This equation can be rearranged to express the non radiative confinement in terms of the total confinement time and the radiated fraction, ζ:

$$\tau_{E_{\text{NR}}} = \frac{\tau_E}{1 - (1 - \zeta)} \qquad (1)$$

Results and Scaling of the Non Radiative Confinement Time:

A series of discharges was run on ZT-40M in which various amounts of Krypton gas were injected to adjust the radiated power from 15% to over 95% of the ohmic input. However, most other macroscopic plasma parameters were held within a narrow range:

$$\begin{gathered} 170\text{kA} \leq I_\phi \leq 190\text{kA} \\ 3.6 \times 10^{13}\text{cm}^{-3} \leq \bar{n}_e \leq 4.4 \times 10^{13}\text{cm}^{-3} \\ \left|\frac{dI}{dt}\right| \leq 5\text{kA/millisecond} \\ 1.3 \leq \Theta \leq 1.43 \end{gathered} \tag{2}$$

The measured results confirm the hypothesis of a dominant, beta dependent transport process: on-axis plasma beta nominally remained the same, and the non radiative confinement improved as radiation was increased. Figure 1 plots the total poloidal beta, $\beta_\theta \equiv \left(1 + \frac{n_i}{n_e}\right) \frac{\bar{n}_e T_e(0)}{I_\phi^2}$, as a function of the radiation fraction. Total β_θ stayed constant or increased slightly as the radiation fraction was increased. Total energy confinement (τ_E) did decrease during Krypton injection, however, it was entirely due to increased plasma resistance, presumably from increased Z_{eff}.

The non radiative confinement time, $\tau_{E_{NR}}$ was calculated using equation 1, and the results are plotted in figure 2. As the radiation fraction was increased, the non radiative confinement time improved over an order of magnitude. The radiation loss more than compensated for the increased ohmic input. This result is perhaps the most dramatic demonstration of the constant beta hypothesis because the transport properties of the plasma were improved by the addition of an impurity.

Radiation Profiles:

In order for the $\tau_{E_{NR}}$ calculation to be meaningful, the radiated emission profile must be nearly flat or center peaked. By contrast, if the emission profile were edge peaked, then the radiation would originate from an annulus surrounding the plasma. This annulus would act as a radiation limiter, but would not affect the internal transport. Radiation was measured with an 8 chord bolometer array,[6] and the data were unfolded to obtain a two parameter representation of the radiation profile.

Although the low radiation discharges were edge peaked[7], the high radiation, Krypton discharges showed a nearly flat profile. Typical ratios of central to edge emission for Krypton shots were: $\frac{P_{\text{rad}_{\text{central}}}}{P_{\text{rad}_{\text{edge}}}} = 50\% - 100\%$. Typical chord averaged, path length normalized, profiles are shown in figure 3 for both the high and low radiation cases. These profiles are nearly flat for high radiation discharges.

Ion Effects:

The calculation of the ion beta assumed that $T_i = T_e$. However, when the data were analyzed using Doppler broadening of the CV impurity line as a measurement of T_i, the ratio $\frac{T_i}{T_e}$ increased with the radiation fraction. The results quoted here are therefore conservatively stated.

The ion beta calculation also included the diluting effect on the Deuterium ions by the Krypton ($\bar{n}_i \leq \bar{n}_e$). The ratio of Krypton to Deuterium ions ($\frac{n_K}{n_D}$) was measured by

the relative pressures recorded on a baratron gauge, and the Krypton charge state was calculated using the electron temperature and assuming coronal equilibrium (which will overestimate the dilution factor). The calculation was checked for self consistency by comparing to the increase in plasma resistance, and assuming that the change was due to a change of Z_{eff}. The ratio of ions to electrons is:

$$\frac{n_i}{n_e} = \frac{1}{1 + Z_K \left(\frac{n_K}{n_D}\right)} \tag{3}$$

For the maximum Krypton concentration of 3.4%, a Krypton charge of $Z_K = 9$, and a $\Delta Z_{\text{eff}} = 2$, the dilution factor is: $\frac{n_i}{n_e} \simeq .75$.

Implications for Future Experiments:

The improved confinement time predicted for future RFP experiments assumes a nearly constant beta. The Krypton injection experiment has provided a window to the next step machines by accessing the higher non radiative confinement properties of the RFP.

Krypton injection has also provided a method for adjustment of the cross mean field transport without changing most of the macroscopic plasma parameters, which permits searching for the mechanism of the transport process directly. For example, by correlating changes in the fluctuation spectrum with the improvement of $\tau_{E_{NR}}$, it may be possible to determine the spectrum of modes directly associated with the transport process.

References:

[1]B. Alper, S. Martini, and S. Ortolani, Nuclear Fusion **26**, 1256 (1986).

[2]K. I. Sato et al., in *Proceedings of the 11'th International Conference on Plasma Physics and Controlled Nuclear Fusion Research (Kyoto)*, p. 413 (Vienna, Austria, 1987) [Volume II].

[3]T. Shimada et al., in *Proceedings of the 11'th International Conference on Plasma Physics and Controlled Nuclear Fusion Research (Kyoto)*, p. 453 (Vienna, Austria, 1987) [Volume II].

[4]T. Tamano et al., in *Proceedings of the 10'th International Conference on Plasma Physics and Controlled Nuclear Fusion Research (London)*, p. 431 (Vienna, Austria, 1985) [Volume II].

[5]J. N. DiMarco, Technical Report LA-UR-REVISED-88-3375, Los Alamos National Laboratory, Los Alamos, NM 87545 (Los Alamos, NM 87545, 1988).

[6]G. Miller, J. C. Ingraham, and L. S. Schrank, Review of Scientific Instruements **59**, 700 (1988).

[7]V. Antoni, A. Buffa, L. Carraro, S. Costa, et al., in *Proceedings of the 11th Conference on Plasma Physics and Controlled Nuclear Fusion Research (Kyoto)*, p. 441 (IAEA, 1986) [Nuclear Fusion Supplement, 1987].

This work is supported by the US DOE.

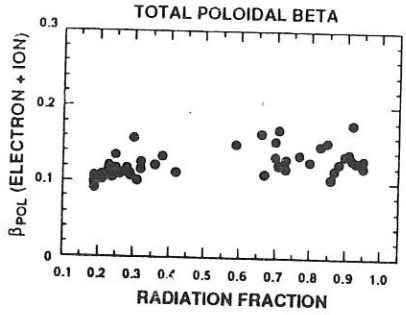

Figure 1: Total poloidal beta, β_θ, as a function of radiated fraction. β_θ is seen to remain constant or slightly improve as ζ is raised.

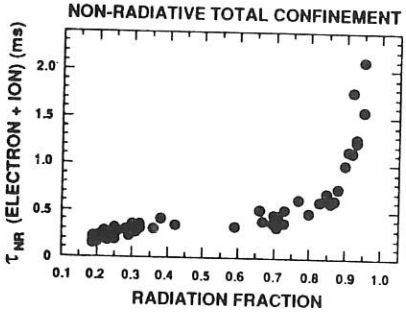

Figure 2: Total non radiative confinement time, $\tau_{E_{NR}}$, as a function of radiated fraction. The non radiative confinement improves an order of magnitude as as ζ is raised from 15% to 95%.

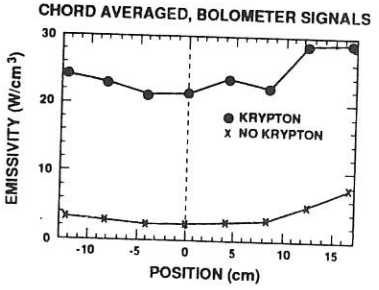

Figure 3: Chord averaged radiation profiles with and without Krypton. Note that the high radiation, Krypton shots have nearly flat chordal radiation profiles.

ION TEMPERATURE MEASUREMENTS IN HBTX1C WITH A THIN SHELL

C A Bunting and P G Carolan

Culham Laboratory, Abingdon, Oxon, OX14 3DB, UK
(UKAEA/Euratom Fusion Association)

Introduction

Results from a number of Reversed Field Pinch (RFP) machines where the shell time constant exceeds the plasma lifetime, can be accommodated in a simple ion power balance model [1]. In this paper, results from HBTX1C using a 'thin shell', and a 'distant secondary shell' are shown to be in broad agreement with this model for both RFP and Ultra Low Q (ULQ) discharges [2]. These new results suggests that the ion power balance model has wider application in systems other than the reversed field pinch.

Here we report measurements of the ion temperature in two new versions of HBTX. Firstly, where the long time constant stabilising shell of HBTX1B is replaced with a "thin shell" where the penetration time of the shell is short compared with the plasma duration, (τ_{shell} = 0.5msec; < τ_{pulse} ~3msec), and secondly where an additional external secondary shell with (τ_{shell} = 5.5msec; τ_{pulse} ~ 5-10msec) is used [3]. The secondary shell is seen to suppress thin shell modes. The plasmas with these new shells exhibited high fluctuations and high anomalous loop voltages for both RFP and ULQ discharges. It has been shown that Spitzer resistivities are inadequate to account for the observed loop voltages. Ion temperatures in these discharges of 0.35keV to 1.7keV are also much higher than can be accounted for by ion electron equipartition. There is a clear similarity between these conditions and those found when a graphite tile is used to intercept field lines at the edge of an RFP plasma which had a long shell time [4,5].

Ion heating model

In the RFP, the ion temperature is observed to be much higher than that expected from collisions. Loop voltages are also much larger than expected from classical considerations. In the ion power balance model [1], it is assumed that the ion heating is derived from the residual input power in excess of that required to heat the electrons through Spitzer resistivities. This residual power may be coupled to the fluid velocity fluctuations and the energy of these fluctuations provides the ion heating. Large loop voltages and high fluctuations levels were observed in both the RFP and ULQ configurations, and this is, at least, qualitatively in accord with the high ion temperatures measured. Since the ion energy density depends on both the input power and ion energy confinement, an evaluation of the ion temperature alone is not a good test of the ion power balance model. A much better comparison is obtained from T_i/T_e where the model provides the scaling:-

$$\frac{T_{io}}{T_{eo}} = \frac{1}{\chi}\,(C_z^{-1}\,\frac{V_\phi}{V_p} - 1)$$

where T_{io} and T_{eo} are the on-axis temperatures. The constants C_z ($\sim$ .48) and χ ($\sim$ 3.5) are calculated profile form factors, V_ϕ is the measured toroidal loop voltage, and V_p is the toroidal voltage calculated using helicity balance from F, θ and the resistivity profile.

Experimental results

The ion temperatures were measured over a range of plasma currents from 80kA to 250kA, for both the RFP and ULQ (q = 0.5) plasmas, using a five channel Neutral Particle Energy Analyser (NPA). Electron densities in these discharges were within the range: $0.5 \times 10^{19}m^3$ to $1.8 \times 10^{19}m^3$.

For the RFP discharges, ion temperatures of 380-500eV with $T_i/T_e = \sim 1.6$, were recorded for the thin shell operation, and $T_i/T_e = \sim 0.8\text{-}1.2$ with the secondary shell in place. These results are in agreement with the ion power balance model (cf Fig 1). For thin shell operation where there is a large anomalous voltage ion heating is high as expected. With the secondary shell fitted, the anomalous voltage is smaller, energy confinement is improved and ion heating is reduced.

In the ULQ plasmas, with the thin shell, T_i = 1.5-1.7keV, and with the secondary shell T_i = 1.0-1.2keV. Corresponding T_i/T_e ratios are 1.8-2.5 for the thin shell and 1.0-1.4 with the secondary shell fitted. This can be seen in Fig. 1 where the corresponding ratios are plotted against the loop voltage from electrical measurements, and the shaded area represents the model predictions for an RFP. The similarity in behaviour of the ratio T_i/T_e for ULQ discharges with that of the model for the RFP based on helicity balance, may be fortuitous. However, it does suggest some of the residual non-Spitzer power provides ion heating. In Fig. 2 are shown the energy spectra of the emitted neutrals from the 220kA ULQ HBTX1C discharges, with and without the secondary shell. These are formed from a collection of spectra, with overlapping energy settings on the NPA, obtained from separate discharges, and indicate the high reproducability of these discharges. The strong curvature of these emitted spectra may be modelled by a Monte Carlo code simulation (eg. ref [5]) using a sharply peaked ion temperature, profile ie. $T_i(r) \sim T_{io}(r)\{1-(\frac{r}{a})^2\}^2$. The comparatively straight portion of the curve, related to the core temperature, does not require the presence of any anomalous concentrations of high energy ions.

Large excursions in the emitted flux from the plasma of an order of magnitude are seen in both ULQ and RFP discharges. In the ULQ these fluctuations are almost coincident in time with excursions in the loop voltage and other electrical diagnostics. These are associated with minor fluctuations in the ion temperature of up to 20%. In Fig 3 are shown the temporal behaviour of the ion temperature in these two types of discharge. These results are obtained by integrating over 0.5 msec time-slots. The ion temperature for the thin and secondary shell cases are about the same as for the RFP. However the electron temperature is increased when the

secondary shell is installed, and so reducing the value of T_i/T_e. In the ULQ the ion temperature is seen to rise during the shot whereas ion temperatures in the RFP remain fairly constant, or fall.

Summary

Ion temperatures for RFPs in HBTX1C with both thin shell and when a secondary shell is fitted are ~380eV to 500eV. The corresponding ratios of T_i/T_e agree with a simple power balance model. For the ULQ configuration ion temperatures in the thin shell case are ~1.5keV to 1.7keV and with the secondary shell fitted are 1keV to 1.25keV. The ratios of T_i/T_e for the ULQ cases are similar to that of the model. The similarity in ion heating behaviour in these disparate discharges suggest that the ion heating model may be applicable to a wider range of discharges than the RFP.

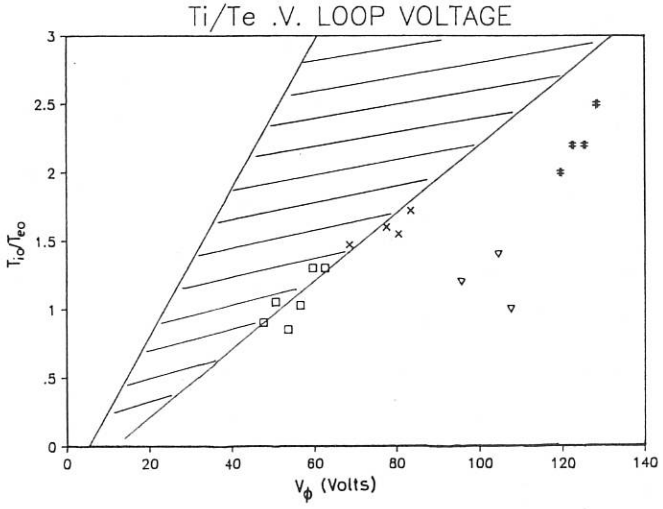

Fig 1 T_i/T_e ratios for RFP (X) and ULQ(#) with the thin shell and RFP (□) and ULQ(Δ) with the secondary shell in place. The shaded area represents the model for RFP for V_p = 11 to 22 Volts.

References
[1] Carolan P G et al, 15th EPS Conf, Dubrovnik (1988) Part II, 557
[2] Tsui H Y W, this conference.
[3] Alper B, La Haye R, this conference.
[4] Carolan P G, et al, 14th EPS Conf, Madrid II 515 (1987)
[5] Wurden G A, et al, Ion Heating Studies in the ZT-40M RFP, 15th EPS Conf, Dubrovnik (1988) Part II, 533.

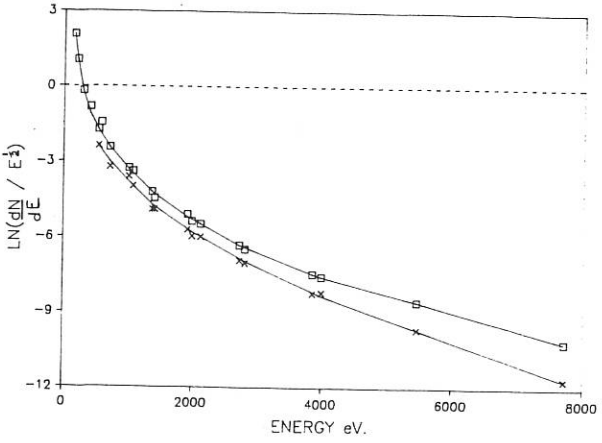

Fig 2 Energy spectrum of ULQ. X with and □ without the secondary shell in place formed from 3 and 4 overlayed spectra respectively.

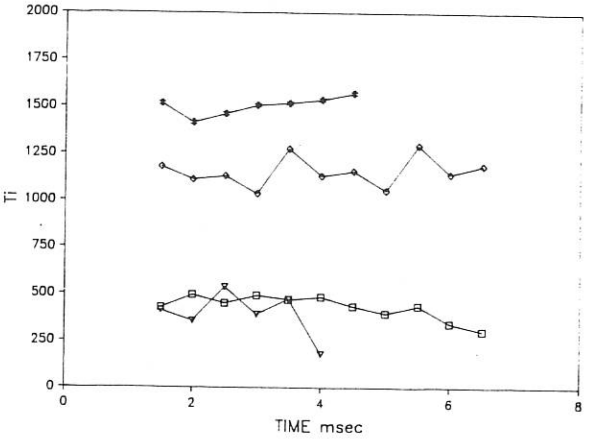

Fig 3 Time history of core ion temperature for # ULQ, ▽ RFP thin shell, and ◇ ULQ, □ RFP secondary shell cases.

A COMPARISON OF THE MAGNETIC BEHAVIOUR IN ULRA-LOW-Q AND RFP DISCHARGES IN HBTX1C

H Y W Tsui, R J La Haye*, J A Cunnane+

Culham Laboratory, Abingdon, Oxon, OX14 3DB, UK
(UKAEA/Euratom Fusion Association)

* General Atomic, San Diego, CA, USA
\+ University College, Cork, Ireland

Abstract The study of Ultra-Low-q (ULQ) and Reversed Field Pinch (RFP) operations in the HBTX1C assembly with a shell of short vertical field time constant (compared with the pulse length) reveals new unstable modes arising from resistive shell instabilities. Their suppression in ULQ discharges has been achieved in experiment by controlling the value of q. Resistivity which arises from low density and rapid particle recycling is larger in ULQ than RFP discharges. Different plasma relaxation phenomena are observed in these two regimes.

Introduction Normal Tokamak discharges have an edge safety factor $q > 3$ and discharges with $1 \leq q < 2$ have been referred to as the Low-q Tokamak (LQ). RFP discharges have negative q values. In between the Tokamak and RFP is the Ultra-low-q (ULQ) regime with $0 < q < 1$. These ULQ states also exist transitorily in the RFP setting up phase. The studies of the ULQ regime can enhance the understanding of both the Tokamak and the relaxing RFP plasma, especially with regard to relaxation and resistive wall stability. Tokamaks have been operating routinely without a conducting shell. Resistive shell operation (i.e. pulse length longer than τ_w, the time constant of the shell for vertical field penetration) of LQ [1], ULQ [2] and RFP [3,4] are also possible. The slinky mode [3] and resistive shell modes [4] have been identified in RFP discharges.

Formation and Sustainment The HBTX1C [4] device (a/R = 0.26m/0.80m) has a resistive shell (τ_w = 0.5ms) located at 1.1 times the plasma minor radius. The setting up of the LQ, ULQ and RFP discharges is similar; after a uniform toroidal field is applied, the plasma current is raised rapidly (< 0.5 ms) to near its maximum value then sustained. The value of q after the current rise is determined by the plasma current and the initial toroidal field. When the ratio is sufficiently large, the edge toroidal field reverses itself naturally to form the RFP configuration. In normal RFP operation, the reversal is assisted by reversing the current in the external poloidal winding during the plasma current rise phase.

In resistive shell RFP operation, the pulse length was normally limited to $< 10\ \tau_w$ by the growing resistive shell modes [4]. These modes have normalized growth rate $\gamma\tau_w = 0.3 \pm 0.1$ and are phase-locked to the wall or rotating very slowly with $\omega\tau_w < 0.1$ [5]. Their presence gives

rise to a slowly growing edge radial magnetic field signal. Such characteristic is absent in the well sustained ULQ and LQ discharges and was not observed in RFP discharges with conducting shells [5].

Current Limitation and Termination With a constant edge toroidal field of B_ϕ = 130 mT, the LQ plasma current remains unchanged at I_ϕ = 45 kA when the loop voltage is increased from 12 to 86 volts (Fig 1). Increasing the loop voltage results in stronger MHD activity observed on edge coils and on the plasma current and the loop voltage. The duration of the discharge can be sustained to $\sim 30\ \tau_w$ and is not dependent on the loop voltage.

The q limit which gives rise to this current limitation at fixed toroidal field also exists in ULQ discharges. The range of V_ϕ is 80 to 130 volts for the 210 kA, q = 1/2 discharges. With sufficiently high loop voltage, quasi-stable q = 1/2 and 2/3 sustainment can last up to 15 τ_w and is limited only by the circuit. As the loop voltage is reduced, the q = 1/2 sustainment shortens (Fig 2). There is a significant level of (m,n) = (1,2) high frequency activity (f > 10 kHz) and a growing non-resonant (1,1) mode develops to larger than 10% of the mean field prior to termination. With a high loop voltage maintaining the plasma current and q at its limiting value, the slowly growing (1,1) mode is absent throughout the discharge indicating that the onset of this mode is related to the edge q value. Fig 3 shows the effect of raising the q value in a q = 1/2 discharge. At t = 2.6 ms, the edge toroidal field is increased and the sustainment period shortens when the increase in q is more than 10%. The shorter pulse length is related to the earlier onset of the (1,1) mode as shown in Fig 4. This mode which has a growth time of 1 ms ($\gamma\tau_w$ = 0.5) and a rotational frequency of 300 Hz ($\omega\tau_w$ = 0.9) has similar characteristics as the resistive shell modes in RFP discharges. In RFP discharges, these modes are not affected by the loop voltage. When an inductor is added to the external power supply to enhance the plasma current sustaining capability, the RFP pulse length is extended to = 14 τ_w but remains limited by the growing modes.

Anomalous Resistance and Relaxation ULQ discharges up to 260 kA at q = 1/2 have been obtained. A typical q = 1/2 discharges has θ = 0.59 ± 0.01 and F = 0.84 ± 0.04. These values are consistent with that of a configuration with parabolic $\mu = \underline{j}.\underline{B}/B^2$, T_e and n profiles and 2% $\beta(0)$. With these profiles, the on axis plasma resistivity of a 210 kA discharge with V_ϕ = 100 V is 4.9 μΩ-m and 5.8 μΩ-m using global magnetic helicity and energy balance calculation. The 17% difference between then is smaller than the 30% to 50% typical of RFP profiles indicating a lower power throughout coupled to fluctuations and, possibly, weaker dynamo activity. These resistivities, which are greater than 100 times the Spitzer resistivity of 3.5×10^{-2} μΩ-m for a 800 eV and Z=1 plasma, can be related to the low density ($\leq 0.5\times10^{18}$ m^{-3}) and short particle confinement time ($t_p \sim 10^{-5}$ s) typical of these ULQ discharges; for instance, the particle recycling induced resistivity [6] η_t is 1.8 μΩ-m for n = 2×10^{18} m^{-3} and $t_p = 10^{-5}$ s. Such turbulent convection

particle loss process also channels input power into ion heating [6]. In experiment, high ion temperature (> 1 keV) has been measured [7].

Increasing V_ϕ of a LQ discharges generates more frequent sawtooth events (see Fig 1). Most of the excess power input above the minimum required to sustained a LQ discharge is channeled through the sawtooth activity; when V_ϕ is 50 V compared to the minimum of 12 V for a 45 kA discharge, the frequency and the amplitude of the sawtooth are ≈ 5 kHz and $\tilde{I}_\phi/I_\phi$ = 15%. Correlation analysis on V_ϕ and I_ϕ fluctuations indicated that they are related by $\tilde{V}_\phi \sim -d\tilde{I}_\phi/dt$ i.e. a positive voltage spike corresponds to a drop in the plasma current. This causal relationship is more apparent at lower loop voltage when these events becomes infrequent. The small collapse in the plasma current or relaxation, which is similar to the familiar sawtooth event in Tokamaks, takes place as q decreases from $1 < q < 2$ to the $q = 1$ boundary, and does not results in termination. In ULQ discharges, there are also significant level of fluctuations in the plasma current and the loop voltage. Correlation analysis shows that these fluctuations have the same characteristics as those seen in LQ discharges. Such correlation, however, is absent in RFP discharges suggesting that the RFP configuration is continuously relaxing in finer scale to relieve the plasma from major sawtooth activity.

Conclusion Resistive shell modes growing on the vertical field penetration timescale of the shell have been observed in both ULQ and RFP operation. Their growth to large amplitude limits the pulse duration. Mode rotation is more significant in ULQ than in RFP discharges. By maintaining q within 10% above its limiting value in ULQ discharges, the resistive shell mode can be suppressed. Resistance anomaly is higher in ULQ than RFP plasma and can be related to the rapid particle recycling. Plasma current fluctuations similar to the sawtooth activity seen in LQ Tokamak discharges are present in ULQ but not in RFP discharges. It is suggested that the continuous relaxation in RFP prevents sawtooth current collapse.

References

[1] T Edlington et al, in Plasma Phys. & Cont. Nuc. Fus. Research (Proc. 9th IAEA Conf, Baltimore, USA, 1982) Vol. 3 p.241
[2] Z Yoshida et al, J Phys. Soc. Japan 55 (1986) 450
[3] T Tamano et al, Phys. Rev. Lett. 59 (1987) 1444
[4] B Alper et al, Plasma Phys. & Cont. Fus. 31 (1989) to be published
[5] J A Cunnane, R J La Haye & H Y W Tsui, 'Magnetic Fluctuation Studies in RFPs with Various Shell Times', this conference
[6] H Y W Tsui & D E Evans, in Proc. 15th EPS, Dubrovnik (1988) 12B Part II, 585
[7] C A Bunting, P G Carolan, 'Ion Temperature Measurements in HBTX1C with a Thin Shell', this conference

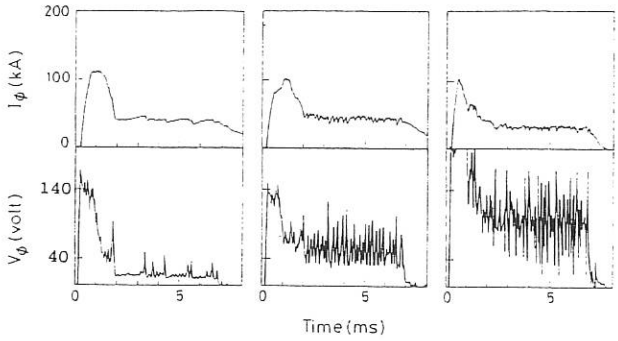

Figure 1 Current limitation in a LQ discharge. Increasing V_ϕ from 12 to 86 volts yields more frequent sawtooth events on I_ϕ and spikes on V_ϕ while the mean I_ϕ remains unchanged at ≈ 45 kA.

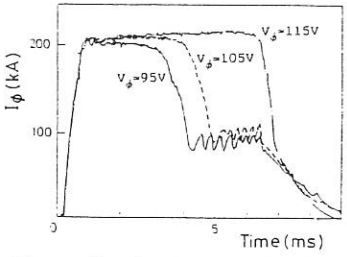

Figure 2 The increase in the q = 1/2 sustainment with higher loop voltage.

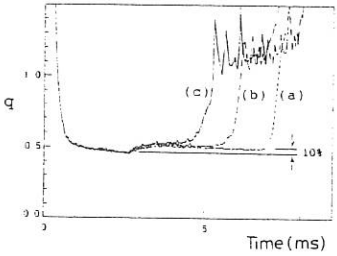

Figure 3 The changes in pulse length when q is increased externally.

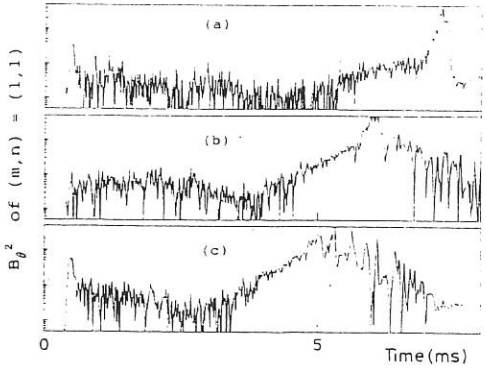

Figure 4 The onset of the (m,n) = (1,1) mode growth. When q is raised more than 10% of its limiting value by increasing the edge toroidal field externally (see Figure 3), the slowing growing non-resonant (1,1) mode develops to discrupt the discharges.

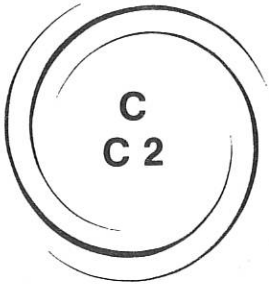

ALTERNATIVE MAGNETIC CONFINEMENT SCHEMES

OTHER ALTERNATIVE MAGNETIC CONFINEMENT SCHEMES

C2

PINCH FORMATION IN TERAWATT FIBER EXPERIMENTS

G. Decker, W. Kies, K. Koshelev*, M. Mälzig, Y. Sidelnikov*,
C. van Calker, G. Ziethen,

Institut für Experimentalphysik, Universität Düsseldorf, FRG.
*Institute of Spectroscopy, Academy of Science, Troitsk, USSR

H. Bluhm, D. Rusch, W. Ratajczak

Institut für Neutronenphysik und Reaktortechnik, Kernforschungszentrum Karlsruhe, FRG.

Introduction

Low power fiber pinch experiments (up to several hundreds of gigawatts) show pinch expansion and subsequent disruptions preventing $n\tau$-values and ion temperatures relevant for thermonuclear fusion /1,2,3/. Nevertheless, these pinches are less prone to macroscopical instabilities than predicted by MHD theory promising thermonuclear fusion conditions of reactor efficiency if magnetic confinement at small pinch radii ($< 100\,\mu$m) could be maintained up to a peak current of about 1.6 MA /4/.
Because of a fixed pinch inductance (typically 100 nH) this seems to be easily realized applying drivers of about 200 kJ to these fibers. However, unavoidable initial pinch expansion and also a limited pinch life time (~100 ns) require high power (> 1 TW) and consequently high voltage (> 1 MV) drivers. On the other hand, high electric fields (E > 200 kV/cm) tend to generate plasma diodes rather than pinches so that not only lower limits of electric field (and current rise Idot $\propto$ E) but also upper ones are likely to exist for fiber pinch experiments.

The Karlsruhe Light Ion Facility KALIF (1.6 TW, > 10 kA/ns, $\lesssim$ 800 kA), though of limited voltage pulse length (60 ns) and current, was used for CD_2 fiber experiments in order to investigate the
(i) initial phase of breakdown and ionization at high power imput and (ii) pinch formation above a current level critical for radiation collapse (several 100 kA for CD_2 depending on temperature /5/).
Unfortunately, the effect of a prepulse (~100 kV, ~50 kA, typical for pulselines) about 100 ns prior to the main pulse was uncertain. This prepulse, attenuated by a pressurized prepulse switch and additionally by a vacuum feed integrated dielectric switch, as yet, cannot be totally eliminated. (Prepulse free operation will hopefully be achieved by means of either capacitive shielding of the water-vacuum interface or vacuum feed integrated plasma opening switches, measures presently in preparation.)

CD_2 fiber experiments

a) Breakdown and ionization

Time correlated electric signals (voltage, current, hard X-rays) and streak pictures show that during the steep voltage rise (~100 kV/ns) of the main pulse breakdown occurs in a radially extended gas or vapor (r~10 mm) (with a density profile peaked on axis) rather than along the fiber surface (r~50 μm). The reason for this is the prepulse totally or partially (depending on prepulse attenuation) vaporizing the fiber and partially ionizing neutrals about 100 ns prior to the main pulse.

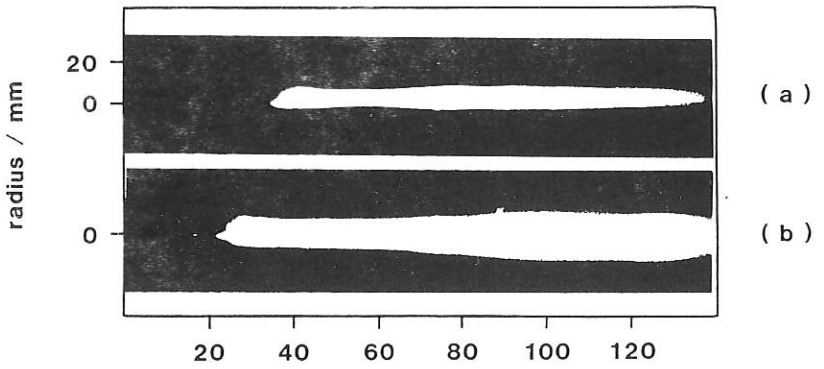

figure 1

Figure 1 shows two examples of streak pictures with (a) normal (prepulse switch pressure 60 psi) and (b) improved (130 psi) prepulse attenuation. While the denser central column initially ($r \sim 1$ mm) is slowly expanding (expansion velocity $\sim 10^4$ m/s) during ionization the coaxial plasma cylinder ($r \sim 10$ mm) is quickly compressed (compression velocity $> 10^5$ m/s) and keeps bouncing with increasing radial amplitude after the first compression. Neither explosive expansion nor pinch disruptions as normally observed in low power experiments take place throughout the current pulse (> 100 ns). The better the prepulse is reduced (i) the shorter is the breakdown delay (fiber surface discharge), (ii) the longer appears the discharge concentrated to the fiber and (iii) the better is the initial hard X-ray emission suppressed /6/.

The radial extension of the vaporized material within less than 100 ns requires a velocity of more than 10^5 m/s, far too high to be explained by a thermal spread (typical 10^4 m/s for a temperature of a few eV) of neutrals or ions. Only an off axis E x B drift can account for this radial extension. Remarkably, the prepulse shows a distinct voltage reversal (several tens of kV) that is likely to drive a surface plasma off axis since the current is not reversed. This also explains the fact that the velocity of radial expansion does not significantly depend on prepulse power but the number of particles does. Thus, effective prepulse reduction results in both a thinner plasma envelope and in better current concentration to the central plasma.
Moreover, the shorter breakdown delay indicates that the discharge is faster initiated along the solid fiber that is not totally vaporized with reduced prepulse power. This means that the electric field at breakdown is lower and electron runaway and therefore hard X-ray emission is effectively suppressed. Hence, prepulse elimination as well as external means for discharge initiation (e. g. matched UV-irradiation of the fiber) should result in much better confinement for fiber experiments.

b) Pinch formation
Time integrated X-ray pinhole pictures show that the visible central pinch plasma (streak pictures) contains a radially less extended ($r \sim 1$ mm) hot (several 100 eV) core from which multiple axially separated micropinches (diameter < 50 μm, $T_e \sim 2$ keV) are formed presumably via radiation collapse. This indicates that the radial current distribution is stronger peaked on axis than one might expect from the streak pictures.

Line radiation (not visible in our X-ray pictures filtered by 10 μm and 20 μm Be) can initiate the collapse but becomes small in the final stage, where radiation loss is primarily due to bremsstrahlung continuum (effective wavelength 6 to 7 Å). Thermal outflow from necked regions locally reduces the line density so that temperature and radiation loss is locally enhanced enabling further compression /7/. However, there are no signs (no hard X-ray emission, no dips in the current trace, no neutron fluence anisotropy) of total pinch disruptions as typical in low power experiments. Either the current quickly reconnects in outer regions during the collapse or the collapse process is stopped by some mechanism not yet identified (e. g. anomalous heating or radiation absorption).

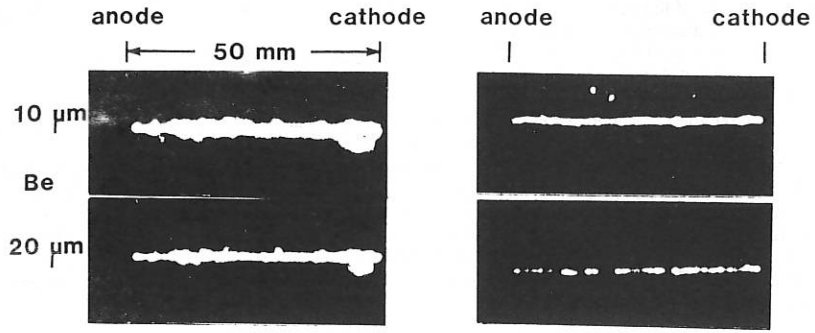

figure 2 (a) (b)

Figure 2 shows two twin pictures with (a) normal (60 psi) and (b) improved (130 psi) prepulse attenuation. The hot core plasma is better confined and the micropinches are more distinct in the latter case that gives further evidence that the current is even more concentrated to the axis in case of prepulse reduction. Although it is not clear yet whether these micropinches are simultaneously formed or not and what their life time is, the pictures show that an axially homogeneous collapse is not likely to take place.
The radially extended anode spots of figure 2(a) are absent in figure 2(b) showing that runaway electrons, primarily generated initially in outer plasma regions, are suppressed in discharges with improved prepulse reduction.

c) Neutron emission
The indium activation technique was used to measure the angular distribution of the neutron fluence. Fairly isotropic emission with a tendency to a side-on enhanced fluence indicates that an axial beam-target process is negligible. This means that runaway ions due to high axial electric fields (pinch voltage and disruptions) are not efficiently generated because of high pinch density and/or high magnetic fields. Nevertheless dynamical compression of the thin plasma envelope may cause radial and/or azimuthal ion runaway so that a non-axial beam-target process may produce most of the neutrons (which would also explain the side-on enhanced fluence).
Most striking, however is that the neutron yield ($\sim 10^{10}$) is the highest (several 10^{10}) in shots with effective prepulse reduction despite the fact that the pinch current is reduced from 800 to 500 kA in these discharges.

Since the outer pinch compression velocity as well as the inner pinch(target) density are especially high in these discharges this enhanced neutron production might be primarily due to an efficient beam-target process but a significant contribution from a thermonuclear process can also not be excluded. (Unfortunately, the neutron energy distribution from side-on and end-on exposed nuclear emulsion plates was not available).

Assuming Bennett equilibrium and the micropinch volume proportional to r^3 the thermonuclear yield of micropinches is independent of radial dimensions for a constant temperature in contrast to the yield of an axially homogeneous column which is proportional to r^{-1}. Therefore, micropinching might limit the fusion efficiency of fiber pinches. Future time and energy resolved X-ray and neutron measurements may clarify the effect of micropinches for fusion.

Conclusions

There is experimental evidence that an investment of several terawatts into fiber experiments is a necessary condition for particle confinement to initial fiber dimensions.
The first KALIF CD_2 fiber experiments showed that current concentration depends primarily on discharge initiation (e. g. prepulse free operation). However, there is also experimental evidence that an axially homogeneous confinement is hardly achieved (even with frozen pure deuterium fibers /1/) because of micropinch formation. Since micropinching inevitably results in axially modulated line density and temperature thermonuclear fusion efficiency can be limited.
Whether or not there is a real chance to prevent this axial inhomogeneity in reducing initial pinch expansion remains to be demonstrated by future prepulse free terawatt fiber experiments.

Acknowledgement

This work was carried out under EC-Project ST 2J-0059-2-D

References

/1/ J. D. Sethian et al. Phys. Rev. Letters, 59, 8, p 892 (1987)
/2/ J. E. Hammel and D. W. Scudder, 14th European Conference on Controlled Fusion and Plasma Physics, Vol: 11 D Part II, Madrid (1987)
/3/ G. Decker et al., 14th European Conference on Controlled Fusion and Plasma Physics, Vol: 11 D Part II, Madrid (1987)
/4/ M. G. Haines, Physica Scripta T2/2, 380 (1982)
/5/ V. V. Vikhrev et al. Sov. J. Plasma Physics 8, 688, (1983)
/6/ G. Decker et al., First KALIF.fiber experiments, z-Pinch and Plasma Focus Workshop, Nice, France (1988)
/7/ K. Koshelev et al., The formation of micropinches in the plasma focus device due to heavy impurities, J. Physics D (in press), (1989)

AN ANALYTIC MODEL OF RADIATIVE COLLAPSE OF A Z-PINCH

M G Haines

Blackett Laboratory, Imperial College, London SW7 2BZ

There is a critical current I_{PB} of about 1 MA (the Pease-Braginskii current) at which Ohmic heating and bremsstrahlung losses balance in a Z-pinch under pressure equilibrium. An analytic zero-dimensional model shows the process of radiative collapse when the prescribed current exceeds the critical current. In particular for a linearly rising current radiative collapse is complete when the current is $\sqrt{3}\, I_{PB}$. However, in practice the voltage limitation imposed by an external circuit prevents such a total collapse, and by including this in the model a maximum density ($10^{30} - 10^{32} m^{-3}$) can occur followed by an expansion and damped oscillation about an equilibrium at which the current equals the Pease-Braginskii current. In the absence of alpha-particle pressure the maximum density is limited by the resistance of the narrow column, the large voltage across which ($\sim 10^8$V) is balanced essentially by a large negative $L\dot{I}$; it occurs when the current is $I_{PB}\,[(\delta - 1)/(\delta - 2)]^{\frac{1}{2}}$ where $\delta = 7/3 + 4/3\ \ln(R/a)$, where a is the pinch radius and R is the radius of the current return. The minimum current following maximum density is shown to be greater than $I_{PB}/\sqrt{2}$. Degeneracy effects can be included in the model.

1. Model

An analytic model is developed for a zero-dimensional description of a Z-pinch, obeying pressure balance through the Bennett relation

$$16\pi N k_B T = \mu_0 I^2 \qquad (1)$$

and a time-dependent energy equation

$$\frac{d}{dt}\left[I^2 a^{4/3} \right] = \frac{16}{3\mu_0 \alpha_\perp I a^{2/3}} \left[\frac{16\pi N k_B}{\mu_0} \right]^{3/2} \left[1 - \frac{I^2}{I^2_{PB}} \right] \qquad (2)$$

Where N is the line density, k_B Boltzmann's constant, T the temperature, I the current, I_{PB} the Pease-Braginskii current (equal to 0.433 $(1n\Lambda)^{\frac{1}{2}}$ MA), a radius of the pinch, and the electrical conductivity is $\alpha_\perp T^{3/2}$. Setting $x(t) = I a^{2/3}$, eq (2) reduces to

$$\frac{dx}{dt} = \frac{B}{x^2}\left[1 - \frac{I^2}{I^2_{PB}} \right] \qquad (3)$$

where

$$B = \frac{8}{3\mu_0 \alpha_\perp}\left[\frac{16\pi N k_B}{\mu_0} \right]^{3/2} \qquad (4)$$

If I is a linear function of t (I = At), eq (3) can be immediately integrated to give

$$\frac{1}{3} A^3 t^3 a^2 = B \left[t - \frac{A^2 t^3}{3 I^2_{PB}} \right] + C \qquad (5)$$

where C is a constant to be determined. It immediately follows that for $C << Bt$ the radius a will vanish when $I = \sqrt{3}\, I_{PB}$. At this time an infinite voltage would be required, and therefore a more realistic circuit equation should be employed.

2. Boundary condition

Eq (5) shows that there is a problem of divergence of the radius a(t) in the limit of $t \to 0$, and it arises for a linearly rising current because of the violation of the prescription $I \propto t^{1/3}$ for small times (Haines, 1960). One-dimensional simulations indicate that dynamical effects cannot be neglected at early times (Chittenden, 1988). The model is therefore commenced at a time t_0 with plasma radius a_0 such that (i) $da/dt|_{t_0} = f_1 c_s|_{t_0}$ and (ii) $a_0|_{t_0} = f_2 c_s/t_0$ where $|f_1| < 1$, $0 < f_2 < 1$ and c_s is the sound speed, $(\gamma k_B T/m_i)^{\frac{1}{2}}$, with $\gamma = 5/3$. The first condition ensures that inertial terms are small, and the second condition ensures that internal dynamics are unimportant i.e. by the time t_0 several sound transit times have occurred so that a quasi-steady pressure profile has developed. These two conditions lead to a cubic equation for a_0 (and t_0)

$$a_0^3 \left[1 + \frac{2 f_1}{3 f_2} \right] + \frac{B a_0}{A I^2_{PB}} - \frac{B f_2}{A^2} \left[\frac{\gamma \mu_0}{16 \pi N n_i} \right]^{\frac{1}{2}} = 0 \qquad (6)$$

which has only one real root. There is a tendancy for t_0 and a_0 to increase with increasing N and decreasing A, for fixed values of f_1 and f_2.

3. Circuit equation

It is envisaged that the z-pinch is driven by a pulse-forming line of characteristic impedance Z_c. Taking into account the forward and reflected power, the circuit equation is given by

$$V = \frac{d}{dt} (LI) + RI + Z_c I \qquad (7)$$

where the pinch inductance and resistance are given respectively by

$$L(t) = \frac{z_0 \mu_0}{4\pi} \left[\frac{1}{2} + 2 \ln \frac{R_w}{a(t)} \right] \qquad (8)$$

and

$$R(t) = \frac{z_0}{\pi a^2(t) \alpha_\perp T^{3/2}(t)} \qquad (9)$$

with z_0 the pinch length and R_w the radius of the return conductor. V is the charging voltage of the line, having a maximum (constant) value, which limits the time during which the current can rise linearly.

4. Solution with a voltage limitation of 4MV

The figure shows the variation of plasma radius a(t) and current I(t) for a generator with a maximum voltage of 4 MV an initial rate of rise of current of 2.4 x 10^{13} amp sec^{-1} and a line density N of 5.6 x 10^{18} m^{-1} (consistent with a value which Haines (1978) derived for satisfying Lawson conditions with end-losses. For deuterium and f_1 = f_2 = 0.5 eq (6) gives a_0 = 57.9μm and t_0 = 1.80ns. For $1.8<t<44$ns the voltage is less than 4MV and the solution (5) applies. Beyond 44ns eqs (3) and (7) are solved self consistently. It can be seen that the current is reduced below the I = At line, reaches a maximum below $\sqrt{3}$ I_{PB} at 72.5ns and then sharply falls to a minimum at 79.9ns and then rises, with a damped oscillation about the equilibrium value of I = I_{PB} (= 1MA for $\ln\Lambda$ = 5.316, chosen to be constant here for simplicity). The radius falls sharply to 0.135μm at 78.37 ns and then rises to oscillate about an equilibrium value of 0.835μm. It is assumed that the pulse length available is 100 to 200 ns. The peak density in this example is almost $10^{32}m^{-3}$, but it is to be noted that there is always a balance of magnetic and plasma pressure, so that the time for this transient is determined by the energy and circuit equations primarily. In particular the radiative loss rate is important, together with the fact that the resistive voltage RI (about 100 MV in this example) is balanced by a large negative value of LdI/dt at peak compression.

Because of these high voltages the terms V and Z_cI can be neglected at the time of peak compression. Putting da^2/dt to zero in eqs (3) and (7) and eliminating dI/dt gives a current of

$$I = \left[\frac{\delta - 1}{\delta - 2} \right]^{\frac{1}{2}} I_{PB} \qquad (10)$$

where

$$\delta = \frac{7}{3} + \frac{4}{3} \ln \frac{R_w}{a} \qquad (11)$$

at minimum radius. The same assumption gives $I = I_{PB}/\sqrt{2}$ at minimum current.

5. Scaling with line density and applied voltage

If for a given line voltage a different line density is employed eqs (3), (4) and (7) show that the constant B scales as $N^{3/2}$ and a^2/B acts as a reduced parameter leading to the pinch raqdius a scaling as $N^{3/4}$, while temperature and number density scale as N^{-1} and $N^{-\frac{1}{2}}$. If the radius of the return conductor R_w is scaled also as $N^{3/4}$ eq (7) gives exactly the same current.

If the voltage instead is being varied as an experimental design parameter, then to attain the same current (relative to the Pease-Braginskii limit) the line characteristic impedance must be changed by the same amount; the pinch radius will scale as $V^{-\frac{1}{2}}$, and the time-scale by V^{-1}.

References

Braginskii, S.I. (1957) Sov. Phys. JETP, 6, 494.
Chittenden, private communication.
Haines, M.G. (1960) Proc Phys Soc 76, 249.
Haines, M.G. (1978) J Phys D Appl Phys 11, 1709.
Pease, R.S. (1957) Proc Phys Soc 70, 11.

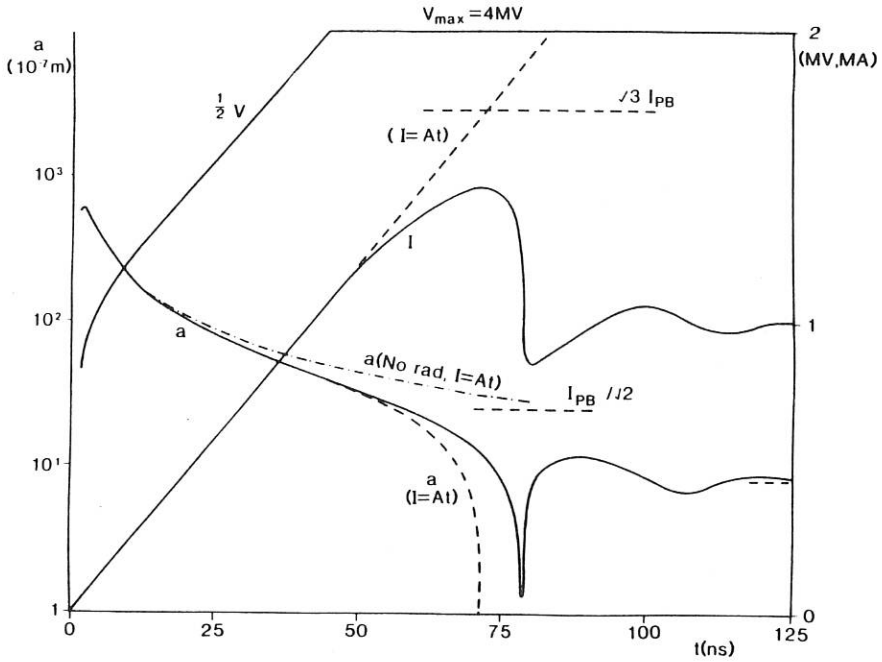

Fig 1. Current I and pinch radius a as a function of time for N = 5.6 x 10^{18} m^{-1}, $\ln\Lambda$ = 5.316 (I_{PB} = 1.0 MA), line impedance 1.25 ohm, R_w = 0.03m, length 0.05m, I = 2.4 x 10^{13} A s^{-1} with maximum line voltage 4 MV. Also shown is a(t) for I = At with (---) and without (-·-·-) bremsstrahlung loss.

RESISTIVE STABILISATION OF A DENSE Z−PINCH

I. D. Culverwell, M. Coppins and M. G. Haines

Blackett Laboratory,
Imperial College of Science, Technology and Medicine,
London SW7 2BZ, UK.

0. ABSTRACT

The stability of an ohmically heated Z−pinch is considered where the unperturbed time-evolving plasma column is in pressure balance. The m = 0 mode only is considered. At first, when cold the Lundquist number (magnetic Reynolds number) S is small (<100) and the pinch is stable. Above a critical value of S exponential growth of an unstable mode occurs. These theoretical results will be compared with the experimental deuterium fibre results from NRL, Washington in which during the current rise phase the Z−pinch was stable. The importance of this result is that because of the small pinch radius a small value of S occurs even at a temperature of 100 eV.

1. INTRODUCTION

The anomalous stability of Z−pinches formed from frozen deuterium fibres is well documented [1,2]. These pinches remain stable during the period of current rise for up to 50 ideal MHD growth times τ_{mhd} (= a/V_A). One possible explanation for this behaviour is that these pinches remain cold for a large fraction of the current rise time and that resistivity could therefore have an important effect on their dynamics. The magnitude of resistivity is measured through the Lundquist number $S = \mu_0 V_A a/\eta$ where $V_A^2 = \mu_0 I^2/4\pi N m_i$, the symbols having their usual meanings. Naively one expects ideal behaviour if S is greater than unity, resistive effects only becoming significant if S falls below this value.

The current required to keep an ohmically heated Z−pinch in pressure balance rises on the ohmic heating timescale $\tau_{ohm} = \mu_0 a^2/\eta$ [3]. It is possible to show that $\tau_{ohm}/\tau_{mhd} = S$, so that when resistivity is important (on the radial length−scale (rather than on the tearing layer length−scale of a localised mode)), so is the time−dependence of the equilibrium.

The purpose of this paper is to report calculations on the growth of axisymmetric instabilities in a time−dependent equilibrium using a one−dimensional linearized initial value code.

2. THEORY

The plasma is assumed throughout to be a single temperature fully ionised deuterium fluid. The equations describing the behaviour of the plasma are: continuity, conservation of momentum (viscosity is ignored), conservation of energy (bremsstrahlung is neglected), Ohm's law (using scalar Spitzer resistivity), Ampere's law, Faraday's law and the perfect gas equation of state. The thermal conductivity is assumed to be infinite to obviate consideration of the complicated perturbed energy equation: in this theory the perturbed temperature is found by distributing the perturbed ohmic heating uniformly across the pinch.

The time−dependent equilibrium used in the code is given in [3].

The equations describing the evolution of the perturbation are obtained by linearising and Fourier analysing the above mentioned equations, perturbed quantities being proportional to exp(ikz). The boundary condition is given by the continuity of the total (thermal + magnetic) pressure across the perturbed boundary. An initial perturbation, random in the radial profile, is applied at an early time ($S << 1$) and the perturbed quantities are advanced using the equilibrium (and perturbed) variables at the current time.

3. RESULTS

A convenient measure of the amplitude of the perturbation is given by its kinetic energy. At early times the pinch appears to be stable, the perturbed kinetic energy remaining approximately constant. When a critical Lundquist number S^* is reached, however, the instability starts to grow exponentially with eigenfunctions and a growth rate given by ideal MHD. S^* therefore defines the stability threshold for an ohmically heated Z−pinch. The variation of S^* with ka is given in table 1.

ka	0.1	0.3	1.0	3.0	10.0
S^*	430	160	33	21	7.5

Table 1. S^* versus ka for m = 0 external modes.

4. DISCUSSION AND CONCLUSIONS

The results shown in table 1 indicate that an ohmically heated equilibrium Z−pinch does not become susceptible to long wavelength m = 0 ideal MHD instabilities until the plasma Lundquist number is of the order of 100, two orders of magnitude greater than might at first be expected. It is hoped to modify the code to include viscous effects and

that doing so will strengthen this conclusion by inhibiting the growth of the short wavelength modes.

Over a wide range of conditions in the NRL fibre experiments the Lundquist number at peak current was never more than 250 [4]. It therefore seems that the stability of these pinches during the current rise can be at least partly explained by the effects of resistivity.

The principle conclusion of this work is that smaller radius fibres should be used in future experiments since $S \propto r_0 T^2$ implies that smaller fibres can reach higher temperatures before attaining the stability threshold of $S^* = 100$.

5. ACKNOWLEDGEMENTS

We would like to thank A. E. Robson (NRL, Washington) for stimulating discussions and for making unpublished experimental results available to us. This work was supported by the UK Science and Engineering Research Council.

6. REFERENCES

1. J. D. Sethian, A. E. Robson, K. A. Gerber and A. W. DeSilva, (1987), Phys. Rev. Lett. 59, 892.
2. J. E. Hammel and D. W. Scudder, (1987), Proc. 14th European Conference on Controlled Fusion and Plasma Physics, Madrid, Contributed Papers, Pt. 2, 450.
3. M. G. Haines, (1960), Proc. Phys. Soc., 76, 250.
4. A. E. Robson, (1988), private communication.

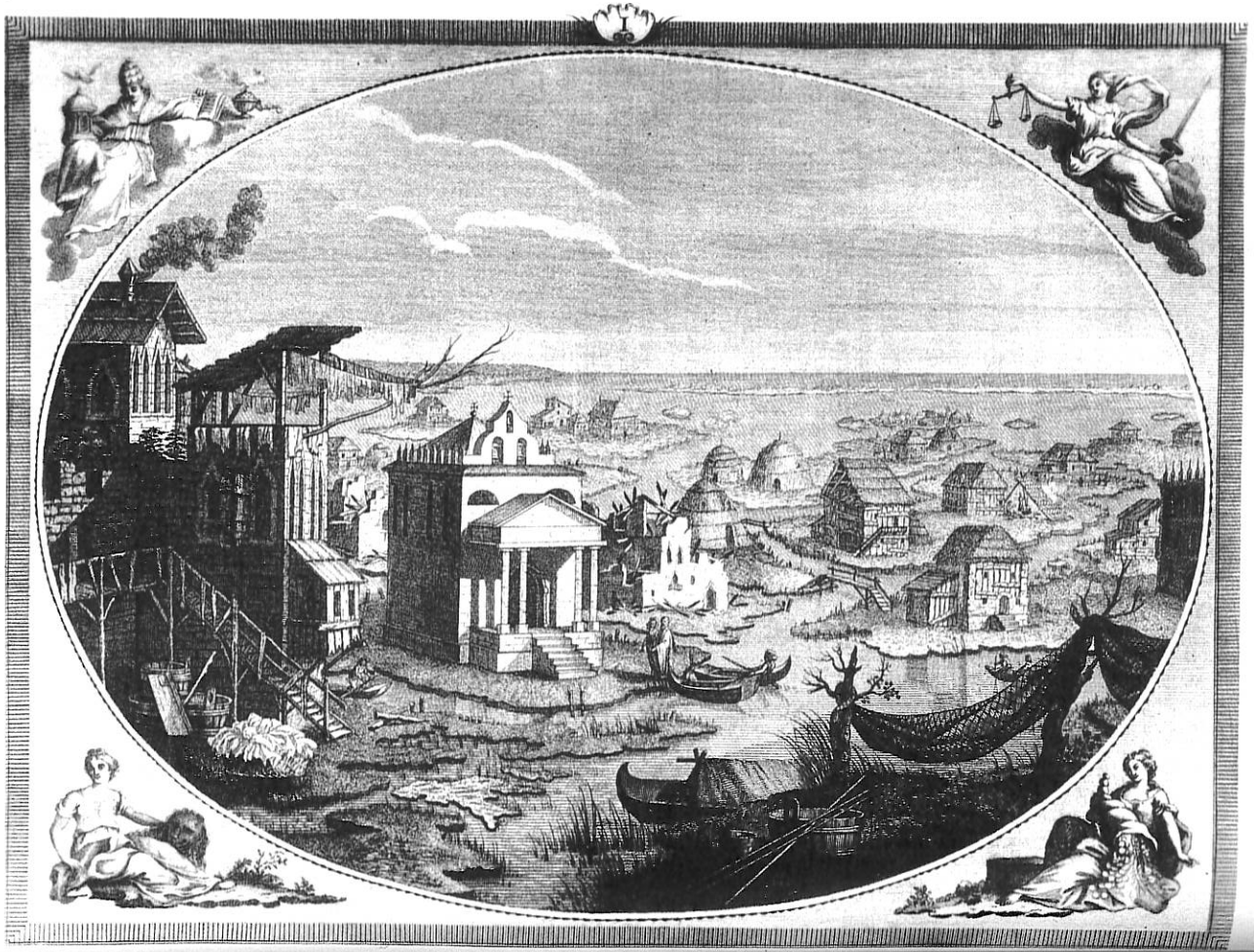

CURRENT DISTRIBUTION MEASUREMENTS ALONG THE ELECTRODES OF PF360 PLASMA-FOCUS FACILITY

K. Kociecka, A.Jerzykiewicz

SOLTAN INSTITUTE FOR NUCLEAR STUDIES, 05-400 SWIERK, POLAND

1.INTRODUCTION

The knowledge of current distribution along the electrodes during a discharge is of primary importance for the optimizing of energy transfer to plasma in a PF facility. Usually the current is calculated from the magnetic field value measured by means of miniature probes or from the Faraday effect. The same value of the field is assumed at a radius "r" or even between electrodes at a distance "z" from their begining. This assuption is incorrect in the case of PF360 device in which a filamentary current flow has been observed. Therefore an effort has been undertaken to measure the current by means of Rogowski coils situated inside the inner electrode.

The paper presents mmeasurement results supplementary to those described previously [1],[2].

2.EXPERIMENTAL ARRANGEMENT.

The measurements have been performed using Mather-type electrodes of 30cm in length. The squirrel-cage type outer electrode (16 bars) was 170mm in diameter. The inner electrode (shown in Fig.1) has been divided into several disks. The Rogowski coil containing disk can be exchanged with three other disks. The extreme distances from the Rogowski coil to the insulator front were d_1=2.5cm and d_4=13cm. The Rogowski coil consisting of 340 turns has been wound on a polyethylene core of 8mm in diameter.The voltage has been integrated on a resistance and recorded by means of an osilloscope placed inside an insulated Faraday cage. The current in the electrode has been compared with the total current measured by means of a Rogowski coil placed between the collector plates. The equality of these currents in the case of shortcircuiting electrodes has been tested at the begining of the measurements. The presented results have been achieved with coils located at the distances 2.5cm (pos.1,index 1) and 13cm (pos.4, index 4) from the front of the insulator at the storage bank energy 90 kJ.

3.RESULTS OF MEASUREMENTS

Three main types of discharges shown in Fig.2 have been discerned. The type "a" has been characterized by a great content of the leakage current in the insulator vicinity. It has been observed mainly during the training procedure after an exchange of the the insulator or electrodes. This type of discharges produced a low neutron emission. During the discharges of "b"

type secondary breakdowns on the insulator occured as a result of the voltage rise caused by the plasma compression. The secondary breakdowns in this case have not influenced the neutron yield. All the measured currents equalized themselves after some delay in the case of type "c" discharges. The highest neutron emission was mostly recorded for the "c" type discharges.

Several parameters shown in Fig.3a have been analized and compared for various initial deuterium pressure, in order to find the correlations between the current distribution and the neutron yield. Evident dependances have been found mainly at the pressure 3 Tr. at which the maximal neutron yield has been observed. The current distribution along the electrode length has been shown in Fig.3b for several time values at the deuterium pressure 3 Tr. To estimate the current shape on the electrode axis, use was made from the fact that at the time 3.85 μs corresponding to the maximal compression the current crest value depended linear on the electrode length. The current rise-time has been estimated using the measured values of current sheath front (14.3 cm/μs) and tail (13 cm/μs) velocities. The estimated current has been shown in Fig.3a using dotted line. It should be stressed that the both velocities have been similar only at the pressure corresponding to the maximal neutron yield [1]. It has also been found that the crest current value, as measured at the time corresponding to the maximal compression in position 4, diminished with rising pressure. The dependance of the neutron yield on the delay of current origin in pos.4 (t4d) has been shown in Fig.4. An evident correlation between these parameters has been found at the pressure 3 Tr. The maximal neutron yield has corresponded approximately to the average value of t4d. This relation is probably connected with the current sheath uniformity. A weak correlation between the current rise-time in pos.4 (t4M) and the neutron yield has been observed (Fig.5). The neutron yield has been higher in the case of faster current rise. The current rise-time is connected with the current sheath width. It has been found that the current sheath has been broader than it had been assumed. This is probably caused by the asymmetry of the sheath. The width of current sheath estimated at the optimal pressure 3 Tr has been about 25cm. Due to this fact only about 7% of energy stored has been available at the end of electrodes at the beginning of collapse phase.

4. CONCLUSIONS

Following conclusions can be drawn as the result of the investigations:

- The main reason of the low neutron yield, seems to be the broad current sheath.
- Theoretical and experimental studies are needed to understand the current sheath properties described above.

5. REFERENCES

[1] Jerzykiewicz A. et al. Plasma Physics and Contr. Nuclear Fusion Research, 1988, (Proc.12th Int.Conf., Nice 1988), IAEA-CN-50/C-5-17.

[2] Jerzykiewicz A., Brandt Sz., Kociecka K., Nawrot W., Plasma Focus and Z-pinch Research 1988 (Proc.Int.Workshop, Nice 1988).

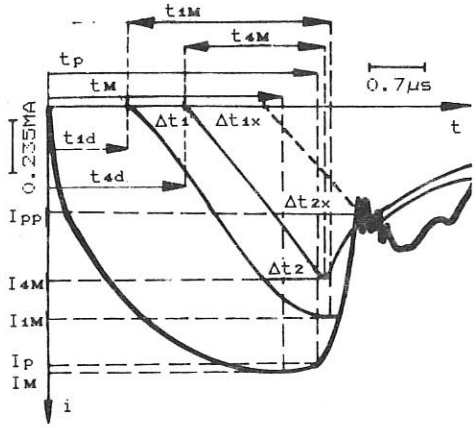

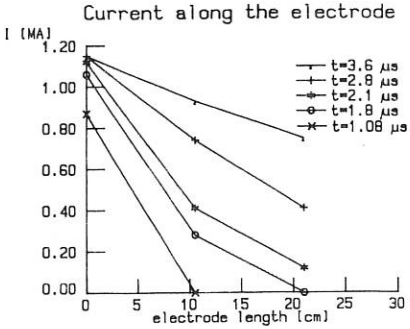

Fig.3 Current distribution along the electrode.

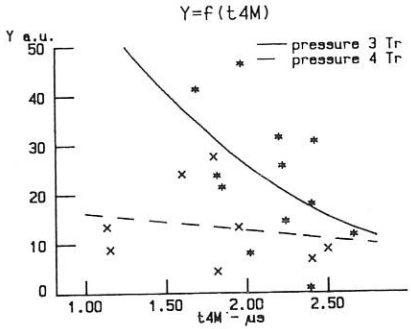

Fig.4

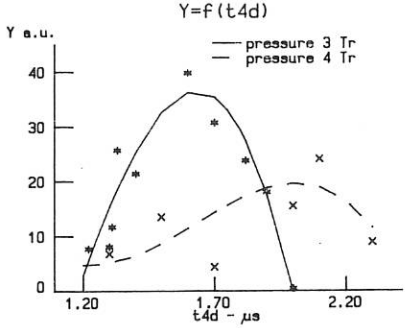

Fig.5

Fig.1 Inner electrode ϕ120mm: 3-exchangeable disk, 4,5-disk with Rogowski coil(7), 9-copper plate.

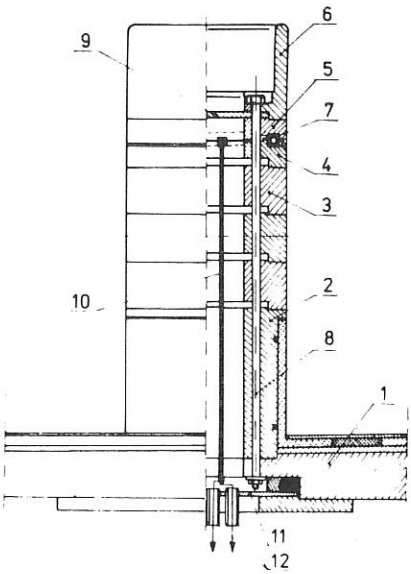

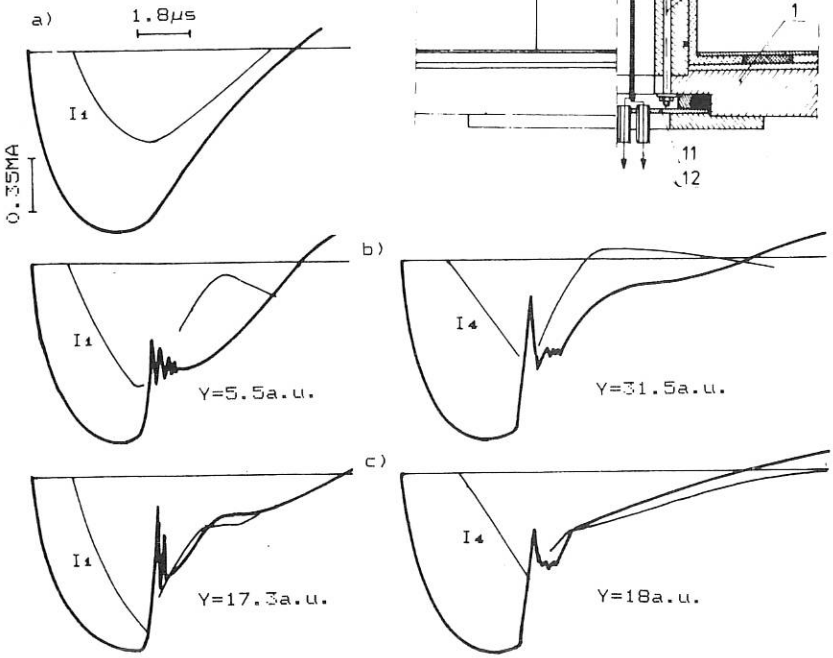

Fig.2 Currents measured by means of Rogowski coils (pressure 3Torr)
—— in collector,
—— in inner electrode.

INFLUENCE OF GAS-PUFFING ON FORMATION OF PF-TYPE DISCHARGES

M. Sadowski, J. Baranowski, L. Jakubowski, E. Rydygier, E. Składnik-Sadowska, A, Szydłowski, J. Żebrowski

Sołtan Institute for Nuclear Studies
05-400 Otwock-Swierk, Poland

Abstract: The paper reports on results of a new gas-puffed plasma-focus /PF/ experiment. Measurements of current- and voltage-waveforms as well as studies of X-rays, high-energy charged particles, and neutrons, are summarized. Also described are measurements of a plasma front propagation velocity.

Introduction

Development of high-current Z-pinch and PF discharges depends strongly on initial gas conditions within an experimental chamber, and particularly on the working gas concentration within the interelectrode gap. Numerous PF experiments were performed under static initial pressure and it was found that there exists the optimum pressure, at which the neutron yield reaches the maximum value [1-2]. On the other hand, many experiments showed that in order to get a high neutron yield the current sheath must demonstrate appropriate features. It has to possess a distinct front structure, to be thick enough, and to move with a high speed, preserving the azimuthal symmetry [2-3]. It should also be noted that the highest ion emission is usually observed at initial pressures lower than the neutron optimized value [2-3].

Some PF experiments have also shown that the final current sheath characteristics depend on the initial breakdown process which usually occurs along the insulator surface. In principle, it seems that an appropriate initial gas distribution along the insulator and electrodes can be created not only under static conditions, but also under dynamic filling, since the break down process is very fast in comparison with a gas thermal flow. Unfortunately, only a few PF experiments have been performed at the pulsed filling of the interelectrode gap [4-7].

In order to study the operation mode in question, a new gas puffed PF experiment has been undertaken at IPJ-Swierk [8-9]. Preliminary results of that experiment have been reported previously [9-10]. This paper reports on the results obtained during successive series of the PF-type discharges performed under different initial gas conditions.

Experimental Results

The studies have been performed with the modified MAJA-PF facility [8-9]. The inner electrode was a copper tube of 72 mm in diameter, while the outer electrode was a squirrel-cage configuration of 124 mm in diameter, consisted of 16 copper rods of 10 mm in diameter each. The both electrodes were 298 mm long, and the main insulator embracing the inner electrode was made of a pyrex tube of 72 mm in length. The whole system was supplied from a 48 μF condenser bank charged up to 40 kV.

In the static mode the initial gas conditions have been similar to those realized in the conventional PF experiments of a comparable size [1-3]. For the dynamic operational mode the initial gas conditions have been formed by means of a fast electromagnetic gas valve situated inside the inner electrode [8-9], and powered by a separate condenser bank.

On the contrary to the old Mather-type experiments, in the present PF-type experiment the gas-puffing was performed through a special nozzle directing a gas stream towards the insulator surface /in so-called A configuration/, and the gas pressure inside the valve plenum was considerably higher /up to 30 atm/. It made possible to form locally a relatively dense neutral gas cloud at the insulator surface, facilitating the formation of a current sheath.

For the purposes of a comparative analysis several series of PF-type discharges have been performed under different initial gas conditions, and the main characteristics of those discharges have been considered. With the appropriate gas-puffing the current- and voltage-waveforms have been very similar to those observed under static initial gas conditions.

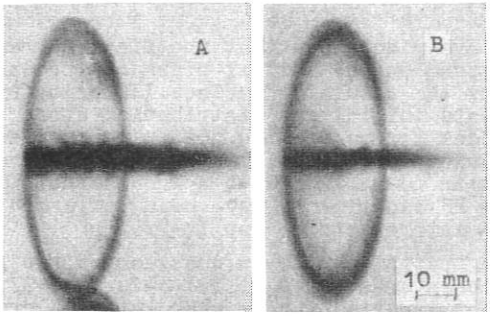

Fig.1. X-ray pinhole pictures taken /A/- for static initial gas conditions at $Y_n = 5.5 \times 10^8$, $I_{xh} = 0.16$ μG; and /B/- with the gas puffing at p_v=10 atm, t = 300 us, $Y_n = 1.3 \times 10^9$, $I_x = 1.2$ μG

The formation of a PF region at the electrode outlet has also been analyzed on the basis of X-ray measurements. A comparison of time-integrated X-ray pinhole pictures taken under different initial gas conditions, has been shown in Fig.1. It can be easy seen that the formation of a distinct

pinch column can also be observed if the gas-puffing is intense enough. The formation of the PF-type discharges with the initial gas-puffing has also been confirmed by time-resolved measurements of hard- and soft-X-rays, as well as of neutron pulses, similar to those presented in Fig.2.

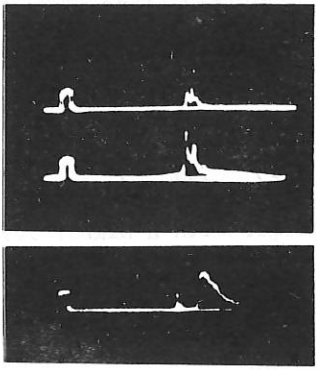

Fig.2. X-ray pulses of hard /upper trace/ and soft /lower trace/ radiation, as observed for a single shot. Below - the corresponding X-ray and neutron pulses at $Y_n = 5 \times 10^8$, $I_{xh} = 0.7$ uG. Time base - 200 ns/div.

Particular attention has been paid to the correlation between the X-ray intensity and the neutron yield. It has been found that with an increase in the neurton emission one can also observe an increase in the X-ray emission, but after some saturation the X-ray intensity decreases for shots with the higher neutron yield. The position of the maximum on the I_X vs Y_n diagram differs for the static- and dynamic-operation mode, as it can be easily seen in Figs 3 and 4. If the gas nozzle volume is reduced, and the initial gas pressure in the valve plenum is increased, the maximum of the X-ray emission appears at a lower neutron yield. It can be explained by the fact that the modification of an initial gas density profile can influence on the generation of primary e-beams interacting with a plasma target. In result, conditions of the electron-ion heating, as well as those of the neutron

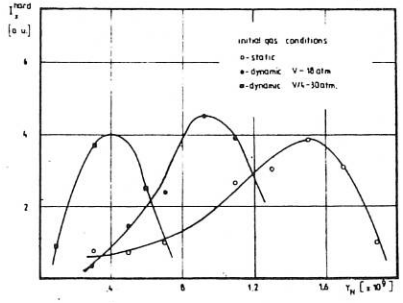

Fig.3. Hard X-ray intensity vs Y_n for different operation modes.

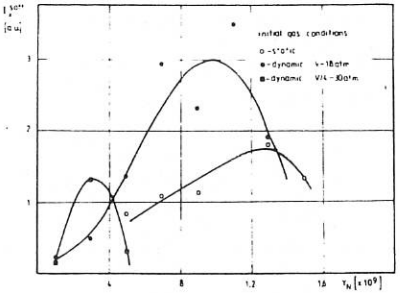

Fig.4. Soft X-ray intensity vs Y_n for different operation modes.

production, can be modified.

During recent gas-puffed experiments particular attention has been paid to observations of the plasma front propagation. The measurements of the front velocity have been performed by means of an optical system consisting of light-pipes and photodetectors. It has been observed that during the run-down phase the plasma front velocity reaches the value of /0.8-2.5/ x 10^7 cm/s. It has also been found that the gas-puffed PF discharges with a higher front velocity are characterized by a higher neutron yield, as shown in Fig.5. This observation confirms that the current sheath characteristics are of particural importance for the PF formation.

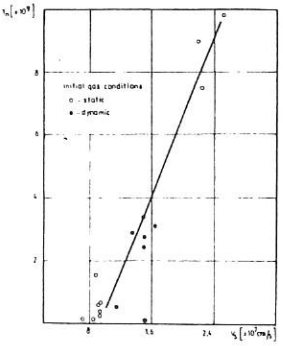

Fig.5. Neutron yield vs a plasma front velocity for different operation modes.

Conclusions

From the gas-puffed PF-type experiments described above, one can get following conclusions:

1. The formation of the PF-type discharges can be carried out also under the dynamic filling, since the breakdown process develops very quickly in comparison with a thermal outflow of the working gas.

2. The application of a fast-acting gas valve with an appropriate nozzle makes possible to create profiled initial gas distributions, and it can be used for the optimization of the X-ray emission.

3. Although the gas-puffed PF experiments performed so far have revealed lower neutron yields, one cannot exclude that an appropriate gas puffing might lead also to an increase in the neutron emission.

References

1. Proc. 3rd Intern. Workshop on PF Research /Stuttgart 1983/.
2. Proc. 4th Intern. Workshop on PF and Z-Pinch /Warsaw 1985/.
3. Proc. 1987 Workshop on PF and Z-Pinch /Toledo 1987/.
4. A. Bernard et al., Proc. 4th Topic. Conf./Palaiseau 1981/.
5. A.G. Tolstolutskij et al., Sov. J. Plasma Phys. 8/1982/141.
6. J.H. Degnan et al., J. Appl. Phys. 61/1987/ 2763.
7. R.G. Sulakvdze et al., Proc. 14th Europ. Conf. /Madrid1987/.
8. M. Sadowski et al., Report SINS 2056/P-V/PP/A /Swierk 1988/.
9. M. Sadowski et al., Proc. Z-Pinch and PF Workshop/Nice1988/.
10. A. Jerzykiewicz et al., Proc. 12th Europ. Conf. /Nice1988/.

NUCLEAR REACTIVITY IN SUBMILLIMETRIC DOMAINS OF FOCUSED DISCHARGES. A PROGRESS REPORT ON SIT-UF EXPERIMENTS *.

A. Bortolotti, J. S. Brzosko, A. Fuschini, V. Nardi, C. Powell

Stevens Institute of Technology, Hoboken, NJ 07030 (USA),
Universitá di Ferrara, Ferrara, 44100 (Italy)
Cooperative Research Program.

Abstract. High nuclear reactivity within submillimetric domains in the space structure of the pinch of focused discharges has been reported since many years [1,2,3]. New evidence from the localized reactivity is reported from a variety of independent diagnostic methods in agreements with the findings of other laboratories [4].

Introduction. We summarize and compare new and previously published data from our experiments which describe the emission of D^+ beams and the occurrence of nuclear fusion reactions within submillimetric domains of plasma focus (PF) discharges. All data have been obtained from PF machines operating in the neutron mode, at an energy level $W = 5 \div 10$ kJ of the powering capacitor bank ($3 \div 8$ Torr of pure D_2 or, alternatively, of $D_2 + N_2$ or $D_2 + CH_4$). The geometry of electrodes, power transmission lines and switches is exactly the same for all machines. Some of the experiments have been repeated with an advanced version of the electrode system (i.e., with a field distortion element in the interelectrode gap [5]) which leads to an increase of the pinch current without changing the basic role of the localized sources of particle beams and of fusion reactions.

Space Resolved Information. In the last eight years, pinhole images of high-density submillimetric domains in the PF pinch have been recorded from the non uniform distributions of ion induced damage on targets of different materials [5] and/or etched tracks of energetic D^+ ions on CR-39 targets [6,7,8] which were covered with a thin filter (a mylar foil) and/or a grid filter; the grid is composed of 50-μm-dia. cylindric yarns of plastic material. With a suitable choice of the filter thickness, of the CR-39 etching procedure and from the difference of track characteristics we determine the ion energy spectrum and the ion species at different points of the pinch image, with a space resolution $\tilde{=}$ 50 μm, or better, with a limitation dictated only by the density of tracks. Hundreds of single-shot images have been collected at different emission angles (0°, 45°, 85°-90° with respect to the electrode axis). These images from the pinch particle emission systematically reveal the presence in each image of a few (1-5) microsources of D^+ ions ($E \gtrsim 2.4$ MeV) with linear dimensions $\lesssim 100$ μm. These microsources of ions are detected for a pure D_2 filling as well as when we use D_2 with C and/or N doping ($\tilde{=}$ 1-10% by pressure). Fig. 1 shows an example of D^+ microsources (D^+ with $E > 2.4$ MeV in Fig. 1a where the CR-39 target at 45° has a grid filter; $E > 1.5$ MeV in Fig. 1b, where the 0° target has a 25 μm-mylar foil as a filter). Conditions for track etching and imaging are chosen in such a way that outside the grid filter area D^+ ions with $E = 0.1$-1 MeV (as well as ion clusters and/or impurity ions with typical 5-9 μm-dia. tracks) are clearly recorded. Under the 50 μm filter

(*) Work supported in part by ONR, Arlington (VA), Enricerche and MPI (I)

D^+ with 2.4 MeV $\lesssim E \lesssim$ 3.5 MeV are detected. Where two yarns overlap (~ 100 μm filter) only fusion protons of energy ≅ 3 MeV are detected. A quantitative estimate of the physical parameters of the localized sources can be based on: (i) The assumption that these sources are isotropically emitting D^+ ions (with energy E > 2.4 MeV) and D-D fusion reaction protons P in agreement with our ion track observations of the pinch, with [7,8] and without [9] limitations of the field of view of the pinch. (ii) The energy spectrum of trapped (in the source self field) and ejected D^+ ions is of the form $d\phi/dE \cong A\, E^{-m}$ (m = 2.5 ± 0.5 for 50 keV $\lesssim E \lesssim$ 10 MeV) in agreement with our previous spectral determinations with five independent methods [5]. This estimate indicates that: (a) A localized source emits a quantity $\gtrsim 10^9$ of D^+ ions with 2.4 MeV $\lesssim E \lesssim$ 3.5 MeV. This agrees with the quantity of the D^+ emission from more recent measurements of the D^+-induced activation of several targets inside the discharge chamber (a foil target covering the internal wall of discharge chamber from 15° to 120° has also been used [10]). (b) The fast ion density in the localized sources is ~ 10^{19} cm^{-3} which fits the electron density $n_e \gtrsim 10^{20}$ cm^{-3} as we have determined from x-ray bremsstrahlung intensity [1,11] and x-ray spectrum with different doping (Ar, N_2) of the gas filling, and is consistent with the value $n_e \gtrsim 10^{20}$ of 40 μm diameter plasma domains which were observed via "overdense" infrared (CO_2 laser) scattering in the post pinch plasma [4]. (c) The fusion proton yield from one microsource is $N_p \sim Y_n/\nu$, where Y_n = 2-8 x 10^8 is the total neutron yield/shot and ν (≅ 1-5) the number of microsources observed in the same shot.

Time Resolved Data. The fine structure in time of the PF-pinch x-ray emission consists of a multiplicity of x-ray bursts (photon energy $\epsilon \gtrsim$ 30 keV) which numerically fits the multiplicity of localized hot spots in the pinch image from x-ray pinhole cameras (at 0°, 45°, 80°) in the same shot [12,1]. Scintillation detectors data indicate also that the x-ray emission and the neutron emission have the same time structure [3]. This is determined by using a paraffin collimator with different values of the collimator gap (usually 1 cm width) in different tests. The collimater gap (110 long) has a rectangular cross section (orthogonal to the electrode axis), viewing a segment of the PF pinch from the front end of the PF anode [3]. The NE-102 collimated detector is embedded in the paraffin block with the lead shielding open in the front for observation of neutrons and x-rays. A second NE-102 scintillation detector (inside a Pb box which screens out all x-rays, outside the paraffin block) monitors the neutron emission of the entire source at a distance of 12 cm from the PF electrode axis in the normal direction (3). Fig. 2 reports typical oscilloscope traces with structure of the signal from both collimated, (a), and noncollimated,(b), detectors. By decreasing the collimator gap width (e.g. to 0.5 cm) we can resolve a neutron-signal spike also in a signal where the time spacing between signal peaks is smaller than the spacing reported in Fig. 2(b). Time resolved observation of the D^+ beam emission has been carried out with a large-angle Faraday cup with a stack of ion collector foils in a series arrangement, so that each foil performs also as an ion filter for the successive foil in the stack [13]. This method is different from that presented in [14] because of the relatively-large angle of collection and because it is not limited to PF shots with a single ion pulse. The signals from different ion collecting foils are displayed simultaneously on different oscilloscope channels. The stack of ion collecting foils is at an axial distance (0°) of 76 cm from the end of the

PF anode in a 10^{-3} Torr drift chamber and is suitably shielded from the EM noises (each foil is also biased by a polarizing ring, to prevent interference from photoelectrons which are generated in the foil stack or in the metallic supports). Fig. 3 reports typical signals from two foils of the collector stack in three different PF shots. The signal from one foil corresponds to D^+ ions of energy 1.7 MeV < E < 2.6 MeV (a) and that from the other foil to D^+ with 2.6 < E < 4 MeV. Time resolved data (beam intensity and energy spectrum of the D^+ at 0°) have been also recorded from Thomson (parabola) spectrometers at 0° with a time resolution of about 1 ns [5]. Time resolved data from the x-ray emission (via x-ray scintillation detectors and collimators) have been reported in the literature with a quantitative description of the correlation (in multiplicity and location) between x-ray signal spikes and localized hot spot in the PF-pinch x-ray image. The number of peaks in the hard x-ray signal matches the localized sources (50 μm dia.) in the x-ray image from the same shot [12] with enhanced space resolution of saturated x-ray films, via a new method as it is described in [15]. The quantitative results of all these tests are: (a) The typical FWHM of emission pulses from a localized source are respectively $\tau_n \lesssim 5$ ns (for 2.5 MeV neutrons), $\tau_d \gtrsim$ (for 1.7-4 MeV D^+ beams at 0°) and $\tau_x \simeq$ 1-5 ns (for $\epsilon \sim 30$ keV x-rays), after corrections for time of flight and instrumental broadening of the signal. (b) The localized sources are emitting over a time interval $\Delta t \simeq$ 50-200 ns, in which ν = 1-5 sources (most frequently $\nu = 2$) are particularly intense. These localized sources generate up to ~ 70% of the total neutron emission, well explain the observed high nuclear reactivity in the plasma and their observed D^+ emission for E > 1.7 MeV fits the (d,n) reaction yield in ^{10}B, ^{12}C, ^{14}N solid external targets [5]. Ion clusters with a wide mass spectrum from the low magic numbers up to $m/Z \simeq 10^{12}$ (in A.U.) and linear dimensions up to ~ 100-200 μm are also ejected from the pinch [8,16]. This indicates the ubiquitous tendency of self-field-dominated plasma toward generating structured and high-density plasma domains. Neutrons spectrum and high-z nuclei reactivity in the suitably-doped gas of the discharge chamber (with ^{12}C or ^{14}N) have been used for the spectrum determination of the D^+ ions which are trapped in the localized sources [5]. This yields the same spectral function $AE^{-2.5}$ and amplitude A for both trapped and ejected ions (the linear correlation coefficient for the spectral amplitudes of ejected and trapped ions is $a_c \geq 0.7$, on 25 shots; Ref. [5,17]). Consistently, we have determined the quantity $n\tau$ (τ is the fast ion confinement time inside the localized sources). We find $3 \cdot 10^{12} \leq n\tau \leq 1.2 \cdot 10^{13}$ cm^{-3}s. For τ = 5 ns (or 1 ns) it follows $6 \cdot 10^{20} < n < 2.4 \cdot 10^{21}$ cm^{-3} (or $3 \cdot 10^{21} \leq n \leq 1.2 \cdot 10^{22}$ cm^{-3}). These values of the localized source density from nuclear reactivity and energy spectrum are in good agreement with the ion-track density on the pinhole image of localized sources (from the particle emission during the microsource disintegration on a ns time scale) if we note that the D^+ population with E > 50 keV (which forms the pinhole image) is about 1% of the total D^+ population within a microsource.

Discussion and Conclusions. An independent assessment of the $n\tau$ and τ values resulting from the above data can be based on the observed quantity of D-T secondary fusion reactions from the tritium which is bred via primary D-D fusion reactions in the initially pure D_2 filling of the discharge chamber [2]. The observed yield in one shot of these secondary D-T reactions is Y_n (D-T) ~ $(1.5 \pm 0.5) \cdot 10^{-4} \cdot Y_n$ (D-D) [2]. If we assume $n \simeq 1.5 \cdot 10^{21}$ and τ = 1 ns (i.e., if we set the tritium confinement time = fast

D^+ confinement time inside a microsource) we estimate from the reaction cross-sections the value $Y(D-T)/Y(D-D) \tilde{=} 1.4 \cdot 10^{-4}$ for the ratio of secondary and primary reactions. This coincidence of the estimated ratio with the experimentally observed ratio [2] supports the validity of the here chosen values for $n\tau$, τ. We conclude that a variety of independent data supports the cogency of the basic idea we have stressed here, i.e., that localized high-density plasma domains with submillimetric dimensions (microsources, say) contributes the bulk ($\gtrsim$ 70%) of the observed fusion reactions in our PF machines. The generality of the observations we have presented here indicates also that the same conclusion is valid for optimized PF machines with any value of W.

References.

1. W.H. Bostick, V.Nardi, W.Prior: J. Plasma Phys. Vol.8,7 (1972)
2. W.H. Bostick, V.Nardi, W.Prior: Nucl.Fusion, Suppl.Vol.3,108 (1975)
3. W.H. Bostick, V.Nardi, W.Prior: Nucl.Fusion, Suppl.Vol.3,497 (1977)
4. G.R. Neil, R.Post: Plasma Phys. 23, 425 (1981)
5. V.Nardi,A.Bortolotti,J.Brzosko et al:IEEE Tr.Plasma Sci.16,368&373(1988)
6. V.Nardi,et al.:Proc.XI Eur.Fusion Conf.(Aachen,1983)Vol.7-D,Pt.1,pg.489
7. V.Nardi,et al: Proc.6th I.C. High-Power Particle Beams(Kobe 1986) p.447
8. V.Nardi: Proc.IV MG Conf.(S.Fe,1986,M.Fowler,ed),Plenum, NY p.269
9. V.Nardi: Energy Storage,Compression&Switching(ESCS)Vol.2,449(1983)
10. J.Brzosko,V.Nardi: Submitted for publication (1989) and foll.Ref.17
11. V.Nardi,W.Bostick,W.Prior:Phys.High Magn. F.CNRS,I.C.Vol.242129 (1975)
12. W.H.Bostick et al.:Energy S.C.&S:Vol.1,261(1975) Plenum, NY
13. J.S.Brzosko,V.Nardi,C.Powell:Bull.Am.Phys.Soc.31,1453 (1986)
14. W.H.Bostick,H.Kilic,V.Nardi,C.Powell:Proc.PF&Z-pinch Work.(Nice'88)
15. W.H.Bostick, et al: En.Stor.C.&S:Vol.2 267(1983)Plenum, NY
16. V.Nardi,C.Luo,C.Powell:Proc.PF Workshop (Warsaw 1985),S.Denus,ed,p.112
17. V.Nardi, et al.:Nuclear Fusion Suppl. (Proc.IAEA 10/1988 Nice Conf.)

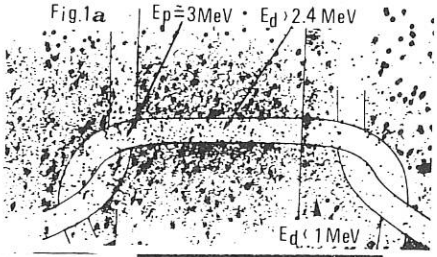

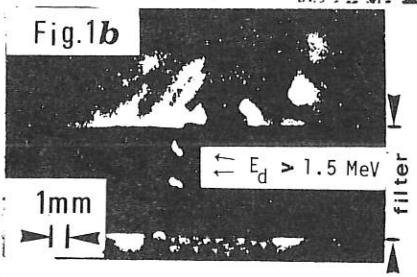

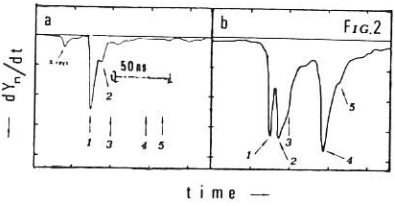

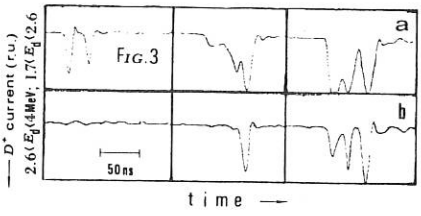

THE DESIGN AND MAGNETIC BEHAVIOUR OF THE SPHEX SPHEROMAK

P.K. Browning, B. Browning, J. Clegg, P. Dooling, K. Gibson, G. Holford, D. Kitson, G. Cunningham, S.J. Gee, M.G. Rusbridge, K. Sebti.

Dept of Pure and Applied Physics, UMIST, Manchester M60 1QD,UK

Abstract. SPHEX is a gun-injected Spheromak similar to CTX at Los-Alamos, but with a solid copper flux-conserver designed to minimise field errors due to flux-loss through the conducting wall. We describe the design and initial performance of the device. We have reached a gun current of 70 kA corresponding to a toroidal circulating current of about 135 kA; the density is $3 - 4 \times 10^{20}$ m^{-3} as measured by an interferometer while from specroscopic evidence we estimate the electron temperature to be about 30 eV.

1. Introduction and Description of Machine. SPHEX is a gun-injected Spheromak similar to CTX at Los-Alamos National Laboratory (Jarboe et al 1983), but with a solid copper flux-conserver 5 mm thick in place of the meshwork of copper rods used in recent work on CTX. Following evidence of the significance of field errors and wall interactions in RFP's (Jarboe and Alper 1987), our design is chosen to minimise the effects of magnetic field penetration into the wall, which remains a flux-surface to a good approximation (Browning et al 1987). The internal profile of the flux-conserver is smooth, sharp corners are avoided, and openings are kept to a minimum: there are 7 4 cm diameter holes near the 'pole' for pumping purposes, and a further 4 on the 'equator' for diagnostic access. Fig.(1) shows a cross-section, similar to that proposed by Browning et al (1987) except that the entry region is tapered to accommodate the return solenoid; this extracts the magnetic flux fed in by the main gun solenoid, much reducing flux penetration into the wall.

The device is powered by a 45o kJ capacitor bank which discharges through a 40 μH inductor in series with the central electrode of the annular gun. The bank is shorted at peak current, and the gun current then decays with an L/R time of ~4 msec; the gun impedance is ~ 5 m Ω, typically half the total circuit resistance. The design aim was a gun current of 100 kA; at present we have achieved 70 kA, and are reconfiguring the bank to raise this limit. The solenoids are powered by a single 50 kJ capacitor, with a rise time of 20 msec.

Diagnostics so far installed a single-chord CO_2 interferometer; a spectrograph and half-metre monochromator; and a set of eight magnetic pick-up coils arranged around the equator to measure the poloidal or toroidal field just inside the wall. An insertable magnetic probe carrying an array of ten coils has been used to measure the magnetic field configuration as far as the toroidal magnetic axis, and preliminary results have also been obtained from an insertable Langmuir probe.

2. Performance. Fig.(2) shows typical results including the bank current, gun current and one of the equatorial poloidal field signals. (The currents are of course identical until the bank is shorted.) The equatorial poloidal field (P.F.) is a rough measure of the toroidal circulating current and shows the formation of the spheromak configuration after the plasma ejects from the gun. For ejection the gun current I_G must exceed a critical value (Barnes et al 1986), we define the

gun μ-value by $\mu_G = \mu_o I_G / \Psi_G$ where Ψ_G is the flux in the gun solenoid, and then find $\mu_G > \mu_{GC} \simeq 26\ m^{-1}$ is required. This appears to be a high value; Barnes et al (1986) quote $\mu_{GC} = 15\ m^{-1}$ for CTX, with similar gun dimensions, but inspection of their results shows that higher values are obtained for lower gun currents, and from their Fig.(2) we find $\mu_{GC} \simeq 33\ m^{-1}$ for $I_G = 60$ kA.

The P.F. pulse terminates when μ_G falls below μ_{GC}, so that the spheromak lasts longer when the peak value of μ_G is raised. However, the P.F. reaches a maximum for $\mu_G \simeq 1.25\ \mu_{GC}$ and thereafter falls roughly as μ_G^{-1}; we normally work at this optimum condition, and the P.F. pulse length is then about 1 msec, as shown in Fig.(2). We infer from results given by Barnes et al (1986) that CTX behaves similarly. The 'efficiency' of injection, measured by the ratio of P.F. to gun current with μ_G kept constant at its optimum value of $34\ m^{-1}$, is a rapidly increasing function of gun current, as shown in Fig.(3). The magnetic field configuration has been measured at $I_G = 70$ kA the highest current reached so far, and from comparison with theoretical models we infer a toroidal circulating current of 135 kA, i.e. a current amplification factor of nearly 2.

3. Magnetic field configuration: model and experiment. In the fully relaxed minimum-energy state satifying $\nabla \wedge \underline{B} = \mu \underline{B}$, with μ determined by the boundary conditions (Taylor 1986), the true spheromak configuration with closed flux surfaces is predicted to form only when μ is very close to the first eigenvalue μ_e; for SPHEX, $\mu_e \simeq 11.1\ m^{-1}$. Solutions with $\mu > \mu_e$ can be found, but they have a different magnetic topology and are not accessible; thus μ cannot exceed μ_e. More realistically, μ is not a constant; for CTX Knox et al (1986) showed that during the driven or sustained phase μ increased from the magnetic axis outwards. They modelled the configuration assuming μ to be a linear function of poloidal flux. We have repeated these calculations and compared them with the measured magnetic fields to obtain the same conclusions: μ increases from $\sim 5\ m^{-1}$ at the magnetic axis to $\sim 16\ m^{-1}$ at the wall. (Our results refer to the sustainment phase only: we do not yet have a crowbar switch and have not observed the decaying phase, with the opposite variation of μ, described by Knox et al, 1986.) We note that the range of μ spans the eigenvalue; this must always be the case if a spheromak is to be formed. It can be shown (Kitson and Browning, to be published) that there is an appropriately weighted average μ which has the property that it cannot exceed the eigenvalue, but must be close to it for spheromak formation.

There is a large mismatch between the gun μ-value ($\simeq 34\ m^{-1}$ at the optimum) and that of the spheromak, only partly resolved by noting that only the outermost field lines, with highest μ, are directly connected to the gun. This means that the gun is providing about twice the current which enters the flux-conserver. There appear to be two possible explanations for this. First, there may be some 'short flux' which links the gun electrodes directly rather than through the flux conserver (Browning et al 1987): then μ may well be non-uniform across the gun, with the excess current confined to the short flux. In this case it is hard to see why all the current does not transfer to the short flux, leading to rapid extinction of the spheromak. Alternatively, there may be no short flux, (T.R. Jarboe, private communication), and the excess current may flow across the magnetic field inside the gun, leading to continuous ejection of newly ionised gas. In this case, the influx of mechanical energy must be as significant as the electrical energy dissipated in the flux-conserver.

Magnetic field fluctuations are dominated by a quasi-regular oscillation at about 15 kHz. Observations of the phasing with the equatorial coil array show that this is an n = 1 mode, confirming the analysis of Knox et al (1986). The mode appears to be basically a 'tilt' mode with an amplitude of about 3 cm. It can also be detected with other diagnostics, including the interferometer, where, as expected for a line-of-sight diagnostic, its frequency is doubled.

4. Plasma Properties. An extensive photographic spectrum at a resolution of 2.5A has been obtained, integrated over several discharges. This shows numerous lines of iron and some chromium, clearly originating from the stainless-steel gun electrodes, and copper from the flux-conserver. Among light impurities, C III and 0 III are both observed and appear to be the dominant ionisation states. Time histories of a representative set of spectral lines are shown in Fig.(4). These show quite different forms. $H\beta$, for example, continues throughout the current pulse at a similar level: it probably represents mainly scattered light from the gun. C III is confined to the P.F. pulse and shows no evidence of burnthrough, from this, and from the observation of 0 III, we estimate that the electron temperature is in the range 30 - 40 eV. Cu I shows a very spiky signal, which from 1.5 msec onwards is related in phase to the n = 1 magnetic field oscillation; it is, however, at the basic frequency rather than twice it, and we infer that the source is local, probably the edges of, or even outside, the flux-conserver viewing opening. We have looked for bulk emission of ionised copper, but the only convenient line is weak and overlaid by Fe II lines; an attempt to subtract these showed no evidence of a Cu II signal, but the sensitivity must be poor. Finally, Fe II shows peaks at the beginning and end of the pulse; presumably it is burnt through, the ionisation energy being only 16 eV.

Finally, from initial interferometer results we infer a peak density of 3 - 4 x 10^{20} m^{-3}, corresponding to $\beta \simeq 10\%$ if the ion and electron temperature are equal. This is about twice the average density in CTX.

5. Discussion and Future Programme. The initial results from SPHEX reported in this paper largely confirm the results obtained from CTX at comparable gun currents; in particular the critical μ-value of the gun, the μ-profile of the spheromak during sustainment, and the dominant n = 1 fluctuation mode are all closely comparable with CTX results. The principal aims of the experiment after the initial period of study, which includes working up to the target gun current and cleaning up the discharge to reduce radiation losses are (1) to examine the effect of an improved flux-conserver structure on the energy balance, and to see whether anomalous dissipation can be reduced by the elimination of field errors, and (2) to investigate the mechanism of the relaxation process.

Acknowlegement: We are grateful to the Science and Engineering Council and to the United Kingdom Atomic Energy Authority for financial support for the building and operation of SPHEX.

References:

C.W. Barnes et al, Phys. Fluids 29, 3415, 1986

P.K. Browning, G. Cunningham, M.G. Rusbridge in "Physics of Mirrors Reversed Field Pinches, and Compact Tori", Proceedings of the Varenna International School of Physics, 1987, vol II, p.449

T.R. Jarboe, B. Alper, Phys. Fluids 30, 1177, 1987

T.R Jarboe et al, Phys. Rev. Lett. 51, 39, 1983

S.O. Knox et al, Phys. Rev. Lett. 56, 842, 1986

J.B. Taylor, Rev. Mod. Phys. 58, 741, 1986

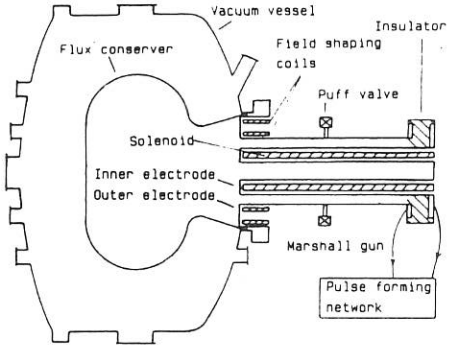

Fig 1. SPHEX cross section

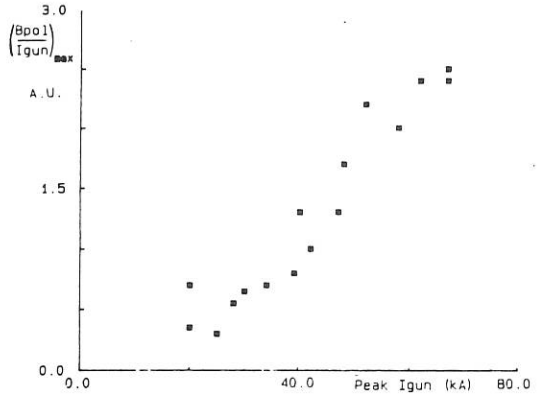

Fig 3. Injection efficiency

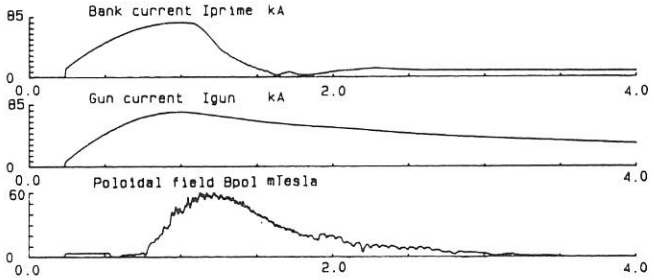

Fig 2. Typical shot characteristic

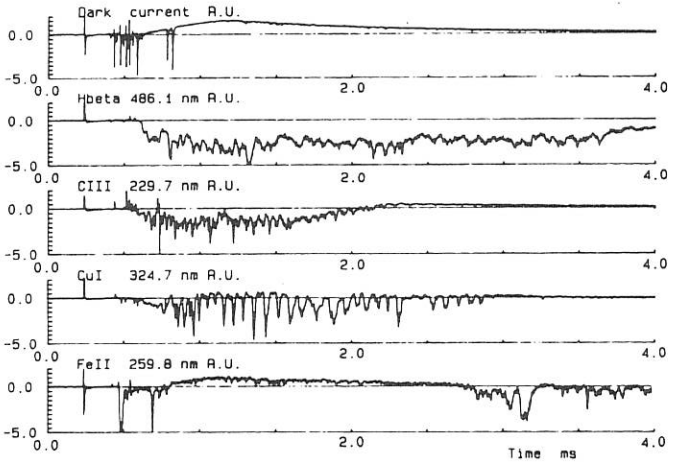

fig 4. Typical spectral line behaviour

FORMATION OF HIGH-β FIELD REVERSED MAGNETIC CONFIGURATIONS USING PLASMA ACCELERATOR

V.A.Burtsev, V.M.Kozhevin, B.V.Ljublin, V.N.Litunovsky, A.N.Makhankov, I.B.Ovchinnikov

D.V.Efremov Scientific Research Institute of Electrophysical Apparatus, 189631, Leningrad, USSR

1. Introduction

The thermonuclear systems based on field reversed configurations (FRC) can be used for developing the fusion reactors with the advanced fuel (D-^{3}He) /1,2/. The possibility of similar configurations formation using quasistationary plasma accelerators /3/ is discussed and the preliminary experimental results of similar accelerator plasma flow dynamics study are given in this paper.

2. The requirements to an accelerator operating conditions

Let's evaluate the requirements to the parameters and operating conditions of an accelerator, used for formation the toroid with particle inventory N, temperature T and $\langle\beta\rangle \sim 1$. From the condition of energy balance and taking into account the condition $\langle\beta\rangle = 1 - x_s^2/2$, ($x_s = r_s/r_w$ -is the relative radius of the toroid separatrix), we can obtain that 2/5 of the plasma flow kinetic energy is spent on creation the toroid magnetic configuration and 3/5 - for plasma heating there. Plasma final temperature is defined by the plasma velocity (V_m) at the accelerator muzzle: $m_i V_m^2 = 5T$. In its turn, $V_m \sim U^{1/2}$, where U - is the voltage at the electrodes /3/, and, consequently, $T \sim U$. For $T_e = T_i = T \simeq 8$ keV, U=200 kV.

On the other hand $V_m \sim B_0$ /3/, where B_0 is the magnetic field at the accelerator muzzle and, consequently, the ejected magnetic flux rises with T-increase. From the discontinuity equation and magnetic field freezing-in condition, it can be easily obtained that $\Phi_T = \langle\mathcal{R}\rangle \cdot N$, where Φ_T -is the ejected toroidal flux, $\langle\mathcal{R}\rangle = \sqrt{2\pi m_i} \cdot V_m / n_0^{1/2} \cdot r_0$ -is the freezing-in parameter. For $\mathcal{R}N$

fixed value Φ_T -magnitude can be minimized due to $\langle \varkappa \rangle$ -reduction,and the plasma mainly should be concetrated in the region with r_0 high values.From the pressure balance in the toroid central cross-section and above said relationships the criterion ofthe toroidal flux minimization is the following view: $n_m < n_0$, where n_m is the plasma density at the toroid magnetic axis.

The second possibility for Φ_T minimization can be attributed to 2-fluid nature of the plasma flow. As the magnetic field is frozen into an electron flow,then the trapped flux can be leaded away from the compression zone if the combined current transfer is organized (ion transfer-in the accelerator channel, electron-at accelerator muzzle).For ion charge compensation the electron flow injection is necessery (for example from the gun solenoid) which will eject its toroidal flux. The coefficient this flux freezing-in $\varkappa_C$ doesn't depend on radius at the current uniform radial distribution. $\varkappa_C \sim n_C^{-1}$ where n_C is plasma density in a compensator. It's easy to obtain that $\varkappa_C \leq (r_0/r_c)^2 \cdot (n_0/n_c) \cdot \varkappa \cdot 2\pi$. The proper choice of n_c/n_0 value permits to reduse Φ_T magnitude.

3.Experimental results

The experimental investigations are carried out on SAPFIR installation,comprising quasistationary plasma accelerator(QPA) and the magnetic system intended for creation the magnetic configuration with "min B" at accelerator muzzle (Fig 1). The preionization sistem comprising 6 plasma accelerators are located at the electrode entrance. QPA is supplied from 5kV and 10kV cappacitive storage modules with the total energy storage 0.8MJ. The current pulse duration is $\sim 100\ \mu s$.

The magnetic system comprises the "gun solenoid",located inside the cathode hole and two coils of "the magnetic flux interseption". The gun magnetic flux magnitude is $\Phi_G \leq 50$ mWb.

The experimental investigation of preionisation system accelerators (PSA) plasma flow dynamics and parameters was aimed at attaining the operating modes with spatial focusing,permitting to programm the density radial profile in QPA accelerating

channel.The process of the ejected current closing to the metallic vacuum chamber wall influences significantly the plasma flow dinamic.Fig.2 shows the discharge current and two Rogovski loops signals located at ~50 mm and~1600 mm distances from PSA. The temporal compression of current plasma,resulted apparently from the fact plasma flow character may change abruptly at threshold value of the discharge current. Current-voltage characteristic of PSA discharge (Fig.3) have two typical bends, corresponding transitions to qualitatively different operating conditions.At discharge current values I_d>70 kA high speed plasma flows ($V_m \simeq 12 \cdot 10^7 cm/s$; $n \sim 10^{15} cm^{-3}$) with the flow power density $p > 5 MW/cm^2$ at the distance ~ 1,5 m where observed.Fig.4 shows high speed photography frame of preionisation system luminousity.PSA outer electrode insulation prevented closing of the current ejected from the discharge chamber wall to the PSA anode and reduced these currents magnitude by an order.

4.Conclusion

The results of analytic evalutions testify to the principle possibility of QPA operation with mimnimized ejected currents, what is the condition necessary for formation of the high $\langle \beta \rangle$ plasma toroid.Found operation conditions with high degree of spatial focussing (p > 5MW/cm) is of interest for tokamak disruption simulation.

REFERENCES

1.V.A.Burtsev,V.M.Kozhevin,A.N.Makhankov.In 11-th IAEA Confer. on Plasma Physics and Contr.Fusion Research,Kyoto,1986, p.CN-47-H-11-2.

2.V.A.Burtsev,V.M.Kozhevin,A.N.Makhankov.Proc.4-th Techn.Comm. Meeting Fusion Reactor.Design and Technology (Yalta,1986), IAEA,1987,v.1,p.413-421.

3.A.I.Morozov,A.P.Shubin.Plasma accelerators.Fizika plasmy,v.5, (Itogi nauki i tekhniki,VINITY AN SSSR),M,1984,s.178-260.

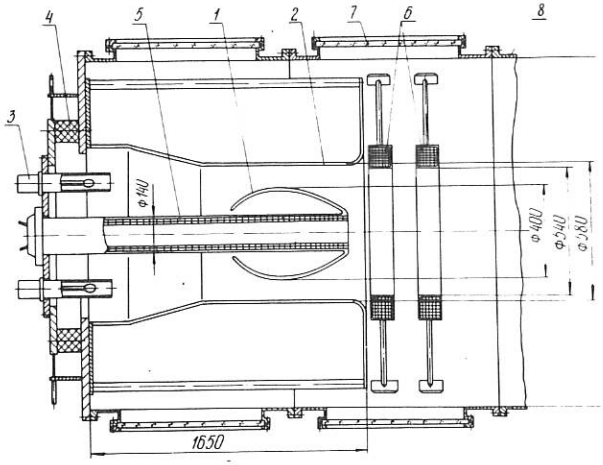

Fig.1

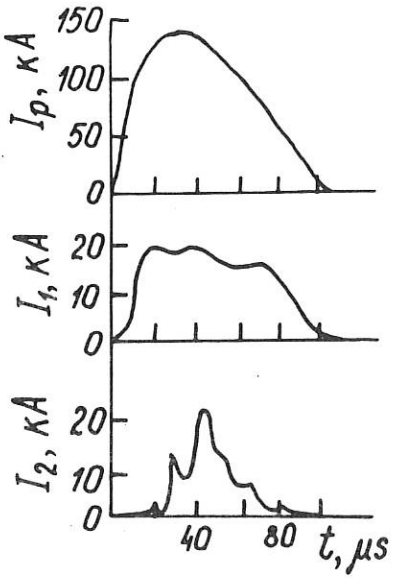

Fig.2

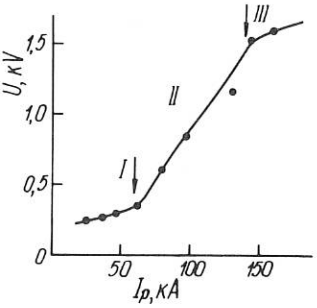

Fig.3

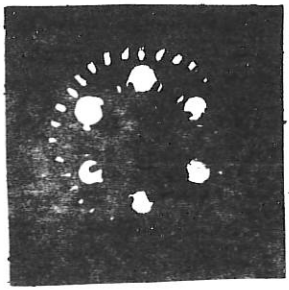

Fig.4

OBSERVATION OF OPPOSITELY ROTATING PLASMA CELLS DURING SPHEROMAK FORMATION

George C. Goldenbaum and Bruce Barrow
Laboratory for Plasma Research
University of Maryland
College Park, Maryland 20742
U.S.A.

It has long been recognized that flow velocity can play an important role in the generation and transport of magnetic fields in conducting fluids. In the context of spheromak formation velocity fields can effect magnetic helicity injection (1), require the need for consideration of cross helicity (2) and act as a source or sink of energy. These considerations may be important in magnetic relaxation to the minimum energy configuration (3),(4). In this paper we report our observation of a gradient in plasma rotation velocity during spheromak formation and compare the resulting magnetic helicity with estimates based on two types of helicity injection.

We have reported (5) the observation of the shift of carbon impurity spectral lines emitted from a plasma during spheromak formation in the PS-3 and PS-3.5 devices. In these experiments the spheromak is formed by a combination of inductive and electrode discharges (6). The experimental geometry is a cylinder with a ring of electrodes at each end and inductive coils near the midplane. The reported spectroscopic measurements have been made in the apparatus mid-plane along chords at right angles to the symmetry axis. The measurements have been analyzed assuming the shifts are due to the Doppler effect. It was concluded that during the time the spheromak is forming the plasma is rotating in the toroidal direction with a velocity of about 2 cm/μs which is about 20% of the Alfven speed. MHD simulations (7) of spheromak formation on a similar type of device has indicated that there should be two counter-rotating plasma rings, one in each of the electrode regions due to oppositely directed $(\mathbf{j} \times \mathbf{B})\cdot\varphi$ forces. The simulation, however, shows no rotation in the midplane where experimentally we see rotation. Subsequent to reporting these spectroscopic measurements it was determined by magnetic probe measurements that the midplane of the magnetic configuration was shifted by about five centimeters from the apparatus midplane where the spectroscopic measurements were made. Computing the toroidal component of the $\mathbf{j} \times \mathbf{B}$ force

from the magnetic probe measurements it was found that regions of oppositely directed forces exist symmetrically placed around the magnetic midplane. The force in the apparatus midplane had the correct direction for the observed Doppler shift. A further check on the possibility of counter-rotating cells was made by measuring the radial component of the induced electric field with double electric probes. The field was measured as a function of z for several different radial positions. The electric field was observed to change sign depending on which ring the probe was located inside. The field also had the correct magnitude for the measured velocity and magnetic field ($E_r = -v_\varphi B_z$). The picture that emerges from these measurements is that of two oppositely rotating cells twisting the initial magnetic field and relaxing to a minimum energy force free state. The rapid dissappearance of the rotational velocity is probably associated with the toroidal $\mathbf{j} \times \mathbf{B}$ force component set up by the currents between the cells which short out the oppositely directed radial $\mathbf{E}$ fields.

Browning (8) has calculated the rate of magnetic helicity injection in solar corona loops using as a model a magnetized cylinder with oppositely rotating ends. For a situation where the relaxation time associated with fine scale turbulence is short compared with the time for gross velocity changes she computes the magnetic injection rate into a cylinder. The injection rate is given by the equations

$$dK/dt = \int (\mathbf{A}\cdot\mathbf{v} + g)\,\mathbf{B}\cdot d\mathbf{S}, \quad \partial\mathbf{A}/\partial t = \mathbf{v} \times \mathbf{B} + \nabla g \ \text{ on } S,$$

where $\mathbf{A}$ is the magnetic vector potential, g is the gauge (which drops out of the result) and the integration is over the cylinder surface. The cylindrical model MHD fluid passes through a sequence of force free states given by Bessel functions $\mathbf{B} = B_0 J_0(kr)\,\mathbf{z} + B_0 J_1(kr)\,\boldsymbol{\varphi}$ where k is the eigenvalue parameter. The magnetic helicity (K) injection rate is then

$$dK/dt = 8\pi B_0^2 \int dr\, r\, J_0(kr)\, J_1(kr)\, v_\varphi(r)/k$$

To estimate the contribution to the internal helicity from counter rotating rings we assume that the measured radial profile of the toroidal velocity in the apparatus midplane is characteristic of the radial velocity profile all along the cylinder, but of course with different direction on opposite sides of the midplane. For small values of k characteristic of the early phase of formation with a peaked velocity profile the injection rate is $dK/dt \approx 2.8 \cdot 10^{-3}\ T^2m^4/s$ ($v_\varphi = 2\ 10^4$ m/s for .02m < r < .07m, $B_0 = 0.1$ T). With a formation time of $1{\cdot}10^5$ s this gives $K \approx 3{\cdot}10^{-8}\ T^2m^4$. Although the resulting spheromak is more nearly

spherical than cylindrical it is interesting to compare the helicity calculated from the measured equilibrium fields with the estimate based on the rotating plasma injection rate. For a spherical spheromak (9) with separatrix radius R_s in an externally applied field B_{ext} the helicity is $K = 0.26 (B_{ext} R_s^2)^2$. Using typical values ($R_s = 0.175$ m, $B_{ext} = 0.02$ T) we find $K \approx 9.7 \cdot 10^{-8}$ $T^2 m^4$.

Electrostatic helicity injection is a competing injection method (4). In this case the injection rate is given by

$$dK/dt = V \cdot \Phi$$

where V is the electrode voltage and Φ is the flux through the 16 electrodes at each end. For values characteristic of P.S.-3.5 we have $V \approx 5$ kV and $\Phi = 16 \int d\mathbf{S} \cdot \mathbf{B} \approx 16 (.0001\ m^2)(0.01\ T) \approx 1.6\ 10^{-7}\ Tm^2$. This gives an injection rate of $dK/dt \approx 30\ 10^{-3}\ T^2 m^4/s$, more than an order of magnitude larger than other calculation. In addition to only being order of magnitude estimates these calculations do not take into account how much of the injected helicity ends up inside the separatrix, consequently it is difficult at this time to determine the dominant mechanism.

References

1) J. Heyvaerts and E.R. Priest, Astron. Astrophys. **137**, 63 (1984).
2) L. Woltjer, Proc. Natl. Acad. Sci. (U.S.A.) **44**, 833 (1958).
3) J. B. Taylor, Phys. Rev. Lett. **33**, 1139 (1974).
4) J. B. Taylor, Rev. of Mod. Phys. **58**, 741 (1986).
5) T. Peyser and G.C. Goldenbaum Phys. Rev. Lett. **61**, 955 (1988).
6) H. Bruhns, C. Chin-Fatt, Y. P. Chong, A. W. DeSilva, G. C. Goldenbaum, H. R. Griem, R. A. Hess, J. H. Irby and R. S. Shaw, Phys. Fluids **26**, 1616 (1983).
7) P. N. Guzdar, J. Finn et al., Phys. Fluids **28**, 3154 (1985).
8) P. K. Browning, J. Plasma Phys. **40**, 263 (1988).
9) M. N. Rosenbluth and M. N. Bussac, Nuclear Fusion **19**, 489 (1979).

Supported by U.S. Department of Energy.

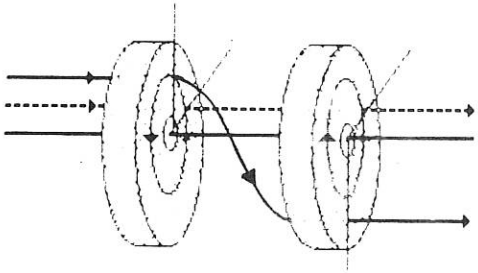

Fig. 1 Geometry of rotating plasma cells and field lines.

Improved Plasma Confinement and Evidence for a Pressure-Driven Instability from Reduced Magnetic Field Errors in the CTX Spheromak*

J. C. Fernández, F. J. Wysocki, T. R. Jarboe, Cris W. Barnes
I. Henins, S. O. Knox, G. J. Marklin

Los Alamos National Laboratory, Los Alamos, NM 87545, USA

The 0.67 m radius mesh flux conserver (MFC) in CTX was replaced by a solid flux conserver (SFC), resulting in greatly reduced field errors. Decreased spheromak open flux led to vastly improved decaying discharges, including increased global energy confinement times τ_E (from 20 to 180 μs) and corresponding magnetic energy decay times τ_{B^2} (from 0.7 to 2 ms). Improved confinement allowed the observation of a pressure-driven instability which ejects plasma from the spheromak interior to the wall [Wysocki, F., et al., Phys. Rev. Lett. **61** (1989) 2457].

In the CTX 0.67 m radius mesh flux conserver (MFC), $\approx 1/4$ of the spheromak poloidal flux forms the "edge", with open flux intersecting the FC wall[1]. Fig. 1 shows one half of a cross section of the MFC, along with the poloidal flux contours for a typical decaying CTX spheromak. $l_{eff} \approx 3$ m represents the effective length between the points where the (poloidal) open field lines intersect the wall[1]. The effective poloidal electric field $E_{eff} = \eta j$ at the edge is also illustrated. To replenish mainly the rapid plasma losses on open field lines, spheromak refueling is achieved with a static H_2 filling pressure surrounding the MFC, typically 1 – 8 mT. Because of low edge T_e, the neutrals penetrate deep into the spheromak, allowing refueling from the electrical breakdown of the neutrals by the spheromak edge currents. $E_{eff} l_{eff}$ agrees with the Paschen voltage[2] for breakdown of neutral H_2 at the given neutral pressure[1].

Maintaining spheromak edge currents causes a high loss rate of spheromak helicity (magnetic-flux linkage). Without external voltages, the helicity decay rate is given by[3]

$$\frac{dK}{dt} = -2 \int E \cdot B \; dvol = -2 \int \eta j \cdot B \; dvol \qquad (1)$$

where $E + (v \times B) = \eta j$ has been used. The high neutral density in the edge increases η much above the Spitzer resistivity. Throughout the plasma, ηj is negligible compared to E_{eff} at the edge, so that $dK/dt \approx -2 E_{eff} \int_{edge} B \; dvol$. The result is spheromak magnetic-energy decay times τ_{B^2} which are uncorrelated with the electron temperature, but which are correlated with the edge neutral pressure[1]. This model is also consistent with the results in the HBTX1B reversed-field pinch discharges with limiters[3].

*This work supported by the US DOE.

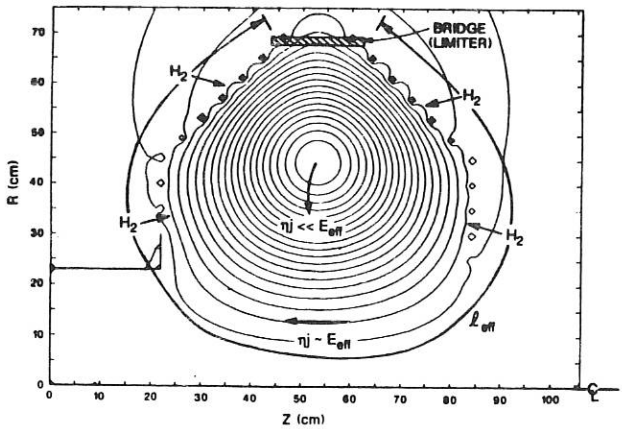

Figure 1: One half of the MFC cross section is shown. Typical normalized spheromak poloidal flux contours (5% increments) during decay are included. The poloidal magnetic field wraps around the magnetic axis in the counter-clockwise direction, while the toroidal field goes into the page.

In decaying CTX spheromaks with high edge resistivity from electron-neutral collisions, the edge currents decay until the resulting peaked current profile becomes unstable. The instabilities which grow up cause relaxation toward the minimum-energy state, which implies a current drive at the edge (which will be called relaxation current drive). It is observed that the poloidal edge $E_{eff} \approx \eta j$ driven by relaxation is up to ten times greater than the electric field produced by toroidal flux decay.

Relaxation current drive is the reason why the edge plasma must be refueled. With negligible edge electron density n_e, relaxation would try unsuccessfully to drive currents in the edge. The resulting large E_{eff} would quickly dissipate the spheromak helicity (Eq. 1). CTX results agree with this model. Without the filling pressure, only the plasma from the helicity source feeds the spheromak. After the source is turned off, the edge n_e decays within a particle confinement time τ_p. After n_e has decreased enough, the spheromak decays extremely rapidly[4,5].

It has been proposed that strong relaxation activity would result in direct ion heating[1]. Fig. 2 shows selected time traces for discharge 15805, one of the nearly identical 47 discharges previously studied[1]. The maximum reproducible Thomson scattering T_e ever achieved in the MFC is $\approx$ 100 eV. The top trace shows the spheromak toroidal current. The middle trace shows the line brightness of the impurity line used, OV at 2781 Å. The bottom trace is the Doppler broadening temperature T_D. Since the calculated ion equilibration time is much shorter than τ_p and similar to the plasma energy confinement time τ_E, T_D should reflect the bulk ion temperature T_i. These high T_D indicate an anomalous ion heating mechanism, as expected from strong relaxation activity. Anomalously high T_i have also been observed in reversed field pinches[6,7]. The oscillations in T_D (Fig. 2) are correlated with the n=1 (sustainment) and n=2,3 (decay) saturated, rotating, current-driven kink-modes[8]. T_D oscillations are most probably due to the mode exposing the

spatial profile of T_i, which we cannot resolve with our single-chord instrument. Accounting for $T_D \gg T_e$, the previously presented[1] energy confinement times $\tau_E \equiv 3/2\langle\beta\rangle_{vol}\tau_{B^2}$ in the MFC should be corrected up to the 50 – 100 μs range, and $\langle\beta\rangle_{vol}$ up to $\approx 5\%$. Still, large charge exchange losses and enhanced transport from excessive relaxation activity (caused by high edge resistivity) almost surely degrade confinement significantly.

A 0.60 m radius solid flux conserver (SFC) has been designed to decrease the relative fraction of open spheromak magnetic flux much below the value in the MFC. The observed result is a much longer τ_p, so the filling pressure has been eliminated. Ti gettering of the SFC walls has produced non-radiation dominated discharges with low edge neutral density. In the SFC, as in the MFC, the spheromak equilibrium is deduced from magnetic field measurements at the FC surface, coupled with a Grad-Shafranov MHD equilibrium solver[8]. The n_e and T_e are diagnosed by an absolutely calibrated multi-point Thomson scattering system. T_e and n_e are combined with the MHD equilibrium calculations to determine the electron β_e and pressure p_e. The result is an accurate calculation of τ_E.

τ_{B^2} in the SFC scales proportionally with T_e at the magnetic axis. With reproducible $T_e \approx 150$ eV, maximum τ_{B^2} is 2 ms. In the SFC the OV T_D is similar to T_e, and maximum global $\tau_E = 180$ μs (using $T_i = T_e$). Fig. 3 shows the increase in τ_E for similar discharges over time as the decaying spheromak plasma heats up. In this figure, only τ_E values measured before the pressure-driven instability (discussed below) are included. These SFC results suggest reduced open magnetic flux resulting in less relaxation activity, which reduces direct ion heating and increases plasma confinement, as also reported for HBTX1B[7].

In the SFC, a pressure-driven instability ejects the spheromak plasma in a distinct event[9]. As the maximum electron pressure gradient ∇p_e increases, $\langle\beta\rangle_{vol}$ remains at $\approx$ 3–6% (using $T_i = T_e$). At a threshold ∇p_e, p_e moves towards the outer flux surfaces within 10–20 μs, indicating a flux interchange. No concurrent signature on the magnetic probes at the wall is observed, as normally occurs with current-driven instabilities.

[1]FERNÁNDEZ, J. C., *et al.*, Nuclear Fusion **28** (1988) 1555.

[2]VON ENGEL, A., *Ionized Gases*, Oxford University Press, Oxford, 1955, see page 172.

[3]JARBOE, T. R. and ALPER, B., Physics of Fluids **30** (1987) 1177.

[4]HOIDA, H. W., *et al.*, in *Controlled Fusion and Plasma Physics*, page 643, Budapest, 1985, European Physical Society, Volume 9F, Part 1 (Budapest Conference).

[5]BARNES, C. W., *et al.*, Nuclear Fusion **24** (1984) 267.

[6]WURDEN, G. A., *et al.*, Nuclear Fusion **27** (1987) 857.

[7]ALPER, B., *et al.*, in *Plasma Physics and Controlled Nuclear Fusion Research, 1986*, pages 399–411, Vienna, 1987, IAEA, Volume II (Kyoto Conference), 1986.

[8]KNOX, S. O., *et al.*, Physical Review Letters **56** (1986) 842.

[9]WYSOCKI, F. J., *et al.*, Physical Review Letters **61** (1988) 2457.

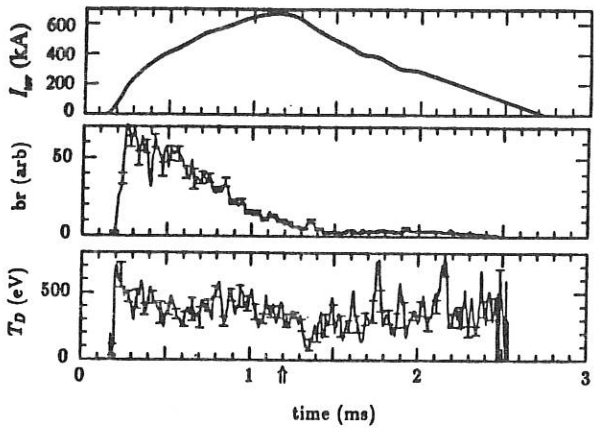

Figure 2: Traces versus time for typical MFC discharge 15805: The top figure shows the spheromak toroidal current, increased by helicity injection until 1.2 ms, when the source is turned off (arrow in the bottom figure). The middle figure shows the "brightness" br, defined as the area under the gaussian fit. The bottom figure shows the Doppler temperature T_D. Error bars at regular intervals illustrate the uncertainty resulting from the fit.

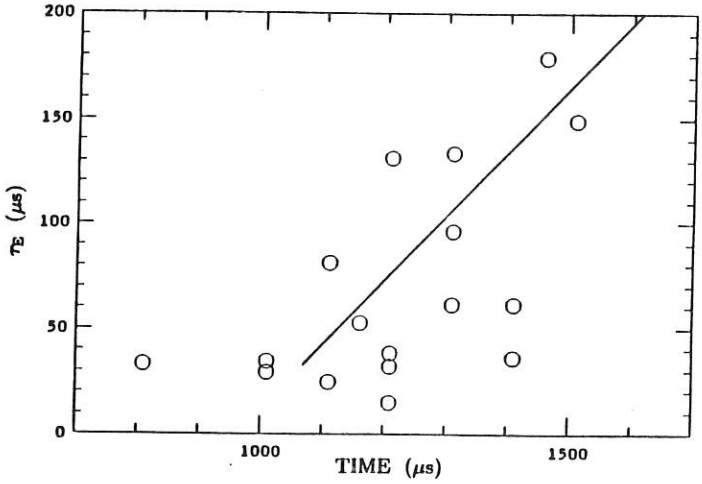

Figure 3: τ_E from similar spheromak discharges in the solid flux conserver are plotted versus time. The helicity source is turned off at 700 μs.

MEASUREMENTS OF AZIMUTHAL ASYMMETRIES IN THE FRX-C/LSM EXPERIMENT†

M. Tuszewski, G.A. Barnes, R.E. Chrien, E.A. Crawford*, S. Okada**,
D.J. Rej, R.E. Siemon, D.P. Taggart, R.B. Webster, B.L. Wright

Los Alamos National Laboratory, NM 87545, USA

Properties of large field-reversed configurations (FRCs) are being investigated in the FRX-C/LSM experiment[1] (coil diameter 0.7 m and length 2.0 m). High beta prolate compact toroids are formed in a theta-pinch coil when an external magnetic field (B_z parallel to the cylindrical axis of the coil) is applied rapidly in the opposite direction to an initial bias field embedded in a preionized plasma. The FRCs thus formed have equilibrium parameters $\langle\beta\rangle \simeq 90\%$, $n = (0.5\text{-}2) \times 10^{21}$ m^{-3}, T_e = 100-200 eV, T_i = 100-600 eV, and B_z(external to FRC) = 3-6 kG. This paper reports on new measurements made with a soft X-ray camera and with external magnetic probes that indicate departures from azimuthal symmetry under conditions where confinement is less than optimum.

As in previous smaller-size experiments, FRCs with good confinement properties have been obtained in FRX-C/LSM[2]. For certain initial conditions (gas fill of 3 mtorr deuterium pressure, 0.75 kG bias field, and experimentally "optimized" preionization timing) the longest FRC confinement times reported to date are observed: $\tau_E = 100\,\mu$s, $\tau_N = 230\,\mu$s and $\tau_\phi = 250\,\mu$s. Also, when the FRC is translated axially into an adjacent coil in which quadrupole fields stabilize the rotational n=2 mode, a total configuration lifetime of 400 μs has been obtained. These conditions are well suited to a combined translation and compressional heating experiment that will begin in 1989.

Also as in previous experiments, the best confinement results are only obtained by careful adjustment of initial parameters, and relatively small departures from the optimum settings result in significant degradation of confinement times. In particular, reproducibly good confinement has been observed only for 2-4 mtorr fill pressures and for moderate bias fields (0.5-0.8 kG). These strong dependences on operating conditions are observed in the present experiments even though the initial dynamic phase of FRC formation is controlled by the use of auxiliary "cusp" coils at the ends of the theta pinch[1]. The formation phase does not appear to be unfavorably influenced by preionization level (usually 40-80%), preionization uniformity (axially uniform according to interferometry), impurity concentration (less than 1% carbon), or symmetry of initial implosion (observed with visible light). For the same range of conditions where confinement varies markedly (fill pressures of 3-5 mtorr and bias of 0.5-1 kG) Thomson scattering shows electron temperatures between 110 and 190 eV with no correlation to confinement.

A soft X-ray plasma imaging method and various arrays of external magnetic field probes are being developed as new diagnostic methods in an effort to better understand the strong dependence on operating conditions. These measurements are complementary in that the imaging system offers good azimuthal resolution while the probes provide axial resolution and complete temporal coverage. An end-viewing X-ray pinhole camera (wavelength response 10-20 nm) has been used to view selectively the high temperature FRC plasma within the separatrix. One 2-μs exposure was obtained on each discharge. In most cases a symmetric circular image is seen for the optimum conditions with 3 mtorr, while at 5 mtorr the X-ray images are noticeably less symmetric with n = 6-10 flutes often observed at the separatrix[2] (these flutes are probably not related to the probe measurements described below). So far no strong correlation has been found between image symmetry and plasma confinement properties.

Two arrays of magnetic probes oriented to measure B_r and B_θ have been used to investigate possible departures from symmetry in the external magnetic fields. A total of twelve B_θ probes are

located at $\pm$ 0.3 and $\pm$ 0.7 m from the center of the coil at θ = 0, 180, 230 degrees. Six B_r probes are located at $\pm$ 0.2 m at θ = 0, 180, 270 degrees. Azimuthal symmetry is investigated in the case of B_r by monitoring the three differences between the probe signals at a given axial position. B_θ and differenced -B_r signals in the 1 to 100 gauss range are observed after subtracting a small amount of B_z pickup. The following general features are observed: 1) The B_r and B_θ signals near the midplane are comparable in magnitude and have similar time histories, 2) The largest B_θ signals are observed on the probes near the midplane, 3) Variations in probe amplitudes for the conditions studied are much too large to be accounted for by the relatively small variations in plasma radius, 4) At a given axial position the maximum B_θ signal varies from one azimuthal location to another, and 5) The signals do not appear to arise from a net axial current.

Representative B_θ data for a scan of bias field at 3 mtorr are shown in Fig. 1. From top to bottom the bias field increases, confinement times decrease, and progressively larger B_θ signals are observed. Low bias (< 0.7 kG) FRCs consistently show small amplitude signals (Fig. 1a). As the bias field increases the amplitude of B_θ generally increases, and a peak in the amplitude usually occurs around 10 - 20 μs, after axial contraction (the peak in $\int$ndr at about 6 μs is associated with the axial contraction) and well before the n=2 rotational mode (oscillations that develop after 50 μs). Comparison of signals on the probes separated by 180 degrees suggests mainly odd toroidal mode number (possibly n=1) but the small number of probes did not allow a definitive characterization. It is also difficult to distinguish oscillation from growth in the signal levels. A feature that was observed on a number of discharges is seen in Figure 1c at around 20 μs. At about the time of peak B_θ the line-integrated density displays a sudden decrease followed by slower decay. Measurement of midplane diamagnetism shows a sudden decrease at about the same time. For this type of high bias discharge a rapid initial flux loss (inferred to be dropping from about 9 to 3 mWb) is often followed by a slower decay of flux and $\int$ndr.

For the purpose of a preliminary analysis of the probe results, the peak B_θ amplitude ($B_{\theta m}$), or peak B_r difference signal (B_{rm}), has been taken as a measure of asymmetry. For example in Fig. 1c the value is 20 gauss (peak at 19 μs). There is good correlation between B_{rm} and $B_{\theta m}$ as shown in Fig. 2. We take τ_ϕ as a reasonable indicator of overall plasma confinement, and compare it with $B_{\theta m}$ for various fill pressures in Fig. 3. One observes that good confinement (τ_ϕ > 100 μs) is consistently obtained for small $B_{\theta m}$ values. All of the τ_ϕ values are small for the 5 and 7.5 mtorr data shown in Fig. 3b, and the corresponding $B_{\theta m}$ signals are consistently of large amplitude. At 10 mtorr pressure the correlation between τ_ϕ and $B_{\theta m}$ is less clear and occasional discharges have relatively good τ_ϕ (X-ray images also show generally better symmetry at 10 mtorr than at the intermediate pressures). The time of peak amplitude on the probes tends to occur earlier as the fill pressure increases.

In summary, the B_z and B_θ probes show larger signal amplitudes under conditions where confinement is degraded. This is the first clear correlation we have found between measurements of localized quantities and global confinement behavior. Although the asymmetries implied by the probe signals develop after formation for 3-5 mtorr cases, the FRCs are still far from equilibrium when they start to occur. It is therefore difficult to assess whether asymmetries result from a dynamic state associated with FRC formation or from growing unstable modes. A larger number of probes are needed to clarify the spatial and temporal structure of the asymmetries. Future detailed comparisons of such probe data and of multi-frame X-ray image data appear most promising.

†Work supported by the USDOE
*Spectra Technology, Inc., Bellevue, WA, USA
**Osaka University, Osaka, Japan

REFERENCES

/1/ Siemon, R.E., et al., Proc. 14th EPS, Madrid (1987) Vol. 1, p. 485.
/2/ Siemon, R.E., et al., Proc. 12th IAEA, Nice (1988) paper CN-50/C-4-1.

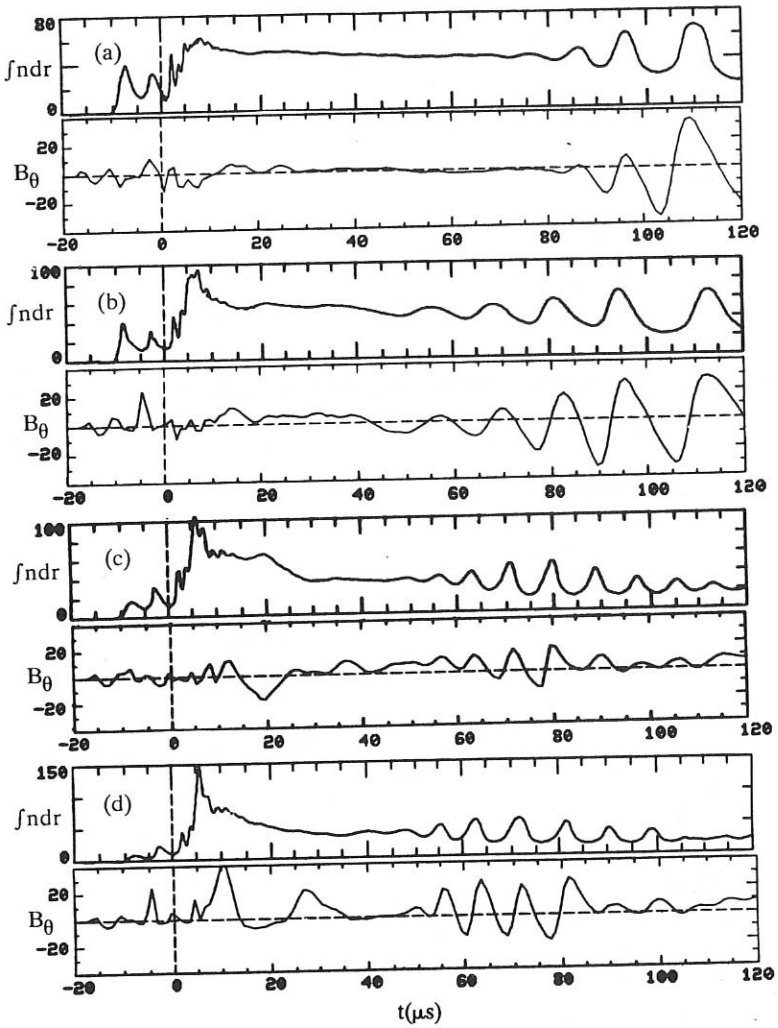

Fig. 1 3 mtorr bias scan: time history of FRCs formed with (a) 0.64, (b) 0.83, (3) 0.93, and (d) 0.96 kG bias. Top trace: $\int ndr$ (10^{21} m^{-2}) across a diameter at z = 0. Bottom trace B_θ (G) at z = 0.3 m and θ = 230°.

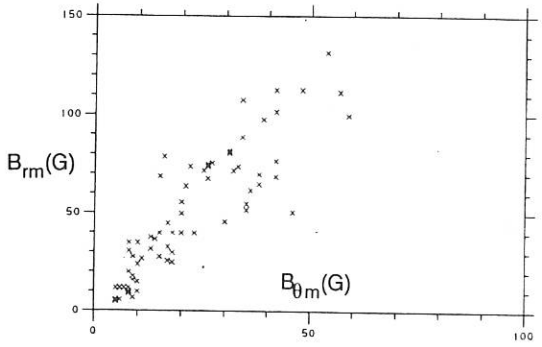

Fig. 2 Correlation between maximum amplitudes of the B_r and B_θ probe signals.

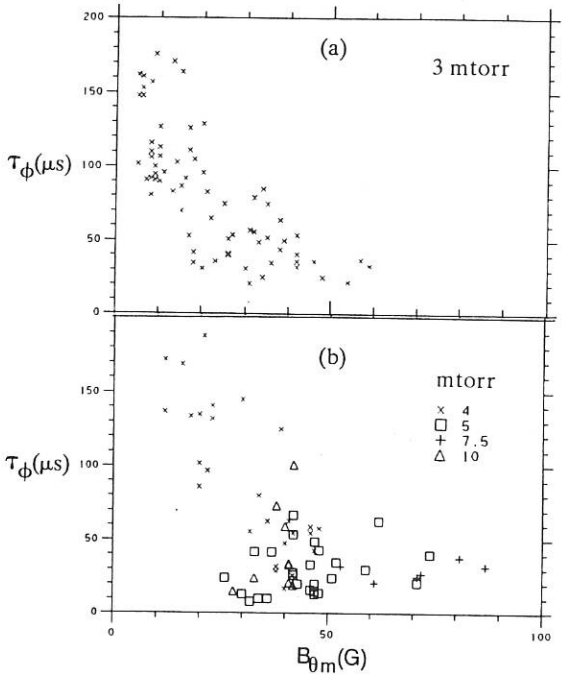

Fig. 3 Correlation between flux confinement time and maximum B_θ amplitude.

COMPARATIVE ANALYSIS AT SK/CG-1 MACHINE FOR SPHEROMAK PLASMA HEATING

S. Sinman, A. Sinman *

Plasma Engineering Laboratory, Electrical and Electronic Engineering Department, Middle East Technical University
* Nuclear Fusion Laboratory, Nuclear Research and Training Centre, Turkish Atomic Energy Authority
Ankara, Turkey

INTRODUCTION

The SK/CG-1 machine (World Survey of Activities in Controlled Fusion Research, 1986 Edition, IAEA, Vienna, p. 197), has been constructed to generate compact toroids (CT's) such as spherical torus, spherical pinch and spheromak.

In previous studies they have been investigated the new magnetically driven plasma gun (C-gun) with high injection efficiency together with the system description of SK/CG-1 /1/, the magnetic helicity and injection /2/,the Taylor state and formation for the production of alternative CT's /3-5/.

In this study, in order to understand the heating mechanism at SK/CG-1 more accurately, successive processes of ionization rate, formation, reconnection and plasma radiation loss have comparatively been evaluated. For this purpose, the data taken by the total flux loop, the electrical surface and Langmuir probes the charge exchange cell or other magnetic tools and the visible optical spectrometer have been used.

EXPERIMENTAL OBSERVATIONS AND THEIR INTERPRETATIONS

The maximum value of self generated toroidal magnetic field, perpendicular to the effective poloidal cross - section of dense (10^16 - 10^17 cm-3) and hot (50 - 70 eV) paraboloid plasma belt, produced by the C-gun is about 10 - 15 KG. At the begining, the shock heated thermal electrons, either ionize the back ground Helium gas or heat the produced plasma ohmically.

By the influence of this toroidal magnetic field, the active ion-cyclotron waves of 10-15 MHz are generated, as a result of the W3 instability, which is normally formed in ordinary beam plasma interaction systems.

As it is shown in Fig. 1, after rising to maximum amplitude in first 400-500 ns, this wave damps just looking like to magnetic beach model. Due to the self resonance heating, in spheromak plasma the ion-cyclotron resonance heating is very effective for a short time. Using a terminated magnetic loop, the measurements carried out at an angular distance of 135 degree from the C-gun and the analysis of current and voltage transients of discharge taken from the same distance have shown that this ion-cyclotron wave packet is equivalent to the high frequency pulse power of 25 - 30 MW.

On the other hand, the shock and ohmic heated thermal electrons, interacting with the self generated toroidal magnetic field, under different angles with respect to the magnetic field vector, moves on the alternative helical orbits having various long pitches. Thus, in the first 5 us which is the half period of the C-gun, the system arrives into equilibrium state, and the current channel confines itself by reconnecting the toroidal field of helices and the poloidal field of the pitches.

Operating period of the C-gun is about 50-60 us and the discharge is in the underdamping mode. In the first half period of 5 us, the 70 % of capacitor bank energy has been used on the C-gun directly. The average sustainment time of the toroid formed by the C-gun is approximately 20-30 us.

The time resolved optical spectral line (Fig. 2), the Langmuir probe signals (Fig. 3) and the total magnetic flux variations (Fig. 4) have been determined after the turn-off of the C-gun. Thus, the comparative results obtained have characterized all of the spheromak plasma specifications which are confined in the flux conserver for a definite duration.

As it is known, in the time resolved spectral line profile, the FWHM is given by a relation between the ionization and the loss rates /6/. Distribution of the spectral lines for high level impurity ions such as He II (54.40 eV), N III (47.43 eV), O III (54.89 eV) and Cu III (36.4 eV) are falling on the wave length range of 250-700nm. The FWHM in integrated line profile determined in this band width (Fig. 2) is 220 us.

When the transitions between the high level shells are investigated in the band width of 750-900 nm, the FWHM has been found as 250 us. On the other hand, the effective energy confinement time calculated by the experimental data is 360 us.

When the space potential of the Langmuir probe is evaluated with respect to time, a drop on the space potential level to the floating level in 1.5 ms after turn-off of the C-gun and then a rising up to last space potential value again in 1.5 ms have been observed (Fig. 3). Successively, the space potential has remained constant for 6 ms and finally, an after glow region has appeared for 12 ms. Due to the gas pressure is not changed, this drop and successively rising on the electron density can be attributed to the increase of ionization rate or in other words to the contribution of new hot electrons. The total period of this event is about 3 ms, and this result is very close to the total flux period. The flat space potential region of 6 ms which probably characterizes the E-layer, can define a quiscent and warm plasma cloud. As a matter of fact, during this period the toroidal and the poloidal fields are zero.

On the total flux measuremets, it has been observed that the diamagnetism is begining at the initial phase of the discharge. After turn-off the C-gun, the diamagnetism is translated into paramagnetism. Depending on the total flux decay time, duration of the paramagnetism is about 2.5-3.5 ms (Fig. 4).

In addition, the data taken from the Langmuir, electrical surface and magnetic probe, the paramagnetic and total flux loops

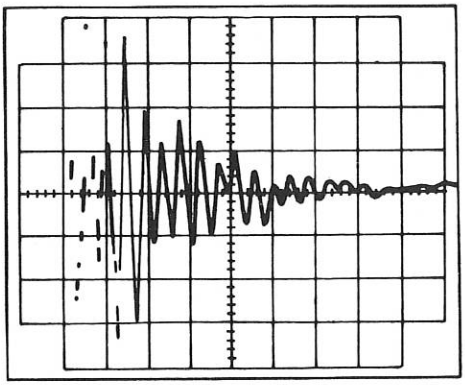

Fig. 1.

Ion cyclotron damping,
cycl. freq. 10-15 MHz.,
X axis = 200 ns/div.,
Y axis = 50 mV/div.

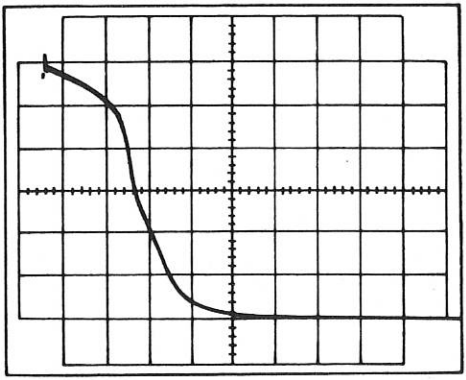

Fig. 2.

Optical radiation signal,
detection range 250-700nm
X axis = 0.1 ms/div.,
Y axis = 100 mV/div.

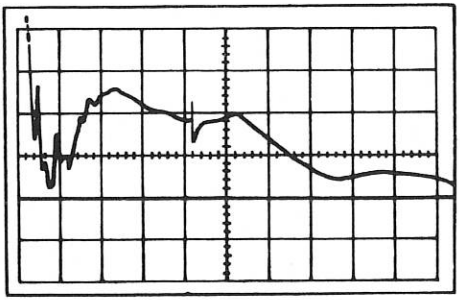

Fig. 3.

Langmuir probe signal,
X axis = 2 ms/div.,
Y axis = relative units.

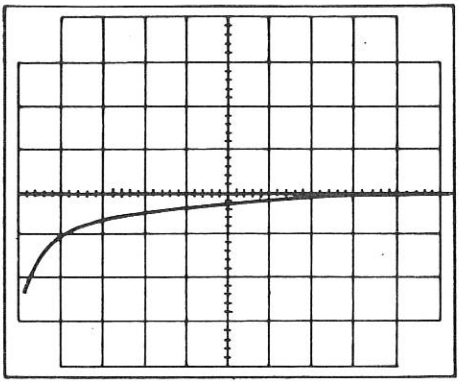

Fig. 4.

Total magnetic flux decay
X axis = 0.5 ms/div.,
Y axis = relative units.

and lastly the toroidal and poloidal magnetic loops near to the wall of flux conserver have also been evaluated.

Consequently some parameters of spheromak plasmas are as follows: volume averaged beta is 0.085, electron density is 4X10^14 cm-3, average electron temperature is 25-35 eV and energy confinement time is 300-400 us.

CONCLUSIONS

The comparative analysis of experimental results taken from the SK/CG-1 have been shown that there exist a complex but very systematical heating mechanism in time at the machine. In this content, the shock heating, the ohmic heating and the ion-cyclotron resonance heating mechanisms have successively been determined. It has lastly observed that this evaluation fits very closely to self organization process.

ACKNOWLEDGEMENT

This work was performed under a cooperative agreement between the Turkish Atomic Energy Authority and the International Atomic Energy Agency, Vienna, Contract No.: 3828/R3/RB.

REFERENCES

/1/ Sinman,S., Sinman,A., in Plasma Phys. and Cont. Nucl. Fusion Research (Proc. 11th Int. Conf. Kyoto, 1986) Vol. 2, IAEA, Vienna (1987) 731.
/2/ Sinman,S.,Sinman,A., in Cont. Fusion and Plasma Phys. (Proc. 14th Europ. Conf. Madrid), Vol. 11D, (1987) 465.
/3/ Sinman,S., Sinman,A., in Cont. Fusion and Plasma Phys. (Proc. 15th Europ. Conf. Dubrovnik), Vol. 12B, (1988) 617.
/4/ Sinman,A., Sinman,S., ibid., p.621.
/5/ Taylor,J.B., Phys. Rev. Lett. 33 (1974) 1139.
/6/ McWhirter,P.W.P., Ch. 5,of Plasma Diag. Tech., Huddlestone,H.R., Stanley,L.L.,eds. Academic Press, (1965).

POTENTIAL MEASUREMENT AND RADIAL TRANSPORT IN GAMMA 10 TANDEM MIRROR

K.Ishii, I.Katanuma, T.Segawa, H.Ohkawara, A.Mase and S.Miyoshi

Plasma Research Center, University of Tsukuba
Tsukuba, Ibaraki 305 Japan

INTRODUCTION

GAMMA 10 is an effectively axisymmetric tandem mirror with thermal barriers / 1 / . Potential information is important to investigate the plasma confinement. The barrier and central space potentials are determined by means of two gold neutral beam probes. Two-dimensional potential profiles have been measured in the barrier cell. In GAMMA 10, to assure magneto-hydrodynamic (MHD) stability, the nonaxisymmetric minimum-B mirror cells are contained between the central-solenoid and the plug/barrier cells at the ends of the machine. From the point of view of neoclassical resonant-plateau transport in circular equipotential contours, this effective axi-symmetrization is successful / 2 /. The measured potential profiles are slightly elongated during the onset of ω_{ce} ECRH. In this paper we report the beam probe potential measurement, the neoclassical ion radial transport in the noncircular equipotential surface and the thermal barrier potential.

MACHINE STATUS

GAMMA 10 consists of a central cell, anchor cells and axisymmetric end mirror cells as shown in Fig.1-a. The anchor cells are minimum-B mirrors. Plug and thermal barrier potentials are formed in the axisymmetric mirrors. The vacuum vessel with a total volume of 150 m^3 has total length of 27.1 m. The central cell axial length is 6 m. Heating systems are operated as follows : An initial plasma is injected by magneto-plasma dynamic (MPD) guns from both ends of the machine. Neutral beams with 20 keV and 35 keV injection energies produce sloshing ions in the plug/barrier cells and hot ions in the anchor cells, respectively. Four gyrotrons with a frequency of 28 GHz and 100 kW output power each are used to produce magnetically trapped hot electrons near the midplane ($\omega=2\omega_{ce}$ ECRH) and plug warm electrons in the off-midplane ($\omega=\omega_{ce}$ ECRH) region of the plug/barrier cells. Ion cyclotron resonance heating (ICRH) with 9.6 MHz, 200 kW is employed to heat the plasma in the central cell.

GOLD NEUTRAL BEAM PROBE

The tandem mirror experiment requires the space potentials in the barrier and the central cells which are adjacent to the minimum-B anchors. The irregular leakage magnetic field caused by the anchor coils affects the orbits of the probing beam, and in addition the strong magnetic field covers a wide area as shown in Figs.1-b,1-c. Finally, it is found that neutral

beam injection is the most suitable after calculation of the orbits for various types of probing beams. We adopt a method of neutralizing the gold negative ions by hydrogen gas to avoid undesired gas inflow into the plasma. By using a hydrogen gas puffer valve with a neutralizing gas box and a differential pumping volume between the gas box and the barrier cell, the gas loading on the plasma is reduced effectively. The increment of the gas pressure is less than 2 % of the nominal gas pressure during the GAMMA 10 discharge. A gold atom has a large mass number of 197 and the largest affinity for electron capture in stable isotopes, except for halogen atoms. The sputtering yield of the gold atom is the largest for heavy elements which have an atomic number greater than 60. Figure 2 shows a schematic outline of the gold beam probe at the east barrier. The accuracy of space potential measurement is better than 30 V in the experiment, and spatial accuracy is within ±0.8 cm as determined from the results of the calibration using gas cells and beam trajectory calculations. Potential contours over a cross-section of the barrier plasma are measured by sweeping the probing beams with different beam energies. A typical result is shown in Fig.3. The central beam probe system is similar to the barrier system. However, the radial potential measurement location is presently limited to a diameter of 7 cm about the axis.

NEOCLASSICAL ION RADIAL TRANSPORT

Neoclassical radial transport is one of the most imprtant process in considering the plasma confinement in tandem mirrors, and is enhanced due to the deviation of the noncircular equipotential contour from the circular magnetic flux surface. The electrostatic potential is dominantly determined by the ω_{ce} ECRH power density distribution on the $\omega=\omega_{ce}$ resonance surface at the plug. The microwave is injected obliquely upwards in both region consists of the axisymmetric mirror cell. Experimentally it is observed that the radial profile of the potential approximately coincides with that of the deposition of microwave power at the plug and also with that of the end flux of the heated electrons /3/. Figure 3 shows an example of the two dimensional plots of the electrostatic potential at the barrier cell. The equipotential contours are slightly elongated. We estimate the enhancement of the neoclassical transport caused by the noncircular equipotential contours /4/. In the magnetic configuration of GAMMA 10 a circular magnetic flux atarting at the central cell becomes circular again at the barrier and the plug cells. It is supposed that the equipotential contour at the barrier cell is the same as that at the central and the magnetic field lines lie on the equipotential surface. In the present GAMMA 10 parameters, the $\vec{E}\times\vec{B}$ drift is much larger than the $\vec{\nabla}B$ drift during ECRH injection. Therefore the plasma is rotating along equipotential surface in the equilibrium. There are two kinds of effects of noncircular cross-section on the neoclassical transport. One is that the magnitude of magnetic field line curvature changes because the curvature is proportional to the radius. The other is that the surface of a magnetic tube deforms so that the normal curvature also drives the particle drift across the magnetic surface. The radial particle flux averaged over the flux surface is approximated to be

$$\Gamma \cong \{ 1 + (b/a)^2 (\xi_1^2 + \xi_2^2) \} \Gamma^{RS} . \qquad (1)$$

Here Γ^{RS} is the radial particle flux for the case of circular equipotential

surface, the quantity (b/a) corresponds to the ratio of the particle drift coming from the normal curvature to that from the geodesic curvature. ξ is derived from the angle between the tangents of the circle and the noncircular surface. In this case, the particle flux is estimated to be about $1.7\times \Gamma^{RS}$. Therefore the enhancement of the neoclassical resonant transport due to the noncircular equipotential surface is small. The noncircular equipotential distribution depends on the ω_{ce} ECRH power. However, in GAMMA10 the neoclassical radial transport is not serious, because the potential contours may be circularized by adjusting the shining optics of the ECRH for the reason that the plug/barrier region consists of the axisymmetric mirror cell.

THERMAL BARRIER POTENTIAL

Figure 4 plots the time evolution of the potentials on axis at the central cell and the barrier cell, respectively. When the plug ECRH turned on, the central cell potential grows up suddenly and the thermal barrier potential is observed. The floating potential of the end plate also becomes negative with respect to the wall which is grounded. The warm passing electrons, the parallel temperature of which is 5 ~ 10 times as high as the electron temperature at the central cell, have been measured at each end of the machine by use of end-loss analyzers. This indicates that the warm passing electrons may be concerned with the thermal barrier potential. Conventionally the thermal barrier potential is described by Boltzmann relation derived from a full Maxwellian plasma, which is based on an assumption that the barrier electrons consist of magnetically trapped hot electrons and low energy Maxwellian electrons. The low energy electrons, however, are subject to rf heating due to the strong $2\omega_{ce}$ wave field. The effect leads to the conventional Boltzmann low to the modified one /5/. In the case of a low density ($< 2 \times 10^{11}$ cm^{-3}), however, a more enhanced potential depth has been observed. Figure 5 shows the potential enhancement. By taking account of the warm passing electrons, it is shown that the thermal barrier potential is enhanced /6/.

SUMMARY

Gold neutral beams have been used successfully for measuring the space potential in GAMMA 10. Two-dimensional potential profiles have been measured in the barrier cell. The potential profile is elongated during the onset of the ω_{ce} ECRH. The eiliptic pattern enhance the neoclassical resonant-plateau transport appreciably. Passing electrons having a warm parallel component are important for the thermal barrier formation in a low density plasma.

REFERENCES

/1/ M.Inutake, et al., Fusion Reactor Design and Technology, Vol.1 IAEA, Vienna (1983) 429.
/2/ I.Katanuma, et al., Nucl. Fusion 27 (1987) 2041.
/3/ T.Kariya, et al., Phys. Fluids 31 (1988) 1815.
/4/ I.Katanuma, et al., Submitted to Phys. Fluids.
/5/ I.Katanuma, et al., Phys. Fluids 29 (1986) 4138.
/6/ K.Ishii, et al., Submitted to Nucl.Fusion.

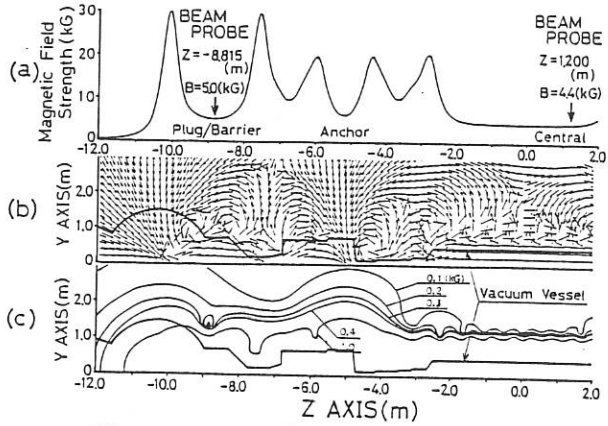

Fig.1
(a) Axial profile of magnetic field strength.
(b) Directions of magnetic field.
(c) Mod-B contours.

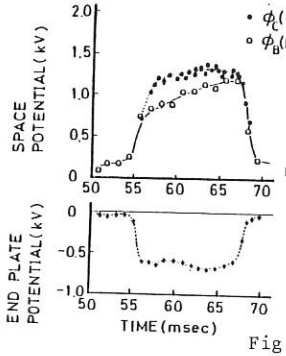

Fig.4
Temporal evolution.

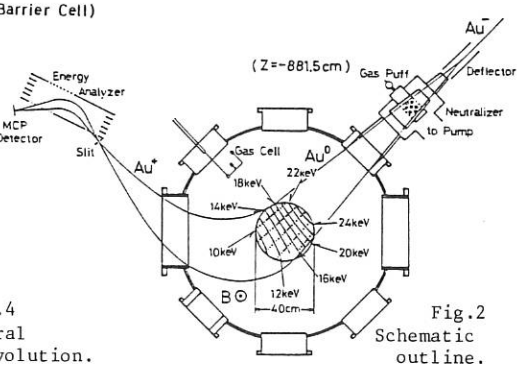

Fig.2
Schematic outline.

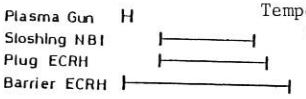

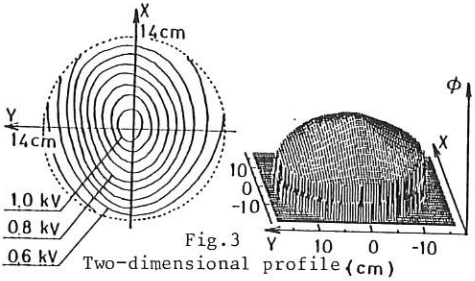

Fig.3
Two-dimensional profile

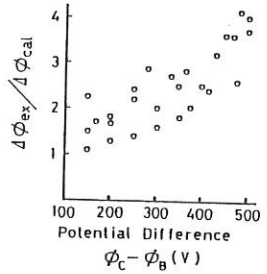

Fig.5
Potential enhancement.

AXISYMMETRIC TANDEM MIRROR AMBAL-M

G.I.Dimov, V.I.Davydenko, P.B.Lysyansky

Institute of Nuclear Physics, 630090, Novosibirsk, USSR

The using of a completely axisymmetric geometry of the magnetic field allows practically the suppression of the transverse neoclassical losses, opens the possibility to increase substantially the magnetic field strength in the mirrors and leads to a considerable simplification of the design of the open systems.

For these reasons, despite all difficulties of realization of the MHD-stable axisymmetric systems, the fully axisymmetric Tandem Mirror is now being developed in our Institute. Fig.1 shows a plan view of the device. The vacuum volume of the device consists of a cylindrical chamber of the central cell, of two vacuum chambers of the plugs, of two chambers for MHD-stabilizers and adjacent to them two end tanks.

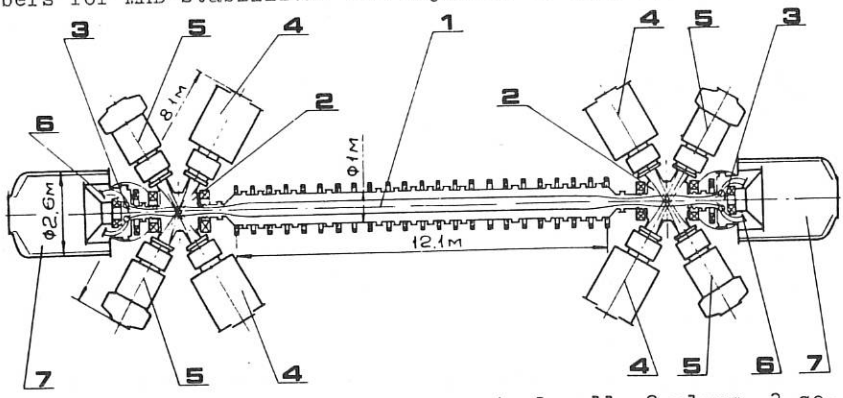

Fig. 1. AMBAL-M general view. 1-central cell, 2-plugs, 3-semicusps, 4-NB injectors, 5-beam dumps, 6-plasma dumps, 7-cryopumps.

Magnetic field strength in the central solenoid is 4.5 kG, plasma diameter is 40 cm, plasma volume is 1.7 m^3. Magnetic field in the plug mirrors is 60 kG, mirror-to-mirror distance is 1.7 m, mirror ratio in the plug is 4, plasma volume (reduced to the peak density) is 7 l. The initial design of the MHD stabilizer in that of semicusp with a bell-like shape of the field lines. Mirror to mirror distance along the axis of the device is 26 cm, diameter of the external (ring shaped) mirror is 75 cm. The design value of the external plasma diameter in the magnetic field minimum is 14 cm, plasma thickness in this region is 6 cm. Magnetic field strength in the mirrors is 23.5 kG; the minimum value of the magnetic field changes across the plasma size from 6.7 to 12.2 kG. The magnetic field lines, the plasma position, and NB cross-section in semicusp are shown in Fig.2. Also shown is the gas discharge cell producing warm plasma stream for the MHD-stabilization of inner plasma surface.

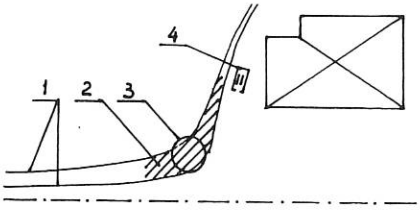

Fig. 2. Semicusp schematic 1-magnetic field lines, 2--plasma positon, 3-NB cross--section, 4-annular gas discharge cell.

We plan to organize the work in two phases [1]. First, we will construct only the end system to which instead of the solenoid we will add second end tank together with the vacuum chamber for the second MHD-stabilizer. In this chamber an additional plasma gun will be installed with a solenoid creating pulse magnetic field up to 20 kG. This gun would allow us to build up the target plasma both in the plug and the semicusp.

The plug is fed by neutral beams of deuterium atoms with energy of 25 keV and total current 160 A. The semicusp is fed by neutral beams of hydrogen with energy of 6 keV and total

current ~ 70 A. For providing the high NB current density in semicusp the ion sources with high brightness and geometric focusing is being developed now.

The expected plasma parameters in the plug are the following: $\hat{n}=3\cdot10^{13}cm^{-3}$, $\langle E_i\rangle$ ~12 keV, T_e ~100 eV, β ~7%. For the cusp we expect $\hat{n}=10^{13}cm^{-3}$, $\langle E_i\rangle$ ~5 keV, T_e ~100eV, β ~2%. Plasma radius in the plug is 6.6 gyroradius of D^+ ions and the width of the bell-shaped plasma equals to 7 gyroradius of H^+ ions.

MHD plasma stability with respect to high m-modes is provided by FLR effect |2|. Rigid $m=1$ mode should be stabilized by the nonparaxial contribution to the perturbation energy coming from the semicusp.

The adiabaticity boundary in the semicusp was calculated using numerical simulation |3|. The details of the proposal for the first phase of the AMBAL-M is published in Ref. |4|. Also planned to study is the MHD-stabilization of the plasma in the plug by means of hot disk-like electron population with β ~ 0,7 produced by ECRH |5|. The MHD stabilizer based on the supernonparaxial mirror cell proposed in Ref. |6| is being considered now.

The main issue for studying at the first phase in AMBAL-M is MHD plasma stability in axisymmetric system.

At the first step of the second phase the center solenoid and the second end system will be installed. To produce in a solenoid a target plasma, the radial plasma gun, circumferencing the plasma, will be mounted. The plasma penetration into the near axis region of solenoid will occur by virtue of fast connection of the solenoid magnetic field. The plasma escaping through the end of the solenoid, will be used for much more effective plasma built up in the plugs and MHD stabilizer.

As a result, it is expected to obtain at first step the following parameters of the central cell plasma: $\hat{n}\sim10^{13}cm^{-3}$, $T\sim100$ eV.

At second step four gyrotrons producing microwave radiation with a power of 200 kW (each) will be installated in the plugs. It is supposed that ECRH at the first and second harmonics will be performed in two planes of each plug. The ICRH system with the power of 1 MW is to be installed in the solenoid. The possibility of MHD-stabilization of the central solenoid plasma by inclusion the sections with high β and conducting shell is investigated |5|. It is assumed that high β in section will be achieved by the decrease in magnetic field and the generation of trapped particle population by ICR slot antenna heating.

The main goal to be achieved as a result of the phase (as a whole) is production of the solenoidal plasma with parameters: $\hat{n} \sim 10^{13}\,cm^{-3}$, $T \sim 1$ keV, $n\tau \sim 10^{12}\,cm^{-3}s$.

REFERENCES

1. G.I.Dimov. "Axisymmetric tandem mirror AMBAL-M" - In the Proc. of Intern. School of Plasma Physics, Varenna, 1987, v.2, p.703-709.
2. G.I.Dimov, P.B.Lysyansky. "Flute MGD-stability of an axisymmetric system mirror-semicusp", Intern. Conf. on Plasma Physics, Kiev, 1987.
3. S.V.Kuzmin, P.B.Lysyansky. Preprint of the Institute of Nuclear Physics N 88-5, Novosibirsk, 1988.
4. G.I.Dimov, P.B.Lysyansky. Preprint of the Institute of Nuclear Physics N86-102, Novosibirsk, 1986.
5. H.L.Berk, H.V.Wong and K.T.Tsang. Report of Institute for Fusion Studies IFSR 235, Texas, 1986.
6. D.D.Ryutov, G.V.Stupakov. Pis'ma Zh. E.T.F., 1985, 42, 29.

RESPONSIBLE AUTHOR

INDEX *

* (First author is listed when responsible author was not indicated)